

Reading human motives
pp. 1028 & 1074

Light-emitting stretchable
electronics p. 1077

Antibody analysis of an
Ebola survivor p. 1069

Science

57%
& MARTIN JAMES
INTERVIEW

AAAA5

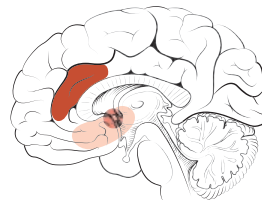
THE LONG AFTERMATH OF FUKUSHIMA

p. 1018



CONTENTS

4 MARCH 2016 • VOLUME 351 • ISSUE 6277



1028 & 1074

Brain circuitry
and generous behavior



FEATURES

1018 SLOW BURN

Five years after the meltdowns at the Fukushima atomic plant, evacuees are weighing the prospect of living near a nuclear disaster zone for decades to come

By D. Normile

1020 TRIAL BY MELTDOWN

At Fukushima, robots performed poorly at first but are now critical players in the cleanup

By T. Hornyak

1022 EPIDEMIC OF FEAR

A bumper crop of thyroid abnormalities, including cancer, in Fukushima children has perplexed scientists and alarmed locals

By D. Normile

ON THE COVER



Japanese media tour the Fukushima Daiichi Nuclear Power Station (Unit 4 reactor building shown here). On 11 March, Japan marks the fifth anniversary

of the earthquake and tsunami that triggered meltdowns at this site. Tokyo Electric Power Company is in the early stages of a decades-long, \$9 billion decommissioning effort that is spurring advances in robotics. Area residents, meanwhile, are wrestling with the possible health effects of long-term exposure to low doses of radiation. See page 1018. Photo: Tomohiro Ohsumi/Bloomberg via Getty Images

NEWS

IN BRIEF

1009 News at a glance

IN DEPTH

1012 FAST RADIO BURSTS TEASE ASTRONOMERS

Conflicting results suggest the potent blasts come in two flavors

By G. Schilling

1013 'PATIENT ZERO' NO MORE

Sleuthing clarifies HIV's history

By J. Cohen

1014 SURVEY FRAUD TEST SPARKS BATTLE

Pew Research Center challenges statistical test

By J. Bohannon

1015 SCIENTISTS TO DRILL INTO DINOSAUR-KILLING BLAST

Cores from Chicxulub crater could illuminate how life returned after the cataclysm

By E. Hand

1017 NSF MAKES A NEW BID TO BOOST DIVERSITY

Initiative aims for fresh answers, but researchers are still framing the questions

By J. Mervis

INSIGHTS

PERSPECTIVES

1024 LIBERATING FIELD SCIENCE SAMPLES AND DATA

Promote reproducibility by moving beyond "available upon request"

By M. McNutt et al.

► EDITORIAL P. 1005; EDITOR'S NOTE P. 1007

1026 ELECTRONS GO WITH THE FLOW IN EXOTIC MATERIAL SYSTEMS

Electronic hydrodynamic flow—making electrons flow like a fluid—has been observed

By J. Zaane

► REPORTS PP. 1055, 1058, & 1061

1028 WIRING THE ALTRUISTIC BRAIN

Communication between brain regions uncovers hidden motives for generous behavior

By S. Gluth and L. Fontanesi

► REPORT P. 1074

1029 A COPY-AND-PASTE GENE REGULATORY NETWORK

Transposable elements provide a ready-made route to regulate complex gene networks

By V. J. Lynch

► REPORT P. 1083

1030 SURPRISED BY SELECTIVITY

A bifunctional catalyst enables olefin synthesis from carbon monoxide and hydrogen at high selectivity

By K. P. de Jong

► REPORT P. 1065

1032 AN RNA TWIST TO T_H17 CELLS

A long noncoding RNA and RNA helicase constitute a new layer of T cell control

By M. K. Atianand and K. A. Fitzgerald

BOOKS ET AL.

1033 WHEN WE ARE NO MORE

By A. S. Rumsey,

reviewed by C. B. Anderson

1034 STRANGE GLOW

By T. J. Jorgensen, reviewed by A. N. Creager

LETTERS

1036 SEEING THE GRASSLANDS THROUGH THE TREES

By S. DeWitt et al.

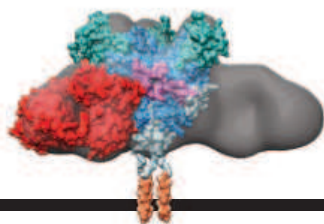
1036 RESPONSE

By W. Bond

1037 GOVERNMENT: PLAN FOR ECOSYSTEM SERVICES

By L. N. Joppa et al.

1037 TECHNICAL COMMENT ABSTRACT



1078

Targeting Ebola



1094

Cellular heterogeneity

RESEARCH

IN BRIEF

1038 From *Science* and other journals

RESEARCH ARTICLES

1041 NEURAL COMPUTATION

Spiking neurons can discover predictive features by aggregate-label learning *R. Gütig*

RESEARCH ARTICLE SUMMARY; FOR FULL TEXT:

[dx.doi.org/10.1126/science.aab4113](https://doi.org/10.1126/science.aab4113)

1042 CANCER BIOLOGY

Activation of PKA leads to mesenchymal-to-epithelial transition and loss of tumor-initiating ability *D. R. Pattabiraman et al.*

RESEARCH ARTICLE SUMMARY; FOR FULL TEXT:

[dx.doi.org/10.1126/science.aad3680](https://doi.org/10.1126/science.aad3680)

1043 STRUCTURAL BIOLOGY

Cryo-EM structure of a native, fully glycosylated, cleaved HIV-1 envelope trimer

J. H. Lee et al.

1048 IMMUNOLOGY

Visualizing antibody affinity maturation in germinal centers *J. M. J. Tas et al.*

REPORTS

ELECTRON TRANSPORT

1055 Negative local resistance caused by viscous electron backflow in graphene *D. A. Bandurin et al.*

1058 Observation of the Dirac fluid and the breakdown of the Wiedemann-Franz law in graphene *J. Crossno et al.*

1061 Evidence for hydrodynamic electron flow in PdCoO₂ *P. J. W. Moll et al.*

► PERSPECTIVE P. 1026

1065 CATALYSIS

Selective conversion of syngas to light olefins *F. Jiao et al.*

► PERSPECTIVE P. 1030

1068 QUANTUM COMPUTING

Realization of a scalable Shor algorithm *T. Monz et al.*

1071 FLEXIBLE ELECTRONICS

Highly stretchable electroluminescent skin for optical signaling and tactile sensing *C. Larson et al.*

► PODCAST

1074 HUMAN ALTRUISM

The brain's functional network architecture reveals human motives *G. Hein et al.*

► PERSPECTIVE P. 1028

1078 EBOLA VIRUS

Isolation of potent neutralizing antibodies from a survivor of the 2014 Ebola virus outbreak *Z. A. Bornholdt et al.*

1083 IMMUNOGENOMICS

Regulatory evolution of innate immunity through co-option of endogenous retroviruses *E. B. Chuong et al.*

► PERSPECTIVE P. 1029

1087 GENE EXPRESSION

Expression homeostasis during DNA replication *Y. Voickek et al.*

1090 TRANSCRIPTION

Multiplexed protein-DNA cross-linking: Scrunching in transcription start site selection *J. T. Winkelman et al.*

1094 DNA REPAIR

Stochastic activation of a DNA damage response causes cell-to-cell mutation rate variation *S. Uphoff et al.*

DEPARTMENTS

1005 EDITORIAL

#IAmAResearchParasite
By Marcia McNutt

► EDITOR'S NOTE P. 1007; PERSPECTIVE P. 1024

1007 EDITOR'S NOTE

Data sharing
By Marcia McNutt

► EDITORIAL P. 1005; PERSPECTIVE P. 1024

1106 WORKING LIFE

Making a game of science
By Elizabeth Pennisi

Science Staff	1002
New Products	1101
Science Careers	1102

1030
& 1065

SCIENCE (ISSN 0036-8075) is published weekly on Friday, except the last week in December, by the American Association for the Advancement of Science, 1200 New York Avenue, NW, Washington, DC 20005. Periodicals mail postage (publication No. 484460) paid at Washington, DC, and additional mailing offices. Copyright © 2016 by the American Association for the Advancement of Science. The title SCIENCE is a registered trademark of the AAAS. Domestic individual membership and subscription (51 issues): \$165 (\$74 allocated to subscription). Domestic institutional subscription (51 issues): \$1522. Foreign postage extra: Mexico, Caribbean (surface mail) \$55; other countries (air assist delivery) \$89. First class, airmail, student, and emeritus rates on request. Canadian rates with GST available upon request. GST #R1254 88122. Publications Mail Agreement Number 1069624. Printed in the U.S.A. **Change of address:** Allow 4 weeks, giving old and new addresses and 8-digit account number. **Postmaster:** Send change of address to AAAS, P.O. Box 96178, Washington, DC 20090-6178. **Single-copy sales:** \$15.00 current issue, \$20.00 back issue prepaid includes surface postage; bulk rates on request. **Authorization to photocopy** material for internal or personal use under circumstances not falling within the fair use provisions of the Copyright Act is granted by AAAS to libraries and other users registered with the Copyright Clearance Center (CCC) Transactional Reporting Service, provided that \$35.00 per article is paid directly to CCC, 222 Rosewood Drive, Danvers, MA 01923. The identification code for Science is 0036-8075. Science is indexed in the Reader's Guide to Periodical Literature and in several specialized indexes.

Editor-in-Chief Marcia McNutt

Executive Editor Monica M. Bradford **News Editor** Tim Appenzeller

Managing Editor, Research Journals Katrina L. Kelner

Deputy Editors Barbara R. Jasny, Andrew M. Sugden(UK), Valda J. Vinson, Jake S. Yeston

Research and Insights

SR. EDITORS Caroline Ash(UK), Gilbert J. Chin, Lisa D. Chong, Julia Fahrenkamp-Uppenbrink(UK), Pamela J. Hines, Stella M. Hurlty(UK), Paula A. Kiberstis, Marc S. Lavine(Canada), Kristen L. Mueller, Ian S. Osborne(UK), Beverly A. Purnell, L. Bryan Ray, Guy Riddihough, H. Jesse Smith, Jelena Stajic, Peter Stern(UK), Phillip D. Szurmi, Sacha Vignieri, Brad Wible, Nicholas S. Wigginton, Laura M. Zahn **ASSOCIATE EDITORS** Brent Grocholski, Keith T. Smith **ASSOCIATE BOOK REVIEW EDITOR** Valerie B. Thompson **ASSOCIATE LETTERS EDITOR** Jennifer Sills **CHIEF CONTENT PRODUCTION EDITOR** Cara Tate **SR. CONTENT PRODUCTION EDITORS** Harry Jach, Lauren Kmec **CONTENT PRODUCTION EDITORS** Jeffrey E. Cook, Chris Filiatreau, Cynthia Howe, Barbara P. Ordway, Catherine Wolner **SR. EDITORIAL COORDINATORS** Carolyn Kyle, Beverly Shields **EDITORIAL COORDINATORS** Jo S. Granger, Lisa Johnson, Anita Wynn **PUBLICATIONS ASSISTANTS** Aneera Dobbins, Jeffrey Hearn, Dana Mathieu, Le-Toya Mayne Flood, Shannon McMahon, Scott Miller, Caitlyn Phillips, Jerry Richardson, Rachel Roberts(UK), Alice Whaley(UK), Brian White **EXECUTIVE ASSISTANT** Anna Bashkirova **ADMINISTRATIVE SUPPORT** Janet Clements(UK), Lianne Newton(UK), Maryrose Madrid, John Wood(UK)

News

NEWS MANAGING EDITOR John Travis **INTERNATIONAL EDITOR** Richard Stone **DEPUTY NEWS EDITORS** Daniel Clery(UK), Robert Coontz, Elizabeth Culotta, David Grimm, David Malakoff, Leslie Roberts **CONTRIBUTING EDITOR** Martin Enserink(Europe) **SR. CORRESPONDENTS** Jeffrey Mervis, Elizabeth Pennisi **NEWS WRITERS** Adrian Cho, Jon Cohen, Jennifer Couzin-Frankel, Carolyn Gramling, Eric Hand, Jocelyn Kaiser, Catherine Maticic, Kelly Servick, Robert F. Service, Erik Stokstad(Cambridge, UK), Emily Underwood **INTERNS** Hanae Armitage, Catherine Monahan, Nala Rogers **CONTRIBUTING CORRESPONDENTS** Michael Balter(Paris), John Bohannon, Warren Cornwall, Ann Gibbons, Mara Hvistendahl, Sam Kean, Eli Kintisch, Kai Kupferschmidt(Berlin), Andrew Lawler, Christina Larson(Beijing), Mitch Leslie, Charles C. Mann, Eliot Marshall, Virginia Morell, Dennis Normile(Shanghai), Heather Pringle, Tania Rabesandratana(London), Gretchen Vogel(Berlin), Lizzie Wade(Mexico City) **CAREERS** Donisha Adams, Rachel Bernstein(Editor) **COPY EDITORS** Julia Cole, Dorie Cheven, Jennifer Levin (Chief) **ADMINISTRATIVE SUPPORT** Jessica Adams

Executive Publisher Rush D. Holt

Interim Publisher Bill Moran **Chief Digital Media Officer** Rob Covey

BUSINESS OPERATIONS AND PORTFOLIO MANAGEMENT DIRECTOR Sarah Whalen **PRODUCT DEVELOPMENT DIRECTOR** Will Schweitzer **PRODUCT DEVELOPMENT ASSOCIATE** Hal Moore **BUSINESS SYSTEMS AND FINANCIAL ANALYSIS DIRECTOR** Randy Yi **MANAGER OF FULFILLMENT SYSTEMS** Neal Hawkins **SYSTEMS ANALYST** Nicole Mehmedovic **ASSISTANT DIRECTOR, BUSINESS OPERATIONS** Eric Knott **MANAGER, BUSINESS OPERATIONS** Jessica Tierney **BUSINESS ANALYST** Cory Lipman **FINANCIAL ANALYST** Robert Clark **RIGHTS AND PERMISSIONS ASSISTANT DIRECTOR** Emilie David **PERMISSIONS ASSOCIATE** Elizabeth Sandler **RIGHTS, CONTRACTS, AND LICENSING ASSOCIATE** Lili Kiser

MARKETING DIRECTOR Elise Swinehart **ASSOCIATE DIRECTOR OF ACQUISITION AND RETENTION** Julianne Wielga **MARKETING ASSOCIATE** Elizabeth Sattler **SR. MARKETING EXECUTIVE** Jennifer Reeves **ASSOCIATE DIRECTOR, CREATIVE SERVICES** Tzeitel Sorrosa **ART ASSOCIATE** Seil Lee **JR. ART ASSOCIATE** Kim Huynh **ASSISTANT COMMERCIAL EDITOR** Selby Frame **MARKETING PROJECT MANAGER** Angelissa McArthur **PROGRAM DIRECTOR, AAAS MEMBER CENTRAL** Peggy Mihelich **FULFILLMENT SYSTEMS AND OPERATIONS** membership@aaas.org **MANAGER, MEMBER SERVICES** Pat Butler **SPECIALISTS** Terrance Morrison, Latasha Russell **MANAGER, DATA ENTRY** Mickie Napoleoni **DATA ENTRY SPECIALISTS** Brenden Aquilino, Fiona Giblin

PUBLISHER RELATIONS MANAGER Catherine Holland **PUBLISHER RELATIONS, EASTERN REGION** Keith Layson **PUBLISHER RELATIONS, WESTERN REGION** Ryan Rexroth **SALES RESEARCH COORDINATOR** Aiesha Marshall **MANAGER, SITE LICENSE OPERATIONS** Iqoo Edim **SENIOR PRODUCTION SPECIALIST** Robert Koepeke **SENIOR OPERATIONS ANALYST** Lana Guo **FULFILLMENT ANALYST** Judy Lillibridge **ASSOCIATE DIRECTOR, MARKETING** Christina Schlecht **MARKETING ASSOCIATES** Thomas Landreth, Isa Sesay-Bah

WEB TECHNOLOGIES SR. DEVELOPER Chris Coleman **DEVELOPERS** Dan Berger, Jimmy Marks, Ryan Jensen **SR. PROJECT MANAGER** Trista Smith **PROJECT MANAGER** Nick Fletcher

DIGITAL MEDIA DIRECTOR OF ANALYTICS Enrique Gonzales **DIGITAL REPORTING ANALYST** Eric Hossinger **SR. WEB PRODUCER** Sarah Crespi **WEB PRODUCER** Alison Crawford **VIDEO PRODUCER** Nguyen Nguyen **SOCIAL MEDIA PRODUCER** Brice Russ

DIRECTOR OF OPERATIONS PRINT AND ONLINE Lizbeth Harman **DIGITAL/PRINT STRATEGY MANAGER** Jason Hillman **QUALITY TECHNICAL MANAGER** Marcus Spiegler **PROJECT ACCOUNT MANAGER** Tara Kelly **DIGITAL PRODUCTION MANAGER** Lisa Stanford **ASSISTANT MANAGER** DIGITAL/PRINT Rebecca Doshi **SENIOR CONTENT SPECIALISTS** Steve Forrester, Antoinette Hodal, Lori Murphy, Anthony Rosen **CONTENT SPECIALISTS** Jacob Hedrick, Kimberley Oster

DESIGN DIRECTOR Beth Rakouskas **DESIGN EDITOR** Marcy Atarod **SENIOR DESIGNER** Garvin Grullón **DESIGNER** Chrystal Smith **GRAPHICS MANAGING EDITOR** Alberto Cuadra **SENIOR SCIENTIFIC ILLUSTRATORS** Chris Bickel, Katharine Sutliff **SCIENTIFIC ILLUSTRATOR** Valerie Altounian **SENIOR ART ASSOCIATES** Holly Bishop, Nathalie Cary, Preston Huey **PHOTOGRAPHY MANAGING EDITOR** William Douthitt **PHOTO EDITORS** Leslie Blizard, Christy Steele

DIRECTOR, GLOBAL COLLABORATION, CUSTOM PUBLICATIONS, ADVERTISING Bill Moran **EDITOR, CUSTOM PUBLISHING** Sean Sanders: 202-326-6430 **ASSISTANT EDITOR, CUSTOM PUBLISHING** Tianna Hicklin: 202-326-6463 **ADVERTISING MARKETING MANAGER** Justin Sawyers: 202-326-7061 **science_advertising@aaas.org** **ADVERTISING SUPPORT MANAGER** Karen Foote: 202-326-6740 **ADVERTISING PRODUCTION OPERATIONS MANAGER** Deborah Tompkins **SR. PRODUCTION SPECIALIST/GRAPHIC DESIGNER** Amy Hardcastle **SR. TRAFFIC ASSOCIATE** Christine Hall **SALES COORDINATOR** Shirley Young **ASSOCIATE DIRECTOR, COLLABORATION, CUSTOM PUBLICATIONS/CHINA/TAIWAN/KOREA/SINGAPORE** Ruoli Wu: +86-186 0082 9345, rwu@aaas.org **COLLABORATION/CUSTOM PUBLICATIONS/JAPAN** Adarsh Sandhu + 81532-81-5142 asandhu@aaas.org **EAST COAST/E. CANADA** Laurie Faraday: 508-747-9395, FAX 617-507-8189 **WEST COAST/W. CANADA** Lynne Stickrod: 415-931-9782, FAX 415-520-6940 **MIDWEST** Jeffrey Dembski: 847-498-4520 x3005, Steven Lohr: 847-498-4520 x3006 **UK EUROPE/ASIA** Roger Goncalves: TEL/FAX +44 143 243 1358 **JAPAN** Katsuyoshi Fukamizu(Tokyo): +81-3-3219-5777 kfukamizu@aaas.org **CHINA/TAIWAN/Ruoli Wu**: +86-186 0082 9345, rwu@aaas.org

WORLDWIDE ASSOCIATE DIRECTOR OF SCIENCE CAREERS Tracy Holmes: +44 (0) 1223 326525, FAX +44 (0) 1223 326532 tholmes@science-int.co.uk **CLASSIFIED** advertise@sciencecareers.org **U.S. SALES** Tina Burks: 202-326-6577 **Nancy Toema**: 202-326-6578 **EUROPE/ROW SALES** Sarah Lelarge **SALES ASSISTANT** Kelly Grace **JAPAN** Hiroyuki Mashiki(Kyoto): +81-75-823-1109 hmashiki@aaas.org **CHINA/TAIWAN** Ruoli Wu: +86-186 0082 9345 rwu@aaas.org **MARKETING MANAGER** Allison Pritchard **MARKETING ASSOCIATE** Aimee Aponte

AAAS BOARD OF DIRECTORS, CHAIR Geraldine L. Richmond **PRESIDENT** Barbara A. Schaaf **PRESIDENT-ELECT** Susan Hockfield **TREASURER** David Evans **Shaw CHIEF EXECUTIVE OFFICER** Rush D. Holt **BOARD** Cynthia M. Beall, May R. Berenbaum, Carlos J. Bustamante, Stephen P.A. Fodor, Claire M. Fraser, Michael S. Gazzaniga, Laura H. Greene, Elizabeth Loftus, Mercedes Pascual

SUBSCRIPTION SERVICES For change of address, missing issues, new orders and renewals, and payment questions: 866-434-AAAS (2227) or 202-326-6417, FAX 202-842-1065. Mailing addresses: AAAS, P.O. Box 96178, Washington, DC 20090-6178 or AAAS Member Services, 1200 New York Avenue, NW, Washington, DC 20005

INSTITUTIONAL SITE LICENSES 202-326-6730 **REPRINTS:** Author Inquiries 800-635-7181 **COMMERCIAL INQUIRIES** 803-359-4578 **PERMISSIONS** 202-326-6765, permissions@aaas.org **AAAS Member Services** 202-326-6417 or http://membercentral.aaas.org/discourts

Science serves as a forum for discussion of important issues related to the advancement of science by publishing material on which a consensus has been reached as well as including the presentation of minority of conflicting points of view. Accordingly, all articles published in Science—including editorials, news and comment, and book reviews—are signed and reflect the individual views of the authors and not official points of view adopted by AAAS or the institutions with which the authors are affiliated.

INFORMATION FOR AUTHORS See pages 624 and 625 of the 5 February 2016 issue or access www.sciencemag.org/authors/science-information-authors

SENIOR EDITORIAL BOARD

Gary King, Harvard University, Susan M. Rosenberg, Baylor College of Medicine, Ali Shilatifard, Northwestern University Feinberg School of Medicine

BOARD OF REVIEWING EDITORS (Statistics board members indicated with \$)

Adriano Aguzzi, U. Hospital Zurich
Takuzo Aida, U. of Tokyo
Leslie Aiello, Wenner-Gren Foundation
Judith Allen, U. of Edinburgh
Sonia Altizer, U. of Georgia
Sebastian Amigorena, Institut Curie
Kathryn Anderson, Memorial Sloan-Kettering Cancer Center
Meinrat O. Andreae, Max-Planck Inst. Mainz
Paola Ariotta, Harvard U.
Johan Auwerx, EPFL
David Awschalom, U. of Chicago
Clare Baker, University of Cambridge
Jordi Bascompte, University of Zurich
Fausto Batista, London Research Inst.
Ray H. Baughman, U. of Texas, Dallas
David Baum, U. of Wisconsin
Carlo Beenakker, Leiden U.
Kamran Behnia, ESPCI-ParisTech
Yasmine Belkaid, NIAID, NIH
Philip Benfey, Duke U.
May Berenbaum, U. of Illinois
Gabriele Bergers, U. of California, San Francisco
Bradley Bernstein, Massachusetts General Hospital
Peer Bork, EMBL
Bernard Bourdon, Ecole Normale Supérieure de Lyon
Chris Bowler, Ecole Normale Supérieure
Ian Boyd, U. of St. Andrews
Emily Brodsky, U. of California, Santa Cruz
Ron Brookmeyer, U. of California Los Angeles (\$) **Christian Büchel**, U. Hamburg-Eppendorf
Joseph A. Burns, Cornell U.
Carter Tribley Butts, U. of California, Irvine
György Buzsáki, New York U. School of Medicine
Blanche Capel, Duke U.
Mats Carlsson, U. of Oslo
Ib Chorkendorff, U. of Denmark
David Clapham, Children's Hospital Boston
Joel Cohen, Rockefeller U., Columbia U.
James J. Collins, MIT
Robert Cook-Deegan, Duke U.
Lisa Coussens, Oregon Health & Science U.
Alan Cowman, Walter & Eliza Hall Inst.
Robert H. Crabtree, Yale U.
Roberta Croce, Vrije Universiteit
Janet Currie, Princeton U.
Jeff L. Dangl, U. of North Carolina
Tom Daniel, U. of Washington
Frans de Waal, Emory U.
Stanislas Dehaene, Collège de France
Robert Desimone, MIT
Claude Desplais, New York U.
Dennis Discher, U. of Pennsylvania
Gerald W. Dorn II, Washington U. School of Medicine
Jennifer A. Doudna, U. of California, Berkeley
Bruce Dunn, U. of California, Los Angeles
William Dunphy, Caltech
Christopher Dye, WHO
Todd Ehlers, U. of Toebingen
David Ehrhardt, Carnegie Inst. of Washington
Tim Elston, U. of North Carolina at Chapel Hill
Gerhard Ertl, Fritz-Haber-Institut, Berlin
Barry Everitt, U. of Cambridge
Ernst Fehr, U. of Zurich
Anne C. Ferguson-Smith, U. of Cambridge
Michael Feuer, The George Washington U.
Toren Finkel, NHLBI, NIH
Kate Fitzgerald, U. of Massachusetts
Peter Fratzl, Max-Planck Inst.
Elaine Fuchs, Rockefeller U.
Daniel Geschwind, UCLA
Karl-Heinz Glassmeier, TU Braunschweig
Ramon Gonzalez, Rice U.
Julia R. Greer, Caltech
Elizabeth Grove, U. of Chicago
Nicolas Gruber, ETH Zurich
Kip Guy, St. Jude's Children's Research Hospital
Taekjip Ha, U. of Illinois at Urbana-Champaign
Christian Haass, Ludwig Maximilians U.
Michael Hasselmo, Boston U.
Martin Heimann, Max-Planck Inst. Jena
Yka Helariutta, U. of Cambridge
James A. Hendler, Rensselaer Polytechnic Inst.
Janet G. Hering, Swiss Fed. Inst. of Aquatic Science & Technology
Kai-Uwe Hinrichs, U. of Bremen
David Hodell, U. of Cambridge
David Holden, Imperial College
Lora Hooper, UT Southwestern Medical Ctr. at Dallas
Tamas Horvath, Yale University
Raymond Huey, U. of Washington
Fred Hughson, Princeton U.
Auke Ijspeert, EPFL Lausanne
Stephen Jackson, USGS and U. of Arizona
Steven Jacobsen, U. of California, Los Angeles
Kai Johnson, EPFL Lausanne
Peter Jonas, Inst. of Science & Technology (IST) Austria
Matt Kaeberlein, U. of Washington
William Kaelin Jr., Dana-Farber Cancer Inst.
Daniel Kahne, Harvard U.
Daniel Kammen, U. of California, Berkeley
Abby Kavner, U. of California, Los Angeles
Masashi Kawasaki, U. of Tokyo
V. Narry Kim, Seoul National U.
Joel Kingsolver, U. of North Carolina at Chapel Hill
Robert Kingston, Harvard Medical School
Etienne Kochlin, Ecole Normale Supérieure
Alexander Kolodkin, Johns Hopkins U.
Thomas Langer, U. of Cologne
Mitchell A. Lazar, U. of Pennsylvania
David Lazer, Harvard U.
Thomas Lecuit, IBDM
Virginia Lee, U. of Pennsylvania
Stanley Lemon, U. of North Carolina at Chapel Hill
Ottoline Leyser, Cambridge U.
Wendell Lim, U.C. San Francisco
Marcia C. Linn, U. of California, Berkeley
Luis Liz-Marzan, CIC biomAGUNE
Jonathan Losos, Harvard U.
Ke Lu, Chinese Acad. of Sciences
Christian Lüscher, U. of Geneva
Laura Machesky, CRUK Beatson Inst. for Cancer Research
Anne Magurran, U. of St. Andrews
Oscar Marin, CSIC & U. Miguel Hernández
Charles Marshall, U. of California, Berkeley
C. Robertson McClung, Dartmouth College
Graham Medley, U. of Warwick
Tom Misteli, NCI
Yasushi Miyashita, U. of Tokyo
Mary Ann Moran, U. of Georgia
Richard Morris, U. of Edinburgh
Alison Motsinger-Reif, NC State U. (\$) **Thomas Murray**, The Hastings Center
Daniel Neumarck, U. of California, Berkeley
Kitty Nijmeijer, U. of Twente
Per Nordlund, Karolinska Inst.
Haig Nowotny, European Research Advisory Board
Ben Olken, MIT
Jo Chorkendorff, U. of Denmark
Barkeley & Lawrence Berkeley National Lab
Harry Orr, U. of Minnesota
Pilar Ossorio, U. of Wisconsin
Andrew Oswald, U. of Warwick
Steve Palumbi, Stanford U.
Jane Parker, Max-Planck Inst. of Plant Breeding Research
Giovanni Parmigiani, Dana-Farber Cancer Inst. (\$) **John H. J. Petrini**, Memorial Sloan-Kettering Cancer Center
Samuel Pfaff, Salk Institute for Biological Studies
Joshua Plotkin, U. of Pennsylvania
Albert Polman, FOM Institute AMOLF
Philippe Poulin, CNRS
Jonathan Pritchard, Stanford U.
David Randall, Colorado State U.
Felix Rey, Institut Pasteur
Trevor Robbins, U. of Cambridge
Jim Roberts, Fred Hutchinson Cancer Research Ctr.
Barbara A. Romanowicz, U. of California, Berkeley
Amy Rosenzweig, Northwestern University
Mike Ryan, U. of Texas, Austin
Mitinori Saitou, Kyoto U.
Shimon Sakaguchi, Kyoto U.
Miquel Salmeron, Lawrence Berkeley National Lab
Jürgen Sandkühler, Medical U. of Vienna
Alexander Schier, Harvard U.
Vladimir Shalae, Purdue U.
Robert Siliciano, Johns Hopkins School of Medicine
Denis Simon, Arizona State U.
Uri Simonson, U. of Pennsylvania
Alison Smith, U. of Pennsylvania
Richard Smith, U. of North Carolina (\$) **John Speakman**, U. of Aberdeen
Allan C. Spradling, Carnegie Institution of Washington
Jonathan Sprent, Garvan Inst. of Medical Research
Eric Steig, U. of Washington
Paula Stephan, Georgia State U. and National Bureau of Economic Research
Molly Stevens, Imperial College London
V. S. Subrahmanian, U. of Maryland
Ira Tabas, Columbia U.
Sarah Teichmann, Cambridge U.
John Thomas, North Carolina State U.
Shubha Tole, Tata Institute of Fundamental Research
Christopher Tyler-Smith, The Wellcome Trust Sanger Inst.
Herbert Virgin, Washington U.
Bert Vogelstein, Johns Hopkins U.
Cynthia Volkert, U. of Göttingen
David Wallach, Weizmann Inst. of Science
Ian Walmsley, U. of Oxford
Jane-Ling Wang, U. of California, Davis (\$) **Dana A. Wardle**, Swedish U. of Agric. Sciences
David Waxman, Fudan U.
Jonathan Weissman, U. of California, San Francisco
Chris Wikle, U. of Missouri (\$) **Ian A. Wilson**, The Scripps Res. Inst. (\$) **Timothy D. Wilson**, U. of Virginia
Rosemary Wyse, Johns Hopkins U.
Jan Zaenen, Leiden U.
Kenneth Zaret, U. of Pennsylvania School of Medicine
Jonathan Zehr, U. of California, Santa Cruz
Len Zon, Children's Hospital Boston
Maria Zuber, MIT

BOOK REVIEW BOARD

David Bloom, Harvard U. Samuel Bowring, MIT, Angela Creager, Princeton U., Richard Sweder, U. of Chicago, Ed Wasserman, DuPont

#IAmAResearchParasite

In the midst of steady progress in policies for data sharing, a recent editorial expressed a contrarian view.* The authors described the concern of some scientists about the rise of an underclass of “research parasites” who exploit data sets that are collected and curated by others. Even worse, these parasites might use such data to try to disprove the conclusions posited in the data’s original source studies. The editorial raised the points of how anyone not involved in the original study could use the data without misrepresenting it, and the danger of perhaps arriving at erroneous conclusions. The editorial advised instead that data sharing be implemented by involving the authors of the original study as coauthors in follow-up research. The research community immediately took to Twitter under the hashtag #IAmAResearchParasite to voice opposition to the editorial.

Much of what we know about the large-scale features of this planet is apparent thanks to widespread data-sharing practices and the early establishment of data banks in the geosciences. Aspects such as determining the shape of the ocean floor, ocean chemistry, the internal structure of Earth’s deep interior, the physics and chemistry of the atmosphere, and many other topics could not have been ascertained from a single investigator’s field program. One meta-analysis I published on the South Pacific benefited from observations of my own and those of others, including the 18th-century British explorer Captain James Cook. Involving Cook as a coauthor on my paper was clearly not an option, any more than it would have been feasible or desirable to include the dozens of others, living or dead, who had contributed to the data repository. Many fields, including the biomedical sciences, are now benefiting from meta-analyses of data to better understand the big picture.

Effective data sharing is not trivial or inexpensive

to implement, and it takes more than community acceptance of the practice. Agencies supporting research in oceanography have long funded data and sample repositories and have encouraged data and sample deposition by making new awards contingent on compliance. Repositories are *instrumental* in setting formats for data, so much so that standard programs and apps accept and output data in the standard format. The marine community supports data professionals who are responsible for the quality control of data collected on ships and from other major observing programs.

Often overlooked is the importance of community-established metadata, so that those not involved in the original research will know what the data mean. As an example, in an oceanographic temperature data base, the community had to agree on what T(0) meant. Was it temperature at atmospheric pressure? Temperature at the sea surface?

Communities must discourage low-quality data collection. A well-attended poster presentation at one prominent scientific meeting some years ago compared the crossover errors (misfits) of non-time-dependent measurements (such as depth soundings) from ships’ tracks where they intersected in the

world’s oceans. Any discrepancy at a crossing could be attributed to poor data quality control on either ship, but with thousands of crossings, institutions with systematically more misfits than others stand out. The results did not escape the attention of the funding agencies that support ship time.

There are costs to implementing data reuse, but there are also costs for irreproducible research and for re-collecting data for new uses. And no amount of funding can reconstruct lost ephemeral or time-dependent phenomena for which the data were not well curated. No more excuses: Let’s step up to data sharing.

– Marcia McNutt



Marcia McNutt is
Editor-in-Chief,
Science Journals



*“There are costs...
for re-collecting data
for new uses.”*

*D. L. Longo, J. M. Drazen, *N. Engl. J. Med.* **374**, 276 (2016).

Data sharing

The *Science* family of journals is committed to sharing data relevant to public health emergencies, and therefore we are signatories to, and wholeheartedly endorse, the following statement by funders and journals.*

Statement on Data Sharing in Public Health Emergencies

The arguments for sharing data, and the consequences of not doing so, have been thrown into stark relief by the Ebola and Zika outbreaks.

In the context of a public health emergency of international concern, there is an imperative on all parties to make any information available that might have value in combatting the crisis.

We are committed to working in partnership to ensure that the global response to public health emergencies is informed by the best available research evidence and data, as such:

- Journal signatories will make all content concerning the Zika virus free to access. Any data or preprint deposited for unrestricted dissemination ahead of submission of any paper will not pre-empt its publication in these journals.
- Funder signatories will require researchers undertaking work relevant to public health emergencies to set in place mechanisms to share quality-assured interim

and final data as rapidly and widely as possible, including with public health and research communities and the World Health Organisation.

We urge other organisations to make the same commitments.

This commitment is in line with the consensus statement agreed at a WHO expert consultation on data sharing last year whereby researchers are expected to share data at the earliest opportunity, once they are adequately controlled for release and subject to any safeguards required to protect research participants and patients.

Signatories to the Statement

Academy of Medical Sciences, UK
 Bill and Melinda Gates Foundation
 Biotechnology and Biological Sciences Research Council (BBSRC)
 Bulletin of the World Health Organization
 Canadian Institutes of Health Research
 Centers for Disease Control and Prevention
 Chinese Academy of Sciences
 Chinese Centre for Disease Control and Prevention
 Department of Biotechnology, Government of India
 Department for International Development (DFID)
 Deutsche Forschungsgemeinschaft (DFG)
 eLife
 Faculty of 1000 (F1000)
 Fondation Mérieux
 Fundação Oswaldo Cruz (Fiocruz)
 Institut Pasteur
 Japan Agency for Medical Research and Development (AMED)
 The JAMA Network
 The Lancet
 Médecins Sans Frontières/Doctors Without Borders (MSF)
 National Academy of Medicine
 National Institutes of Health, USA
 National Science Foundation
 The New England Journal of Medicine (NEJM)
 PLOS
Science Journals
 South African Medical Research Council
 Springer Nature
 UK Medical Research Council
 Wellcome Trust
 ZonMw—The Netherlands Organisation for Health Research and Development

– Marcia McNutt



Marcia McNutt is Editor-in-Chief, Science Journals



Aedes aegypti mosquito

“Precision medicine is not a replacement for making sure people have just basic health care.”

President Obama, 25 February, at a White House summit marking 1 year of the Precision Medicine Initiative, when asked what the initiative can do to address opioid drug abuse in rural communities. <http://scim.ag/PM1year>

IN BRIEF

Rewilding led to hybrid orangutans



Many orangutans at Camp Leakey in Borneo now carry a “cocktail” of genes from different subspecies.

From 1971 to 1985, primatologists have released more than 90 rehabilitated orangutans—most confiscated from the illegal pet trade—into the wilds of Borneo. At the time, orangutans were considered a single species; however, they are now thought to be two separate species with at least three reproductively distinct subspecies. Those early rewildings, a new study shows, inadvertently introduced the wrong subspecies into local populations. Primatologist Graham Banes of the University of Cambridge in the United Kingdom and colleagues analyzed 44 years of data from Borneo’s Camp Leakey and also used fecal samples to study the genetics of the camp’s ape population. Two reintroduced females were not from the local subspecies; one has at least 14 descendants, whereas the other has had few offspring, many with health issues that could be the result of mixing populations. Meanwhile, an estimated nine males from mixed-species unions have carried their “cocktail” of genes into the wilds of Tanjung Puting National Park—with unknown repercussions. Given the number of orangutan reintroductions and the likelihood that other wildlife sanctuaries have also reintroduced the wrong species, this may be the tip of the iceberg, the researchers wrote last week in *Scientific Reports*.

PHOTOS: (LEFT TO RIGHT) GRAHAM L BANES, KEEGAN HOUSER/UC BERKELEY

AROUND THE WORLD

Average innovator? Not Steve Jobs

WASHINGTON, D.C. | If you think the archetypal U.S. researcher-entrepreneur is a young white college dropout building a startup in his garage, then think again, argues a new study of the demographics of U.S. innovators in the information, life, and materials sciences. The face behind the next big thing could easily belong to a middle-aged male Ph.D. from India or China, working at a large firm, conclude researchers from the Information Technology and Innovation Foundation in Washington, D.C., and George Mason University in Fairfax, Virginia. The team used patents and awards to identify and send surveys to more than 6000 U.S. innovators. Of the 923 who responded, 46% are immigrants or the children of immigrants. More than half hold doctorates and work at firms with more than 500 employees. The median age is 47, and just 12% are women. Fewer than 8% belong to a minority group. <http://scim.ag/avginnovator>

Budget crunch at Berkeley

BERKELEY, CALIFORNIA | The University of California (UC), Berkeley, may disband the university’s College of Chemistry to help cope with a cash crunch. Faced with \$150 million in debt, as well as flat income from tuition and rising costs, the university is considering saving money by closing the college and absorbing its departments into other university colleges. No decisions have yet been made; so far, more than 2250



Latimer Hall at UC Berkeley’s College of Chemistry.

Softball-sized *Rafflesia consueloae* is the smallest species in the giant flower family.



Corpse flower's cousin smells like coconut

The world's largest and perhaps stinkiest flower has a newly discovered—and much smaller and much more pleasant-smelling—cousin. The genus *Rafflesia* has produced some of the largest flowers on Earth; the largest known individual flower is about a meter across and was produced by *R. arnoldii*, which some call the corpse flower for its distinctive odor (and not to be confused with another giant flower commonly called a corpse flower, *Amorphophallus titanum*). Now, in the mountains of the Philippines's Luzon Island, scientists have found *R. consueloae*, a parasitic flowering plant (like its larger cousins) that has a far less offensive smell. It measures only 10 centimeters across, making it the smallest of the giants, they reported last week in *PhytoKeys*.

people have signed a petition asking UC Berkeley Chancellor Nicholas Dirks to scrap the idea of disbanding the school, which is home to 101 faculty and 1492 students and postdocs. Thirteen of its faculty have won Nobel Prizes.

Nanopore pioneer sued

SAN DIEGO, CALIFORNIA | The first company to bring nanopore DNA sequencing to market is facing charges of patent infringement from genetic sequencing giant Illumina. The company filed a lawsuit against U.K.-based Oxford Nanopore Technologies last week, claiming that the nanopore platforms it has made available to researchers since 2014 use patented technology Illumina controls. Hailed as a revolution in cheap and portable DNA analysis (*Science*, 19 February, p. 800), nanopore sequencing reads long strands of DNA by measuring changes in electrical current as different nucleotides of a strand pass through a bacterial pore. Oxford hasn't revealed what type of pore is inside its devices, but Illumina contends that they rely on the *Mycobacterium smegmatis* porin (Msp). The Msp pore is described in two

patents Illumina has exclusively licensed from the University of Washington and the University of Alabama, Birmingham.

Ebola risk, ZMapp limits revealed

BOSTON | Worrisome findings about the 2013–16 Ebola epidemic in West Africa are continuing to emerge. Many survivors of the disease have experienced long-term effects, including joint pain, neurological



Ebola survivors, like this mother and daughter, face possible long-term symptoms.

problems, and eye damage, researchers reported last week at a special session of the Conference on Retroviruses and Opportunistic Infections in Boston. Another group reported that many men harbor Ebola RNA in their semen after they recover, and for far longer than imagined—which suggests that fresh outbreaks caused by sexual transmission can remain a threat for nearly a year. And a third team of scientists presented disappointing results from a clinical trial of what was once considered the most promising Ebola treatment: an antibody cocktail called ZMapp. The study, started late in the epidemic, enrolled fewer people than planned, and failed to provide statistically significant results. Although the conference focuses on HIV/AIDS, meeting organizers included the Ebola findings because of overlap in the HIV and Ebola research communities and because of the magnitude of the epidemic. http://scim.ag/_Ebolanews

Scientists decry spending plan

NEW DELHI | Science spending in India is slated to rise by 11% in the 2016–17 fiscal year, according to the budget proposal presented this week by Prime Minister Narendra Modi. But inflation, projected to be 5% in the coming year, will consume much of the increase, many scientists say—and far greater investments will be needed to revamp crumbling infrastructure. “We have very few laboratories and institutions comparable to the best in the world,” says C.N.R. Rao, a chemist and adviser to the previous prime minister, Manmohan Singh. “We need to provide much more support for improving this state.” In the new budget, agricultural research gets a 19% boost, and earth sciences and renewable energy increase by 16% each. Space research and atomic energy would get increases of just 6.6% and 5.1%, respectively. The Council for Scientific and Industrial Research, which runs a network of 38 national labs, will get a 4.6% increase, in line with orders it received last year to self-finance half of its budget within the next 2 to 3 years. <http://scim.ag/Indiascience>

NEWSMAKERS

Surgeon facing dismissal

Pressure on surgeon **Paolo Macchiarini** is increasing as the Karolinska Institute (KI) in Stockholm says it will try to cut ties with him before his contract runs out in November. Macchiarini, a surgeon who implanted artificial tracheae into

patients at KI and elsewhere, is under a cloud of controversy after colleagues and media reports questioned the ethics of the operations and the accuracy of papers he published about their success (*Science*, 5 February, p. 546). Meanwhile, *The Lancet* published a letter on 23 February detailing problems with a 2011 paper by Macchiarini that described early success with the first patient to receive the polymer trachea seeded with stem cells. The journal has previously declined to amend or retract the paper. <http://scim.ag/Macchiarini>

Califf confirmed as FDA head

President Barack Obama's new pick to head the Food and Drug Administration (FDA) was confirmed by the U.S. Senate


on 24 February. Cardiologist **Robert Califf** has faced opposition from several senators since his nomination in September 2015. Some labeled him an industry insider for his role in overseeing large company-funded trials at Duke University Medical Center in Durham, North Carolina. Others, meanwhile, used the nomination as a chance to take the agency to task over various issues not related to Califf, including FDA's response to the epidemic of opioid abuse. The opposition was blunted by a procedural vote last week that limited floor debate, and the Senate approved the nomination by a vote of 89 to four. Califf will take the helm as FDA faces pressure from Congress to speed the approval of medical products to patients. http://scim.ag/_Califf



Return of the monarchs

The number of monarch butterflies wintering in Mexico is up for the second year in a row—but their famous migration remains imperiled, researchers said in a press conference in Mexico City 26 February. Every year, millions of butterflies journey from their breeding grounds in the U.S. Midwest and Canada to their winter habitat in the oyamel fir and pine forests of central Mexico. Since 1993, researchers have estimated the butterflies' numbers based on the total forest area they inhabit. Monarchs covered 4 hectares of forest this winter, according to a December 2015 survey released last week. That's nearly four times as much area as last year (1.13 hectares), and suggests an ongoing rebound from the all-time recorded low of 0.67 hectares in the winter of 2013–14. But monarch numbers remain low compared with the late 1990s and early 2000s, when the butterflies often covered 8 hectares or more. Their main threat is still the loss of milkweed in the United States (*Science*, 23 January 2015, p. 357), says Omar Vidal, the director general of the World Wildlife Fund Mexico in Mexico City, which administers the annual count.

IN DEPTH



Young pulsars like the one at the heart of the Crab Nebula (shown in this artist's conception) may spark repeating fast radio bursts.

RADIO ASTRONOMY

Fast radio bursts tease astronomers

Conflicting results suggest the potent blasts come in two flavors

By **Govert Schilling**

The more radio astronomers learn about the potent bursts of radio waves called fast radio bursts (FRBs), the deeper their confusion becomes. Last week, a scientific paper suggested that these milliseconds-long radio bursts result when superdense burnt-out stars called neutron stars collide and perish in remote galaxies. But this week, another paper reports multiple bursts from an FRB—something merging neutron stars cannot explain.

“These are some papers!” says astrophysicist Chryssa Kouveliotou of George Washington University in Washington, D.C. “The first one already presented a major discovery, showing that the progenitor of the FRB was destroyed in the process. Now, the second one has a completely different result: Not only did the progenitor survive, but it kept giving. It’s extremely interesting.”

FRBs last on the order of a millisecond and pop up all over the sky, probably thousands of times per day across the observable universe. Without knowing their distance, it’s impossible to say how energetic they are. Unfortunately for researchers, they are extremely hard to detect, mainly because most radio telescopes can view only minute patches of sky. David Narkevic, a graduate student working with radio astronomer Duncan Lorimer at West Virginia University in Morgantown, serendipitously found the

first one in 2007, in archival data collected in 2001 by the 64-meter Parkes Observatory radio telescope in Australia. Since then, 16 more of the mysterious signals have been detected, most at Parkes, but no one knew what to make of them. Theories about their origin—including speculative ideas about black holes turning inside out—vastly outnumber the discoveries themselves.

One thing astronomers do agree on is that FRBs originate in remote galaxies. That’s because longer radio waves from the bursts arrive slightly later than shorter waves do. That so-called dispersion results from an interaction between the radio waves and tenuous clouds of electrons in space. The space between the stars in our own Milky Way galaxy contains too few electrons to cause the large dispersion that astronomers see, so the bursts must have originated much farther away.

Last week’s paper, which Evan Keane of the Square Kilometre Array Organisation, in Manchester, U.K., and colleagues published in the 26 February issue of *Nature*, appeared to prove that FRBs are extremely remote, one-time cataclysms. On 18 April 2015, the Parkes telescope detected a new millisecond burst, FRB 150418, in the constellation Canis Major. Just a few hours later, the six-dish Australia Telescope Compact Array in Narrabri found a faint source of radio waves at the same location, slowly fading over 6 days—presumably the afterglow of a catastrophic event. Subsequent observa-

tions with the Japanese 8.2-meter Subaru Telescope on Mauna Kea, Hawaii, revealed a dim elliptical galaxy some 6 billion light-years from Earth—apparently FRB 150418’s host galaxy.

Not everyone is convinced, however. On 26 February, in a note on the arXiv preprint server, astrophysicists Peter Williams and Edo Berger of Harvard University proposed that the fading radio source could be a naturally varying signal from the distant galaxy’s nucleus—and unrelated to the FRB. The researchers say new radio observations they carried out on 27 and 28 February with the Very Large Array radio telescope on the Plains of San Agustin in New Mexico support that interpretation.

But if Keane and his colleagues are correct about the extremely remote location, the most plausible source of the burst may be two ultracompact neutron stars coalescing into a black hole—an event energetic enough to explain the burst’s estimated power of 10^{35} watts and its long radio afterglow, presumably from a cooling fireball. Such neutron star mergers are also the prime candidate for explaining another cosmic mystery, short gamma ray bursts: fleeting blasts of radiation that can outshine entire galaxies for a few seconds. No gamma rays have been detected from FRB 150418, Keane says, but that could be because the radiation is focused in a tight beam not aimed at Earth.

But a one-time catastrophe can’t explain the phenomenon reported in this week’s

issue of *Nature* by Laura Spitler of the Max Planck Institute for Radio Astronomy in Bonn, Germany; Jason Hessels of the University of Amsterdam and ASTRON, the Netherlands Institute for Radio Astronomy; and colleagues. They reobserved the region of the sky where the 305-meter Arecibo Observatory radio telescope in Puerto Rico had detected FRB 121102 in November 2012. In 3 hours of follow-up observations from May and June 2015, Paul Scholz, a postdoctoral student at McGill University in Montreal, Canada, identified two more bursts on 17 May and another eight on 2 June. Many others may have gone unnoticed. The additional radio blips leave no doubt that the object they come from is not destroyed in the process, Lorimer says: "It's basically impossible for a cataclysmic event to produce repeating bursts."

So if this can't be a neutron star merger, what are the alternatives? One once-promising candidate—so-called "giant flares" on young, highly magnetized neutron stars known as magnetars—has fallen from favor, Kouveliotou says. No known magnetar in our own galaxy has produced more than one giant flare in almost half-a-century of observing. A stronger possibility, Kouveliotou and the authors agree, is that the repeating bursts of FRB 121102 are irregular giant explosions on a pulsar: a rapidly spinning neutron star. The pulsar at the heart of the famous Crab Nebula (which also sends out regular weaker pulses of radio waves) is known to produce incidental giant pulses.

The bottom line, Lorimer says, is that "the results in the two papers immediately divide the sample of fast radio bursts into two classes." Similar things have happened before in astronomy: In the 1930s, astronomers discovered that supernova explosions come in several varieties, and in the early 1990s, they realized that different mechanisms produce long and short gamma ray bursts. In fact, says Kouveliotou, "the current situation with FRBs is starting to make me feel like some 24 years ago, when I was working on gamma ray bursts and then magnetars popped in to add to the mystery and the confusion. It's all very exciting."

Lorimer expects FRBs to become a major focus of astrophysical research. To find more of them, astronomers need wide-field instruments like the Canadian Hydrogen Intensity Mapping Experiment, under construction in British Columbia, or ASTRON's upgraded Westerbork Synthesis Radio Telescope, which will become operational later this year. To capture other signals from each radio source before they fade, astronomers also need to build systems for quickly alerting other telescopes. Lorimer says: "There's an awful lot of work ahead of us." ■

INFECTIOUS DISEASE

'Patient Zero' no more

Sleuthing clarifies HIV's history

By Jon Cohen, in Boston

A new study pinpoints with greater precision than ever before when and where HIV entered the United States and sparked North America's AIDS epidemic. It also puts to rest a media-fueled theory about a peripatetic flight attendant with a very active sex life: so-called "Patient Zero," who after his death became infamous for supposedly bringing the virus into the country and seeding the infection in different locales.

In *And the Band Played On*, the 1987 best-selling account of the U.S. epidemic's early years, journalist Randy Shilts wrote in detail about Patient Zero, a Canadian named Gaëtan Dugas who died from AIDS 3 years before the book was published. "[T]here's no doubt that Gaëtan [sic] played a key role in spreading the new virus from one end of the United States to the other," Shilts wrote. He did not say Dugas introduced the disease to North America, but subsequent media accounts, including one in *Time* magazine, did make that claim—and vilified Dugas. A front-page *New York Post* headline went so far as to proclaim, "THE MAN WHO GAVE US AIDS." HIV/AIDS researchers have long been skeptical about the Patient Zero claim.

Last week at the Conference on Retroviruses and Opportunistic Infections here, Michael Worobey, an evolutionary biologist at the University of Arizona in Tucson, solidly debunked that claim, saying Dugas was far from what epidemiologists refer to as the "index patient" in the United States. Worobey's new work will help put "the myth of Patient Zero" to rest, says epidemiologist Harold Jaffe of the Centers for Disease Control and Prevention (CDC) in Atlanta, who helped unravel the early spread of the disease.

The first AIDS cases surfaced in five gay men in Los Angeles, California, and were reported in CDC's *Morbidity and Mortality Weekly Report* in June 1981. After HIV was

proven to be the culprit in 1984, researchers analyzed stored blood samples from gay and bisexual men collected in the late 1970s in San Francisco, California, and New York City and found that the men already carried antibodies to the virus. Worobey plucked the virus from eight of those samples, which dated from 1978 and 1979, and obtained nearly the complete genetic sequences of each one. Jaffe, who had helped piece together Dugas's connection to a cluster of early AIDS cases in California and New York, supplied a 1983 sample of the flight attendant's blood, which also yielded a near-complete HIV genome.

HIV mutates at a constant rate each time it copies itself, so Worobey could use the differences among the sequences to create a family tree of the viruses and estimate when each isolate emerged. His work suggests the U.S. epidemic most likely began in New York City around 1970, when the real index case brought in a virus that closely matched the sequences of older HIVs isolated from people in Haiti and a few other Caribbean countries. Although his sample size is small, Worobey said the probability that New York City was the origin of the U.S. epidemic "is very, very

high indeed." He estimates the virus reached San Francisco around 1975.

On the family tree of the early U.S. isolates, Dugas's HIV genome fell in about the middle. "There's nothing special about his genome," Worobey said. Although Dugas had been to Haiti—in 1977—there is no sign that he was either the index patient or key to spreading the virus around the country. Worobey notes that when CDC researchers were piecing together how the first AIDS cases were linked to each other, they originally referred to Dugas not by the number "0" but by the letter "O," because he was from "outside" California. Later, for reasons that remain murky, Dugas morphed into Patient Zero.

So rather than Dugas sparking the U.S. epidemic, his case, historically speaking, really is just an "oh." ■



Gaëtan Dugas, infamously, and wrongly, labeled Patient Zero.



SCIENTIFIC INTEGRITY

Survey fraud test sparks battle

Pew Research Center challenges statistical test

By John Bohannon

With grants from charitable donations, the Pew Research Center funds dozens of surveys a year, on everything from Americans' views about science and religion to what people in African countries see as national priorities and problems. So it's not surprising that Pew wouldn't take kindly to the suggestion that some, perhaps more than a quarter, of its international surveys are marred by data fabrication. Indeed, the organization is vigorously challenging that claim—from two former Pew researchers.

At a meeting on survey data fabrication in Washington, D.C., last week, the pair, Michael Robbins and Noble Kuriakose, presented an update on a newly developed statistical test that has been roiling the survey research community for the past year. When they apply the test to more than 1000 public data sets from international surveys, about one in five of the surveys fail, indicating a high likelihood of fabricated data. At the meeting, they debuted an analysis focusing on 309 of Pew's international studies that found a failure rate of 30%.

"Robbins and Kuriakose have uncovered a massive problem," says Michael Spagat, an economist at Royal Holloway, University of London, who has investigated high-profile cases of possible survey data fabrication in war zones. But Pew officials dismiss the test, saying it is prone to false

positives. The organization has gone so far as to request Robbins and Kuriakose desist from publishing their original analysis, which is now in press. Pew's actions are "pretty disappointing," says Kuriakose, now a research scientist at SurveyMonkey in Palo Alto, California. "This problem isn't going to just go away."

Robbins and Kuriakose originally met at Pew, which is based Washington, D.C. "Michael was doing methodology work on Pew's international surveys and we connected about data quality," Kuriakose says. Surveying communities in the developing world often requires face-to-face interviews, done house-by-house in dangerous environments. To avoid risk or save time, Robbins says, interviewers sometimes resort to "curbstoning": sitting on the curb and inventing survey responses, often by duplicating answers.

To detect such fabrication, their test looks for highly similar responses from multiple respondents. How similar is too similar? After running a simulation of data fabrication scenarios, they settled on 85% as the cutoff. In a 100-question survey of 100 people, for example, fewer than five people would be expected to have identical answers on 85 of the questions if the data are genuine. The 85% rule isn't appropriate for all kinds of surveys, the pair acknowledges—some types tend to produce more uniform answers. But for the large-scale opinion surveys typically carried out in the developing world "this is

Surveys, like this one collecting family information in Guatemala, may often be marred by fabricated data, a new statistical test suggests.

exactly the appropriate method for detecting fabrication," Kuriakose says.

After he left Pew, Robbins became director of Arab Barometer, which surveys opinion across the Arab world. He tested data from that project and found signs of fabrication, which subsequent investigation confirmed. Wondering about the scale of the problem, Robbins and Kuriakose refined their test and applied it to 1008 international surveys, including many from Pew, though they only reported the aggregate results. Their test flagged 17% as likely to contain a significant portion of fabricated data—and the figure shot up to 26% for surveys done in the developing world.

"We found out about this study and were very alarmed," says Courtney Kennedy, director of survey research for Pew. She and her colleagues used the same test on Pew's surveys and found that a "certain share" failed by Robbins and Kuriakose's standards, Kennedy says, but follow-up investigation left the organization convinced only a "handful" were suspicious.

Late last year, after the pair submitted a paper on their method and findings to the peer-reviewed *Statistical Journal of the IAOS*, one of the field's leading publications, they received an email from Kennedy and other top officials at Pew. "We strongly suggest that you retract the paper," the email stated, "as we believe the analysis is severely underspecified and will give both survey vendors and contractors a false metric for identifying fraud." Kennedy calls the letter "appropriate" because "our organization's reputation is on the line. You can't make cavalier claims like that."

Kuriakose and Robbins did not withdraw their paper. It was accepted in December 2015 and is in press, and at last week's meeting they lobbed a second bombshell: their analysis of Pew surveys. Kennedy responded with an attack on the test's methodology. For example, she points out, it does not account for the number of questions on a survey, the number of respondents, or other factors that can skew the results. (Pew has posted its analysis online.)

Before the meeting, co-organizer Steven Koczele, president of the MassINC Polling Group in Boston and a previous survey research leader for the U.S. State Department told *Science* that the case laid out by Kuriakose and Robbins "seems unassailable." Now that both sides have hashed it out publicly, the community is digging into the issue, he says. "I am encouraged by the sense of momentum and common purpose." ■

Scientists to drill into dinosaur-killing blast

Cores from Chicxulub crater could illuminate how life returned after the cataclysm

By Eric Hand

This month, a drilling platform will rise in the Gulf of Mexico, but it won't be aiming for oil. Scientists will try to sink a diamond-tipped bit into the heart of Chicxulub crater—the buried remnant of the asteroid impact 66 million years ago that killed off the dinosaurs, along with most other life on the planet. They hope that the retrieved rock cores will contain clues to how life came back in the wake of the cataclysm, and whether the crater itself could have been a home for novel microbial life. And by drilling into a circular ridge inside the 180-kilometer-wide crater rim, scientists hope to settle ideas about how such “peak rings,” hallmarks of the largest impact craters, take shape.

“Chicxulub is the only preserved structure with an intact peak ring that we can get to,” says University of Texas, Austin, geophysicist Sean Gulick, co-chief scientist for the \$10 million project, sponsored by the International Ocean Discovery Program (IODP) and the International Continental Scientific Drilling Program. “All the other ones are either on another planet, or they’ve been eroded.”

At the end of March, a specially equipped vessel will sail from the Mexican port of Progreso to a point 30 kilometers offshore. There, in water 17 meters deep, the boat will sink three pylons and raise itself above the waves, creating a stable platform. By 1 April, the team plans to start drilling, quickly churning through 500 meters of limestone that were deposited on the sea floor since the impact. After that, the drillers will extract core samples, in 3-meter-long increments, as they go deeper. For 2 months, they will work day and night in an attempt to go down another kilometer, looking for changes in rock types, cataloging microfossils, and collecting DNA samples (see figure, p. 1016). “We’ve got one shot to try and get this down to 1500

meters,” says David Smith, the IODP operations manager at the British Geological Survey in Edinburgh, U.K.

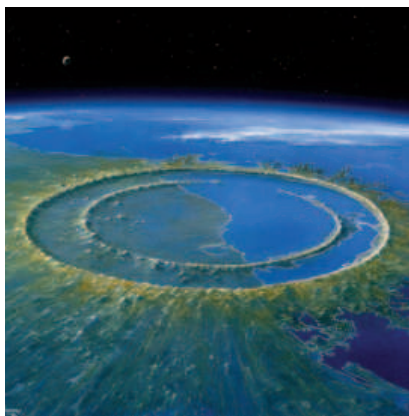
Although this is the first offshore attempt to drill into the crater, roughnecks have sunk wells into it on land—even before scientists knew a crater was there. In the 1950s, geologists for Pemex, Mexico’s national oil company, conducted gravity and magnetic surveys of the Yucatán Peninsula and were intrigued to see underground circular structures—possible oil traps. They drilled several exploratory wells but lost

interest when they got volcanic rocks instead of oil-bearing sediments. “When they found the igneous rocks, they said, ‘Oh, this is a volcanic center,’” says Alan Hildebrand, a geologist at the University of Calgary in Canada.

In 1980, however, Nobel laureate Luis Alvarez and others called attention to a thin layer of iridium—possible material from an asteroid—found all over the world in

rocks from the time of the dinosaur extinctions. It was the signature, they said, of a previously unsuspected cause of the extinctions: a giant impact. In 1991 Hildebrand and colleagues fingered the village of Chicxulub as the site of the cataclysm, finding quartz crystals shocked by an impact in samples from the Pemex wells—samples that had sat around for more than a decade. “Some people are a little embarrassed about that these days,” he says.

The data from the Pemex wells were spotty, and so scientists have always wanted to go back for a detailed look at the impact and its aftermath, says co-chief scientist Joanna Morgan of Imperial College London. “It seems like a lifetime’s ambition coming true,” says Morgan, who first proposed a scientifically cored well to the IODP in 1998. Although offshore drilling is expensive, she says that working at sea means the team will face fewer hassles with environmental permitting and won’t have to cope with the Yucatán’s poor roads. In 2005, Morgan and Gulick led a \$2 mil-



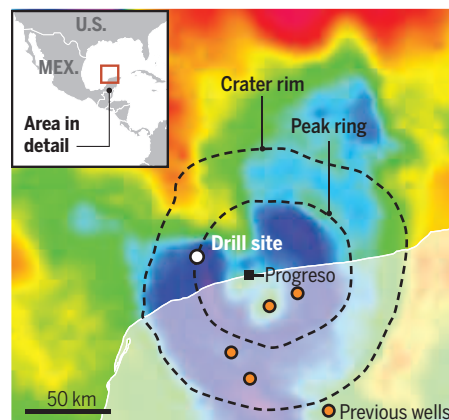
Artist's reconstruction of Chicxulub crater soon after impact, 66 million years ago.

Probing ground zero

In April, scientists will drill into Chicxulub crater, where an asteroid impact 66 million years ago led to one of Earth's biggest mass extinctions. They hope to reach a buried peak ring, Earth's only preserved example.

Buried treasure

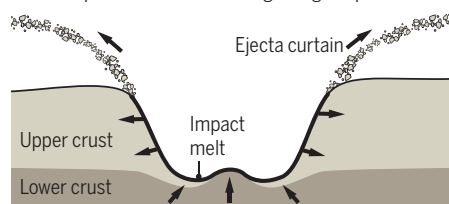
Offshore from Progreso, Mexico, scientists will drill into the crater's peak ring, partially seen in geophysical remote sensing data (below). Onshore wells have been drilled into the crater before, but few were cored and none reached the peak ring.



Making the mounds

One model for peak ring formation predicts that impact shocks would make rocks behave like fluids. Deep crustal rocks could end up on top of rocks of shallower origin.

1. Postimpact excavation and beginning of uplift.



2. Central uplift becomes unstable.



3. Uplift collapses to form peak ring.



lion remote-sensing campaign that used small seismic explosions to help illuminate the subterranean structures and pinpoint the best spot to reach the peak ring.

As the drill approaches the crater, 800 meters down, scientists expect to find fewer species of the shell-producing animals that make up the limestone, because life was just recovering from the impact. Some scientists think that carbon dioxide released by the impact would have acidified

the oceans, contributing to the extinctions, so the drill team will look at whether seafloor animals just after the impact were species that tolerate low pH.

Just above the crater lies an impact layer, 100 meters or more thick, that would have been deposited in the weeks after the cataclysm. At its base, scientists expect to find a hodgepodge of chunks of bedrock blasted up by the impact and once-molten rock that fell back into the crater in the minutes af-

ter impact. Above that would be sediments, since hardened into rock, that were swept in as the ocean rushed into the vast new depression. The impact layer may be capped by hardened deposits of ash that persisted in the atmosphere for weeks or more before falling out.

For many of the IODP scientists, the main event will be reaching the peak ring. Peak rings abound on the moon, Mercury, and Mars. But on Earth, there are just two craters larger than Chicxulub that should also have peak rings: the 2-billion-year-old Vredefort crater in South Africa, and the 1.8-billion-year-old Sudbury crater in Canada—yet they are so old that the peak rings have eroded away.

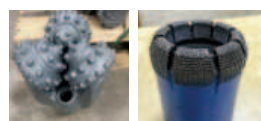
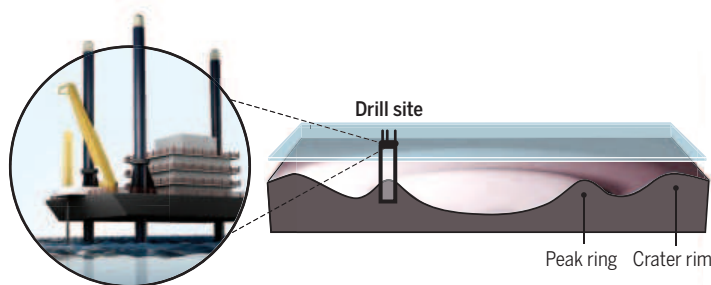
The IODP team wants to test a leading model for peak ring formation, in which granite from Earth's depths rebounds after a major impact, like water struck by stone, to form a central tower, taller than the crater rim. In minutes, the tower would collapse and collide with material slumping in from the rims to form the peak ring. Confirmation for the model could come from finding rocks "out of order": deep rocks, probably granite, brought up in the central tower, lying atop originally shallower younger rocks. "They're going to test whether our numerical models are making any sense or not," says Jay Melosh, a planetary scientist at Purdue University in West Lafayette, Indiana, who helped develop the model.

The team is interested not just in the structure of the peak ring rocks but in what life they might host. Remote sensing has already suggested that the peak ring is less dense than expected for a granite—a sign that the rocks are porous and fractured in places. It is possible that these fractures, in the wake of the impact, were filled with hot fluids. "Those will be preferred spots for microbes to grow, but it depends whether the fractures have energy and nutrients," says Charles Cockell, an astrobiologist on the IODP team at the University of Edinburgh. When the drill bit encounters mineral veins or other fracture zones in the peak ring, Cockell and his colleagues will take a sub-core from the core: a biopsy on the geopsy. They will count and culture any microbes still living in the fractures, and sequence DNA to look for the genes responsible for metabolic pathways.

Those genes might show that peak ring microbes—descendants of those that lived after the impact—derive their energy not from carbon and oxygen, like most microbes, but from iron or sulfur deposited by hot fluids percolating through the fractured rock. And that would mean the impact crater, harbinger of death, was also a habitat for life. ■

Going deep

Using a three-legged lift boat to create a stable drilling platform, scientists will drill 1500 meters deep, and back in time. Some layers took millions of years to form, whereas others were laid down in minutes.



1 Switching of the bits (500 m)

At first, no cores will be taken in layers of limestone. After casing the hole with steel, scientists will switch from a tungsten-carbide roller cutter to a diamond-tipped system that can retrieve 3-meter-long cores.



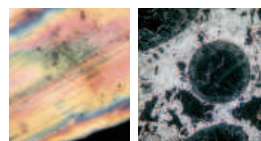
2 Paleocene–Eocene Thermal Maximum (550 m)

A time 55 million years ago when Earth was 5°C warmer. The warmth may have triggered algal blooms that died and fell to the sea floor. These might show up in the rock record as black shales amid the limestone.



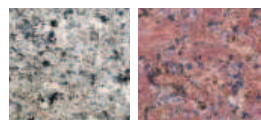
3 Life returns (550–650 m)

The scientists will look for life coming back after the impact, as the shelled animals that make up limestone return and evolve into new species. Moving downhole and back in time to the impact, the size and number of species of forams and coccolithophores is expected to shrink.



4 Impact layer (650–800 m)

Rocks at the base may contain chunks of rock and impact melt. The ocean rushing in to fill the crater hole could have deposited overlying sediment, perhaps containing glassy impact spherules. Settling on top could be fine ash containing crystals of shocked quartz.



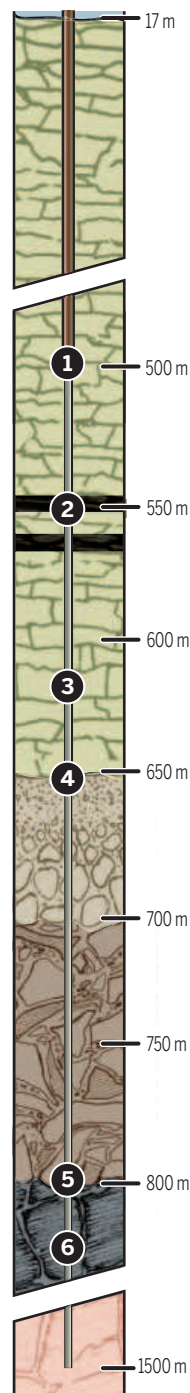
5 Peak ring (800–1500 m)

If formation models are correct, peak ring rocks—probably volcanic granites—could be sitting "out of order." Deeper granites, with darker minerals, could rest on top of granites with lighter minerals.



6 Microbial life (800–1500 m)

The peak ring is expected to be fractured and filled with mineral veins that were once part of a vast hydrothermal system. Scientists will look for DNA evidence that chemosynthetic microbes live in the cracks.



NSF makes a new bid to boost diversity

Initiative aims for fresh answers, but researchers are still framing the questions

By Jeffrey Mervis

In what could be the signature program of her 6-year term, National Science Foundation (NSF) Director France Córdova last week launched a 5-year, \$75 million initiative aimed at creating a more diverse technical community. It's a laudable goal, say researchers who attended an NSF-organized workshop on "the science of broadening participation" held just 2 days after the new program was announced. But it may be out of reach, they add, without a greater federal investment in understanding the problem.

Despite decades of work, scholars are still struggling to understand why women, many minorities, people with disabilities, and other groups are underrepresented in U.S. science and engineering. "NSF may be putting the cart before the horse" in funding potential solutions without knowing the underlying factors, says Kaye Husbands Fealing, an economist at Georgia Institute of Technology in Atlanta, who organized the workshop and says she welcomes the new program. Córdova promises that the initiative will break new ground. "I'm not interested in funding more of the same," she told *Science*.

Since arriving at NSF in March 2014, Córdova has spoken repeatedly about why broadening participation is not just the right thing to do, but also how diversity fuels better research and bolsters the U.S. economy. The new initiative—dubbed INCLUDES (Inclusion across the Nation of Communities of Learners of Underrepresented Discoverers in Engineering and Science)—will give 40 researchers \$300,000 each this year to test their ideas on fostering inclusion. Next year, a second competition will award \$12.5 million each over 5 years to five larger teams, called alliances.

NSF wants proposals that lay out a convincing strategy for scaling up efforts through partnerships with industry, local and state governments, schools, and nonprofit groups. The NSF solicitation offers the hypothetical examples of sponsoring

more community-based science programs or boosting the number of underrepresented minorities earning Ph.D.s in STEM (science, technology, engineering, and mathematics) fields.

The INCLUDES launch generated some positive buzz at the 25–26 February workshop, held next door to NSF headquarters in northern Virginia. The 60 participants have extensive experience in both the research and practice of broadening participation, and the fact that there were three times as many women of color in the room as white men reflected the inclusiveness that NSF aims to foster. Fealing, a former NSF program manager, said she hoped

needs to be based on good theory." The agency convened the meeting to help "create a science-based approach to reach conclusions on what works and what doesn't work," said Mumpower, who last year returned to Texas A&M University, College Station. "But for the moment we are forced to rely on intuition and seat-of-the-pants efforts."

INCLUDES traces its roots to a 2012 report by an NSF advisory committee on equal opportunity that called for a "bold new initiative." Last summer Córdova assembled an internal working group to flesh out the idea and build support for it both inside and outside the agency.

Ira Harkavy, a social scientist at the University of Pennsylvania and chair of the advisory committee, says he's "thrilled" that Córdova has embraced the initiative. The committee plans to keep a close eye on INCLUDES, he adds, with an upcoming report on how to ensure that the results of INCLUDES won't simply become fodder for scholarly articles and future grant applications.

Córdova offered few specifics in an interview this week. "While we will continue to fund the programs we already have—and I want to underline that, because they are really good programs—we are looking for something very different here." She cited a long-running NSF program to help women succeed in academic science—known as ADVANCE—as an example of the limitations

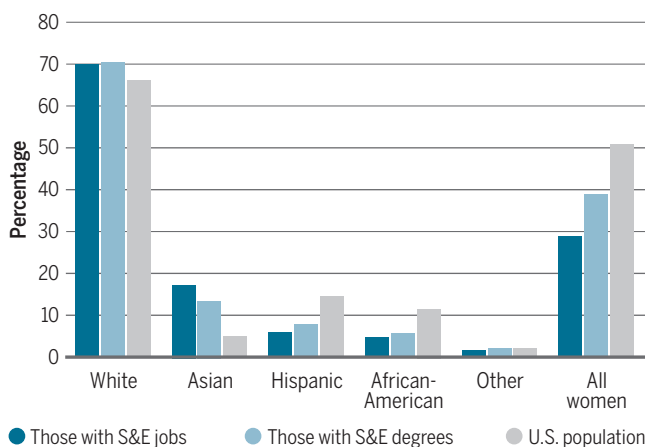
of current approaches.

"I was an ADVANCE [principal investigator] at Purdue University," she recalled. "But as hard as we were working and as effective as the program was locally, the nationwide problem was not getting much better. And with the country's changing demographics, one could argue that the gap between those with access to STEM and those who don't is actually increasing."

"There's an old saying that if you keep doing the same thing to achieve a different solution, you're not going to make progress," Córdova added. "And the smaller amount of money [for INCLUDES] is because we need to test new approaches. And if they are successful, we can build on that investment." ■

Too little diversity in science

A new National Science Foundation initiative aims to find ways to broaden participation of women, Hispanics, African-Americans, and other minority groups underrepresented in the U.S. science and engineering workforce.



some INCLUDES pilot projects will lead to standard NSF grants that strengthen the science of broadening participation.

But there were also expressions of concern, starting with how INCLUDES will differ from NSF's existing \$750-million-a-year portfolio of dozens of programs that pursue similar goals, and how it might affect them. Researchers wondered how NSF would measure the success or failure of INCLUDES projects. There were also worries that a 15 April deadline for preliminary proposals is too soon.

In his opening remarks at the workshop, Jeryl Mumpower, former director of NSF's division of social and economic sciences, cited a broader concern: "Good policy



SLOW BURN

Five years after the meltdowns at the Fukushima atomic plant, evacuees face the prospect of living near a nuclear disaster zone for decades to come

By **Dennis Normile**

A long, grinding struggle back to normal is underway at Fukushima. As workers make progress in cleaning up contaminated land surrounding the reactor, evacuees are grappling with whether to return to homes sealed off since the accident. The power plant itself remains a dangerous disaster zone, with workers just beginning the complex, risky job of locating the melted fuel and figuring out how to remove it.

The magnitude 9.0 earthquake that struck northeastern Japan on 11 March 2011 and the 40-meter tsunami that followed left 15,893 dead and 2572 missing, destroyed 127,290 buildings, and damaged more than a million more. It also triggered the meltdowns at the Fukushima Daiichi Nuclear Power Plant and the evacuation of 150,000 people from

A crane lifts a panel—part of a temporary canopy—to gauge the effects of dust suppression inside the wreckage of Fukushima Daiichi's Unit 1 reactor building.



within 20 kilometers of the nuclear plant as well as from areas beyond that were hard hit by fallout.

Now, the nuclear refugees face a dilemma: How much radiation in their former homes is safe? In a herculean effort, authorities have so far scooped up some 9 million cubic meters of contaminated soil and leaves and washed down buildings and roadways with the goal of reducing outdoor radiation exposure to 0.23 microsieverts per hour. Last September, the government began lifting evacuation orders for the seven municipalities wholly or partly within 20 kilometers of the plant. As the work progresses, authorities expect that 70% of the evacuees will be allowed to return home by spring 2017.

But evacuees are torn over safety and compensation issues. Many claim they are being compelled to go home, even though ra-

diation exposure levels, they feel, are still too high. "There has been no education regarding radiation," says Katsunobu Sakurai, the mayor of Minamisoma, where 14,000 people were evacuated after the accident. "It's difficult for many people to make the decision to return without knowing what these radiation levels mean and what is safe," he says. Some citizen groups are suing the national government and Tokyo Electric Power Company (TEPCO), the Fukushima plant's owner, over plans to end compensation payments for those who choose not to return home. Highly contaminated areas close to the nuclear plant will remain off limits indefinitely.

Conditions at the plant are "really stable," the plant manager, Akira Ono, recently told reporters. Radioactivity and heat from the nuclear fuel have fallen substantially in the past 5 years, he says. But cleanup is off to a slow start, hampered by sketchy knowledge of where the nuclear fuel is located. Last year managers agreed to a road map for decommissioning the site over the next 30 to 40 years that calls for removing melted nuclear fuel masses and demolishing the plant's four reactor halls at a cost that could top \$9 billion. TEPCO intends to start removing nuclear debris from the reactors in 2021.

Ono puts the decommissioning at "around 10%" complete. One big hurdle was cleared in December 2014, when crews removed the last of 1535 fuel rods stored in the Unit 4 spent fuel pool. At the time of the accident, some feared that cooling water had drained out of the pool and exposed the fuel to air, which might have led to overheating and melting. It hadn't, but the fuel remained a threat.

The biggest challenge at present, Ono says, is contaminated water. Cooling water is continuously poured over the melted cores of units 1, 2, and 3 to keep the fuel from overheating and melting again. The water drains into building basements, where it mixes with groundwater. To reduce the amount of contaminated water seeping into the ocean, TEPCO collects and stores it in 10-meter-tall steel tanks. They now fill nearly every corner of the grounds, holding some 750,000 tons of water. The government is evaluating experimental techniques for cleansing the water of a key radioisotope, tritium (*Science*, 12 December 2014, p. 1278). Ono says a solution is sorely needed before the plant runs out of room for more tanks.

TEPCO has found ways to divert groundwater from the site, cutting infiltration to about 150 tons per day. Now it's about to freeze out the rest. Borrowing a technique for making temporary subsurface barriers during tunnel construction, a contractor has driven 1500 pipes 30 meters down to bedrock, creating something akin to an underground picket fence encircling the four crippled reactor units. Brine chilled to -30°C circulating in the pipes will freeze the soil between the pipes; the frozen wall should keep groundwater out and contaminated water in. TEPCO was planning to start the operation shortly after *Science* went to press.



The Fukushima plant is crowded with 10-meter-tall tanks storing tainted water used to cool melted nuclear fuel masses and groundwater that infiltrated the site—some 750,000 tons in all.

The most daunting task is recovering the fuel debris. TEPCO modeling and analyses suggest that most, if not all, of the fuel in the Unit 1 reactor melted, burned through the reactor pressure vessel, dropped to the bottom of the containment vessel, and perhaps ate into the concrete base. Units 2 and 3 suffered partial meltdowns, and some fuel may remain in the cores.

To try to confirm the location and condition of the melted fuel, the International Research Institute for Nuclear Decommissioning, set up by TEPCO and other entities, has been probing the reactors' innards with muons. Wispy cousins of the electron, muons are generated by the trillions each minute when cosmic rays slam into the upper atmosphere. A few muons are absorbed or scattered, at a rate that depends on a material's density. Because uranium is denser

than steel or concrete, muon imaging can potentially locate the fuel debris.

In February 2015, a group at Japan's High Energy Accelerator Research Organization in Tsukuba supplied two van-sized muon detectors, which TEPCO placed adjacent to the Unit 1 reactor at ground level. After a month of collecting muons, the detectors confirmed there was no fuel left in the core. Because they were positioned at ground level, the devices could not image the reactor building basements and so could not pin down where the fuel is or its condition. TEPCO plans to use robots to map the location of the fuel debris so it can develop a strategy for removing it (see story, right).

A second team has developed detectors that observe muons before and after they pass through an object of interest, promising a more precise picture of reactor interiors. For Fukushima, the researchers—from Los Alamos National Laboratory in New Mexico and Japan's Toshiba Corp.—built mammoth detectors, 7 meters across, which they intended to place outside Unit 2. That work has been postponed because TEPCO decided to first send a robot into the containment vessel; high radiation levels have delayed that plan. "Our current task is to reduce that exposure," Ono says, using robotic floor and wall scrubbers in the area workers need to access to deploy the robot.

While the authorities struggle to clean up the site and resettle residents, some locals are judging safety for themselves. In 2014, a group of enterprising high school students in Fukushima city, outside the evacuation zone, launched an international radiation-dosimetry project. Some 216 students and teachers at six schools in Fukushima Prefecture, six elsewhere in Japan, four in France, eight in Poland, and two in Belarus wore dosimeters for 2 weeks while keeping detailed diaries of their whereabouts and activities. "I wanted to know how high my exposure dose was and I wanted to compare that dose with people living in other places," explains Haruka Onodera, a member of Fukushima High School's Super Science Club, which conceived the project. The students published their findings last November in the *Journal of Radiological Protection*. Their conclusion: "High school students in Fukushima [Prefecture] do not suffer from significantly higher levels of radiation" than those living elsewhere, Onodera says.

That's good news for Fukushima city residents, perhaps, but cold comfort to displaced people now weighing the prospect of moving back to homes closer to the shattered nuclear plant. ■

With reporting by Timothy Hornyak.

TRIAL BY MELTDOWN

At Fukushima, robots performed poorly at first but are now critical players in the cleanup

By Timothy Hornyak, in Tokyo

Watch Honda's Asimo humanoid robot up close, and you may fall under its spell. As it walks gracefully across a stage, sometimes opening bottles or serving tea, the elegant mechatronic man seems at home anywhere. So after a 9.0-magnitude earthquake and tsunami waves struck Japan's Fukushima Daiichi plant on 11 March 2011, it was no wonder that one of Asimo's fans tweeted, "Can't Asimo be dispatched to survey the interior of Unit 4, where radiation is too high for human workers?"

If only. In the early days of the crisis, engineers were desperate to learn about the damaged reactors' cores and the radiation levels inside the buildings, data that robots should have been able to provide. Alas, neither Asimo—designed to navigate sedate offices—nor any other of Japan's vaunted robots was up to the challenge of navigating Fukushima's complex, debris-strewn interiors. The plant's operator, Tokyo Electric Power Company (TEPCO), had to turn to U.S. military-grade robots, such as iRobot's 510 PackBot, to get its first glimpses inside the facility. Only in June 2011, 2 months later, did a modified Japanese rescue robot called Quince enter one of the ruined complex buildings.

"When Fukushima occurred, I was astounded that Japan had no robots to help out in any significant way," says Frederik Schodt near San Francisco, California, author of *Inside the Robot Kingdom: Japan, Mechatronics, and the Coming Robotopia*. "It practically brought me to tears."

Five years after the accident, however, robots are finally ready to enter the ruined reactors en masse. They are now expected to play an essential part in the daunting

task of decontaminating and dismantling the reactors. Roboticists are making halting progress in developing machines for specific tasks, such as decontaminating and removing melted nuclear fuel masses, but they know that their creations need to be adaptable. "We must prepare for unforeseen situations beyond the scope of expectation and imagination," says Satoshi Tadokoro, a roboticist at Tohoku University in Sendai, Japan, who led development of Quince.

THE STRUGGLES of Japanese roboticists came despite a national program in the 1980s to develop robotics for nuclear power plants. One of the first was AMOOTY, which Toshiba and University of Tokyo researchers built in 1985. The radiation-hardened crawler could climb stairs and manipulate objects in mock power plants. But in 1999,

when an accident at a uranium reprocessing facility in Tokaimura killed two workers and contaminated the plant, AMOOTY was still considered too experimental to use.

In the years after Tokaimura, Japan developed other nuclear disaster robots and imported Menhir, a large mobile unit built by France's Cybernetix that's equipped with radiation shielding, cameras, and a

manipulator. But well before the Fukushima disaster, TEPCO and other industry testers judged them to be too big, slow, and ineffective. Government funding ran out, and Menhir is now on display at Tohoku University. The other machines were mothballed or cannibalized for parts, according to *The Asia-Pacific Journal: Japan Focus*; misplaced faith in the safety of nuclear plants and lack of long-term funding scuppered the program.

After the catastrophe of 11 March 2011, the first task for robots was to survey dam-

"We must prepare for unforeseen situations beyond the scope of expectation and imagination."

Satoshi Tadokoro,
Tohoku University

age, radiation, and variables such as temperature and humidity in areas that were too hazardous for workers. The PackBot droids explored the ground floors of the Unit 1 and Unit 3 reactor buildings, and found maximum radiation levels of tens of millisieverts (mSv) per hour. Workers exposed to such levels for less than a workday would exceed their emergency safety limit for an entire year, 250 mSv. The radiation and temperature maps made by the PackBots and two iRobot 710 Kobra bots allowed TEPCO workers to plot paths for quick forays into the reactor buildings with the least radiation exposures, says iRobot Vice President Tim Trainer in Bedford, Massachusetts.

But the complex structure of the reactor buildings' ground and upper floors, with many staircases and thick concrete walls, challenged robot mobility and wireless communications. The iRobot bots couldn't climb slippery stairs or turn corners easily. Once it was clear that more capable machines were needed, TEPCO and the government contacted roboticists at Chiba Institute of Technology and Tohoku University. They hastily modified Quince, a survey droid on caterpillar treads that climbs stairs and debris, by equipping it with two cameras, a dosimeter, and a power and communications cable that stretched hundreds of meters. Quince explored the upper floors of the Unit 2 re-

actor building. More sophisticated versions, dubbed Rosemary and Sakura, were also sent into the reactor buildings. Sakura acts as a communications relay, and Rosemary is equipped with a U.K.-developed system that combines radiation meters, a fisheye camera, and a laser rangefinder to produce 3D radiation maps.

By now, nearly a dozen robots have been developed to get closer looks at the heart of the plant. Some float or swim through pools that have formed in the building's bowels because of the constant need to inject water to cool the damaged cores. Two snake-like robots crawled through a pipe leading into the 48-meter-tall primary containment vessel in the Unit 1 reactor to ascertain the state of melted fuel masses. Although one got stuck, the machines returned valuable video and dose information, according to TEPCO. In the dark and vaporous interior, the robots measured radiation in one area as high as 25 sieverts per hour—enough to kill a person in minutes.

Makers are now developing robots that can tackle specific decommissioning chores. For example, Toshiba has developed machines that decontaminate surfaces with blasts of dry ice, inspect vent pipes for leaks, and cut and remove debris covering fuel rod assemblies in the Unit 3 building, which was damaged by a hydrogen explo-

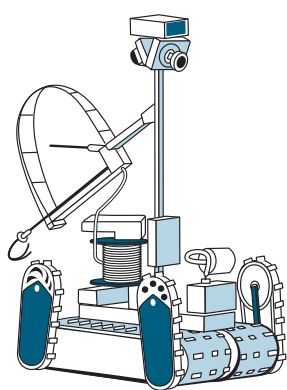
sion. Honda developed a robot based on Asimo's joint-stabilization technology that can extend 7 meters vertically to inspect upper nooks. "Every robot needed differs according to its purpose and the damage," says Tomohisa Ito, a spokesperson for the International Research Institute for Nuclear Decommissioning here, a consortium of nuclear plant companies that aims to develop new technologies for cleaning up the Fukushima plant.

Robots' slow start at Fukushima holds a broader lesson, says Gill Pratt in Boston, an engineer who led the Defense Advanced Research Projects Agency Robotics Challenge from 2012 to 2015 before joining Toyota to head its new artificial intelligence lab. Roboticists, he says, need to develop emergency robotic equipment that can be deployed immediately without the need for additional training or adaptation. "The great lesson of Fukushima," Pratt says, "is that disasters are often fast moving and difficult to predict events, where the window of time for effective intervention is small." In the immediate aftermath of a future nuclear accident, robots, and their masters, will have to be far nimbler. But at least at Fukushima, they are evolving. ■

Timothy Hornyak is a freelance reporter based in Tokyo.

Into the hot zone

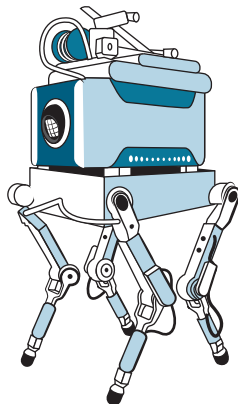
At the stricken Fukushima nuclear power plant, robots are performing an increasing variety of tasks in areas that are too radioactive for people to work in. Here are a few of the top performers.



Quince, Rosemary, and Sakura

TOHOKU UNIVERSITY/CHIBA KODAI

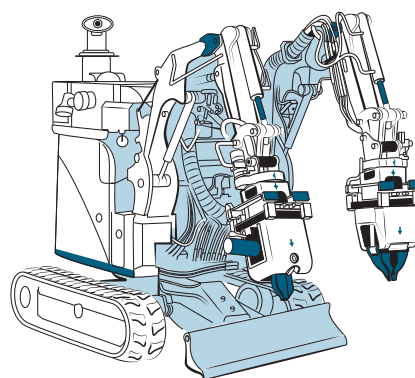
A modified earthquake rescue robot, Quince was the first Japanese bot to enter the nuclear plant's wrecked buildings. Smaller and nimbler than its U.S. military counterparts, Quince and its successors Rosemary and Sakura have gathered data for radiation maps, sampled airborne radioactive particles, and monitored radiation dose rates.



Quadraped inspection robot

TOSHIBA

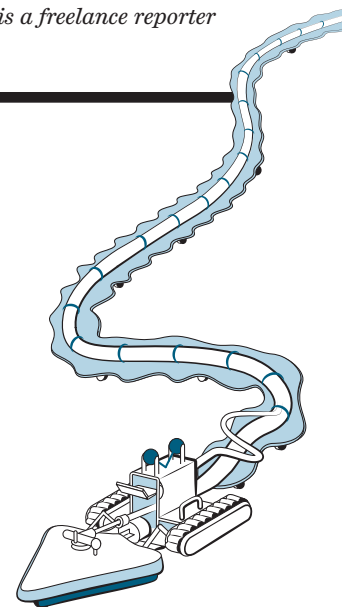
With its four multijointed legs, this 65-kilogram droid has a mobility advantage over crawling robots: It can climb stairs and access hard-to-reach crannies. The quadraped inspection robot verified that there were no leaks in the Unit 2 primary containment vessel, the crucible holding the partially melted down reactor.



ASTACO-SoRa

HITACHI GE NUCLEAR ENERGY

Whereas most robots at the Fukushima plant have been used for surveys, this 2.5-ton shovel-welding robot has done yeoman's work removing debris such as sheet metal, fallen ducts, concrete chunks, and nitrogen canisters from reactor Units 1 and 3. Its two arms are equipped with swappable manipulators such as grippers and rotating blades.



Raccoon

ATOX

Working with a relay robot that wrangles its water hoses, Raccoon is a nuclear-hardened maid that has been scrubbing the floors of Unit 2. Its decontamination work has helped tamp down radiation levels to the point that human workers can access the interior for decommissioning tasks. Raccoon doesn't do walls or windows.

EPIDEMIC OF FEAR

A bumper crop of thyroid abnormalities in Fukushima children, including cancer, has perplexed scientists and alarmed locals

By Dennis Normile

The March 2011 meltdowns at the Fukushima Daiichi Nuclear Power Plant caused extensive human suffering—evacuations, emotional trauma and premature deaths, disrupted jobs and schooling. What they have not caused, so far, is radiation-related illness among the general public, and few specialists expect dramatic increases in cancers or other ailments. The reactors spewed just a tenth of the radiation emitted by the Chernobyl disaster, winds blew much of that out to sea, and evacuations were swift. Yet one wave of illness has been linked to the disaster—the ironic result of a well-intentioned screening program.

Months after the disaster, Fukushima Prefecture set about examining the thyroids of hundreds of thousands of children and teens for signs of radiation-related cancers. The screening effort was unprecedented, and no one knew what to expect. So when the first round of exams started turning up thyroid abnormalities in nearly half of the kids, of whom more than 100 were later diagnosed with thyroid cancer, a firestorm erupted.

One result, says Kenji Shibuya, a public health specialist at University of Tokyo, was “overdiagnosis and overtreatment,” leading dozens of children to have their thyroids removed, perhaps unnecessarily. Activists trumpeted the findings as evidence of the dangers of nuclear power. The large number of abnormalities appearing so soon after the accident “would indicate that these children almost certainly received a very high dose of thyroid radiation from inhaled and ingested radioactive iodine,” antinuclear crusader Helen Caldicott wrote in a post on her homepage.

Scientists emphatically disagree. “The evidence suggests that the great majority and perhaps all of the cases so far discovered are not due to radiation,” says Dillwyn Williams, a thyroid cancer specialist at University of Cambridge in the United Kingdom. In journal papers and in a series of letters published last month in *Epidemiology*, scientists have attacked the alarmist

interpretations. Many acknowledge that baseline data from noncontaminated areas were needed from the outset and that the public should have been better educated to understand results and, perhaps, to accept watchful waiting as an alternative to immediate surgery. But most also say the findings hint at a medical puzzle: Why are thyroid abnormalities so common in children? The “surprising” results of the screening, Williams says, show that “many more thyroid carcinomas than were previously realized must originate in early life.”

MEMORIES OF CHERNOBYL got Japanese authorities worrying about thyroid cancer. The fallout from that April 1986 accident included radioactive iodine, which settled across swathes of Belarus, Russia, and Ukraine, contaminating pastures grazed by dairy cows. Children who drank the tainted milk accumulated the radioactive iodine in their thyroids. (Adult thyroids absorb less iodine.) A 2006 World Health Organization (WHO) study found that in the most contaminated areas, there had been about 5000 thyroid cancer cases among those who were under 18 at the time of the accident, though the report noted that more cases could emerge over time. The United Nations in 2006 attributed 15 childhood thyroid cancer deaths to Chernobyl. Caught early, the cancer is almost always cured by removal of the thyroid gland.

With that in mind, Japanese authorities set out to screen the thyroids of all 368,651 Fukushima residents who were 18 and under at the time of the accident (*Science*, 5 August 2011, p. 684). Most experts were not anticipating a bumper crop of thyroid problems. For starters, the potential radiation exposure of Fukushima residents was slight compared with Chernobyl victims. More-

over, the day after the meltdowns, Japanese authorities evacuated some 150,000 people living within 20 kilometers of the plant, and a week later they started screening for contaminated food. In addition, Fukushima residents were offered iodine tablets after the accident to block absorption of any radioactive iodine that managed to find its way into the food supply.

In 2013, WHO estimated that the 12 to 25 millisieverts (mSv) of exposure in the first year after the accident in the hardest hit areas might result in minuscule increases in cancer rates. (Worldwide, people receive on average 2.4 mSv per year from background radiation; a medical chest x-ray delivers about 0.1 mSv.) WHO noted that females have a 0.75% lifetime risk of

developing thyroid cancer; it estimated that the highest exposures in the Fukushima area raised that risk by an additional 0.5%.

The initial round of thyroid screening, started in late 2011, was simply to provide baseline data, as any radiation-induced tumors were not expected to emerge for at least 4 years. Children with nodules larger than 5.0 mm or cysts bigger than 20.1 mm underwent a second, more detailed examination and, if necessary, fine needle aspiration. After the initial screening, children will have their thyroids examined every 2 years until age 20 and every 5 years after that.

Results were released as screening progressed, and right from the start there were surprisingly high rates

of abnormalities. Findings from the initial round of screening, completed in April 2015 and released in August 2015, showed that nearly 50% of the 300,476 subjects had solid nodules or fluid-filled cysts on their thyroids. Smaller studies elsewhere had hinted that tiny thyroid cysts and nodules were common in all ages. But “specialists

300,476

Number of Fukushima residents 18 and under whose thyroid screening results were available as *Science* went to press.

50%

Approximate fraction of those screened with solid nodules or fluid-filled cysts on their thyroids.

110

Number of thyroid cancer cases identified by December 2014 as a result of the screening.



In Iwaki, a town south of the Fukushima nuclear plant, a doctor conducts a thyroid examination on 4-year-old Maria Sakamoto. Scientists are puzzled over a high number of thyroid abnormalities observed so soon after the accident.

did not know whether the frequency [in the Fukushima results] was high or low,” says Noboru Takamura, a radiation health scientist at the Atomic Bomb Disease Institute at Nagasaki University in Japan.

As the number of confirmed cancers rose, worries grew about a link to radiation—and those concerns gained a high-profile proponent. In 2013, Toshihide Tsuda, an environmental epidemiologist at Okayama University in Japan, started presenting analyses at international conferences claiming the number of thyroid cancers in the Fukushima screening was unusually high. Last October, he published his results online in *Epidemiology*, concluding that the first round of screening indicated cancer incidence rates ranging from 0 to 605 cases per million kids, depending on location, but overall “an approximately 30-fold increase” over the normal childhood cancer rate. That claim fed alarming headlines.

Other scientists were swift and severe in their criticism. A fundamental error, according to several epidemiologists, is that Tsuda compared the results of the Fukushima survey, which used advanced ultrasound devices that detect otherwise unnoticeable growths, with the roughly three cases of thyroid cancer per million found by tra-

ditional clinical examinations of patients who have lumps or symptoms. “It is inappropriate to compare the data from the Fukushima screening program with cancer registry data from the rest of Japan where there is, in general, no such large-scale screening,” Richard Wakeford, an epidemiologist at the University of Manchester in the United Kingdom, wrote on behalf of 11 members of a WHO expert working group on Fukushima health consequences. Theirs was one of seven letters to *Epidemiology* published online last month that blasted Tsuda’s methodology and conclusions.

To see what comparable screening would find in a population not exposed to radiation, Takamura’s team used the Fukushima survey protocol to examine 4365 children aged 3 to 18 from three widely separated prefectures. They found similar numbers of nodules and cysts and one cancer, for a prevalence of 230 cancers per million people, as they reported in *Scientific Reports* in March 2015. Other Japanese studies reported thyroid cancer rates of 300, 350, and even 1300 per million. “The prevalence of thyroid cancer detected by advanced ultrasound techniques in other areas of Japan does not differ meaningfully from that in Fukushima Prefecture,” Takamura

wrote in *Epidemiology*. In a letter to *Epidemiology*, Tsuda claims to have addressed the screening effect by adjusting the number of cancer cases to account for the lag time between when an ultrasound examination would catch the cancers and when they could be clinically identified. He did not address other criticisms or respond to repeated requests for comment from *Science*.

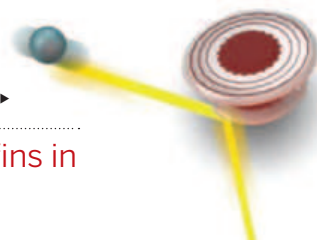
Although many scientists disagree with the spin Tsuda and activists have put on the findings, they endorse the screening effort. “A thyroid screening program would be expected to save lives by detecting cancers early, whether or not the cancers were caused by radioactivity,” says Timothy Jorgensen, a radiation health physicist at Georgetown University in Washington, D.C.

Yet it has become clear the public and even many doctors did not have the background to put the results in perspective. Even though the vast majority of thyroid abnormalities are safe to ignore, “finding small lesions causes patients anxiety,” says Seiji Yasumura, vice director of the Fukushima Prefecture Health Management Survey. Virtually all of those diagnosed with thyroid cancer have had the glands removed, even

though accumulating evidence suggests in many cases it might have been better to wait, the University of Tokyo’s Shibuya adds. “Careful observation would be the best option.”

South Korea offers a cautionary tale. In 1999, the South Korean government initiated a health program in which care providers offered ultrasound thyroid screening for a small additional fee—and thyroid cancer diagnoses exploded. In 2011, the rate of thyroid cancer diagnosis was 15 times what it was in 1993, yet there was no change in thyroid cancer mortality, Heyong Sik Ahn of Korea University in Seoul and colleagues reported in *The New England Journal of Medicine* in November 2014. Virtually all those diagnosed underwent total or partial thyroid removal. Most required lifelong thyroid-hormone replacement therapy. To stem this “epidemic,” Ahn and others discourage routine thyroid cancer screening.

Williams says the evidence suggests that thyroid growths among children are far more common than previously thought and must be considered normal. The Fukushima survey, he says, promises a “better understanding of the origins and development” of such growths and may lead to better treatment protocols. ■



PERSPECTIVES

RESEARCH INTEGRITY

Liberating field science samples and data

Promote reproducibility by moving beyond “available upon request”

By Marcia McNutt,^{1*} Kerstin Lehnert,²
Brooks Hanson,³ Brian A. Nosek,⁴ Aaron
M. Ellison,⁵ John Leslie King⁶

Transparency and reproducibility enhance the integrity of research results for scientific and public uses and empower novel research applications. Access to data, samples, methods, and reagents used to con-

duct research and analysis, as well as to the code used to analyze and process data and samples, is a fundamental requirement for transparency and reproducibility. The field sciences (e.g., geology, ecology, and archaeology), where each study is temporally (and often spatially) unique, provide exemplars for the importance of preserving data and samples for further analysis. Yet field sciences, if

POLICY

they even address such access, commonly do so by simply noting “data and samples available upon request.” They lag behind some laboratory sciences in making data and samples available to the broader research community. It is time for this to change. We discuss cultural, financial, and technical barriers to change and ways in which funders, publishers, scientific societies, and others are responding.

ILLUSTRATION: D. BONAZZI/@SALZMANART

Repeating a study from start to finish using new samples and equivalent procedures under identical conditions is the ideal. This may be practical in laboratory sciences but is rarely possible in field sciences. Objects of study might be ephemeral (Superstorm Sandy), exceptionally rare (*Dreadnoughtus*), or forever changing (succession in a forest or how climate affects a prairie ecosystem). Nevertheless, transparency and reproducibility have substantial value for field sciences. Independent analysis of original data can uncover statistical or coding errors, data selection bias, or problems with observations that are “too good to be true.” Original analyses may be augmented with new techniques to test novel questions. Data and samples can be combined across studies for more precise or generalizable tests [e.g., the Paleobiological Database (1) or PetDB database (2)].

Such efforts must recognize that motivations for promoting transparency and reproducibility vary by stakeholder. Researchers want to produce knowledge in new directions and to get credit for their contributions. Funders want to see greater value from their investment. Journals want to facilitate reproducible science. Repositories want to support their communities and streamline data flow.

FUNDING, PUBLISHING, AND CULTURE CHANGE. Transparency and reproducibility in scientific research require investment. Quality control is costly, and even large projects can have difficulty curating data to make them useful for others. For example, many data sets in ecology and evolution publications are incomplete or inaccessible (3). Funders that support domain-specific data and sample repositories do so because they advance science by facilitating preservation and reuse, as well as support data professionals who help with collection, management, and curation.

U.S. and UK funding agencies require publicly supported researchers to provide data management plans and use open repositories for data and samples. Investigators are often allowed reasonable amounts of time between collection and deposition (e.g., up to 2 years) for quality control or publication priority, but making data and samples available sooner can advance science more rapidly [e.g., (4)]. The U.S.

National Science Foundation’s PASSCAL (Portable Array Seismic Studies of the Continental Lithosphere) and OOI (Ocean Observatory Initiative) projects are examples of programs that are acclimating communities to more progressive data-sharing policies, demonstrating research gains, and undermining arguments against open data.

Initiatives such as OpenAIRE and the Center for Open Science are advancing principles and guidelines for transparent research and publication. More than 500 journals have indicated intent to review the TOP (Transparency and Openness Promotion) (5) publication guidelines for potential implementation. However, journals that require that data and samples be deposited upon publication may suffer if journal staff lack resources to verify deposition, evaluate metadata, or check code accessibility of code or other materials.

“All should credit data creators and accelerate recognition of the value of data in the...system.”

Funding agencies and journals can guide expectations and set requirements, but top-down mandates alone are unlikely to foster needed cultural changes in scientific communities. Research culture prioritizes publications, innovation, and insight, which puts data stewardship and reuse far down the list. Data professionals in large projects too often are invisible team members. To change this, bottom-up approaches are needed to earn community buy-in and effect culture change to recognize researchers who develop and curate original data (6): Principal investigators can lead by example; universities can offer education in data and samples management; and scholarly societies can recognize excellence in data and samples stewardship in their awards, selection of fellows, and leadership. Development of data journals with citable output can provide data experts acknowledged leadership roles.

REPOSITORIES, CITATIONS, AND CURATION. Although general-purpose repositories are useful for data that do not fit easily within a specific domain, the value of preserved data is best maximized by discipline-specific repositories. They can provide services informed by community priorities, which can promote cultural change.

Repositories can improve quality control and compliance, but progress will be faster if repositories move beyond curation and provide value-added services, such as certi-

fying to journals completion of deposition requirements. Because deposition alone does not guarantee that data or samples are discoverable or usable, machine-readable, quality-controlled, public metadata would help researchers find, understand, and use the resources. Automated services can promote cost-effective and data-conscious research cultures, while providing incentives to data collectors by demonstrating impact through metrics of views, downloads, and data and sample uses. The Open Science Framework (<http://osf.io/>) connects repositories so authors can find domain-specific repositories and provides links to general-purpose repositories for unusual classes of data (7).

Repositories can expand assignments of digital object identifiers (DOIs) to data sets to aid citation. International initiatives, including DataCite (www.datacite.org) and the IGSN e.V. (www.igsn.org, International Geo Samples Numbers), develop and promote common conventions for unambiguous identification and citation of data and samples to enhance usability, to guard against loss, and to provide credit to creators. Publishers can adopt resolutions such as the Joint Declaration

of Data Citation Principles (8) that specify data citation in the references. Journals can publish descriptions of data sets and methods. All should credit data creators and accelerate recognition of the value of data in the scientific reward system.

Despite many efforts, there remains widespread disagreement regarding data and sample availability and metadata, as well as uneven sample deposition across the field sciences. Journals might use DOIs for data or accession numbers for curated samples (e.g., IGSNs), but these are not used routinely. Journals that ensure precise descriptions of variables, data, or sample provenance and that provide details concerning collecting permits and requirements or restrictions for reuse can help. However, such information must come from those closest to the data and samples—the researchers themselves. Scientists and technical staff must know how to create such information and be supported by funding agencies to do so. Repositories could provide user-friendly software and training to field teams to overcome resistance to sharing data and samples.

Scientific societies can work with stakeholders to set guidelines for provenance of metadata; access; and security or ethical restrictions (e.g., for protecting human subjects or rare and endangered samples); and cooperate with all journals, not just those they own or sponsor. Community partnerships [e.g., COPDESS (Coalition for Publishing Data in the Earth and Space Sci-

¹Editor-in-Chief, *Science*, Washington, DC 20005 USA.

²Columbia University, Palisades, NY 10964 USA. ³American Geophysical Union, Washington, DC 20009 USA. ⁴University of Virginia and Center for Open Science, Charlottesville, VA 22903 USA. ⁵Harvard University, Petersham, MA 01366 USA.

⁶University of Michigan, Ann Arbor, MI 48109 USA.

^{*}E-mail: mmcnutt@aaas.org

ences) (9)] can provide discipline-specific metadata and effective quality control with secure badging for journal verification. The Research Data Alliance (RDA) is developing approaches and infrastructure for the publishing community.

Finally, not every sample can be saved. Museums and other special-purpose repositories (e.g., ice-core labs) face resource and space limitations. Curators must decide what to keep. Samples supporting peer-reviewed publications should have priority. Digitized samples and collection information or other metadata will facilitate remote examination. Digital catalogs can provide persistent access to metadata on samples used in publications. These should include information on access linked to publications via resolvable unique identifiers such as the IGSN. The System for Earth Sample Registration (SESAR), iDigBio, and Cyverse provide examples of metadata profiles.

By working together, stakeholders can create a virtuous cycle of increasing data and sample accessibility. The days when scientists held on to samples and data hoping to squeeze out one more publication are ending. Sharing can be more productive than hoarding when researchers get credit for use of their data or samples. The citation advantage for papers with open data (10) suggests that stakeholders help themselves by promoting transparency and reproducibility. ■

REFERENCES AND NOTES

1. Paleobiological Database, <https://paleobiodb.org/#/>.
2. D. B. Pet, <http://www.earthchem.org/petdb>.
3. D. G. Roche, L. E. B. Kruuk, R. Lanfear, S. A. Binning, *PLOS Biol.* **13**, e1002295 (2015).
4. D. Lindenmayer, G. E. Likens, *Ecol. Soc. Am. Bull.* **94**, 338 (2013).
5. B. A. Nosek, G. Alter, G. C. Banks, D. Borsboom, S. D. Bowman, S. J. Breckler, S. Buck, C. D. Chambers, G. Chin, G. Christensen, M. Contestabile, A. Dafoe, E. Eich, J. Freese, R. Glennerster, D. Goroff, D. P. Green, B. Hesse, M. Humphreys, J. Ishiyama, D. Karlan, A. Kraut, A. Lupia, P. Mabry, T. A. Madon, N. Malhotra, E. Mayo-Wilson, M. McNutt, E. Miguel, E. L. Paluck, U. Simonsohn, C. Soderberg, B. A. Spellman, J. Turitto, G. VandenBos, S. Vazire, E. J. Wagenmakers, R. Wilson, T. Yarkoni, Promoting an open research culture. *Science* **348**, 1422–1425 (2015).
6. J. A. Mills *et al.*, *Trends Ecol. Evol.* **30**, 581 (2015).
7. S. Buck, *Science* **348**, 1403 (2015).
8. Data Citation Synthesis Group, Joint Declaration of Data Citation Principles, M. Martone, Ed. (FORCE11, San Diego CA; 2014); www.force11.org/group/joint-declaration-data-citation-principles-final.
9. B. Hanson, K. Lehnert, J. Cutcher-Gershenfeld, *Eos* **96**, 10.1029/2015EO022207 (2015).
10. H. A. Piwowar, T. J. Vision, *Peer J.* **1**, e175 (2013).

ACKNOWLEDGMENTS

These recommendations resulted from a workshop supported by the Laura and John Arnold Foundation. Attendees who helped shape these recommendations include P. G. Brewer, B. Clement, C. Duke, D. Erwin, L. Ferguson, R. Freckleton, A. Friedlander, T. Gardner, B. Grocholski, L. Hale, S. Hageman, J. Kratz, W. J. Kress, M. Morovati, M. Parsons, K. Ram, M. Ramamurthy, H. J. Smith, A. Sugden, M. Uhen, J. VanDecar, T. Vision, N. Wigginton, and R. Wakimoto.

10.1126/science.aad7048

PHYSICS

Electrons go with the flow in exotic material systems

Electronic hydrodynamic flow—making electrons flow like a fluid—has been observed

By Jan Zaanen

Turn a switch and the light goes on. The layman's perception is that this is like opening a tap so that the water starts running. But this analogy is misleading. The flow of water is governed by the theory of hydrodynamics, whereby the behavior of the fluid does not require knowledge of the motions of individual molecules. Electrical currents in solids, however, are formed from electrons. In metals, these do not collide with each other, but they do scatter from lattice imperfections. The resulting “Knudsen flow” of electrons is reminiscent of the avalanche of balls cascading through a dense forest of pins, as in a Pachinko machine. On pages 1058, 1055, and 1061 of this issue, evidence is presented that electrons can actually yield to the laws of hydrodynamics (1–3). What is additionally surprising is that these observations are in agreement with mathematical techniques borrowed from string theory (4). These techniques have been applied to describe strongly interacting forms of quantum matter, predicting that they should exhibit hydrodynamic flows (5).

The experiments have been made possible by progress in new materials and nanofabrication techniques. Two of the papers report on complementary aspects of the electron hydrodynamics in graphene (1, 2). The third paper deals with an oxide material that exhibits highly surprising transport properties. By confining the electrical currents to nanoscale pipes, hydrodynamic flow is demonstrated (3).

The flow of substances is governed by simple conservation laws: Matter, energy, and electrical charge are naturally conserved, while in a perfectly homogeneous space the velocity of an aggregate of matter is not changing either; that is, momentum is also conserved. A classical fluid, such as water, looks like a dense traffic of colliding water molecules exchanging momentum at a very high rate. However, their combined momentum does not change unless

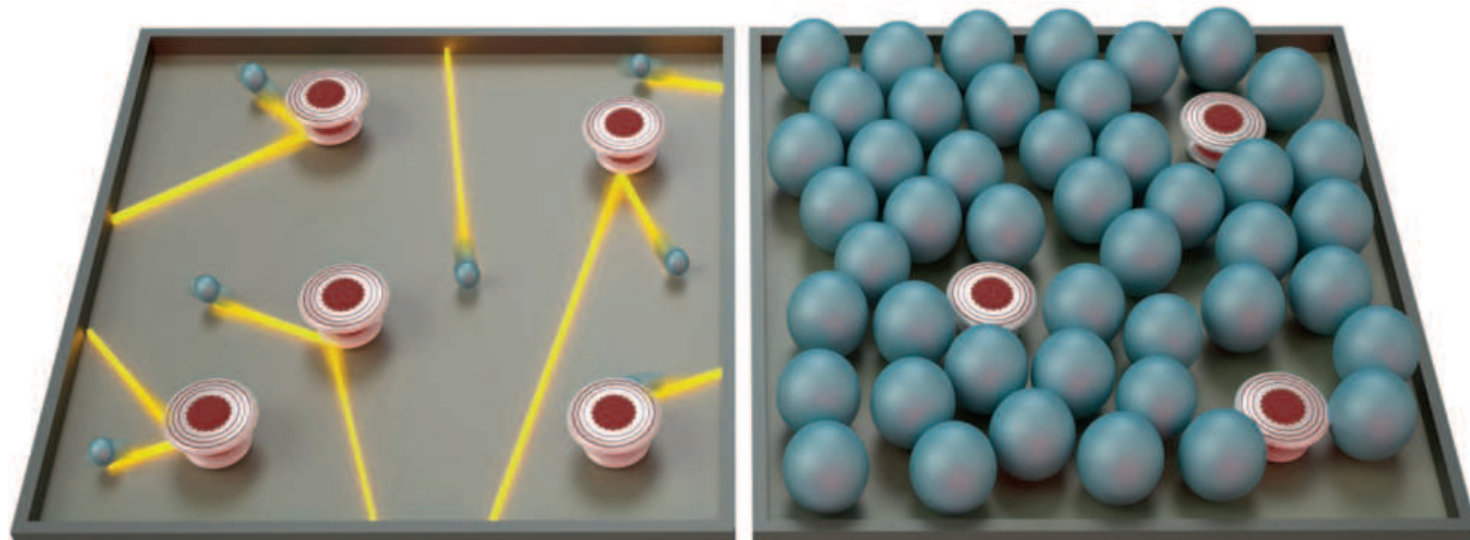
the space they are moving in is made inhomogeneous by, for example, putting the water in a pipe such that the overall momentum relaxes and the kinetic energy turns into heat. Electrons in solids, however, move in a background of static ions, breaking this translational invariance, and imperfections occur even in the most perfect periodic crystals. It is now a matter of numbers. Could it be the case that an individual electron can lose its momentum because of scattering from the ionic disorder before it meets another electron (Knudsen flow) (see the figure, left panel), or will the electron fluid equilibrate first through many electron-electron collisions without noticing the imperfections (hydrodynamic regime) (right panel)?

To better understand the situation, we must invoke quantum physics. On the microscopic scale, electrons in solids are strongly interacting, but quantum many-body systems submit to the principle of

“...hydrodynamic flows are much richer than the diffusive currents that have been the traditional mainstay of solid-state electronics.”

renormalization, in which the electrons' behavior is dependent on the scale at which the system is observed. In conventional metals, the renormalized electrons increasingly ignore each other as the energy decreases. On the macroscopic scale, the electrons behave like the individual balls of the Pachinko machine. However, it might well happen that the effects of the interactions increase as the energy decreases (giving rise to a complex quantum soup), and until now we did not have the mathematical tools to describe transport in the resulting highly collective quantum state. Recently, it has been shown that the mathematical machinery developed by string theorists can

Instituut-Lorentz for Theoretical Physics, Leiden University, Leiden, Netherlands. E-mail: jan@lorentz.leidenuniv.nl



Distinguishing different flow regimes. (Left) In conventional metals, the flow of electrical current is due to electrons (balls) moving independently as a consequence of quantum physics while scattering against crystal imperfections (bumpers). **(Right)** In normal fluids such as water, the molecules collide with each other, equilibrating in a macroscopic fluid that is described by the theory of hydrodynamics. Electrons in particular solids that form strongly interacting quantum systems are also found to exhibit hydrodynamic transport properties (1–3).

be used to describe general features of such quantum soups (4), predicting that at finite temperature they have a strong tendency to form hydrodynamic fluids. Evidence for such behavior has surfaced in seemingly unrelated areas of physics (4): the quark-gluon plasma created in high-energy colliders, and the unitary fermion gas of cold-atom physics. These findings raised the question of whether such behavior could also occur for electrons in metals (5).

Graphene is a strong candidate to meet the required conditions. An advantage of this material is the remarkable perfection of its crystal structure. Its electrons are also known to mimic the behavior of the relativistic fermions of high-energy physics (6). Considering their many-body physics, the electrons in graphene exhibit the special renormalization property that the interactions are marginally irrelevant, meaning that at zero temperature the electrons behave as independent particles, but upon raising energy or temperature the interactions grow rapidly, tending toward the quantum soup of string theory (7).

To observe the predicted hydrodynamic behavior, Crossno *et al.* (1) exploited the property of the graphene electron system that it is like a “Dirac vacuum” with no net density of particles. Upon raising temperature, negatively and positively charged “particles” and “antiparticles” are thermally excited, but they occur in precisely the same amount. In an electrical field, the particles and antiparticles move in opposite directions, with the effect that the whole system does not move. However, by applying a temperature difference, a heat current is

induced with the particles and antiparticles moving in the same direction; this current is sensitive to momentum conservation (8). The data signatures of hydrodynamical behavior can then be discerned, which on closer inspection appear to be consistent with the notion that these are rooted in the strongly interacting quantum nature of this electron system (9).

Bandurin *et al.* (2) present complementary evidence. They exploited qualitative differences in the flow patterns associated with hydrodynamic versus Knudsen flows. They manufactured a device to probe the current patterns that are formed upon injecting a current through a narrow nozzle in a graphene sheet. These turn out to be impossible to explain on the basis of Knudsen flow, but are in accord with the whirling patterns formed by a hydrodynamic description (10).

Moll *et al.* (3) studied PdCoO_3 , a material as disorder-free as graphene but entirely different in other respects. Although oxide metals are strongly interacting electron systems, this one is known to be a weakly interacting metal. But its transport properties are anomalous—it is exceptionally conductive. Moll *et al.* flowed electrons in long conduction channels, or pipes, with variable widths. In hydrodynamic flow, the resistance is determined by the channel width in such a way that it can be sharply distinguished from the Knudsen flow (11).

It is a remarkable coincidence that three groups have presented independent evidence for electron hydrodynamics. Such hydrodynamic flows are much richer than the diffusive currents that have been the

traditional mainstay of solid-state electronics. It will therefore be interesting to see whether behavior associated with hydrodynamics (shocks, turbulence, etc.) can be incorporated into electronic device technology. There is also the possibility of using hydrodynamic flow as a diagnostic to detect whether the states of strongly interacting quantum matter predicted by theory are actually realized in nature. Although these applications represent tantalizing possibilities, it will be a grand challenge for experimentalists to tame these usually difficult materials to a degree that they can be subjected to the controlled nanofabrication required to detect the hydrodynamic flow. ■

REFERENCES

1. J. Crossno, J. K. Shi, K. Wang, X. Liu, A. Harzheim, A. Lucas, S. Sachdev, P. Kim, T. Taniguchi, K. Watanabe, T. A. Ohki, K. C. Fong, *Science* **351**, 1058 (2016).
2. D. A. Bandurin, I. Torre, R. Krishna Kumar, M. Ben Shalom, A. Tomadin, A. Principi, G. H. Auton, E. Khestanova, K. S. Novoselov, I. V. Grigorieva, L. A. Ponomarenko, A. K. Geim, M. Polini, *Science* **351**, 1055 (2016).
3. P. J. W. Moll *et al.*, *Science* **351**, 1061 (2016).
4. J. Zaanen, Y.-W. Sun, Y. Liu, K. Schalm, *Holographic Duality in Condensed Matter Physics* (Cambridge Univ. Press, 2015).
5. S. A. Hartnoll, P. K. Kovtun, M. Mueller, S. Sachdev, *Phys. Rev. B* **76**, 144502 (2007).
6. A. H. Castro Neto *et al.*, *Rev. Mod. Phys.* **81**, 109 (2009).
7. M. Mueller, J. Schmalian, L. Fritz, *Phys. Rev. Lett.* **103**, 025301 (2009).
8. M. S. Foster, I. L. Aleiner, *Phys. Rev. B* **79**, 085415 (2009).
9. A. Lucas, J. Crossno, K. C. Fong, P. Kim, S. Sachdev, <http://arxiv.org/abs/1510.01738> (2015).
10. L. Levitov, G. Falkovich, <http://arxiv.org/abs/1508.00836> (2015).
11. M. J. M. de Jong, L. W. Molenkamp, *Phys. Rev. B* **51**, 13389 (1995).

10.1126/science.aaf2487

NEUROSCIENCE

Wiring the altruistic brain

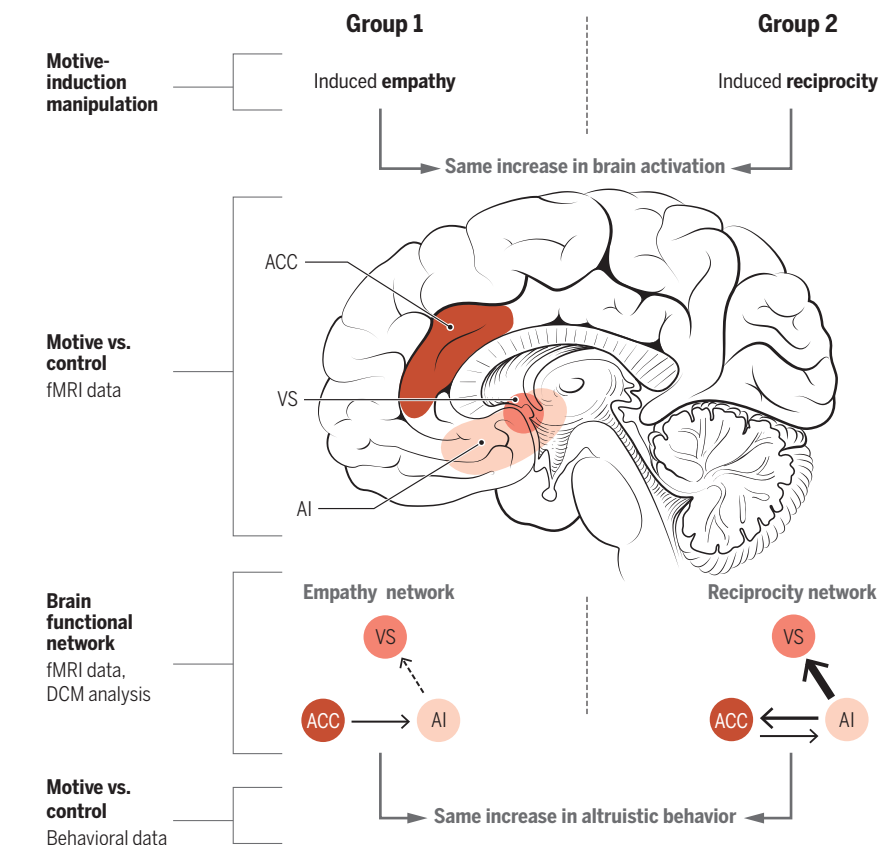
Communication between brain regions uncovers hidden motives for generous behavior

By Sebastian Gluth and Laura Fontanesi

Contrary to classical economic supposition (1), understanding people's preferences and decisions is not as simple as observing their actions. Indeed, there are many reasons for behaving altruistically, such as being moved by someone's suffering (empathy) or feeling obliged to return a favor (reciprocity) (2, 3). One of the major challenges for social psychologists and neuroscientists is to characterize the different motives underlying our interactions with other people. On page 1074 in this issue, Hein *et al.* (4) show that knowing how distinct areas in the human brain communicate with each other can tell us why someone behaves altruistically.

To induce different motives for altruism, Hein *et al.* developed a clever experimental design in which a participant first interacts with two partners (who received specific instructions from the authors) in one of two scenarios. In one experimental group, a participant observes one partner receiving painful shocks, thereby eliciting an empathic response in the participant (empathy group). In the other group, a participant observes a partner sacrificing money to save the participant from receiving painful shocks, thereby eliciting a desire in the participant to return the kind behavior (reciprocity group). In both groups, the participant is also paired with a second partner who serves as a control—that is, a second person who does not receive painful shocks in the empathy group, or who does not sacrifice money to relieve the participant's shock treatment in the reciprocity group.

Following this phase of motive induction, all participants performed a money allocation task. They chose between maximizing a partner's monetary payoff by reducing their own (prosocial behavior) or holding on to the money at a cost to the other person (selfish behavior). During this task, the participants'



The altruistic brain. By eliciting different motives, the same increase in brain activation and in altruistic behavior is observed, but the functional coupling between activated brain regions differs. Continuous and dashed arrows indicate positive and negative connections, respectively. Thicker arrows indicate stronger connections. ACC, anterior cingulate cortex; AI, anterior insula; VS, ventral striatum.

brains were scanned by functional magnetic resonance imaging (fMRI)—which uses changes in local blood flow as an indicator of neural activity changes—while they chose how to allocate the money. As expected, participants sacrificed more money to the empathy or reciprocity partner than to the control partner. Critically, this increased altruism did not differ between the groups, so that the hidden motive could not be accurately inferred from behavior alone. Hein *et al.* analyzed the neural data using a conventional contrast of brain activation during altruistic decisions toward the empathy/reciprocity partner versus the control partner. In line with previous work (5, 6), a brain network including anterior cingulate cortex (ACC), anterior insula (AI), and ventral striatum (VS) was identified. But again, this analysis did not reveal any differences between the two motives. However, when the authors examined how these brain areas interact with each other during altruistic decisions using dynamic causal modeling (DCM) (7), they observed a distinction. The connectivity patterns differed remarkably between empathy and reciprocity, and, by using a novel DCM-based classification technique (8), the authors successfully categorized par-

ticipants to their motive-induction treatment (see the figure). Hence, the reasons for being gracious to someone appear to be hidden in how cortical and subcortical structures communicate with each other.

The study of Hein *et al.* is an intriguing example of the richness and power of fMRI data, when we do not simply look for “activated blobs” in brain images, but investigate the flow of information between brain areas. In this spirit, the authors report that the functional networks of the empathy and the control condition are very similar to each other but dissimilar to the reciprocity network. This indicates that empathy-motivated altruism is perhaps (phylogenetically) more common than reciprocal altruism.

Hein *et al.* provide yet another striking finding. After categorizing participants as either selfish or prosocial on the basis of their behavior toward the control partner, they find that only selfish participants increase their donations toward the empathy partner, whereas only prosocial participants

Department of Psychology, University of Basel, Missionsstrasse 62a, 4055 Basel, Switzerland. E-mail: sebastian.gluth@unibas.ch

act (even) more generously toward the reciprocity partner. Provided that this result can be established as robust and generalizable to nonlaboratory contexts, it bears high relevance for social policy and for treatments of antisocial behavior: Whether we want to increase altruism in an already cooperative group or in individuals with deficits in prosocial skills, we should focus on emphasizing reciprocity or empathy, respectively.

The study raises many new questions, including whether these connectivity patterns are specific to pain-related altruism or general to any altruistic behavior. Furthermore, it remains open whether there is a causal relationship between the proper functioning of these networks and altruism—in other words, whether we can alter altruistic behavior by disrupting specific connections within the networks. In addition, how (differently motivated) altruistic decisions develop over time appears to be a particularly pressing question, given that Hein *et al.* did not model the decision process itself. Sequential sampling models, which describe decisions as a noisy process of accumulating evidence up to a response threshold, can explain exactly how and when decisions are made (9). These models have a long and successful history in accounting for perceptual and preferential decision-making, such as when we react to a red or green traffic light or when we choose between ice cream flavors, respectively. But their application to social interactions is just emerging (10). Because sequential sampling models take not only choices but also response times into account and break the decision process down into its elements (e.g., response conflict, decision urgency), they would offer an in-depth comparison of empathy- and reciprocity-based altruistic behavior. Moreover, given that sequential sampling model predictions can be used to inform DCM-based analyses of fMRI data (11), a closer inspection of the process that leads to selfish or prosocial actions is a promising avenue for future research. ■

REFERENCES AND NOTES

1. P. Samuelson, *Economica* **5**, 61 (1938).
2. E. Fehr, U. Fischbacher, *Nature* **425**, 785 (2003).
3. C. D. Batson, *The Altruism Question: Toward a Social Psychological Answer* (Erlbaum, Hillsdale, NJ, 1991).
4. G. Hein *et al.*, *Science* **351**, 1074 (2016).
5. K. L. Phan, C. S. Sripada, M. Angstadt, K. McCabe, *Proc. Natl. Acad. Sci. U.S.A.* **107**, 13099 (2010).
6. T. Singer *et al.*, *Nature* **439**, 466 (2006).
7. K. J. Friston *et al.*, *NeuroImage* **19**, 1273 (2003).
8. K. H. Brodersen *et al.*, *PLOS Comput. Biol.* **7**, e1002079 (2011).
9. P. L. Smith, R. Ratcliff, *Trends Neurosci.* **27**, 161 (2004).
10. C. A. Hutcherson, *et al.*, *Neuron* **87**, 451 (2015).
11. S. Gluth *et al.*, *Neuron* **86**, 1078 (2015).

ACKNOWLEDGMENTS

This work is supported by a Swiss National Science Foundation grant (100014_153616) to both authors.

10.1126/science.aaf4688

GENETICS

A copy-and-paste gene regulatory network

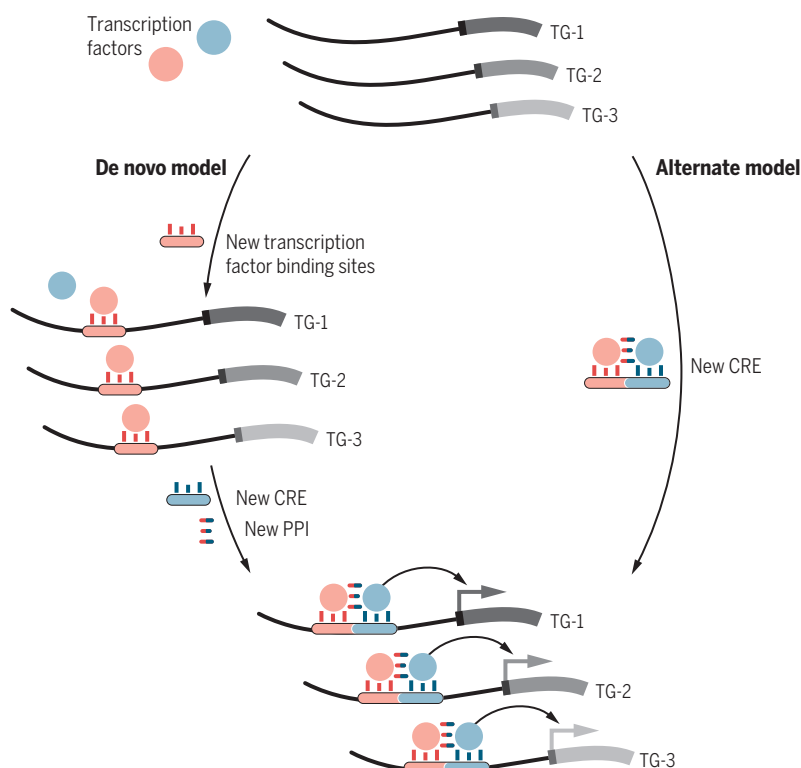
Transposable elements provide a ready-made route to regulate complex gene networks

By Vincent J. Lynch

Changes in gene regulatory networks (GRNs) underlie many phenotypic differences between species. However, the mechanisms of GRN evolution are still being debated (1–5). Explaining how GRNs originate, diversify, and maintain their identities despite regulatory element turnover is essential for developing mechanistic explanations for the origin, diversification, and conservation of homologous characters between species. Among the major outstanding questions in GRN evolution is whether individual cis-regulatory elements arise de novo through the gradual accumulation of mutations that increase the regulatory potential of existing DNA or

whether cis-regulatory elements originate more rapidly through concerted processes. On page 1083 of this issue, Chuong *et al.* provide evidence that concerted processes, involving endogenous retroviruses (ERVs), which are remarkably abundant in mammalian genomes, have contributed to the evolution of the regulatory systems that control the mammalian immune system (6).

Transposable element (TE)-mediated origination of cis-regulatory elements is an attractive alternative to the de novo appearance of such elements. TEs provide a mechanism to rapidly distribute nearly identical copies of regulatory elements across the genome that can respond to the same input signals (7–9) rather than requiring that each gene in a GRN evolve cis-regulatory



Plug-and-play gene regulatory network formation. The de novo model of GRN formation requires that each gene in the network (TG-1 to TG-3) independently evolve a new cis-regulatory element (CRE) that can bind to the same sets of transcription factors (red and blue circles). However, individual transcription factor binding sites may not be sufficient to activate target gene expression, requiring the evolution of additional binding sites for cooperating transcription factors or novel protein-protein interactions (PPIs) to recruit more transcription factors and cofactors. Alternatively, TEs can generate new regulatory networks by donating already functional cis-regulatory elements to neighboring genes.

elements capable of responding to the same stereotyped signals *de novo* (see the figure). The *de novo* origination model, for example, would require the independent evolution of the same transcription factor binding site(s) in many genes distributed across the genome, whereas TEs can donate the same sets of transcription factor binding sites to nearby genes upon their integration into the genome.

Although TE-mediated rewiring of GRNs provides a simple and straightforward model of gene regulatory evolution, and numerous cis-regulatory elements for individual genes in mammalian genomes are derived from TEs (10), few studies have demonstrated that TEs actually have globally rewired GRNs (11). Among the most notable barriers to developing mechanistic explanations for the role of TEs in the origin and diversification of GRNs is a lack of model networks that are both amenable to detailed functional studies and that evolve rapidly enough that TEs can be caught in the act of remodeling the regu-

“TEs provide a mechanism to rapidly distribute nearly identical copies of regulatory elements...”

latory landscape. The mammalian immune system is an ideal model in which to explore the molecular mechanisms that underlie GRN evolution because numerous genomic and experimental resources have been developed for mammals. In addition, immune responses evolve fast enough that evolutionary changes can occur between relatively closely related species, yet slow enough that the functional significance of TE-derived regulatory elements can be inferred and experimentally validated.

Proinflammatory cytokines, such as interferon- γ (IFNG), are essential signaling molecules in the innate immune response that are released upon infection and that regulate a battery of downstream immunity factors called IFN-stimulated genes (ISGs). ISGs are regulated by cis-regulatory elements containing binding sites for interferon regulatory factor (IRF) and signal transducer and activator of transcription (STAT) transcription factors that are activated by IFN signaling. Although the innate immune response is conserved as a process, the specific genes activated by IFNG signal-

ing have diverged within mammals, potentially reflecting lineage-specific adaptations to host-pathogen interactions. Chuong *et al.* found that 27 TE families were enriched within IFNG-responsive cis-regulatory elements. Remarkably, 20 of these TE families originated from long terminal repeat (LTR) promoter regions of ERVs. These data suggest that many TE-derived IFNG-responsive cis-regulatory elements arose from ancient retroviral infections.

Previous studies have implicated ERVs in the genesis of cis-regulatory elements important for the evolution of mammalian pregnancy (12), placentation (13), and most notably the core regulatory networks in embryonic stem cells (14). ERVs are normally repressed in somatic cells by histone modifications and methylation, suggesting that ERVs escape silencing in some contexts, such as the placenta and embryonic stem cells, which appear to have pervasive expression of ERVs. Chuong *et al.*, for example, speculate that IFNG-responsive cis-regulatory elements in LTRs are remnants of ancient retroviral enhancers that used host signaling to promote viral transcription and replication; thus, ERVs may have evolved to be derepressed upon IFNG stimulation. This conjecture suggests an answer to a nagging question: What is it about TEs that predisposes them to act as tissue-specific regulatory elements? In this case, ERVs may be predisposed to act as regulatory elements in IFNG-responsive cells because they already possess functional IRF and STAT binding sites. More generally, TEs may be biased in the kinds of transcription factor binding sites they contain because of their own biology, leading to domestication as regulatory elements in cell types that already express those transcription factors. Although more detailed experimental approaches will be required to reconstruct the exact mechanisms by which TEs rewire gene regulatory networks, the experimental framework provided by Chuong *et al.* will lead the way. ■

REFERENCES

1. S. B. Carroll, *Cell* **134**, 25 (2008).
2. S. B. Carroll, *PLOS Biol.* **3**, e245 (2005).
3. B. Prud'homme, N. Gompel, S. B. Carroll, *Proc. Natl. Acad. Sci. U.S.A.* **104**, 8605 (2007).
4. G. P. Wagner, V. J. Lynch, *Curr. Biol.* **20**, R48 (2010).
5. V. J. Lynch, G. P. Wagner, *Evolution* **62**, 2131 (2008).
6. E. B. Chuong, N. C. Elde, C. Feschotte, *Science* **351**, 1083 (2016).
7. R. J. Britten, E. H. Davidson, *Science* **165**, 349 (1969).
8. E. Davidson, R. Britten, *Science* **204**, 1052 (1979).
9. B. McClintock, *Science* **226**, 792 (1984).
10. R. Rebollo, M. T. Romanish, D. L. Mager, *Annu. Rev. Genet.* **46**, 21 (2012).
11. F. S. J. de Souza, L. F. Franchini, M. Rubinstein, *Mol. Biol. Evol.* **30**, 1239 (2013).
12. V. J. Lynch *et al.*, *Cell Rep.* **10**, 551 (2015).
13. E. B. Chuong *et al.*, *Nat. Genet.* **45**, 325 (2013).
14. G. Kunarso *et al.*, *Nat. Genet.* **42**, 631 (2010).

Department of Human Genetics, The University of Chicago, 920 East 58th Street, CLSC 319C, Chicago, IL 60637, USA. E-mail: vijlynch@uchicago.edu

10.1126/science.aaf2977

CHEMISTRY

Surprised by selectivity

A bifunctional catalyst enables olefin synthesis from carbon monoxide and hydrogen at high selectivity

By Krijn P. de Jong

Lower olefins, particularly ethylene (C_2H_4), propylene (C_3H_6), and butylenes (C_4H_8), are important intermediates in the manufacture of products such as plastics, solvents, paints, and medicines. They are produced worldwide in amounts exceeding 200 million tons per year (see the photo) (1), mostly from crude oil. More recent approaches use methanol or synthesis gas (syngas; a mixture of carbon monoxide and hydrogen) as feedstocks, but capital investments are high and/or selectivities to lower olefins limited. A bifunctional catalyst reported by Jiao *et al.* on page 1065 of this issue (2) enables the direct conversion of synthesis gas to lower olefins with a surprisingly high selectivity.

Synthesis gas is an important intermediate in the chemical industry for the production of ammonia, hydrogen, and methanol. Any carbon-containing feedstock such as coal, natural gas, or biomass can be converted via steam reforming or gasification into a mixture of carbon monoxide and hydrogen. In previous studies, lower olefins have been produced in one step from synthesis gas with selectivities of 50 to 60% (1, 3), a process referred to as FTO (Fischer-Tropsch to olefins).

Methanol can also be converted to olefins with the help of zeolite catalysts (4). Using this MTO (methanol to olefins) process, high yields of ethylene and propylene have been obtained, but catalyst deactivation poses challenges. Recently, the MTO technology was implemented at industrial scale in China, using coal as feedstock for the production of methanol. Since the shale-gas revolution in the United States, methanol production has become economically much more attractive. In the coming decade, transport of an additional 30 million tons per annum of methanol from the United States to China for use in MTO technology in Asia is foreseen (5). How-

Inorganic Chemistry and Catalysis, Debye Institute for Nanomaterials Science, Utrecht University, Utrecht, Netherlands. E-mail: k.p.dejong@uu.nl



Large-scale olefin production. At this chemical plant in Ludwigshafen, Germany, steam cracking is used to make olefins from crude oil.

ever, methanol needs to be produced from methane, making olefin production more complex and expensive. Direct conversion of methane to chemicals (including lower olefins) seems attractive, but product yields have been limited (6) or process conditions harsh (7).

Jiao *et al.* now report selectivities for lower olefins of about 80% of total hydrocarbons, produced directly from synthesis gas at 17% CO conversion under industrially attractive conditions—400°C, 25 bar, and H_2/CO volume ratio of 1.5—and catalyst lifetimes exceeding 100 hours. Their bifunctional catalyst, OX-ZEO, consists of a metal oxide (Zn-CrO_x) and a zeolite (MSAPO). CO and H₂ are activated on the metal oxide surface, leading to formation of CH₂ species and subsequently of ketene (CH₂CO). The latter diffuses via the gas phase to the zeolite and is converted to lower olefins (see the figure).

The authors provide extensive experimental and theoretical data in support of this mechanism for converting synthesis gas to

hydrocarbons. On metal or metal carbide surfaces, CH_x species polymerize, resulting in a statistical distribution of hydrocarbon chain lengths called the Anderson-Schulz-Flory (ASF) distribution. This statistical distribution of products leads to a maximum lower-olefin yield of around 60% (3). By using a metal oxide catalyst to activate CO, the authors prevent polymerization of CH_x species, allowing CO insertion followed by ketene formation. Mass spectrometry data show that ketene is indeed present in the gas phase. The authors use ketene from the decomposition of acetic acid anhydride to provide evidence for olefin formation over the zeolite from this intermediate. Well-known MTO catalysts (8) did not perform well as the second component of the bifunctional catalyst; the authors therefore tailored the acidity of the MSAPO zeolite, using temperature-programmed desorption of ammonia as an indicator for acid site strength.

The main components of the OX-ZEO catalyst resemble a methanol synthesis cata-

lyst and an MTO catalyst. However, as noted by the authors, previous attempts to combine methanol synthesis and MTO catalysts mainly yielded paraffin and aromatics. Furthermore, they show that when methanol is fed to the MSAPO catalyst as an intermediate, catalyst stability does not reach the >100 hours found for the OX-ZEO catalyst.

Most important, by disconnecting CO activation and C-C bond formation in hydrocarbons, the authors circumvent ASF distribution in the FTO process. This leads to the surprisingly high 80% selectivity to lower olefins.

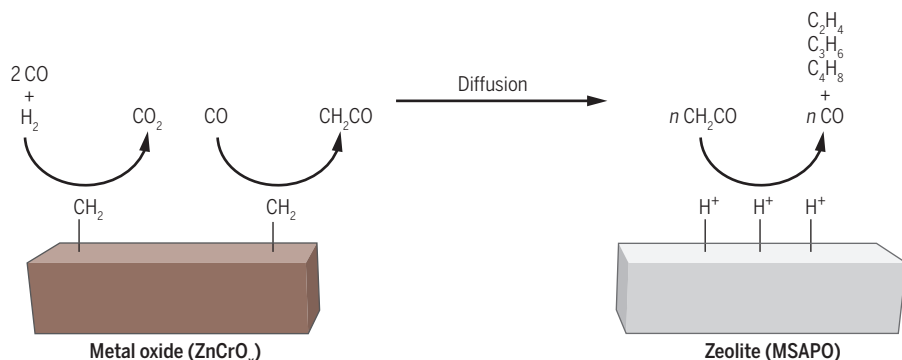
The research reported by Jiao *et al.* should be of interest to both academia and industry. It remains to be shown whether ketene or the thermodynamically more stable methanol is the key intermediate in the new process. The bifunctional nature of the catalyst invites structure performance studies including the effects of proximity of oxide and acid functions (9). The new process could become a serious competitor for industrial processes such as FTO (3) and MTO (4, 8). ■

REFERENCES AND NOTES

1. H. M. Torres Galvis, K. P. de Jong, *ACS Catal.* **3**, 2130 (2013).
2. F. Jiao *et al.*, *Science* **351**, 1065 (2016).
3. H. M. Torres Galvis *et al.*, *Science* **335**, 835 (2012).
4. P. Tian, Y. Wei, M. Ye, Z. Liu, *ACS Catal.* **5**, 1922 (2015).
5. A. H. Tullo, *Chem. Eng. News* **92**, 12 (11 August 2014).
6. R. Horn, R. Schlögl, *Catal. Lett.* **145**, 23 (2015).
7. X. Guo *et al.*, *Science* **344**, 616 (2014).
8. U. Olsbye *et al.*, *Angew. Chem. Int. Ed.* **51**, 5810 (2012).
9. J. Zecevic *et al.*, *Nature* **528**, 245 (2015).

ACKNOWLEDGMENTS

Supported by the European Research Council (EU FP7 ERC Advanced Grant no. 338846).



Two steps in one. Schematic representation of the OX-ZEO catalyst and the reaction scheme proposed by Jiao *et al.*

IMMUNOLOGY

An RNA twist to T_H17 cells

A long noncoding RNA and RNA helicase constitute a new layer of T cell control

By Maninjay K. Atianand and Katherine A. Fitzgerald

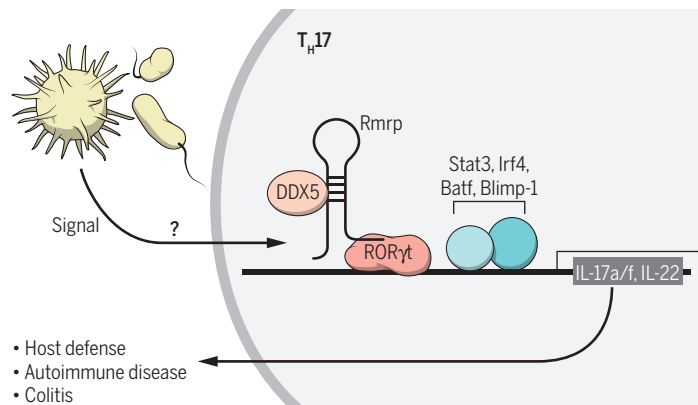
T helper lymphocytes play essential roles in the adaptive immune system. They come in distinct types defined by unique transcriptional programs that control their development and functions. Among these, T helper 17 (T_H17) cells are important in protecting mucosal surfaces against fungal and bacterial infections. In addition, T_H17 cells contribute to the pathogenesis of multiple autoimmune diseases (1). A recent study (2) adds yet another layer of complexity to the biology of these complex cells—an RNA helicase and a long noncoding RNA (lncRNA) that act together to control their effector functions.

Differentiation of naïve T helper cells into distinct populations depends on a cytokine milieu that governs the expression of lineage-defining transcription factors (3). The induced expression of the nuclear hormone receptor retinoic acid receptor-related orphan nuclear receptor gamma t (ROR γ t) drives T_H17 cell differentiation and functions by controlling the expression of interleukin-17a (IL-17a), IL-17f, and IL-22 cytokines, among others (4, 5). Using mass spectrometry, the recent study identified a coactivator for ROR γ t called DEAD-box protein 5 (DDX5; also known as p68). DDX5 belongs to a large family of more than 70 evolutionarily conserved RNA helicases that hydrolyze adenosine 5'-triphosphate to unwind RNA (6). These helicases are involved in diverse aspects of RNA biogenesis, including gene transcription, splicing, and messenger RNA decay.

In T_H17 cells, DDX5 mediates the transcription of nearly 40% of ROR γ t target genes by binding to regulatory regions of these genes. DDX5 was also found to contribute to ROR γ t-mediated inflammatory pathologies in a mouse model of T cell-induced colitis

and autoimmune encephalomyelitis. The study furthers our understanding of ROR γ t-dependent gene regulation and the coactivator functions of DDX5, which also cooperates with Runt-related transcription factor 2 (Runx2), a key transcription factor important in osteoblast differentiation (7).

Determining how DDX5 cooperates with ROR γ t began with the observation that the RNA helicase activity of DDX5 was essential for inducing ROR γ t-regulated gene expression. Wild-type DDX5, but not a helicase-dead DDX5 mutant, rescued the expression of IL-17a and IL-17f in DDX5-deficient T cells under T_H17 -polarizing conditions. RNA sequencing was used to screen for endogenous RNAs associated with DDX5 in T_H17 cells.



A T_H17 cell effector program. In response to infection, the DDX5-Rmrp complex is recruited to ROR γ t-occupied DNA to drive the expression of genes that promote host defense and autoimmunity. The signals that trigger this pathway are not yet clear.

This revealed RNA component of mitochondrial ribonuclease (RNase) protein complex (Rmrp) as a major constituent of the DDX5 complex. Through elegant biochemical, genome-wide, and in vivo studies, Rmrp was shown as essential for the assembly and recruitment of DDX5-ROR γ t complexes to regulatory regions of ROR γ t target genes in T_H17 cells (see the figure).

Rmrp is a lncRNA (a non-protein-coding RNA larger than 200 nucleotides) that functions in mitochondrial RNA processing (MRP; hence, it is also known as RNase MRP) and maturation of 5.8S ribosomal RNA (8). Rmrp also functions as a precursor to microRNAs. Interestingly, genetic mutations in this lncRNA had previously been linked to a rare autosomal recessive disorder known as

cartilage-hair hypoplasia (CHH), an early-onset genetic disease characterized by skeletal malformations and immune dysfunction (9). Using clustered regularly interspaced short palindromic repeats (CRISPR)-Cas9-based genome editing, mice were generated that expressed a mutant form of Rmrp bearing a mutation corresponding to that found in CHH patients. Cells from these mice had impaired Rmrp functions in the context of DDX5-ROR γ t-dependent regulation of T_H17 cell effector functions.

The discovery of Rmrp as a functional partner of DDX5 and a regulator of ROR γ t target genes reveals a new layer of regulation of T_H17 cell function. However, important questions arise regarding the signals that trigger formation of the DDX5-Rmrp complex. DDX5 and Rmrp are both abundantly expressed in T_H17 cells, as well as in many other cell types. The precise molecular signals that trigger the assembly of the complex in T_H17 cells therefore remain to be defined. It is likely that specific environmental cues present at mucosal surfaces unleash this complex in a specific manner under T_H17 -

polarizing conditions. Commensal bacteria or their products could provide such a signal. It will also be important to determine how DDX5 and Rmrp interface with other factors such as signal transducer and activator of transcription 3 (Stat3), interferon regulatory factor 4 (Irf4), basic leucine zipper transcription factor, ATF-like (Batf), and B lymphocyte-induced maturation protein-1 (Blimp-1), all of which control ROR γ t target gene expression in T_H17 cells (10, 11). It will also be interesting to assess the potential contribution of DDX5-Rmrp complexes in controlling IL-17

gene transcription in other immune cells, such as innate lymphoid cells. The identification of DDX5 and Rmrp raises the intriguing possibility that additional RNA helicase-lncRNA complexes await discovery that might function similarly to control gene expression in other T helper cell subsets. ■

REFERENCES

1. D. D. Patel, V. K. Kuchroo, *Immunity* **43**, 1040 (2015).
2. W. Huang et al., *Nature* **528**, 517 (2015).
3. S. Nakayama et al., *Curr. Opin. Immunol.* **24**, 297 (2012).
4. I. I. Ivanov et al., *Cell* **126**, 1121 (2006).
5. T. Korn et al., *Annu. Rev. Immunol.* **27**, 485 (2009).
6. P. Linder, E. Jankowsky, *Mol. Cell. Biol.* **12**, 505 (2011).
7. E. D. Jensen et al., *J. Cell. Biochem.* **103**, 1438 (2008).
8. C. L. Hsieh et al., *Genomics* **6**, 540 (1990).
9. A. N. Martin, Y. Li, *Cell Res.* **17**, 219 (2007).
10. M. Ciofani et al., *Cell* **151**, 289 (2012).
11. R. Jain et al., *Immunity* **44**, 131 (2016).

Program in Innate Immunity, Division of Infectious Diseases and Immunology, Department of Medicine, University of Massachusetts Medical School, 364 Plantation Street, Worcester, MA 01605, USA. E-mail: kate.fitzgerald@umassmed.edu

10.1126/science.aaf4691

BIG DATA

The future of memory

A deluge of digital data threatens to destroy our collective identity

By Clifford B. Anderson

A surprising fact about professional archivists and librarians is their unsentimental readiness to turn away books, documents, and other tidbits of information, an act known as “appraisal.” Archivists are skilled at making these evaluations because they are charged with curating coherent collections rather than assembling hodgepodes of stuff.

The art of appraisal makes sense when the material in question must be stored in a physical space. Archivists would be overwhelmed if they tried to keep every item delivered to their doorsteps. But what about in the digital world? If technological advances allow us to keep every bit of digital data, should we? How would the resulting proliferation of information affect our ability to make sense of it all? And if we come to depend on this digital record, how can we ensure that it persists into the future? In *When We Are No More*, Abby Smith Rumsey, a professional historian and consultant to libraries and other memory organizations, explores these questions through the wide lens of human history.

Rumsey adopts an evolutionary perspective on the function of memory in society, arguing that our ability to transmit information by encoding it in physical media is what enables us not only to develop a sense of the past but also to meet future challenges. However, the externalization of memory has its downside. We become reliant on the material artifacts of culture. This dependence becomes fraught as we move to more ephemeral media. Clay tablets, although not capable of recording much information, have survived over millennia. Burn down a Mesopotamian archive and the “fired” tablets become more durable.



Opened in 1878, the Peabody Library Building in Baltimore houses more than 300,000 titles.

By contrast, digital artifacts like websites change constantly. And if you unplug a data center, you stand to lose everything.

Rumsey tells her story through a series of vignettes, focusing on significant episodes in cultural history. She sketches the development of writing in the ancient Near East, the organization of libraries in the Hellenistic world, the invention of movable type and the rise of the first “print natives,” and the Jeffersonian dream of a universal library. These inflection points paved the way for our current understanding of the material world as one that encodes its own history. “Nature is the ultimate archive, the most complete set of records about the past, the Universal Library itself,” she writes, and science is “the ultimate library card.”

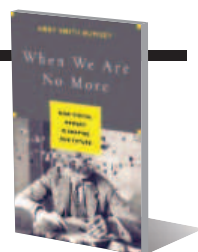
The digital age has vastly increased our ability to collect and recollect data, although perhaps at the cost of our personal memories. Our reliance on smart devices, which summon facts on demand, decreases our need to recall facts unaided. In part, this is an old worry. Socrates fretted about how the technology of writing affected wisdom. Committing something to memory is,

after all, among other things, a moral act. We are what we know. However, as Rumsey notes, forgetting also serves a critical purpose, freeing up our minds to incorporate new experiences.

Is there a danger that computers may supplant us as our cognitive systems struggle to keep up with all the data we now produce? Rumsey is skeptical; she regards brains and computers as different and largely complementary. Drawing on contemporary neuroscience, she contends that, unlike computers, the brain relies on affective, emotional experiences of the world to organize facts into patterns and to produce narratives about future courses of action.

Rumsey also issues a warning against the temptation to overoptimize our preservation strategies. Although we may consider certain forms of information unimportant or useless at present, that same information may turn out to be vital in the future. She points, for example, to information about climate change that scholars have retrieved from the antiquarian logbooks of naval voyages.

The goal of *When We Are No More* is not to have the final word on the subject of information management but to challenge us to consider more seriously how the consequences of our current data deluge will influence society moving forward. In that, Rumsey succeeds admirably.



When We Are No More
How Digital Memory Is
Shaping Our Future

Abby Smith Rumsey
Bloomsbury, 2016. 246 pp.

The reviewer is Director of Scholarly Communications,
Vanderbilt University, Nashville, TN 37240, USA.
E-mail: clifford.anderson@vanderbilt.edu

HISTORY OF SCIENCE

Risky business

Hard-won lessons shed light on the promise and perils of radiation and nuclear power

By **Angela N. Creager**

In 1953, President Dwight D. Eisenhower launched his “Atoms for Peace” initiative, aimed at increasing energy production, improving agriculture, and advancing health care. The following year, the U.S. Pacific atomic test Castle Bravo showered a Japanese fishing vessel with radioactive fallout, resulting in 23 cases of radiation sickness (including one death) and a boatload of contaminated tuna. These events—even more than the use of nuclear weapons at the end of World War II—launched an ongoing public debate over whether the risks of radiation exposure outweigh the benefits of nuclear technology. For many, the verdict is still out. Or, more to the point, it is hard to reach a verdict even today, because unbiased, comprehensible information on radiation risk is hard to come by.

Timothy J. Jorgensen’s book *Strange Glow: The Story of Radiation* fills this gap, using history to explain how we encounter radiation and how it affects us. His goal is to provide readers with the basic facts so that they can make decisions about the risks they want to live with.

Jorgensen, a radiation biologist at Georgetown University, notes that quantitative approaches to educating the public about radiation have failed. He believes that people learn through stories more easily than through statistics. The book begins by comparing radioactivity to electricity, which at the time of Edison was not well understood by the public and was feared for its deadliness. Over time, however, people began to see how the dangers might be managed and were ultimately persuaded that the potential benefits outweighed the risks. He believes this illustrates that effective education as well as experience can change risk perception.

Jorgensen is a good storyteller, with an eye for compelling details. In chapter 6, for example, he explains how a homeopathic

medical practitioner at the turn of the century pioneered the use of x-rays to treat cancer.

In chapter 7, Jorgensen recounts in detail the dreadful injuries caused by the atomic weapons detonated over Hiroshima and Nagasaki. He also notes the deadly consequences of the shock waves and firestorms from those blasts, which together represented 85% of the energy released. Those victims “didn’t live to tell their tales.” But if they had, we might have a fuller understanding of the horrors of atomic warfare.

Most Americans are more afraid of nuclear power plants than stored nuclear warheads. In chapter 17, Jorgensen illustrates



Data collected from atomic bomb survivors help scientists estimate the cancer risk associated with radiation-based medical treatments and diagnostics.

why these fears may be misplaced. Power reactors are not without hazards, but they cannot explode in the same way as atomic weapons are designed to do. Jorgensen recounts chillingly many near accidents during the Cold War, including one example in which a B-52 bomber broke open in midair over a farm in North Carolina, releasing two hydrogen bombs. Although both bombs remained intact, the ensuing investigation revealed that all but one of the seven steps required to detonate had occurred. So long as nuclear warheads remain in the custody of fallible people, their accidental detonation is by far the greatest large-scale radiation-related threat to humankind.

Aside from this catastrophic possibility, routine medical usage of x-rays delivers the greatest amount of man-made radiation

Strange Glow**The Story of Radiation**

Timothy J. Jorgensen

Princeton University Press,
2016. 506 pp.



exposure to most people. Especially worrisome to Jorgensen is the recent popularity of whole-body CT scans, which can expose individuals to 20,000 times the radiation dose of an x-ray to the arm—roughly the same as experienced by the lower-dose Japanese atomic bomb survivors. In addition, many physicians are unaware of how many false positives are generated by medical tests based on x-rays (such as mammograms) (1). Such results can precipitate further tests and surgeries, which are at best unnecessary and at worst bring their own complications.

Ionizing radiation is now the single best-studied carcinogen on Earth, in no small measure due to the long-term studies of survivors from Hiroshima and Nagasaki. Even so, uncertainty bedevils many of the best risk assessments about dose estimates, particularly when it comes to exposures from environmental contamination.

For the most part, I find Jorgensen’s recounting of radiation’s uses and their hazards clarifying, if not reassuring. But I wonder about his assumption that individuals can make choices about their exposures. As Ulrich Beck observed in his landmark book *Risk Society*, social status is now reflected in the distribution of risk rather than (simply) the distribution of wealth (2). Not everyone in the world gets to choose how they encounter radioactivity, which argues for the importance of just policies as well as informed consumers.

Although I doubt that the risks of radiation will ever seem as manageable as those of electricity, I am ultimately convinced by Jorgensen’s approach. His book gave me a more commonsense understanding of the risks associated with radiation exposure than either my scientific training or my historical research on this topic (3).

REFERENCES

1. G. Gigerenzer, *Risk Savvy: How to Make Good Decisions* (Viking, New York, 2014).
2. U. Beck, *Risk Society: Towards a New Modernity*, Mark Ritter, Transl. (Sage, Los Angeles, 1986).
3. A. N. H. Creager, *Life Atomic: A History of Radioisotopes in Science and Medicine* (University of Chicago Press, Chicago, 2013).

The reviewer is at the Department of History, Princeton University, Princeton, NJ 08544, USA.
E-mail: creager@princeton.edu

10.1126/science.aaf3339

LETTERS

Edited by Jennifer Sills

Seeing the grasslands through the trees

IN HIS PERSPECTIVE “Ancient grasslands at risk” (8 January, p. 120), W. J. Bond makes a compelling argument for the need to identify, study, and preserve ancient grassland ecosystems because of their ecological importance. We strongly agree. However, we disagree with his claim that our Atlas of Forest Landscape Restoration Opportunities (1–3) promotes activities that threaten these grasslands by targeting them for afforestation or reforestation beyond their natural level of tree cover.

Bond claims that the Atlas “is linked to a global plan to reforest degraded lands to offset anthropogenic CO₂ emissions.” This indicates a fundamental misunderstanding of the concept of Forest and Landscape Restoration (FLR) and of the Atlas. As we have previously indicated (4), FLR is not a “forest plantation project” and is not focused solely on offsetting CO₂ emissions (though sequestering carbon is one of many benefits of FLR). FLR does not call for increasing tree cover beyond what would be ecologically appropriate for a particular location, nor should it cause any loss or conversion of natural forests, grasslands, or other ecosystems.

Rather, FLR is a process that seeks to regain the ecological integrity and enhance human well-being in deforested or degraded forest landscapes (5). The FLR approach includes a wide range of sustainable land-management practices applicable to both forest and nonforest ecosystems (5–7). A fundamental first step in the FLR process involves understanding the ecosystem at the landscape level, including its historical and cultural values, before making decisions on a restoration approach (8). FLR under this definition would promote exactly the same conservation of ancient grasslands that Bond advocates.

Bond’s claims also highlight disagreement over how certain ecosystems should be classified. Grasslands and sparse forests are not mutually exclusive, often occurring together in mosaic ecosystems (9).

Bond’s Perspective and Veldman *et al.* (10) define grassland biomes broadly, whereas the Atlas defines forest landscapes as those with a potential tree canopy cover as low as 10%, consistent with the widely accepted FAO definition (11) but at a much lower level of resolution (1 by 1 km). As a result, some grassland biomes identified by Bond and by Veldman *et al.* overlap with forest landscapes identified by our Atlas. These mosaic areas require individual assessment, including identifying the natural level of tree cover before deciding on the appropriate management approach.

Further research and collaboration are needed to explore areas where “forests” and “grasslands” overlap. Agreement on terminology, refinement of maps, and identification of the appropriate management policies and practices for these complex ecosystems are among the outcomes we can achieve through collaboration. We invite Bond to work with



Wildebeests graze in Serengeti National Park, Tanzania.

us on these objectives, with the end goal of leveraging the principles of FLR to both preserve critical ecosystems and improve local livelihoods.

**Sean DeWitt,^{1*} James Anderson,¹
Chetan Kumar,² Lars Laestadius,⁴
Stewart Maginnis,² S. Minnemeyer,¹
Peter V. Potapov,³ Katie Reynter,¹
Carole Saint-Laurent²**

¹World Resources Institute, Washington, DC 20002, USA. ²International Union for Conservation of Nature, 1196, Gland, Switzerland. ³Department of Geographical Sciences, University of Maryland, College Park, MD 20742, USA. ⁴Silver Spring, MD 20901, USA.

*Corresponding author. E-mail: sdewitt@wri.org

REFERENCES

1. World Resources Institute, “Atlas of forest landscape restoration opportunities” (World Resources Institute, Washington, DC, 2014); www.wri.org/applications/maps/flr-atlas/#.

2. S. Minnemeyer, L. Laestadius, N. Sizer, C. Saint-Laurent, P. Potapov, “A world of opportunity” (World Resources Institute, Washington, DC, 2011).
3. L. Laestadius *et al.*, *Unasylva* 238 **62**, 47 (2011/2).
4. L. Laestadius *et al.*, *Science* **347**, 6227 (2015).
5. ITTO and IUCN, “Restoring forest landscapes,” *ITTO Technical Series No. 23* (2005).
6. IUCN and World Resources Institute, “A guide to the Restoration Opportunities Assessment Methodology (ROAM)” (IUCN and WRI, Gland, Switzerland, 2014); http://cmsdata.iucn.org/downloads/roam_handbook_lowres_web.pdf.
7. R. Winterbottom, “Restoration: It’s about more than just the trees” (2014); www.wri.org/blog/2014/05/restoration-it%E2%80%99s-about-more-just-trees.
8. IUCN, “Restoring the world’s ecosystems: More than planting trees” (2015); www.iucn.org/about/work/programmes/forest/?22210/restoring-the-worlds-ecosystems-more-than-planting-trees.
9. W. A. Hoffman *et al.*, *Ecol. Lett.* **15**, 759 (2012).
10. J. W. Veldman *et al.*, *BioScience* **65**, 1011 (2015).
11. FAO, “FRA 2015 Terms and Definitions,” *Forest Resources Assessment Working Paper 180* (2012).

Response

DEWITT *ET AL.* claim that the Forest Landscape Restoration (FLR) plan (1–3) would not return tree cover beyond

what would be ecologically appropriate. However, the labeling system of the Atlas of Forest Landscape Restoration Opportunities stymies this goal. The Atlas defines a landscape as “degraded” if it is subject to any process that reduces the volume and canopy cover of trees. Consequently, misclassifications of ancient ecosystems, maintained by fire and/or herbivory, are inevitable. Under these assumptions, the FLR handbook would mark such areas as suitable for reforestation.

It has long been assumed that tropical grassy ecosystems were originally forests degraded by cutting, and especially burning (4, 5). However, as shown by

the studies I reviewed in my Perspective, evidence of fire does not mean that the landscape originated as forest. In striking contrast to closed forests, ancient grassy ecosystems are maintained, not degraded, by fire and herbivory. Yet they are misclassified by the Atlas as degraded forest. For example, the western Serengeti and Kruger National Park are mapped as deforested instead of as ancient savannahs, and the natural species-rich montane grasslands of South Africa and southern Brazil are both mapped as deforested and/or degraded.

The Atlas label of “forest” for any landscape with more than 10% tree canopy is also misleading. Restoration strategies differ for forests and grasslands. The FLR handbooks promote fire suppression as one of the tools to restore forests and landscapes (6, 7). Although appropriate

for closed forests, fire suppression can be disastrous for ancient grassy systems defined, inappropriately, as forests based on the tree cover definition (8). A full restoration program would not only recognize ancient grasslands but also promote fire and herbivory to help maintain them. It would call for repeal of fire suppression legislation that inhibits grassland fire management and endorse active burning programs along with livestock farming as suitable land practices.

I appreciate DeWitt *et al.*'s call for collaboration with experts in open grassy ecosystems. Laestadius *et al.* (3) also noted the need for wider consultation. If the grassy biomes and the processes key to their ecological integrity are formally included in the restoration agenda, we will, at last, have put a century of misunderstanding of tropical vegetation behind us.

William Bond

South African Environmental Observation Network,
National Research Foundation, Claremont, 7735,
South Africa and Department of Biological Sciences,
University of Cape Town, Rondebosch, 7701,
South Africa. E-mail: William.Bond@uct.ac.za

REFERENCES

1. World Resources Institute, "Atlas of forest landscape restoration opportunities" (World Resources Institute, Washington, DC, 2014); www.wri.org/applications/maps/flr-atlas/#.
2. S. Minnemeyer, L. Laestadius, N. Sizer, C. Saint-Laurent, P. Potapov, "A world of opportunity" (World Resources Institute, Washington, DC, 2011).
3. L. Laestadius *et al.*, *Unasylva* 238 **62**, 47 (2011/2012).
4. A. M. Aubréville, *Unasylva* **1**, 5 (1947).
5. J. P. H. Acocks, *Veld Types of South Africa* (Botanical Research Institute, ed. 3, 1953).
6. ITTO and IUCN, "Restoring forest landscapes," *ITTO Technical Series* No. 23 (2005).
7. IUCN and World Resources Institute, "A guide to the Restoration Opportunities Assessment Methodology (ROAM)" (IUCN and WRI, Gland, Switzerland, 2014); http://cmsdata.iucn.org/downloads/roam_handbook_lowres_web.pdf
8. C. L. Parr *et al.*, *Trends Ecol. Evol.* **29**, 205 (2014).

Government: Plan for ecosystem services

NATURAL AND MANAGED ecosystems provide food, water, and other valuable services to human societies. Unnoticed by many in the scientific community, the values associated with ecosystem services have been integrated into U.S. government policy. A recent administration memo (1) put U.S. federal agencies on notice: The clock is ticking to integrate ecosystem services into their planning and decision-making. By 30 March 2016, agencies are to describe approaches for "conducting decision-relevant and scale-specific ecosystem-services assessments, as well as plans for effective monitoring and evaluation." The administration stresses that

such policies may be most effective when incorporated into existing decision-making frameworks.

As members of the Ecological Society of America's (ESA's) Steering Committee on the Intergovernmental Platform for Biodiversity and Ecosystem Services (IPBES) (2), we urge U.S. federal agencies to consider how this recent mandate provides opportunities to leverage the global impact of IPBES while achieving national policy objectives. IPBES, which was established with support from the United States but not mentioned in the administration's memo, provides scientific assessments of the state of biodiversity and ecosystem services (3). At its fourth plenary, one month before the administration's deadline, IPBES will likely approve the first of its global ecosystem service assessments.

We encourage U.S. federal agencies to familiarize themselves with these assessments and the ongoing IPBES work program. Creating a cross-agency policy agenda for understanding, monitoring, and managing ecosystem services in the United States would reduce the risk of scattered and inconsistent national-level policy mechanisms and would align U.S. policy and IPBES goals. Seeking input from the country's scientific community would help build a secure foundation for these policies and offer U.S. scientists an opportunity to contribute their knowledge to the scientific foundations upon which effective environmental policy rests.

Lucas N. Joppa,^{1*} James W. Boyd,² Clifford S. Duke,³ Stephanie Hampton,⁴ Stephen T. Jackson,⁵ Katharine L. Jacobs,⁶ Karim-Aly S. Kassam,⁷ Harold A. Mooney,⁸ Laura A. Ogden,⁹ Mary Ruckelshaus,¹⁰ Jason F. Shogren¹¹

¹Microsoft Research, Redmond, WA 98052, USA. ²Resources for the Future, Washington, DC 20036, USA. ³Ecological Society of America, Washington, DC 20036, USA. ⁴Washington State University, Center for Environmental Research, Education and Outreach, Pullman, WA 99164, USA. ⁵United States Geological Survey, Southwest Climate Science Center, Tucson, AZ 85721, USA. ⁶University of Arizona, Center for Climate Adaptation Science and Solutions, Tucson, AZ 85721, USA. ⁷Cornell University, Department of Natural Resources, Ithaca, NY 14850, USA. ⁸Stanford University, Department of Biological Sciences, Stanford, CA 94305, USA. ⁹Dartmouth University, Department of Anthropology, Hanover, NH 03755, USA. ¹⁰The Natural Capital Project, Stanford University, Stanford, CA 94305, USA. ¹¹University of Wyoming, College of Business, Laramie, WY 82071, USA.

*Corresponding author.

E-mail: ljoppa@microsoft.com

REFERENCES

1. S. Donovan, C. Goldfuss, J. Holdren, "Incorporating Ecosystem Services into Federal Decision Making" (2015); www.whitehouse.gov/sites/default/files/omb/memoranda/2016/m-16-01.pdf.
2. ESA, IPBES (<http://esa.org/ipbes/>).
3. IPBES (<http://ipbes.net/>).

TECHNICAL COMMENT ABSTRACTS

Comment on "Estimating the reproducibility of psychological science"

Daniel T. Gilbert, Gary King, Stephen Pettigrew, Timothy D. Wilson

A paper from the Open Science Collaboration (Research Articles, 28 August 2015, [aac4716](https://doi.org/10.1126/science.aac4716)) attempting to replicate 100 published studies suggests that the reproducibility of psychological science is surprisingly low. We show that this article contains three statistical errors and provides no support for such a conclusion. Indeed, the data are consistent with the opposite conclusion, namely, that the reproducibility of psychological science is quite high.

Full text at <http://dx.doi.org/10.1126/science.aad7243>

Response to Comment on "Estimating the reproducibility of psychological science"

Christopher J. Anderson, Štěpán Bahník, Michael Barnett-Cowan, Frank A. Bosco, Jesse Chandler, Christopher R. Chartier, Felix Cheung, Cody D. Christopherson, Andreas Cordes, Edward J. Cremata, Nicolas Della Penna, Vivien Estel, Anna Fedor, Stanka A. Fitneva, Michael C. Frank, James A. Grange, Joshua K. Hartshorne, Fred Hasselman, Felix Henninger, Marije van der Hulst, Kai J. Jonas, Calvin K. Lai, Carmel A. Levitan, Jeremy K. Miller, Katherine S. Moore, Johannes M. Meixner, Marcus R. Munafò, Koen I. Neijenhuijs, Gustav Nilsson, Brian A. Nosek, Franziska Plessow, Jason M. Prenoveau, Ashley A. Ricker, Kathleen Schmidt, Jeffrey R. Spies, Stefan Steiger, Nina Strohming, Gavin B. Sullivan, Robbie C. M. van Aert, Marcel A. L. M. van Assen, Wolf Vanpaemel, Michelangelo Vianello, Martin Voracek, Kellylynn Zuni

Gilbert *et al.* conclude that evidence from the Open Science Collaboration's Reproducibility Project: Psychology indicates high reproducibility, given the study methodology. Their very optimistic assessment is limited by statistical misconceptions and by causal inferences from selectively interpreted, correlational data. Using the Reproducibility Project: Psychology data, both optimistic and pessimistic conclusions about reproducibility are possible, and neither are yet warranted.

Full text at <http://dx.doi.org/10.1126/science.aad9163>

TECHNICAL COMMENT

PSYCHOLOGY

Comment on “Estimating the reproducibility of psychological science”

Daniel T. Gilbert,^{1*}† Gary King,¹ Stephen Pettigrew,¹ Timothy D. Wilson²

A paper from the Open Science Collaboration (Research Articles, 28 August 2015, aac4716) attempting to replicate 100 published studies suggests that the reproducibility of psychological science is surprisingly low. We show that this article contains three statistical errors and provides no support for such a conclusion. Indeed, the data are consistent with the opposite conclusion, namely, that the reproducibility of psychological science is quite high.

The replication of empirical research is a critical component of the scientific process, and attempts to assess and improve the reproducibility of science are important. The Open Science Collaboration (OSC) (1) conducted “a large-scale, collaborative effort to obtain an initial estimate of the reproducibility of psychological science” by attempting to replicate 100 original studies that had been published in one of three top-tier psychology journals in 2008. Depending on the criterion used, only 36 to 47% of the original studies were successfully replicated, which led many to conclude that there is a “replication crisis” in psychological science (2). Here, we show that when these results are corrected for error, power, and bias, they provide no support for this conclusion. In fact, the data are consistent with the opposite conclusion, namely, that the reproducibility of psychological science is quite high.

First, we will discuss the issue of error. If an original study reports a true effect, and if a replication study uses the original procedures with a new sample of subjects drawn from the original population, the replication study will sometimes fail to replicate the original effect because of sampling error alone. If all 100 of the original studies examined by OSC had reported true effects, then sampling error alone should cause 5% of the replication studies to “fail” by producing results that fall outside the 95% confidence interval of the original study and 8% to “fail” by producing results that are not also statistically significant (with the same sign). OSC used the latter figure as the benchmark to which the actual replication failure rate in their data was compared. Neither of these figures provides an appropriate benchmark, however, because both assume that sampling error is the only source of error in the data. In other words, these bench-

marks assume that the one and only way in which OSC’s replication studies differed from the original studies is that they drew new samples from the original population. In fact, many of OSC’s replication studies differed from the original studies in other ways as well.

For example, many of OSC’s replication studies drew their samples from different populations than the original studies did. An original study that measured American’s attitudes toward African-Americans (3) was replicated with Italians, who do not share the same stereotypes; an original study that asked college students to imagine being called on by a professor (4) was replicated with participants who had never been to college; and an original study that asked students who commute to school to choose between apartments that were short and long drives from campus (5) was replicated with students who do not commute to school. What’s more, many of OSC’s replication studies used procedures that differed from the original study’s procedures in substantial ways: An original study that asked Israelis to imagine the consequences of military service (6) was replicated by asking Americans to imagine the consequences of a honeymoon; an original study that gave younger children the difficult task of locating targets on a large screen (7) was replicated by giving older children the easier task of locating targets on a small screen; an original study that showed how a change in the wording of a charitable appeal sent by mail to Koreans could boost response rates (8) was replicated by sending 771,408 e-mail messages to people all over the world (which produced a response rate of essentially zero in all conditions).

All of these infidelities are potential sources of random error that the OSC’s benchmark did not take into account. So how many of their replication studies should we expect to have failed by chance alone? Making this estimate requires having data from multiple replications of the same original study. Although OSC did not collect such data, the corresponding author of OSC, Brian Nosek,

referred us to another of his projects that did. The “Many Labs” project (MLP) (9) involved 36 independent laboratories that attempted to replicate each of 16 original psychology studies, resulting in 574 replication studies. These replication studies, like OSC’s replication studies, did not always use original populations and procedures, so their data allow us to estimate the amount of error that sampling and infidelity together introduce. To make this estimate, we simply treated each of the studies reported by MLP as an “original effect” and then counted how many of the remaining “replications” of that particular study observed that original effect. This analysis revealed that when infidelities were allowed, only 65.5% of the “replication effects” fell within the confidence intervals of the “original effects.” Applying this estimate to OSC’s data produces a sobering conclusion: If every one of the 100 original studies that OSC attempted to replicate had described a true effect, then more than 34 of their replication studies should have failed by chance alone. [All information and code necessary to replicate our results are archived in Dataverse (10).] The bottom line is that OSC allowed considerable infidelities that introduced random error and decreased the replication rate but then compared their results to a benchmark that did not take this error into account.

Second, we will discuss the issue of power. OSC attempted to replicate each of 100 studies just once, and that attempt produced an unsettling result: Only 47% of the original studies were successfully replicated (i.e., produced effects that fell within the confidence interval of the original study). In contrast, MLP attempted to replicate each of its studies 35 or 36 times and then pooled the data. MLP’s much more powerful method produced a much more heartening result: A full 85% of the original studies were successfully replicated. What would have happened to MLP’s heartening result if they had used OSC’s method? Of MLP’s 574 replication studies, only 195 produced effects that fell within the confidence interval of the original, published study. In other words, if MLP had used OSC’s method, they would have reported an unsettling replication rate of 34% rather than the heartening 85% they actually reported. (A similar result occurs when we limit our analysis to those MLP replication studies that had sample sizes at least as large as the original studies.) Clearly, OSC used a method that severely underestimates the actual rate of replication.

Third, we will discuss the issue of bias. The foregoing analyses generously assume that infidelities are a source of random error that are equally likely to increase or decrease the likelihood of successful replication. Is this assumption true, or were the infidelities in OSC’s replication studies more likely to decrease than to increase the likelihood of successful replication? Answering this question requires an indicator of the fidelity of each replication study, which OSC attempted to provide. Before conducting each replication study, OSC asked the authors of the original study whether they endorsed the methodological

¹Harvard University, Cambridge, MA, USA. ²University of Virginia, Charlottesville, VA, USA.

*Corresponding author. E-mail: gilbert@wjh.harvard.edu

†Authors are listed alphabetically.

protocol for the to-be-attempted replication. Only 69% of the original authors did. Although endorsement is an imperfect indicator that may overestimate the fidelity of a replication study (e.g., some of the original authors may have knowingly endorsed low-fidelity protocols and others may have discovered that the replication studies were low fidelity only after they were completed) or may underestimate the fidelity of a replication study (e.g., endorsement decisions may be influenced by original authors' suspicions about the weakness of their studies rather than by the fidelity of the replication protocol), it is nonetheless the best indicator of fidelity in OSC's data. So what does that indicator indicate?

When we compared the replication rates of the endorsed and unendorsed protocols, we discovered that the endorsed protocols were nearly four times as likely to produce a successful replication (59.7%) as were the unendorsed protocols (15.4%). This strongly suggests that the infidelities did not just introduce random error but instead biased the replication studies toward failure. If OSC had limited their analyses to endorsed studies, they would

have found that 59.7% [95% confidence interval (CI): 47.5%, 70.9%] were replicated successfully. In fact, we estimate that if all the replication studies had been high enough in fidelity to earn the endorsement of the original authors, then the rate of successful replication would have been 58.6% (95% CI: 47.0%, 69.5%) when controlling for relevant covariates. Remarkably, the CIs of these estimates actually overlap the 65.5% replication rate that one would expect if every one of the original studies had reported a true effect. Although that seems rather unlikely, OSC's data clearly provide no evidence for a "replication crisis" in psychological science.

We applaud efforts to improve psychological science, many of which have been careful, responsible, and effective (*II*), and we appreciate the effort that went into producing OSC. But metascience is not exempt from the rules of science. OSC used a benchmark that did not take into account the multiple sources of error in their data, used a relatively low-powered design that demonstrably underestimates the true rate of replication, and permitted considerable infidelities that almost certainly biased their replication studies toward

failure. As a result, OSC seriously underestimated the reproducibility of psychological science.

REFERENCES AND NOTES

1. Open Science Collaboration, *Science* **349**, aac4716 (2015).
2. B. Carey, Psychology's fears confirmed: Rechecked studies don't hold up. *New York Times* (27 August 2015), p. A1.
3. B. K. Payne, M. A. Burkley, M. B. Stokes, *J. Pers. Soc. Psychol.* **94**, 16–31 (2008).
4. J. L. Risen, T. Gilovich, *J. Pers. Soc. Psychol.* **95**, 293–307 (2008).
5. E. J. Masicampo, R. F. Baumeister, *Psychol. Sci.* **19**, 255–260 (2008).
6. N. Shnabel, A. Nadler, *J. Pers. Soc. Psychol.* **94**, 116–132 (2008).
7. V. LoBue, J. S. DeLoache, *Psychol. Sci.* **19**, 284–289 (2008).
8. M. Koo, A. Fishbach, *J. Pers. Soc. Psychol.* **94**, 183–195 (2008).
9. R. A. Klein *et al.*, *Soc. Psychol.* **45**, 142–152 (2014).
10. D. T. Gilbert, G. King, S. Pettigrew, T. D. Wilson, Replication data for Comment on "Estimating the reproducibility of psychological science," Harvard Dataverse, V1; <http://dx.doi.org/10.7910/DVN/5LKVH2> (2016).
11. J. P. Simmons, L. D. Nelson, U. Simonsohn, *Psychol. Sci.* **22**, 1359–1366 (2011).

ACKNOWLEDGMENTS

We acknowledge the support of NSF Grant BCS-1423747 to T.D.W. and D.T.G.

26 October 2015; accepted 28 January 2016
10.1126/science.aad7243

TECHNICAL RESPONSE

PSYCHOLOGY

Response to Comment on “Estimating the reproducibility of psychological science”

Christopher J. Anderson,^{1*} Štěpán Bahník,² Michael Barnett-Cowan,³ Frank A. Bosco,⁴ Jesse Chandler,^{5,6} Christopher R. Chartier,⁷ Felix Cheung,⁸ Cody D. Christopherson,⁹ Andreas Cordes,¹⁰ Edward J. Cremata,¹¹ Nicolas Della Penna,¹² Vivien Estel,¹³ Anna Fedor,¹⁴ Stanka A. Fitneva,¹⁵ Michael C. Frank,¹⁶ James A. Grange,¹⁷ Joshua K. Hartshorne,¹⁸ Fred Hasselman,¹⁹ Felix Henninger,²⁰ Marije van der Hulst,²¹ Kai J. Jonas,²² Calvin K. Lai,²³ Carmel A. Levitan,²⁴ Jeremy K. Miller,²⁵ Katherine S. Moore,²⁶ Johannes M. Meixner,²⁷ Marcus R. Munafò,²⁸ Koen I. Neijenhuijs,²⁹ Gustav Nilsson,³⁰ Brian A. Nosek,^{31,32} Franziska Plessow,³³ Jason M. Prenoveau,³⁴ Ashley A. Ricker,³⁵ Kathleen Schmidt,³⁶ Jeffrey R. Spies,^{31,32} Stefan Stieger,³⁷ Nina Strohminger,³⁸ Gavin B. Sullivan,³⁹ Robbie C. M. van Aert,⁴⁰ Marcel A. L. M. van Assen,^{40,41} Wolf Vanpaemel,⁴² Michelangelo Vianello,⁴³ Martin Voracek,⁴⁴ Kellylynn Zuni⁴⁵

Gilbert *et al.* conclude that evidence from the Open Science Collaboration's Reproducibility Project: Psychology indicates high reproducibility, given the study methodology. Their very optimistic assessment is limited by statistical misconceptions and by causal inferences from selectively interpreted, correlational data. Using the Reproducibility Project: Psychology data, both optimistic and pessimistic conclusions about reproducibility are possible, and neither are yet warranted.

Across multiple indicators of reproducibility, the Open Science Collaboration (1) (OSC2015) observed that the original result was replicated in ~40 of 100 studies sampled from three journals. Gilbert *et al.* (2) conclude that the reproducibility rate is, in fact, as high as could be expected, given the study methodology. We agree with them that both methodological differences between original and replication studies and statistical power affect reproducibility, but their very optimistic assessment is based on statistical misconceptions and selective interpretation of correlational data.

Gilbert *et al.* focused on a variation of one of OSC2015's five measures of reproducibility: how often the confidence interval (CI) of the original study contains the effect size estimate of the replication study. They misstated that the expected replication rate assuming only sampling error is 95%, which is true only if both studies estimate the same population effect size and the replication has infinite sample size (3, 4). OSC2015 replications did not have infinite sample size. In fact, the expected replication rate was 78.5% using OSC2015's CI measure (see OSC2015's supplementary information, pp. 56 and 76; <https://osf.io/k9rnd>). By this measure, the actual replication rate was only 47.4%, suggesting the influence of factors other than sampling error alone.

Within another large replication study, “Many Labs” (5) (ML2014), Gilbert *et al.* found that 65.5% of ML2014 studies would be within the CIs

of other ML2014 studies of the same phenomenon and concluded that this reflects the maximum reproducibility rate for OSC2015. Their analysis using ML2014 is misleading and does not apply to estimating reproducibility with OSC2015's data for a number of reasons.

First, Gilbert *et al.*'s estimates are based on pairwise comparisons between all of the replications within ML2014. As such, for roughly half of their failures to replicate, “replications” had larger effect sizes than “original studies,” whereas just 5% of OSC2015 replications had replication CIs exceeding the original study effect sizes.

Second, Gilbert *et al.* apply the by-site variability in ML2014 to OSC2015's findings, thereby arriving at higher estimates of reproducibility. However, ML2014's primary finding was that by-site variability was highest for the largest (replicable) effects and lowest for the smallest (nonreplicable) effects. If ML2014's primary finding is generalizable, then Gilbert *et al.*'s analysis may leverage by-site variability in ML2014's larger effects to exaggerate the effect of by-site variability on OSC2015's nonreproduced smaller effects, thus overestimating reproducibility.

Third, Gilbert *et al.* use ML2014's 85% replication rate (after aggregating across all 6344 participants) to argue that reproducibility is high when extremely high power is used. This interpretation is based on ML2014's small, ad hoc sample of classic and new findings, as opposed to OSC2015's effort to examine a more representa-

tive sample of studies in high-impact journals. Had Gilbert *et al.* selected the similar Many Labs 3 study (6) instead of ML2014, they would have arrived at a more pessimistic conclusion: a 30% overall replication success rate with a multisite, very high-powered design.

That said, Gilbert *et al.*'s analysis demonstrates that differences between laboratories and sample populations reduce reproducibility according to the CI measure. Also, some true effects may exist even among nonsignificant replications (our additional analysis finding evidence for these effects is available at <https://osf.io/smjge>). True effects can fail to be detected because power calculations for replication studies are based on effect sizes in original studies. As OSC2015 demonstrates, original study effect sizes are likely inflated due to publication bias. Unfortunately, Gilbert *et al.*'s focus on the CI measure of reproducibility neither addresses nor can account for the facts that the OSC2015 replication effect sizes were about half the size of the original studies on average, and 83% of replications elicited smaller effect sizes than the original studies. The combined results of OSC2015's five indicators of reproducibility suggest that, even if true, most effects are likely to be smaller than the original results suggest.

Gilbert *et al.* attribute some of the failures to replicate to “low-fidelity protocols” with methodological differences relative to the original, for which they provide six examples. In fact, the original authors recommended or endorsed three of the six methodological differences discussed

¹Russell Sage College, Troy, NY, USA. ²University of Würzburg, Würzburg, Germany. ³University of Waterloo, Waterloo, Ontario, Canada. ⁴Virginia Commonwealth University, Richmond, VA, USA. ⁵University of Michigan, Ann Arbor, MI 48104, USA. ⁶Mathematica Policy Research, Washington, DC, USA. ⁷Ashland University, Ashland, OH, USA. ⁸Michigan State University, East Lansing, MI, USA. ⁹Southern Oregon University, Ashland, OR, USA. ¹⁰University of Göttingen, Institute for Psychology, Göttingen, Germany. ¹¹University of Southern California, Los Angeles, CA, USA. ¹²Australian National University, Canberra, Australia. ¹³Technische Universität Braunschweig, Braunschweig, Germany. ¹⁴Parmenides Stiftung, Munich, Germany. ¹⁵Queen's University, Kingston, Ontario, Canada. ¹⁶Stanford University, Stanford, CA, USA. ¹⁷Keele University, Keele, Staffordshire, UK. ¹⁸Boston College, Chestnut Hill, MA, USA. ¹⁹Radboud University Nijmegen, Nijmegen, Netherlands. ²⁰University of Koblenz-Landau, Landau, Germany. ²¹Erasmus Medical Center, Rotterdam, Netherlands. ²²University of Amsterdam, Amsterdam, Netherlands. ²³Harvard University, Cambridge, MA, USA. ²⁴Occidental College, Los Angeles, CA, USA. ²⁵Willamette University, Salem, OR, USA. ²⁶Arcadia University, Glenside, PA, USA. ²⁷University of Potsdam, Potsdam, Germany. ²⁸University of Bristol, Bristol, UK. ²⁹Vrije Universiteit Amsterdam, Amsterdam, Netherlands. ³⁰Karolinska Institutet, Stockholm University, Stockholm, Sweden. ³¹Center for Open Science, Charlottesville, VA, USA. ³²University of Virginia, Charlottesville, VA, USA. ³³Harvard Medical School, Boston, MA, USA. ³⁴Loyola University, Baltimore, MD, USA. ³⁵University of California, Riverside, CA, USA. ³⁶Wesleyan University, Middletown, CT, USA. ³⁷University of Konstanz, Konstanz, Germany. ³⁸Yale University, New Haven, CT, USA. ³⁹Coventry University, Coventry, UK. ⁴⁰Tilburg University, Tilburg, Netherlands. ⁴¹Utrecht University, Utrecht, Netherlands. ⁴²University of Leuven, Leuven, Belgium. ⁴³University of Padova, Padova, Italy. ⁴⁴University of Vienna, Vienna, Austria. ⁴⁵Adams State University, Alamosa, CO, USA. *Authors are listed alphabetically. †Corresponding author. E-mail: nosek@virginia.edu

by Gilbert *et al.*, and a fourth (the racial bias study from America replicated in Italy) was replicated successfully. Gilbert *et al.* also supposed that non-endorsement of protocols by the original authors was evidence of critical methodological differences. Then they showed that replications that were endorsed by the original authors were more likely to be replicated than those not endorsed (nonendorsed studies included 18 original authors not responding and 11 voicing concerns). In fact, OSC2015 tested whether rated similarity of the replication and original study was correlated with replication success and observed weak relationships across reproducibility indicators (e.g., $r = 0.015$ with $P < 0.05$ criterion; supplementary information, p. 67; <https://osf.io/k9rnd>). Further, there is an alternative explanation for the correlation between endorsement and replication success; authors who were less confident of their study's robustness may have been less likely to endorse the replications. Consistent with the alternative account, prediction markets administered on OSC2015 studies showed that it is possible to predict replication failure in advance based on a brief description of the original finding (7). Finally, Gilbert *et al.* ignored correlational

evidence in OSC2015 countering their interpretation, such as evidence that surprising or more underpowered research designs (e.g., interaction tests) were less likely to be replicated. In sum, Gilbert *et al.* made a causal interpretation for OSC2015's reproducibility with selective interpretation of correlational data. A constructive step forward would be revising the previously non-endorsed protocols to see if they can achieve endorsement and then conducting replications with the updated protocols to see if reproducibility rates improve.

More generally, there is no such thing as exact replication (8–10). All replications differ in innumerable ways from original studies. They are conducted in different facilities, in different weather, with different experimenters, with different computers and displays, in different languages, at different points in history, and so on. What counts as a replication involves theoretical assessments of the many differences expected to moderate a phenomenon. OSC2015 defined (direct) replication as “the attempt to recreate the conditions believed sufficient for obtaining a previously observed finding.” When results differ, it offers an opportunity for hypothesis generation and then

testing to determine why. When results do not differ, it offers some evidence that the finding is generalizable. OSC2015 provides initial, not definitive, evidence—just like the original studies it replicated.

REFERENCES AND NOTES

1. Open Science Collaboration, *Science* **349**, aac4716 (2015).
2. D. T. Gilbert, G. King, S. Pettigrew, T. D. Wilson, *Science* **351**, 1037 (2016).
3. G. Cumming, R. Maillardet, *Psychol. Methods* **11**, 217–227 (2006).
4. G. Cumming, J. Williams, F. Fidler, *Underst. Stat.* **3**, 299–311 (2004).
5. R. A. Klein *et al.*, *Soc. Psychol.* **45**, 142–152 (2014).
6. C. R. Ebersole *et al.*, *J. Exp. Soc. Psychol.* **65** (2016); <https://osf.io/csygd>.
7. A. Dreber *et al.*, *Proc. Natl. Acad. Sci. U.S.A.* **112**, 15343–15347 (2015).
8. B. A. Nosek, D. Lakens, *Soc. Psychol.* **45**, 137–141 (2014).
9. Open Science Collaboration, *Perspect. Psychol. Sci.* **7**, 657–660 (2012).
10. S. Schmidt, *Rev. Gen. Psychol.* **13**, 90–100 (2009).

ACKNOWLEDGMENTS

Preparation of this response was supported by grants from the Laura and John Arnold Foundation and the John Templeton Foundation.

2 December 2015; accepted 28 January 2016
10.1126/science.aad9163

RESEARCH ARTICLE SUMMARY

NEURAL COMPUTATION

Spiking neurons can discover predictive features by aggregate-label learning

Robert Gütiġ

INTRODUCTION: Opportunities and dangers can often be predicted on the basis of sensory clues. The attack of a predator, for example, may be preceded by the sounds of breaking twigs or whiffs of odor. Life is easier if one learns these clues. However, this is difficult when clues are hidden within distracting streams of unrelated sensory activity. Even worse, they can be separated from the events that they predict by long and variable delays. To discover those clues, a learning procedure must bridge the gap between the short epochs within which clues occur and the time when feedback arrives. This “temporal credit-assignment problem” is a core challenge in biological and machine learning.

RATIONALE: A neural detector of a sensory clue should fire whenever the clue occurs but

remain silent otherwise. Hence, the number of output spikes of this neuron should be proportional to the number of times that the clue occurred. The reversal of this observation is the core hypothesis of this study: A neuron can identify an unknown clue when it is trained to fire in proportion to the clue’s number of occurrences. This “aggregate-label” hypothesis entails that when a neuron is trained to match its number of output spikes to the magnitude of a feedback signal, it will identify a set of clues within its input activity whose occurrences predict the feedback. This learning requires neither knowledge of the time nor of the absolute number of individual clues.

RESULTS: To implement aggregate-label learning, I calculated how neurons should modify their synaptic efficacies in order to most ef-

fectively adjust their number of output spikes. Because a neuron’s discrete number of spikes does not provide a direction of gradual improvement, I derived the multi-spike tempotron learning rule in an abstract space of continuous spike threshold variables. In this space, changes in synaptic efficacies are directed along the steepest path, reducing the discrepancy between a neuron’s fixed biological spike threshold and the closest hypothetical threshold at which the neuron would fire a desired number of spikes. With the resulting synaptic learning rule, aggregate-label learning enabled simple neuron models to solve the temporal credit assignment problem. Neurons reliably identified all clues whose occurrences contributed to a delayed feedback signal. For instance, a neuron could learn to respond with different numbers of spikes to individual clues without being told how many different clues existed, when they occurred, or how much each one of them contributed to the feedback. This learning was robust to high levels of feedback and input noise and performed well on a connected speech-recognition task.

Aggregate-label learning enabled populations of neurons to solve unsupervised learning tasks by relying on internally generated feedback

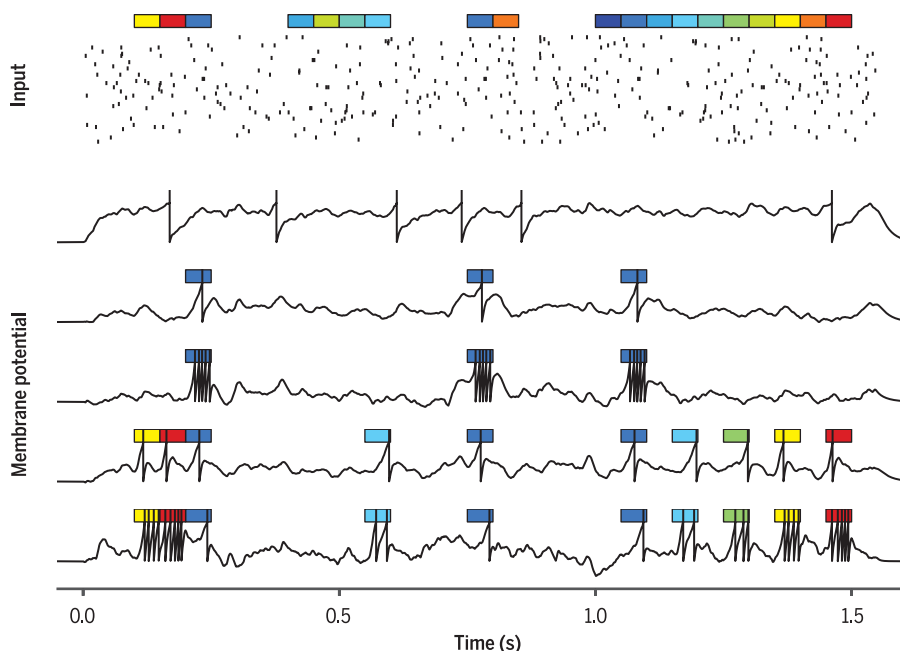
ON OUR WEB SITE

Read the full article at <http://dx.doi.org/10.1126/science.aab4113>

signals that amplified correlations between the neurons’ output spike counts. These self-supervised networks discovered reoccurring constellations of input patterns even if they were

rare and distributed over spatial and temporal scales that exceeded the receptive fields of individual neurons. Because learning in self-supervised networks is driven by aggregate numbers of feature occurrences, it does not require temporal alignment of the input activities of individual neurons. When competitive interactions between individual neurons were mediated through the internal feedback circuit, the formation of feature maps was possible even when the features’ asynchrony incapacitated lateral inhibition.

CONCLUSION: Aggregate-label learning solves the long-standing question of how neural systems can identify features within their input activity that predict a delayed feedback. This solution strongly enhances the known learning capabilities of simple neural circuit models. Because the feedback can be external or internal, these enhancements apply to supervised and unsupervised learning. In this framework, both forms of learning converge onto the same rule of synaptic plasticity, inviting future research on how they cooperate when brains learn. ■



Membrane potential traces of a model neuron before and after learning to detect reward predictive sensory clues. Before learning, top trace; after learning, second through fifth traces from top; clues, colored squares. Each clue occurrence is represented as a spike pattern within the neuron’s input activity (raster plot). After learning, the number of output spikes (vertical deflections) elicited by each clue encodes the clue’s contribution to a delayed reward.

RESEARCH ARTICLE

NEURAL COMPUTATION

Spiking neurons can discover predictive features by aggregate-label learning

Robert Gütig

The brain routinely discovers sensory clues that predict opportunities or dangers. However, it is unclear how neural learning processes can bridge the typically long delays between sensory clues and behavioral outcomes. Here, I introduce a learning concept, **aggregate-label learning**, that enables biologically plausible model neurons to solve this temporal credit assignment problem. Aggregate-label learning matches a neuron's number of output spikes to a feedback signal that is proportional to the number of clues but carries no information about their timing. Aggregate-label learning outperforms stochastic reinforcement learning at identifying predictive clues and is able to solve unsegmented speech-recognition tasks. Furthermore, it allows unsupervised neural networks to discover reoccurring constellations of sensory features even when they are widely dispersed across space and time.

The fitness of an individual depends on its ability to recognize circumstances that require specific actions to procure reward or avoid punishment. The approach of a predator, for example, may be preceded by one or more brief sensory clues, such as the sounds of breaking twigs or whiffs of odor. Humans and other animals are very good at learning such associations, even when clues are hidden within distracting streams of unrelated sensory activity of similar structure, and the delays between clues and outcomes are variable and orders of magnitudes longer than the durations of individual clues. To discover those clues, a learning procedure must bridge the gap between the short epochs within which clues occur and the long delays after which feedback arrives. This “temporal credit-assignment problem” is a core challenge in biological and machine learning (1–4). Often, the assignment of credit to a particular sensory clue is made even harder by the fact that the learner must not only discover when but also in which sensory channel a predictive clue can be found. This is the “spatial credit assignment problem.”

To forecast opportunities or dangers, a neural feature detector should be active whenever a predictive sensory clue occurs but remain silent otherwise. If the timing of the clues is known, synaptic learning rules (5–8) that resemble perceptron learning (9) can realize such desired responses by strengthening synapses that depolarize the cell at the time of a clue and weakening those that do otherwise. However, when the timing of the clues is unknown, an appropriate objective function that

can provide the direction of synaptic changes in spiking neurons has remained elusive (10). Applications of stochastic reinforcement learning have resulted in slow learning and limited performance (3, 4, 11–13). Other, non-neuromorphic solutions rely on complex iterative optimization algorithms such as expectation-maximization (14). Their biologically plausible implementation has remained challenging. Here, I show that the temporal credit assignment problem can be solved by training a neuron to match its number of output spikes to the magnitude of a feedback signal.

Results

Aggregate-label learning

A reliable clue detector should fire at least one action potential whenever the clue occurs but must remain silent otherwise. Hence, the number of spikes elicited within a given sensory episode should grow with the number of clue occurrences. Because we have only aggregate feedback information, I used the total number of spikes when constructing an objective function to drive learning (15). Here, I introduce the learning concept of **aggregate-label learning**: The temporal credit assignment problem is solved by a broad class of synaptic learning rules that credit individual synapses according to their ability to reduce the mismatch between the number of output spikes and the magnitude of the aggregate feedback. This feedback is only assumed to be proportional to the number of clues but provides no information about their timing or absolute numbers. Aggregate-label learning entails that neurons can learn to respond synchronously to predictive sensory clues from delayed feedback signals (16). I implemented aggregate-label learning with two specific synaptic learning rules: the multi-spike tempotron, a gradient-based learning rule that adjusts synaptic efficacies along

the steepest path toward the desired number of output spikes, and an approximation that is biologically more plausible.

The multi-spike tempotron

The “minimum disturbance principle” (17) posits that a neural implementation of aggregate-label learning should use a synaptic learning rule that adjusts a neuron's synaptic efficacies in the direction along which its number of output spikes changes most rapidly. Naive gradient-based approaches to find this direction fail in spiking neurons because of the discrete nature of the number of output spikes. Its derivatives with respect to a neuron's synaptic efficacies are zero almost everywhere and infinite at points where a new spike appears or an existing one disappears. To circumvent this problem, stochastic approaches have been tried with mixed success (11, 18, 19). Here, I introduce an alternative approach that is based on a continuous deterministic objective function for spiking neurons, the spike-threshold-surface. For each synaptic configuration and presynaptic activity pattern, the spike-threshold-surface is defined as the mapping between the neuron's firing threshold and the number of elicited output spikes (materials and methods, spike-threshold-surface) (fig. S1). On the basis of this curve, the discrete number of elicited output spikes is replaced with the distance between the fixed biological firing threshold of a neuron and the closest hypothetical threshold at which the neuron would fire the desired number of spikes. When this distance is zero, the neuron responds to the input pattern with the desired number of spikes. The multi-spike tempotron is defined as the gradient-based learning rule that approaches the desired number of spikes along the (locally) steepest path (materials and methods, multi-spike tempotron) (fig. S1D). I implemented the multi-spike tempotron by calculating the exact gradient (materials and methods, ∂^* -gradient). I also approximated the learning rule with a biologically established form of synaptic plasticity that is driven by correlations between presynaptic firing and postsynaptic depolarization. Specifically, in this correlation-based learning each synapse maintains a local trace of eligibility by correlating its own activity with the postsynaptic membrane potential (materials and methods, correlation-based learning). Beyond these eligibilities, this learning does not require a memory of past inputs or membrane potential values.

Learning predictive sensory clues

I tested aggregate-label learning within a family of generic feature learning tasks for single neurons. Each task consisted of a fixed set of brief (50 ms long) activity patterns that represented responses of a neuron's afferent periphery to occurrences of distinct features within an organism's sensory environment (Fig. 1A). In each trial, a random number of feature activity patterns was embedded within a long stream of random background activity at random times (materials and methods, embedded features). Each feature was either a clue or a distractor. The task of the neuron was to signal all clues by

Max Planck Institute of Experimental Medicine, Hermann-Rein-Strasse 3, 37075 Göttingen, Germany.
E-mail: guetig@em.mpg.de

firing a specific number of action potentials whenever the corresponding feature activity pattern occurred within its input stream. In contrast, the neuron had to remain silent during intervals of background activity or when encountering a distractor. In a first test, I trained the multi-spike tempotron to detect a single clue (out of 10 features) by matching each trial's aggregate label to the clue's number of occurrences. All remaining features were distractors. Whenever the cell fired fewer or more spikes than there were clues, the learning rule adjusted the neuron's synaptic efficacies along the direction of the steepest path toward the synaptic configuration that elicited one more or one less spike, respectively (materials and methods, multi-spike tempotron, and Eq. 7). Neural responses (materials and methods, neural responses) to random background activity and to all distractor features declined rapidly, and the cell learned to fire exactly one spike whenever the clue occurred (Fig. 1, B, second trace, and C, left; and fig. S2A) (response statistics are provided in table S1). I have checked that the correlation-

based approximation of the multi-spike tempotron resulted in a similar learning performance (fig. S3A).

Aggregate-label learning is not limited to a particular gain between a clue's number of occurrences and the feedback signal. When the desired number of output spikes corresponded to five times the number of the clues, the neuron learned to fire a burst of five spikes in response to each clue (Fig. 1B, third trace; fig. S2A; and table S1). Aggregate-label learning also enables neurons to decompose the feedback signal and identify the individual values of multiple sensory clues whose occurrences are mixed within a sensory scene (Fig. 1, B, fourth and fifth traces, and C, right; fig. S2B; and table S1). This problem arises in many ethological settings (2) whenever feedback signals incorporate contributions from several sources, such as food quality being associated with different color and odor clues. Our neural implementation of aggregate-label learning remains efficient even when applied to long sensory episodes dominated by background activity (Fig. 2A and fig. S2C) or when the number of distractor features is high

(Fig. 2A). It also tolerates a wide range of clue frequencies (Fig. 2B). The learning is robust to substantial correlations between clue and distractor occurrences (materials and methods, correlated feature occurrences) (Fig. 2C) and reproduces the phenomenon of "blocking" (2) when correlations are high (fig. S2D). When compared with a recent neural implementation of reinforcement learning (4), aggregate-label learning required much fewer synapses and learning trials to solve a feature learning task that was similar (although substantially simpler) to the ones studied here (materials and methods, reinforcement learning comparison task) (table S2) (20). Last, when sensory clues were not discrete but instead drawn from a continuous feature dimension, aggregate-label learning enabled neurons to learn continuous tuning curves (supplementary text S1 and fig. S4). The outcome of seeing a face, for instance, is likely to depend on its direction of gaze (ranging from looking straight at us to looking away) or its emotional expression (between angry and friendly).

Noisy feedback

In many learning tasks, the relation between clues and feedback can be unreliable. For instance, sensory clues can be occluded or feedback signals corrupted by noise. To test aggregate-label learning in such conditions, I modified the desired number of spikes on each trial by adding or subtracting (with equal probabilities) random Poisson noise. I found that neurons continued to reliably identify sensory clues even when the feedback noise was high (Fig. 2D). However, increasing levels of noise caused a gradual decline in the average number of spikes elicited by the clues in favor of spikes elicited by random background activity. This behavior reflects the inability of the identified clues to fully account for the (corrupted) feedback signal and could be interpreted as the neuron's attempt to search for a better predictor within the background activity. However, when the teacher is wrong, definitions of good and bad learning become circumstantial.

Prompted by its robustness to noise in the above scenario, I next considered whether aggregate-label learning can be extended to a well-studied probabilistic feature learning task. In the "weather prediction task" (27), relations between clues and feedback are not deterministic, but rather, clue occurrences increase the probability of a binary reward at the end of a trial (materials and methods, probabilistic reward contingencies). In addition to introducing feedback noise through probabilistic rewards, this scenario also relaxes our previous assumption that the feedback is proportional to the number of clue occurrences. Instead, here the number of clue occurrences is related to the reward (probability) through a saturating nonlinearity whose steepness is determined by the clue's reward contingency. The higher the contingency, the more step-like this mapping becomes. Because of this task's stochastic nature, the relation between clues and rewards has to be acquired and maintained across trials—for example, the absence of a reward on a single trial should not cause the immediate unlearning

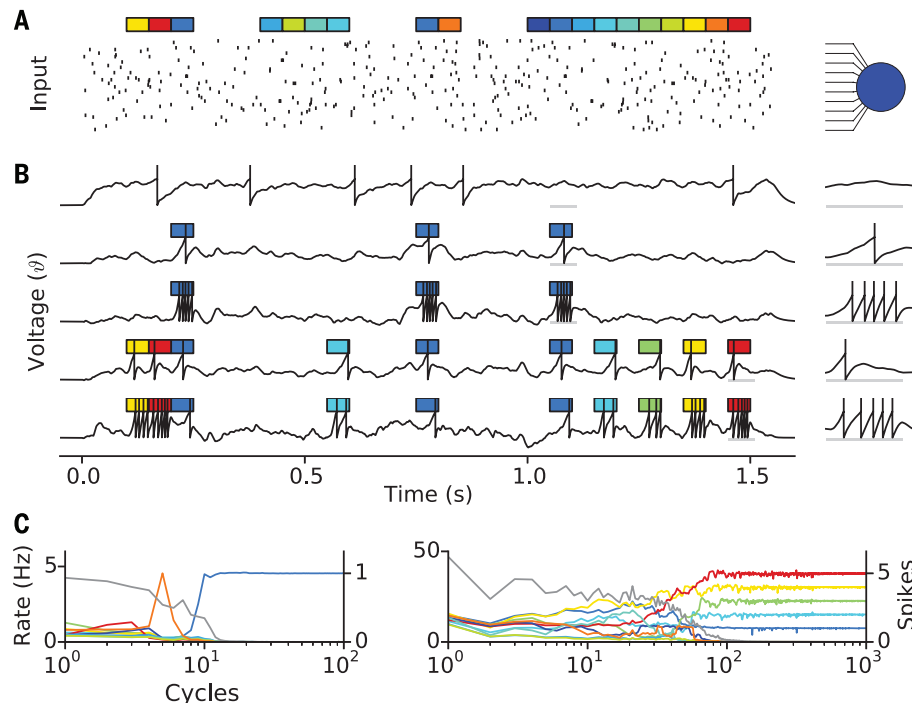


Fig. 1. Supervised learning of sensory clues. (A) Input activity (left raster plot) and schematic of a postsynaptic readout neuron (right). For visibility, only spikes (black ticks) of 10% of the neuron's 500 synaptic afferents are shown. Colored rectangles depict occurrences of $N_f = 10$ distinct sensory features (color coded) whose corresponding 50-ms activity patterns have been embedded within a stream of random background activity. (B) Voltage traces of the readout neuron before (top trace) and after being trained to fire one (second trace) or five (third trace) spikes in response to a single clue (dark blue rectangles), respectively. For the fourth and fifth traces, the neuron was trained to respond to five clues out of the 10 features (colored rectangles). The neuron either had to fire one spike in response to each of the clues (fourth trace) or one, two, three, four, and five spikes in response to the dark blue, light blue, green, yellow, and red clues, respectively (fifth trace). (Right) Enlargements of the underlined (gray horizontal lines) clue intervals. (C) Neural responses (materials and methods, neural responses) as a function of learning cycles (each containing 100 trials) for the two tasks underlying the second (left) and fifth (right) voltage traces in (B), respectively. Colored lines show the mean numbers of spikes (right y axis) elicited by each feature [color coded as in (A)], and gray lines show the mean responses to background activity (left y axis). Population learning curves are provided in fig. S3, left.

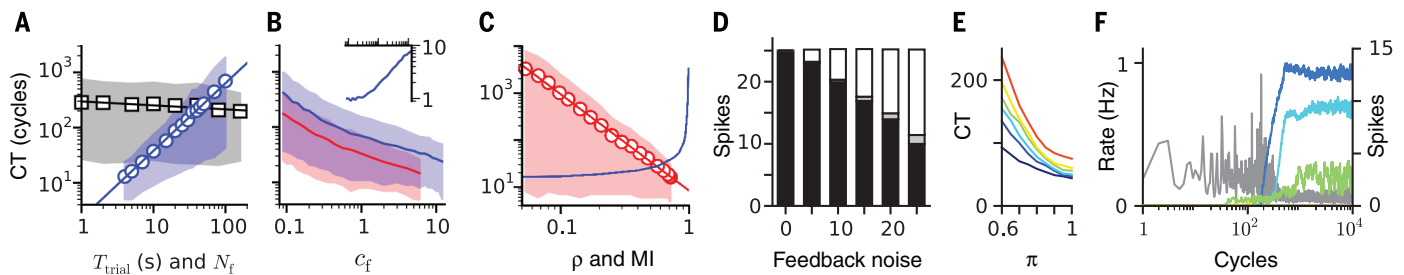


Fig. 2. Robustness of aggregate-label learning. (A to C) Mean convergence times (CT) of a neuron that was trained to fire one spike in response to a single clue for different task parameters. (A) For a fixed mean feature count $c_f^{\text{mean}} = 5$ as a function of the mean trial duration T_{trial} (blue circles) and for a fixed mean trial duration $T_{\text{trial}} = 50$ s as a function of the number of features N_f (black squares). Solid lines depict exponential fits with slopes of 1.23 and -0.07 , respectively. (B) For fixed mean trial durations $T_{\text{trial}} = 5$ s (red) and $T_{\text{trial}} = 10$ s (blue) as a function of the mean feature count c_f^{mean} . (Inset) The expected number of clue encounters before convergence in the $T_{\text{trial}} = 10$ s condition as a function of c_f^{mean} (same interval as in the main data) normalized to the value at $c_f^{\text{mean}} = 0.1$ (37.33). (C) For a fixed mean trial duration $T_{\text{trial}} = 5$ s and a fixed mean feature count $c_f^{\text{mean}} = 5$ as a function of feature correlations ρ (blue curve) or the corresponding normalized mutual information MI between the aggregate-label and the clue identity (red circles). The red line shows an inverse power-law relationship, with a nearly quadratic exponent of -2.05 . Shaded areas in (A), (B), and (C) correspond to regions between the 10th and 90th

percentile of 1000 independent simulations. (D) Learned responses of a neuron that was trained to fire five spikes in response to a single clue $c_f^{\text{mean}} = 5$ as function of the average noise that corrupted the feedback signal on each trial. Neural responses were averaged over the last 100 of 1000 cycles of training and converted to the expected number of spikes that were elicited by occurrences of the clue (black), the nine distractors (gray), or the 7.5 s of background activity (white) during each trial. All measurements were averaged over 1000 independent simulations. (E) Mean convergence times in the probabilistic single-clue detection task as a function of the clue's reward contingency π . Colors (cool to warm) depict rising noise levels in the input activity patterns implemented by an increasing spike deletion probability of 0, 0.1, 0.2, 0.3, 0.4, and 0.5. (F) Neural responses as in Fig. 1C, but for the probabilistic reward scenario. Three clues had reward contingencies of $\pi_1 \approx 1$ (dark blue), $\pi_2 \approx 0.8$ (light blue), and $\pi_3 \approx 0.6$ (green), respectively, and on each trial, a quarter of all input spikes were randomly deleted. Except the black line in (A), $N_f = 10$ throughout this figure.

of the corresponding clue. I therefore modified the learning scheme so that each rewarded trial invoked a learning step toward increasing the neuron's output spike number regardless of its response. In contrast, unrewarded trials triggered a learning step to reduce the number of output spikes only in the case of a "false alarm," when the neuron had fired at least one spike. This asymmetric learning continues to strengthen the neuron's responses to the sensory clues even after they have been identified, increasing their robustness. In addition, selectivity of the learned neural responses is enhanced by synaptic competition (22) that was induced here by bounding the overall strength of the neuron's synaptic efficacies through divisive normalization (materials and methods, probabilistic reward contingencies). The resulting learning reliably identified predictive clues, even if their reward contingencies were far from perfect and, in addition, all activity patterns were corrupted by random deletions of presynaptic spikes on each trial (Fig. 2E). I checked that the learned neural responses were hardly affected by the presence of false rewards that were not predicted by any of the available clues. The main effect of such false rewards was to slow down the clue acquisition (fig. S5A). When the reward probability resulted from the combination of several different clues, the relative strengths of the average learned responses reflected each clue's individual predictive strength (Fig. 2F and fig. S5, B and C). Thus, learned responses of multi-spike tempotrons with stochastic feedback resembled recordings in the lateral intraparietal cortex of rhesus monkeys performing a similar task (21).

Application to speech recognition

In machine learning approaches to automatic speech recognition, it is easy to count occurrences

of words or phonemes within a known text. However, their temporal alignment with a corresponding speech signal has been notoriously difficult and requires complex optimization algorithms (14). I tested whether word counts are sufficient to successfully apply aggregate-label learning to continuous speech recognition problems. I addressed this question by extending a recent neural model of spoken digit recognition (materials and methods, auditory front-end) (23) from binary to multi-spike tempotrons. In contrast to the previously used TI46 database, which is limited to utterances of single digits, I used the TIDIGITS speech corpus (24), which also contains sequences of digits of variable length (ranging from 2 to 7). With all utterances of single digits reserved to test performance, training was based on unsegmented digit sequences only. Specifically, I used the number of occurrences of a single target digit as aggregate-label to train neurons to discriminate between this target and the remaining distractor digits. I found that multi-spike tempotrons reliably learned to fire a single spike whenever their target digit occurred and to remain silent otherwise (Fig. 3A). Across all digits, the majority of simulations achieved zero errors over the test set (Fig. 3B), with an average test error of 0.0055 (materials and methods, TIDIGITS-task). For comparison with the binary tempotron model (12), I also evaluated the test error under a binary decision rule, which only required the neuron to fire at least one spike when the target digit occurred within its input. With this looser performance measure, the test error of the multi-spike tempotron reduced to 0.0021, outperforming the binary tempotron by 23%. I next exploited that $\sim 20\%$ of the training sequences in which a target digit occurred contained multiple occurrences. To expose the role of aggregate-label learning,

I repeated the comparison with a strongly reduced training set in which target digits, if present, occurred multiple times. Indeed, the performance gap between the two models widened to 47%. In contrast, the difference fell to 16% when trials with multiple target digit occurrences were excluded. This remaining difference shows that the ability of the multi-spike tempotron learning rule to enforce a single output spike, as opposed to realizing at least one, resulted in an advantage over the binary tempotron, even when the labels of a task were binary. I expect that the advantages of aggregate-label learning will become even more pronounced in applications to neural models of phoneme detection that will encounter higher numbers of target feature occurrences.

Self-supervised neural networks

Consider the above family of feature learning tasks, however, without any feedback (25, 26). How can neurons still "discover" synaptic activity patterns that represent repeated occurrences of sensory features in the environment? In general, structure is discriminated from noise through correlations. Indeed, existing models of unsupervised learning in spiking neural networks have typically relied on spatiotemporally local correlations between the pre- and postsynaptic activity of individual neurons to detect structure within a networks input activity (27)—for instance, through spike-timing-dependent synaptic plasticity (25, 26, 28). Can aggregate-label learning enable populations of neurons to detect structure across much larger scales in space and time by amplifying correlations between the neurons' output spike counts? In contrast, neurons that respond to random inputs typically generate uncorrelated numbers of output spikes. I tested this hypothesis by modeling a neural processing

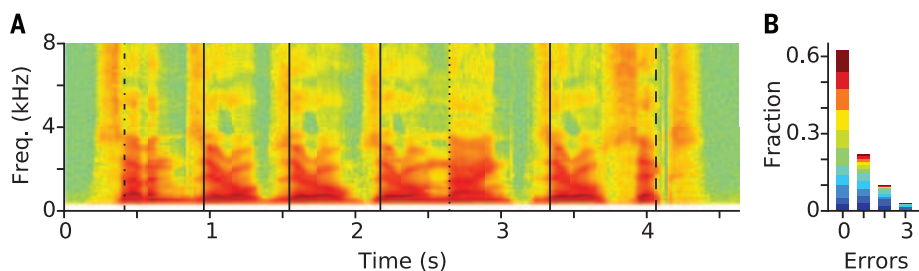


Fig. 3. Application of aggregate-label learning to continuous speech recognition. (A) Spectrogram of one example utterance of the TIDIGITS database (file “7zzz9z6a.wav” of male speaker “ka”) containing the spoken digit sequence “seven,” “zero,” “zero,” “zero,” “nine,” “zero,” “six.” Vertical lines show the output spike times of four neurons that were trained with the occurrence counts of the digits “seven” (dot-dashed), “zero” (solid), “nine” (dotted), and “six” (dashed). Each of the neurons responds to the occurrence of its target digit by firing a single spike. (B) Histogram of individual test errors over the isolated digits subset of the database. The histogram comprises error counts of 10 independent simulations for each of the 242 task conditions (11 target digits \times 22 dialects). Colors depict contributions from individual digits [starting with “zero” (darkest blue) followed by “oh,” numerical values increase with color temperature].

layer as a population of multi-spike tempotrons that were driven by a common sensory periphery. Learning in this population was controlled by a feedback signal that was generated internally by a single downstream supervisor unit (Fig. 4A) and signaled a common desired number of output spikes to all processing layer neurons. To amplify correlations between the processing layer responses—to drive neurons to respond to structure within their input activity—the common feedback signal was based on the average number of spikes fired within the processing layer during the preceding sensory episode. This self-supervision entailed that all processing neurons that fired more spikes than the population average implemented a learning step toward a reduced spike response. Vice versa, neurons that fired fewer spikes than their peers’ average response adjusted their synaptic efficacies toward an increased output spike count. If by chance a subset of neurons responded to occurrences of the same sensory feature, their elevated joint weight within the average population response biased the remaining neurons to search for a feature that occurred the same number of times. This learning will come to an end when all processing layer neurons generate an equal number of output spikes (materials and methods, zero labels, correlations in synaptic efficacies and synaptic learning noise)—in particular, when neurons cease to respond to random background activity and respond with the same number of spikes to all sensory features. Indeed, when applied to the embedded feature detection task, processing layer neurons of self-supervised networks converged (materials and methods, convergence in unsupervised learning tasks) to subsets of the recurring features and encoded each of their occurrences by firing the same number of spikes while remaining silent otherwise (Fig. 4, B and C; population data is provided in fig. S6A). The ability of aggregate-label learning to overcome long feedback delays permits the network’s supervisory circuit to integrate the activity of the processing layer over long time windows. Within these windows, features are bound together across

the individual receptive fields of different neurons on the basis of their common occurrence counts, irrespective of their timing. In particular, features can occur asynchronously across the processing layer. To demonstrate this capability, I implemented a self-supervised network architecture in which each processing layer neuron received individual input activity (Fig. 4D): For each neuron, sensory features were represented by individual activity patterns that occurred at independent random times within independent random background activity. Such individual input architectures mimic neural integration stages of segregated or even multimodal sensory input streams—such as visual, auditory, and olfactory—whose activity might not be temporally aligned. Self-supervised learning functioned also within this network architecture (Fig. 4B, inset). Detailed analyses (supplementary text S2) showed that self-supervised learning is sensitive to the number and the timing of spikes within a feature’s activity pattern (fig. S6, C and E). It can tolerate high levels of input noise (fig. S6F) and operate over a wide range of processing layer sizes (fig. S6D). Furthermore, the learning mechanism can be implemented with various functional forms of the internal feedback signal, including a neural implementation in which the feedback is driven by output spikes of a neural supervisor (fig. S6G). I have ensured that self-supervised learning was unaffected when synaptic plasticity in the processing layer used the approximate, correlation-based learning rule (fig. S3C). Last, self-supervised learning functioned analogously when the unknown features were not discrete but drawn from continuous feature dimensions (fig. S7).

Neural interactions mediated through internal feedback signals

An important question in unsupervised neural learning is what mechanisms of interactions can ensure the formation of neural maps in which different neurons represent different features. One intuitive and long established mechanism for competitive interactions between neurons is lateral inhibition (27). Indeed, recurrent inhibitory

connections between the processing layers of several self-supervised networks (materials and methods, lateral inhibition) ensured that each of the networks converged to a nonoverlapping region of feature space (fig. S8, A and B). This mechanism did not require fine tuning of the strength of inhibition (fig. S8B) and accommodated different numbers of participating networks by automatically increasing each network’s selectivity when the number of networks grew (fig. S8C).

Lateral inhibition shaped the neural activity profiles that emerged from the unsupervised learning dynamics by introducing a complex interference between feedforward inputs and recurrent inhibitory activity. The complexity of these highly nonlinear interactions makes it difficult (presumably also for evolutionary processes) to control the exact shape of the emerging neural tuning profiles. In addition, this tuning remains dependent on the continued presence of the recurrent inhibition even after the learning has converged. Last, because direct lateral inhibition operates on the fast time scale of the processing layer, it requires the tight temporal alignment of all sensory feature streams. This conflicts with the inherent capability of self-supervised networks to discover temporal structures that extend over the much slower time scale of the supervisory feedback circuit. These three drawbacks can be resolved by replacing the direct interactions between processing layer neurons with indirect interactions through a more refined supervisory circuit. Specifically, I assume that instead of the common supervisory signal introduced above, a group of supervisory units maps the activity of the processing layer onto an array of supervisory signals $\vec{\ell}$ whose components ℓ_i specify the individual desired spike counts of each processing neuron (Fig. 5A). In its simplest form, these labels are given by a linear projection,

$$\ell_i = \sum_{j=1}^{N_p} S_{ij} a_j \quad (1)$$

which has a straightforward neural interpretation (materials and methods, neuron specific feedback signals in self-supervised networks) and suffices to expose the basic principle underlying the proposed mechanism. Nevertheless, nonlinearities within this supervisory pathway, such as the saturation of individual feedback signals, can have important functional consequences (compare with Fig. 6). In the above equation, N_p is the number of processing layer neurons, and the component S_{ij} of the $N_p \times N_p$ supervisory matrix specifies how much the activity a_j of the j th processing neuron contributes to the supervisory signal ℓ_i of the i th processing neuron. The regulation of this coupling between the supervisory circuit and the processing layer is assumed to take place over much slower (developmental or evolutionary) time scales than that of learning in the processing layer.

In any unsupervised neural network, the shape of the emerging neural activity profiles depends on the network’s architecture. In self-supervised networks, this dependence is particularly simple:

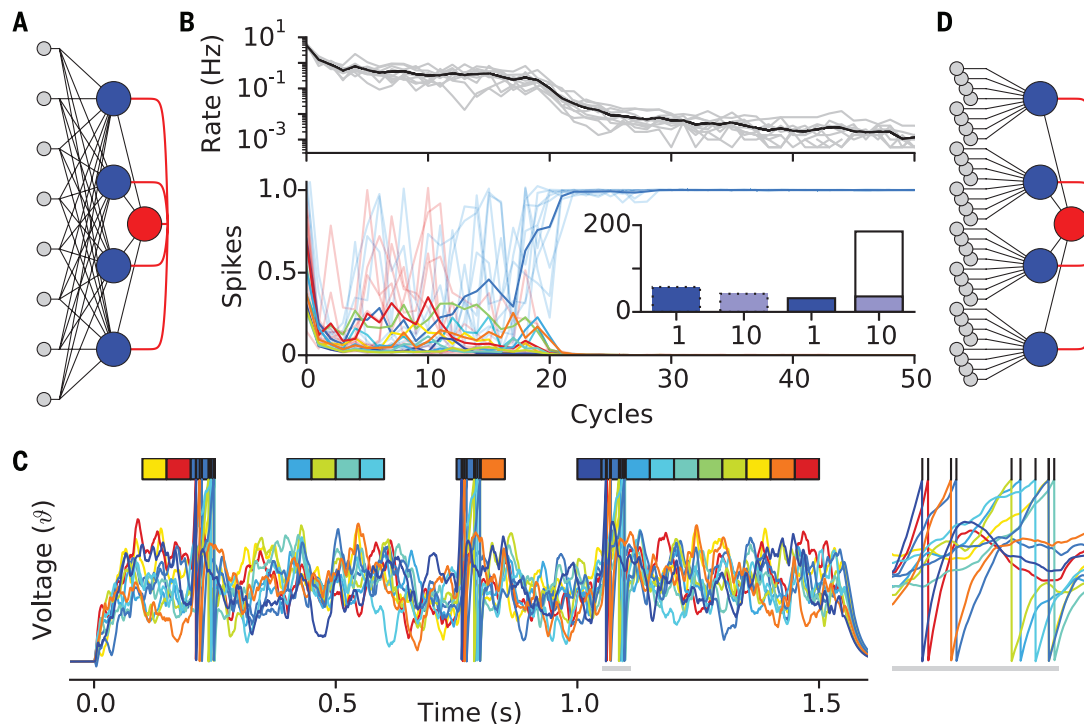


Fig. 4. Self-supervised neural networks. (A) Network scheme with shared input architecture. A layer of processing neurons (blue) receives input activity from a common input layer (gray). These multi-spike tempotrons project to a single supervisor unit (red), which feeds back a common feedback signal (red lines) to each neuron of the processing layer. (B) Learning curves of a shared input network showing the evolution of the processing-layer responses to the background activity (top, black line) and to each of the individual features [bottom; color code as in (C)]. Full colors denote the mean responses over all 10 processing-layer neurons of the network, and light tones depict responses of individual cells. (Inset) The mean convergence times (over 1000 independent

simulations) of shared [(A), dotted lines] and individual [(D), solid lines] input architectures for tasks with 1 (dark blue) and 10 (light blue) features. The open bar represents tasks in which the independent features of each processing-layer neuron were not ordered with respect to their spike counts (supplementary text S2) (C) Example voltage traces of all 10 processing-layer neurons (color coded) at the end (500 cycles) of the simulation shown in (B). Although individual voltage traces have remained diverse, all neurons have learned to respond the dark-blue feature. (Right) The 10 traces within one of the feature occurrences (gray horizontal line). (D) Network scheme as in (A), but with individual input architecture.

The learning dynamics in self-supervised networks reaches a fixed point when all supervisory signals match the activities of the recipient processing layer neurons so that all discrepancies between feedback signals and neural responses vanish. This is the case when the supervisory circuit projects the processing layer activities onto themselves—when, mathematically, \vec{a} is an eigenvector of the supervisory matrix S with eigenvalue 1. This observation immediately explains the behavior of the self-supervised networks with a single supervisor that corresponds to a uniform supervisory matrix with constant $S_{ij} = 1/N_p$. With uniform supervision, the only eigenvector of S with nonzero eigenvalue is also uniform, so that convergence requires all neurons to respond with the same number of spikes to each input pattern. Although uniform supervision offers the simplest neural implementation, neural circuits can use multiple supervisor units as an efficient mechanism to stabilize more complex neural activity profiles across feedforward sensory processing stages. In fact, with appropriate supervisory connections the learned neural responses to a discovered sensory feature can be shaped almost arbitrarily (materials and methods, supervisory matrices, neural population tuning for discrete features) (Fig. S5B and fig. S9, A

and B). When exposed to sensory features from a continuous dimension, self-supervised networks with saturating supervisory signals (materials and methods, continuous feature maps) are capable of generating continuous sensory feature maps without requiring lateral inhibition or temporal alignment of incoming sensory features (materials and methods, continuous feature maps) (Fig. 6 and fig. S9C).

Discussion

I have demonstrated that aggregate-label learning enables simple neural architectures to solve the temporal credit-assignment problem underlying learning tasks with delayed feedback. This approach remains robust even when input signals are corrupted by noise or when the feedback is stochastic and binary. Aggregate-label learning outperforms reinforcement learning and can solve connected-speech recognition tasks without temporally annotated training data. Although organisms rarely have access to the timing of an unknown clue, a clue's number of occurrences is often related to the strength or likelihood of the feedback signal that it predicts. Hence, the concept applies to a large class of ethological learning scenarios. The learning requires neural representations of the discrepancy between ag-

gregate rewards and the integrated neural responses. The existence of such reward prediction errors, such as within responses of midbrain dopamine neurons, has long been established (2, 29). I have shown that a simple binary readout (increase versus decrease) of such error signals (2, 29, 30) is sufficient to drive aggregate-label learning. At the core of aggregate-label learning lies the challenge to credit the right synapses when a neuron's discrete number of output spikes requires adjustment. The gradient-based multi-spike tempotron learning rule establishes a normative solution of this fundamental problem. Thus, it provides an important frame of reference for experimental measurements of synaptic plasticity. Its essential capabilities can be reproduced by an approximation (materials and methods, correlation-based learning) (fig. S3) that is based on temporal correlations between presynaptic activity and postsynaptic depolarization (12, 31, 32). Although performing well on easier tasks, this simple approximation becomes unstable for difficult tasks in which it requires early stopping or stabilization—for instance, through divisive weight normalization (fig. S3B). I expect that refinements, such as nonlinear eligibilities or the incorporation of corrections from elicited postsynaptic spikes (33), will further improve the performance and stability

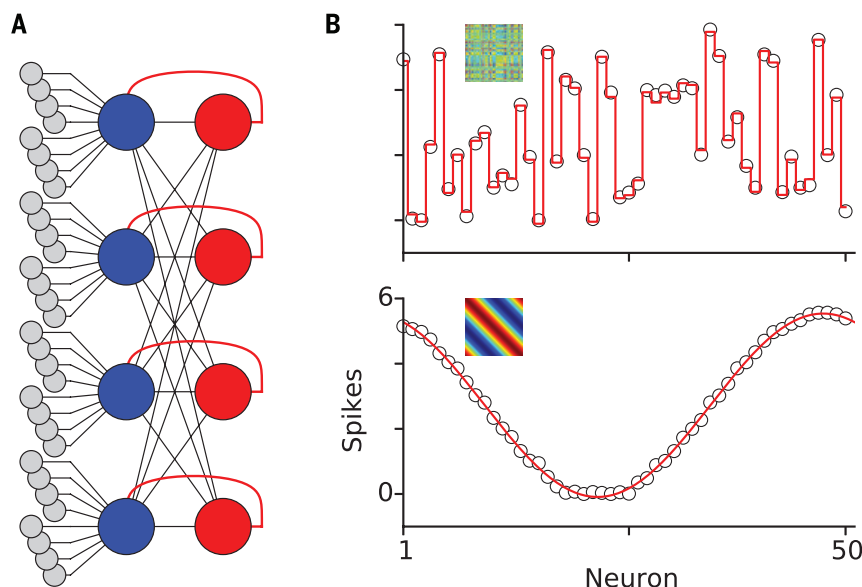


Fig. 5. Feedback-mediated neural interactions. (A) Network scheme (Fig. 4D) of a generalized self-supervised network in which each processing layer neuron receives an individual feedback signal (red lines) from a dedicated supervisor unit (red circles). (B) Learned neural responses (open circles, y axis) of 50 processing layer neurons (x axis) in a single feature task ($N_f = 1$). Responses were measured after 200 cycles of unsupervised learning (materials and methods, neural population tuning for discrete features) with two different supervisory matrices. (Top) The supervisory matrix (inset) stabilized a generic population tuning profile v whose individual components were drawn from a uniform distribution (materials and methods, supervisory matrices). The red line shows a two-parameter (baseline and scale) fit of v with $R^2 = 0.9973$. (Bottom) The circulant supervisory matrix (inset) stabilized a sinusoidal neural tuning profile. The red line shows a first-order harmonic fit (baseline, amplitude, and phase) with $R^2 = 0.9987$. Background intervals were $T_\phi = 2$ s long, and mean feature counts were $c_f^{\text{mean}} = 25$.

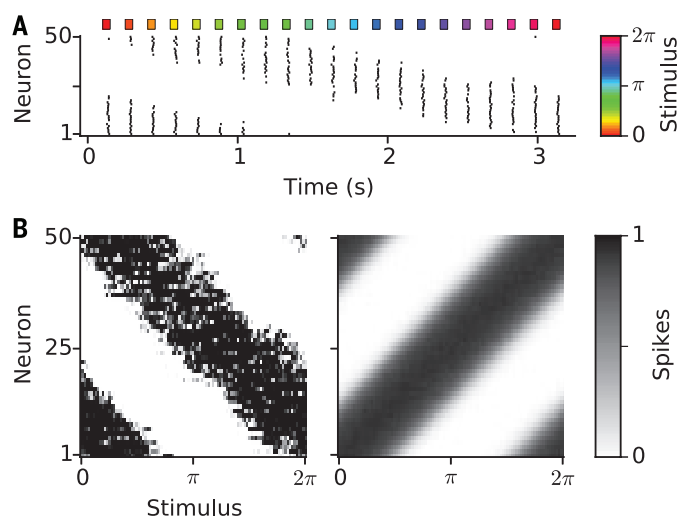


Fig. 6. Emergence of continuous feature maps. (A and B) Learned neural responses when the generalized self-supervised network from Fig. 5B, bottom, was driven with features from a continuous dimension (materials and methods, continuous feature dimensions). The emergence of these continuous maps required the supervisory signals to be saturating (materials and methods, continuous feature maps) to enforce an even distribution of neural responses across the processing layer. (A) Example output spike raster of a processing layer (after learning) when driven by a probe trial containing 21 features (colored rectangles) embedded within background activity at evenly spaced times (x axis). The features evenly span the feature dimension (color bar). (B) Mean neural responses (gray scale) of all 50 processing-layer neurons (y axis) to feature from the continuous dimension (x axis) for a single network (left) and the mean map (right) over 1000 independent simulations. Phases and directions of individual maps (fig. S9C) were aligned before averaging. Background intervals were $T_\phi = 1$ s long, and mean feature counts were $c_f^{\text{mean}} = 2$.

of neural implementations of the multi-spike tempotron. I have focused on the computationally hardest scenario and applied aggregate-label learning to single-step prediction problems (1), within which no feedback at all is available until the end of a trial. Extensions of the concept to multistep prediction problems—within which some feedback can also arrive throughout a trial, such as in the context of temporal difference learning (1)—will further boost learning performance. These extensions will need to elaborate how the neural feedback circuit should segment the learning in time when consecutive feedback signals become available. One possibility is that the circuit initiates a learning step whenever the discrepancy between the available external feedback and its internal prediction reaches a critical value. The neural implementation of aggregate-label learning can be interpreted as a continuous (temporal) form of multiple-instance learning [reviewed in (34)], establishing an unexplored cross-link between neurobiological and machine learning.

The concept of aggregate labels gives rise to a form of unsupervised learning that enables populations of neurons to discover reoccurring constellations of input patterns even if they are rare and distributed over spatial and temporal scales that exceed the receptive fields of single neurons. This detection of global structure through the amplification of correlations is related to the long established statistical technique of canonical correlation analysis (35, 36). Implemented within an information maximization approach, the underlying principle has previously enabled abstract neural networks with analog (sigmoidal) units to detect “instantaneous” spatial structure across neural populations (36, 37). Through aggregate-label learning, this principle could be realized in the time domain and implemented within a spiking neural network. The resulting self-supervised learning is consistent with observed increases in response coherence (within local groups of neurons) accompanying the emergence of direction selectivity in early cortical development (38) and captures the process’s sensitivity to stimulus statistics (39). Self-supervised networks are robust to extensive temporal misalignments between feature occurrences across their processing layers. Overcoming the inability of direct lateral inhibition to introduce competitive interactions between neurons that are processing asynchronous features, I have demonstrated that such interactions can be straightforwardly mediated through internal supervisory signals, offering a simple yet powerful mechanism with which to mold the emerging neural maps. After convergence, the supervisory circuit can disengage without affecting the learned neural responses. By detecting common numbers of occurrence, self-supervised networks realize a general principle for invariance learning that encompasses (as a special case) the recently proposed principle of “temporal contiguity” (40, 41). Nevertheless, constraints on the time evolution of the internal supervisory signals could be considered to further extend the window of “temporal contiguity” beyond the time frame of the supervisory signaling.

The mechanisms through which self-supervision segments learning in time, such as through thresholding the total number of processing layer spikes, will be important constituents of its specific neural implementations. The structural and computational simplicity of self-supervised networks permits a number of neural implementations at different spatial scales. I have shown that the internal feedback signal can be realized by the spiking activity of a simple model neuron, demonstrating that modulatory feedback of neural origin could be provided to local as well as distributed (multimodal) processing layers. Alternatively, I speculate that a local supervisory signal could be provided by astrocytes that have been implicated in modulating synaptic plasticity and also monitor the activity levels of neighboring neural circuits (42). Last, the computational similarity between a two-layer neural network and dendritic nonlinearities that converge onto a soma (43) invites the intriguing thought that the principle of self-supervision could be used by a neuron's somatic compartment to guide its dendritic branches in a search for structure within the cell's presynaptic activity (44).

Materials and methods

Embedded features

High-dimensional spike patterns of $N = 500$ sensory afferents were modeled as Poisson point processes with an average firing rate of $r_f = 5$ Hz. Each multineural input spike pattern consisted of random background activity of duration $T_{\mathcal{O}}$, which was interleaved by a random number of feature activity patterns. Feature activity patterns were $T_f = 50$ ms long and remained fixed across all trials of a given learning task. In tasks that mimicked learning of discrete sensory features, N_f independent realizations of feature activity patterns were generated from the background firing statistics. For each trial, the number of each feature's occurrences was drawn from a Poisson distribution with mean c_f^{mean} . Thus, the average total number of features within each trial was given by $N_f c_f^{\text{mean}}$, and the mean trial duration was

$$T = T_{\mathcal{O}} + N_f c_f^{\text{mean}} T_f \quad (2)$$

For each feature occurrence of a given trial, an occurrence time was drawn from a uniform distribution over $[0, T_{\mathcal{O}}]$. After sorting all feature occurrence times, the input activity pattern was constructed by successively inserting the feature activity patterns into the background. Overlap was avoided by delaying all background spikes after a feature occurrence and all subsequent feature occurrence times by T_f whenever a feature activity pattern was inserted.

Fixed feature activity spike counts

In fig. S6, D to F, I studied the convergence times of self-supervised networks with feature activity patterns whose total spike counts were fixed instead of drawn from Poisson count statistics. Specifically, for each feature activity pattern the predetermined number of spikes was randomly distributed across all N afferents by randomly

sampling (with replacement) from a uniform distribution over $\{1, 2, \dots, N\}$.

Correlated feature occurrences

In Fig. 2C and fig. S2D, homogeneous pairwise correlations $0 \leq \rho \leq 1$ between the numbers of occurrences C_i of all features $i = 1, \dots, N_f$ were introduced through a common source Y . Specifically, on each trial each feature's number of occurrences was realized through the sum of two Poisson random variables, $C_i = Y + X_i$. With the mean of the common Y set to ρc_f^{mean} and the means of the individual X_i set to $(1 - \rho)c_f^{\text{mean}}$, the resulting C_i were Poisson distributed with mean c_f^{mean} and pairwise correlations $\text{Corr}[C_i, C_j] = \rho$ for $i \neq j$. The mutual information (MI) between the labeled numbers of occurrences \vec{C}_{ℓ} —that is, $\vec{C} = (C_1, \dots, C_{N_f})$ and the corresponding aggregate-label ℓ —and the identity of the clue is given by the reduction in the clue's uncertainty, $\text{MI} = H_{\text{clue}} - H_{\text{clue}|\vec{C}_{\ell}}$ (materials and methods: mutual information between feedback signal and clue identity).

Reinforcement learning comparison task

To compare aggregate-label learning with the performance of a recent implementation of reinforcement learning (4), I studied a feature learning task in which no background activity was present and the desired response to each feature was binary: at least one spike versus no spike. In addition, the duration $T_f = 500$ ms of the $N_f = 10$ Poissonian feature activity patterns with mean firing rates of $r_f = 6$ Hz was much longer. Each trial consisted of a random sequence of all features. To mimic the feedback delay of 1350 ms (4), each input activity pattern was partitioned into 10 segments of 1350 ms duration whose starting times were locked to the beginning of each of the 10 features. Half of the features were targets and the neuron required to respond with at least one spike within the 500 ms feature interval, whereas the other half were distractors, for which the neuron had to remain silent. After a miss, the neuron was trained to increase its number of output spikes over the preceding 1350-ms input activity pattern by one spike, and after a false alarm, the neuron was trained to decrease its number of output spikes. The convergence criterion required 90% correct feature responses (4).

Probabilistic reward contingencies

In Fig. 2, E and F, and fig. S5 I study an adapted version of the “weather prediction task” (21), in which the occurrences of sensory features increment the probability p_R that a binary reward is delivered at the end of a trial. In each trial, the reward probability was given by

$$p_R = 1 - \exp \left[\sum_{i=1}^{N_f} c_i \log(1 - \pi_i) \right] \quad (3)$$

where the sum runs over all existing sensory features and $c_i \in \mathbb{N}_0$ denotes their independent Poissonian occurrence counts (with mean $c_f^{\text{mean}} = 0.1$). The reward contingency of each feature i was controlled by the parameter $\pi_i \in [0, 1]$, which determined by how much each individual occurrence

of the feature increased the reward probability. On trials that contain only a single feature—only one of the $c_i = 1$ while the others are zero—the reward probability reduces to $p_R = \pi_i$. In fig. S5A, I test the effect of false rewards. These were generated by additional features with nonzero reward contingencies, however, which were invisible to the neuron because their occurrences did not contribute to the neuron's input spike train. In learning tasks with probabilistic reward contingencies, synaptic potentiation was invoked after each rewarded trial irrespective of the neuron's response. Specifically, the neuron performed a multi-spike tempotron learning step toward increasing the current response by one spike. In contrast, depression was dependent on the neuron's response, and a learning step toward decreasing the neuron's response by one spike was only invoked when the neuron fired at least one spike during a nonrewarded trial (false alarm). I used divisive normalization to bound the resulting learning dynamics: Whenever, after a learning step, the Euclidean norm $|\vec{w}|$ of the synaptic efficacies surpassed the fivefold multiple of its initial value $|\vec{w}_{\text{ini}}|$, all efficacies were multiplied by $5|\vec{w}_{\text{ini}}|/|\vec{w}|$.

Continuous feature dimensions

To mimic sensory features from a continuous dimension I modeled a sensory encoding stage that mapped each feature parameter $\alpha \in [0, 2\pi]$ to a feature activity pattern of $T_f = 50$ ms duration. This deterministic map was constructed by specifying how the feature spike trains of each individual afferent—the number and timing of spikes within the 50 ms feature interval—depended on the feature parameter α . For each afferent, this mapping was defined through interpolation between a set of spike train templates. The number of templates assigned to each afferent was a random number $m = 1 + \Gamma$ with Γ drawn from a Poisson distribution with mean γ . Each of these m templates was randomly assigned to a fixed position α_i^* ($i = 1, \dots, m$) within the feature dimension, drawn from a uniform distribution over $[0, 2\pi]$. Each template i stored a spike count c_i drawn from the background statistics and a vector of spike times drawn from a uniform distribution over $[0, T_f]$. The number of spike times stored in each template was equal to the maximal spike count of the afferent over all of its m templates. For any feature parameter $\alpha \in [0, 2\pi]$, a vector of spike times was given by linear interpolation between the two spike time vectors of the adjacent templates k and $k + 1$ with $\alpha_k^* < \alpha < \alpha_{k+1}^*$. For afferents with only one spike train template, $m = 1$, the spike train remained unchanged for all α and did not carry any information about the feature parameter. If the two adjacent templates had the same spike counts—if $c_k = c_{k+1}$ — α was mapped to a spike train of c_k spikes that occurred at the first c_k components of the interpolated spike time vector. If the spike counts were different, $\Delta c_k = |c_k - c_{k+1}| > 0$, an additional set of transition values α_j^{Δ} ($j = 1, \dots, \Delta c_k$) from a uniform distribution over $[\alpha_k^*, \alpha_{k+1}^*]$ was stored with the templates. These transition values determined the positions of incremental changes

in the number of spikes as α transitioned through $\alpha_k^* < \alpha_1^* < \alpha_2^* < \dots < \alpha_{\Delta k}^* < \alpha_{k+1}^*$. The appearance and disappearance of spikes along the feature dimension was ordered according to a “last-in-first-out” principle, so that the most recently added spike was always the first to disappear when the spike count began to decrease. The only internal parameter of the above encoding stage is γ , which controls the density of independent spike train templates along the feature dimension and thus determines how quickly the activity patterns of two feature parameters become uncorrelated as their distance along the dimension grows (fig. S4A). Except in fig. S4A where I varied γ , I used $\gamma = 5$ throughout the present work.

Encoding schemes

In fig. S4, D to F, I compare the learning performance for different encoding stages. In addition to the above encoding in which both spike counts and spike times carry information about the feature parameter α , I implemented three additional alternatives: In a count-based encoding, the feature parameter α only determined the deterministic number of spikes that each afferent contributed to the feature activity pattern, but their timing was drawn independently for each feature realization. In a variation of this scheme, these deterministic spike counts were interpreted as the mean values of random Poisson spike count variables that were redrawn for each realization of a feature activity pattern and the corresponding number of spikes placed randomly within the feature interval. In contrast, the spike-timing-based encoding stage was constrained so that the spike counts of all spike train templates of a given afferent remained constant along the entire feature dimension. Here, only the relative timing of spikes within the feature activity pattern, but not their numbers, carried information about the feature parameter.

Continuous tuning curves

Random periodic target tuning curves of the form

$$f_O(\alpha) = A_0 + \beta \sum_{k=1}^O B_k \cos(k\alpha + \phi_k) \quad (4)$$

were generated by drawing the amplitudes B_k from a uniform distribution over $[0, 1]$ and the phases ϕ_k from a uniform distribution over $[0, 2\pi]$. The parameter $O \in \mathbb{N}$ determined the order of the highest nonzero Fourier coefficient in the above expansion. For each realization, the baseline A_0 and the global scale β were set so that the minimum and maximum of f_O were $f_O^{\min} = 0$ and $f_O^{\max} = 10$, respectively. In fig. S4C, I used the gray-level values of Leonardo da Vinci's Mona Lisa as target tuning curves. The image data was based on the file `Mona_Lisa_by_Leonardo_da_Vinci_from_C2RMF_retouched.jpg` downloaded from <http://commons.wikimedia.org/wiki> in a resolution of 687 by 1024 pixels. A 100- by 100-pixel region was extracted, converted to gray-scale, and rescaled so that the minimum value was 0 and the maximum 10. Each target tuning function corresponded to a row of the resulting

matrix. During training, feature parameters were rounded to a discrete grid that matched the column resolution of the image.

Input noise

I used two types of input noise: First, random deletion of input spikes that mimicked synaptic transmission failures (Fig. 2, E and F, and figs. S4F, S5, and S6F), and second, presynaptic spike time jitter (Fig. 3 and fig. S4E). Spike deletion was parameterized through a probability p_{del} , which determined for each spike of an input activity pattern (including background spikes) the independent probability that it was not transmitted to the postsynaptic compartment. Spike jitter was realized by adding independent Gaussian noise with zero mean and standard deviation σ to each spike time of the input activity. Neural responses were measured with the same noise settings that were used during training.

Neuron model

The multi-spike tempotron was implemented as current-based leaky integrate-and-fire neuron model with reset. Specifically, the neuron's postsynaptic membrane potential $V(t)$ was given by integration of exponentially decaying currents from $N = 500$ synaptic afferents, yielding

$$V(t) = V_{\text{rest}} + \sum_{i=1}^N \omega_i \sum_{t_i^j < t} K(t - t_i^j) - \vartheta \sum_{t_{\text{spike}}^j < t} \exp\left(-\frac{t - t_{\text{spike}}^j}{\tau_m}\right) \quad (5)$$

Here, t_i^j denote the arrival times of individual presynaptic spikes of the i th afferent, and t_{spike}^j are the times of output spikes elicited in the postsynaptic compartment. Each input spike at time t_i^j contributes a postsynaptic potential (PSP), whose shape is given by the kernel $K(t - t_i^j) = V_{\text{norm}} \left[\exp\left(-\frac{t - t_i^j}{\tau_m}\right) - \exp\left(-\frac{t - t_i^j}{\tau_s}\right) \right]$ and whose peak amplitude is determined by the afferent's individual synaptic efficacy ω_i . Normalization of K to unit amplitude resulted from setting $V_{\text{norm}} = \eta^{1/(\eta - 1)}/(\eta - 1)$ with $\eta = \tau_m/\tau_s$. The temporal shape of PSPs is governed by the integration time constant of the postsynaptic membrane, $\tau_m = 20$ ms, and the decay time constant of synaptic currents, $\tau_s = 5$ ms. PSPs are causal; $K(t - t_i^j)$ is defined to vanish for $t < t_i^j$. Whenever $V(t)$ crosses the firing threshold ϑ , the neuron emits an output spike, and the voltage resets to $V_{\text{rest}} = 0$ by the last term in Eq. 5. I used $\vartheta = 1$ for the fixed biological firing threshold of the neuron. Numerical simulations of the neuron model were event-driven and based on exact solutions of Eq. 5. In simulations underlying table S2, I also tested readout neurons with $N = 80$ and $N = 20$ synaptic afferents.

Spike-threshold-surface

To formulate a continuous objective function for a neuron's discrete number of spikes, I defined, for a given input spike pattern, the spike-threshold-surface (STS) of a neuron as the function $\text{STS} :$

$\mathbb{R}^+ \rightarrow \mathbb{N}_0$, which maps each threshold value ϑ to the number of elicited output spikes, $\vartheta \mapsto \text{STS}(\vartheta)$ (fig. SIC). The STS can be characterized by the decreasing sequence of critical threshold values ϑ_k^* :

$$\vartheta_k^* = \sup\{\vartheta \in \mathbb{R}^+ : \text{STS}(\vartheta) = k\}, k \in \mathbb{N} \quad (6)$$

The critical threshold ϑ_k^* denotes the threshold value (supremum) at which the number of output spikes jumps from $k - 1$ to k . For thresholds between two critical values, the STS is constant, $\text{STS}(\vartheta_{k+1}^* < \vartheta < \vartheta_k^*) = k$. Because a neuron remains silent if its firing threshold lies above the maximum postsynaptic voltage V_{max} , the STS is zero for thresholds above V_{max} , $\text{STS}(\vartheta > V_{\text{max}}) = 0$. The first output spike is generated when the threshold equals to V_{max} , $\vartheta_1^* = V_{\text{max}}$. In general, each ϑ_k^* corresponds to a voltage value described by Eq. 5 and hence is a function of the neurons synaptic efficacies ω and differentiable with respect to them. When I use the STS for the definition of gradient-based synaptic learning rules, I ignore the possible existence of singular points in the space of synaptic efficacies where a required ϑ_k^* and/or its derivatives might not exist—for example, when two adjacent critical thresholds coalesce and the output spike count of a neuron jumps by two spikes at a single critical value. I have not encountered such pathologies in any of the simulations underlying the present work.

Multi-spike tempotron

The goal of multi-spike tempotron learning is to modify a neuron's synaptic efficacies so that it fires a desired number of output spikes in response to a given input spike pattern. A simplified version of this problem has been solved with the binary tempotron (12), which is a supervised synaptic learning rule that can train a neuron to respond to a given input spike pattern by either firing at least one spike or remaining silent. Because of the original tempotron's binary decision, the learning could be formulated as a gradient-based learning rule operating on the maximum postsynaptic potential: increasing it toward the cell's firing threshold when the neuron should fire at least one spike, and lowering it below the firing threshold when the neuron should remain silent. However, this reliance on the maximal postsynaptic potential as its objective function prevents the binary tempotron learning rule from controlling the number of spikes beyond one, when the nonlinearity of spike generation renders the maximum postsynaptic potential insensitive to the number of elicited spikes. To overcome this problem, the multi-spike tempotron implements a gradient-based learning rule whose objective is to shape the neuron's STS by modifying the positions of the critical thresholds ϑ_k^* (Eq. 6). Although many objective functions can be defined on the basis of the STS, I focus here on the simplest form in which each learning step operates along the gradient of only a single ϑ_k^* with $k \in \mathbb{N}$; that is, the neuron's synaptic efficacies are changed by $\Delta \omega \propto \nabla_{\omega}^* \vartheta_k^*$ after each error trial.

To generate the desired number of output spikes d in response to a given input spike pattern,

a neuron's STS must be aligned with its firing threshold ϑ so that $\vartheta_{d+1}^* < \vartheta < \vartheta_d^*$. If this condition is violated on a given trial—if the neuron misclassifies its input spike pattern—an “absolute” learning rule would decrease ϑ_{d+1}^* through $\bar{\Delta}\omega \propto -\nabla_{\omega} \vartheta_{d+1}^*$ whenever the neuron fired more spikes than required. If the neuron had fired less spikes than desired, absolute learning would increase ϑ_d^* through $\bar{\Delta}\omega \propto \nabla_{\omega} \vartheta_d^*$. Such absolute learning (fig. S2C) would require the supervisory signal to provide the exact value of desired output spike count. In contrast, a simpler, biologically more plausible, and from an incremental learning perspective perhaps also more intuitive learning rule is based on a binary feedback signal that only specifies whether the neuron should increase or decrease its current output spike count o :

$$\bar{\Delta}\omega = \begin{cases} -\lambda \nabla_{\omega} \vartheta_o^* & \text{if } o > d \\ \lambda \nabla_{\omega} \vartheta_{o+1}^* & \text{if } o < d \end{cases} \quad (7)$$

where the learning rate $\lambda > 0$ controls the step size of individual updates. The present work is based on this “relative” multi-spike tempotron learning rule (Eq. 7) (materials and methods, ϑ^* -gradient).

Correlation-based learning

In correlation-based learning (12), the synaptic credit assignment of the multi-spike tempotron learning rule is approximated on the basis of the correlation between presynaptic activity and postsynaptic voltage. Given the i th synapse's presynaptic spike train with spike times t_i^j , its eligibility $\mathcal{E}_i = \sum_{t_i^j} V_i^j$ was defined by the sum over all individual correlations $V_i^j = \int_{t_i^j}^{\infty} dt V(t) K(t - t_i^j)$, where $V(t)$ is the postsynaptic voltage given by Eq. 5 and K is the PSP kernel. In neurons, eligibilities of this or similar form could be realized on the basis of intracellular calcium signals, which are sensitive to the coincidence of pre- and postsynaptic activity through the voltage dependence of synaptic *N*-methyl-D-aspartate (NMDA) receptors. It is well established that the induction of long-term synaptic changes requires these calcium signals to reach specific plasticity induction thresholds (31, 45, 46). Correspondingly, I defined correlation-based learning so that all synapses whose eligibility reached a plasticity induction threshold ψ on a given error trial became eligible to undergo potentiation or depression. To ensure sufficient specificity of this learning, the induction threshold should be adjusted so that on average, only a limited fraction of synapses undergo change. In the present work, I have simplified this adjustment of ψ by automatically selecting the 10% most eligible synapses on each error trial. Specifically, all synapses whose V_i exceeded the 9th, (the highest) decile D_9 were updated:

$$\Delta\omega_i^{\pm} = \begin{cases} \pm\lambda_V & \text{if } \mathcal{E}_i > D_9 \\ 0 & \text{if } \mathcal{E}_i \leq D_9 \end{cases} \quad (8)$$

Positive updates applied to trials in which the neuron fired less than the desired number of

spikes, and negative updates applied to trials in which the neuron fired too many.

Noninteger labels in supervised learning tasks

In tasks involving supervised learning of continuous tuning curves (fig. S4), aggregate-labels were not restricted to integer values (supplementary materials, equation 41) and could not be directly interpreted as the desired number of output spikes d . Although technically the relative learning rule defined in Eq. 7 does not require d to be an integer, I probabilistically mapped noninteger labels ℓ to integer values d , being either the nearest lower L^- or higher L^+ integer adjacent to ℓ . Specifically, on each trial ℓ was mapped to $d = L^-$ with probability $p = L^+ - \ell$ and to $d = L^+$ with probability $1 - p = \ell - L^-$. As a result, the average integer label $\langle d \rangle = pL^- + (1 - p)L^+ = (L^+ - \ell)L^- + (\ell - L^-)L^+ = \ell$ matched the noninteger aggregate.

Learning rate and annealing

In simulations of the multi-spike tempotron, I used a learning rate of $\lambda = 10^{-5}$ (Eq. 7) in all supervised learning tasks with discrete target features. This value resulted in near optimal convergence times in the single-clue detection tasks, but the minimum was shallow (fig. S2C, inset). In supervised learning tasks of continuous tuning curves (fig. S4), learning convergence was improved by the use of a simple annealing schedule: If the fraction of error trials within the past 2500 trials failed to decrease relative to the preceding 2500 trial interval, the learning rate λ was reduced by a multiplicative factor of 0.9. Correspondingly, a higher initial learning rate of $\lambda = 10^{-4}$ was used in these simulations. In all self-supervised network simulations with a single supervisor unit, the learning rate was $\lambda = 5 \times 10^{-4}$ and remained fixed (Fig. 4 and figs. S6, S7, and S8). In simulations of self-supervised networks with generalized supervisory architectures, I lowered the learning rate to $\lambda = 1 \times 10^{-5}$ during the critical and consolidation phases of the discrete feature learning task (Fig. 5 and fig. S9, A and B) and used $\lambda = 5 \times 10^{-5}$ when studying the formation of continuous maps (Fig. 6 and fig. S9C). For correlation-based learning (Eq. 8), I used a constant learning rate of $\lambda_V = 1 \times 10^{-5}$ for supervised learning and $\lambda_V = 5 \times 10^{-4}$ in self-supervised networks. In the simulations summarized in table S2, I used the optimized learning rates given there.

Momentum heuristic

Following previous studies (12, 23), I used a momentum heuristic (47) to accelerate convergence in all supervised learning tasks. Specifically, synaptic updates combined the learning rule correction $\bar{\Delta}\omega$ of the current error trial (Eq. 7) with a fraction of the previous synaptic change $\bar{\Delta}\omega^{\text{previous}}$, so that $\bar{\Delta}\omega^{\text{current}} = \bar{\Delta}\omega + \mu \bar{\Delta}\omega^{\text{previous}}$. If on a given error trial the individual learning rule correction of an efficacy $i \in \{1, \dots, N\}$ was zero ($\Delta\omega_i = 0$), neither the synapse nor its previous change were updated. I used $\mu = 0.99$ for the momentum parameter, implementing a decaying trace of former synaptic changes (12). The momen-

tum heuristic was not engaged in self-supervised networks, in which I set $\mu = 0$.

Initialization

Before learning, the initial synaptic efficacies $\bar{\omega}_{\text{ini}}$ of all multi-spike tempotrons were initialized so that the neurons fired with ~ 5 Hz when driven by the 5-Hz Poisson background activity. Specifically, after efficacies were drawn from a Gaussian distribution with zero mean and a standard deviation of 0.01, neurons were trained with 1-s-long trials of background activity with random Poisson labels with a mean of 5. During this initialization, the momentum heuristic was disengaged ($\mu_{\text{ini}} = 0$), and the learning rate was set to $\lambda_{\text{ini}} = 10^{-3}$. Initialization proceeded over independent blocks of 100 trials and terminated when the mean firing rate of the neuron over the last block exceeded 5 Hz. Subsequently, the parameters λ and μ were set to their simulation values, and previous synaptic changes (materials and methods, momentum heuristic) were initialized to zero ($\bar{\Delta}\omega^{\text{previous}} = 0$). The above initialization was important for self-supervised networks to avoid the trivial fixed point at which all processing layer neurons remain silent. When self-supervised networks were studied with noisy input spike trains (fig. S6F), the spike deletion probability p_{del} was also applied to the Poisson background activity used during the initialization, but the target spike rate remained at 5 Hz. For supervised learning tasks, initialization was not crucial and had only appreciable effects on the convergence times when convergence was fast (fig. S2C).

Neural responses

The mean response R_y^{mean} of a neuron to a feature activity pattern y during and after learning was measured through dedicated batches of probe trials during which the learning rule was not engaged. The index y refers either to a particular feature $f \in \{1, \dots, N_f\}$ from the set of discrete features or to the feature activity pattern of a particular feature parameter $\alpha \in [0, 2\pi]$ when feature activity patterns belonged to a continuous manifold. Each probe trial consisted of a $T_{\text{probe}} = 2$ s segment of background activity within which a central gap of 50 ms was inserted. For each probe trial, the output spike count of a neuron was measured twice: once giving $s_{\mathcal{O}}$, with the central gap being empty, and once giving s_y , with the feature activity pattern placed within the gap. The response R_y^{mean} was defined as the mean difference in the number of output spikes elicited in these two conditions, $R_y^{\text{mean}} = \langle s_y - s_{\mathcal{O}} \rangle$, with the average taken over 1000 independent probe trials. The embedding of the feature activity pattern within background activity ensured that the neuron's responses were measured in the same conditions as present during learning. The averaging captured the stochasticity of the neuron's responses due to the random background activity that surrounded the feature activity pattern or additional input noise, whose statistics were kept identical to the training conditions of a given task. Responses to background activity $R_{\mathcal{O}}^{\text{mean}}$ were defined as the mean spike rate elicited in the absence of the feature activity pattern, $R_{\mathcal{O}}^{\text{mean}} = \langle s_{\mathcal{O}} \rangle / T_{\text{probe}}$.

Response variability (table S1) was quantified through the corresponding standard deviations $R_y^{\text{std}} = \text{STD}[s_y - s_\emptyset]$ and $R_\emptyset^{\text{std}} = \text{STD}[s_\emptyset]/T_{\text{probe}}$.

Neural tuning curves

The tuning of neurons that were exposed to features from a continuous dimension (Fig. 6 and figs. S4, S7, S8, and S9C) was characterized by measuring the neural responses to 100 probe features that were linearly spaced along the continuous feature dimension. The mean responses shown in fig. S7A are the average of these responses over the networks processing layer. Tuning width in figs. S7, B and C, and S8C were defined as the fraction of the continuous feature dimension over which the processing layer's average response exceeded 0.5 spikes per feature.

Convergence in supervised tasks

Convergence times for the supervised single-feature learning tasks in Fig. 2, A to C and E, and fig. S2C were defined as the number of learning cycles required until neural responses converged to firing one spike in response to the clue and remaining silent in response to distractors and background activity. Specifically, neural responses were evaluated after each cycle of 100 independent learning trials. Convergence required all distractor feature and background responses to satisfy $R_{\text{distractor}}^{\text{mean}} < 0.01$ and $R_\emptyset^{\text{mean}} < 0.01/T_r$, respectively. In addition, in deterministic feedback tasks (Fig. 2, A to C, and fig. S2C) convergence required the mean discrepancy between the clue responses and the desired single spike to fall below $|\langle s_{\text{target}} - s_\emptyset - 1 \rangle| < 0.01$. In probabilistic feedback tasks (Fig. 2E), convergence required the mean clue response to exceed one spike, $R_{\text{clue}}^{\text{mean}} > 1$. Mean convergence times report the number of cycles after which the criterion was first satisfied, averaged over 1000 independent simulations.

Convergence in unsupervised tasks

Depending on the learning task, I used different definitions of convergence for self-supervised networks. In Fig. 4B, inset, and fig. S6, C, E, and G, I studied the convergence times of networks with a fixed number of $N_p = 10$ processing layer neurons that were engaged in discrete feature detection tasks without input noise. In these simulations, I used a direct convergence criterion that required convergence of all individual processing-layer neurons. As in the supervised tasks, learning proceeded in cycles of 100 learning trials that were interleaved by measurements of the neural responses, giving the individual mean feature iR_f^{mean} ($f \in \{1, \dots, N_f\}$) and background $iR_\emptyset^{\text{mean}}$ responses of each processing layer neuron $i \in \{1, \dots, N_p\}$ (materials and methods, neural responses). On the basis of these, I defined the population feature responses \mathcal{R}_f as the average feature responses across the processing layer $\mathcal{R}_f = \sum_{i=1}^{N_p} iR_f^{\text{mean}}/N_p$ and its rounded integer value as $\mathcal{R}_f^{\text{int}} = \text{round}(\mathcal{R}_f)$. Convergence required the background responses of all individual processing neurons to fall below $iR_\emptyset^{\text{mean}} < 0.05$ Hz, while at least one of the rounded population feature responses $\mathcal{R}_f^{\text{int}}$ had to be greater than zero.

In addition, for all feature activity patterns f , the deviations between the individual responses of each processing layer neuron and the population mean had to lie below 5%, $|iR_f^{\text{mean}} - \mathcal{R}_f| < 0.05\mathcal{R}_f^{\text{int}}$, when $\mathcal{R}_f^{\text{int}} \geq 1$ or $|iR_f^{\text{mean}} - \mathcal{R}_f| < 0.05$ when $\mathcal{R}_f^{\text{int}} = 0$.

When comparing convergence times of networks with varying processing-layer sizes and also different levels of input noise, the above convergence criterion was not suitable. Instead, successful detection of the single feature in the tasks of fig. S6F was based on a population criterion that required the total number of spikes elicited within the processing layer in response to the feature activity pattern $S_f = \sum_{i=1}^{N_p} (i s_{f_i} - i s_\emptyset)$ to exceed the population response to the 2-s background activity interval $S_\emptyset = \sum_{i=1}^{N_p} i s_\emptyset$ of the probe trials. Specifically, I required that over 1000 independent probe trials, the minimum of S_f was greater than the maximum of S_\emptyset . The comparison of the above two convergence measures in the absence of noise is shown in fig. S6D. Although both measures give similar values for small populations, the strictness of the second, population-based convergence criterion does not increase with growing network size, so that convergence times do not grow.

In fig. S7, B, C, and E, I report the tuning statistics of self-supervised networks that were exposed to feature activity patterns from a continuous feature dimension. For continuous dimensions, the computational costs of the above convergence criteria that required an ongoing evaluation of the processing layers' responses were not practical. As an efficient albeit indirect alternative, I defined convergence on the basis of spike count coherence (SCC), which is the agreement between the spike counts of all processing layer neurons during successive learning cycles of 100 trials (fig. S7D, bottom). Specifically, convergence required that throughout a cycle, an average of 99% of the processing-layer neurons fired in agreement with the mode value of the processing-layer spike counts—that the peak in the processing layer's spike count histogram would on average contain over 99% of the individual neural responses. The tuning of multiple self-supervised networks with recurrent inhibition (fig. S8) was evaluated after a fixed simulation length of 1000 cycles.

Temporal alignment of sensory features

To highlight the capability of self-supervised networks to identify structure within their input activity across long temporal distances, I did not align the random occurrence times of feature activity patterns in simulations of individual input networks. However, as motivated in the text, I did enforce such alignment in simulations of networks with recurrent lateral inhibition between multiple self-supervised groups (fig. S8).

Scalar feedback signals in self-supervised networks

In self-supervised networks, all processing-layer neurons implemented the same relative multi-

spike tempotron learning rule that was used in the supervised tasks. However, in contrast to receiving an external feedback signal, self-supervised networks generated their training labels internally as a function of the spiking activity within their processing layers. After each learning trial, the components of the activity vector $\vec{a} \in \mathbb{N}_0^{N_p}$ consisted of the N_p individual spike counts a_i ($i = 1, \dots, N_p$) that were elicited in the processing layer throughout a given learning trial. In self-supervised networks with a single supervisor (Fig. 4 and figs. S3C, S6, S7, and S8), each activity vector \vec{a} was mapped to a common label ℓ through a scalar feedback function $\mathcal{L}: \mathbb{N}_0^{N_p} \rightarrow \mathbb{N}_0$ with $\vec{a} \mapsto \ell = \mathcal{L}(\vec{a})$. I defined \mathcal{L} to be the mean spike count, $\mathcal{L}(\vec{a}) = \sum_{i=1}^{N_p} a_i/N_p$, except in fig. S6G, where I also tested self-supervised learning with nonlinear feedback functions that realized the mode and the median of the processing-layer spike counts. When \mathcal{L} implemented the mean spike count, noninteger labels were rounded to the nearest integers. In fig. S6G, I also tested the learning performance under a neural implementation of the scalar feedback function \mathcal{L} , defined as the normalized spike count of a supervisor neuron. Specifically, the same integrate-and-fire model that was used for the multi-spike tempotrons of the processing layer, but with fast synaptic time constants of $\tau_s = 0.5$ ms, received excitatory projections from all processing-layer neurons. These connections had fixed strong individual efficacies of $\omega = 1.01$ so that in essence, every processing-layer spike caused a spike in the supervisor neuron. As a result, when normalized by the number of processing-layer neurons N_p , its spike count approximated the mean spike count within the processing layer.

Neuron-specific feedback signals in self-supervised networks

I generalized the concept of self-supervised neural networks by replacing the scalar feedback function \mathcal{L} by a vector valued projection $\vec{\mathcal{L}}: \mathbb{N}_0^{N_p} \rightarrow \mathbb{N}_0^{N_s}$ with $\vec{a} \mapsto \vec{\ell} = \vec{\mathcal{L}}(\vec{a})$, whose components specify an individual label for each processing-layer neuron. Having in mind a neural implementation of this feedback function through a back-projecting layer of N_s supervisor units, I considered $\vec{\mathcal{L}}$ to be a linear projection of the form $\vec{\mathcal{L}}(\vec{a}) = S\vec{a}$ (Eq. 1). In addition, all labels were rounded to the nearest non-negative integers. In the context of a neural implementation, the $N_p \times N_s$ supervisor matrix S can be thought of as the product of two sets of connections, $S = \mathcal{BF}$: A $N_s \times N_p$ matrix \mathcal{F} denoting feed-forward connections of neural activity from the processing to the supervisor layer, and a $N_p \times N_s$ matrix \mathcal{B} denoting feedback connections of supervisory signals from the supervisor units to the processing neurons. In this interpretation, the number of supervisory units required for the implementation of a particular projection S is given by its rank.

Zero labels

The learning dynamics of self-supervised networks has a trivial fixed point at which all

processing-layer neurons remain silent ($\vec{a} = 0$) for all input spike patterns. To prevent convergence to this state, I enforced that any given processing-layer neuron would refrain from learning on an individual trial when its feedback was zero.

Stability of self-supervised learning dynamics

When feedback signals were implemented as the rounded mean of the processing-layer activity, the resulting self-supervised learning dynamics was susceptible to a runaway instability in which all processing-layer responses continued to grow in response to background activity. This was in contrast to the stable learning dynamics that emerged under the nonlinear scalar feedback functions that implemented the mode or median because of the well-known robustness of these measures to outliers. Although this instability could be effectively countered by a small bias in the rounding operation that mapped the mean processing-layer spike counts to integer-valued labels, I followed an alternative approach: Whenever a neuron's output exceeded its label, the multi-spike tempotron learning step was followed by an additional attenuation of all weights by a factor of 0.995. In addition to stabilizing the learning dynamics, this attenuation step substantially accelerated the convergence of the processing-layer neurons to stop firing in response to background activity. It was implemented in all reported simulations of self-supervised networks, except in the critical and consolidation phases of Figs. 5B and 6 and fig. S9.

Lateral inhibition

Lateral inhibition between multiple self-supervised networks was introduced by recurrent inhibitory connections between all processing neurons that did not belong to the same self-supervised network. Specifically, each multi-spike tempotron in these networks received inhibitory afferents, with a fixed efficacy $\omega_l < 0$, that were driven by the output spikes of all processing-layer neurons of the other networks.

Correlations in synaptic efficacies and synaptic learning noise

In biological implementations, neurons in the processing layer would neither be identical in terms of their morphologies or biophysical properties, nor would they receive exactly identical input spike trains. However, as a worst-case scenario I also studied this limiting case in which the self-supervised learning dynamics of the shared input architectures had a pathological fixed point at which all neurons converged to identical synaptic efficacies. In this case, the learning would stop even if the processing-layer neurons had failed to lock onto a sensory feature and instead responded to the random background activity. Indeed, in the shared input scenario, correlations between the synaptic efficacies within the processing layer grew during learning (fig. S6B). Although the probability that a network would enter the pathological state be-

fore converging onto a sensory feature was limited for a broad range of task parameters that I explored in this study, the problem could be alleviated by introducing an additive Gaussian learning noise at each synaptic update. Specifically, after any learning step invoked in a processing-layer neuron, all synaptic efficacies received additive noise, so that

$$\vec{\omega} = \vec{\omega} + \vec{\xi} \quad (9)$$

with individual ξ_i drawn independently from a Gaussian distribution with zero mean and standard deviation $\sigma_{\omega} = 10^{-3}$. With such synaptic learning noise, which also highlights the robustness of the present learning scheme, neural responses remained diverse even over extended learning periods. For comparability, the synaptic update noise was also applied to individual input architectures in Fig. 4 and figs. S3C, S6 and S7, although by construction these architectures could not develop correlations between the efficacies of their processing-layer neurons (fig. S6B).

Supervisory matrices

I studied supervisor-mediated interactions between processing-layer neurons with two types of supervisory matrices S that stabilized different tuning profiles across the processing-layer population. In the first type, S corresponded to the sum of two matrices $S = S_{\text{hom}} + \lambda_{\text{inhom}} S_v$, each of which contributed one eigenvector with nonzero eigenvalue, λ_{hom} and λ_{inhom} , respectively, to S . The constant matrix S_{hom} with elements $(S_{\text{hom}})_{ij} = (1/N_p)$ was normalized by the processing-layer size N_p so that the eigenvalue of the homogeneous eigenvector became one, $\lambda_{\text{hom}} = 1$. This component of the supervisory circuit ensured that the learning dynamics preserved the mean processing layer activity. In contrast, the second contribution $S_v = \vec{v} \vec{v}^T$ with eigenvector \vec{v} is used to stabilize an arbitrary activity profile \vec{v} with zero mean. Specifically, in the simulations of Fig. 5B, top, and fig. S9, A, top, and B, top, the components of \vec{v} were drawn randomly from a uniform distribution, centralized by subtraction of their mean and scaled so that each \vec{v} had unit norm. In the second type of supervisory matrices (Figs. 5B, bottom, and 6 and figs. S9, A, bottom, B, bottom, and C, S was constructed as a circulant matrix whose only nonzero eigenvalues λ_{hom} and λ_{inhom} corresponded to the homogeneous (one eigenvector) and the first-order harmonic modes (two eigenvectors), respectively. Specifically, I set the first row of S to $S_{1,j} = [\lambda_{\text{hom}} + 2\lambda_{\text{inhom}} \cos(2\pi j/N_p)]/N_p$ where $j = 1, \dots, N_p$, which fixed the circulant matrix S .

Neural population tuning for discrete features

To demonstrate that the steady-states of the self-supervised learning dynamics can be controlled by the structure of the supervisory matrix S , I used a triphasic learning schedule that consisted of an initialization period, a critical period, and a consolidation period. Specifically, each simulation started by a brief initialization period of 50 cycles, during which the supervisory matrix

was neutral ($\lambda_{\text{hom}} = 1$ and $\lambda_{\text{inhom}} = 1$), and the processing layer ceased responding to background activity. In the following critical period, which lasted only a single cycle, the supervisory signaling amplified the desired mode of the processing layer responses by operating with $\lambda_{\text{inhom}} = 4$. During a subsequent consolidation phase, the supervisory circuit returned to $\lambda_{\text{inhom}} = 1$, and the responses stabilized. Fit parameters between the learned processing layer feature responses ${}_i R_i^{\text{mean}} (i = 1, \dots, N_p)$ and the inhomogeneous mode are shown in fig. S9B. Specifically, each random tuning profile \vec{v} (fig. S9B, top) was fitted (least squares) to the learned response profile by optimizing a baseline b and an amplitude a parameter, minimizing $\sum_{i=1}^{N_p} [{}_i R_i^{\text{mean}} - (b + a v_i)]^2$. Because of the two first-order harmonic eigenvectors of the circulant S , harmonic fits (fig. S9B, bottom) required an additional phase parameter ϕ so that the corresponding fits minimized the discrepancies between ${}_i R_i^{\text{mean}}$ and $b + a \cos[2\pi(i-1)/N_p + \phi]$.

Continuous feature maps

The emergence of continuous maps required longer periods of amplifying supervisory signaling. Specifically, I used the circulant supervisory matrix (materials and methods, supervisory matrices) with a strong amplification of the first harmonic mode, whose eigenvalue was set to $\lambda_{\text{inhom}} = 20$. Task parameters were as in lateral inhibition case, $T_{\text{O}} = 1$ s and $c_i^{\text{mean}} = 2$. A saturation of each neuron's individual feedback signal at $\Delta = 2$ spikes per trial resulted in the distribution of neural activity across the processing layer. Specifically, each neuron's individual label ℓ (Eq. 1) was mapped to $\tilde{\ell}$ by the saturating nonlinearity

$$\tilde{\ell} = \Delta \left[1 - \exp(-\ell/\Delta) \right] \quad (10)$$

In addition, this saturation of neural feedback signals prevented the unbounded growth of neural responses within the processing layer due to the strongly amplifying harmonic mode. Results in Fig. 6 and fig. S9C were obtained by running the above self-supervised learning dynamics for 1000 cycles. For each simulation, the learned neural response map (Fig. 6B, left) was characterized by the dependence of the center response (across the processing layer) on the continuous stimulus parameter. Specifically, for each stimulus parameter $a_j = 2\pi j/100$ with $j = 0, \dots, 99$ of the learned response map, the center of the processing layer's response was measured by the weighted circular mean

$$\hat{m}(a_j) = \text{atan2} \left[\frac{1}{N_p} \sum_{k=1}^{N_p} {}_k R_{a_j}^{\text{mean}} \sin \left(\frac{2\pi k}{N_p} \right), \frac{1}{N_p} \sum_{k=1}^{N_p} {}_k R_{a_j}^{\text{mean}} \cos \left(\frac{2\pi k}{N_p} \right) \right] \quad (11)$$

and converted back to the processing layer locations (neuron id) of the center responses $\hat{u}(a_j) = N_p \hat{m}(a_j) / (2\pi)$. These center responses were fitted

by a straight line whose y -intercept (phase), slope, and coefficient of determination (R^2) values were used to characterize the learned maps over 1000 independent simulations (fig. S9C).

Auditory front-end

Following the auditory brain stem model used in (23), speech samples from the TIDIGITS database were converted to spike patterns through the following sequence of processing steps: Audio files (20 kHz sampling frequency) were converted into spectrograms by using the specgram function of the matplotlib python package, with a sliding window of 512 samples and a temporal resolution of 1 ms. These spectrograms were smoothed in frequency space into 16 overlapping channels between 360 and 8000 Hz. Specifically, the signal in each channel corresponded to the dot product between the spectrogram and a triangular frequency filter. Each of the 16 filters spanned three adjacent values of the logarithmic (Mel-scale) frequency list (360, 500, 658, 837, 1039, 1269, 1528, 1822, 2155, 2531, 2957, 3439, 3984, 4602, 5301, 6092, 6987, and 8000) and peaked at the center value. The resulting frequency averaged spectrogram S was normalized to its global maximum, logarithmically rescaled by $S = \log(S + \epsilon) - \log(\epsilon)$ with $\epsilon = 10^{-5}$, and again peak normalized. Last, the signal in each channel of S was smoothed in time by a Gaussian filter with a time constant of 20 ms. For spike generation, the final signals were rescaled to the interval $[0, 1]$ by subtraction of the global minimum and subsequent division by the global maximum. Spikes were generated by threshold crossings. Specifically, in each frequency band 15 threshold values (0.0625, 0.125, 0.1875, 0.25, 0.3125, 0.375, 0.4375, 0.5, 0.5625, 0.625, 0.6875, 0.75, 0.8125, 0.875, and 0.9375) triggered onset (crossings from below) and offset (crossings from above) spikes, respectively, and fed these into separate output channels. One additional threshold placed at 1 fed into a single output channel. In total, each speech sample was converted into a spike pattern over $16 \times (2 \times 15 + 1) = 496$ afferents that traced the envelope of the spectrotemporally smoothed spectrogram.

TIDIGITS-task

In Fig. 3, I used continuous digit sequences from the TIDIGITS database to train multi-spike tempotrons with aggregate-label learning to detect one out of the 11 English digit words “zero,” “oh,” “one,” “two,” “three,” “four,” “five,” “six,” “seven,” “eight,” and “nine,” which served as the clue. For each training example, the neuron’s supervisory signal consisted only of the aggregate-label, the number of times that the clue occurred within the speech sequence. The neuron’s task was to learn to fire one spike in response to each clue occurrence. I divided the speech data from all 111 male speakers (21 to 70 years of age) of the database into a training and a test set. The test set consisted of the isolated digit subset of the database and contained 22 utterances of isolated digits (two productions of each digit) from each speaker. In contrast, I defined the training set as

the remaining 55 connected digit sequences from each speaker. The lengths of these sequences were variable, comprising two, three, four, five, and seven digits (11 each). The TIDIGITS database comprises 22 distinct dialect groups (five to six speakers each), which were used separately in the present application and resulted in $22 \times 11 = 242$ individual tasks. Generalization performance was improved by training margins and spike time noise (23), which I optimized over a three-dimensional grid spanning Gaussian spike time jitters $\sigma \in \{0, 5, 10\}$ ms and independent spike threshold margins $\kappa^+ = \{0, 0.1, 0.2, 0.3, 0.4, 0.5\}$. The two margin parameters refer to a positive margin, $\vartheta = 1 + \kappa^+$, when at least one output spike was required, and a negative margin, $\vartheta = 1 - \kappa^-$ when the neuron should remain silent. For each of the $3 \times 6 \times 6$ different parameter combinations, the performance was measured by the mean minimal error (over 1000 learning cycles) over 10 independent simulations. The histogram in Fig. 3B reports the test errors of all 10 simulations for the best parameter combination for each digit and dialect—a total of $10 \times 11 \times 22 = 2420$ values. Accommodating the dimensions of the front-end, the number of afferents in this application of the multi-spike tempotron was set to $N = 496$. All other parameters—except the learning rate, which was increased to $\lambda = 5 \times 10^{-5}$ —remained unaltered.

ϑ^* -gradient

The multi-spike tempotron learning rule requires the evaluation of the gradient $\nabla_{\vec{\omega}} \vartheta^*$ of the appropriate critical threshold ϑ^* in the space of synaptic efficacies $\vec{\omega}$. After an error trial, ϑ^* is determined numerically in two steps: First, the ϑ^* is bracketed by interval halving until the extra spike that is elicited when the spike threshold ϑ corresponds to the lower bound can be analytically associated with a local subthreshold voltage maximum $v_{\max}(\vartheta)$ when ϑ is set to the upper bound. In the second step, ϑ^* is determined numerically (with accuracy 10^{-13}) as the root of the analytic expression for $[\vartheta - v_{\max}(\vartheta)]$. At the critical spike threshold ϑ^* , the post-synaptic voltage $V(t)$ (Eq. 5) that is elicited by the presynaptic spike pattern with spike times t_s^j is given by

$$V(t) = V_o(t) - \vartheta^* \sum_{t_s^j < t} \exp\left[-\frac{(t - t_s^j)}{\tau_m}\right] \quad (12)$$

where

$$V_o(t) = \sum_{i=1}^N \omega_i \sum_{t_s^j < t} K(t - t_s^j) \quad (13)$$

is the unreset subthreshold voltage and the sum over t_s^j in Eq. 12 runs over all output spikes elicited before time t . We assume (materials and methods, spike-threshold-surface) that for any given ϑ^* there exists a unique t^* so that

$$\begin{aligned} \vartheta^* &= V(t^*) \\ &= V_o(t^*) - \vartheta^* \sum_{j=1}^m \exp\left[-\frac{(t^* - t_s^j)}{\tau_m}\right] \end{aligned} \quad (14)$$

where m denotes the number of output spikes that the neuron fires before t^* , $t_s^j < t^*$ for $j \in \{1, \dots, m\}$. By definition of the neuron model and the critical threshold ϑ^* , all spike times t_s^j and t^* satisfy

$$\vartheta^* = V(t^*) = V(t_s^j) \quad (15)$$

so that for each afferent $i \in \{1, \dots, N\}$

$$\vartheta_i^{*'} \equiv \frac{d}{d\omega_i} \vartheta^* = \frac{d}{d\omega_i} V(t^*) = \frac{d}{d\omega_i} V(t_s^j) \quad (16)$$

where we introduced the abbreviation $\vartheta_i^{*'}$ for the i th component of the wanted gradient.

Because ϑ^* depends on the synaptic efficacy ω_i also through the previous spike times $t_s^j < t^*$ (Eq. 14), its derivative with respect to ω_i is given by

$$\vartheta_i^{*'} = \frac{\partial}{\partial \omega_i} V(t^*) + \sum_{j=1}^m \frac{\partial}{\partial t_s^j} V(t^*) \frac{d}{d\omega_i} t_s^j \quad (17)$$

where we dropped the vanishing

$$\frac{\partial}{\partial t^*} V(t^*) \frac{d}{d\omega_i} t^* = 0 \quad (18)$$

The above relation holds because $V(t^*)$ is either a local maximum with $\partial V(t^*)/\partial t^* = 0$ or t^* is the time of an inhibitory input spike whose arrival time does not depend on ω_i . Similarly, for each $k \in \{1, \dots, m\}$

$$\begin{aligned} \frac{d}{d\omega_i} V(t_s^k) &= \frac{\partial}{\partial \omega_i} V(t_s^k) \\ &+ \sum_{j=1}^k \frac{\partial}{\partial t_s^j} V(t_s^k) \frac{d}{d\omega_i} t_s^j \end{aligned} \quad (19)$$

from which we obtain

$$\begin{aligned} \frac{d}{d\omega_i} t_s^k &= \frac{1}{\dot{V}(t_s^k)} \left[\vartheta_i^{*'} - \frac{\partial}{\partial \omega_i} V(t_s^k) - \sum_{j=1}^{k-1} \frac{\partial}{\partial t_s^j} V(t_s^k) \frac{d}{d\omega_i} t_s^j \right] \end{aligned} \quad (20)$$

with the time derivatives

$$\dot{V}(t_s^k) \equiv \left. \frac{\partial}{\partial t} V(t) \right|_{t=t_s^k} \quad (21)$$

evaluated from the left, before the spike reset.

To solve Eq. 17 for $\vartheta_i^{*'}$, we refactor the right hand side of Eq. 20 into the form

$$\frac{d}{d\omega_i} t_s^k = \frac{1}{\dot{V}(t_s^k)} [\vartheta_i^{*'} A_k + B_k] \quad (22)$$

where the coefficients A_k and B_k are given by the recursive equations

$$A_k = 1 - \sum_{j=1}^{k-1} \frac{A_j}{\dot{V}(t_s^j)} \frac{\partial}{\partial t_s^j} V(t_s^k) \quad (23)$$

and

$$B_k = -\frac{\partial}{\partial \omega_i} V(t_s^k) - \sum_{j=1}^{k-1} \frac{B_j}{\dot{V}(t_s^j)} \frac{\partial}{\partial t_s^j} V(t_s^k) \quad (24)$$

With the analogous definitions

$$A_* = 1 - \sum_{j=1}^m \frac{A_j}{\dot{V}(t_s^j)} \frac{\partial}{\partial t_s^j} V(t^*) \quad (25)$$

and

$$B_* = -\frac{\partial}{\partial \omega_i} V(t^*) - \sum_{j=1}^m \frac{B_j}{V(t_s^j)} \frac{\partial}{\partial t_s^j} V(t^*) \quad (26)$$

for t^* , insertion of Eq. 22 into Eq. 17 yields

$$\vartheta_i^* = -\frac{B_*}{A_*} \quad (27)$$

To calculate A_* and B_* , we consider all times t_x at which the voltage reaches the spike threshold, when $t_x \in \{t_s^1, t_s^2, \dots, t_s^m, t^*\}$. At these times, Eq. 12 reduces to

$$V(t_x) = \frac{V_o(t_x)}{C_{t_x}} \quad (28)$$

with

$$C_{t_x} \equiv 1 + \sum_{t_s^j < t_x} \exp\left[\frac{-(t_x - t_s^j)}{\tau_m}\right] \quad (29)$$

and gives the derivatives

$$\begin{aligned} \frac{\partial}{\partial \omega_i} V(t_x) &= \frac{1}{C_{t_x}} \frac{\partial}{\partial \omega_i} V_o(t_x) \\ &= \frac{1}{C_{t_x}} \sum_{t_s^j < t_x} K(t_x - t_s^j) \end{aligned} \quad (30)$$

$$\frac{\partial}{\partial t_s^k} V(t_x) = \frac{-V_o(t_x)}{C_{t_x}^2} \frac{\exp\left[\frac{-(t_x - t_s^k)}{\tau_m}\right]}{\tau_m} \text{ for } t_s^k < t_x \quad (31)$$

and

$$\begin{aligned} \dot{V}(t_x) &= \frac{1}{C_{t_x}^2} \left\{ C_{t_x} \frac{\partial}{\partial t_x} V_o(t_x) \right. \\ &\quad \left. + \frac{V_o(t_x)}{\tau_m} \sum_{t_s^j < t_x} \exp\left[\frac{-(t_x - t_s^j)}{\tau_m}\right] \right\} \end{aligned} \quad (32)$$

Mutual information between feedback signal and clue identity

In the discrete feature detection task, the sensory environment is composed of N_f distinct features, one of which is randomly selected as target feature $t \in \{1, \dots, N_f\}$. Hence, a priori the uncertainty about the target feature identity is given by the entropy $H_t = \ln N_f$. On a given learning trial, the occurrence counts of all sensory features $i \in \{1, \dots, N_f\}$ are realizations c_i of Poisson random variables C_i each with mean rate c_i^{mean} . Homogeneous pairwise correlations of strength $\rho \in [0, 1]$ between these occurrences counts are introduced by implementing each individual feature count $C_i = Y + X_i$ as the sum of a common count variable Y and a feature specific variable X_i , with mean rates ρc_i^{mean} and $(1 - \rho) c_i^{\text{mean}}$, respectively. On each learning trial, information about the target feature identity is provided by a label ℓ that specifies the occurrence count of the target feature, $\ell = c_\ell$. To quantify the amount of information that the resulting labeled vector of occurrence counts $\vec{C}_\ell = (c_1, c_2, \dots, c_{N_f}; \ell)$ provides about the target feature identity, we calculate the mutual information

$$I_{t, \vec{C}_\ell} = H_t - H_{t|\vec{C}_\ell} = \ln N_f - H_{t|\vec{C}_\ell} \quad (33)$$

where the conditional entropy

$$H_{t|\vec{C}_\ell} = \sum_{\vec{c}} p(\vec{c}) H_{t|\vec{c}_\ell = \vec{c}} \quad (34)$$

quantifies the average uncertainty in the target feature identity after a labeled occurrence count vector has been provided.

For a specific realization of the labeled occurrence count vector \vec{c}_ℓ , the entropy $H_{t|\vec{c}_\ell = \vec{c}_\ell} = \ln m$ only depends on the number of features m whose occurrence counts are equal to the label. Hence,

$$H_{t|\vec{c}} = \sum_{\vec{c}} p(\vec{c}) H_{t|\vec{c} = \vec{c}} = \sum_{m=1}^{N_f} p(m) \ln m \quad (35)$$

where $p(m)$ can be written as the total probability

$$p(m) = \sum_{k=0}^m p(X_t = k) p(m|X_t = k) \quad (36)$$

Because all individual feature counts X_i for $i \in \{1, \dots, N_f\}$ are iid, we can define

$$\begin{aligned} p_k &\equiv p(X_i = k) \\ &= \frac{[(1 - \rho) c_i^{\text{mean}}]^k \exp[-(1 - \rho) c_i^{\text{mean}}]}{k!} \end{aligned} \quad (37)$$

and obtain

$$p(m|X_t = k) = \binom{N_f - 1}{m - 1} p_k^{m-1} (1 - p_k)^{N_f - m} \quad (38)$$

so that

$$p(m) = \binom{N_f - 1}{m - 1} \sum_{k=0}^m p_k^m (1 - p_k)^{N_f - m} \quad (39)$$

and

$$\begin{aligned} I_{t, \vec{C}_\ell} &= \ln N_f - \sum_{m=1}^{N_f} \ln m \binom{N_f - 1}{m - 1} \times \\ &\quad \sum_{k=0}^m p_k^m (1 - p_k)^{N_f - m} \end{aligned} \quad (40)$$

In Fig. 2C, I use the normalized mutual information, $I_{t, \vec{C}_\ell} = I_{t, \vec{C}_\ell} / \ln N_f$, which measures the fraction of bits of the target feature uncertainty that can on average be inferred from a given trial. The pairwise correlations ρ only enter the mutual information through the probabilities p_k of the individual count variables X_i .

REFERENCES AND NOTES

- R. S. Sutton, Learning to predict by the methods of temporal differences. *Mach. Learn.* **3**, 9 (1988).
- W. Schultz, P. Dayan, P. R. Montague, A neural substrate of prediction and reward. *Science* **275**, 1593–1599 (1997). doi: [10.1126/science.275.5306.1593](https://doi.org/10.1126/science.275.5306.1593); pmid: [9054347](https://pubmed.ncbi.nlm.nih.gov/9054347/)
- E. M. Izhikevich, Solving the distal reward problem through linkage of STDP and dopamine signaling. *Cereb. Cortex* **17**, 2443–2452 (2007). doi: [10.1093/cercor/bhl152](https://doi.org/10.1093/cercor/bhl152); pmid: [17220510](https://pubmed.ncbi.nlm.nih.gov/17220510/)
- J. Friedrich, R. Urbanczik, W. Senn, Spatio-temporal credit assignment in neuronal population learning. *PLOS Comput. Biol.* **7**, e1002092 (2011). doi: [10.1371/journal.pcbi.1002092](https://doi.org/10.1371/journal.pcbi.1002092); pmid: [21738460](https://pubmed.ncbi.nlm.nih.gov/21738460/)
- F. Ponulak, A. Kasinski, Supervised learning in spiking neural networks with ReSuMe: Sequence learning, classification, and spike shifting. *Neural Comput.* **22**, 467–510 (2010). doi: [10.1162/neco.2009.11.08.901](https://doi.org/10.1162/neco.2009.11.08.901); pmid: [19842989](https://pubmed.ncbi.nlm.nih.gov/19842989/)

- R. V. Florian, The chronotron: A neuron that learns to fire temporally precise spike patterns. *PLOS ONE* **7**, e40233 (2012). doi: [10.1371/journal.pone.0040233](https://doi.org/10.1371/journal.pone.0040233); pmid: [22879876](https://pubmed.ncbi.nlm.nih.gov/22879876/)
- Y. Xu, X. Zeng, S. Zhong, A new supervised learning algorithm for spiking neurons. *Neural Comput.* **25**, 1472–1511 (2013). doi: [10.1162/NECO_a.00450](https://doi.org/10.1162/NECO_a.00450); pmid: [23517101](https://pubmed.ncbi.nlm.nih.gov/23517101/)
- R. M. Memmesheimer, R. Rubin, B. P. Olveczky, H. Sompolinsky, Learning precisely timed spikes. *Neuron* **82**, 925–938 (2014). doi: [10.1016/j.neuron.2014.03.026](https://doi.org/10.1016/j.neuron.2014.03.026); pmid: [24768299](https://pubmed.ncbi.nlm.nih.gov/24768299/)
- F. Rosenblatt, *Principles of Neurodynamics: Perceptrons and the Theory of Brain Mechanisms* (Spartan Books, 1962).
- R. Güti, To spike, or when to spike? *Curr. Opin. Neurobiol.* **25**, 134–139 (2014). doi: [10.1016/j.conb.2014.01.004](https://doi.org/10.1016/j.conb.2014.01.004); pmid: [24468508](https://pubmed.ncbi.nlm.nih.gov/24468508/)
- H. S. Seung, Learning in spiking neural networks by reinforcement of stochastic synaptic transmission. *Neuron* **40**, 1063–1073 (2003). doi: [10.1016/S0896-6273\(03\)00761-X](https://doi.org/10.1016/S0896-6273(03)00761-X); pmid: [14687542](https://pubmed.ncbi.nlm.nih.gov/14687542/)
- R. Güti, H. Sompolinsky, The tempotron: A neuron that learns spike timing-based decisions. *Nat. Neurosci.* **9**, 420–428 (2006). doi: [10.1038/nn1643](https://doi.org/10.1038/nn1643); pmid: [16474393](https://pubmed.ncbi.nlm.nih.gov/16474393/)
- I. R. Fiete, M. S. Fee, H. S. Seung, Model of birdsong learning based on gradient estimation by dynamic perturbation of neural conductances. *J. Neurophysiol.* **98**, 2038–2057 (2007). doi: [10.1152/jn.01311.2006](https://doi.org/10.1152/jn.01311.2006); pmid: [17652414](https://pubmed.ncbi.nlm.nih.gov/17652414/)
- L. R. Rabiner, A tutorial on hidden Markov models and selected applications in speech recognition. *Proc. IEEE* **77**, 257–286 (1989). doi: [10.1109/5.18626](https://doi.org/10.1109/5.18626)
- At first sight, it seems that losing the clue timing eliminates almost all the necessary feedback information, and asking for a specific number of spikes seems irrelevant because we do not really care about the total number of spikes if we only get at least one spike for each clue. However, a varying spike count per clue would indicate that the detector is operating in a regime in which noise could suppress or add spikes, which implies that the detector would not function reliably when the clues are embedded in background activity. This suggests that the number of spikes could serve as an objective function to stabilize an effective synaptic configuration and might also suffice for learning such a configuration from random initial conditions.
- Because a neuron's memory for previous inputs decays rapidly (neural membrane time constants rarely exceed a few tens of milliseconds), it has to fire rather promptly in response to a clue, if at all.
- B. Widrow, M. A. Lehr, 30 years of adaptive neural networks: Perceptron, Madaline, and backpropagation. *Proc. IEEE* **78**, 1415–1442 (1990). doi: [10.1109/5.58323](https://doi.org/10.1109/5.58323)
- D. Barber, "Learning in spiking neural assemblies" in *Advances in Neural Information Processing Systems*, S. Becker, S. Thrun, K. Obermayer, Eds. (MIT Press, 2002), vol. 15, pp. 149–156.
- J. P. Pfister, T. Toyozumi, D. Barber, W. Gerstner, Optimal spike-timing-dependent plasticity for precise action potential firing in supervised learning. *Neural Comput.* **18**, 1318–1348 (2006). doi: [10.1162/neco.2006.18.6.1318](https://doi.org/10.1162/neco.2006.18.6.1318); pmid: [16764506](https://pubmed.ncbi.nlm.nih.gov/16764506/)
- Although a population of 135 neurons (with 80 synapses each) required more than 3000 trials of reinforcement learning (4), the single integrate-and-fire neuron underlying the present study required an average of eight or four trials, when learning was implemented with the multi-spike tempotron or the correlation-based approximation (discussion and materials and methods, correlation-based learning), respectively. In fact, based on aggregate labels the task could be readily solved by a single neuron with only 20 synapses (table S2). Similarly strong performance differences between other neural implementations of gradient-based and reinforcement learning (11) have been reported (12) in the context of a binary classification task.
- T. Yang, M. N. Shadlen, Probabilistic reasoning by neurons. *Nature* **447**, 1075–1080 (2007). doi: [10.1038/nature05852](https://doi.org/10.1038/nature05852); pmid: [17546027](https://pubmed.ncbi.nlm.nih.gov/17546027/)
- L. F. Abbott, S. B. Nelson, Synaptic plasticity: Taming the beast. *Nat. Neurosci.* **3** (suppl.), 1178–1183 (2000). doi: [10.1038/81453](https://doi.org/10.1038/81453); pmid: [11127835](https://pubmed.ncbi.nlm.nih.gov/11127835/)
- R. Güti, H. Sompolinsky, Time-warped-invariant neuronal processing. *PLOS Biol.* **7**, e1000141 (2009). doi: [10.1371/journal.pbio.1000141](https://doi.org/10.1371/journal.pbio.1000141); pmid: [19582146](https://pubmed.ncbi.nlm.nih.gov/19582146/)
- R. G. Leonard, G. Doddington, *TIDIGITS*, vol. LDC93S10 (Linguistic Data Consortium, 1993).
- T. Masquelier, R. Guyonnet, S. J. Thorpe, Spike timing dependent plasticity finds the start of repeating patterns in continuous spike trains. *PLOS ONE* **3**, e1377 (2008). doi: [10.1371/journal.pone.0001377](https://doi.org/10.1371/journal.pone.0001377); pmid: [18167538](https://pubmed.ncbi.nlm.nih.gov/18167538/)

26. B. Nessler, M. Pfeiffer, L. Buesing, W. Maass, Bayesian computation emerges in generic cortical microcircuits through spike-timing-dependent plasticity. *PLoS Comput. Biol.* **9**, e1003037 (2013). pmid: [23633941](#)
27. R. Linsker, Perceptual neural organization: Some approaches based on network models and information theory. *Annu. Rev. Neurosci.* **13**, 257–281 (1990). doi: [10.1146/annurev.ne.13.030190.001353](#); pmid: [2183677](#)
28. R. Gütiğ, R. Aharonov, S. Rotter, H. Sompolinsky, Learning input correlations through nonlinear temporally asymmetric Hebbian plasticity. *J. Neurosci.* **23**, 3697–3714 (2003). pmid: [12736341](#)
29. W. Schultz, Updating dopamine reward signals. *Curr. Opin. Neurobiol.* **23**, 229–238 (2013). doi: [10.1016/j.conb.2012.11.012](#); pmid: [23267662](#)
30. V. Pawlak, J. R. Wickens, A. Kirkwood, J. N. Kerr, Timing is not everything: Neuromodulation opens the STDP gate. *Front. Synaptic Neurosci.* **2**, 146 (2010). doi: [10.3389/fnsyn.2010.00146](#); pmid: [21423532](#)
31. A. Artola, S. Bröcher, W. Singer, Different voltage-dependent thresholds for inducing long-term depression and long-term potentiation in slices of rat visual cortex. *Nature* **347**, 69–72 (1990). doi: [10.1038/347069a0](#); pmid: [1975639](#)
32. D. E. Feldman, The spike-timing dependence of plasticity. *Neuron* **75**, 556–571 (2012). doi: [10.1016/j.neuron.2012.08.001](#); pmid: [22920249](#)
33. V. Pawlak, D. S. Greenberg, H. Sprekeler, W. Gerstner, J. N. Kerr, Changing the responses of cortical neurons from sub- to suprathreshold using single spikes in vivo. *eLife* **2**, e00012 (2013). doi: [10.7554/eLife.00012](#); pmid: [23359858](#)
34. J. Amores, Multiple instance classification: Review, taxonomy and comparative study. *Artif. Intell.* **201**, 81–105 (2013). doi: [10.1016/j.artint.2013.06.003](#)
35. H. Hotelling, Relations between two sets of variates. *Biometrika* **28**, 321–377 (1936). doi: [10.1093/biomet/28.3-4.321](#)
36. S. Becker, G. E. Hinton, Self-organizing neural network that discovers surfaces in random-dot stereograms. *Nature* **355**, 161–163 (1992). doi: [10.1038/355161a0](#); pmid: [1729650](#)
37. S. Becker, Mutual information maximization: models of cortical self-organization. *Network* **7**, 7–31 (1996). doi: [10.1088/0954-898X/7/1/003](#)
38. Y. Li, S. D. Van Hooser, M. Mazurek, L. E. White, D. Fitzpatrick, Experience with moving visual stimuli drives the early development of cortical direction selectivity. *Nature* **456**, 952–956 (2008). doi: [10.1038/nature07417](#); pmid: [18946471](#)
39. S. D. Van Hooser *et al.*, Initial neighborhood biases and the quality of motion stimulation jointly influence the rapid emergence of direction preference in visual cortex. *J. Neurosci.* **32**, 7258–7266 (2012). doi: [10.1523/JNEUROSCI.0230-12.2012](#); pmid: [22623671](#)
40. L. Wiskott, T. J. Sejnowski, Slow feature analysis: Unsupervised learning of invariances. *Neural Comput.* **14**, 715–770 (2002). doi: [10.1162/089976602317318938](#); pmid: [11936959](#)
41. N. Li, J. J. DiCarlo, Unsupervised natural experience rapidly alters invariant object representation in visual cortex. *Science* **321**, 1502–1507 (2008). pmid: [18787171](#)
42. R. Min, M. Santello, T. Nevian, The computational power of astrocyte mediated synaptic plasticity. *Front. Comput. Neurosci.* **6**, 93 (2012). doi: [10.3389/fncom.2012.00093](#); pmid: [23125832](#)
43. P. Poirazi, T. Brannon, B. W. Mel, Pyramidal neuron as two-layer neural network. *Neuron* **37**, 989–999 (2003). doi: [10.1016/S0896-6273\(03\)00149-1](#); pmid: [12670427](#)
44. M. Larkum, A cellular mechanism for cortical associations: An organizing principle for the cerebral cortex. *Trends Neurosci.* **36**, 141–151 (2013). doi: [10.1016/j.tins.2012.11.006](#); pmid: [23273272](#)
45. J. A. Cummings, R. M. Mulkey, R. A. Nicoll, R. C. Malenka, Ca²⁺ signaling requirements for long-term depression in the hippocampus. *Neuron* **16**, 825–833 (1996). doi: [10.1016/S0896-6273\(00\)80102-6](#); pmid: [8608000](#)
46. R. C. Malenka, R. A. Nicoll, Long-term potentiation—A decade of progress? *Science* **285**, 1870–1874 (1999). doi: [10.1126/science.285.5435.1870](#); pmid: [10489359](#)
47. J. Hertz, A. Krough, R. G. Palmer, *Introduction to the Theory of Neural Computation* (Westview Press, 1991).

ACKNOWLEDGMENTS

It is a pleasure to thank W. Denk, D. Hansel, and P. Dayan for very insightful discussions throughout all stages of this work and L. Abbott, J. Hillmann, A. Schaefer, S. Shamma, T. Sharpee, and F. Wolf for helpful comments on this manuscript. I thank D. Fliegner and U. Haase for outstanding technical support and the Max Planck Society for making this research possible.

SUPPLEMENTARY MATERIALS

www.sciencemag.org/content/351/6277/aab4113/suppl/DC1

Materials and Methods

Supplementary Text S1 and S2

Figs. S1 to S9

Tables S1 and S2

References (48–56)

26 April 2015; accepted 20 January 2016
10.1126/science.aab4113

RESEARCH ARTICLE SUMMARY

CANCER BIOLOGY

Activation of PKA leads to mesenchymal-to-epithelial transition and loss of tumor-initiating ability

Diwakar R. Pattabiraman, Brian Bierie, Katharina Isabelle Kober, Prathapan Thiru, Jordan A. Krall, Christina Zill, Ferenc Reinhardt, Wai Leong Tam, Robert A. Weinberg*

INTRODUCTION: Tumor-initiating cells (TICs) have emerged in recent years as important targets for cancer therapy owing to their elevated resistance to conventional chemotherapy and their tumor-initiating ability. Although their mode of generation and biological properties have been explored in a diverse array of cancer types, our understanding of the biology of TICs remains superficial. The epithelial-to-mesenchymal transition (EMT) is a cell-biological program that confers mesenchymal traits on both normal and neoplastic epithelial cells, which enables both to acquire stemlike properties. In the case of carcinoma cells, entrance into a more mesenchymal state is associated with elevated resistance to a variety of conventional chemotherapeutics. This association between the EMT program and

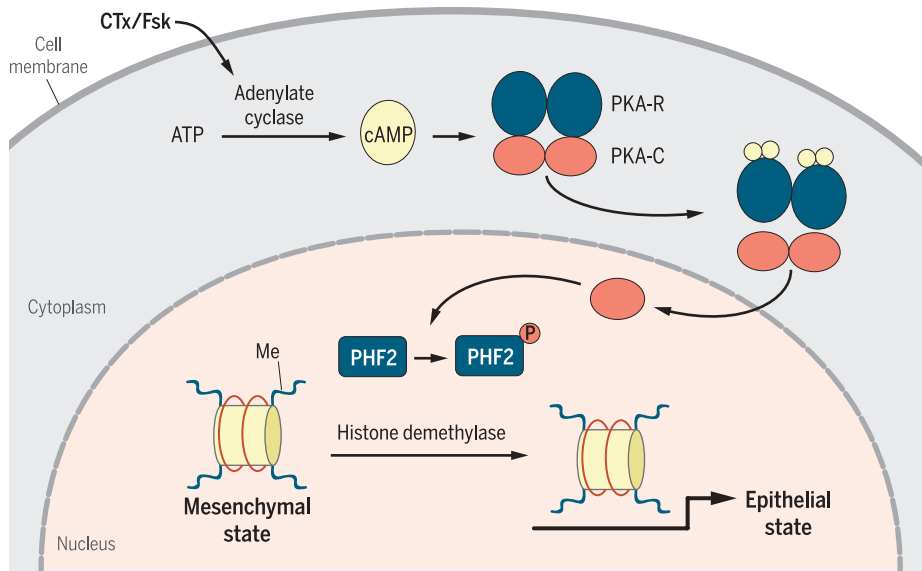
the TIC state has presented an attractive opportunity for drug development using agents that preferentially target more mesenchymal carcinoma cells, rather than their epithelial counterparts, in an effort to eliminate TICs. Adenosine 3',5'-monophosphate (cAMP) is a second messenger that transmits intracellular signals through multiple downstream effectors; the most well studied of these is protein kinase A (PKA). In this study, we explore the role of PKA in determining the epithelial versus mesenchymal properties of mammary epithelial cells and how this signaling pathway affects the tumor-initiating ability of transformed cells.

RATIONALE: At least two approaches might be taken to target mesenchymal TICs. One

strategy that has been used previously is the development of agents that show specific or preferential cytotoxicity toward TICs. In the current study, we have embraced an alternative strategy that is designed to induce TICs to undergo a mesenchymal-to-epithelial transition (MET). This “induced differentiation” approach would trigger cells to exit the more mesenchymal tumor-initiating state and enter into an epithelial non-stemlike state. In principle, this transition would make the cells more vulnerable to conventional cytotoxic treatments and thereby reduce the likelihood of metastasis and clinical relapse.

RESULTS: To identify agents that might induce an MET in mesenchymal mammary epithelial cells, we performed a screen for compounds that stimulate transcription of *CDH1*, which encodes E-cadherin, a key epithelial protein. Through this screen, compounds that activate adenylate cyclase (cholera toxin, CTx; and forskolin, Fsk) were identified as key inducers of the epithelial state. We found that mesenchymal cells treated with either CTx or Fsk differentiated into benign epithelial derivatives that had lost their ability to effectively initiate tumors and that were more susceptible to conventional chemotherapeutic agents in vitro. Further interrogation revealed that these agents elevated the intracellular levels of cAMP, which in turn activates PKA. PHF2, a histone H3 with acetylated lysine 9 (H3K9) histone demethylase and PKA substrate, was found to be essential for the cAMP-induced MET. By studying the genome occupancy of PHF2 and the epigenomic state of the cells before and after PKA activation, we determined that PHF2 promotes the demethylation and derepression of epithelial genes that ultimately contribute to acquisition of an epithelial state.

CONCLUSION: We conclude that PKA participates in the differentiation of TICs by enforcing residence in the epithelial state and preventing or reversing the EMT program. Our study reveals a new direction for targeting the TIC population. We propose that pharmacological induction of epigenetic reprogramming of these cells could promote their differentiation to a more epithelial state and increase their susceptibility to conventional chemotherapeutic drugs. ■



Induction of the MET as a potential cancer therapy. TICs have mesenchymal attributes that contribute to their ability to seed new tumors. Treatment of TICs with compounds that increase cAMP levels (e.g., CTx and Fsk) activates PKA. This leads to epigenetic reprogramming through subsequent activation of the histone demethylase PHF2, a PKA substrate, which in turn promotes differentiation of the cells into a more epithelial state, accompanied by a loss of their tumor-initiating ability. Drugs targeting various steps of this signaling pathway might be developed into a differentiation-based cancer therapy for certain breast cancers.

The list of author affiliations is available in the full article online.

*Corresponding author. E-mail: weinberg@wi.mit.edu

Cite this article as D. R. Pattabiraman et al., *Science* 351, aad3680 (2016). DOI: 10.1126/science.aad3680

RESEARCH ARTICLE

CANCER BIOLOGY

Activation of PKA leads to mesenchymal-to-epithelial transition and loss of tumor-initiating ability

Diwakar R. Pattabiraman,¹ Brian Bierie,¹ Katharina Isabelle Kober,¹ Prathapan Thiru,¹ Jordan A. Krall,¹ Christina Zill,¹ Ferenc Reinhardt,¹ Wai Leong Tam,^{1,2,3} Robert A. Weinberg^{1,4,5,*}

The epithelial-to-mesenchymal transition enables carcinoma cells to acquire malignancy-associated traits and the properties of tumor-initiating cells (TICs). TICs have emerged in recent years as important targets for cancer therapy, owing to their ability to drive clinical relapse and enable metastasis. Here, we propose a strategy to eliminate mesenchymal TICs by inducing their conversion to more epithelial counterparts that have lost tumor-initiating ability. We report that increases in intracellular levels of the second messenger, adenosine 3',5'-monophosphate, and the subsequent activation of protein kinase A (PKA) induce a mesenchymal-to-epithelial transition (MET) in mesenchymal human mammary epithelial cells. PKA activation triggers epigenetic reprogramming of TICs by the histone demethylase PHF2, which promotes their differentiation and loss of tumor-initiating ability. This study provides proof-of-principle for inducing an MET as differentiation therapy for TICs and uncovers a role for PKA in enforcing and maintaining the epithelial state.

Tumor-initiating cells (TICs), also known as cancer stem cells, are defined operationally by their ability to seed new tumors when implanted in appropriate hosts. They have emerged in recent years as important targets for cancer therapy, owing to their elevated resistance to conventional chemotherapy and their tumor-initiating ability—the latter allows them to metastasize and to drive clinical relapse (1, 2). Although their mode of generation and biological properties have been explored in a diverse array of cancer types (3), our understanding of the biology of TICs remains superficial. Cytotoxic therapies designed specifically to eliminate TICs might be targeted, for example, to interdict the signaling pathways that are used preferentially or uniquely by these cells (4). At present, however, the nature of such TIC-specific signaling pathways remains to be fully elucidated.

The epithelial-to-mesenchymal transition (EMT) is a cell-biological program that confers mesenchymal traits on both normal and neoplastic epithelial cells (5). In addition, activation of an EMT program enables both classes of cells to acquire stemlike properties (6, 7). Indeed, TICs from several carcinoma types have distinct mes-

enchymal attributes, which suggests that they have passed, at least partially, through an EMT (7–9). This association between the EMT program and the TIC state has presented an attractive opportunity for drug development using agents that preferentially target more mesenchymal carcinoma cells, rather than their epithelial counterparts, in an effort to eliminate TICs.

At least two approaches might be taken to target mesenchymal TICs. One strategy would be to develop agents that show specific or preferential cytotoxicity toward TICs (1). In this study, we have embraced an alternative strategy that is designed to induce TICs to exit the more mesenchymal tumor-initiating state and enter into an epithelial non-stemlike state. Such induced differentiation should, we reasoned, place cells in a state where they would become more vulnerable to conventional cytotoxic treatments. Accordingly, we screened for agents that could induce a mesenchymal-to-epithelial transition (MET) and, thereby, uncovered the central role of adenosine 3',5'-monophosphate (cyclic AMP or cAMP) and its downstream target, protein kinase A (PKA), in governing the transition of cells from the mesenchymal to the epithelial state.

cAMP is a second messenger that transmits intracellular signals when certain hormones and neurotransmitters interact with receptors on the plasma membrane (10). cAMP regulates multiple downstream effectors; the first of these to be identified and the most well studied is PKA (11), which plays numerous roles in various cell types and operates in several subcellular locations (12).

Because PKA is initially assembled as a heterotetrameric holoenzyme, its activity depends on cAMP binding to its two regulatory subunits, which leads to the release of active catalytic subunits and the phosphorylation of a diverse array of substrates (12).

In previous work, PKA has been shown, under some conditions, to promote an EMT; PKA was shown to regulate the transcription factor Snail in one study; and another study demonstrated that hypoxia-inducible factor 1 α (HIF-1 α) could regulate transcription of *PRKACA* under hypoxic conditions (13, 14). However, PKA signaling has been shown to favor the epithelial state, but the mechanistic understanding of this phenomenon is limited. One report showed that schwannomas in mice without *Prkar1a* (encoding the PKA regulatory subunit) exhibited loss of vimentin and gain of cytokeratins and E-cadherin (15), whereas another study revealed inhibition of the formation of mesoderm-derived structures in *Prkar1a* null mice (16). A recent study reported that deletion of the *Gas* subunit repressed the activity of PKA, which limited the proliferative potential of epithelial hair follicle stem cells (17). Nevertheless, the connection of PKA signaling to TICs and the stemlike state is poorly understood, and the exploitation of this pathway as a differentiation-based cancer therapy has not been explored.

Identification of agents that induce an MET in mammary epithelial cells

Human breast cancers are characterized by cells that show various degrees of epithelial and mesenchymal properties, as revealed by the expression pattern of markers, such as cytokeratins and vimentin (fig. S1). Almost 85% of the carcinomas we examined showed varied expression patterns of cytokeratins, which indicated that the loss of epithelial properties is a commonly occurring event. Notably, ~10% of the carcinomas we examined exhibited high degrees of intratumoral heterogeneity, created in part by the presence of subpopulations of neoplastic cells that have both epithelial and mesenchymal properties. These are reminiscent of cells that have undergone an EMT, which resemble TICs that have a higher tumor-initiating propensity and an increased resistance to chemotherapy (18). To model the behavior of these subpopulations of carcinoma cells from human basal-like breast cancers, we used immortalized human mammary epithelial cells (HMLE cells) (19), which display an epithelial morphology; express E-cadherin at adherens junctions; and have low levels of mesenchymal markers, such as vimentin and fibronectin. They also exhibit a CD44^{lo}/CD24^{hi} cell surface marker phenotype that is characteristic of previously reported cells that lack stemlike properties (non-CSCs) (20). We also used their spontaneously arising mesenchymal derivatives, termed NAMEC8 (N8) cells (21). Relative to their HMLE counterparts, N8 cells express mesenchymal markers, such as vimentin and fibronectin, as well as the EMT-inducing transcription factors Snail and Zeb1 at higher levels; lack expression of E-cadherin at prominent cell junctions; and display a CSC-like

¹Whitehead Institute for Biomedical Research, Cambridge, MA 02142, USA. ²Genome Institute of Singapore, 60 Biopolis Street, Singapore. ³Cancer Science Institute of Singapore, 14 Medical Drive, Singapore. ⁴Department of Biology, Massachusetts Institute of Technology, Cambridge, MA 02139, USA. ⁵Ludwig Center for Molecular Oncology at MIT, Cambridge, MA 02142, USA.

*Corresponding author. E-mail: weinberg@wi.mit.edu

CD44^{hi}/CD24^{lo} cell surface marker profile (Fig. 1, A to C). They also have a greater propensity to form mammospheres (Fig. 1, D and E), which is often used as an *in vitro* surrogate assay for the stemness of mammary epithelial cells. They are more efficient at migration through a trans-well membrane and invasion through a Matrigel-coated Boyden chamber membrane (Fig. 1, F and G); both *in vitro* assays represent models of cancer cell invasiveness *in vivo*. N8 cells are also more resistant to treatment with chemotherapeutic drugs, such as doxorubicin and paclitaxel (Fig. 1, H and I), as shown previously (27). Hence, two cell types represent epithelial and mesenchymal derivatives of mammary epithelial cells of common origin that were used to model the two cell states and how they affect tumor initiation and progression.

To search for agents that can induce an MET, we performed a screen to identify compounds that could induce transcription of *CDHI*, which

encodes E-cadherin, a key epithelial protein, in N8 cells. As a reporter for the activity of the *CDHI* gene, we constructed a lentiviral vector that expresses a portion of the *CDHI* promoter fused to luciferase (fig. S2A). We performed a screen using a 400-compound library for agents that were able to induce the *CDHI*-driven luciferase expression in N8 cells (fig. S2B). Most striking was the behavior of forskolin (Fsk), an adenylate cyclase activator that induced a 40-fold increase in luciferase activity (fig. S2C). Another adenylate cyclase activator, cholera toxin (CTx), was also able to induce an increase in luciferase activity (fig. S2D), which suggested that activation of adenylate cyclase could induce the acquisition of epithelial properties.

Fsk or CTx and the induction of an MET in mammary epithelial cells

We found that treatment of N8 cells in monolayer culture with either CTx or Fsk for a period of 14 days induced the formation of islands of

cells with the characteristic cobblestone morphology of epithelial cells; such cells acquired the expression of E-cadherin at adherens junctions along with a loss of mesenchymal markers, such as vimentin (Fig. 1, A and C). Also, the cell surface marker expression profile of the N8 cells switched from a stemlike CD44^{hi}/CD24^{lo} to a nonstem CD44^{lo}/CD24^{hi} phenotype after this treatment (20) (Fig. 1B). These shifts were accompanied by a 100-fold increase in *CDHI* mRNA levels, as well as decreases in the mRNA levels of *Snail*, *Twist1*, and *Zeb1* EMT-inducing transcription factors (EMT-TFs) to 25%, 20%, and 14%, respectively, of the N8 cells before the transition (fig. S3, A and B). Treatment of N8 cells with either CTx or Fsk resulted in a near-complete loss of mammosphere-forming ability (Fig. 1, D and E), as well as their ability to migrate and invade (Fig. 1, F and G). There were no significant differences in the rates of proliferation between the N8 cells and their CTx- and Fsk-treated derivatives

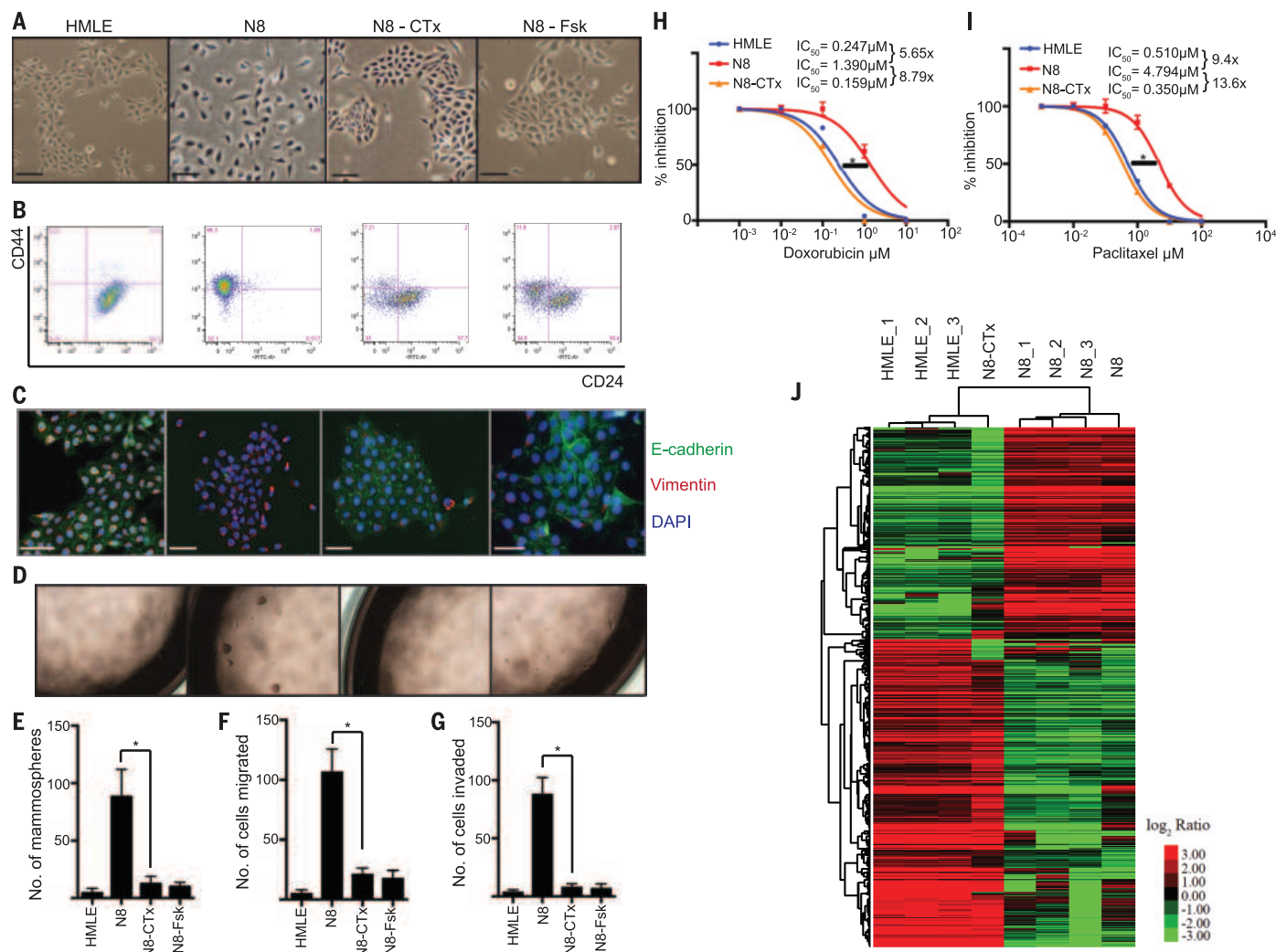


Fig. 1. Induction of an MET on treatment of N8 cells with CTx or Fsk. Mesenchymal N8 cells acquire an epithelial morphology as adjudged by their morphology (**A**), loss of a stemlike CD44^{hi}/CD24^{lo} profile to assume a predominantly CD44^{lo}/CD24^{hi} profile (**B**), and expression of E-cadherin at cell junctions and loss of vimentin (**C**). Reverted N2-CTx and N3-Fsk cells lose their ability to form (**D** and **E**) mammospheres ($P < 0.05$, $n = 4$), (**F**) to migrate

($P < 0.05$, $n = 4$) and (**G**) to invade in transwell assays ($P < 0.05$, $n = 4$) and to acquire increased sensitivity to treatment with (**H**) doxorubicin and (**I**) paclitaxel ($P < 0.05$, $n = 4$). (**J**) Heat map of mRNA-Seq data, which demonstrates similarity in gene expression between HMLE, N8, and N8-CTx cells. Data (means \pm SD) in (E), (F), and (G) were analyzed by Student's *t* test; (H) and (I) were analyzed by Bonferroni correction. All scale bars, 25 μm .

(fig. S3C). Of additional interest, withdrawal of CTx after 14 days of treatment led to cell populations that continued to reside in an epithelial state for >2 months in culture.

Reversion to an epithelial state, ostensibly similar to that of HMLE cells, rendered the N8 cells 8 times as sensitive to killing by doxorubicin [lowered the median inhibitory concentration (IC_{50}) from 1.39 μ M to 0.159 μ M] and 13 times as sensitive to paclitaxel (lowered the IC_{50} from 4.79 μ M to 0.35 μ M) (Fig. 1, H and I). Also, the induced MET resulted in increased sensitivity to a range of chemotherapeutic drugs and inhibitors including methotrexate, 90-kD heat shock protein (HSP90) inhibitors, proteasome inhibitors, and epidermal growth factor receptor-mitogen-activated protein kinase (EGFR-MAPK) pathway inhibitors, as observed when we screened against two small-molecule libraries (Selleck Anticancer Compound Library and Enzo Kinase Inhibitor Library) (fig. S4). Hence, the induction of an MET rendered the N8 cells more sensitive to a range of drugs and inhibitors, which points to its utility as a means of overcoming therapeutic resistance. It also reinforces the notion that mesenchymal cells are more resistant to a range of cytotoxic agents.

We then performed mRNA sequencing (mRNA-Seq) to compare the global gene expression profiles of the mesenchymal N8 and the reverted N8-CTx cells in order to view the transcriptional changes that occur after the induction of MET. As deter-

mined by differential gene expression (Fig. 1J and tables S1 and S2) and principal component analyses (fig. S3D), the N8-CTx cells assume a gene expression profile that is almost completely converted to that of the epithelial HMLE cells and is significantly different from the mesenchymal N8 cells (Fig. 1J). Gene set enrichment analyses showed that the changes in gene expression from N8 to the N8-CTx cells are highly similar to several previously published EMT and MET gene signatures (22–24) (fig. S3E). Taken together, these observations demonstrated a transition of the N8 cells from a mesenchymal-like state to a bona fide epithelial state, which rendered these cells more sensitive to a variety of drugs with potentially important therapeutic implications.

Effects of Fsk and CTx on intracellular cAMP levels and PKA

To confirm that both Fsk and CTx were working through alteration of cAMP levels, we measured the levels of this second messenger in both HMLE and N8 cells using liquid chromatography-mass spectrometry (LC-MS). Treatment with CTx resulted in a six- to eightfold increase in the intracellular levels of cAMP, which could be dampened by exposure to SQ22536, an inhibitor of adenylate cyclase, the enzyme responsible for the formation of cAMP (Fig. 2A).

The major downstream targets of cAMP are exchange proteins activated by cAMP (EPAC1/2)

(25); cyclic nucleotide-gated ion channels that are primarily found in cells of the kidney, heart, testis, and central nervous system (26); and the most commonly studied downstream effector, PKA (11). To delineate the downstream pathways that are activated in response to increase in cAMP levels, we treated N8 cells with two cAMP analogs—8-bromoadenosine 3',5'-cyclic monophosphate (8-Br-cAMP), which is known to preferentially activate PKA (27), or 8-(4-chlorophenylthio)-2'-O-methyladenosine-3',5'-cyclic monophosphate (8-CPT-2Me-cAMP), which is a selective activator of the exchange proteins activated by cAMP (EPACs) (28). As was seen with Fsk or CTx, treatment with 8-Br-cAMP was also able to induce an MET in N8 cells, whereas 8-CPT-2Me-cAMP treatment had no effect on their mesenchymal properties (Fig. 2B). This allowed us to conclude that PKA, rather than the cAMP-activated exchange proteins, was more likely to play a central role in the MET process.

Knockdown of the catalytic subunit of PKA using two different small hairpin RNAs (shRNAs) (fig. S5A) abrogated the CTx-induced MET process in N8 cells, as demonstrated by their inability to develop a clear epithelial morphology; to acquire junctional E-cadherin; and to shed mesenchymal markers, such as fibronectin (Fig. 2, C and D). Moreover, treatment of these PKA-knockdown cells with CTx failed to induce an effective transition from the CD44^{hi}/CD24^{lo} stemlike

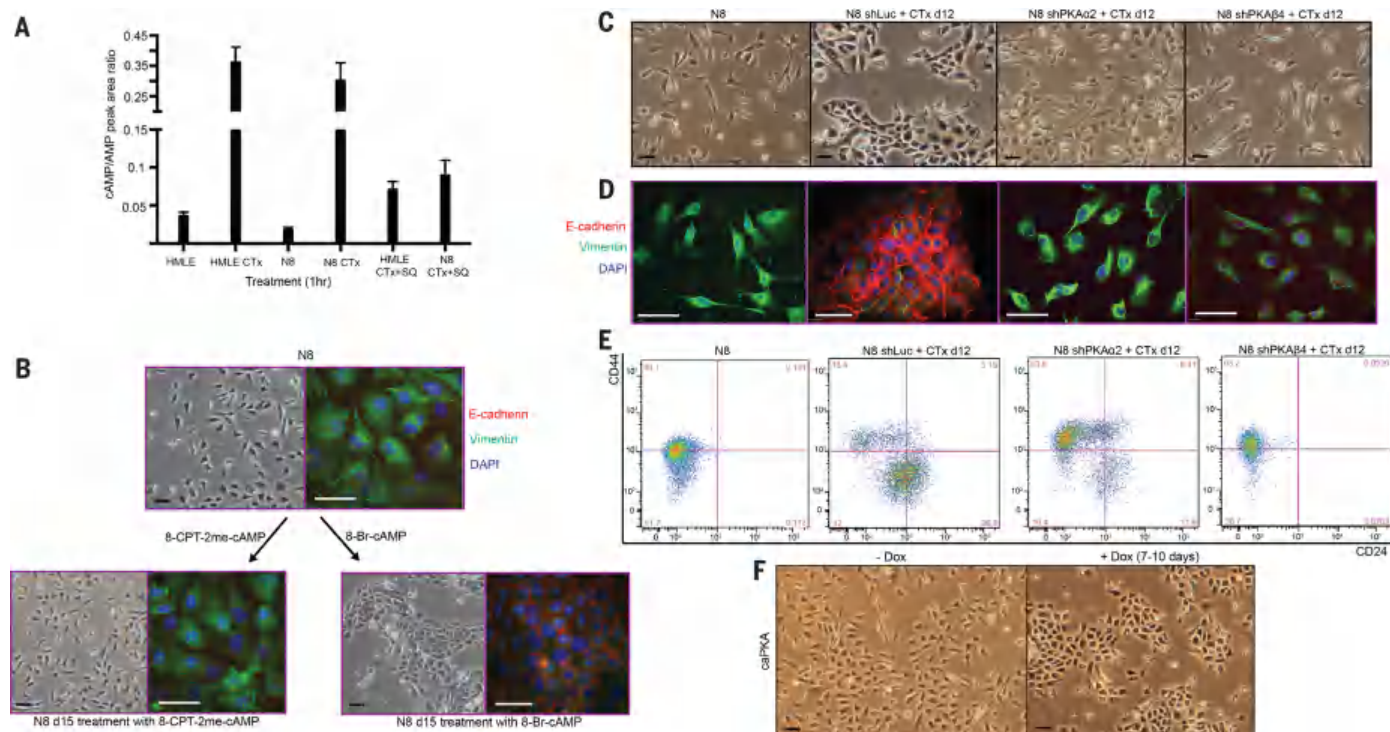


Fig. 2. cAMP increases activate PKA, which is both necessary and sufficient for the induction of an MET in N8 cells. (A) Mass-spectrometry measurement of cAMP levels in N8 cells that have been treated with CTx or Fsk alone and in combination with adenylate cyclase inhibitor SQ22536 (means \pm SD, $P < 0.05$, $n = 3$). (B) Treatment of N8 cells with either 8-CPT-2me-cAMP or 8-Br-cAMP to identify downstream pathways that are responsible

for induction of an MET. Knockdown of either PRKACA or PRKACB prevents CTx from inducing an MET in N8 cells as observed by changes in (C) morphology, (D) immunofluorescence for E-cadherin and vimentin, and (E) CD44/CD24 status. (F) Morphological changes of N8 cells undergoing an MET upon ectopic expression of an active mutant of PKA (caPKA). Data in (A) were analyzed using the Student's t test. All scale bars, 25 μ m.

state to the CD44^{lo}/CD24^{hi} non-stemlike state, which was otherwise observable in the absence of PKA knockdown (Fig. 2E). These results further reinforced the important role of PKA in the MET process.

Then, we tested whether PKA activity, independent of cAMP, was sufficient to induce an MET. Thus, we ectopically expressed a doxycycline-inducible constitutively active, cAMP-independent, constitutively active mutant form of PKA (caPKA) (29) in N8 cells and found that it was capable of inducing a reversion to the epithelial state in 7 to 10 days (Fig. 2F). Hence, it appears as though PKA is both necessary and sufficient to induce the acquisition of epithelial properties in the N8 cells.

We tested the role of CTx or Fsk in inducing an epithelial state in other cell systems to assess the generality of our observations. Removing CTx from the standard culture medium of MCF10A immortalized human mammary epithelial cells (30), caused them to acquire mesenchymal properties, to lose cell-cell adherens junctions, to lose their characteristic cobblestone morphology, and to gain a CD44^{hi}/CD24^{lo} cell surface marker profile. They also lost E-cadherin expression and exhibited an increase in expression of *Zeb1*, *Vim*, and *FN1* (fig. S6, A to E). Readdition of CTx or forced expression of caPKA led to the reacquisition of epithelial features (fig. S6, A to E). Moreover, the MCF10A cells that lost epithelial properties upon CTx withdrawal were 4 times as resistant to treatment with doxorubicin and so extended our observations made in N8 cells that the mesenchymal variants were more resistant to conventional chemotherapeutic agents (fig. S6F).

We then proceeded to test the role of CTx and/or Fsk in a series of other cell lines. MCF7-Ras human breast cancer cells (31) can be induced to undergo an EMT through the ectopic expression of EMT-inducing transcription factors, such as Slug. Cotreatment of the cells undergoing an EMT with CTx led to a 48-hour delay in the acquisition of mesenchymal morphology and CD44^{hi} cell surface marker expression (fig. S7A). Similarly, the ability of HMLE-Ras cells to undergo an EMT upon ectopic expression of *Zeb1* was also hampered upon cotreatment with CTx (fig. S7B). PANC1 pancreatic adenocarcinoma cells undergo an EMT upon treatment with transforming growth factor- β 1 (TGF- β 1) for 48 hours (32). Cotreatment of PANC1 cells undergoing an EMT with either CTx or Fsk delayed the ability of TGF- β 1 to induce an EMT by 48 to 72 hours, which enabled the temporary retention of epithelial properties (fig. S7, C and D).

Treatment with CTx or Fsk induced the acquisition of epithelial properties in a range of cell lines that have mesenchymal traits, including the Hs578T triple-negative breast cancer cell line (fig. S8A), the NCI-H596 lung adenocarcinoma cell line (fig. S8B), and the mesenchymal EpCAM^{lo} CD24^{lo} fraction of the EF021 ovarian carcinoma cell line (fig. S8C). Induction of epithelial properties was also observed in PB3 cells (fig. S8D), which constitute an aggressive cell line isolated from mammary tumors of the genetically

engineered MMTV-PyMT transgenic mouse model of breast cancer, in which the expression of the oncogene is driven by the mouse mammary tumor virus promoter (33). Finally, we note that others have recently reported that Fsk promotes the maintenance of an epithelial morphology in primary human mammary epithelial cells, the absence of which led spontaneously to acquisition of mesenchymal attributes, such as down-regulation of E-cadherin expression and up-regulation of mesenchymal markers (34).

Taken together, these data signify the importance of PKA signaling in maintaining epithelial characteristics in a variety of normal and neoplastic epithelial cells. These data give an indication that these responses might be a general property of cAMP-induced activation of PKA in the reversal of phenotypes created by activation of an EMT program.

Although CTx was able to induce entrance of the N8 cells and a range of other cell systems into a stably maintained epithelial state, there were some models in which neither CTx nor Fsk was able to do so, namely, the MDA-MB-231 and SUM159 human breast cancer cell lines, amongst others. These cell lines are maintained in the mesenchymal state through the deletion or stable silencing of several key epithelial genomic loci, which includes the repression of E-cadherin through strong DNA promoter hypermethylation (35). Hence, although the observed effects of PKA activation are applicable to some breast cancer lines and other carcinomas, they are not universal and depend instead on the specific genetic or epigenetic state of the cells.

Essential role of PKA-induced activation of PHF2 in MET

PKA is known to act on many substrates in both the cytoplasm and nucleus (36). Treatment of HMLE and N8 cells with CTx resulted in an immediate increase in the presence of both isoforms of the catalytic subunit in the nucleus (fig. S9, A and B), which suggested that PKA might be regulating nuclear substrates after activation by cAMP. The most well-studied substrate of PKA, CREB1, translocates to the nucleus upon phosphorylation by PKA at Ser¹³³, thereafter altering the transcription of hundreds of target genes (37). In fact, about 300 distinct physiologic stimuli have been described in the literature that can induce CREB Ser-133 phosphorylation (38). It was, therefore, not surprising that CREB was already phosphorylated and present in the nucleus of the N8 cells even before their treatment with either CTx or Fsk (Fig. 3A). Note that knockdown of CREB1 by the use of at least two shRNAs (fig. S5C) did not affect the ability of CTx to induce an MET in the N8 cells (Fig. 3B). Moreover, loss of CREB1 alone induced a partial MET in N8 cells (Fig. 3B), consistent with previous reports of its role in the induction of an EMT (39, 40). On the basis of these observations, we conclude that CREB1 did not play an important role in the PKA-induced MET. We then assessed the localization of Gli1, Gli2, and Gli3, which have

been previously reported to be PKA substrates that are retained in the cytoplasm after phosphorylation (41) and found no retention of any of the Gli proteins in the cytoplasm after treatment with CTx or Fsk (fig. S9C). These observations suggest that the Gli proteins may not play a role in the observed PKA-induced MET.

Having explored the two most commonly reported nuclear substrates of PKA, we then focused on PHF2, a histone H3 with acetylated lysine 9 (H3K9) histone demethylase, which is known to become activated upon phosphorylation by PKA (42). We found that knockdown of PHF2 expression in N8 cells using either of two shRNAs (fig. S5B) phenocopied the effects of PKA knockdown in that it prevented CTx-induced MET (Fig. 3, C and D). In contrast, knockdown of PHF2 did not alter the ability of HMLE cells to undergo an EMT (Fig. 3, F and G), which indicated that this enzyme, although necessary for induction of an MET, apparently plays no role in the reverse process—the EMT—which suggested that it is specifically important for the derepression of silenced epithelial genes through its function as a H3K9 histone demethylase.

PHF2 can be phosphorylated by PKA at four serine residues in its C terminus (42) (Fig. 3E). Accordingly, we engineered a phospho-mimetic form of PHF2 in which all four of these serines were replaced by aspartate residues. Although expression of this mutant in N8 cells was not sufficient on its own to induce an MET, the phospho-mimetic PHF2 was able to accelerate the rate of CTx-induced transition from the mesenchymal to the epithelial state from 14 days to 7 days (Fig. 3, H and I). Hence, although PHF2 is required for the acquisition of epithelial traits, it appears to be only one of the effectors of the PKA operating during induction of epithelial transition.

To test whether PHF2 can be directly phosphorylated by PKA in our system, we performed an immunoprecipitation of PHF2 followed by immunoblotting using an antibody that recognizes the phospho-PKA substrate motif. As shown in Fig. 3J, 24 hours after treatment of N8 cells with CTx, phosphorylation of PHF2 by PKA can be observed, which provides evidence that PKA phosphorylates PHF2 in the N8 cells. Together, these results suggest an important role for PHF2 as a PKA substrate in the induction of an MET.

PKA-induced activation of PHF2 and the epigenetic reprogramming of mesenchymal cells

The H3K9me2 and H3K9me3 marks have been associated with repression of gene transcription (43). Given the previously reported role of PHF2 as an H3K9me2/3 demethylase, we performed chromatin immunoprecipitation followed by deep sequencing (ChIP-Seq) using antibodies against histone 3 with trimethylated lysine 9 (H3K9me3) and H3K9me2 marks to observe the presence of these marks in untreated N8 cells as well as CTx-treated counterparts in which PHF2 is active. In addition we also performed ChIP-Seq for PHF2, comparing genome-wide occupancy in N8 cells

to the N8-CTx cells. We did so in order to monitor PHF2-associated alterations that might enable phenotypic shifts from the mesenchymal to epithelial states, including shifts that might relieve the H3K9-mediated silencing of epithelial genes.

As seen in Fig. 4A, there was a striking inverse correlation at specific loci of the presence of PHF2 with the repressive H3K9me2 or H3K9me3 marks. This suggests that presence of this demethylase may, on its own, suffice to relieve histone-mediated transcriptional silencing. As

previously reported, PHF2 appears to occupy the promoter region of genes where it recognizes the H3K4me3 histone mark (Fig. 4B) (9). Interestingly, the total H3K9me3 counts (>4-fold enrichment above control) in N8-CTx cells was almost half of the total counts of the same mark in N8

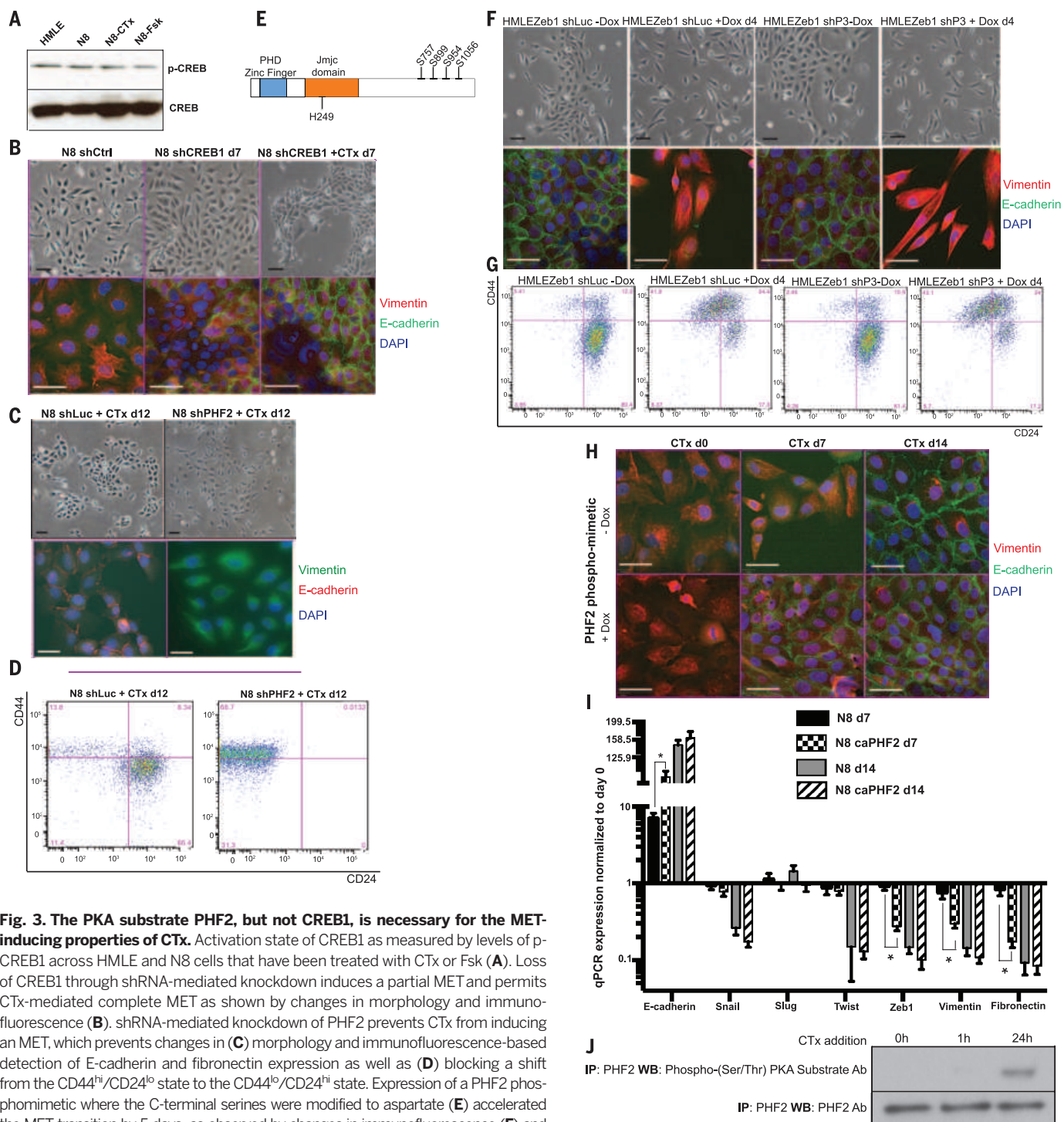


Fig. 3. The PKA substrate PHF2, but not CREB1, is necessary for the MET-inducing properties of CTx. Activation state of CREB1 as measured by levels of p-CREB1 across HMLE and N8 cells that have been treated with CTx or Fsk (A). Loss of CREB1 through shRNA-mediated knockdown induces a partial MET and permits CTx-mediated complete MET as shown by changes in morphology and immunofluorescence (B). shRNA-mediated knockdown of PHF2 prevents CTx from inducing an MET, which prevents changes in (C) morphology and immunofluorescence-based detection of E-cadherin and fibronectin expression as well as (D) blocking a shift from the CD44^{hi}/CD24^{lo} state to the CD44^{lo}/CD24^{hi} state. Expression of a PHF2 phosphomimetic where the C-terminal serines were modified to aspartate (E) accelerated the MET transition by 5 days, as observed by changes in immunofluorescence (F) and quantitative EMT marker analysis by qPCR (G). Effects of shRNA-mediated knockdown of PHF2 on the ability of HMLE cells to undergo an EMT upon ectopic expression of Zeb1 (H and I) (qPCR data, means \pm SD, $P < 0.05$, $n = 3$). Immunoprecipitation of PHF2 followed by immunoblotting with a phospho-PKA substrate antibody showed phosphorylation of PHF2 by PKA 24 hours after treatment of N8 cells with CTx (J). (I) was analyzed using the Student's t test. All scale bars, 25 μ m.

cells (35,455 versus 18,675). Similarly, the total H3K9me2 counts in N8-CTx cells were also less than a half of that in the N8 cells (1295 vs 473). As shown in the representative circos plots, these data indicate a widespread loss of H3K9-mediated repression of genomic regions upon treatment of N8 cells with CTx and subsequent activation of PHF2 (Fig. 4C).

We then sorted for genomic regions present in the N8-CTx but not N8 cells that contained PHF2 binding and lacked repressive H3K9me2/3 marks (table S3). This provided us with a list of genomic regions that were relieved of H3K9me2/3-mediated silencing in the N8-CTx cells, as compared to the N8 cells, owing to PHF2 occupancy. To ensure that these changes were specific for the loss of PHF2, we performed ChIP-Seq for H3K9me2/3 and PHF2 in CTx-treated N8 cells that had an shRNA against PHF2 preventing the MET (table S4). These cells that remained morphologically mesenchymal also demonstrated an epigenetic profile more like that of N8 cells with an overlap of 11,807 peaks compared with the reverted N8-CTx cells, which had an overlap of 6864 peaks. Hence, the list of altered genomic regions outlined in table S3 represents genes that were relieved of H3K9-mediated repression upon CTx-induced activation of PHF2. This suggests that PHF2 activity could be directly responsible for the derepression of these genes that are characteristic of the epithelial cell state. In addition, the expression values of genes that correspond to these genomic loci were also measured in reverted N8-CTx (epithelial) and parental N8 (mesenchymal) cells by RNA-seq, which verified that gain of PHF2 occupancy and loss of H3K9 marks did indeed lead to increased expression (table S3).

Several genes that play a major role in the phenotype and profile of cells in the epithelial state were activated by CTx treatment. The list of genes that were relieved of silencing when treated with CTx includes *CDH1* and *CDH3* (among other cadherin genes) that code for E-cadherin and P-cadherin (fig. S10A), respectively, which are essential components of adherens junctions and hallmark proteins of basal epithelial cells; *KRT8* and *KRT18* (fig. S10B), whose gene products are characteristic components of the cytoskeleton of epithelial cells; and *AJAPI* and *CLDN4* (fig. S10, C and D), which specify genes coding for constituents of adherens and tight junctions that are formed by epithelial but not mesenchymal cells. Other regions include the *TP63* gene (fig. S10E), whose product is a hallmark transcription factor of basal mammary epithelial cells, and *ITGB2*, *ITGB6* (fig. S10F), and *ITGB8*, which code for integrins that are typically expressed on epithelial cells. These observations reveal a mechanism by which activation of this demethylase enables the transcription of genes that induce the acquisition of epithelial properties, ultimately defining the state of the cells.

Activation of PKA and the differentiation of TICs in vivo

We tested the tumor-initiating ability of cells that have been induced to undergo an MET by

activation of PKA in vitro. We transplanted at limiting dilutions the neoplastic, *R4S*-transformed derivatives of HMLE, N8, and the reverted N8-CTx cells, termed HMLE-Ras, N8-Ras, and N8-CTx-Ras, into the mammary fat pads of nonobese diabetic-severe combined immunodeficient (NOD/SCID) mice. As anticipated, the frequency of TICs in the N8-Ras cells was far greater than in the HMLE-Ras cell population, in this case 100-fold as high. Note that the N8-CTx-Ras cells were as inefficient at tumor-initiation as the HMLE-Ras cells (Fig. 5A). The primary tumors that arose upon orthotopic mammary stromal fat pad implantation of N8-Ras tumors spawned 20 to 30 micrometastases in the lungs by 12 weeks after implantation. This property was lost upon induction of an MET by CTx treatment before transplantation (Fig. 5C and fig. S11A), which nevertheless formed primary tumors of comparable size (Fig. 5B). Moreover, this confirmed previous observations that the phenotypic state of these cells before neoplastic transformation strongly influenced their behavior after transformation.

To better mimic a clinical scenario, we next asked how the induction of an MET would affect preestablished tumors derived from mesenchymal N8 cells. Although we wished to pharmacologically treat mice that already had established N8-Ras tumors, CTx is too toxic to be administered systemically, and the rapid clearance and poor pharmacodynamics of Fsk made it difficult to study its effects upon systemic administration. Such difficulties in treating mice with PKA agonists have also been reported previously (44, 45). For this reason, we focused our efforts on studying the proof-of-principle effects of PKA activation in vivo using the doxycycline-inducible version of constitutively active PKA (caPKA). Thus, we induced expression of the caPKA in already formed N8-Ras tumors of 5-mm diameter (Fig. 5D). On visual inspection, the tumors that had been exposed for 14 days to doxycycline contained pasty, fluid-filled necrotic cores when compared with the tumors that had never been exposed to doxycycline: The latter were solid with a hard center of viable cells. Tumors from mice that received doxycycline weighed less than those that did not receive any (Fig. 5F). Moreover, those tumors in which expression of caPKA had been induced developed a more differentiated histomorphology as revealed by hematoxylin and eosin (H&E) staining of tumor sections (fig. S11, B and C). When tumors were harvested and subjected to fluorescence-activated cell sorting (FACS) analysis, the doxycycline-treated tumors showed a decrease in expression of the CD44 cell surface marker associated with the stemlike population (20), in contrast to the untreated tumors (fig. S11D).

Secondary transplantation of cells isolated from the doxycycline-exposed tumors at limiting dilutions revealed a 20-fold loss of tumor-initiating ability (Fig. 5E), which showed that activation of PKA induces differentiation of TICs and diminishes their ability to subsequently seed new tumors. This result demonstrates that constitutive expression of PKA for a 14-day period in a

growing tumor suffices on its own to reduce the tumor-initiating properties of its cells, as indicated by their subsequent inability to propagate upon secondary transplantation.

Discussion

Cyclic AMP and its main effector, PKA, have been studied for four decades in a variety of cell-biological and physiologic settings, where its effects in activating a number of distinct, tissue-specific traits have been repeatedly documented (11). A role that it might play in governing the epithelial cell state and thus suppressing entrance into the alternative mesenchymal state in breast cancers has not been described. The present work makes it clear that this second messenger and its main effector, PKA, play a key role in determining this epithelial versus mesenchymal balance of mammary epithelial cells, as well as epithelial cells of other tissues. Indeed, in light of these results, it becomes plausible that maintenance of the residence of cells in an epithelial state depends on tonic elevated levels of intracellular cAMP. In retrospect, it now seems likely that the use of cholera toxin as an ingredient in the tissue culture medium of various epithelial cell types [including cells of the epidermis, mammary gland, and bronchus (46, 47)] was motivated by the observation that loss of such cells in culture was accompanied by an overgrowth of fibroblast-like cells (46).

These results collectively indicate a role for PKA in the differentiation of TICs by enforcing residence in the epithelial state and preventing or reversing the EMT program. Although PKA can act via a large number of substrates, we identified PHF2 as an important downstream effector of PKA that mediates the induction of epithelial characteristics through epigenetic reprogramming to a chromatin state that is more favorable for residence in the epithelial state. We find that activating this histone demethylase enables PKA to induce the transcription of genes that play a role in the entrance into and maintenance of residence in the epithelial state.

The EMT program is known to represent one defined route for the generation of both normal and neoplastic epithelial stem cells (6, 7, 48). The observations that PKA-induced activation of PHF2 can either reverse or curtail this program present an opportunity to exploit such a mechanism for therapeutic gain. Indeed, the differentiation of TICs through the induction of an MET is an attractive proposition—one that could be pursued through the induced increase of intracellular cAMP levels, activation of PKA, or activation of PHF2. Nonetheless, it is likely that many such approaches will result in widespread side-effect toxicities, owing to the multitude of signaling pathways that are activated downstream of cAMP increase (11). Specific activation of the PHF2 histone-modifier enzyme may serve as a means of derepressing genes that are essential for the differentiated epithelial state without eliciting many of the toxicities of induced cAMP increases. Along the same lines, identification of a histone methyltransferase that counteracts

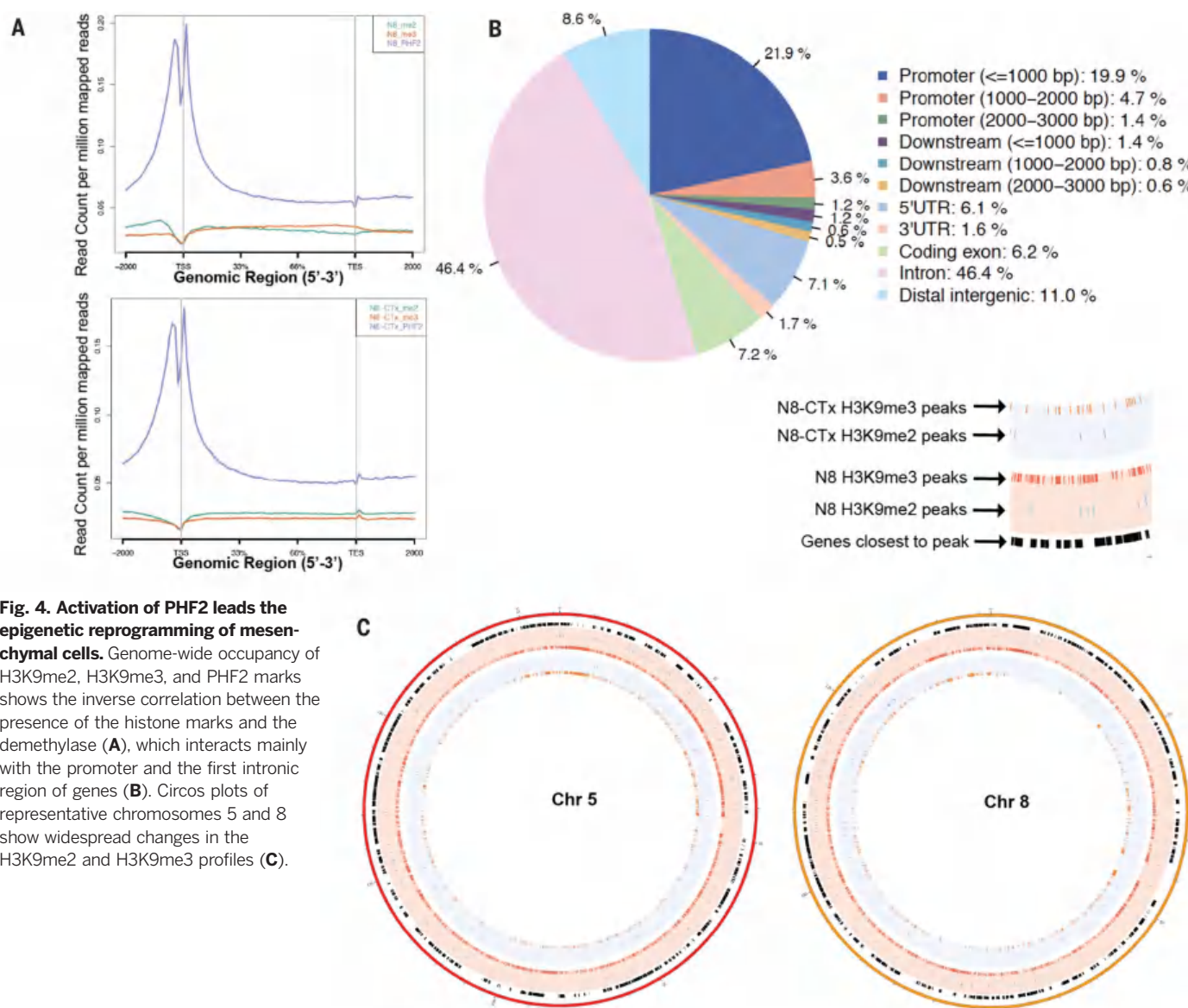


Fig. 4. Activation of PHF2 leads the epigenetic reprogramming of mesenchymal cells. Genome-wide occupancy of H3K9me2, H3K9me3, and PHF2 marks shows the inverse correlation between the presence of the histone marks and the demethylase (A), which interacts mainly with the promoter and the first intronic region of genes (B). Circos plots of representative chromosomes 5 and 8 show widespread changes in the H3K9me2 and H3K9me3 profiles (C).

PHF2 function may also provide an attractive target for therapeutic inhibition, a strategy that has proven successful in the case of DOT1L inhibition against mixed lineage leukemia (MLL)-driven leukemias (49). The role of the G9a histone methyltransferase in establishing the H3K9me2 mark for repression of the *CDH1* promoter in breast cancer cells has been reported previously (50).

This study provides mechanistic insight into the benefits of targeting such an enzyme in epithelial tumors, which prevents the constituent cells from undergoing an EMT and thereby acquiring aggressive characteristics, including increases in the numbers of TICs. The pathways explored in this study provide insight into the functions of PKA in the induction of an MET and the differentiation of the more aggressive TICs within a tumor. This study reveals a new direction for targeting the TIC population

through epigenetic rewiring that ultimately results in their differentiation and increased susceptibility to conventional chemotherapeutic drugs.

Materials and methods

Cell culture and treatments

HMLE, NAME8, and all derived cell lines were grown in Mammary Epithelial Cell Growth Medium medium (Lonza, USA); MCF10A cells were grown in Dulbecco's minimum essential medium; nutrient mixture F-12 (DMEM/F12) containing 5% horse serum (Sigma, USA; H0146); epidermal growth factor, 20 ng/ml; hydrocortisone, 0.5 mg/ml; CTx, 100 ng/ml; and insulin, 10 μ g/ml. EF021 and H596 cells were grown in Roswell Park Memorial Institute (RPMI) medium containing 10% fetal bovine serum. MCF7Ras cells were grown in DMEM containing 10% fetal bovine serum. Hs578T were grown in DMEM containing 10% fetal bovine serum and

insulin at 10 μ g/ml. Cells were treated with either 100 ng/ml of CTx (Calbiochem, USA; 227036), which was replenished every 2 days, or 1 μ M Fsk (Tocris Biosciences, USA; 1099), which was replenished daily over a period of 14 to 16 days. Cells were split to a ratio of 1:6 every 2 to 3 days during the treatments. MCF10A and EF021 cells were a gift from N. Kalaany and R. Drapkin, respectively.

Screening

For the *CDH1* reporter screen, 500 N8 cells bearing wild-type (wt) *CDH1* promoter luciferase were seeded into 384-well plates in a volume of 40 μ l. Twenty-four hours later, 100 nl of each compound (200 μ M stock) were added using a CyBio liquid handler, which resulted in a final screen concentration of 0.5 μ M. Four days later, the plates were read for either firefly luciferase activity (Pierce, 16177) or CellTiter-Glo (Promega, USA; G7572). The Enzo compound library (plate A and plate

B; 451 compounds, including repeats) was obtained from the Koch Institute Screening Facility at MIT. Firefly luciferase and CellTiter-Glo assays were performed in triplicates.

The vulnerabilities of the reverted cells were assessed by screening against the Selleck anti-cancer compound library (400 compounds) and the Enzo kinase library (80 compounds) at the Koch Institute Screening Facility at MIT. N8 or N8-CTx cells (1000 each) were seeded in 384-well plates in a volume of 50 μ l. Twenty-four hours later, 50 nl of each compound were added to assay a 5-point dose response. Three days later, the plates were read for CellTiter-Glo, and assays were performed in duplicate.

Flow cytometry

Cells were prepared according to standard protocols and suspended in 2% inactivated fetal bovine serum with phosphate-buffered saline (IFS/PBS). The fluorescent stain 4',6'-diamidino-2-phenylindole

(DAPI) (Life Technologies, USA; D1306) was used to exclude dead cells. Cells were sorted on BD FACSaria SORP and analyzed on BD LSRII, using BD FACSDiva Software (BD Biosciences, USA). Antibodies used were against CD44-PE-Cy7 (Biolegend, USA; 103029); against CD24-PE (BD Biosciences, USA; 555428); against CD45-Pacific Blue (Biolegend, USA; 103125); and against CD31-Pacific Blue (Biolegend, USA; 102421).

Mammosphere and tumorsphere culture

Mammosphere culture was performed as previously described (57). Cells (1000) were seeded per well of a 96-well Corning Ultra-Low attachment plate (Corning, USA; CLS3474) in replicates of 10; sphere numbers were counted between days 8 to 12.

Migration and invasion assays

Cells (25,000) were seeded into 24-well cell culture inserts with 8 μ m pores (BD Falcon, USA).

After 12 to 24 hours, the cells on the upper surface of the filters were removed with a cotton swab. For visualization, cells on lower filter surfaces were fixed and stained with a Diff-Quick staining kit (Dade Behring/Siemens, Germany). Three to five fields per filter were counted. Data are presented as migrated cells per field.

RNA preparation and polymerase chain reaction analysis

Total RNA was isolated using the RNeasy Plus Mini kit (Qiagen, USA; 74136) and reverse transcription was performed with the High Capacity RNA-to-cDNA kit (Life Technologies, USA; 4387406), both according to the manufacturer's protocols. A cDNA sample prepared from 1 μ g total RNA was used for quantitative reverse transcription polymerase chain reaction (RT-PCR). The PCR reactions were performed with the Fast SYBR Green Master Mix (Life Technologies; 4385612), data collection and data analysis were

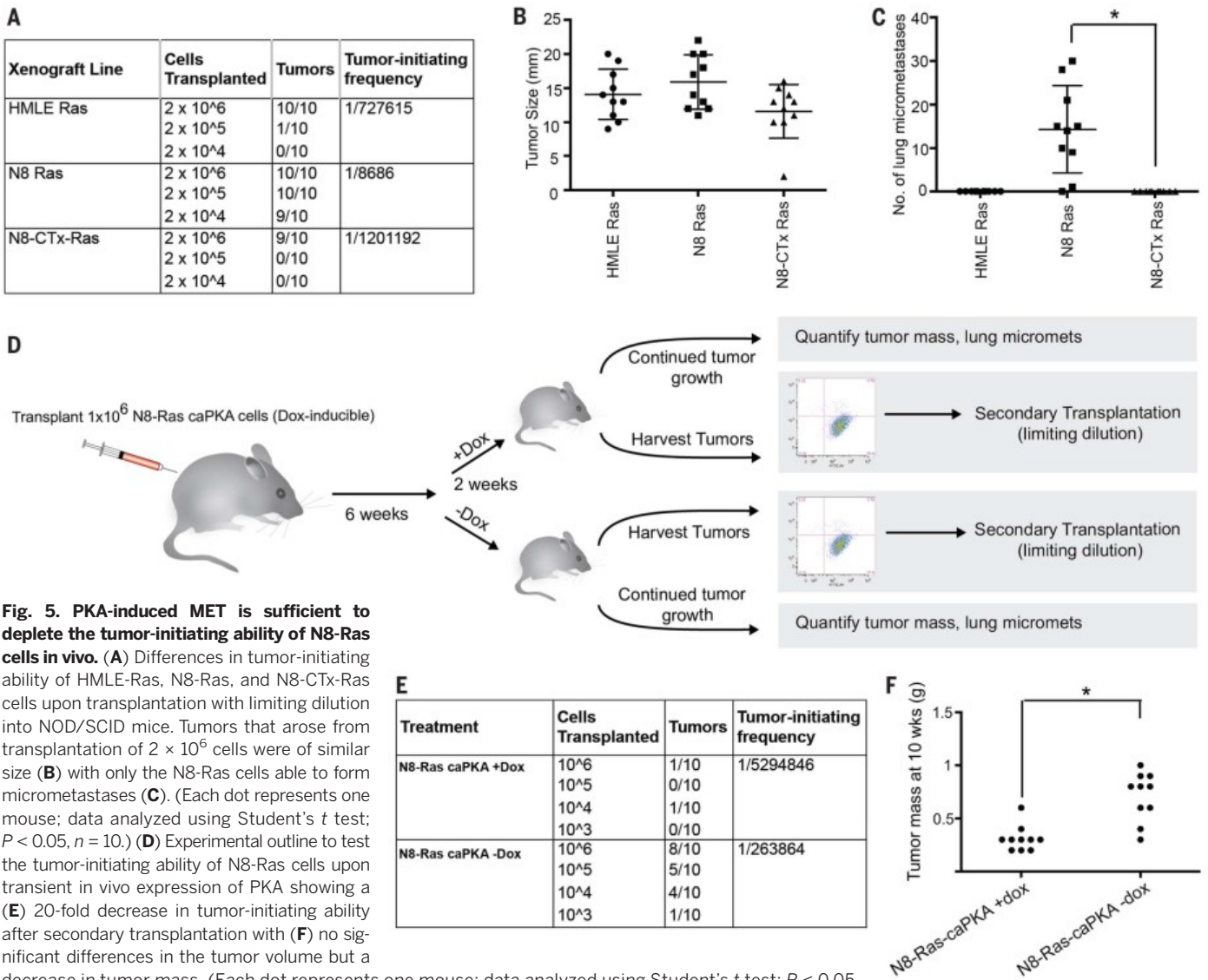


Fig. 5. PKA-induced MET is sufficient to deplete the tumor-initiating ability of N8-Ras cells in vivo. (A) Differences in tumor-initiating ability of HMLE-Ras, N8-Ras, and N8-CTx-Ras cells upon transplantation with limiting dilution into NOD/SCID mice. Tumors that arose from transplantation of 2×10^6 cells were of similar size (B) with only the N8-Ras cells able to form micrometastases (C). (Each dot represents one mouse; data analyzed using Student's *t* test; *P* < 0.05, *n* = 10.) (D) Experimental outline to test the tumor-initiating ability of N8-Ras cells upon transient in vivo expression of PKA showing a (E) 20-fold decrease in tumor-initiating ability after secondary transplantation with (F) no significant differences in the tumor volume but a decrease in tumor mass. (Each dot represents one mouse; data analyzed using Student's *t* test; *P* < 0.05, *n* = 10.)

performed on the ABI7900 machine (Applied Biosystems, USA) by using the SDS2.0 and RQ manager software. The thermal-cycling parameters for the PCR were as follows: 95°C for 5 min, followed by 45 cycles each of 95°C for 10 s, 49°C for 7 s, and 72°C for 25 s. The relative mRNA quantity was normalized against the relative quantity of *HPRT1* mRNA in the same sample. The primer sequences in a 5' to 3' orientation are shown in table S1.

Immunofluorescence (cultured cells)

Cells were cultured on dishes containing coverslips for 2 to 3 days, after which coverslips were washed in cold PBS, fixed in 4% paraformaldehyde for 10 min at 4°C and permeabilized in 0.2% TritonX in PBS for 2 min. Cells were then washed in PBS, blocked for 1 hour at room temperature in PBS containing 3% normal horse serum (Vector Labs, USA; S-2000). Fixed cells were then incubated with the primary antibody in PBS containing 1% bovine serum albumen (BSA) solution overnight at 4°C. Cells were washed in PBS three times, and secondary antibody was added in PBS containing 1%BSA solution for 1 to 2 hours at room temperature in the dark. Cells were washed three times in PBS and were incubated for 2 min in DAPI solution, after which they were washed in PBS and mounted with a drop of Prolong Gold antifade reagent (Life Technologies, USA; P36961) and placed on coverslips. Slides were viewed on a PerkinElmer Ultraview Spinning Disk Confocal imager and analyzed using Volocity software.

Immunofluorescence (tissue microarrays)

Slides were rehydrated by incubating in Histo-clear solution twice for 5 min each, followed by incubation in 100% ethanol twice for 5 min each, in 95% ethanol twice for 5 min each, 70% ethanol twice for 5 min each, once in 35% ethanol for 5 min, and in water for 5 min. Pressure cooker-mediated heat-induced epitope retrieval was carried out in 250 ml of unmasking buffer containing sodium citrate at pH 6. After retrieval, slides were blocked for 30 min in PBS containing 3% normal horse serum after which they were incubated with primary antibody in blocking solution overnight at 4°C. Slides were washed twice with PBS and incubated with secondary antibody at room temperature for 1 hour in the dark. After two PBS washes, 20 µl of mounting medium was added, then slide contents were topped with coverslips, and stored in the dark for 24 hours before imaging. A table of the antigens with source, host, and dilution is shown in table S2.

Proliferation assays

To measure rate of proliferation, 1000 cells were seeded onto a 96-well plate in quadruplicate. Proliferation was measured using CyQuant (Life Technologies, USA; C7026), according to the manufacturer's protocols.

Protein extraction and Western blotting

To obtain protein extracts, cells were washed with chilled PBS and scraped from culture dishes in

aqueous lysis buffer (50 mM Tris pH 7.5, 150 mM NaCl, 10 mM EDTA pH 8.0, 0.2% sodium azide, 50 mM NaF, and 0.5% NP40) containing complete miniprotease inhibitor cocktail (Roche, USA; 04693159001) and stored at -80°C. The proteins names, sources, and dilutions are shown in table S3. After thawing, they were centrifuged at top speed on a benchtop centrifuge at 4°C for 20 min, and the supernatant was assayed for protein concentration with Bradford Reagent (Bio-Rad; 500-0006). Of the total protein, 30 µg were separated by SDS-polyacrylamide gel electrophoresis (SDS-PAGE) on NuPage gels (Invitrogen, USA) and transferred to Hybond-P polyvinylidene difluoride membrane (GE Healthcare, USA). Membranes were probed with specific primary antibodies and antibody-protein complex detected by horseradish peroxidase (HRP)-conjugated secondary antibodies and SuperSignal West Dura Extended Duration Substrate (Life Technologies, USA; 34075).

Immunoprecipitation

N8 cells in 15-cm dishes were scraped and harvested in 0.5 ml of ice-cold immunoprecipitation (IP) buffer (Cell Signaling Technology, USA) containing protease and phosphatase inhibitors (Roche, Germany) after which they were sonicated with three pulses on ice. Lysates were spun down at 14,000g for 10 min, and supernatants were collected for IP. PHF2-specific antibody (Cell Signaling Technology, USA; 3497) was added at 1:25 and incubated overnight at 4°C rotating. The following morning, 40 µl of magnetic protein A/G beads (Thermo Scientific, USA; 26162) were added and incubated for 30 min on a rotator, after which beads were washed five times by using a magnetic separator with cold IP buffer. Beads were then boiled in lithium dodecyl sulfate buffer and run on an SDS-PAGE gel followed by immunoblotting.

RNAi-mediated knockdown

To generate shRNA-expressing plasmids, double-stranded oligonucleotides (oligos) encoding the desired shRNA were cloned into a Tet-pLKO-puro lentiviral vector (Addgene, plasmid 21915). In the absence of doxycycline, shRNA expression is repressed by constitutively expressed TetR protein. With the addition of doxycycline to the growth medium, shRNA expression is triggered, which results in target gene knockdown. The cloning vector has a 1.9-kb stuffer that is released by digestion with Age I and Eco RI. shRNA oligos are cloned into the Age I and Eco RI sites in place of the stuffer. PKA hairpins are shown in tables S4 to S6.

Animal studies

Research involving animals complied with protocols approved by the MIT Committee on Animal Care. For tumor studies, cells suspended in 15 µl 30% Matrigel (GFR)/PBS mix (BD Biosciences; 356230) were injected into the inguinal mammary gland fat pads of age-matched female NOD/SCID mice (Jackson Laboratory). Mice were killed after 10 weeks or when tumors reached a diameter of >1 cm. Lung sur-

face metastases were counted with a fluorescent microscope.

Chromatin IP followed by sequencing

ChIP for PHF2, H3K9me2, and H3K9me3 was carried out using the SimpleChIP Plus Enzymatic Chromatin IP Kit (Cell Signaling Technology, USA; 9005) and the protocols within. The PHF2 rabbit monoclonal antibody (Cell Signaling Technology, USA; 3497) was used at 1:25 per IP; the H3K9me2 mouse monoclonal (Abcam, USA; ab1220); and the H3K9me3 rabbit polyclonal antibodies (Abcam, ab8898) were used at 1:50 (10 µg) per IP. The ChIP DNA was used to prepare libraries for sequencing, which was carried out in the Genome Technology Core at the Whitehead Institute.

Library preparation for sequencing

To prepare libraries for RNA-Seq, the TruSeq stranded mRNA protocol was followed to prep the libraries as described in the kit (Illumina, USA; RS-122-2101) manual. To prepare libraries for the ChIP-Seq, the TruSeq ChIP protocol was followed as described in the kit (Illumina, USA; IP-202-1012) manual.

Deep sequencing and data analysis

Libraries were pooled together and sequenced on the HiSeq 2500 sequencer using the standard sequencing protocols. Images analysis and base calling was done using the Standard Illumina pipeline, and then demultiplexed into FASTQ files. RNASeq paired-end reads from Illumina 1.5 encoding were aligned using TopHat (version 2.0.13) (52) to the human genome (GRCh37) with Ensembl annotation (GRCh37.75) in gtf format. Differential expression was assayed using HTSeq count (53) and DESeq (54). ChIPSeq data were aligned to the human genome (GRCh37) using Bowtie2 (version 2.2.5) (55), base encoding as above, and peaks were called using MACS2 (version 2.1.0.20150420) (56) with -nomodel option, and fragment length was determined by strand cross-correlation (using phantompeakqualtools; <https://code.google.com/p/phantompeakqualtools/>). Differential binding was determined by using MACS' bdgdiff tool. Peaks were annotated using Cis-regulatory Element Annotation System (CEAS) (57), and ChIPSeq data profiles were viewed in ngsplot (58). Overlap between peaks, and with expression data, was determined using bedtools (59). ChIPSeq data profiles were viewed in ngsplot (58) and the Integrative Genomics Viewer (60). RNA-seq and ChIP-seq data have been submitted to GEO under the generic stream encapsulation (GSE) ID GSE74883.

LC/MS-based metabolite profiling

LC/MS analyses were conducted on a QExactive benchtop Orbitrap mass spectrometer equipped with an Ion Max source and a HESI II probe, which was coupled to a Dionex UltiMate 3000 high-performance liquid chromatography system (Thermo Fisher Scientific, San Jose, CA). External mass calibration was performed using the standard calibration mixture every 7 days.

Polar metabolites were extracted using 1 ml of ice-cold 80% methanol with 10 ng/ml phenylalanine- d_8 or phenylalanine- $^{13}C_9$ - ^{15}N as an internal standard. After 10 min of using a vortex and centrifugation for 10 min at 10,000g, both at 4°C, samples were dried in a centrifugal evaporator. Dried samples were stored at -80°C and then resuspended in 100 μ l water; 2.5 μ l of each sample was injected onto a ZIC-pHILIC 2.1 \times 150 mm (5- μ m particle size) column (EMD Millipore). Buffer A was 20 mM ammonium carbonate, 0.1% ammonium hydroxide; buffer B was acetonitrile. The chromatographic gradient was run at a flow rate of 0.150 ml/min as follows: 0 to 20 min, linear gradient from 80% to 20% B; 20 to 20.5 min, linear gradient from 20% to 80% B; 20.5 to 28 min, hold at 80% B. The column oven was held at 25°C. The mass spectrometer was operated with the spray voltage set to 3.0 kV, the heated capillary held at 275°C, and the HESI probe held at 350°C; the sheath gas flow was set to 40 units, the auxiliary gas flow was set to 15 units, and the sweep gas flow was set to 1 unit. To measure cAMP, a positive targeted SIM (tSIM) scan was performed at a resolution of 70,000, an automatic gain control (AGC) target of 1×10^5 , and the maximum injection time at 250 ms. The tSIM window was set to a width of 1.0 m/z and centered at 330.05980 m/z, corresponding to the $[M+H]^+$ ion of cAMP. To monitor other endogenous polar metabolites and the internal standard, the tSIM scans were interspersed with positive and negative mode scans in the range of 70 to 1000 m/z, with the resolution set to 70,000, the AGC target at 10^6 , and the maximum injection time at 80 ms. Relative quantitation of polar metabolites was performed with XCalibur QuanBrowser 2.2 (Thermo Fisher Scientific) by using a 5 parts per million mass tolerance and referencing an in-house library of chemical standards.

Statistical analysis

Data are presented as means \pm SD. A Student's *t* test (two-tailed) was used to compare two groups (*P* < 0.05 was considered significant) unless otherwise indicated.

REFERENCES AND NOTES

- P. B. Gupta *et al.*, Identification of selective inhibitors of cancer stem cells by high-throughput screening. *Cell* **138**, 645–659 (2009). doi: [10.1016/j.cell.2009.06.034](#); pmid: [19682730](#)
- J. Chen *et al.*, A restricted cell population propagates glioblastoma growth after chemotherapy. *Nature* **488**, 522–526 (2012). doi: [10.1038/nature11287](#); pmid: [22854781](#)
- A. Kreso, J. E. Dick, Evolution of the cancer stem cell model. *Cell Stem Cell* **14**, 275–291 (2014). doi: [10.1016/j.stem.2014.02.006](#); pmid: [24607403](#)
- D. R. Pattabiraman, R. A. Weinberg, Tackling the cancer stem cells—what challenges do they pose? *Nat. Rev. Drug Discov.* **13**, 497–512 (2014). doi: [10.1038/nrd4253](#); pmid: [24981363](#)
- B. De Craene, G. Bex, Regulatory networks defining EMT during cancer initiation and progression. *Nat. Rev. Cancer* **13**, 97–110 (2013). doi: [10.1038/nrc3447](#); pmid: [23344542](#)
- S. A. Mani *et al.*, The epithelial-mesenchymal transition generates cells with properties of stem cells. *Cell* **133**, 704–715 (2008). doi: [10.1016/j.cell.2008.03.027](#); pmid: [18485877](#)
- A. P. Morel *et al.*, Generation of breast cancer stem cells through epithelial-mesenchymal transition. *PLOS ONE* **3**, e2888 (2008). doi: [10.1371/journal.pone.0002888](#); pmid: [18682804](#)
- C. Chen *et al.*, Evidence for epithelial-mesenchymal transition in cancer stem cells of head and neck squamous cell carcinoma. *PLOS ONE* **6**, e16466 (2011). doi: [10.1371/journal.pone.0016466](#); pmid: [21304586](#)
- N. Ahmed, K. Abubaker, J. Findlay, M. Quinn, Epithelial mesenchymal transition and cancer stem cell-like phenotypes facilitate chemoresistance in recurrent ovarian cancer. *Curr. Cancer Drug Targets* **10**, 268–278 (2010). doi: [10.2174/15680091079190175](#); pmid: [20370691](#)
- J. A. Beavo, L. L. Brunton, Cyclic nucleotide research — still expanding after half a century. *Nat. Rev. Mol. Cell Biol.* **3**, 710–718 (2002). doi: [10.1038/nrm911](#); pmid: [12209131](#)
- K. Taskén, E. M. Aandahl, Localized effects of cAMP mediated by distinct routes of protein kinase A. *Physiol. Rev.* **84**, 137–167 (2004). doi: [10.1152/physrev.00021.2003](#); pmid: [14715913](#)
- S. S. Taylor, R. Ilouz, P. Zhang, A. P. Kornev, Assembly of allosteric macromolecular switches: Lessons from PKA. *Nat. Rev. Mol. Cell Biol.* **13**, 646–658 (2012). doi: [10.1038/nrm3432](#); pmid: [22992589](#)
- M. R. MacPherson *et al.*, Phosphorylation of serine 11 and serine 92 as new positive regulators of human Snail1 function: Potential involvement of casein kinase-2 and the cAMP-activated kinase protein kinase A. *Mol. Biol. Cell* **21**, 244–253 (2010). doi: [10.1091/mbc.E09-06-0504](#); pmid: [19923321](#)
- D. Shaikh *et al.*, cAMP-dependent protein kinase is essential for hypoxia-mediated epithelial-mesenchymal transition, migration, and invasion in lung cancer cells. *Cell. Signal.* **24**, 2396–2406 (2012). doi: [10.1016/j.cellsig.2012.08.007](#); pmid: [22954688](#)
- K. S. Nadella *et al.*, Targeted deletion of Prkar1a reveals a role for protein kinase A in mesenchymal-to-epithelial transition. *Cancer Res.* **68**, 2671–2677 (2008). doi: [10.1158/0008-5472.CAN-07-6002](#); pmid: [18413734](#)
- P. S. Amieux *et al.*, Increased basal cAMP-dependent protein kinase activity inhibits the formation of mesoderm-derived structures in the developing mouse embryo. *J. Biol. Chem.* **277**, 27294–27304 (2002). doi: [10.1074/jbc.M200302200](#); pmid: [12004056](#)
- R. Iglesias-Bartolome *et al.*, Inactivation of a G α (s)-PKA tumour suppressor pathway in skin stem cells initiates basal-cell carcinogenesis. *Nat. Cell Biol.* **17**, 793–803 (2015). doi: [10.1038/ncb3164](#); pmid: [25961504](#)
- X. Li *et al.*, Intrinsic resistance of tumorigenic breast cancer cells to chemotherapy. *J. Natl. Cancer Inst.* **100**, 672–679 (2008). doi: [10.1093/jnci/djn123](#); pmid: [18445819](#)
- B. Elenbaas *et al.*, Human breast cancer cells generated by oncogenic transformation of primary mammary epithelial cells. *Genes Dev.* **15**, 50–65 (2001). doi: [10.1101/gad.828901](#); pmid: [11156605](#)
- M. Al-Hajj, M. S. Wicha, A. Benito-Hernandez, S. J. Morrison, M. F. Clarke, Prospective identification of tumorigenic breast cancer cells. *Proc. Natl. Acad. Sci. U.S.A.* **100**, 3983–3988 (2003). doi: [10.1073/pnas.0530291100](#); pmid: [12629218](#)
- W. L. Tam *et al.*, Protein kinase C α is a central signaling node and therapeutic target for breast cancer stem cells. *Cancer Cell* **24**, 347–364 (2013). doi: [10.1016/j.ccr.2013.08.005](#); pmid: [24029232](#)
- T. T. Onder *et al.*, Loss of E-cadherin promotes metastasis via multiple downstream transcriptional pathways. *Cancer Res.* **68**, 3645–3654 (2008). doi: [10.1158/0008-5472.CAN-07-2938](#); pmid: [18483246](#)
- D. Anastassiou *et al.*, Human cancer cells express Slug-based epithelial-mesenchymal transition gene expression signature obtained in vivo. *BMC Cancer* **11**, 529 (2011). doi: [10.1186/1471-2407-11-529](#); pmid: [22208948](#)
- E. Charafe-Jauffret *et al.*, Gene expression profiling of breast cell lines identifies potential new basal markers. *Oncogene* **25**, 2273–2284 (2006). doi: [10.1038/sj.onc.1209254](#); pmid: [16288205](#)
- J. de Rooij *et al.*, Epac is a Rap1 guanine-nucleotide-exchange factor directly activated by cyclic AMP. *Nature* **396**, 474–477 (1998). doi: [10.1038/24884](#); pmid: [9853756](#)
- M. C. Broillet, S. Firestein, Cyclic nucleotide-gated channels. Molecular mechanisms of activation. *Ann. N. Y. Acad. Sci.* **868**, 730–740 (1999). doi: [10.1111/j.1749-6632.1999.tb11352.x](#); pmid: [10414360](#)
- R. B. Meyer Jr., J. P. Miller, Analogs of cyclic AMP and cyclic GMP: General methods of synthesis and the relationship of structure to enzymic activity. *Life Sci.* **14**, 1019–1040 (1974). doi: [10.1016/0024-3205\(74\)90228-8](#); pmid: [4362776](#)
- J. M. Enserink *et al.*, A novel Epac-specific cAMP analogue demonstrates independent regulation of Rap1 and ERK. *Nat. Cell Biol.* **4**, 901–906 (2002). doi: [10.1038/ncb874](#); pmid: [12402047](#)
- G. S. McKnight, Mutations in the catalytic subunit of cAMP-dependent protein kinase result in unregulated biological activity. *Proc. Natl. Acad. Sci. U.S.A.* **89**, 4726–4730 (1992). doi: [10.1073/pnas.89.10.4726](#); pmid: [1584809](#)
- H. D. Soule *et al.*, Isolation and characterization of a spontaneously immortalized human breast epithelial cell line, MCF-10. *Cancer Res.* **50**, 6075–6086 (1990). pmid: [1975513](#)
- C. L. Sommers, A. Papageorge, G. Wilding, E. P. Gelmann, Growth properties and tumorigenesis of MCF-7 cells transfected with isogenic mutants of rasH. *Cancer Res.* **50**, 67–71 (1990). pmid: [2403419](#)
- V. Ellenrieder *et al.*, Transforming growth factor beta1 treatment leads to an epithelial-mesenchymal transdifferentiation of pancreatic cancer cells requiring extracellular signal-regulated kinase 2 activation. *Cancer Res.* **61**, 4222–4228 (2001). pmid: [11358848](#)
- C. T. Guy, R. D. Cardiff, W. J. Muller, Induction of mammary tumors by expression of polyomavirus middle T oncogene: A transgenic mouse model for metastatic disease. *Mol. Cell. Biol.* **12**, 954–961 (1992). doi: [10.1128/MCB.12.3.954](#); pmid: [1312220](#)
- J. R. Linnemann *et al.*, Quantification of regenerative potential in primary human mammary epithelial cells. *Development* **142**, 3239–3251 (2015). doi: [10.1242/dev.123554](#); pmid: [26071498](#)
- A. Hollestelle *et al.*, Distinct gene mutation profiles among luminal-type and basal-type breast cancer cell lines. *Breast Cancer Res. Treat.* **121**, 53–64 (2010). doi: [10.1007/s10549-009-0460-8](#); pmid: [19593635](#)
- J. B. Shabb, Physiological substrates of cAMP-dependent protein kinase. *Chem. Rev.* **101**, 2381–2412 (2001). doi: [10.1021/cr000236j](#); pmid: [11749379](#)
- G. A. Gonzalez, M. R. Montminy, Cyclic AMP stimulates somatostatin gene transcription by phosphorylation of CREB at serine 133. *Cell* **59**, 675–680 (1989). doi: [10.1016/0092-8674\(89\)90013-5](#); pmid: [2573431](#)
- M. Johannessen, M. P. Delghandi, U. Moens, What turns CREB on? *Cell. Signal.* **16**, 1211–1227 (2004). doi: [10.1016/j.cellsig.2004.05.001](#); pmid: [15337521](#)
- D. Wu *et al.*, cAMP-responsive element-binding protein regulates vascular endothelial growth factor expression: Implication in human prostate cancer bone metastasis. *Oncogene* **26**, 5070–5077 (2007). doi: [10.1038/sj.onc.1210316](#); pmid: [17310988](#)
- R. Singh, B. S. Shankar, K. B. Sainis, TGF- β 1-ROS-ATM-CREB signaling axis in macrophage mediated migration of human breast cancer MCF7 cells. *Cell. Signal.* **26**, 1604–1615 (2014). doi: [10.1016/j.cellsig.2014.03.028](#); pmid: [24705025](#)
- T. Sheng, S. Chi, X. Zhang, J. Xie, Regulation of Gli1 localization by the cAMP/protein kinase A signaling axis through a site near the nuclear localization signal. *J. Biol. Chem.* **281**, 9–12 (2006). doi: [10.1074/jbc.C500300200](#); pmid: [16293631](#)
- A. Baba *et al.*, PKA-dependent regulation of the histone lysine demethylase complex PHF2-ARID5B. *Nat. Cell Biol.* **13**, 668–675 (2011). doi: [10.1038/ncb2228](#); pmid: [21532585](#)
- P. Hublitz, M. Albert, A. H. F. M. Peters, Mechanisms of transcriptional repression by histone lysine methylation. *Int. J. Dev. Biol.* **53**, 335–354 (2009). doi: [10.1387/ijdb.082717ph](#); pmid: [19412890](#)
- M. P. Saunders *et al.*, A novel cyclic adenosine monophosphate analog induces hypercalcemia via production of 1,25-dihydroxyvitamin D in patients with solid tumors. *J. Clin. Endocrinol. Metab.* **82**, 4044–4048 (1997). doi: [10.1210/jcem.82.12.4410](#); pmid: [9398710](#)
- D. J. Propper *et al.*, Phase I study of the novel cyclic AMP (cAMP) analogue 8-chloro-cAMP in patients with cancer: Toxicity, hormonal, and immunological effects. *Clin. Cancer Res.* **5**, 1682–1689 (1999). pmid: [10430069](#)
- J. Taylor-Papadimitriou, P. Purkis, I. S. Fentiman, Cholera toxin and analogues of cyclic AMP stimulate the growth of cultured human mammary epithelial cells. *J. Cell. Physiol.* **102**, 317–321 (1980). doi: [10.1002/jcp.1041020306](#); pmid: [6248570](#)
- H. Green, Cyclic AMP in relation to proliferation of the epidermal cell: A new view. *Cell* **15**, 801–811 (1978). doi: [10.1016/0092-8674\(78\)90265-9](#); pmid: [83196](#)
- W. Guo *et al.*, Slug and Sox9 cooperatively determine the mammary stem cell state. *Cell* **148**, 1015–1028 (2012). doi: [10.1016/j.cell.2012.02.008](#); pmid: [22385965](#)
- S. R. Daigle *et al.*, Selective killing of mixed lineage leukemia cells by a potent small-molecule DOT1L inhibitor. *Cancer Cell* **20**, 53–65 (2011). doi: [10.1016/j.ccr.2011.06.009](#); pmid: [21741596](#)
- C. Dong *et al.*, G9a interacts with Snail and is critical for Snail-mediated E-cadherin repression in human breast cancer. *J. Clin. Invest.* **122**, 1469–1486 (2012). doi: [10.1172/JCI57349](#); pmid: [22406531](#)

51. G. Dontu *et al.*, In vitro propagation and transcriptional profiling of human mammary stem/progenitor cells. *Genes Dev.* **17**, 1253–1270 (2003). doi: [10.1101/gad.1061803](https://doi.org/10.1101/gad.1061803); pmid: [12756227](https://pubmed.ncbi.nlm.nih.gov/12756227/)
52. D. Kim *et al.*, TopHat2: Accurate alignment of transcriptomes in the presence of insertions, deletions and gene fusions. *Genome Biol.* **14**, R36 (2013). doi: [10.1186/gb-2013-14-4-r36](https://doi.org/10.1186/gb-2013-14-4-r36); pmid: [23618408](https://pubmed.ncbi.nlm.nih.gov/23618408/)
53. S. Anders, P. T. Pyl, W. Huber, HTSeq—a Python framework to work with high-throughput sequencing data. *Bioinformatics* **31**, 166–169 (2015). doi: [10.1093/bioinformatics/btu638](https://doi.org/10.1093/bioinformatics/btu638); pmid: [25260700](https://pubmed.ncbi.nlm.nih.gov/25260700/)
54. S. Anders, W. Huber, Differential expression analysis for sequence count data. *Genome Biol.* **11**, R106 (2010). doi: [10.1186/gb-2010-11-10-r106](https://doi.org/10.1186/gb-2010-11-10-r106); pmid: [20979621](https://pubmed.ncbi.nlm.nih.gov/20979621/)
55. B. Langmead, S. L. Salzberg, Fast gapped-read alignment with Bowtie 2. *Nat. Methods* **9**, 357–359 (2012). doi: [10.1038/nmeth.1923](https://doi.org/10.1038/nmeth.1923); pmid: [22388286](https://pubmed.ncbi.nlm.nih.gov/22388286/)
56. Y. Zhang *et al.*, Model-based analysis of ChIP-Seq (MACS). *Genome Biol.* **9**, R137 (2008). doi: [10.1186/gb-2008-9-9-r137](https://doi.org/10.1186/gb-2008-9-9-r137); pmid: [18798982](https://pubmed.ncbi.nlm.nih.gov/18798982/)
57. H. Shin, T. Liu, A. K. Manrai, X. S. Liu, CEAS: Cis-regulatory element annotation system. *Bioinformatics* **25**, 2605–2606 (2009). doi: [10.1093/bioinformatics/btp479](https://doi.org/10.1093/bioinformatics/btp479); pmid: [19689956](https://pubmed.ncbi.nlm.nih.gov/19689956/)
58. L. Shen, N. Shao, X. Liu, E. Nestler, ngs.plot: Quick mining and visualization of next-generation sequencing data by integrating genomic databases. *BMC Genomics* **15**, 284 (2014). doi: [10.1186/1471-2164-15-284](https://doi.org/10.1186/1471-2164-15-284); pmid: [24735413](https://pubmed.ncbi.nlm.nih.gov/24735413/)
59. A. R. Quinlan, I. M. Hall, BEDTools: A flexible suite of utilities for comparing genomic features. *Bioinformatics* **26**, 841–842 (2010). doi: [10.1093/bioinformatics/btq033](https://doi.org/10.1093/bioinformatics/btq033); pmid: [20110278](https://pubmed.ncbi.nlm.nih.gov/20110278/)
60. J. T. Robinson *et al.*, Integrative genomics viewer. *Nat. Biotechnol.* **29**, 24–26 (2011). doi: [10.1038/nbt.1754](https://doi.org/10.1038/nbt.1754); pmid: [21221095](https://pubmed.ncbi.nlm.nih.gov/21221095/)

ACKNOWLEDGMENTS

We thank the Keck Microscopy Facility, Metabolite Profiling Core Facility, Genome Technology Core, Bioinformatics and Research Computing Core, and Proteomics Core Facility at the Whitehead Institute; the Koch Institute Swanson Biotechnology Center (SBC), specifically the Histology Facility and the High-Throughput Screening Facility; J. Benson (SBC) for providing the compound library; D. Bachovchin (Broad Institute) for assistance with automation; and T. DiCesare for assistance with scientific illustration. We thank A. Dongre, S. Iyer, and J. Fröse for technical assistance; all members of the Weinberg laboratory for helpful discussions; and A. Lambert, K. Krishnan, and S. Rajavasireddy for critical reading of the manuscript. D.R.P. is supported by a C. J. Martin Overseas Biomedical Fellowship from the National Health and Medical Research Council of Australia (NHMRC APP1071853). W.L.T. is supported by the National Research

Foundation, Singapore (NRF-NRFF2015-04); and National Medical Research Council, Singapore (NMRC/TCR/007-NCC/2013). This research was supported by the Ludwig Center for Molecular Oncology at MIT (R.A.W.), Breast Cancer Research Foundation (R.A.W.), Samuel Waxman Cancer Research Foundation (R.A.W.) and NIH R01-CA078461 (R.A.W.). R.A.W. is an American Cancer Society and D. K. Ludwig Foundation Cancer Research Professor. R.A.W. is a shareholder in and the chairman of the Scientific Advisory Board of Verastem, Inc., a company focused on developing drugs to treat cancer by the targeted killing of cancer stem cells. The Whitehead Institute and the authors (R.A.W., D.R.P., B.B., and W.L.T.) have filed a patent application (PCT/US2015/028239) that covers methods of differentiating cancer stem cells through the induction of a MET and the use of these methods for treating cancer. RNA-Seq and ChIP-Seq data from this study have been deposited at GEO under accession number GSE74883.

SUPPLEMENTARY MATERIALS

www.sciencemag.org/content/351/6277/aad3680/suppl/DC1
Figs. S1 to S11
Tables S1 to S10
References

3 September 2015; accepted 7 January 2016
[10.1126/science.aad3680](https://doi.org/10.1126/science.aad3680)

RESEARCH ARTICLES

STRUCTURAL BIOLOGY

Cryo-EM structure of a native, fully glycosylated, cleaved HIV-1 envelope trimer

Jeong Hyun Lee, Gabriel Ozorowski, Andrew B. Ward*

The envelope glycoprotein trimer (Env) on the surface of HIV-1 recognizes CD4⁺ T cells and mediates viral entry. During this process, Env undergoes substantial conformational rearrangements, making it difficult to study in its native state. Soluble stabilized trimers have provided valuable insights into the Env structure, but they lack the hydrophobic membrane proximal external region (MPER, an important target of broadly neutralizing antibodies), the transmembrane domain, and the cytoplasmic tail. Here we present (i) a cryogenic electron microscopy (cryo-EM) structure of a clade B virus Env, which lacks only the cytoplasmic tail and is stabilized by the broadly neutralizing antibody PGT151, at a resolution of 4.2 angstroms and (ii) a reconstruction of this form of Env in complex with PGT151 and MPER-targeting antibody 10E8 at a resolution of 8.8 angstroms. These structures provide new insights into the wild-type Env structure.

The HIV-1 envelope glycoprotein (Env) houses the receptor binding site and fusion machinery to infect target cells. The intrinsic instability of and glycosylation on Env have made solving a high-resolution structure a daunting task. Low-resolution tomographic reconstructions of Env on the viral surface have described the overall shape of the trimer (1, 2), and more recently, structures of an engineered, soluble clade A BG505 SOSIP.664 trimer have been solved at high resolution (3–9). The BG505 SOSIP.664 trimer interacts preferentially with broadly neutralizing antibodies (bnAbs) but not with nonneutralizing antibodies (10) and has promising immunogenic properties (11, 12). Although these data suggest that this soluble trimer recapitulates native Env, it is not known what effect the stabilizing mutations or the lack of the membrane proximal external region (MPER) and transmembrane domain (TM) have on the Env structure.

BG505 SOSIP.664 shares a highly similar architecture with wild-type Env

We studied the JR-FL Env strain with the cytoplasmic tail (CT) deleted (hereafter referred to as EnvΔCT). In some isolates, the deletion of the CT has been shown to increase the exposure of non-neutralizing epitopes (13), but the deletion of CT in JR-FL does not abolish the ability of the trimer to fuse and infect (14, 15). Our previously described protocol (16) for extracting the complex formed by JR-FL EnvΔCT and the bnAb PGT151 was modified

to make the sample amenable for cryogenic electron microscopy (cryo-EM) (fig. S1, A and B), resulting in a 4.2 Å-resolution reconstruction (Fig. 1, A and B, and figs. S1 to S3). Similar to our negative-stain reconstructions (16), PGT151 Fab bound in an asymmetric manner, with a maximum of two Fabs per trimer. Because the three gp140 interfaces of the Env trimer were nonequivalent, we hereafter refer to them as interfaces 1, 2, and 3 (Fig. 1A).

The clade B JR-FL EnvΔCT shares a similar topology to BG505 SOSIP.664, despite the lack of stabilizing mutations and the difference in subtypes (68.5% sequence identity) (fig. S4 and fig. S5, A and E). Differences were observed at the trimer apex and the N-terminal region of heptad repeat 1 (HR1_N) of gp41. In the JR-FL trimer, the inter-V1/V2 loop region of the trimer apex is more loosely associated than in the unliganded BG505 SOSIP.664 [Protein Data Bank identifier (PDB ID) 4ZMJ] (fig. S5B). This phenomenon is consistent with fluorescence resonance energy transfer studies of viral Env (17), as well as studies of clades B and C SOSIP.664 trimers in which loop mobility and flexibility have been observed (18, 19). Despite this weaker interaction, the V3 loop in all three protomers remains in contact with the base of V2 on the adjacent protomer (figs. S5B and S6A), and therefore it probably confers the majority of the stability at the trimer apex.

In the published BG505 SOSIP.664 structures, HR1_N does not adopt a regular secondary structure (4–9), whereas in our JR-FL EnvΔCT model, this region is helical (fig. S5D). We attribute this difference to the I559P mutation in SOSIP that disrupts the propensity of the HR1 peptide to form an extended and stable α-helix during fusion (20). In contrast, the SOS disulfide bond does not cause any major conformational differences relative to the wild-type structure (fig. S5C). As in the BG505

SOSIP.664 structures (4–9), most of the C terminus of HR2 is helical until residue 664. However, hydrogen deuterium exchange mass spectrometry (HDXMS) studies (21) have demonstrated that the C-terminal region of HR2 in BG505 SOSIP.664 has a flexible topology. Whereas the C-terminal region of gp41 is observed in our JR-FL EnvΔCT structure, the micelle-embedded MPER and TM just downstream of HR2 were both unresolved (Fig. 1A; fig. S1, D and E; and fig. S2C). Crystal structures of MPER peptide–Fab complexes have also shown that MPER can adopt different conformations (22–24).

Model building of newly resolved regions

We used the BG505 SOSIP.664 and PGT151 Fab x-ray structure coordinates [PDB IDs 4TVP (6) and 4NUG (16), respectively] as starting models for building and refinement (figs. S3, S5F, and S6 and table S1). The fusion peptide (FP, residues 512 to 527) and HR1_N (548 to 568) (Fig. 1C and fig. S4) regions of gp41 were both resolved in the current structure. The HR1_N helix in interfaces 2 and 3 was tilted by ~24° away from the center of the trimer and ~26° to the right in comparison with interface 1 (Fig. 2A), when viewed normal to the threefold axis of the trimer. The HR1_N and HR1_C form a helix-turn-helix-type motif but contain residues with high helical propensity in the turn region (Fig. 2A and fig. S4). The HR1_N region in the unliganded protomer is less well defined than the liganded HR1_N helices (fig. S5D), as would be expected for a conformationally variable segment.

In the BG505.664 x-ray structure, the N terminus of the FP (residues A512 to A518) is disordered and appears to project into the solvent. Similarly, at interface 1 of the cryo-EM model, residues A512 to L520 are unresolved, but a density adjacent to HR1_N could be attributed to the FP (fig. S7A); this suggests that the hydrophobic N terminus of the FP may be inserted into the trimer core in wild-type Env, as observed in another class I viral fusion protein, influenza hemagglutinin (25). At the PGT151 liganded interfaces, there are changes in both the antibody and the FP. The majority of the Fab heavy- and light-chain residues adopt the same conformation as when the Fab is unliganded, except for the heavy-chain complementarity-determining region 3 (CDRH3) of PGT151 (P100a to Y100l), which is substantially different in the two structures (fig. S7B). Upon PGT151 binding, the entire FP is resolved (fig. S7C), where it projects away from the trimer and is sequestered in a pocket formed between the PGT151 Fab CDRH2, CDRH3, and CDRL3 (L, light chain) loops via hydrophobic and backbone interactions (Fig. 2B and fig. S7D). Because the FP is pulled away from the trimer core in both BG505 SOSIP.664 and PGT151-bound Env, which stabilizes the prefusion trimer, this conformation of the FP may counterintuitively contribute to trimer stability.

Newly revealed glycans in the wild-type Env trimer

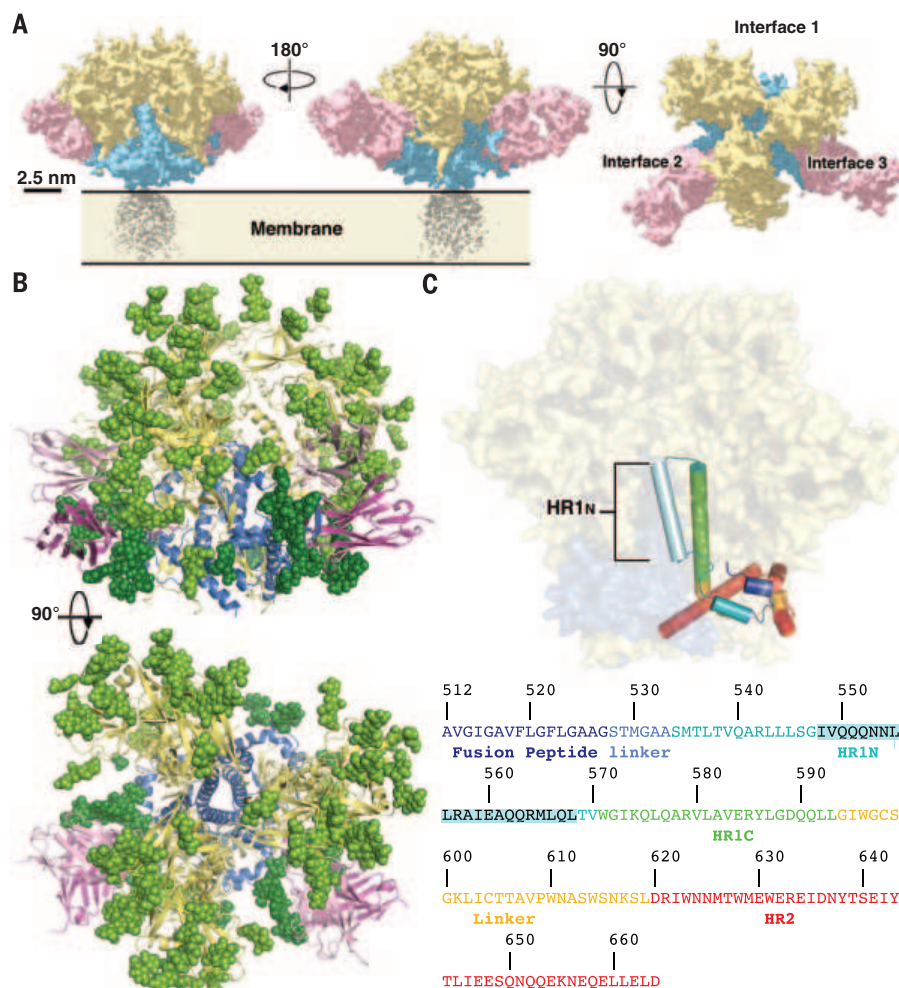
The Env trimers in our studies contain fully processed native glycans. Similar to the two other cryo-EM structures (5, 9), at least the two core

Department of Integrative Structural and Computational Biology, Center for HIV/AIDS Vaccine Immunology and Immunogen Discovery, International AIDS Vaccine Initiative Neutralizing Antibody Center, and Collaboration for AIDS Vaccine Discovery, The Scripps Research Institute, La Jolla, CA 92037, USA.

*Corresponding author. E-mail: abward@scripps.edu

Fig. 1. Cryo-EM reconstruction of JR-FL EnvΔCT.

(A) Reconstruction of JR-FL EnvΔCT in complex with PGT151 Fab at 4.2 Å resolution, segmented to highlight densities corresponding to gp120 (yellow), gp41 (blue), PGT151 Fab (pink), and the micelle surrounding the MPER and TM domain (gray). The three possible PGT151 binding sites are labeled as interface 1 (unliganded), interface 2, and interface 3. (B) Model of the EnvΔCT ectodomain, colored as in (A). The Fab light and heavy chains are colored in pink and magenta, respectively. Glycans are shown as spheres, with the gp120 and gp41 glycans shown in light and dark green, respectively. (C) Simplified cartoon of gp41. Most of the portion of HR1 that does not have a regular secondary structure in SOSIP trimers (residues 548 to 568) is here revealed to be an α -helix. To distinguish this region from the central HR1 helix (residues 571 to 593), we call these two helices HR1_N and HR1_C, respectively. The complete HR1 spans residues 534 to 593. The cartoon cylinder and loops are colored according to the sequence shown at the bottom.



N-acetylglucosamine (GlcNAc) moieties are visible at the majority of glycosylation sites, except in disordered peptide regions such as V1 and V4 (fig. S6, B to D, and table S1). The glycans in the PGT151 epitope are ordered, allowing us to resolve four highly branched glycans at N241 and N448 in gp120 and N611 and N637 in gp41.

Gp120 glycans have been studied extensively, but much less is known about gp41 glycans. In our structure, glycans at positions N625 and N616 were only resolved up to the core GlcNAc residues (table S1). The ordered glycans at positions N611 and N637 that interact with PGT151 were built as complex glycans with *N*-acetylglucosamine (GlcNAc) branching, which is consistent with published glycan array binding data (Fig. 3, A to D, and figs. S8 and S9) (26). The base GlcNAc residues of the N611 and N637 glycans were core-fucosylated (Fig. 3, A and B, and figs. S8 and S9), which is consistent with glycan array data demonstrating fucose-dependent binding differences by some clonal relatives of PGT151 (26) and with binding studies (fig. S10).

The N611 glycan is minimally a tri-antennary glycan, with the two LacNAc units of the mannose(α 1-6) [Man(α 1-6)] arm resolved. The LacNAc(β 1-6) branch packs against the heavy-chain framework region 3 (FRWH3). The LacNAc(β 1-2) interacts with

a highly conserved CDRH2 region of the PGT151 family and also extends far enough to make potential contacts with the FP of the adjacent gp41 (Fig. 3, A and C; fig. S8; and fig. S12, A and B).

The N637 glycan is a tetra-antennary glycan (Fig. 3, B and D, and fig. S9), and the core trisaccharide interacts along the length of CDRH3 (Fig. 3B). The interactions are probably backbone-mediated, because the PGT151-family CDRH3 sequences in this stretch are variable (fig. S12, A and C). The Man(α 1-3) branch projects between the heavy chain and light chain, with the LacNAc(β 1-4) unit primarily interacting with CDRH1 and the LacNAc(β 1-2) branch interacting with the C terminus of CDRL2. The GlcNAc(β 1-6)Man(α 1-6) branch interacts with another well-conserved region in CDRL2 (Fig. 3B and fig. S12, A and C).

Previous low-resolution modeling and glycan knockout neutralization assays allowed us to predict that glycans from N262 and N448 in one gp120 protomer, and from N276 in the adjacent gp120 protomer on a BG505 trimer, could interact with the PGT151 Fab (16). In this study, we observed a density for a glycan at N241 (glycosylation site ~96% conserved, not present in BG505), which, along with the N448 glycan, extends toward FWRH3 (Fig. 3E and fig. S11, A and B). The N276 glycan is the least resolved of the four PGT151-

proximal gp120 glycans (fig. S11C), suggesting that it makes considerably fewer contacts relative to N448 or N241, although is positioned to restrict accessibility to the PGT151 epitope.

In TZM-bl neutralization assays, the IC₅₀ (half-minimal inhibitory concentration) improved slightly when the N241 or N448 glycan was knocked out in JR-FL pseudovirus (26), corroborating our structural observations. In the same assay, the presence of either the N611 or the N637 glycan alone in gp41 was sufficient for neutralization, albeit with decreased potency (26). In JR-FL, the reduced neutralization potency due to the knockout of N637 was recovered by a second, simultaneous knockout of the N448 glycan. This effect is not observed for BG505 pseudovirus, which naturally lacks the N241 glycan. Furthermore, in BG505 pseudovirus, the N637A glycan knockout does not cause as large a decrease in neutralization potency as in JR-FL (26). We therefore hypothesize that the N448 glycan imposes a steric hurdle for PGT151 binding, but only in the presence of the highly conserved N241 glycan (Fig. 4A). The N241 glycan probably limits the range of motion of the N448 glycan, which in turn limits access to the PGT151 epitope, in a similar manner to steric restriction of epitopes by glycans that has been observed with other bnAbs (27–29). It has also

been suggested that the presence or absence of one glycan can affect the conformational space that can be occupied by adjacent glycans (30). This type of mechanism illustrates the complex nature of Env surface accessibility and the difficulty of determining complete epitopes outside of high-resolution structures. Lastly, the D2/D3 branch of the very highly conserved N262 oligomannose glycan is in close proximity to the FWRL3 of PGT151; this suggests interactions with the D2 arm, although it is unclear whether this glycan is hindering or enhancing PGT151 binding (fig. S11D).

Trimers of different genotypes may contain different glycoforms, especially in gp41 (31), and variation at these sites may be responsible for a neutralization plateau (26). Our model illustrates that the PGT151 epitope extends beyond the gp41 glycans and includes gp120 glycans that may also contribute to incomplete neutralization. Overall, PGT151 is highly glycan-dependent, with up to six glycans in JR-FL (N241, N262, N276, N448, N611, and N637) surrounding the antibody (Fig. 4A).

Mechanism of trimer stabilization

Unlike any other bnAb identified so far, including gp41-gp120 interface antibodies such as 35O22 (fig. S13A) (32), PGT151 stabilizes the metastable prefusion Env for prolonged periods (16). Contact with both N611 and N637 glycans probably prevents the HR2 helix from progressing to the postfusion conformation (Fig. 4B). PGT151 and its clonal relatives all have a long CDR1 of 16 residues and a conserved N28 (D28 in PGT154 to -158; fig. S12A) at the CDR1 tip that interacts with a conserved region at the end of HR1_N (sequence conservation: Q551 to Q552, 100%; N553, 58%; N554, 99%). Additionally, CDRH3 is wedged between the HR1_N and the FP-proximal HR1 region. In this manner, the CDR1 and CDRH3 cap the end of a short helix to prevent it from extending into a longer helix and thereby thwart the transition to a postfusion conformation (Fig. 4C). PGT151 has an unusual binding stoichiometry of two Fabs per trimer, even though there is no obvious steric barrier to the binding of the third Fab (fig. S13B). Rather, binding of two PGT151 antibodies appears to have an allosteric effect, altering the conformation of the third binding site (Fig. 4D).

10E8-bound conformation of Env

To visualize the MPER, we added MPER-specific bnAb 10E8 to the complex and analyzed the JR-FL EnvΔCT-PGT151 Fab-10E8 Fab complex by means of cryo-EM (fig. S14, A and B). Although 10E8 had some stabilizing effect on the MPER, we still observed flexibility in this region (Fig. 5A and fig. S14C), which is consistent with a previously solved crystal structure of the MPER peptide-10E8 Fab complex (Fig. 5C) (22). Despite variation in the protein conformation and binding occupancies on the trimer, we obtained an 8.8 Å-resolution reconstruction from a subset of the JR-FL EnvΔCT-PGT151 Fab-10E8 Fab complexes (Fig. 5A and fig. S14D). This reconstruction revealed that the center of the trimer at the base is empty, similar to the JR-FL EnvΔCT-PGT151 structure. Again, we did not observe a three-helix bundle formed

by the TM, but MPER bound to 10E8 and the HR2-MPER interface could be visualized (Fig. 5B and fig. S15A). The HR2-MPER connectivity was substantially different from the crystal struc-

ture and emphasizes the flexibility in this region (Fig. 5C and fig. S15A).

10E8 recognizes Env primarily via CDRH3 contacts with MPER helix 672 to 683, with additional

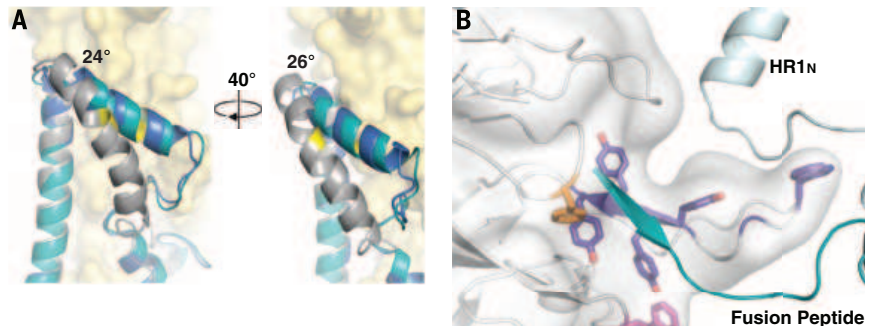


Fig. 2. Conformational changes induced by PGT151 binding. (A) Compared with interface 1 (gray), HR1_N in interfaces 2 (blue) and 3 (teal) is shifted about 24° outwards toward the Env surface and 26° toward gp120 of the same protomer (yellow surface). The position of the I559 residue is shown in bright yellow. (B) The FP (teal) is inserted into a hydrophobic pocket formed by the PGT151 CDR loops (CDRH2, magenta; CDRH3, purple; CDRL3, orange). The hydrophobic aromatic residues in these CDRs are shown as sticks.

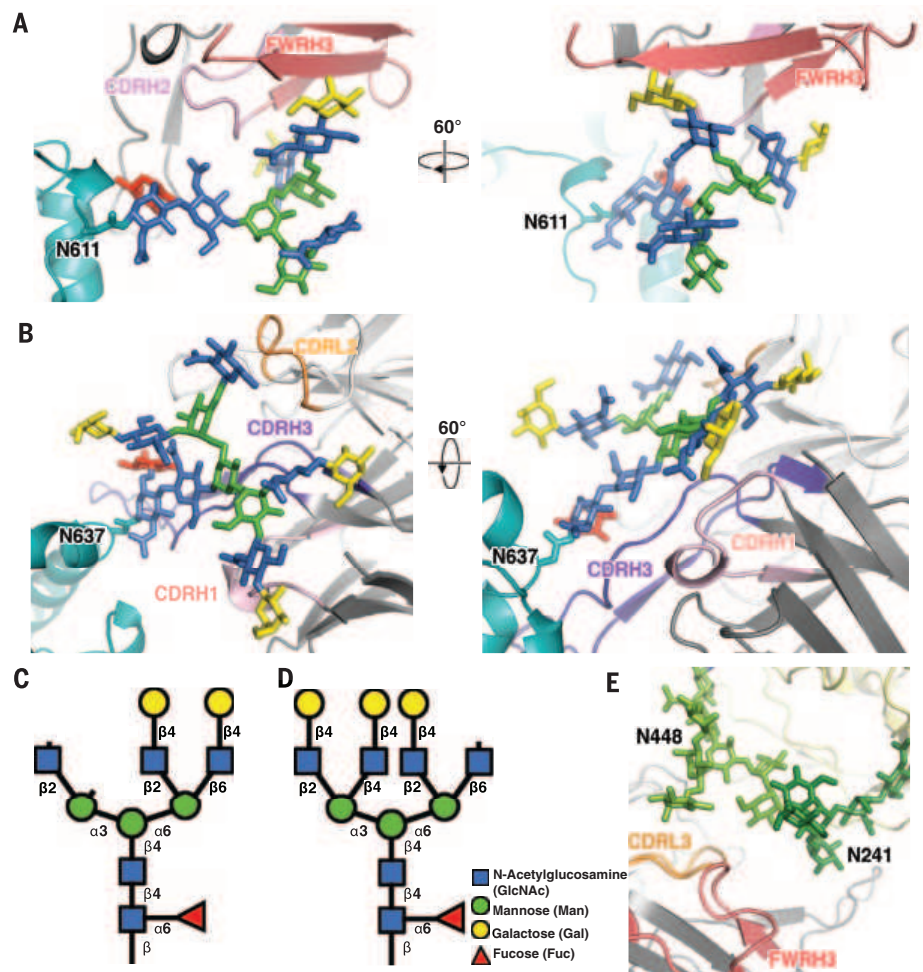
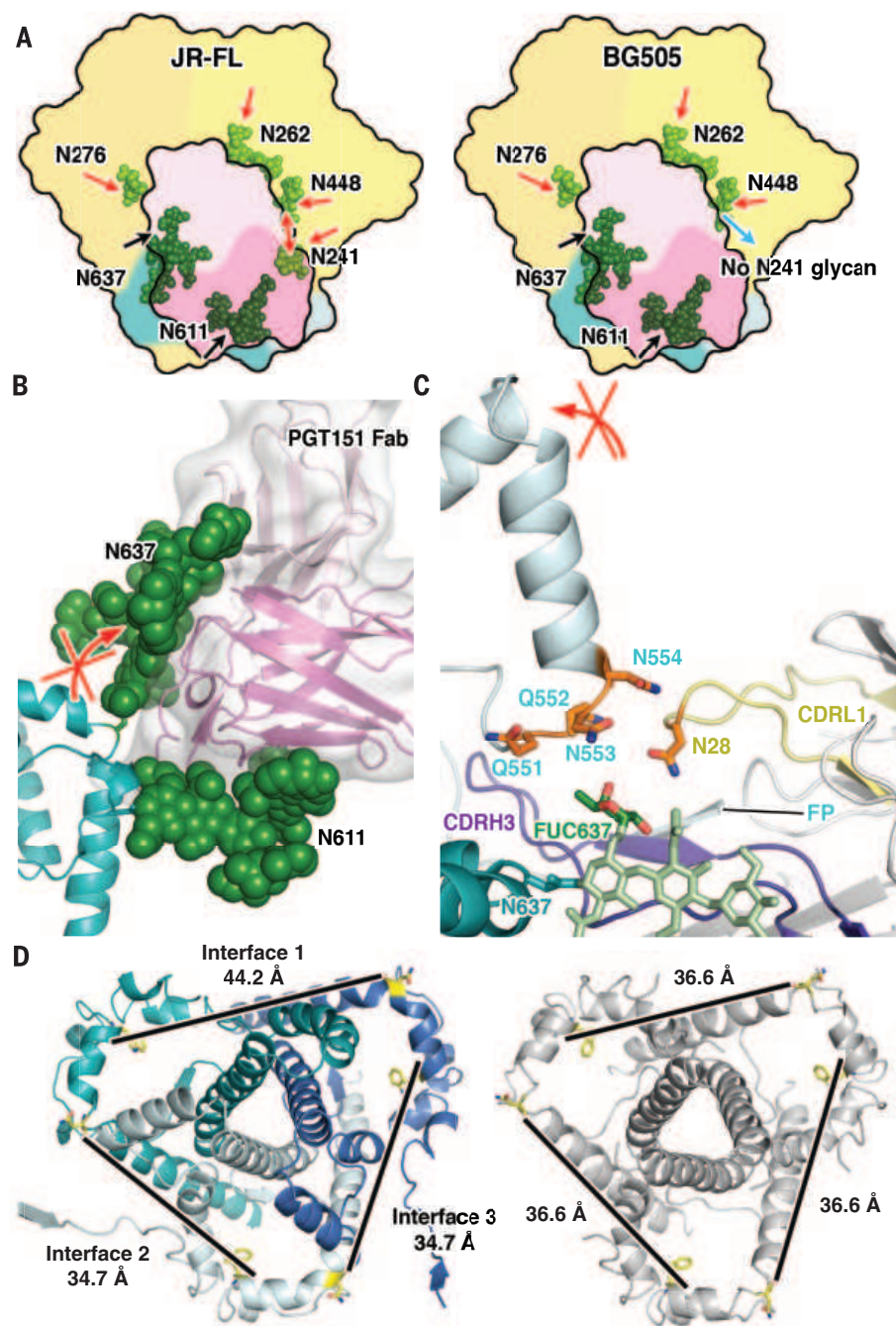


Fig. 3. Glycan structures on the Env trimer. (A) The glycan at position N611 makes extensive contacts with PGT151 Fab. The glycan residues are colored according to the diagram in (C) and (D). (B) As in (A), but for the N637 glycan. (C) The glycans modeled at N611 and (D) N637. Only sugar moieties resolved in the current structure are shown. (E) The N241 and N448 glycans (different shades of green) are in close proximity to the CDRL3 and FWRH3 of PGT151.

Fig. 4. The complete PGT151 epitope. (A) A model of PGT151-glycan interactions. Glycans from up to four different subunits (two from gp120 and two from gp41) of two protomers of the trimer can lock the Fab in its bound form (left). Some of the glycans bind PGT151 with high affinity (black arrows), but there are numerous steric barriers that need to be overcome (red arrows). Glycans N241 and N448 probably have an inhibitory effect on PGT151 binding by influencing the conformations of each other. The lack of the N241 glycan (right) alleviates steric pressure by N448 (blue arrow). Different gp120 subunits are shown in shades of yellow, gp41 subunits in shades of blue, Fab light and heavy chains in pink and magenta, gp120 glycans in green, and gp41 glycans in dark green. (B) When PGT151 is bound to glycans at N611 and N637, HR2 is locked in a bent conformation and therefore cannot undergo conformational changes into the extended post-fusion form. Colors are as in (A). (C) PGT151 CDR1L1 (yellow) and the N637 glycan fucose (Fuc, dark green) interact with a glutamic acid- and asparagine-rich region of HR1_N on the adjacent gp41 (Q551 to N554). The CDRH3 (purple) inserts between HR1_N and the FP, and these interactions cap HR1_N to lock gp41 in the prefusion conformation. The interacting residues in the Fab and HR1_N are shown in orange. Only the core Man(Fuc)GlcNAc₂ residues are shown for the N637 glycan for clarity. In (B) and (C), red arrows with crosses show that gp41 regions are blocked from undergoing conformational changes. (D) A measurement of the inter-gp41 distances in PGT151-bound JR-FL (left) compared with the unliganded BG505 trimer (right). The unliganded BG505 trimer measures ~37 Å between the C α of N628 and N637 (residues shown in yellow) on the adjacent protomer, whereas the distance between the same two residues measures ~35 Å at the PGT151-liganded interfaces. However, the inter-gp41 distance at interface 1 (~44 Å) is ~9 Å farther apart in comparison with the liganded interfaces, indicating that the trimer becomes asymmetric in the PGT151-bound form. The three shades of blue differentiate the three gp41 monomers.



interactions between FWRH3 and the gp41-gp120 interface (Fig. 6, A and B). Moreover, N88 and N625 glycans are positioned to sterically block 10E8 binding. The N88 glycan, built as a ManGlcNAc₂, in the 4.2 Å model, clashes with FWRH1, and a complete glycan at N625 would also clash with the 10E8 Fab constant region (Fig. 6, A and B). The N625Q mutation increases maximum neutralization of JR2, and glycoforms affect the degree of neutralization plateauing (33). In the trimer structure, both the N88 and N625 glycans are accessible for glycan processing and have been predicted to be complex (34–36). Thus, these glycans could restrict access to the MPER epitope. Most MPER antibodies bind to gp41

fusion intermediates (37–39), but although 10E8 potentially neutralizes virus after CD4 attachment (33), it also neutralizes the prefusion trimer (22, 32). Other studies have suggested that the CD4-bound form of Env may be lifted from the membrane and would therefore provide greater accessibility to membrane proximal epitopes (32). CD4 binding opens Env via a rotation in gp120, which moves the N88 glycan farther away from the base of the trimer (Fig. 6C). Nuclear magnetic resonance structures of MPER peptides, as well as our EnvΔCT model (fig. S16), suggest that the ground-state MPER epitope is embedded in the membrane (15). Thus, although MPER is difficult to access, MPER antibodies can either bind MPER while membrane-

embedded or during some transient exposure when the trimer is lifted off the membrane surface.

In the negative-stain reconstruction of 10E8 in complex with MPER-containing BG505 SOSIP.683 (fig. S15, B and C), the Fab does not induce an opening of the trimer, as it does when soluble CD4 or CD4-induced antibodies are bound (2). Although the 2D class averages of 10E8-bound BG505 SOSIP.683 trimers display distinguishable Fab densities (fig. S15B), the particles refine poorly in the 3D reconstruction, and the 10E8 Fab binds at a different angle than in EnvΔCT (fig. S15C), which again is consistent with MPER flexibility. Without the TM, however, the Fab approaches from the bottom of the trimer, which

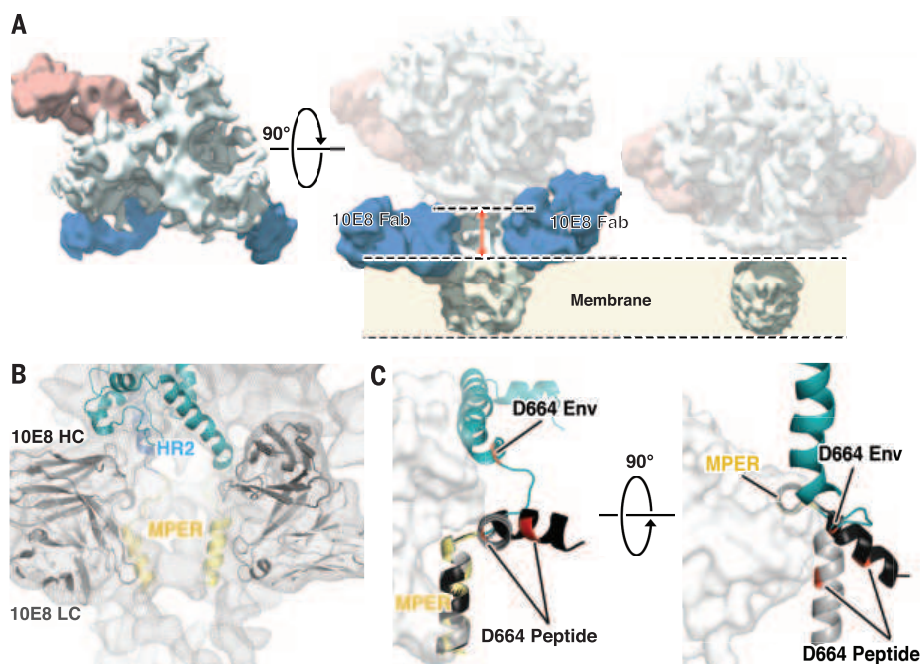


Fig. 5. JR-FL Env Δ CT bound to PGT151 and 10E8.

(A) Cryo-EM reconstruction of JR-FL Env Δ CT (gray) in complex with both PGT151 (pink) and the MPER-binding antibody 10E8 (blue) at 8.8 Å resolution (left). The JR-FL Env Δ CT–PGT151 reconstruction (low pass-filtered to 8.8 Å) is shown on the right for comparison. The reconstructions indicate that when 10E8 is bound, the trimer is lifted off the membrane (red arrow), suggesting a conformational change in the MPER and TM. (B) The Env HR2-MPER connectivity in the 10E8-bound form is modeled into the EM density. (C) A comparison of the position of residues 659 to 670 in the two asymmetric units of the 10E8-bound MPER peptide x-ray model (dark and light gray), superimposed on the complete Env model (teal), in which the primary MPER epitope (residues 671 to 685) is shown in yellow. This N-terminal segment exhibits different conformations in the two asymmetric units. D664 is colored in red as a point of reference. 10E8 is shown as the white surface.

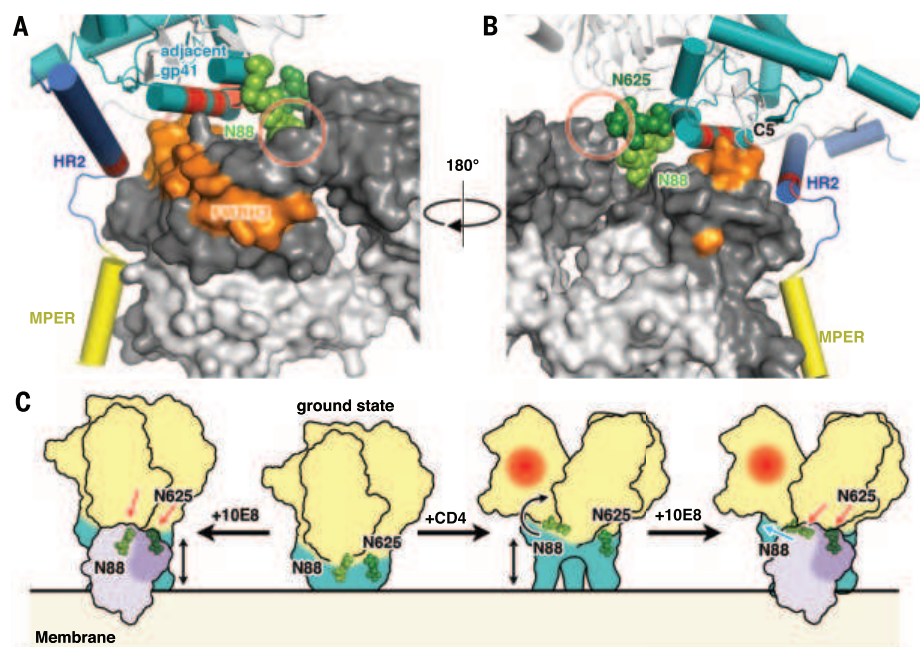


Fig. 6. 10E8 contact analysis in the context of the Env ectodomain.

(A and B) A model of the 10E8 epitope in the context of the intact Env trimer. The Fab constant region (dark and light gray surface) and the nearby Env gp120 (white) are also shown. On the left in (A) and the middle-lower right in (B) is the gp41 in which the 10E8 Fab makes primary interactions with MPER residues 671 to 685 (yellow). Additional contacts could be made with the HR2 and C-terminal region of the FP in the adjacent gp41 (teal), as well as regions in gp120 (white). These additional contacts to Env within a 4 Å radius of 10E8 are colored red. Many of these interactions are probably mediated by FWRH3 (orange). The model also demonstrates that the N88 (A) and N625 (B) glycans could sterically obstruct 10E8 binding (red circles). The glycans modeled here are ManGlcNAc₂ for N88 and GlcNAc for N625 (table S1), but they are expected to be larger in native Env. (C) Glycans at N88 and N625 sterically hinder 10E8 binding to the trimer (left, red arrows). Binding of 10E8 (left, purple) or CD4 (center right) lifts the MPER up from the membrane relative to the ground state (center left). In the CD4-bound conformation, the opening of the

trimers results in rotation of the gp120s, moving N88 away from the 10E8 binding site and relieving some steric hindrance (right, blue arrow). Colors are as in Fig. 4A. The red-orange areas in the cartoons on the right indicate the CD4-bound state.

would be impossible in the context of the viral membrane. Cross-linking the ectodomain of full-length Env also has no effect on MPER-bnAb binding, despite the reduced CD4 binding (40). Together, these observations indicate that (i) MPER is largely inaccessible on the viral membrane, with the membrane imposing a steric hurdle for the Fab approach angle, and (ii) 10E8 binds a transiently exposed MPER, which is not necessarily the CD4-bound conformation of Env nor a fusion-transition conformation, in contrast with previous observations (41). The appearance of a gap between

the HR2 C terminus and the micelle in our 10E8-bound structure (Fig. 5A) probably represents the optimal display of the membrane-anchored MPER epitope with all additional constraints in place. The epitope of 10E8, and perhaps of other MPER antibodies, is therefore more complex than previously thought, involving elements from multiple gp41 protomers, as well as from gp120.

Discussion

Here we present the cryo-EM reconstruction of a cleaved wild-type JR-FL Env Δ CT trimer in com-

plex with PGT151 Fab at 4.2 Å resolution, demonstrating the structure not only of wild-type Env but also of a type I viral fusion protein with an intact TM, which unexpectedly was found to be flexible. The PGT151 epitope includes the FP and an extensive network of primary and secondary glycan interactions that stabilize the prefusion conformation of the Env trimer. The MPER appears to be sequestered in the detergent micelle in the unliganded state, but it is outside the micelle in the 10E8-bound structure, suggesting a dynamic topology. This property—in combination

with steric constraints from gp120, gp41, and glycans at N88 and N625—effectively shields the conserved MPER. Thus far, MPER peptide vaccines, though immunogenic, produce nonneutralizing antibodies, probably because of the lack of the additional constraints provided by the trimer and membrane (42, 43); our model suggests that the minimalistic MPER epitope peptide presentation may not be the most ideal strategy to elicit MPER bnAbs. Overall, our data indicate that Env is a pliable structure in which several of the protein-protein interfaces can be remodeled, making it a difficult moving target for the immune system.

REFERENCES AND NOTES

1. J. Liu, A. Bartsaghi, M. J. Borgnia, G. Sapiro, S. Subramaniam, *Nature* **455**, 109–113 (2008).
2. E. E. Tran et al., *PLOS Pathog.* **8**, e1002797 (2012).
3. J. P. Julien et al., *Proc. Natl. Acad. Sci. U.S.A.* **110**, 4351–4356 (2013).
4. J. P. Julien et al., *Science* **342**, 1477–1483 (2013).
5. D. Lyumkis et al., *Science* **342**, 1484–1490 (2013).
6. M. Pancera et al., *Nature* **514**, 455–461 (2014).
7. Y. Do Kwon et al., *Nat. Struct. Mol. Biol.* **22**, 522–531 (2015).
8. F. Garces et al., *Immunity* **43**, 1053–1063 (2015).
9. J. H. Lee, N. de Val, D. Lyumkis, A. B. Ward, *Structure* **23**, 1943–1951 (2015).
10. R. W. Sanders et al., *PLOS Pathog.* **9**, e1003618 (2013).
11. R. W. Sanders et al., *Science* **349**, aac4223 (2015).
12. P. Dosenovic et al., *Cell* **161**, 1505–1515 (2015).
13. J. Chen et al., *Science* **349**, 191–195 (2015).
14. L. G. Abrahamyan et al., *J. Virol.* **79**, 106–115 (2005).
15. Z. Y. Sun et al., *J. Mol. Biol.* **426**, 1095–1108 (2014).
16. C. Blattner et al., *Immunity* **40**, 669–680 (2014).
17. J. B. Munro et al., *Science* **346**, 759–763 (2014).
18. P. Pugach et al., *J. Virol.* **89**, 3380–3395 (2015).
19. J. P. Julien et al., *Proc. Natl. Acad. Sci. U.S.A.* **112**, 11947–11952 (2015).
20. R. W. Sanders et al., *J. Virol.* **76**, 8875–8889 (2002).
21. M. Guttman et al., *Structure* **22**, 974–984 (2014).
22. J. Huang et al., *Nature* **491**, 406–412 (2012).
23. R. Pejchal et al., *J. Virol.* **83**, 8451–8462 (2009).
24. S. Bryson, J. P. Julien, R. C. Hynes, E. F. Pai, *J. Virol.* **83**, 11862–11875 (2009).
25. I. A. Wilson, J. J. Skehel, D. C. Wiley, *Nature* **289**, 366–373 (1981).
26. E. Falkowska et al., *Immunity* **40**, 657–668 (2014).
27. F. Garces et al., *Cell* **159**, 69–79 (2014).
28. D. Sok et al., *Sci. Transl. Med.* **6**, 236ra63 (2014).
29. J. H. Lee et al., *Nat. Commun.* **6**, 8167 (2015).
30. R. Derking et al., *PLOS Pathog.* **11**, e1004767 (2015).
31. L. K. Pritchard et al., *J. Virol.* **89**, 6952–6959 (2015).
32. J. Huang et al., *Nature* **515**, 138–142 (2014).
33. A. S. Kim, D. P. Leaman, M. B. Zwick, *PLOS Pathog.* **10**, e1004271 (2014).
34. J. M. Cutolo, L. J. Deterding, K. B. Tomer, *J. Am. Soc. Mass Spectrom.* **15**, 1545–1555 (2004).
35. E. P. Go et al., *J. Virol.* **89**, 8245–8257 (2015).
36. E. P. Go et al., *J. Virol.* **85**, 8270–8284 (2011).
37. E. T. Crooks et al., *Hum. Antibodies* **14**, 101–113 (2005).
38. R. M. Cardoso et al., *Immunity* **22**, 163–173 (2005).
39. G. Frey et al., *Proc. Natl. Acad. Sci. U.S.A.* **105**, 3739–3744 (2008).
40. D. P. Leaman, J. H. Lee, A. B. Ward, M. B. Zwick, *J. Virol.* **89**, 6725–6745 (2015).
41. J. Chen et al., *J. Virol.* **88**, 1249–1258 (2014).
42. J. Guenaga et al., *PLOS ONE* **6**, e16074 (2011).
43. G. Ofek et al., *Proc. Natl. Acad. Sci. U.S.A.* **107**, 17880–17887 (2010).

ACKNOWLEDGMENTS

We thank C. Blattner for the PGT151 and JR-FL EnvΔCT plasmids, J. Torres and N. Overney for helping with plasmid preparations, T. Nieuwsma for technical assistance, A. Sarkar and L. Kong for advice on glycan modeling, and I. A. Wilson for helpful comments and discussion. The data from this study are tabulated in the main paper and in the supplementary materials. The cryo-EM reconstructions of JR-FL EnvΔCT–PGT151 and JR-FL EnvΔCT–PGT151 Fab–10E8 Fab and the model of JR-FL EnvΔCT–PGT151 have been submitted to the PDB and the Electron Microscopy Data

Bank with accession codes PDB-5FUU, EMD-3308, EMD-3309, and EMD-3312. This work was supported by the NIH (grant UM1 AI100663), the International AIDS Vaccine Initiative (IAVI) Neutralizing Antibody Consortium through the Collaboration for AIDS Vaccine Discovery (grants OPP1084519 and OPP1115782), and the California HIV/AIDS Research Program Dissertation Award (to J.H.L.). This work was partially funded by IAVI with the generous support of the U.S. Agency for International Development (USAID), the Ministry of Foreign Affairs of the Netherlands, and the Bill and Melinda Gates Foundation; a full list of IAVI donors is available at www.iavi.org. The contents of this manuscript are the responsibility of the authors and do not necessarily reflect the views of USAID or the U.S. government. The EM work was

conducted at the cryogenic electron microscopy facility at The Scripps Research Institute. This is manuscript number 29175 from the Scripps Research Institute.

SUPPLEMENTARY MATERIALS

www.sciencemag.org/content/351/6277/1043/suppl/DC1
Materials and Methods
Figs. S1 to S16
Table S1
References (44–64)

13 August 2015; accepted 3 February 2016
10.1126/science.aad2450

IMMUNOLOGY

Visualizing antibody affinity maturation in germinal centers

Jeroen M. J. Tas,^{1*} Luka Mesin,^{1*} Giulia Pasqual,¹ Sasha Targ,¹ Johanne T. Jacobsen,¹ Yasuko M. Mano,¹ Casie S. Chen,¹ Jean-Claude Weill,² Claude-Agnès Reynaud,² Edward P. Browne,^{3,4} Michael Meyer-Hermann,^{5,6} Gabriel D. Vitoria^{1†}

Antibodies somatically mutate to attain high affinity in germinal centers (GCs). There, competition between B cell clones and among somatic mutants of each clone drives an increase in average affinity across the population. The extent to which higher-affinity cells eliminating competitors restricts clonal diversity is unknown. By combining multiphoton microscopy and sequencing, we show that tens to hundreds of distinct B cell clones seed each GC and that GCs lose clonal diversity at widely disparate rates. Furthermore, efficient affinity maturation can occur in the absence of homogenizing selection, ensuring that many clones can mature in parallel within the same GC. Our findings have implications for development of vaccines in which antibodies with nonimmunodominant specificities must be elicited, as is the case for HIV-1 and influenza.

The average affinity of specific antibodies increases dramatically over the course of an immune response (1, 2). This phenomenon is known as affinity maturation and is the result of a Darwinian process that alternates stochastic somatic hypermutation (SHM) of immunoglobulin (Ig) genes with the selection and clonal expansion of B cells that have acquired affinity-enhancing mutations (2). Successive iterations of this cycle drive an increase in the overall affinity of antibodies over time, which is essential for their effectiveness in curtailing and preventing infection.

Affinity maturation takes place in germinal centers (GCs), defined microanatomical clusters

containing up to a few thousand B cells that emerge in multiple copies within secondary lymphoid organs upon infection or immunization (3–7). Each GC is traditionally viewed as arising from a handful of independent “founder clones,” many of which are lost as affinity-based competition leads to progressive focusing of the repertoire on the most successful progeny (which we refer to as “homogenizing selection”) (8). Although it is inducible under experimental settings (9), the extent to which homogenizing selection takes place during normal immunization or infection has been difficult to determine, mostly due to technical limitations in the methods used to measure clonal diversity within individual GCs (10–14).

Measuring clonal diversity in GCs using multiphoton microscopy

As an approach to estimating GC clonal diversity by imaging, we made use of a “rainbow” allele for multicolor fate mapping to permanently tag individual B cells and their progeny with different combinations of fluorescent proteins (15). This method, as implemented in the *Rosa26*^{Confetti} allele (16), relies on stochastic Cre-mediated recombination to commit cells to expression of one of four possible fluorescent proteins, generating 10 different color combinations when two alleles are recombined in homozygous mice (fig. S1, A

¹Whitehead Institute for Biomedical Research, Cambridge, MA 02142, USA. ²Institut Necker-Enfants Malades, INSERM U1151-CNRS UMR 8253, Sorbonne Paris Cité, Université Paris Descartes, Faculté de Médecine-Site Broussais, 75014 Paris, France. ³Koch Institute for Integrative Cancer Research, Massachusetts Institute of Technology (MIT), Cambridge, MA 02142, USA. ⁴Broad Institute of Harvard and MIT, Cambridge, MA 02142, USA. ⁵Department of Systems Immunology and Braunschweig Integrated Centre of Systems Biology, Helmholtz Centre for Infection Research, Inhoffenstraße 7, 38124 Braunschweig, Germany. ⁶Institute for Biochemistry, Biotechnology and Bioinformatics, Technische Universität Braunschweig, Braunschweig, Germany.

*These authors contributed equally to this work. †Corresponding author. E-mail: vitoria@wi.mit.edu

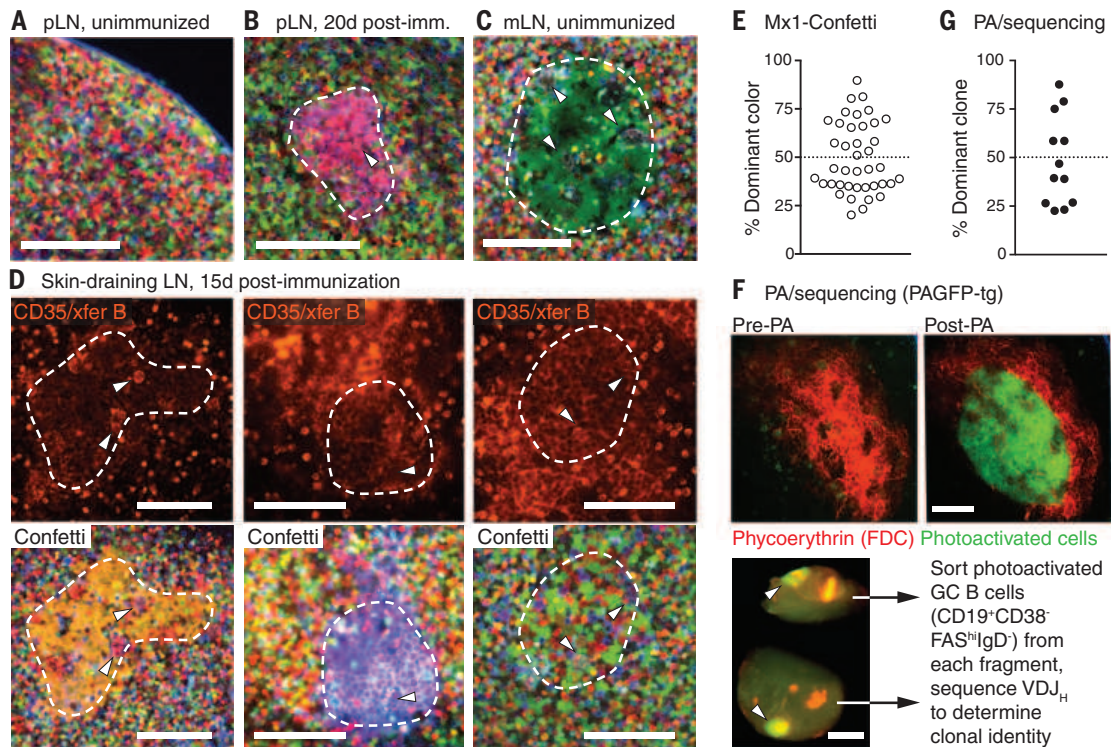


Fig. 1. Visualizing clonal expansions in GCs using a brainbow allele. (A) pLN of an unimmunized *Rosa26^{Confetti/Confetti}*.Mx1-Cre mouse, imaged by multiphoton microscopy. (B) pLN of a mouse immunized 20 days previously with 10 μ g CGG in alum in the hind footpad. The image shows a cluster of similar-colored cells corresponding to a GC (dashed line), as evidenced by the presence of tingible body macrophages (arrowheads). (C) Single-colored GC (dashed line) in a mesenteric lymph node (mLN) from an unimmunized mouse. (D) GCs in draining LN of mice immunized subcutaneously with CGG in alum 15 days before imaging. The location of the GC dark zone (dashed line) was determined by injection of labeled antibody to CD35 and surface-labeled naïve B cells (top panels; fluorescence is from Alexa 633 label). For each GC, Confetti colors (bottom panels) were imaged independently and used for quantification. Confetti colors are as shown in fig. S1B. GC identity is confirmed by presence of tingible-body macrophages (arrowheads). Scale bars, 100 μ m. Second-harmonic generation from collagen fibers is shown in blue. (E) Quan-

tification of data as in (D). Each symbol represents one GC. Graph shows percentage of cells expressing the most abundant color combination. Data pooled from four mice, two independent experiments. (F) Quantifying GC clonality by photoactivation (PA). Photoactivatable-GFP-transgenic mice were immunized in the footpad with 10 μ g CGG in alum and imaged 15 days later. FDC networks were labeled with phycoerythrin immune complexes. (Top) Images of a single GC within a pLN, before and after photoactivation. Scale bar, 100 μ m. (Bottom) Single pLN containing two photoactivated GCs (arrowheads) dissected into two fragments, each of which is separately processed for sorting of PA⁺ GC B cells and *Igh* sequencing. Scale bar, 500 μ m. (G) Quantification of clonal dominance in multiple GCs. Data obtained as in (F), with clonal identity assigned based on *Igh* sequence. Each symbol represents one GC, with two GCs sequenced per LN (full clonality charts in fig. S2). The percentage of cells belonging to the most abundant clone is given. Data are from five mice, three independent experiments.

and B). Because recombination stops upon cessation of Cre activity, selective proliferation of an individual GC B cell would lead to the appearance of clusters of daughter cells of the same color.

We generated *Rosa26^{Confetti/Confetti}* mice carrying the Mx1-Cre transgene, which triggers Confetti recombination spontaneously during early life (17). Multiphoton imaging of popliteal lymph nodes (pLN) in naïve Mx1-Confetti mice showed that, in the absence of immunization, cells of different colors are intermixed, as expected from the polyclonal nature and migratory behavior of naïve lymphocytes (Fig. 1A and movie S1). In contrast, subcutaneous immunization with alum-adsorbed chicken gamma globulin (CGG) induced the appearance in the draining lymph node (LN) of clusters of cells of the same color, suggestive of monoclonal expansion (Fig. 1B and movies S2 and S3). Such clusters could also be found in mesenteric LNs (Fig. 1C), and even occasionally

in Peyer's patches (fig. S1C) of unimmunized mice, where GCs form spontaneously in response to intestinal microbiota. Thus, clonal expansions within GCs can be readily detected by multicolor fate mapping, even in cases where the driving antigen is unknown.

Quantification of cell colors in GC dark zones at 15 days after immunization (Fig. 1D) revealed a wide range of color dominances (from 20.2 to 89.7%; median, 44.0%) and a relative paucity of predominantly single-colored GCs [6 of 40 (15%) GCs with color dominance > 70%] (Fig. 1E). To validate these estimates, we used in situ photoactivation followed by fluorescence-activated cell sorting (9, 18) to obtain single B cells from individual GCs, the clonal identity of which we then determined by *Igh* mRNA sequencing (Fig. 1F). This approach again showed varying degrees of clonal dominance among individual GCs [3 of 12 (25%) GCs with dominance > 70%; range, 22.5% to 87.5%; median, 43.0%] (Fig. 1G and fig. S2). It

also revealed the frequent presence of clones that were shared between two individual GCs in the same LN, indicative of synchronous origin (colored slices in fig. S2). We conclude that GCs display variable degrees of clonal dominance, even when induced synchronously by immunization. Although predominantly monoclonal GCs do exist, these are relatively rare at the time point assayed.

Early GCs are highly diverse

The diversity of clonal dominance levels among mature GCs led us to question the generalizability of reports proposing that GCs are seeded pauciclonally (11, 12, 19). To address this, we generated mice expressing the photoactivatable-GFP (green fluorescent protein) transgene along with Cre recombination driven by the endogenous *Aicda* locus (*Aicda^{Cre}*) (20), expressed in activated B cells, and a *Rosa26^{lox-stop-lox-tdTomato}* reporter. At 6 days after immunization with CGG in alum, early GCs were identifiable in these mice as clusters of

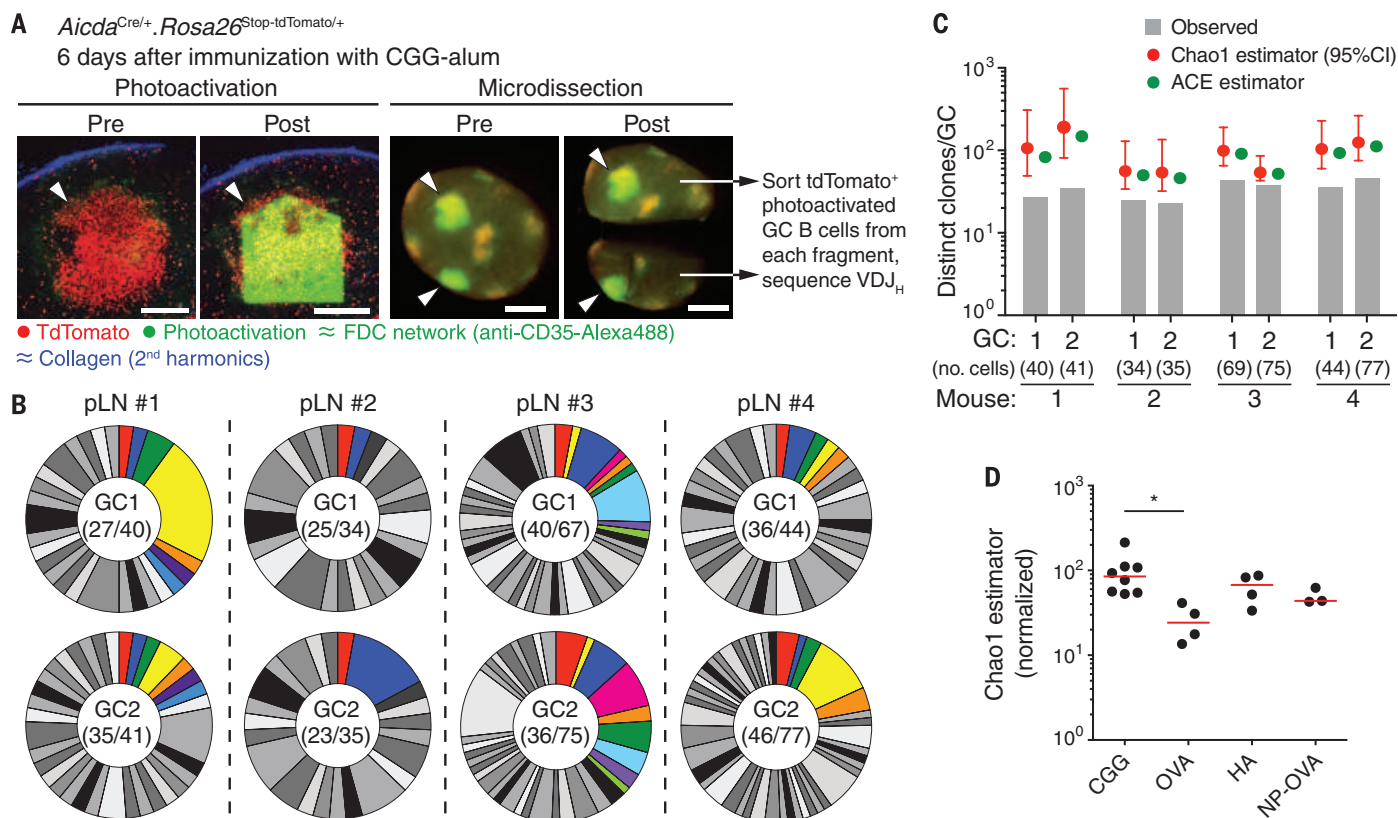


Fig. 2. Clonal diversity in early GCs. (A) Photoactivation of single early GC clusters. Photo activatable-GFP-transgenic.*Aicda*^{Cre}.*Rosa26*^{lox-stop-lox-tdTomato} mice were immunized in the footpad with 10 μ g CGG in alum and imaged 6 days later. FDC networks were marked by injection of labeled antibody to CD35. Left panels show images of a single tdTomato⁺ cluster (arrowheads) within a pLN before and after photoactivation. Scale bar, 200 μ m. Right panels show dissection of a single pLN with two photoactivated GCs (arrowheads) into two fragments, each of which is separately processed for cell sorting. Scale bar, 500 μ m. **(B)** Pie charts showing clonal diversity in early GCs. Each slice represents one clone. Colored slices represent clones that were found in both GCs (upper and lower pie charts) from the same pLN. Numbers in the center of each chart are number of clones observed/total number of cells sequenced. Clonal identity was assigned based on *Igh* sequence. Pairs are from four

different mice in three independent experiments. **(C)** Estimation of total clonal richness in individual GCs using the Chao1 and ACE estimators. Graphs show observed clonal richness [from (B)] and total richness according to the indicated estimator. **(D)** Estimated clonal richness (Chao1) in GCs elicited by various antigens. Mice were immunized with 10 μ g of the indicated antigen and then imaged/photoactivated as in (A). Each symbol represents one GC; bar indicates median. CGG, chicken gamma globulin; OVA, chicken ovalbumin; HA, influenza hemagglutinin (H3); NP-OVA, 4-hydroxy-3-nitrophenylacetyl-OVA. For comparison purposes, estimates are normalized by interpolation to the size of the smallest sample (34 cells). Numbers for CGG GCs in (D) differ from those in (C) due to normalization. Further details are in fig. S3. **P* < 0.05, Kruskal-Wallis test with Dunn's post-test. All other comparisons were not significant.

tdTomato⁺ cells within follicular dendritic cell (FDC) networks. We photoactivated two such clusters per LN and sorted photoactivated GC B cells from each cluster for *Igh* sequencing (Fig. 2A and fig. S3A). Early GCs were highly and uniformly polyclonal, with 23 to 46 unique variable/diversity/joining (VDJ) rearrangements detected when sequencing 34 to 77 single cells per GC (Fig. 2B). Extrapolation of these numbers using the Chao1 and abundance coverage-based estimator (ACE) estimators of species richness (21) gave rough estimates of GC clonality that ranged from ~50 to ~200 clones per GC (median Chao1, 102 clones) for the four pairs of GCs analyzed (Fig. 2C). Overall mutation and class-switching levels were low at this time point (fig. S3B), confirming that these were indeed early GCs. We were again able to identify B cell clones that were shared between two GCs in the same pLN (colored slices, Fig. 2B) [mean 15.8% (SD 6.4) of clones found in one GC were also found in its neigh-

bor]. Similar experiments using other antigens showed that, although the extent of early GC diversity can vary depending on the immunizing antigen, high diversity is not a unique feature of the response to CGG (Fig. 2D and fig. S3, C to E). Diversity was also not the result of nonspecific recruitment of B cells to early GCs (figs. S3C and S4). We conclude that early GCs are highly diverse, containing tens to hundreds of distinct clones, depending on the antigen used for immunization. The progression from uniform diversity (Fig. 2) to variable degrees of clonal dominance (Fig. 1) in the CGG response implies that individual GCs display different rates of homogenizing selection acting subsequently to this coalescence.

Extent of homogenizing selection in individual GCs

Clonal dominance in GCs may arise by parallel selection of multiple members of a clone present in

the early GC or by strong expansion of single SHM variants over cells of the same and of different clones. To investigate these dynamics, we generated mice in which recombination of *Rosa26*^{Confetti} was driven by the tamoxifen-inducible *Aicda*^{CreERT2} allele, specifically expressed in activated B cells (22). We thus delayed recombination until after GC formation, allowing different members of the same clone to express different color combinations, each giving origin to an independent early GC "lineage." In this system, GCs dominated by the descendants of a single SHM variant would be identifiable as having "resolved" to a single dominant color (Fig. 3A).

Administration of tamoxifen to *Rosa26*^{Confetti/Confetti}.*Aicda*^{CreERT2/+} (AID-Confetti) mice at 5 days after CGG immunization triggered recombination, often of a single Confetti allele, in ~40 to 50% of GC B cells (fig. S5, A and B) by the end of the 3- to 5-day period during which tamoxifen is active (23). Recombination thus ends near the onset

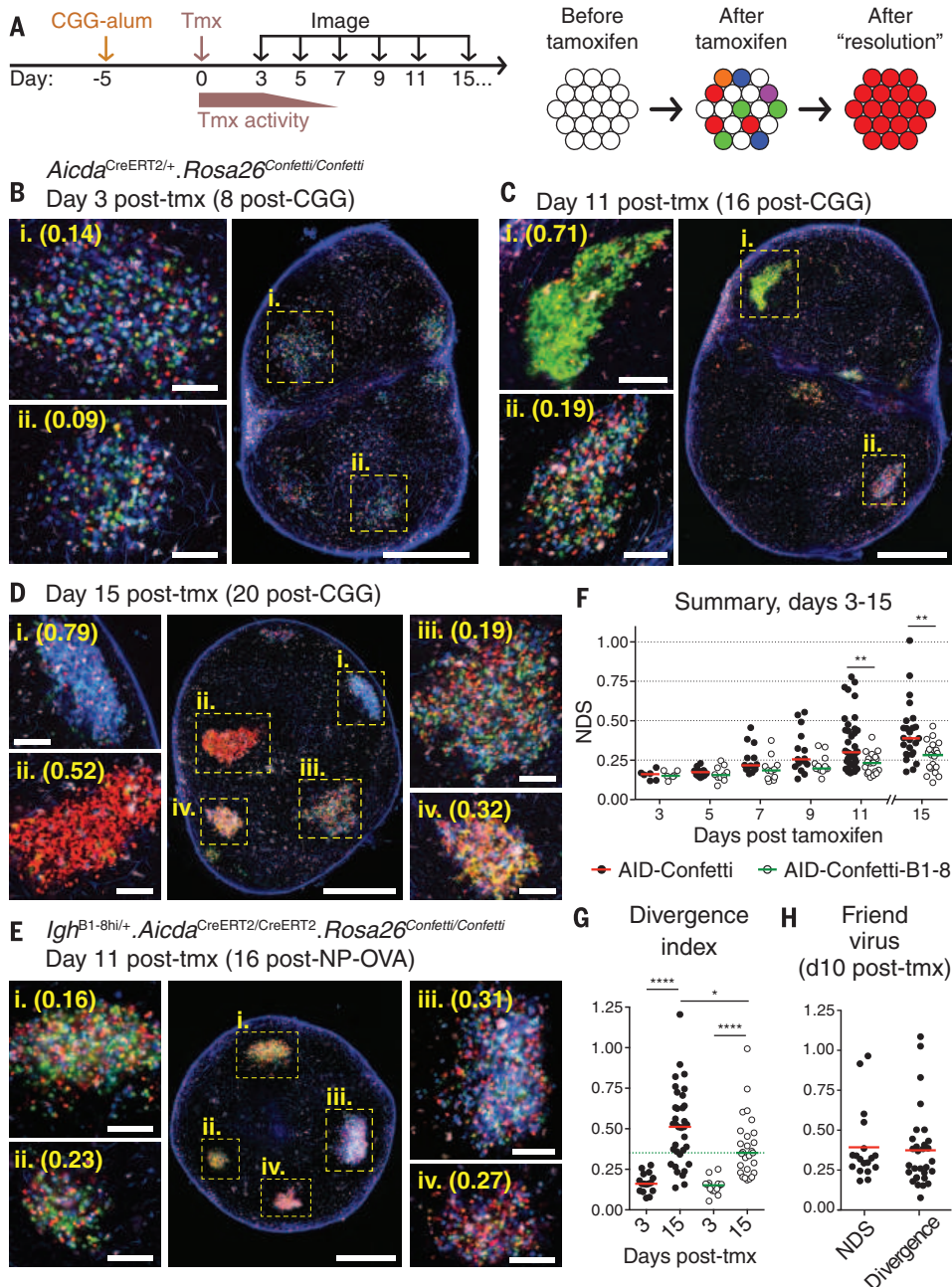


Fig. 3. Kinetics of color dominance in individual GCs. (A) Graphic representation of the experimental protocol. AID-Confetti mice were immunized in the footpad with 10 μ g CGG in alum, treated with tamoxifen (tmx) 5 days later, and imaged at the indicated time points. Tamoxifen triggers recombination of one or both Confetti alleles in individual GC B cells, independent of clonal origin. (B to E) Whole lymph node (large panel; scale bar, 500 μ m) and higher-magnification images (side panels; scale bar, 100 μ m) showing GCs at different times after tamoxifen administration. Cell colors as in fig. S1B. Second-harmonic generation from collagen fibers is shown in blue. Numbers in parentheses are the normalized dominance score (NDS). [(B) to (D)] AID-Confetti mice imaged at the time points indicated. (E) Wild-type (WT) recipients of 1 to 2×10^4 adoptively transferred AID-Confetti-B1-8 $\text{Ig}\lambda^+$ B cells, immunized with NP-OVA as in (A) and imaged 11 days post-tmx. Higher-magnification panels show independently acquired images of the GCs indicated in the overview panel. (F) Quantification of data as shown in (B) to (E). Bars represent the median. (G) Divergence index for AID-Confetti and AID-Confetti-B1-8 mice at days 3 and 15 post-tmx. Bars represent the median. A green dotted line is placed at the median of the day 15 AID-Confetti-B1-8 data for reference. (H) Quantification of GC selection in AID-Confetti mice infected with FV as detailed in fig. S7. Graph shows NDS and divergence index at day 10 post-tmx (day 30 after infection). Bars represent the median. For panels (F) to (H), each symbol represents one GC. Data are pooled from 2 to 6 replicate experiments. For NDS quantification, we exclude GCs with density of fluorescent cells below 0.4 cells per $100 \mu\text{m}^2$ (equivalent to $\sim 40\%$ of cells having recombined a Confetti allele; see the supplementary text). * $P < 0.05$; ** $P < 0.01$; **** $P < 0.0001$, Mann-Whitney U test.

of T cell-driven selection, at the beginning of the second week of the response (24) (Fig. 3A). GCs analyzed 3 days after tamoxifen treatment (8 days after immunization) displayed roughly equal proportions of CFP⁺, YFP⁺, and RFP⁺ (cyan, yellow, and red fluorescent protein, respectively) cells and a lower proportion of GFP⁺ and doubly recombined cells (Fig. 3B), as expected from the original description of the Confetti allele (16). Only residual, if any, GCs containing recombined cells could be detected in unimmunized or alum-only control mice (fig. S5C).

Color distribution changed over time, with progressive emergence of GCs dominated by a single color/combination (Fig. 3, B to G). To quantify color dominance, we calculated a normalized dom-

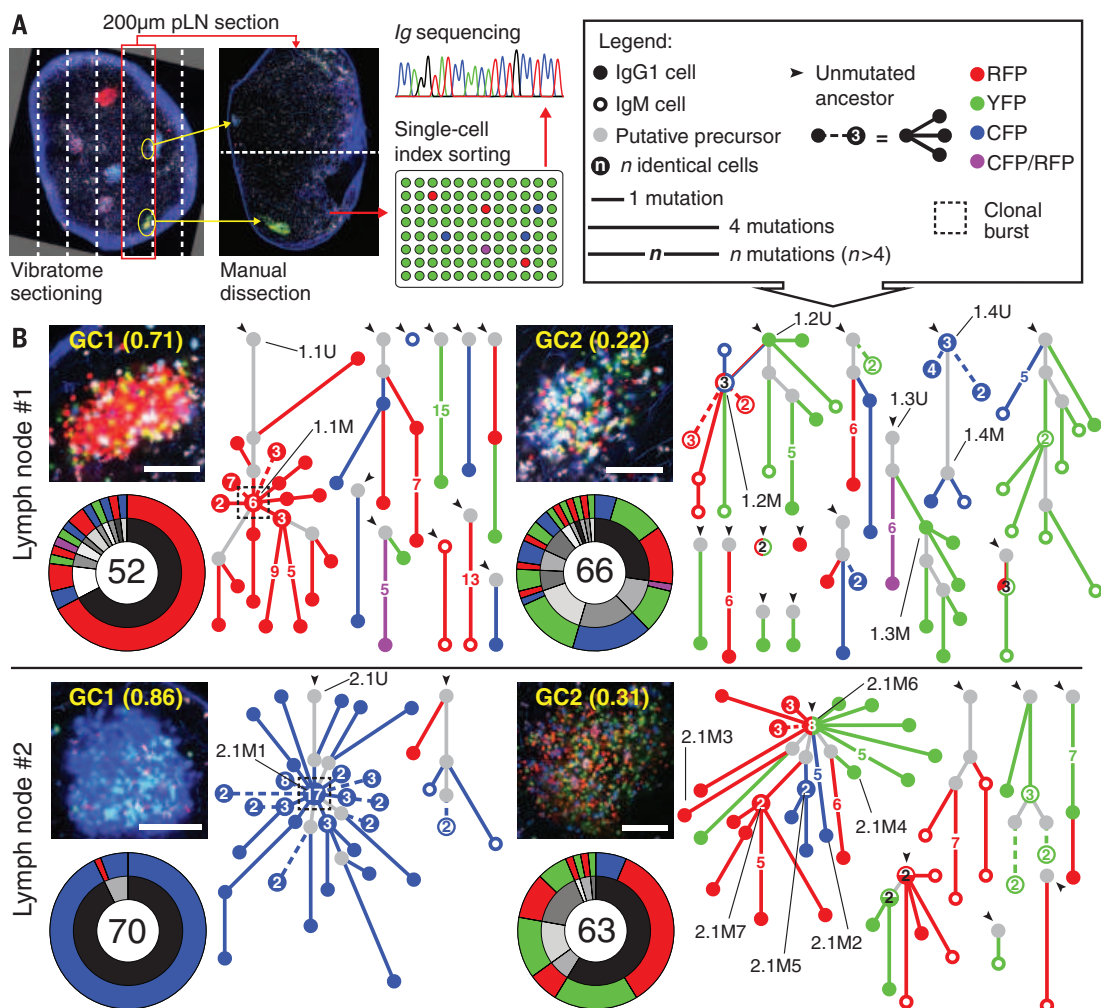
inance score (NDS) for each GC, which approximates (25) the fraction of cells belonging to a single lineage originating at the time of recombination (fig. S5D). Kinetic analysis was extended to 15 days after tamoxifen treatment (20 days after immunization), near the end of the CGG-alum-induced GC response in most LNs. Median dominance increased monotonically, from 0.16 at day 3 to 0.39 at day 15 after tamoxifen. GCs with NDS of 0.5 or more (corresponding to $\sim 50\%$ of all GC cells displaying the same color combination) appeared as early as day 9 after tamoxifen, and a single color could account for close to 80% of GC B cells at day 11 and virtually all cells in a GC 4 days later (Fig. 3F). However, progression among GCs varied markedly, as dominance in the lowest-scoring

GCs at days 11 and 15 after tamoxifen remained close to day 3 levels. Evaluation of color distribution in exceptional LNs in which GCs could still be found at very late time points showed that low-dominance GCs were present up to the very end of the response (fig. S6, A to C). Therefore, GC selection does not inevitably lead to high color dominance within the lifetime of the response to CGG-alum.

To determine the extent to which progression of color dominance depends on affinity-based competition, we generated an adoptive transfer model in which wild-type hosts received B cells from *Aicda*^{CreERT2/CreERT2}.*Rosa26*^{Confetti/Confetti}.*Igh*^{B1-8hi/+} (AID-Confetti-B1-8) donors (in which $\text{Ig}\lambda^+$ B cells have uniformly high affinity to the

Fig. 4. Clonal relationships among cells obtained from GCs with high or low color dominance. (A) Method used to obtain *Ig* sequences. (B) *Igh* sequence relationship among B cells from two pairs of individual GCs from two pLNs of different mice, obtained 10 days after tamoxifen administration (15 days after immunization), as described in Fig. 3. Each panel contains: (Top left) Multi-

photon image (scale bar, 100 μ m; cell colors as in fig. S1B; second-harmonic generation from collagen fibers is shown in blue; number in parentheses is the normalized dominance score (NDS). (Bottom left) Clonal distribution pie chart (with clones represented in gray-scale in the inner ring and Confetti colors in the outer ring; number of cells sequenced is indicated in the center). (Right) Trees representing the phylogeny of *Ig* heavy-chain V-segment sequences within each clone (symbols according to the legend in the top right corner). Dashed lines within phylogenies indicate multiple variants distanced the same number of mutations from the originating node. IDs of variants for which affinity was measured in Fig. 5 are indicated by black lines. For each LN, GC1 and GC2 were considered as displaying high and low color dominance, respectively.



NP hapten and do not undergo affinity maturation due to lack of a functional *Aicda* allele). 4-Hydroxy-3-nitrophenylacetyl-ovalbumin (NP-OVA)-induced GCs in recipient mice approached high color dominance only rarely and with much delayed kinetics (Fig. 3, E and F, and fig. S6D). Therefore, differences in affinity between competing B cells likely contribute toward the rapid rise in dominance observed in a fraction of GCs. To quantify the effect of neutral competition—defined as the change in lineage abundances over time due to stochastic factors, in the absence of differences in affinity—in AID-Confetti-B1-8 GCs, we calculated a divergence index, which computes the difference between the expected and observed proportions of all 10 colors in each GC (fig. S5E) and is thus more sensitive to small changes in color abundance than the NDS. This metric showed marked divergence from baseline distribution in this population (Fig. 3G and fig. S6D), highlighting the effect on GC selection of factors unrelated to affinity. Moreover, the least divergent GCs in polyclonal and SHM-proficient AID-Confetti mice remained relatively close to baseline color distribution

(at day 15 after tamoxifen, 25.7% of AID-Confetti GCs scored below the median of the AID-Confetti-B1-8 distribution) (Fig. 3G). We conclude that individual GCs are highly heterogeneous with respect to selection: Although a fraction of these structures become heavily dominated by cells of one color in a matter of days—suggesting strong expansion of the descendants of a single SHM variant arising at or after the onset of GC selection—others deviate from baseline color distribution at levels that do not exceed those attained by neutral competition.

We extended our findings to a different antigenic system by measuring clonal dominance in GCs elicited by infection with Friend retrovirus (FV) (26). We treated infected AID-Confetti mice with tamoxifen at 20 days after infection (an early time point in the delayed GC response to FV) and imaged spleen slices 10 days later (fig. S7, A and B). A wide range of NDS and divergence scores were also observed in FV-induced GCs (Fig. 3H and fig. S7C). Therefore, heterogeneity in the outcome of selection is a common property of GCs induced by model antigens and

by viral infection, and thus likely represents an intrinsic property of GC evolution.

Homogeneous GCs are the product of “clonal bursts”

To investigate the underlying clonal structure of the variation in homogenizing selection rates among GCs, we determined the *Igh* gene sequences of fluorescent B cells isolated from GCs with different degrees of color dominance. To achieve this, we dissected pLNs from immunized AID-Confetti mice into fragments containing single GCs using vibratome sectioning guided by multiphoton microscopy (Fig. 4A and fig. S8). From each LN, we sorted cells from one high-dominance GC and from a neighboring low-dominance GC for *Ig* sequencing.

We obtained *Igh* sequences from 52 to 74 single cells per GC from three pairs of pLN GCs harvested 10 days after tamoxifen treatment (15 days after immunization with CGG-alum) (Fig. 4B and fig. S9A). Comparison of SHM levels between high- and low-dominance GCs from the same LN (fig. S9B) and between *Aicda*-sufficient and haploinsufficient GCs (fig. S9C) indicated that heterogeneity was

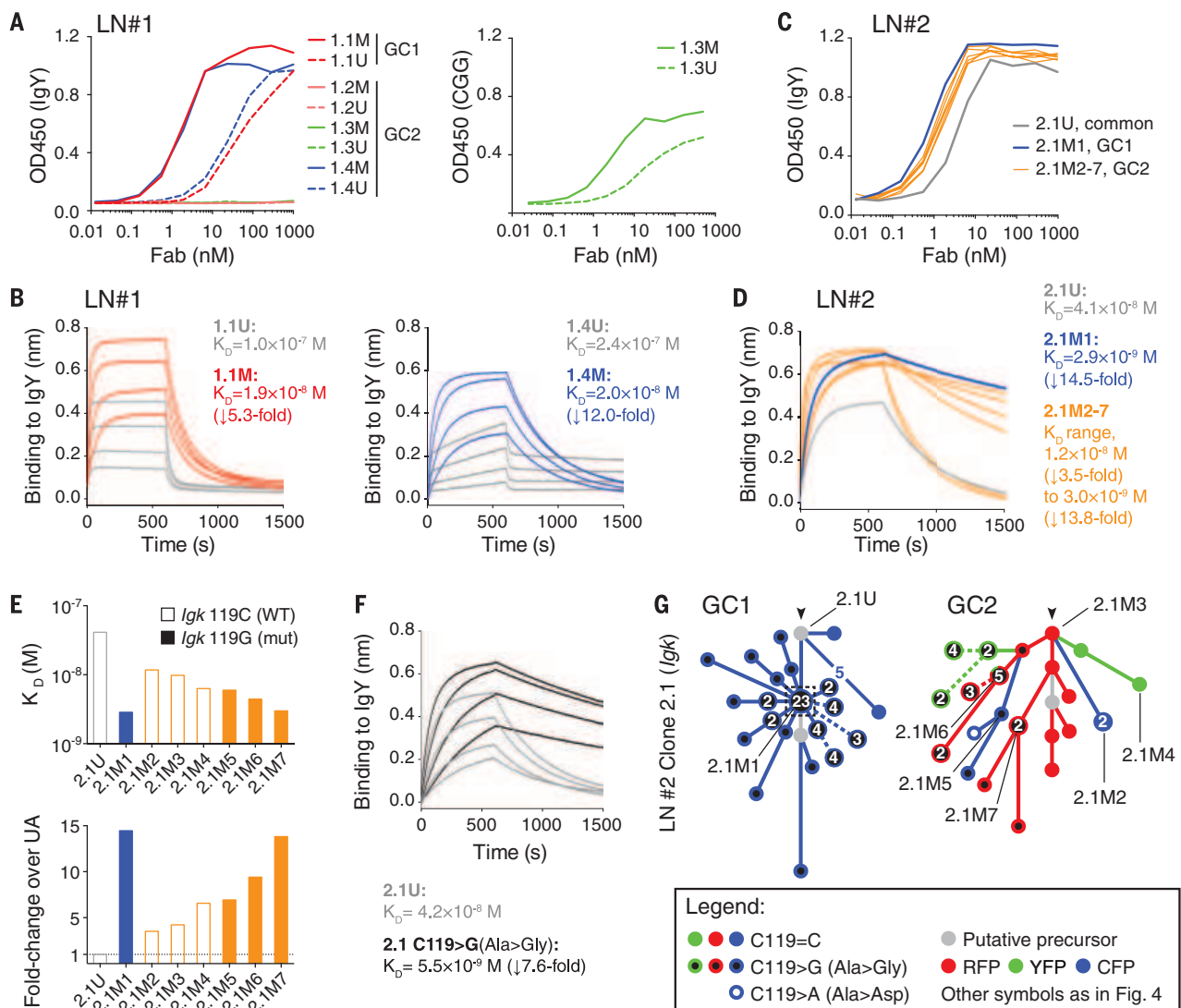


Fig. 5. Affinity maturation in GCs with high or low color dominance. Affinity measurements for reconstructed Fabs derived from B cell clones/variants indicated in Fig. 4B. **(A)** Binding of Fabs cloned from LN1 to IgY (right) or CGG (left), measured by enzyme-linked immunosorbent assay. **(B)** Biolayer interferometry for Fabs cloned from LN1 binding to IgY. **(C and D)** As in (A) and (B), respectively, but using Fabs cloned from LN#2. **(E)** Affinity for IgY among variants of clone 2.1 (Fig. 4B) from LN2/GC1 (blue) and LN2/GC2 (orange), shown as K_D (top) and fold change over UA (bottom). The unmutated ancestor (2.1U) is shown in gray. Open bars have the WT nucleotide (C) in the 119 position; closed bars have the C119→G (Ala→Gly) mutation. **(F)** Affinity of Fabs reconstructed

from clone 2.1, either unmutated (gray lines) or with replacement of a single *Igk* nucleotide [C119→G (Ala→Gly), black lines]. **(G)** *Igk* sequence relationships among B cells from clone 2.1 from LN2/GC1 (left) or LN2/GC2 (right). Symbols according to the legend below the figure and in Fig. 4B. Cloned Fab IDs are indicated by black lines. Although not all cells yielded both *Igk* and *Igh* sequences, clonal relationships are drawn from all available data, and therefore exact correspondence between the trees in (G) and in Fig. 4B is not expected. Biolayer interferometry was performed with Fabs at 20, 40, 80, and 160 nM. **(D)** shows only the 160-nM measurement. Reported affinities are the average of two measurements fitted globally at the 20- to 160-nM range.

not the consequence of asynchronous GC formation or of substantially impaired AID activity, respectively. Most cells of the dominant color in the three high-dominance GCs (Fig. 4B and fig. S9A, left panels) derived from a single expanded clone. In all three GCs, dominance could be readily attributed to the selective expansion of a single SHM variant, three to five heavy-chain variable segment (V_H) mutations (four to nine total mutations) distanced from the unmutated ancestor (UA) (dashed boxes in Fig. 4B and fig. S9A). Thus, high-dominance GCs are predominantly monoclonal and appear to result from “clonal bursts,” in which a single SHM variant is heavily ex-

panded over a short period of time, leading to extensive loss of clonal diversity concomitant with broad diversification of the expanded variant. On the other hand, low-dominance GCs (Fig. 4B and fig. S9A, right panels) were more clonally diverse than their high-dominance neighbors. Low color dominance is unlikely to be the result of failure to identify a dominant nonfluorescent lineage, because fluorescent and nonfluorescent B cells obtained from two independently sequenced low-dominance GCs were largely clonally related (fig. S10). Although low-dominance GCs consisted predominantly of small independent expansions, one of three GCs sequenced (LN2/GC2) contained

a larger clone (accounting for 59% of all recombined cells), within which multiple colors were represented. This expanded clone carried heavy- and light-chain V(D)J rearrangements identical to the dominant clone in the single-colored GC sequenced from the same LN (LN2/GC1), indicative of a common cell of origin. In contrast to the clonal bursts of single-colored GCs, however, this multicolored expansion branched off from the *Igh* UA itself and developed in parallel along several distinct lineages. Thus, expansion of this clone began in the pre/early GC period, before the end of the tamoxifen pulse, and subsequent competition in the mature GC failed to focus on a single dominant

SHM variant. Together, these data indicate that, although clonal dominance in GCs can arise by parallel expansion of members of the same clone, loss of diversity is greatest in GCs in which strong clonal bursts rapidly expand and diversify single SHM variants.

Affinity maturation in the absence of homogenizing selection

To investigate the relationship between clonal bursting and affinity maturation, we measured the affinity of recombinant F_{ab} fragments derived from B cells originating from high- and low-dominance GCs (Fig. 4B), as well as from their deduced or sequenced UAs. F_{ab} affinities varied markedly between clones, from undetectable to low nanomolar dissociation constants (K_D) (Fig. 5). As expected, the two F_{ab} s obtained from SHM variants that underwent clonal bursts had higher affinity for the immunizing antigen than their respective UAs [5.3-fold increase (1.0×10^{-7} to 1.9×10^{-8}) for clone 1.1 and 14.5-fold increase (4.1×10^{-8} to 2.9×10^{-9}) for clone 2.1] (Fig. 5). However, affinity maturation was also evident in F_{ab} s cloned from low-dominance GCs. Of the three clones obtained from LN1/GC2, SHM variants of two clones (1.3 and 1.4) showed increased affinity over their UAs, whereas the affinity of the third clone (1.2) remained below detection level (Fig. 5). Clone 1.4 showed a gain in affinity of 12-fold (2.4×10^{-7} to 2.0×10^{-8}), notably larger than the 5.4-fold change observed for clone 1.1 (associated with a clonal burst in the neighboring single-colored GC). We also determined the affinity of six additional variants of clone 2.1 from LN2/GC2 (which shared its UA with the dominant clone of LN2/GC1 and is thus directly comparable between GCs). Gains in affinity were evident in all of these variants, ranging from 3.5- to 13.8-fold (K_D 1.2×10^{-8} and 3.0×10^{-9} , respectively) (Fig. 5, C to E). Although the highest of these was close in magnitude to the 14.5-fold change seen in variant 2.1M1 (associated with the clonal burst in LN2/GC1), the increase in affinity among GC2 F_{ab} s was in general lower (median increase of 6.8-fold). Thus, affinity maturation can occur in the absence of clonal bursts, although limited data from the two LN2 GCs suggests that selection of high-affinity mutants in these cases may not be as efficient.

Finally, detailed analysis of the SHM trajectory of variant 2.1M1 showed that this burst was associated with a somatic mutation in *Igk* (C119→G, Ala→Gly) that alone increased the F_{ab} affinity by 7.6-fold (Fig. 5, E to G). This mutation was also found to have occurred independently at least twice in LN2/GC2, but without the accompanying burst. Thus, identical mutations occurring within the same clone may still have distinct outcomes when in different GCs, again suggesting a role for stochastic factors in GC selection.

Conclusions

Using a combination of imaging methods and single-cell sequencing, we show that (i) early GCs can be highly diverse, containing up to hundreds

of distinct B cell clones; (ii) individual GCs approach homogeneity at different rates, leading to variable loss of diversity; (iii) homogeneous GCs are the product of clonal bursts that lead to rapid expansion and further diversification of SHM variants with improved affinity; and (iv) affinity maturation can take place in the presence or absence of such bursts and thus does not necessarily require radical loss of clonal diversity.

We speculate that affinity maturation arises through a balance between slow but steady elimination of lower-affinity clones and variants, punctuated by sporadic clonal bursts of various magnitudes that generate a wealth of SHM variants of a clone at the expense of clonal diversity. This balance would ensure that the polyclonality of the GC response is maintained at the same time as very successful clones can be heavily diversified and exported to effector or memory fates, generating the range of GC outcomes observed by us and others (14, 27). Although it cannot be ruled out that differences in outcomes between GCs may be related to factors such as initial clonal composition or timing of the appearance of key mutations, the finding that GCs can deviate substantially from baseline color distribution even when all cells have equal affinity and cannot undergo SHM (Fig. 3, F and G, and fig. S6D) suggests that stochastic factors unrelated to affinity can strongly influence GC selection. A system in which B cell selection is driven by dynamic encounters with a limiting number of T helper cells would be especially sensitive to such effects (9, 27). The explosive B cell proliferation that can be driven by such encounters would provide a mechanistic basis for the clonal burst phenomenon (28, 29).

The finding that early GCs can contain a large diversity of clones is in contrast to the widely held view that these structures form pauciclonally (10–12, 30). Although this discrepancy may be partly attributable to methodological issues (31), Küppers *et al.* (13) reported higher clonal diversity in one of two GCs originating from different reactive human lymph nodes and speculated that pauciclonal GCs were likely the product of extensive selection acting on originally polyclonal early GCs. Our current data strongly support this view.

Our findings have implications for the design of vaccines against highly variable pathogens such as influenza and HIV, where broadly protective antibodies targeting conserved, nonimmunodominant epitopes must be elicited (32, 33). Understanding whether GC competition restricts the appearance of such clones, and how clonal bursts may promote the somatic diversification required for broad neutralization to emerge, may prove key to the successful generation of broadly protective antibodies by vaccination.

REFERENCES AND NOTES

- H. N. Eisen, G. W. Siskind, *Biochemistry* **3**, 996–1008 (1964).
- H. N. Eisen, *Cancer Immunol. Res.* **2**, 381–392 (2014).
- I. C. MacLennan, *Annu. Rev. Immunol.* **12**, 117–139 (1994).
- K. Rajewsky, *Nature* **381**, 751–758 (1996).
- C. D. Allen, T. Okada, J. G. Cyster, *Immunity* **27**, 190–202 (2007).
- D. M. Tarlinton, *Immunol. Cell Biol.* **86**, 133–138 (2008).

- G. D. Victora, M. C. Nussenzweig, *Annu. Rev. Immunol.* **30**, 429–457 (2012).
- G. D. Victora, L. Mesin, *Curr. Opin. Immunol.* **28**, 90–96 (2014).
- G. D. Victora *et al.*, *Cell* **143**, 592–605 (2010).
- J. Jacob, R. Kassir, G. Kelsoe, *J. Exp. Med.* **173**, 1165–1175 (1991).
- F. G. Kroese, A. S. Wubbena, H. G. Seijen, P. Nieuwenhuis, *Eur. J. Immunol.* **17**, 1069–1072 (1987).
- Y. J. Liu, J. Zhang, P. J. Lane, E. Y. Chan, I. C. MacLennan, *Eur. J. Immunol.* **21**, 2951–2962 (1991).
- R. Küppers, M. Zhao, M. L. Hansmann, K. Rajewsky, *EMBO J.* **12**, 4955–4967 (1993).
- M. Ziegner, G. Steinhauser, C. Berek, *Eur. J. Immunol.* **24**, 2393–2400 (1994).
- J. Livet *et al.*, *Nature* **450**, 56–62 (2007).
- H. J. Snippert *et al.*, *Cell* **143**, 134–144 (2010).
- Materials and methods are available as supplementary materials on Science Online.
- Z. Shulman *et al.*, *Science* **341**, 673–677 (2013).
- J. Jacob, J. Przylepa, C. Miller, G. Kelsoe, *J. Exp. Med.* **178**, 1293–1307 (1993).
- D. F. Robbiani *et al.*, *Cell* **135**, 1028–1038 (2008).
- N. J. Gotelli, R. K. Colwell, in *Biological Diversity: Frontiers in Measurement and Assessment*, A. E. Magurran, B. J. McGill, Eds. (Oxford University Press, Oxford, 2010), pp. 39–54.
- I. Dogan *et al.*, *Nat. Immunol.* **10**, 1292–1299 (2009).
- M. Jarjour *et al.*, *J. Exp. Med.* **211**, 1109–1122 (2014).
- D. Dominguez-Sola *et al.*, *Nat. Immunol.* **13**, 1083–1091 (2012).
- See the supplementary materials for mathematical validation of the NDS.
- S. Nair *et al.*, *Retrovirology* **8**, 76 (2011).
- M. D. Radmacher, G. Kelsoe, T. B. Kepler, *Immunol. Cell Biol.* **76**, 373–381 (1998).
- A. D. Gitlin, Z. Shulman, M. C. Nussenzweig, *Nature* **509**, 637–640 (2014).
- A. D. Gitlin *et al.*, *Science* **349**, 643–646 (2015).
- J. Jacob, G. Kelsoe, *J. Exp. Med.* **176**, 679–687 (1992).
- J. Faro, M. Or-Guil, *BMC Bioinformatics* **14** (Suppl 6), S8 (2013).
- G. D. Victora, P. C. Wilson, *Cell* **163**, 545–548 (2015).
- F. Klein *et al.*, *Science* **341**, 1199–1204 (2013).

ACKNOWLEDGMENTS

We thank M. Carroll, A. Schmidt, and S. Harrison (Harvard Medical School), H. Wardemann (German Cancer Research Center), and K. Hasenkrug (National Institute of Allergy and Infectious Diseases) for essential reagents, and R. K. Colwell (University of Connecticut) and S. Binder (Helmholtz Centre for Infection Research) for help with statistical analysis. We are especially thankful to the late Herman N. Eisen (1918–2014) for the lengthy discussions of affinity maturation on which the present study is based. The data presented in this manuscript are tabulated in the main paper and in the supplementary materials. Antibody sequences are also available from the GenBank database, accession numbers KU613419 to KU615568. Aicda-CreERT2 mice are available from C. A. Reynaud and J. C. Weill under a material transfer agreement with INSERM. This work was supported by NIH grant 5DP5OD012146 (G.D.V.), with additional support from Human Frontier Science Program Grant RGP0033/2015 (G.D.V. and M.M.H.), German Federal Ministry of Education and Research within the Measures for the Establishment of Systems Medicine, eMed project SYSIMIT, FKZ: 01ZX1308B (M.M.H.), Swiss National Science Foundation Postdoctoral Mobility Fellowship and Cancer Research Institute Irvington Postdoctoral Fellowship (G.P.), and Norwegian Research Council Fri Prosjektstøtte (FRIPRO) mobility grant (J.T.J.). The Octet RED96 Bio-Layer Interferometry System was supported by NIH grant S10 OD016326 to the MIT Biophysical Instrumentation Facility.

SUPPLEMENTARY MATERIALS

www.sciencemag.org/content/351/6277/1048/suppl/DC1
Materials and Methods
Supplementary Text
Figs. S1 to S11
Tables S1 and S2
Movies S1 to S3
Database S1
References (34–55)

1 September 2015; accepted 2 February 2016
Published online 18 February 2016
10.1126/science.1234393

REPORTS

ELECTRON TRANSPORT

Negative local resistance caused by viscous electron backflow in graphene

D. A. Bandurin,¹ I. Torre,² R. Krishna Kumar,^{1,3} M. Ben Shalom,^{1,4} A. Tomadin,⁵ A. Principi,⁶ G. H. Auton,⁴ E. Khestanova,^{1,4} K. S. Novoselov,⁴ I. V. Grigorieva,¹ L. A. Ponomarenko,^{1,3} A. K. Geim,^{1*} M. Polini^{7*}

Graphene hosts a unique electron system in which electron-phonon scattering is extremely weak but electron-electron collisions are sufficiently frequent to provide local equilibrium above the temperature of liquid nitrogen. Under these conditions, electrons can behave as a viscous liquid and exhibit hydrodynamic phenomena similar to classical liquids. Here we report strong evidence for this transport regime. We found that doped graphene exhibits an anomalous (negative) voltage drop near current-injection contacts, which is attributed to the formation of submicrometer-size whirlpools in the electron flow. The viscosity of graphene's electron liquid is found to be ~ 0.1 square meters per second, an order of magnitude higher than that of honey, in agreement with many-body theory. Our work demonstrates the possibility of studying electron hydrodynamics using high-quality graphene.

The collective behavior of many-particle systems that undergo frequent interparticle collisions has been studied for more than two centuries and is routinely described by the theory of hydrodynamics (1, 2). The theory relies only on the conservation of mass, momentum, and energy and is highly successful in explaining the response of classical gases and liquids to external perturbations that vary slowly in space and time. More recently, it has been shown that hydrodynamics can also be applied to strongly interacting quantum systems, including ultrahot nuclear matter and ultracold atomic Fermi gases in the unitarity limit (3–6). In principle, the hydrodynamic approach can also be used to describe many-electron phenomena in condensed matter physics (7–13). The theory becomes applicable if electron-electron scattering provides the shortest spatial scale in the problem, so that $\ell_{ee} \ll W, \ell$, where ℓ_{ee} is the electron-electron scattering length, W is the characteristic sample size, $\ell \equiv v_F \tau$ is the mean free path, v_F is the Fermi velocity, and τ is the mean free time with respect to momentum-nonconserving collisions,

such as those involving impurities and phonons. The above inequalities are difficult to meet experimentally. At low temperatures (T), ℓ_{ee} varies approximately $\propto T^{-2}$, reaching a micrometer scale at liquid helium T (14), which necessitates the use of ultraclean systems to satisfy $\ell_{ee} \ll \ell$. At higher T , electron-phonon scattering rapidly reduces ℓ . However, for two-dimensional (2D) systems in which acoustic phonon scattering dominates, ℓ

decays only $\propto T^{-1}$, slower than ℓ_{ee} , which should in principle allow the hydrodynamic description to apply over a certain temperature range, until other phonon-mediated processes become important. So far, there has been little evidence for hydrodynamic electron transport. An exception is an early work on 2D electron gases in ballistic devices ($\ell \sim W$) made from GaAlAs heterostructures (15). These devices exhibited nonmonotonic changes in differential resistance as a function of a large applied current I , which was used to increase the electron temperature (making ℓ_{ee} short) while the lattice temperature remained low (allowing long ℓ). The nonmonotonic behavior was attributed to the Gurzhi effect, a transition between Knudsen ($\ell_{ee} \gg \ell$) and viscous electron flows (7, 15). Another possible hint about electron hydrodynamics comes from an explanation (16) of the Coulomb drag measured between two graphene sheets at the charge neutrality point (CNP) (17).

Here we address electron hydrodynamics by using a special measurement geometry (Fig. 1) that amplifies the effects of the shear viscosity ν and, at the same time, minimizes a contribution from ballistic effects that can occur not only in the Knudsen regime but also in viscous flows in graphene. A viscous flow can lead to vortices appearing in the spatial distribution of the steady-state current (Fig. 1, A and B). Such “electron whirlpools” have a spatial scale $D_v = \sqrt{\nu \tau}$, which depends on electron-electron scattering through ν and on the electron system's quality through τ (18). To detect the whirlpools, electrical probes should be placed at a distance comparable to D_v . By using single- and bi-layer graphene (SLG and BLG, respectively) encapsulated between boron nitride crystals (19–21), we were able to reach a D_v of 0.3 to 0.4 μm thanks to the high viscosity of graphene's Fermi liquid and its high carrier

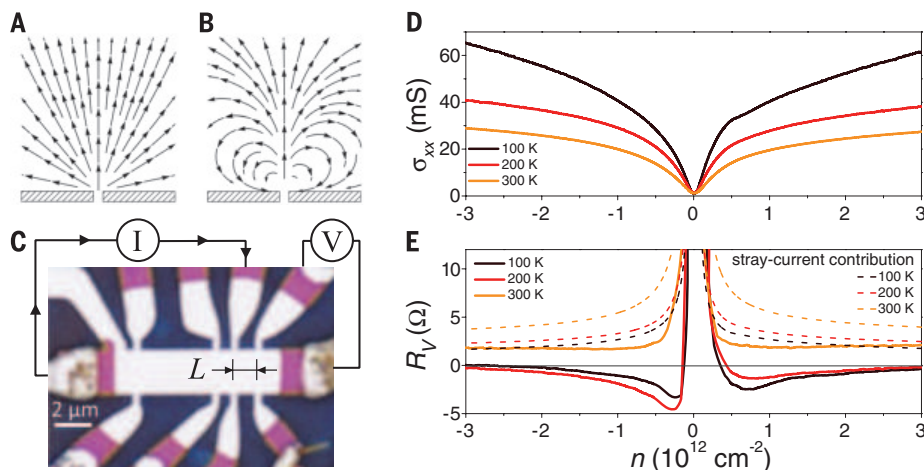


Fig. 1. Viscous backflow in doped graphene. (A and B) The calculated steady-state distribution of a current injected through a narrow slit for (A) a classical conducting medium with zero ν and (B) a viscous Fermi liquid. (C) Optical micrograph of one of our SLG devices. The schematic explains the measurement geometry for vicinity resistance. The top gate electrode appears in white and the mesa, which is etched in encapsulated graphene and not covered with a metal, appears in purple. Mixed colors at the periphery are areas of metallic contacts on top of the mesa. (D and E) Longitudinal conductivity σ_{xx} and R_V as a function of n , induced by applying gate voltage. The dashed curves in (E) show the contribution expected from classical stray currents in this geometry (18). $I = 0.3 \mu\text{A}$; $L = 1 \mu\text{m}$; $W = 2.5 \mu\text{m}$.

¹School of Physics and Astronomy, University of Manchester, Oxford Road, Manchester M13 9PL, UK. ²National Enterprise for nanoScience and nanoTechnology, Scuola Normale Superiore, I-56126 Pisa, Italy. ³Department of Physics, Lancaster University, Lancaster LA14YB, UK. ⁴National Graphene Institute, University of Manchester, Manchester M13 9PL, UK. ⁵National Enterprise for nanoScience and nanoTechnology, Istituto Nanoscienze-Consiglio Nazionale delle Ricerche and Scuola Normale Superiore, I-56126 Pisa, Italy. ⁶Institute for Molecules and Materials, Radboud University, NL-6525 AJ Nijmegen, Netherlands. ⁷Istituto Italiano di Tecnologia, Graphene Labs, Via Morego 30, I-16163 Genova, Italy.

*Corresponding author. E-mail: geim@man.ac.uk (A.K.G.); marco.polini@iit.it (M.P.)

Fig. 2. Vicinity resistance maps. (A and B)

$R_v(n, T)$ for SLG and BLG, respectively. The black curves indicate zero R_v . For each n away from the CNP, there is a wide range of T over which R_v is negative. For the SLG device, $W = 2.5 \mu\text{m}$ and $L = 1 \mu\text{m}$; for the BLG device, $W = 2.3 \mu\text{m}$ and $L = 1.3 \mu\text{m}$.

All measurements for BLG presented in this work were taken with zero displacement between the graphene layers (18).

mobility μ , even at high T . Such a large D_v , which is unique to graphene, nevertheless necessitates submicron resolution to probe the electron backflow. To this end, we fabricated multiterminal Hall bars with narrow ($\sim 0.3 \mu\text{m}$) and closely spaced ($\sim 1 \mu\text{m}$) voltage probes (Fig. 1C and fig. S1). Details of the device fabrication are given in (18).

All our devices were first characterized in the standard geometry by applying I along the main channel and using side probes for voltage measurements. The typical behavior of longitudinal conductivity σ_{xx} at a few characteristic values of T is shown in Fig. 1D. At liquid helium T , the devices exhibited $\mu \sim 10$ to $50 \text{ m}^2 \text{ V}^{-1} \text{ s}^{-1}$ for carrier concentrations n over a wide range of the order of 10^{12} cm^{-2} , and μ remained above $5 \text{ m}^2 \text{ V}^{-1} \text{ s}^{-1}$ up to room T (fig. S2). Such values of μ allow ballistic transport with $\ell > 1 \mu\text{m}$ at $T < 300 \text{ K}$. At $T \geq 150 \text{ K}$, ℓ_{ee} decreases to 0.1 to $0.3 \mu\text{m}$ over the same range of n (figs. S3 and S4) (22, 23). This allows the essential condition for electron hydrodynamics ($\ell_{ee} \ll W, \ell$) to be satisfied within this temperature range. If one uses the conventional longitudinal geometry of electrical measurements, viscosity has little effect on σ_{xx} (figs. S5 to S7), essentially because the flow in this geometry is uniform, whereas the total momentum of the moving Fermi liquid is conserved in electron-electron collisions (18). The only evidence for hydrodynamics that we could find in the longitudinal geometry was the Gurzhi effect that appeared as a function of the electron temperature, which is controlled by applying large I , similar to the observations in (15) (fig. S8).

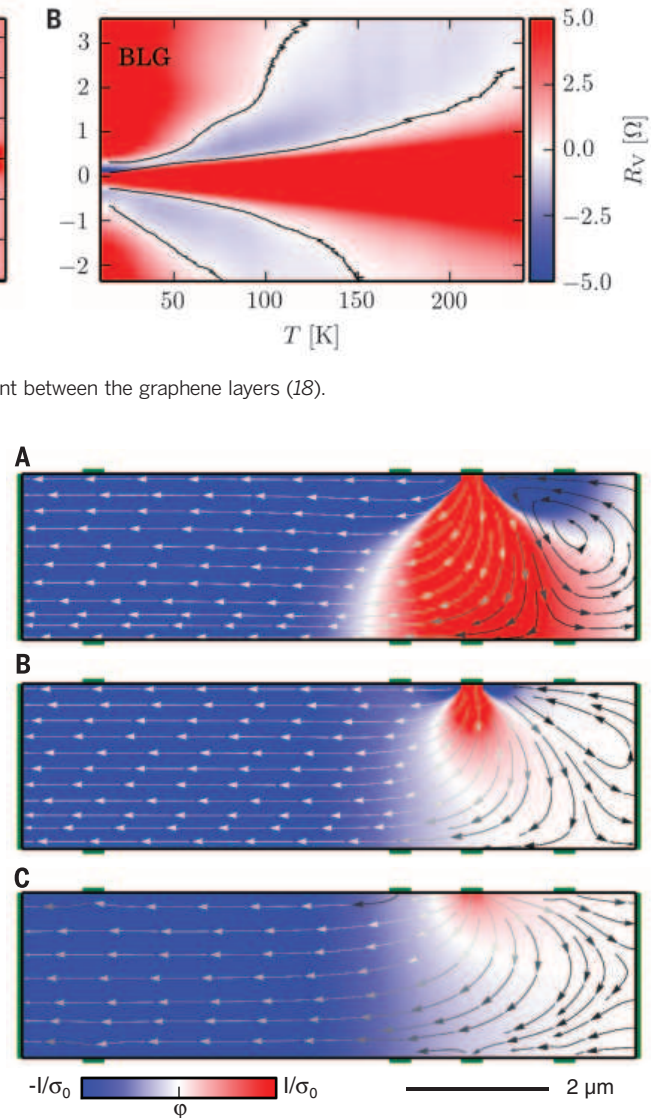
To look for hydrodynamic effects, we used the geometry shown in Fig. 1C. In this setup, I is injected through a narrow constriction into the graphene bulk, and the voltage drop V_v is measured at the nearby side contacts located at the distance $L \sim 1 \mu\text{m}$ away from the injection point. These can be considered as nonlocal measurements, although the stray currents are not exponentially small (dashed curves in Fig. 1E). To distinguish from the proper nonlocal geometry (24), we refer to the linear-response signal measured in our geometry as vicinity resistance, $R_v = V_v/I$. The idea is that, in the case of a viscous flow, whirlpools emerge as shown in Fig. 1B, and their appearance can then be detected as sign reversals of V_v , which is positive for the con-

Fig. 3. Whirlpools in electron flow. (A to C)

Calculated $\mathbf{J}(\mathbf{r})$ and $\phi(\mathbf{r})$ for a geometry similar to that shown in Fig. 1C, with the green bars indicating voltage contacts. $D_v = 2.3, 0.7$, and $0 \mu\text{m}$ for (A), (B), and (C), respectively. Vortices are evident in the top right corners of (A) and (B), where the current flow is in the direction opposite to that in (C), which shows the case of zero viscosity. In each panel, the current streamlines also change from white to black to indicate that the current density $|\mathbf{J}(\mathbf{r})|$ is lower to the right of the injecting contact.

ventional current flow (Fig. 1A) and negative for viscous backflow (Fig. 1B). Figure 1E shows examples of R_v for the same SLG device as in Fig. 1D, and other SLG and BLG devices exhibited similar behavior (18). Away from the CNP, R_v is negative over a wide range of intermediate T , despite an expected substantial offset due to stray currents. Figure 2 details our observations further by showing maps of $R_v(n, T)$ for SLG and BLG. The two Fermi liquids exhibited somewhat different behavior, reflecting their different electronic spectra, but R_v was negative over a large range of n and T for both. Two more R_v maps are provided in fig. S9. In total, seven multiterminal devices with W ranging from 1.5 to $4 \mu\text{m}$ were investigated, showing vicinity behavior that was highly reproducible both for different contacts on the same device and for different devices, independently of their W , although we note that the backflow was more pronounced for devices with the highest μ and lowest charge inhomogeneity.

The same anomalous vicinity response was also evident when we followed the method of

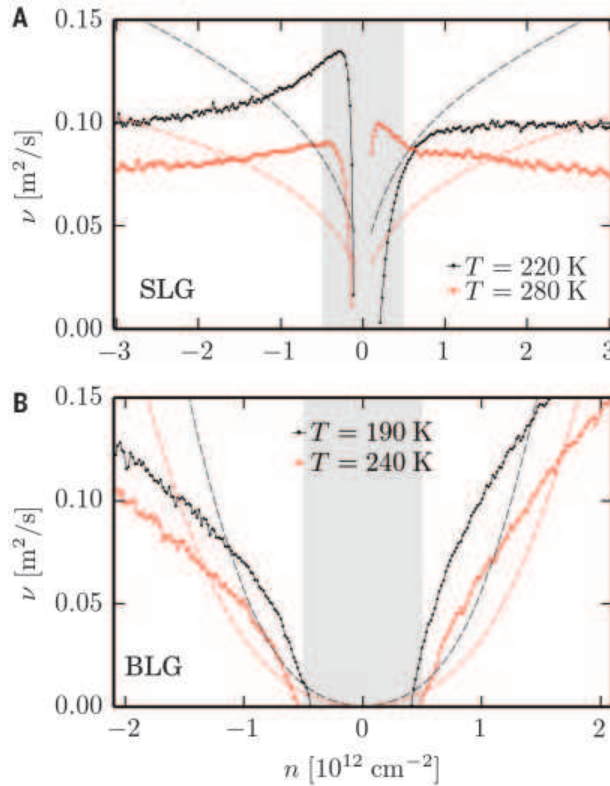


(15) and used the current I to increase the electron temperature. In this case, V_v changed its sign as a function of I from positive to negative to positive again, reproducing the behavior of R_v with increasing T of the cryostat (fig. S10). Comparing figs. S8 and S10, it is clear that the vicinity geometry strongly favors the observation of hydrodynamic effects: The measured vicinity voltage changed its sign, whereas in the standard geometry, the same viscosity led only to relatively small changes in dV/dI . We also found that the magnitude of negative R_v decayed rapidly with L (fig. S11), in agreement with the finite size of electron whirlpools.

Negative resistances can in principle arise from other effects, such as single-electron ballistic transport ($\ell_{ee} \gg \ell$) or quantum interference (18, 20, 24). The latter contribution is easily ruled out, because quantum corrections rapidly wash out at $T > 20 \text{ K}$ and have a random sign that rapidly oscillates as a function of magnetic field. Also, our numerical simulations using the Landauer-Büttiker formalism and the realistic device geometry showed

Fig. 4. Viscosity of the Fermi liquids in graphene.

(A and B) Solid curves show values of ν for SLG and BLG, respectively. Dashed curves represent calculations based on many-body diagrammatic perturbation theory (no fitting parameters). The gray shaded areas indicate regions around the CNP where our hydrodynamic model is not applicable (18).



that no negative resistance could be expected for the vicinity configuration in zero magnetic field (19, 21). Nonetheless, we carefully considered the possibility of any accidental spillover of single-electron ballistic effects into the vicinity geometry of our experiment. The dependences of the negative vicinity signal on T , n , I , and the device geometry allowed us to unambiguously rule out any such contribution (18). For example, the single-electron ballistic phenomena should become more pronounced for longer ℓ (that is, with decreasing T or electron temperature and with increasing n), in contrast to the nonmonotonic behavior of V_v .

Turning to theory, we can show that negative R_v arises naturally from whirlpools that appear in a viscous Fermi liquid near current-injecting contacts. As discussed in (18), electron transport for sufficiently short ℓ_{ee} can be described by the hydrodynamic equations

$$\nabla \cdot \mathbf{J}(\mathbf{r}) = 0 \quad (1)$$

and

$$\frac{\sigma_0}{e} \nabla \phi(\mathbf{r}) + D_v^2 \nabla^2 \mathbf{J}(\mathbf{r}) - \mathbf{J}(\mathbf{r}) = 0 \quad (2)$$

where $\mathbf{J}(\mathbf{r})$ is the (linearized) particle current density, and $\phi(\mathbf{r})$ is the electric potential in the 2D plane. If $D_v \rightarrow 0$, Eq. 2 yields Ohm's law $-e\mathbf{J}(\mathbf{r}) = \sigma_0 \mathbf{E}(\mathbf{r})$ with a Drude-like conductivity $\sigma_0 = ne^2\tau/m$, where $-e$ and m are the electron charge and the effective mass, respectively (\mathbf{E} , electric field). The three terms in Eq. 2 describe (i) the electric force generated by the steady-state charge distribution in response to the applied current I , (ii) the viscous force (1, 2), and (iii) friction caused by

momentum-nonconserving processes that are parameterized by the scattering time $\tau(n, T)$.

Equations 1 and 2 can be solved numerically (18), and Fig. 3 shows examples of spatial distributions of $\phi(\mathbf{r})$ and $\mathbf{J}(\mathbf{r})$. For experimentally relevant values of D_v , a vortex appears in the vicinity of the current-injecting contact. This is accompanied by the sign reversal of $\phi(\mathbf{r})$ at the vicinity contact on the right of the injector, which is positive in Fig. 3C (no viscosity) but becomes negative in Fig. 3, A and B. Our calculations for this geometry show that R_v is negative for $D_v \gtrsim 0.4 \mu\text{m}$ (18). Because both τ and ν decrease with increasing T , D_v also decreases, and stray currents start to dominate the vicinity response at high T . This explains why R_v in Figs. 1 and 2 becomes positive close to room T , even though our hydrodynamic description has no high-temperature cutoff (18). Despite positive R_v values, the viscous contribution remains considerable near room T (Fig. 1D and fig. S12). At low T , the electron system approaches the Knudsen regime, and our hydrodynamic description becomes inapplicable because $\ell_{ee} \sim \ell$ (18). In the latter regime, the whirlpools should disappear and R_v should become positive (fig. S13), in agreement with the experiment and our numerical simulations based on the Landauer-Büttiker formalism.

The numerical results in Fig. 3 can be understood if we rewrite Eqs. 1 and 2 as

$$\mathbf{J}(\mathbf{r}) = \frac{\sigma_0}{e} \nabla \phi(\mathbf{r}) - nD_v^2 \nabla \times \omega(\mathbf{r}) \quad (3)$$

where $\omega(\mathbf{r}) \equiv n^{-1} \nabla \times \mathbf{J}(\mathbf{r}) = \omega(\mathbf{r}) \hat{z}$ is the vorticity (\hat{z} is the unit vector perpendicular to the graphene plane) (2). Taking the curl of Eq. 3, the

vorticity satisfies the equation $\omega(\mathbf{r}) = D_v^2 \nabla^2 \omega(\mathbf{r})$, where D_v plays the role of a diffusion constant. The current I injects vorticity at the source contact, which then exponentially decays over the length scale D_v . For $\nu = 0.1 \text{ m}^2 \text{ s}^{-1}$ [as estimated in (25)] and $\tau = 1.5 \text{ ps}$ (fig. S2), we find that $D_v \approx 0.4 \mu\text{m}$, in qualitative agreement with the measurements in fig. S11.

Lastly, we can combine the measurements of R_v and resistivity ρ_{xx} with the solution of Eqs. 1 and 2 in Fig. 3 to extract the kinematic viscosity for SLG and BLG. Because the observed Gurzhi effect in ρ_{xx} is small at low currents (fig. S6), we can use $\rho_{xx} = 1/\sigma_0 = m/(ne^2\tau)$ to determine $\tau(n, T)$ (18). Furthermore, for the experimentally relevant values of D_v , we find that R_v is a quadratic function of D_v

$$R_v = (b + aD_v^2)\sigma_0^{-1} \quad (4)$$

where a and b are numerical coefficients dependent only on the measurement geometry and boundary conditions, and b describes the contribution from stray currents (fig. S14). For the specific device in Fig. 3, we determined that $a = -0.29 \mu\text{m}^{-2}$ and $b = 0.056$, and this allows us to estimate $D_v(n, T)$ from measurements of R_v . For the known τ and D_v , we find that $\nu(n, T) = D_v^2/\tau$. The applicability limits of this analysis are discussed in (18), and the results are plotted in Fig. 4 for one of our devices. The figure shows that, at carrier concentrations of $\sim 10^{12} \text{ cm}^{-2}$, the Fermi liquids in both SLG and BLG are highly viscous, with $\nu \approx 0.1 \text{ m}^2 \text{ s}^{-1}$. In comparison, liquid honey has typical viscosities of ~ 0.002 to $0.005 \text{ m}^2 \text{ s}^{-1}$.

Figure 4 also shows the results of fully independent microscopic calculations of $\nu(n, T)$, which were carried out by extending the many-body theory of (25) to the case of 2D electron liquids hosted by encapsulated SLG and BLG. Within the range of applicability of our analysis in Fig. 4 ($n \sim 10^{12} \text{ cm}^{-2}$), the agreement in absolute values of the electron viscosity is good, especially taking into account that no fitting parameters were used in the calculations. Because the strong inequality $\ell_{ee} \gg \ell$ required by the hydrodynamic theory cannot be reached even for graphene, it would be unreasonable to expect better agreement (18). In addition, our analysis does not apply near the CNP, because the theory neglects contributions from thermally excited carriers, spatial charge inhomogeneity, and coupling between charge and energy flows, which can play a substantial role at low doping (16, 18). Further work is needed to understand electron hydrodynamics in the intermediate regime $\ell \gtrsim \ell_{ee}$ and, for example, to explain ballistic transport ($\ell > W$) in graphene at high T in terms of suitably modified hydrodynamic theory. The naive single-particle description that is routinely used for graphene's ballistic phenomena even above 200 K (19, 21) cannot be justified; a more complete theory is needed to describe the injection of a collimated electron beam into a strongly interacting 2D liquid. As for experimental approaches, the highly viscous Fermi liquids in graphene and their accessibility offer a promising opportunity to use various scanning probes for visualization and further understanding of electron hydrodynamics.

REFERENCES AND NOTES

1. L. D. Landau, E. M. Lifshitz, *Fluid Mechanics* (Pergamon Press, 1987).
2. G. K. Batchelor, *An Introduction to Fluid Dynamics* (Cambridge Univ. Press, 1967).
3. B. V. Jacak, B. Müller, *Science* **337**, 310–314 (2012).
4. C. Cao *et al.*, *Science* **331**, 58–61 (2011).
5. E. Elliott, J. A. Joseph, J. E. Thomas, *Phys. Rev. Lett.* **113**, 020406 (2014).
6. T. Schäfer, D. Teaney, *Rep. Prog. Phys.* **72**, 126001 (2009).
7. R. N. Gurski, *Sov. Phys. Usp.* **11**, 255–270 (1968).
8. A. O. Govorov, J. J. Heremans, *Phys. Rev. Lett.* **92**, 026803 (2004).
9. R. Bistritzer, A. H. MacDonald, *Phys. Rev. B* **80**, 085109 (2009).
10. M. Müller, J. Schmalian, L. Fritz, *Phys. Rev. Lett.* **103**, 025301 (2009).
11. A. V. Andreev, S. A. Kivelson, B. Spivak, *Phys. Rev. Lett.* **106**, 256804 (2011).
12. A. Tomadin, G. Vignale, M. Polini, *Phys. Rev. Lett.* **113**, 235901 (2014).
13. B. N. Narozhny, I. V. Gornyi, M. Titov, M. Schütt, A. D. Mirlin, *Phys. Rev. B* **91**, 035414 (2015).
14. G. F. Giuliani, G. Vignale, *Quantum Theory of the Electron Liquid* (Cambridge Univ. Press, 2005).
15. M. J. M. de Jong, L. W. Molenkamp, *Phys. Rev. B* **51**, 13389–13402 (1995).
16. J. C. W. Song, L. S. Levitov, *Phys. Rev. Lett.* **109**, 236602 (2012).
17. R. V. Gorbachev *et al.*, *Nat. Phys.* **8**, 896–901 (2012).
18. Supplementary materials are available on Science Online.
19. A. S. Mayorov *et al.*, *Nano Lett.* **11**, 2396–2399 (2011).
20. L. Wang *et al.*, *Science* **342**, 614–617 (2013).
21. T. Taychatanapat, K. Watanabe, T. Taniguchi, P. Jarillo-Herrero, *Nat. Phys.* **9**, 225–229 (2013).
22. Q. Li, S. Das Sarma, *Phys. Rev. B* **87**, 085406 (2013).
23. M. Polini, G. Vignale, <http://arxiv.org/abs/1404.5728> (2014).
24. D. A. Abanin *et al.*, *Science* **332**, 328–330 (2011).
25. A. Principi, G. Vignale, M. Carrega, M. Polini, <http://arxiv.org/abs/1506.06030> (2015).

ACKNOWLEDGMENTS

This work was supported by the European Research Council, the Royal Society, Lloyd's Register Foundation, the Graphene Flagship, and the Italian Ministry of Education, University and Research through the program Progetti Premiali 2012 (project ABNANOTECH). D.A.B. and I.V.G. acknowledge support from the Marie Curie program SPINOGRAPH (Spintronics in Graphene). A.P. received support from the Nederlandse Wetenschappelijk Organisatie. R.K.K. received support from the Engineering and Physical Sciences Research Council.

SUPPLEMENTARY MATERIALS

www.sciencemag.org/content/351/6277/1055/suppl/DC1

Supplementary Text

Figs. S1 to S14

References (26–37)

14 July 2015; accepted 23 December 2015

Published online 11 February 2016

10.1126/science.aad0201

ELECTRON TRANSPORT

Observation of the Dirac fluid and the breakdown of the Wiedemann-Franz law in graphene

Jesse Crossno,^{1,2} Jing K. Shi,¹ Ke Wang,¹ Xiaomeng Liu,¹ Achim Harzheim,¹ Andrew Lucas,¹ Subir Sachdev,^{1,3} Philip Kim,^{1,2*} Takashi Taniguchi,⁴ Kenji Watanabe,⁴ Thomas A. Ohki,⁵ Kin Chung Fong^{5*}

Interactions between particles in quantum many-body systems can lead to collective behavior described by hydrodynamics. One such system is the electron-hole plasma in graphene near the charge-neutrality point, which can form a strongly coupled Dirac fluid. This charge-neutral plasma of quasi-relativistic fermions is expected to exhibit a substantial enhancement of the thermal conductivity, thanks to decoupling of charge and heat currents within hydrodynamics. Employing high-sensitivity Johnson noise thermometry, we report an order of magnitude increase in the thermal conductivity and the breakdown of the Wiedemann-Franz law in the thermally populated charge-neutral plasma in graphene. This result is a signature of the Dirac fluid and constitutes direct evidence of collective motion in a quantum electronic fluid.

Understanding the dynamics of many interacting particles is a formidable task in physics. For electronic transport in matter, strong interactions can lead to a breakdown of the Fermi liquid (FL) paradigm of coherent quasi-particles scattering off of impurities. In such situations, provided that certain conditions are met, the complex microscopic dynamics can be coarse-grained to a hydrodynamic description of momentum, energy, and charge transport on long length and time scales (*1*). Hydrodynamics has been successfully applied to a diverse array of

interacting quantum systems, from high-mobility electrons in conductors (*2*) to cold atoms (*3*) and quark-gluon plasmas (*4*). Hydrodynamic effects are expected to greatly modify transport coefficients compared with their FL counterparts, as has been argued for strongly interacting massless Dirac fermions in graphene at the charge-neutrality point (CNP) (*5–8*).

Many-body physics in graphene is interesting because of electron-hole symmetry and a linear dispersion relation at the CNP (*9, 10*). Together with the vanishing Fermi surface, the ultra-relativistic spectrum leads to ineffective screening (*11*) and the formation of a strongly interacting quasi-relativistic electron-hole plasma known as a Dirac fluid (DF) (*12*). The DF shares many features with quantum critical systems (*13*): most importantly, the electron-electron scattering time is fast (*14–17*) and well suited to a hydrodynamic description. Because of the quasi-relativistic nature of the DF, this hydrodynamic limit is described by equations (*18*) quite different from

those applicable to its nonrelativistic counterparts. A number of unusual properties have been predicted, including nearly perfect (inviscid) flow (*19*) and a diverging thermal conductivity, which results in the breakdown of the Wiedemann-Franz (WF) law at finite temperature (*5, 6*).

Away from the CNP, graphene has a sharp Fermi surface, and the standard FL phenomenology holds. By tuning the chemical potential, we are able to measure thermal and electrical conductivity in both the DF and the FL in the same sample. In a FL, the relaxation of heat and charge currents is closely related, as they are carried by the same quasi-particles. The WF law (*20*) states that the electronic contribution to a metal's thermal conductivity κ_e is proportional to its electrical conductivity σ and temperature T , such that the Lorenz ratio \mathcal{L} satisfies

$$\mathcal{L} \equiv \frac{\kappa_e}{\sigma T} = \frac{\pi^2}{3} \left(\frac{k_B}{e} \right)^2 = \mathcal{L}_0 \quad (1)$$

where e is the electron charge, k_B is the Boltzmann constant, and \mathcal{L}_0 is the Sommerfeld value derived from FL theory. \mathcal{L}_0 depends only on fundamental constants, not specific details of the system such as carrier density or effective mass. As a robust prediction of FL theory, the WF law has been verified in numerous metals (*20*). At high temperatures, the WF law can be violated due to inelastic electron-phonon scattering or bipolar diffusion in semiconductors, even when electron-electron interactions are negligible (*21*). In recent years, several nontrivial violations of the WF law—all of which are related to the emergence of non-FL behavior—have been reported in strongly interacting systems such as Luttinger liquids (*22*), metallic ferromagnets (*23*), heavy fermion metals (*24*), and underdoped cuprates (*25*).

Owing to the strong Coulomb interactions between thermally excited charge carriers, the WF law is expected to be violated at the CNP in a DF. An electric field drives electrons and holes in opposite directions; collisions between them introduce a frictional dissipation, resulting in a finite conductivity even in the absence of disorder (*26*). In contrast, a temperature gradient causes electrons and holes to move in the same direction,

¹Department of Physics, Harvard University, Cambridge, MA 02138, USA. ²John A. Paulson School of Engineering and Applied Sciences, Harvard University, Cambridge, MA 02138, USA. ³Perimeter Institute for Theoretical Physics, Waterloo, Ontario N2L 2Y5, Canada. ⁴National Institute for Materials Science, Namiki 1-1, Tsukuba, Ibaraki 305-0044, Japan.

⁵Quantum Information Processing Group, Raytheon BBN Technologies, Cambridge, MA 02138, USA.

*Corresponding author. E-mail: pkim@physics.harvard.edu (P.K.); kc.fong@bbn.com (K.C.F.)

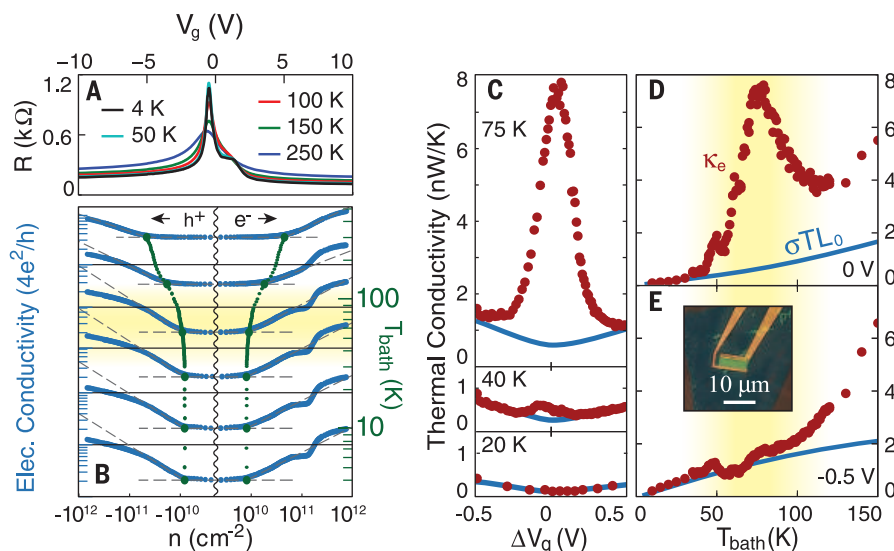


Fig. 1. Temperature- and density-dependent electrical and thermal conductivity. (A) Resistance (R) versus gate voltage (V_g) at various temperatures. kΩ, kilohm. (B) Electrical conductivity (blue) as a function of the charge density set by the back gate for different bath temperatures. The residual carrier density at the neutrality point (green) is estimated by the intersection of the minimum conductivity with a linear fit to $\log(\sigma)$, away from neutrality (dashed gray lines). Curves have been offset vertically such that the minimum density (green) aligns with the temperature axis to the right. Solid black lines correspond to $4e^2/h$. At low temperatures, the minimum density is limited by disorder (charge puddles). Above $T_{\text{dis}} \sim 40$ K (yellow shaded area), thermal excitations begin to dominate, and the sample enters the nondegenerate regime near the neutrality point. (C to E) Thermal conductivity (red points) as a function of (C) gate voltage and [(D) and (E)] bath temperature, compared to with the WF law, $\sigma T L_0$ (blue lines). At low temperature and/or high doping ($|\mu| \gg k_B T$), we find the WF law to hold. This is a nontrivial check on the quality of our measurement. In the nondegenerate regime ($|\mu| < k_B T$), the thermal conductivity is enhanced and the WF law is violated. Above $T \sim 100$ K, electron-phonon coupling becomes appreciable and begins to dominate thermal transport at all measured gate voltages. At this temperature, the yellow shaded background ends. All data from this figure are taken from sample S2 [inset in (E)].

thus inducing an energy current that grows unimpeded by interparticle collisions as the total momentum is conserved. The thermal conductivity is therefore limited by the rate at which momentum is relaxed by residual impurities.

Realization of the DF in graphene requires that the thermal energy be larger than the local chemical potential $\mu(\mathbf{r})$, defined at position \mathbf{r} : $k_B T \gtrsim |\mu(\mathbf{r})|$. Impurities cause spatial variations in the local chemical potential, and even when the sample is globally neutral, it is locally doped to form electron-hole puddles with finite $\mu(\mathbf{r})$ (27–30). At high temperatures, formation of the DF is complicated by phonon scattering, which can relax momentum by creating additional inelastic scattering channels. This high-temperature limit occurs when the electron-phonon scattering rate becomes comparable to the electron-electron scattering rate. These two temperatures set the experimental window in which the DF and the breakdown of the WF law can be observed.

To minimize disorder, we used monolayer graphene samples encapsulated in hexagonal boron nitride (31). All devices used in this study have two terminals, so as to keep a well-defined temperature profile (32), with contacts fabricated using the one-dimensional edge technique (33) to minimize contact resistance. We employed a back-gate voltage V_g applied to the silicon substrate to tune

the charge carrier density $n = n_e - n_h$, where n_e and n_h are the electron and hole densities, respectively (21). All measurements were performed in a cryostat to control the bath temperature T_{bath} . Figure 1A shows the resistance R versus V_g measured at various fixed temperatures for a representative device [see (21) for all samples]. From this, we used the known sample dimensions to estimate the electrical conductivity σ (Fig. 1B). At the CNP, the residual charge carrier density n_{min} can be estimated by extrapolating a linear fit of $\log(\sigma)$ as a function of $\log(n)$ out to the minimum conductivity (34). At the lowest temperatures, n_{min} saturates to $\sim 8 \times 10^9 \text{ cm}^{-2}$. Extraction of n_{min} by this method prompts overestimation of the charge-puddle energy, consistent with previous reports (31). Above the disorder temperature scale $T_{\text{dis}} \sim 40$ K, n_{min} increases as T_{bath} is raised, which suggests that thermal excitations begin to dominate and the sample enters the nondegenerate regime near the CNP.

Electronic thermal conductivity was measured using high-sensitivity Johnson noise thermometry (JNT) (32, 35). We applied a small bias current through the sample, thus injecting a Joule heating power P directly into the electronic system and inducing a small difference between the temperature of the graphene electrons and that of the bath: $\Delta T = T_e - T_{\text{bath}}$. The electron temperature

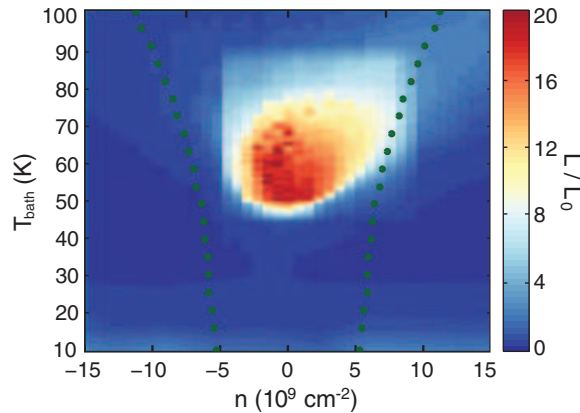
T_e was monitored independently of the lattice temperature through the Johnson noise power emitted at 100 MHz, with a 20-MHz bandwidth defined by an inductor-capacitor matching network. We designed our JNT setup to be operated over a wide temperature range, from 3 to 300 K (35). With a precision of ~ 10 mK, we measured small deviations of T_e from T_{bath} (i.e., $\Delta T \ll T_{\text{bath}}$). In this limit, the temperature of the graphene lattice is well thermalized to the bath (32), and our JNT setup allows us to sensitively measure the electronic cooling pathways in graphene. When the temperature is low enough, electron and lattice interactions are weak (35, 36), and most of the Joule heat generated in graphene escapes via direct diffusion to the contacts (21). As the temperature increases, electron-phonon scattering becomes appreciable, and thermal transport becomes limited by the electron-phonon coupling strength (36–38). The onset temperature of appreciable electron-phonon scattering, $T_{\text{el-ph}}$, depends on the sample disorder and device geometry: $T_{\text{el-ph}} \sim 80$ K (35, 36, 39, 40) for our samples. Below this temperature, the electronic contribution of the thermal conductivity can be obtained from P and ΔT using the device dimensions (21).

Figure 1C shows $\kappa_e(V_g)$ plotted alongside the simultaneously measured $\sigma(V_g)$ at various fixed bath temperatures. Here, for a direct quantitative comparison based on the WF law, we plot the scaled electrical conductivity as $\sigma T L_0$ in the same units as κ_e . In a FL, these two values will coincide, in accordance with Eq. 1. At low temperatures ($T < T_{\text{dis}} \sim 40$ K), where the puddle-induced density fluctuations dominate, we find that $\kappa_e \approx \sigma T L_0$, monotonically increasing as a function of carrier density with a minimum at the neutrality point, confirming the WF law in the disordered regime. As T increases ($T > T_{\text{dis}}$), however, we begin to observe violation of the WF law. This violation appears only close to the CNP, with the measured thermal conductivity maximized at $n = 0$ (Fig. 1C). The deviation is the largest at 75 K, where κ_e is more than an order of magnitude larger than the value expected for a FL. The nonmonotonicity of $\kappa_e(T)$ is consistent with acoustic phonons relaxing momentum more efficiently than impurities as T increases (41). For $T \gtrsim 100$ K in our samples, activation of optical phonons introduces an additional electron-phonon cooling pathway (35), and the measured thermal conductivity is larger than κ_e . This non-FL behavior quickly disappears as $|n|$ increases; κ_e returns to the FL value and restores the WF law. In fact, away from the CNP, the WF law holds for a wide temperature range, consistent with previous reports (35, 36, 39) (Fig. 1E). For this FL regime, we verify the WF law up to $T \sim 80$ K.

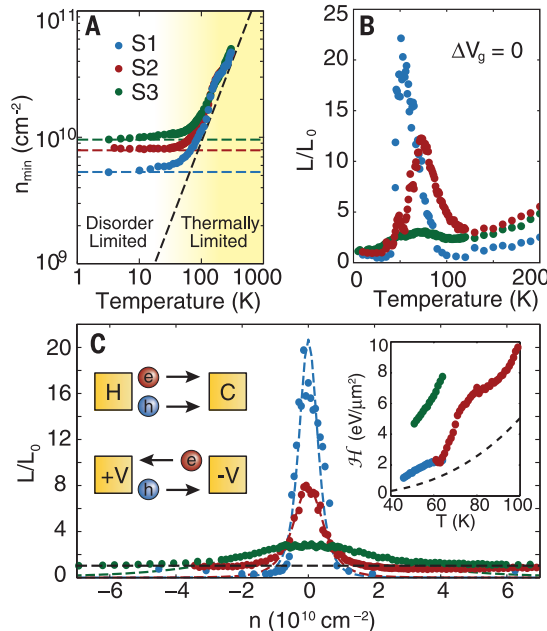
Our observation of the breakdown of the WF law in graphene is consistent with the emergence of the DF. Figure 2 shows the full density and temperature dependence of the experimentally measured Lorenz ratio, highlighting the presence of the DF. The blue region denotes $L \sim L_0$, suggesting that the carriers in graphene exhibit FL behavior. The WF law is violated in the DF (yellow-red region), with a peak Lorenz ratio 22 times larger than L_0 . The green dotted

Fig. 2. Breakdown of the WF law in the DF regime.

The Lorenz ratio is shown as a function of the charge carrier density and bath temperature. Near the CNP and for temperatures above the disorder (charge puddle) regime but below the onset of electron-phonon coupling, the Lorenz ratio is measured to be an order of magnitude greater than the FL value of 1 (blue). The WF law is observed to hold outside of the DF regime. All data from this figure are taken from sample S1. Green dotted lines show the corresponding $n_{\min}(T)$ for this sample.

**Fig. 3. Disorder in the DF.**

Minimum carrier density as a function of temperature for all three samples. At low temperatures, each sample is limited by disorder. At high temperatures, all samples become limited by thermal excitations. Dashed lines are a guide for the eye. **(B)** Lorentz ratio of all three samples as a function of bath temperature. The largest WF violation is seen in the cleanest sample. **(C)** The gate dependence of the Lorenz ratio is well fit to the hydrodynamic theory of (5, 6). Fits of all three samples are shown at 60 K. All samples return to the FL value (black dashed line) at high density. The inset graph shows the fitted enthalpy density as a function of temperature and the theoretical value in clean graphene (black dashed line). The schematic inset illustrates the difference between heat and charge current in the neutral Dirac plasma.



lines show the corresponding $n_{\min}(T)$ for this sample; the DF is found within this regime, indicating the coexistence of thermally populated electrons and holes. Disorder and electron-phonon scattering serve as lower and upper limits, respectively, on the temperature range over which the DF can be observed.

We investigate the effect of impurities on hydrodynamic transport by comparing the results obtained from samples with varying disorder. Figure 3A shows n_{\min} as a function of temperature for three samples used in this study. $n_{\min}(T = 0)$ is estimated as 5×10^9 , 8×10^9 , and $10 \times 10^9 \text{ cm}^{-2}$, respectively, in samples S1, S2, and S3. All devices show qualitatively similar DF behavior: For samples S1, S2, and S3, the largest values of $\mathcal{L}/\mathcal{L}_0$ measured in the DF regime are 22, 12, and 3, respectively (Fig. 3B). Cleaner samples not only have a more pronounced peak but also have a narrower density dependence (Fig. 3C), as predicted (5, 6).

More quantitative analysis of $\mathcal{L}(n)$ in our experiment can be performed by employing a quasi-

relativistic hydrodynamic theory of the DF, incorporating the effects of weak impurity scattering (5, 6, 18)

$$\mathcal{L} = \frac{\mathcal{L}_{\text{DF}}}{[1 + (n/n_0)^2]^2} \quad (2)$$

where

$$\mathcal{L}_{\text{DF}} = \frac{\mathcal{H} v_F l_m}{T^2 \sigma_{\min}} \quad (3)$$

and

$$n_0^2 = \frac{\mathcal{H} \sigma_{\min}}{e^2 v_F l_m} \quad (4)$$

Here, v_F is the Fermi velocity in graphene, σ_{\min} is the electrical conductivity at the CNP, \mathcal{H} is the fluid enthalpy density, l_m is the momentum relaxation length from impurities, and n_0 is the density scale over which \mathcal{L} varies appreciably. Two parameters in Eq. 2, l_m and \mathcal{H} , are undeter-

mined for any given sample. For simplicity, we assume that we are well within the DF limit, where l_m and \mathcal{H} are approximately independent of n . We fit Eq. 2 to the experimentally measured $\mathcal{L}(n)$ for all temperatures and densities in the DF regime to obtain l_m and \mathcal{H} for each sample (Fig. 3C). l_m is estimated to be 1.5, 0.6, and $0.034 \mu\text{m}$ for samples S1, S2, and S3, respectively. For the system to be well described by hydrodynamics, l_m should be long compared with the electron-electron scattering length of $\sim 0.1 \mu\text{m}$ that is expected for the DF at 60 K (19). This is consistent with the pronounced signatures of hydrodynamics in S1 and S2, but not in S3, where only a glimpse of the DF appears in this more disordered sample. We also observe in S1 that $\mathcal{L}(n)$ dips substantially below \mathcal{L}_0 : its minimum is $\sim \mathcal{L}_0/3$. $\mathcal{L} < 1$ occurs in Eq. 2 for $n \gg n_0$. The inset to Fig. 3C shows the fitted enthalpy density as a function of temperature compared with that expected in clean graphene (dashed line) (19), excluding renormalization of the Fermi velocity. In the cleanest sample, \mathcal{H} varies from 1.1 to $2.3 \text{ eV}/\mu\text{m}^2$ in the hydrodynamic regime. This enthalpy density corresponds to $\sim 20 \text{ meV}$ or $\sim 4 k_B T$ per charge carrier—about a factor of 2 larger than the model calculation without disorder (19). The sharp temperature and impurity dependence observed in \mathcal{L} is a prediction of these hydrodynamic models. These effects and the magnitude of \mathcal{L} are inconsistent with alternative models for WF violations, including bipolar diffusion in graphene (21, 42). Furthermore, recent experiments report monotonic behavior in thermopower as a function of T (43), implying that phonon drag is not responsible for the peak in κ_e that we observe as a function of T .

To fully incorporate the effects of disorder, a hydrodynamic theory that treats inhomogeneity nonperturbatively is necessary (41, 44). The enthalpy densities reported here are larger than the theoretical estimation obtained for disorder-free graphene, consistent with the picture that chemical potential fluctuations prevent the sample from reaching the Dirac point. Although we find thermal conductivity well described by (5, 6), electrical conductivity increases more slowly than expected away from the CNP, a result consistent with hydrodynamic transport in a viscous fluid with charge puddles (41).

In a hydrodynamic system, the ratio of shear viscosity η to entropy density s is an indicator of the strength of the interactions between constituent particles. It has been suggested that the DF can behave as a nearly perfect fluid (19): η/s approaches Kovtun *et al.*'s conjecture that $(\eta/s)/(\hbar/k_B) \geq 1/4\pi$ (where \hbar is Planck's constant divided by 2π) for a strongly interacting system (45). A nonperturbative hydrodynamic framework can be employed to estimate η (41). A direct measurement of η is of great interest.

Beyond a diverging thermal conductivity and an ultralow viscosity, other peculiar phenomena are expected to arise in this plasma. The massless nature of the Dirac fermions is expected to result in a large kinematic viscosity, despite a small shear viscosity η . Observable hydrodynamic effects have

also been predicted to extend into the FL regime (46). The study of magnetotransport in the DF will lead to further tests of hydrodynamics (5, 18).

REFERENCES AND NOTES

- L. P. Kadanoff, P. C. Martin, *Ann. Phys.* **24**, 419–469 (1963).
- M. J. M. de Jong, L. W. Molenkamp, *Phys. Rev. B* **51**, 13389–13402 (1995).
- C. Cao *et al.*, *Science* **331**, 58–61 (2011).
- E. Shuryak, *Prog. Part. Nucl. Phys.* **53**, 273–303 (2004).
- M. Müller, L. Fritz, S. Sachdev, *Phys. Rev. B* **78**, 115406 (2008).
- M. Foster, I. Aleiner, *Phys. Rev. B* **79**, 085415 (2009).
- S. S. Apostolov, A. Levchenko, A. V. Andreev, *Phys. Rev. B* **89**, 121104 (2014).
- B. Narozhny, I. Gornyi, M. Titov, M. Schütt, A. Mirlin, *Phys. Rev. B* **91**, 035414 (2015).
- K. S. Novoselov *et al.*, *Nature* **438**, 197–200 (2005).
- Y. Zhang, Y. W. Tan, H. L. Stormer, P. Kim, *Nature* **438**, 201–204 (2005).
- D. A. Siegel, W. Regan, A. V. Fedorov, A. Zettl, A. Lanzara, *Phys. Rev. Lett.* **110**, 146802 (2013).
- D. E. Sheehy, J. Schmalian, *Phys. Rev. Lett.* **99**, 226803 (2007).
- S. Sachdev, B. Keimer, *Phys. Today* **64**, 29 (2011).
- C. H. Lui, K. F. Mak, J. Shan, T. F. Heinz, *Phys. Rev. Lett.* **105**, 127404 (2010).
- M. Breusing, C. Ropers, T. Elsaesser, *Phys. Rev. Lett.* **102**, 086809 (2009).
- K. J. Tielrooij *et al.*, *Nat. Phys.* **9**, 248–252 (2013).
- J. C. Johannsen *et al.*, *Phys. Rev. Lett.* **111**, 027403 (2013).
- S. A. Hartnoll, P. Kovtun, M. Müller, S. Sachdev, *Phys. Rev. B* **76**, 144502 (2007).
- M. Müller, J. Schmalian, L. Fritz, *Phys. Rev. Lett.* **103**, 025301 (2009).
- N. W. Ashcroft, N. D. Mermin, *Solid State Physics* (Brooks Cole, ed. 1, 1976).
- Materials and methods are available as supplementary materials on Science Online.
- N. Wakeham *et al.*, *Nat. Commun.* **2**, 396 (2011).
- R. P. Smith *et al.*, *Nature* **455**, 1220–1223 (2008).
- M. A. Tanatar, J. Paglione, C. Petrovic, L. Taillefer, *Science* **316**, 1320–1322 (2007).
- R. W. Hill, C. Proust, L. Taillefer, P. Fournier, R. L. Greene, *Nature* **414**, 711–715 (2001).
- L. Fritz, J. Schmalian, M. Müller, S. Sachdev, *Phys. Rev. B* **78**, 085416 (2008).
- S. Adam, E. H. Hwang, V. M. Galitski, S. Das Sarma, *Proc. Natl. Acad. Sci. U.S.A.* **104**, 18392–18397 (2007).
- J. Martin *et al.*, *Nat. Phys.* **4**, 144–148 (2008).
- Y. Zhang, V. W. Brar, C. Girit, A. Zettl, M. F. Crommie, *Nat. Phys.* **5**, 722–726 (2009).
- J. Xue *et al.*, *Nat. Mater.* **10**, 282–285 (2011).
- C. R. Dean *et al.*, *Nat. Nanotechnol.* **5**, 722–726 (2010).
- K. C. Fong, K. C. Schwab, *Phys. Rev. X* **2**, 031006 (2012).
- L. Wang *et al.*, *Science* **342**, 614–617 (2013).
- N. J. G. Couto *et al.*, *Phys. Rev. X* **4**, 041019 (2014).
- J. Crossno, X. Liu, T. A. Ohki, P. Kim, K. C. Fong, *Appl. Phys. Lett.* **106**, 023121 (2015).
- K. C. Fong *et al.*, *Phys. Rev. X* **3**, 041008 (2013).
- A. C. Betz *et al.*, *Phys. Rev. Lett.* **109**, 056805 (2012).
- C. B. McKitterick, D. E. Prober, M. J. Rooks, *Phys. Rev. B* **93**, 075410 (2016).
- S. Yiğen, A. R. Champagne, *Nano Lett.* **14**, 289–293 (2014).
- A. Laitinen *et al.*, *Nano Lett.* **14**, 3009–3013 (2014).
- A. Lucas, J. Crossno, K. C. Fong, P. Kim, S. Sachdev, *Phys. Rev. B* **93**, 075426 (2016).
- H. Yoshino, K. Murata, *J. Phys. Soc. Jpn.* **84**, 024601 (2015).
- F. Ghahari *et al.*, <http://arxiv.org/abs/1601.05859> (2016).
- A. Lucas, *New J. Phys.* **17**, 113007 (2015).
- P. K. Kovtun, D. T. Son, A. O. Starinets, *Phys. Rev. Lett.* **94**, 111601 (2005).
- A. Principi, G. Vignale, M. Carrega, M. Polini, <http://arxiv.org/abs/1506.06030> (2015).

ACKNOWLEDGMENTS

We thank M. Foster, D. Efetov, and G.-H. Lee for helpful discussions. The major experimental work at Harvard University is supported by the U.S. Department of Energy (grant DE-SC0012260) and at Raytheon BBN Technologies by Internal Research and Development. J.C. acknowledges support from the Function Accelerated nanoMaterial Engineering (FAME) Center, sponsored by Semiconductor Research Corporation MARCO and Defense Advanced Research Projects Agency. K.W. is supported by Army Research Office (ARO) Multidisciplinary University Research Initiative (MURI) (grant W911NF-14-1-0247). J.K.S. is supported by ARO (grant W911NF-14-1-0638) and the Agency for Science, Technology and Research (A*STAR). P.K. acknowledges partial support from the Gordon and Betty Moore Foundation's EPIQS Initiative (grant GBMF4543) and the Nano Material Technology Development Program through the National Research Foundation of Korea (grant 2012M3A7B4049966). A.L. and S.S. are supported by the NSF under grant DMR-1360789, the Templeton Foundation, and MURI grant W911NF-14-1-0003 from ARO. Research at the Perimeter Institute for Theoretical Physics is supported by the Government of Canada through Industry Canada and by the Province of Ontario through the Ministry of Research and Innovation. K.W. and T.T. acknowledge support

from the Elemental Strategy Initiative conducted by the Ministry of Education, Culture, Sports, Science and Technology, Japan. T.T. acknowledges support from a Grant-in-Aid for Scientific Research (grant 262480621) and a grant on Innovative Areas "Nano Informatics" (grant 25106006) from the Japan Society for the Promotion of Science. T.A.O. and K.C.F. acknowledge support from Raytheon BBN Technologies. This work was performed, in part, at the Center for Nanoscale Systems (CNS), a member of the National Nanotechnology Infrastructure Network, which is supported by the NSF under award no. ECS-0335765. CNS is part of Harvard University.

SUPPLEMENTARY MATERIALS

www.sciencemag.org/content/351/6277/1058/suppl/DC1
Materials and Methods
Figs. S1 to S8
Table S1
References (47–59)

16 July 2015; accepted 6 January 2016
Published online 11 February 2016
10.1126/science.aad0343

ELECTRON TRANSPORT

Evidence for hydrodynamic electron flow in PdCoO₂

Philip J. W. Moll,^{1,2,3} Pallavi Kushwaha,³ Nabhanila Nandi,³ Burkhard Schmidt,³ Andrew P. Mackenzie^{3,4,*}

Electron transport is conventionally determined by the momentum-relaxing scattering of electrons by the host solid and its excitations. Hydrodynamic fluid flow through channels, in contrast, is determined partly by the viscosity of the fluid, which is governed by momentum-conserving internal collisions. A long-standing question in the physics of solids has been whether the viscosity of the electron fluid plays an observable role in determining the resistance. We report experimental evidence that the resistance of restricted channels of the ultrapure two-dimensional metal palladium cobaltate (PdCoO₂) has a large viscous contribution. Comparison with theory allows an estimate of the electronic viscosity in the range between $6 \times 10^{-3} \text{ kg m}^{-1} \text{ s}^{-1}$ and $3 \times 10^{-4} \text{ kg m}^{-1} \text{ s}^{-1}$, versus $1 \times 10^{-3} \text{ kg m}^{-1} \text{ s}^{-1}$ for water at room temperature.

In a quantum fluid without an associated lattice, such as ³He, the momentum of the fluid is conserved except where it interacts with the walls of a channel through which it is flowing. As the temperature decreases and the quasiparticle-quasiparticle mean free path ℓ within the fluid increases (because of the decrease of its quasiparticle scattering rate), interactions with the walls become more probable and the viscosity and flow resistance increase. This is intuitively at odds with the behavior seen for electrons moving in a crystalline lattice, whose flow resistance decreases as ℓ increases. The resolution of this apparent paradox is that coupling to the lattice and its excitations means that the large majority of col-

lisions in the electron fluid (electron-impurity, normal electron-phonon, Umklapp electron-electron, and Umklapp electron-phonon) relax momentum, taking the fluid far from the hydrodynamic limit. At least some of these momentum-relaxing collisions are inevitable in any real material. Strictly speaking, momentum of the electron fluid can never be conserved, even in a bulk sample for which boundary scattering is negligible. However, this does not mean that the electronic viscosity plays no role in determining electrical resistance. A pragmatic benchmark is whether momentum-conserving processes are faster or slower than momentum-relaxing ones. If the electron fluid's momentum is relaxed slowly, it can be thought of as being quasi-conserved, and hydrodynamic signatures might be observable (1–9).

The search for hydrodynamic effects in electrons in solids has been given extra impetus by the introduction of the "holographic correspondence" to condensed matter physics (10). This technique introduced the concept of a minimum viscosity, argued to be applicable to strongly

¹Laboratory for Solid State Physics, ETH Zürich, CH-8093 Zürich, Switzerland. ²Department of Physics, University of California, Berkeley, CA 94720, USA. ³Max Planck Institute for Chemical Physics of Solids, 01187 Dresden, Germany. ⁴Scottish Universities Physics Alliance, School of Physics and Astronomy, University of St. Andrews, St. Andrews KY16 9SS, UK.

*Corresponding author. E-mail: andy.mackenzie@cpfs.mpg.de

Fig. 1. FIB-prepared devices of PdCoO₂ crystals. (A) The crystal used for our channel-thinning experiment, after the first two processing steps. An initial channel 120 μm wide has been reprocessed to produce a narrower conducting channel of width 60 μm . The same channel was subsequently reprocessed seven further times, narrowing it by approximately half each time, until it was 0.7 μm wide. (B) A meander channel processed in a second crystal for use in a search for the Shubnikov–de Haas effect. Its approximate width is 6 μm in the narrowed parts; thickness is 17 μm . Its resistance in a magnetic field of 14 T at a temperature of 2 K is 5.7×10^{-3} ohms.

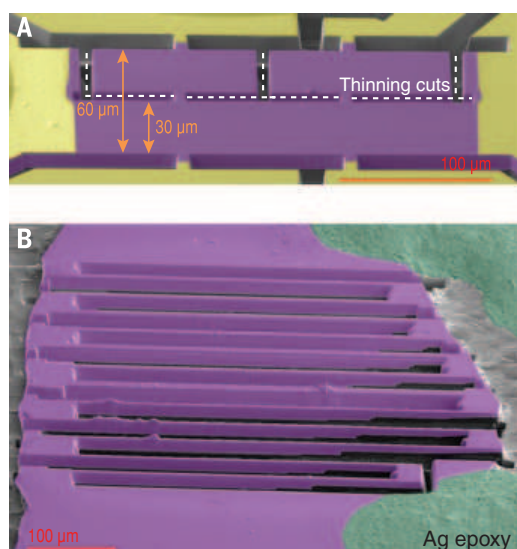
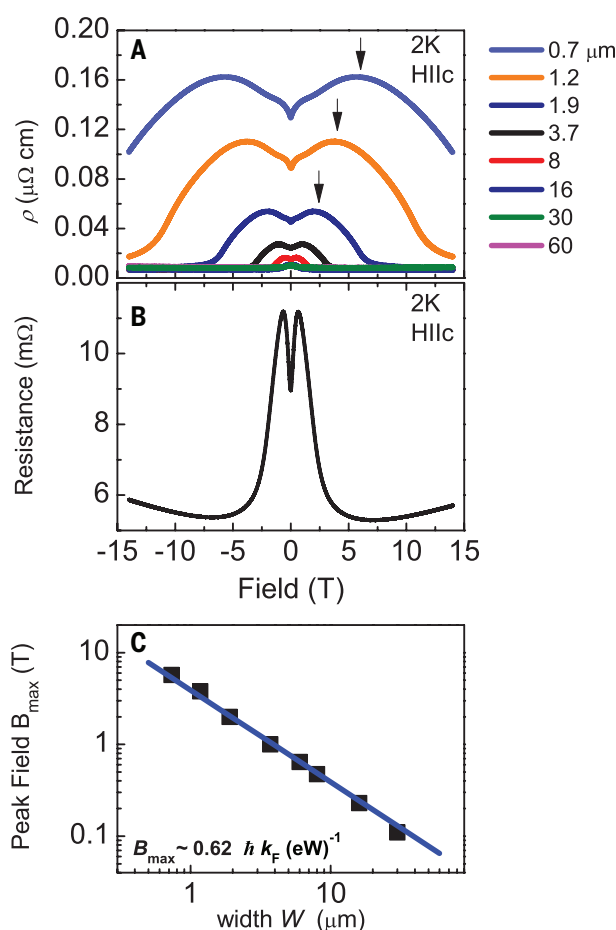


Fig. 2. Effect of channel width W on magnetotransport. (A) Magnetoresistance data from the sample shown in Fig. 1A taken at 2 K after successive channel-thinning steps. (B) Magnetoresistance data from the sample shown in Fig. 1B taken at 2 K. (C) B_{max} [indicated by arrows in (A)] varies as $\alpha(\hbar k_F/We)$ as the device shown in Fig. 1A is successively thinned. Both the functional form and prefactor are in good agreement with theory and with previous measurements on semiconductor wires.



interacting fluids as diverse as the quark-gluon plasma and cold atomic gases (21). Hydrodynamic effects have also been postulated to be at the root of the temperature-linear resistivity of the high-temperature superconductors (6, 7), but because momentum-relaxing scattering is strong in those materials, it is difficult to perform an analysis of the experimental data

that unambiguously separates the two effects. In a pioneering experiment, unusual current-voltage relationships in a semiconductor wire were convincingly ascribed to hydrodynamic effects (3), but that avenue of research has not been widely pursued, even though the large difference between transport and electron-electron scattering rates in semiconductors was later

demonstrated by direct nonequilibrium measurements (12).

To investigate whether a hydrodynamic contribution to electrical transport can be clearly separated from the more standard contributions from momentum-relaxing processes, we sought a material in which momentum-relaxing scattering is anomalously suppressed. The material that we chose was PdCoO₂, a layered metal with a number of unusual properties (13–21). Its electronic structure is deceptively simple, with one highly dispersive band, dominantly of Pd 4d/5s character, crossing the Fermi level (22–26). Its Fermi volume corresponds to one electron per formula unit to high accuracy (18), and the ratio of in-plane to out-of-plane resistivity is approximately 10^3 , justifying the use of a two-dimensional approximation in treating the in-plane properties.

The electrical conductivity of PdCoO₂ is remarkable. At room temperature, its resistivity is just 2.6×10^{-6} ohm-cm, 30% lower per carrier than that of elemental copper. Below 15 K, the resistivity is essentially independent of temperature; in the best single crystals, the resistivity is below 1×10^{-8} ohm-cm (18). This striking behavior might be attributable to phonon drag, in which the phonons follow the electrons into an out-of-equilibrium distribution when an electric field is applied. In PdCoO₂, the activation temperature for Umklapp electron-phonon processes is at least 160 K, unusually high for a metal (18).

These properties make PdCoO₂ a good candidate for a search for hydrodynamic effects. Below 15 K, momentum-relaxing processes are far slower than those observed in most metals. Better still, if phonon drag is indeed taking place, the normal electron-phonon processes that usually impede electrons in solids from approaching the hydrodynamic limit are now helping that process instead, because they contribute a source of momentum-conserving scattering. An important independent hint that the balance between momentum-conserving and momentum-relaxing scattering is both unusual and favorable for the observation of hydrodynamic effects comes from the ratio of the mean free paths deduced, respectively, from the resistivity, which is sensitive to processes that efficiently relax momentum, and from analysis of the de Haas–van Alphen (dHvA) effect, whose amplitude is sensitive to a wider range of scattering processes. The inverse of that ratio is 5 to 10%, an unusually small value approximately an order of magnitude lower than that seen in ordinary metals (18).

In a purely hydrodynamic fluid, flow resistance in channels is determined entirely by momentum-relaxing boundary scattering, the efficiency of which is determined by the fluid's viscosity. Boundary scattering also contributes to the resistance in thin wires or channels of metals in which hydrodynamic effects play no observable role, but the standard theory of this phenomenon is well established (27). We therefore set out to construct a series of PdCoO₂ “wires,” study how their resistance varied with the channel width, and investigate whether there were observable deviations

from the predictions of standard theory. The wires were produced from flux-grown single crystals by focused ion beam (FIB) etching (Fig. 1A). Six such devices were made and shown to have consistent properties (28). We discuss the nature of the boundaries produced by FIB processing in (28) and show that damage is restricted to approximately 20 nm from the edge of the channel. Taking all uncertainties into account, the undamaged channel width can be determined to an accuracy of ± 80 nm. For the main experiment, measurements were done on a single successively etched wire from the same crystal, to remove as many experimental uncertainties as possible. A second crystal (Fig. 1B) was etched into a meander channel ideally suited for a measurement of the Shubnikov–de Haas (SdH) effect. For each experiment, we studied the magnetoresistance of the wire in magnetic fields B ranging from -14 T to $+14$ T. We also fabricated a multicontact device to verify that our data are length-independent at constant width (28).

Data obtained in the channel-narrowing experiment are shown in Fig. 2A for widths ranging from $60\text{ }\mu\text{m}$ to $0.7\text{ }\mu\text{m}$ at a measurement temperature of 2 K . Data from the meander channel are shown in Fig. 2B. Consistent with previous measurements on other single crystals (18), the resistivity in zero field for the $60\text{-}\mu\text{m}$ sample is $9 \times 10^{-9}\text{ ohm-cm}$. The value of the momentum-relaxing mean free path ℓ_{MR} is a crucial parameter in the analysis of the resistance of restricted channels; the single-band electronic structure and well-known Fermi surface shape and volume (16, 18) allow an accurate calculation of $\ell_{\text{MR}} = 18.5 \pm 1.5\text{ }\mu\text{m}$ (28). The wire widths W used for the experiment therefore cover the range $0.3 \leq \ell_{\text{MR}}/W \leq 26$, enabling study of the crossover between a nearly bulk regime and one in which a sample dimension falls far below the bulk mean free path.

We adopt the usual solid-state physics convention of describing the transport properties of our channels in terms of the resistivity ρ . For a channel of width W , length L , thickness T , and resistance R , $\rho \equiv RTW/L$. Conceptually, ρ is a bulk property of the material, so in the absence of boundary effects it should be independent of W . In contrast, at low fields, the overall channel resistivity ρ increases by more than an order of magnitude as the wire width is decreased (Fig. 2). Because this involves repeated exposure to ion beam etching, it is natural to wonder whether this trend is caused by beam damage increasing the scattering in the bulk of the wire. However, extending the data to higher fields proves that this is not the case. First, we note that at high fields, the resistivity is similar at all widths above $0.7\text{ }\mu\text{m}$. Second, the pronounced maximum seen at fields B_{max} in the magnetoresistance for $W \leq 30\text{ }\mu\text{m}$ is a well-known phenomenon from the study of narrow conducting channels for which the bulk mean free path is on the order of the channel width or larger (29–31). For each channel width, the rise in the magnetoresistivity at low fields is stopped when the cyclotron orbit radius falls to less than the channel width, be-

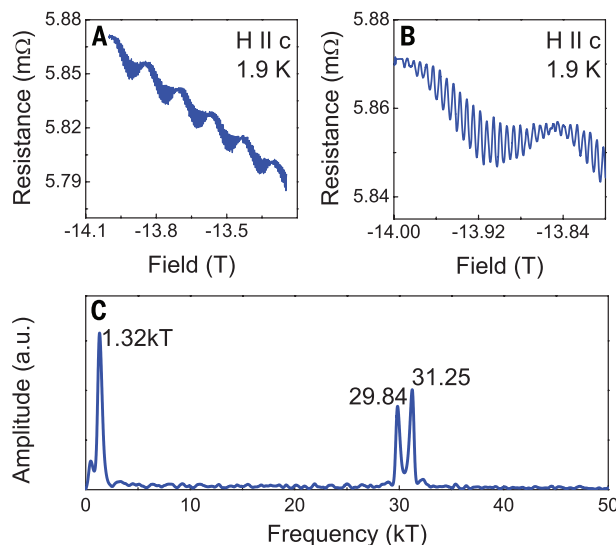


Fig. 3. Shubnikov–de Haas oscillations. (A and B) SdH oscillations from the patterned meander track shown in Fig. 1B. (C) The frequencies of the SdH oscillations extracted by Fourier analysis of the data in (A).

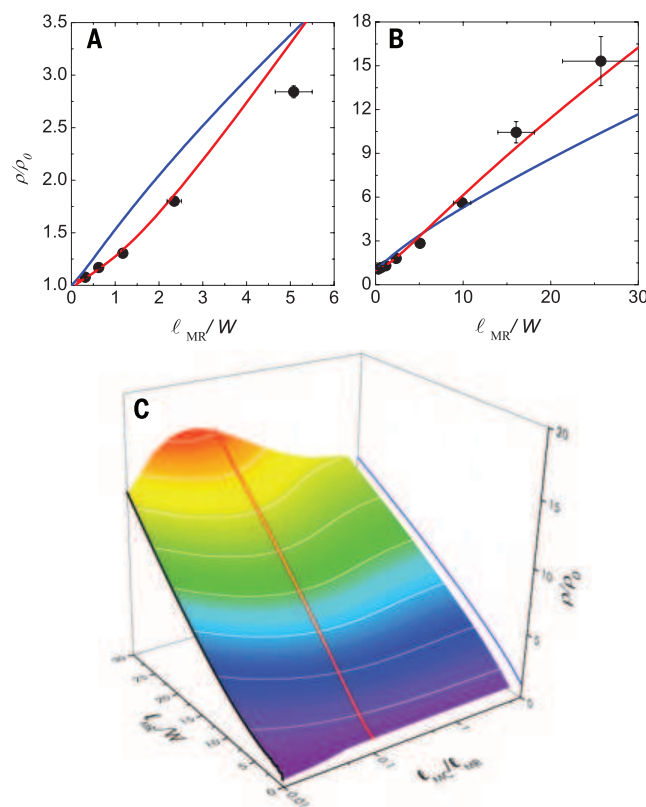


Fig. 4. Hydrodynamic effect on transport.

(A and B) The measured resistivity of PdCoO_2 channels normalized to that of the widest channel (ρ_0), plotted against the inverse channel width $1/W$ multiplied by the bulk momentum-relaxing mean free path ℓ_{MR} (solid black circles). Blue solid line: Prediction of a standard Boltzmann theory including boundary scattering but neglecting momentum-conserving collisions. Red line: Prediction of a model that includes the effects of momentum-conserving scattering (see text). Error bars stem from uncertainties of sample dimension (28). (C) Predictions of the hydrodynamic theory over a wide range of parameter space.

cause the helical pitch of the motion of the drifting electrons becomes so tight that boundary scattering is suppressed, and eventually the bulk, width-independent resistivity is recovered at high fields. Specifically, $B_{\text{max}} = \alpha(\hbar k_F / We)$ (where \hbar is Planck's constant divided by 2π , k_F is the Fermi wave vector, and e is the electronic charge) with constant $\alpha = 0.55$ has been reported for restricted channels of two-dimensional electron gas (30), and a similar functional form with $\alpha = 0.9$ was observed in recent work on graphene

(31). The data shown in Fig. 2C therefore provide further evidence that the overall scale of the resistivity is increasing because of additional boundary scattering rather than additional bulk scattering. Very low field peaks in the magnetoresistance can still be seen in the $30\text{-}\mu\text{m}$ channel, providing further direct geometrical evidence that ℓ_{MR} is long. Further evidence that extremely high bulk purity is retained after ion beam etching comes from the data from the meander sample. Its B_{max} is consistent with the

measured width of 6 μm (Fig. 2, B and C), and at high fields, clear SdH oscillations are seen, with frequencies in agreement with those seen in dHvA oscillations from bulk crystals (18). High frequencies are particularly hard to see by the SdH effect; the 30-KT frequencies shown in Fig. 3B are among the highest ever reported in SdH measurements.

The data presented in Figs. 2 and 3 provide strong evidence that boundary rather than bulk scattering dominates the rise in resistivity seen as we reduce the channel width. As discussed above, boundary scattering is expected even in the absence of hydrodynamic effects as the channel width falls to less than the mean free path and the system enters the ballistic transport regime. The relevant theory (4, 27) can be expressed in a useful dimensionless form, shown as a blue line in Fig. 4. If ρ is normalized to the bulk resistivity ρ_0 of an infinitely wide sample and plotted against ℓ_{MR}/W , the prediction has no free parameters. At $\ell_{\text{MR}}/W = 25$, ρ is calculated to be $10.3 \rho_0$. Our measured value for ρ/ρ_0 is more than 50% larger than this prediction, and our data also show a functional form that is at odds with the simple theory.

To examine whether the large deviations of the data from the predictions of standard transport theory are linked to electronic hydrodynamics, we carefully studied the predictions of a more sophisticated theory that takes momentum-conserving scattering into account (4). Originally formulated to analyze the current-dependent hydrodynamic signatures reported in (3), the theory encodes momentum-relaxing scattering via the role of impurities and momentum-conserving scattering via normal electron-electron scattering processes. In PdCoO_2 , the scale of momentum-conserving electron-electron scattering is uncertain because of Fermi surface faceting (26), and phonons dragged out of equilibrium are also likely to be making a contribution to the momentum-conserving processes. In this sense, even this more sophisticated theory is oversimplified, and it would be dangerous to use it to predict temperature-dependent transport in PdCoO_2 . However, its results at any fixed temperature depend only on the ratio of a momentum-conserving mean free path ℓ_{MC} to the momentum-relaxing mean free path ℓ_{MR} , and the microscopic origin of the scattering that produced that ratio is not relevant. The theory is therefore a useful guide to the consequences of including hydrodynamic effects in experiments performed at constant temperature, such as the one shown in Fig. 4, A and B. For any value of $\ell_{\text{MC}}/\ell_{\text{MR}}$, it predicts a unique functional form and overall magnitude for ρ/ρ_0 versus ℓ_{MR}/W , with no free fitting parameters.

As can be seen from the red lines in Fig. 4, A and B, the hydrodynamic theory for $\ell_{\text{MC}}/\ell_{\text{MR}} = 0.1$ produces an excellent match to our data. In Fig. 4C we show how the predictions of the theory change as a function of $\ell_{\text{MC}}/\ell_{\text{MR}}$, marking the blue and red lines of Fig. 4, A and B, on the contour plot for reference. For large $\ell_{\text{MC}}/\ell_{\text{MR}}$ (i.e., weak momentum-conserving scattering), it limits rapidly to the

prediction of the standard theory. At its other limit of strong momentum-conserving scattering (black line), the prediction for ρ/ρ_0 is approximately quadratic as a function of ℓ_{MR}/W . In this regime, viscous effects dominate, and the W^{-2} dependence of ρ is equivalent to the W^{-3} prediction for flow resistance that is obtained from the purely hydrodynamic Navier-Stokes equation (28).

Our value for $\ell_{\text{MC}}/\ell_{\text{MR}}$ (red line in Fig. 4C) sits between these limiting cases. Because viscosity is inversely proportional to ℓ_{MC} , the initial $\sim W^{-2}$ rise is steeper than for $\ell_{\text{MC}}/\ell_{\text{MR}} = 0.01$. As ℓ_{MR}/W rises toward 10, ℓ_{MC} is no longer much less than W , and the Navier-Stokes prediction evolves smoothly to a solution in which viscous effects are important but the channel constriction is such that we leave the purely hydrodynamic regime. Physically the system is in a hybrid situation in which traditional impurity and boundary scattering mix with viscosity-stimulated boundary scattering to produce the overall evolution of resistivity with channel width. Fig. 4C also shows that the hydrodynamic prediction is insensitive to the precise choice of $\ell_{\text{MC}}/\ell_{\text{MR}}$. Our choice of 0.1 was not the result of fitting, but simply an estimate motivated by the ratio of scattering rates deduced from measurements of resistivity and the dHvA effect. Choices that were larger or smaller by a factor of 2 would give a similar level of agreement with the data.

The data and predictions shown in Fig. 4 and discussed in (28) provide strong evidence that we have observed a substantial hydrodynamic contribution to electrical transport in a bulk material. Further analysis of the theory in its Navier-Stokes limit allows a quantitative estimate of the electronic viscosity itself as a function of the hydrodynamic contribution to ρ/ρ_0 . As a result, we are able to estimate the dynamic viscosity η of the electronic fluid in PdCoO_2 as lying in the range between $6 \times 10^{-3} \text{ kg m}^{-1} \text{ s}^{-1}$ and $3 \times 10^{-4} \text{ kg m}^{-1} \text{ s}^{-1}$. For comparison, the η values of two well-known fluids, water at room temperature and liquid nitrogen at 75 K, are $1 \times 10^{-3} \text{ kg m}^{-1} \text{ s}^{-1}$ and $1 \times 10^{-4} \text{ kg m}^{-1} \text{ s}^{-1}$, respectively.

Although the bounds we can place on the electronic viscosity of PdCoO_2 are not very precise, we stress that this is an issue of theory, not experiment. We believe that there is such a large hydrodynamic contribution to our data that they contain all the information required to estimate the viscosity precisely, and we hope that our experiment motivates further work on this issue. As discussed above, PdCoO_2 is a weakly scattering system, so it is not surprising that a comparison of our estimate of η with measurements of the entropy density s (15, 18) yields $\eta/s \approx 10^6 \hbar/k_B$, far from a proposed minimum viscosity limit (11). It will also be interesting to reexamine a possible role of hydrodynamic effects in explaining the resistivity in systems in which the momentum-conserving scattering is extremely strong (6, 7, 32). In principle, a range of viscosities is to be expected in different electronic fluids, and even the attainment of turbulent electronic flow may be possible.

REFERENCES AND NOTES

1. R. N. Gurzhi, *Zh. Eksp. Teor. Fiz.* **44**, 771 (1963) [*Sov. Phys. Usp.* **17**, 521 (1963)].
2. R. N. Gurzhi, *Usp. Fiziol. Nauk* **94**, 689 (1968) [*Sov. Phys. Usp.* **11**, 255 (1968)].
3. L. W. Molenkamp, M. J. M. de Jong, *Phys. Rev. B* **49**, 5038–5041 (1994).
4. M. J. M. de Jong, L. W. Molenkamp, *Phys. Rev. B* **51**, 13389–13402 (1995).
5. B. Spivak, S. A. Kivelson, *Ann. Phys.* **321**, 2071–2115 (2006).
6. R. A. Davison, K. Schalm, J. Zaanen, *Phys. Rev. B* **89**, 245116 (2014).
7. S. A. Hartnoll, *Nat. Phys.* **11**, 54–61 (2015).
8. A. V. Andreev, S. A. Kivelson, B. Spivak, *Phys. Rev. Lett.* **106**, 256804 (2011).
9. R. Mahajan, M. Barkeshli, S. A. Hartnoll, *Phys. Rev. B* **88**, 125107 (2013).
10. S. A. Hartnoll, P. K. Kovtun, M. Müller, S. Sachdev, *Phys. Rev. B* **76**, 144502 (2007).
11. P. K. Kovtun, D. T. Son, A. O. Starinets, *Phys. Rev. Lett.* **94**, 111601 (2005).
12. C. P. Weber et al., *Nature* **437**, 1330–1333 (2005).
13. R. D. Shannon, D. B. Rogers, C. T. Prewitt, *Inorg. Chem.* **10**, 713–718 (1971).
14. M. Hasegawa, I. Inagawa, M. Tanaka, I. Shirota, H. Takei, *Solid State Commun.* **121**, 203–205 (2002).
15. H. Takatsu et al., *J. Phys. Soc. Jpn.* **76**, 104701 (2007).
16. H.-J. Noh et al., *Phys. Rev. Lett.* **102**, 256404 (2009).
17. H. Takatsu, S. Yonezawa, S. Fujimoto, Y. Maeno, *Phys. Rev. Lett.* **105**, 137201 (2010).
18. C. W. Hicks et al., *Phys. Rev. Lett.* **109**, 116401 (2012).
19. H. Takatsu et al., *Phys. Rev. Lett.* **111**, 056601 (2013).
20. R. Daou, R. Frésard, S. Hébert, A. Maignan, *Phys. Rev. B* **91**, 041113 (2015).
21. N. Kikugawa et al., <http://arxiv.org/abs/1412.5168> (2015).
22. M. Hasegawa et al., *Mater. Trans.* **42**, 961–964 (2001).
23. V. Eyert, R. Frésard, A. Maignan, *Chem. Mater.* **20**, 2370–2373 (2008).
24. K. Kim, H. C. Choi, B. I. Min, *Phys. Rev. B* **80**, 035116 (2009).
25. K. P. Ong, J. Zhang, J. S. Tse, P. Wu, *Phys. Rev. B* **81**, 115120 (2010).
26. K. P. Ong, D. J. Singh, P. Wu, *Phys. Rev. Lett.* **104**, 176601 (2010).
27. C. W. J. Beenakker, H. van Houten, *Solid State Phys.* **44**, 1–228 (1991).
28. See supplementary materials on Science Online.
29. E. Ditlefsen, J. Lothe, *Philos. Mag.* **14**, 759–773 (1966).
30. T. J. Thornton, M. L. Roukes, A. Scherer, B. P. van de Gaag, *Phys. Rev. Lett.* **63**, 2128–2131 (1989).
31. S. Masubuchi et al., *Phys. Rev. Lett.* **109**, 036601 (2012).
32. J. A. N. Bruin, H. Sakai, R. S. Perry, A. P. Mackenzie, *Science* **339**, 804–807 (2013).

ACKNOWLEDGMENTS

We thank J. C. Davis, C. Geibel, A. G. Green, S. A. Hartnoll, C. W. Hicks, S. A. Kivelson, Y. Maeno, T. Oka, J. W. Orenstein, and S. H. Simon for stimulating discussions and the UK Engineering and Physical Sciences Research Council for financial support. The FIB work was supported by the SCOPE-M center for electron microscopy at ETH Zürich. We thank P. Gasser, J. Reuteler, and B. Batlogg for FIB support. The data and/or materials supporting this publication can be accessed at <http://dx.doi.org/10.17630/cdc6c488-2ea4-440e-a68d-e2a2426709171>.

SUPPLEMENTARY MATERIALS

www.sciencemag.org/content/351/6277/1061/suppl/DC1
Materials and Methods
Figs. S1 to S6
References (33–39)

24 June 2015; accepted 23 December 2015
Published online 11 February 2016
10.1126/science.aac8385

CATALYSIS

Selective conversion of syngas to light olefins

Feng Jiao,^{1*} Jinjing Li,^{1*} Xiulian Pan,^{1*†} Jianping Xiao,¹ Haobo Li,¹ Hao Ma,¹ Mingming Wei,¹ Yang Pan,² Zhongyue Zhou,² Mingrun Li,¹ Shu Miao,¹ Jian Li,¹ Yifeng Zhu,¹ Dong Xiao,¹ Ting He,¹ Junhao Yang,¹ Fei Qi,² Qiang Fu,¹ Xinhe Bao^{1†}

Although considerable progress has been made in direct synthesis gas (syngas) conversion to light olefins ($C_2=C_4$) via Fischer-Tropsch synthesis (FTS), the wide product distribution remains a challenge, with a theoretical limit of only 58% for C_2-C_4 hydrocarbons. We present a process that reaches $C_2=C_4$ selectivity as high as 80% and C_2-C_4 94% at carbon monoxide (CO) conversion of 17%. This is enabled by a bifunctional catalyst affording two types of active sites with complementary properties. The partially reduced oxide surface ($ZnCrO_x$) activates CO and H_2 , and C-C coupling is subsequently manipulated within the confined acidic pores of zeolites. No obvious deactivation is observed within 110 hours. Furthermore, this composite catalyst and the process may allow use of coal- and biomass-derived syngas with a low H_2/CO ratio.

Fischer-Tropsch synthesis (FTS) has played an important role as a gas-to-liquid technology, producing synthetic lubricants and synthetic fuels from coal, natural gas, or biomass since it was developed almost a century ago. It is also the only effective technology to date for direct conversion of synthesis gas (syngas) to light olefins—i.e., $C_2=C_4$ —olefins containing two to four carbon atoms, so called Fischer-Tropsch to olefins (FTTO) (1–5). FTS has been under extensive study for more than 50 years, and a variety of metal catalysts, including iron, cobalt,

and ruthenium, have been tested (6). However, application of this technology is still limited by low olefin selectivity and high methane selectivity, as well as severe carbon deposition. These drawbacks arise from the FTS reaction mechanism, which is generally accepted to proceed via surface polymerization of CH_x ($x = 1, 2$, or 3)—i.e., addition of CH_x monomer units to the adsorbed alkyl species on open metal surfaces. Thus, a wide distribution of hydrocarbons with different chain lengths is produced. It can be described by the Anderson-Schulz-Flory (ASF) model (7, 8), which predicts that selectivity of C_2 to C_4 hydrocarbons (C_2-C_4), including $C_2=C_4$ olefins and $C_2^o-C_4^o$ paraffins, does not exceed 58% (6).

Thus, the key challenge of selective formation of light olefins from syngas lies in precise control of C-C coupling while suppressing overhydrogenation and methane formation. We present here a process named OX-ZEO (Oxide-Zeolite),

which separates CO activation and C-C coupling onto two different types of active sites with complementary properties. CO and H_2 are activated over a partially reduced oxide ($ZnCrO_x$) surface, whereas C-C coupling is controlled within the confined environment of zeolite pores with acidic sites. As a result, a C_2-C_4 selectivity up to 94% (including 80% $C_2=C_4$ and 14% $C_2^o-C_4^o$) of all hydrocarbons (carbon atom-based) was achieved with only 2% methane at a CO conversion of 17%. This C_2-C_4 selectivity is far beyond the maximum predicted by the ASF model in FTS.

The composite catalyst contained an oxide ($ZnCrO_x$) that exhibits a typical spinel structure (fig. S1) and a mesoporous SAPO zeolite (MSAPO) exhibiting CHA structure with a hierarchical pore texture (figs. S1 and S2 and table S1) (9). Figure 1A shows that $C_2=C_4$ selectivity reached 74% at CO conversion of 16% over a catalyst with a mass ratio of $ZnCrO_x/MSAPO = 1.4$, under reaction conditions of $H_2/CO = 1.5$, pressure 2.5 MPa, and space velocity 4800 ml/h·g_{cat}. A higher H_2/CO ratio benefits CO conversion, which rose to 30% at $H_2/CO = 3$, for instance, whereas a higher space velocity favored the selective formation of olefins. Selectivities varied in the range from 67 to 80% for $C_2=C_4$ and 81 to 94% for C_2-C_4 in the studied H_2/CO (0.5 to 3.0) and space velocity ranges (1285 to 7714 ml/h·g_{cat}) and different ratios of $ZnCrO_x/MSAPO$. This $C_2=C_4$ selectivity is higher than the best value reported for FTTO (61%) (4) and exceeds the maximum predicted for C_2-C_4 hydrocarbons according to the ASF distribution in typical FTS, as depicted in Fig. 1B. Both CH_4 and C_5+ selectivities were <5% (Fig. 1A), prominently lower than those in FTTO (in a range of 10 to 40% for CH_4 and >10% for C_5+) (4). In contrast, the C_1 and C_5+ products were difficult to suppress simultaneously in FTTO; causing one to decline caused the other to increase (1, 7). The reactivity of this composite catalyst showed good reproducibility, with CO conversion and selectivity fluctuating within 4 and 5%, respectively, among 11 tests (fig. S3). Furthermore, it delivered rather

¹State Key Laboratory of Catalysis, 2011-Collaborative Innovation Center of Chemistry for Energy Materials, Dalian Institute of Chemical Physics, Chinese Academy of Sciences, Zhongshan Road 457, Dalian 116023, China. ²National Synchrotron Radiation Laboratory, University of Science and Technology of China, Hefei 230029, China.

*These authors contributed equally to this work. †Corresponding author. E-mail: panxl@dicp.ac.cn (X.P.); xhbao@dicp.ac.cn (X.B.)

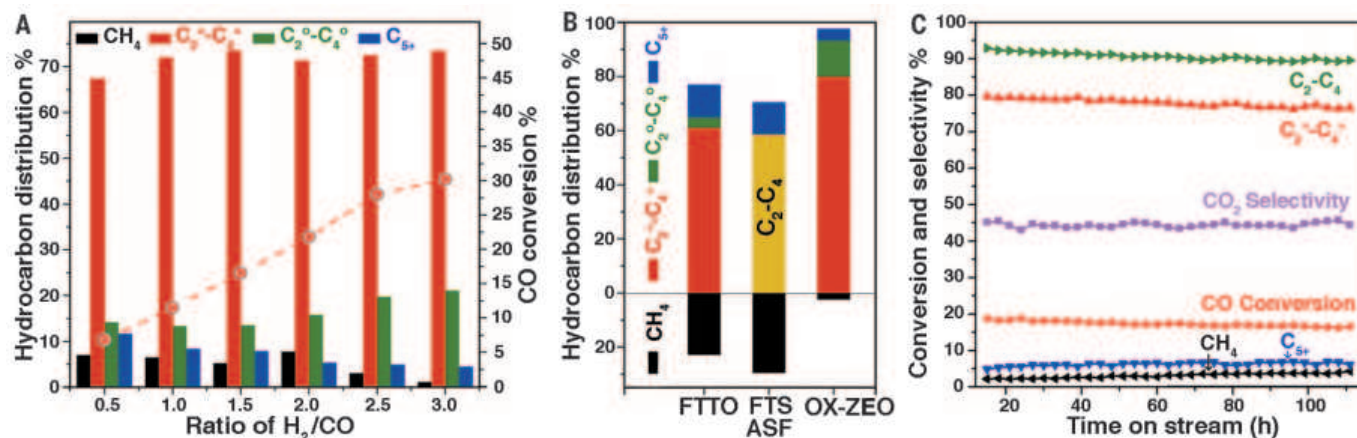


Fig. 1. Catalytic process of OX-ZEO. (A) CO conversion and product distribution at different H_2/CO ratios in syngas over a catalyst with a mass ratio of $ZnCrO_x/MSAPO = 1.4$ at a space velocity of 4800 ml/h·g_{cat}. (B) Hydrocarbon distribution in OX-ZEO in comparison to that reported for FTTO (4) and that in FTS predicted by the ASF model at a chain growth probability of 0.46, with the yellow bar representing selectivity of C_2-C_4 hydrocarbons. (C) A stability test of a composite catalyst with $ZnCrO_x/MSAPO$ ratio = 0.9 at 6828 ml/h·g_{cat} and H_2/CO of 2.5.

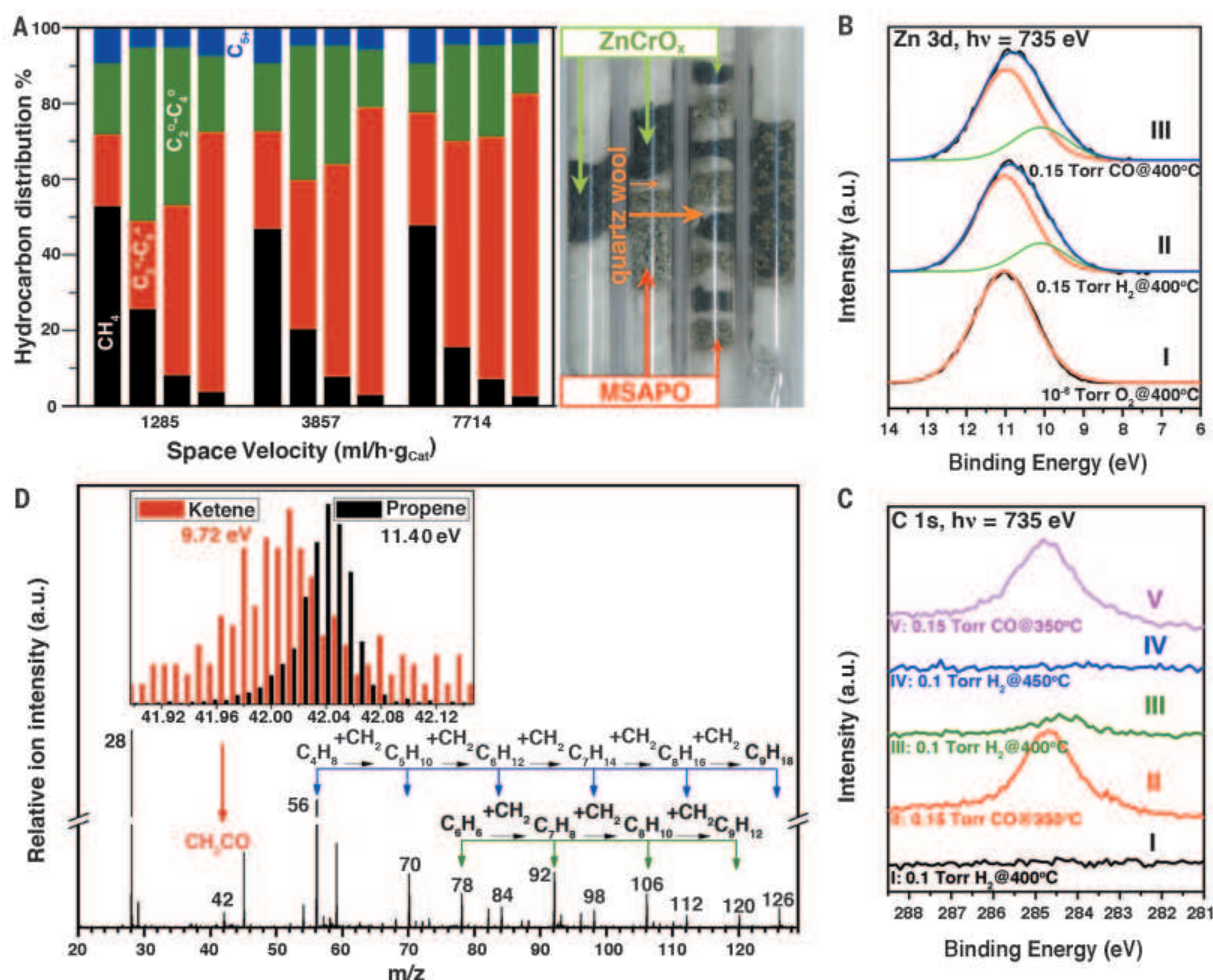


Fig. 2. Bifunctionality of the composite ZnCrO_x/MSAPO catalyst and investigation of the reaction intermediate. (A) Reaction results over the catalysts with the two functionalities packed in different modes under the same conditions. The picture on the right side displays the catalyst beds after reaction, representing Mode 1 to 4 from left to right: Mode 1, the catalyst contains ZnCrO_x only; Mode 2, MSAPO packed below ZnCrO_x, separated by an inert layer of quartz wool; Mode 3, MSAPO and ZnCrO_x packed in an alternating

sequence and separated by quartz wool; Mode 4, MSAPO and ZnCrO_x well mixed. (B) In situ NAP-XPS Zn3d spectra of ZnCrO_x under different conditions. (C) In situ NAP-XPS C1s spectra of ZnCrO_x exposed to H₂, CO, and H₂ sequentially, and then again to CO atmosphere under different conditions. (D) In situ study of syngas conversion over ZnCrO_x by SVUV-PIMS at hν = 9.72 eV. The insets display the signals of m/z = 42.01 (ketene) and m/z = 42.05 (propene) detected at hν = 9.72 and 11.40 eV, respectively.

stable performance (Fig. 1C). The total C₂–C₄ selectivity remained >90%, and that of C₂[–]–C₄[–] ~78% during a 110-hour test at 400°C, 2.5 MPa, and a space velocity of 6828 ml/h-g_{cat}.

Although composite catalysts containing metal oxides such as Cr₂O₃–ZnO and CuO–ZnO, and zeolites such as ZSM-5, Y, and β have been attempted previously for syngas conversion (10–15), the products were mainly dimethylether (10), liquefied petroleum gas (C₃^o–C₄^o) (11–13), or gasoline (14, 15). We attribute the efficiency of the OX-ZEO process to the bifunctionality of the catalyst, with two types of active sites exhibiting complementary and compatible properties. In the absence of MSAPO (corresponding to Mode 1 of Fig. 2A), syngas was converted mainly to CH₄ (selectivity 53%), and selectivity to C₂–C₄ hydrocarbons was only 38% over ZnCrO_x. Upon combination with MSAPO, which was packed below the oxide and separated by a layer of inert quartz wool (Mode 2), the products shifted and C₂–C₄ selectivity increased to

69% containing 23% C₂[–]–C₄[–], whereas CH₄ selectivity dropped to 26%.

This result shows that reaction intermediates generated over the oxides must have transported in the gas phase toward the active sites of MSAPO, where they were converted to C₂–C₄ hydrocarbons, rather than being hydrogenated to CH₄ over the oxide or in gas phase. Thus, any measures that could facilitate the transport of intermediates in gas phase should benefit selective formation of olefins, for example, increasing space velocities, as demonstrated in Fig. 2A. In addition, Mode 3, where the oxides and MSAPO were packed in an alternating sequence and thus the transport distance was reduced, also leads to enhanced C₂[–]–C₄[–] selectivity (65% at 7714 ml/h-g_{cat}). We observed an even higher selectivity of C₂[–]–C₄[–] (80%), with overall C₂–C₄ selectivity reaching 94% and only 2% CH₄ over the well-mixed composite catalyst (Mode 4). Furthermore, CO conversion could be tuned by varying the relative mass ratio of oxide/

zeolite (fig. S4) (9), which lends further support to the above hypothesis that the composite catalyst is bifunctional and that the reaction involves intermediate transport in gas phase.

Activation of the C–O bond has been reported previously for surfaces promoted with oxygen vacancies—for example, Fe₃O₄ (16), CoO_x/TiO₂ (17), Cu/ZnO (0001) (18), and ZnGa₂O₄ (19). However, little is known about subsequent formation of C–C and C–H bonds in the presence of H₂. Density functional theory (DFT) calculations using the ZnCr₂O₄ spinel (111) surface as a model reveal that it is reducible, resulting in a surface with a number of oxygen vacancies (figs. S5 and S6) (9). In situ near-ambient pressure x-ray photoelectron spectroscopy (NAP-XPS) of ZnCrO_x surface (Fig. 2B) revealed a new signal with a lower Zn3d binding energy upon exposure to H₂ and CO, compared with the initial oxidized surface. CO can be activated on such a surface, leading to formation of CO₂, detected by time-of-flight mass spectrometry

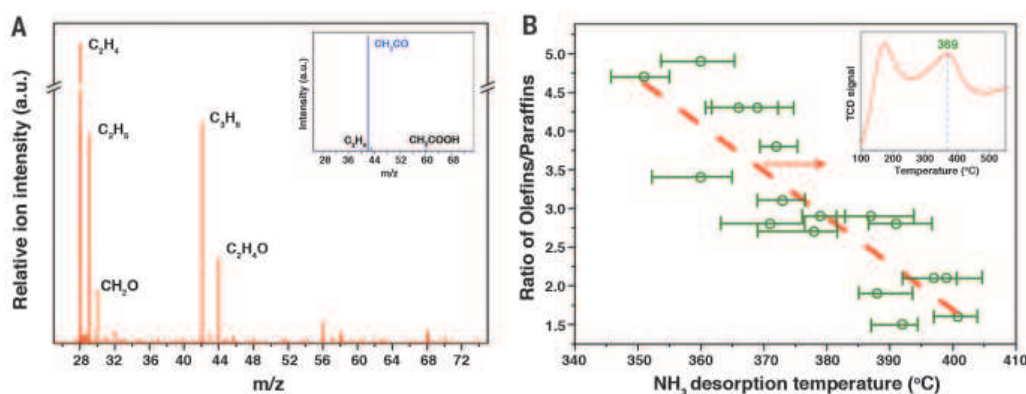


Fig. 3. The role of MSAPO in OX-ZEO.

(A) Catalytic conversion of ketene to olefins over MSAPO at 400°C, with the effluent monitored by SVUV-PIMS. The inset shows the results of the blank experiment with ketene fed to the same reactor containing no catalyst. Spectra are recorded at 10.70 eV. (B) Ratio of olefin/paraffin as a function of the NH_3 desorption peak temperature from the medium-strength acidic sites of MSAPO. The dashed line is only for the purpose of guiding the eyes, and the inset displays a typical NH_3 -TPD profile.

(TOF-MS) (fig. S7) (9) and surface $^*\text{C}$ species in absence of hydrogen, which is evidenced by a strong C1s signal emerging at 284.7 eV, even at 350°C (curve II in Fig. 2C). This C1s signal remained even after heat treatment at 300°C under ultrahigh vacuum (fig. S8) (9), but it remarkably attenuated in H_2 (curve III) and finally vanished at 450°C (curve IV). Analysis of the effluent by TOF-MS shows that $^*\text{C}$ species were removed via hydrogenation forming hydrocarbons (fig. S7, b to d) (9). Thus, the precursor of hydrocarbons, CH_x species formed over ZnCrO_x , are likely the intermediates in the OX-ZEO process.

To detect the intermediate in gas phase, we turned to the highly sensitive synchrotron-based vacuum ultraviolet photoionization mass spectrometry (SVUV-PIMS) (9), which has been widely used in the field of combustion to detect active intermediates and radicals with low concentrations in gas phase (20, 21). It provides a tunable photon energy, soft ionization, and superior signal-to-noise ratio. The schemes of SVUV-PIMS and the reactor are shown in fig. S9. When syngas was fed into the reactor in the absence of catalysts (a blank experiment), no other signal was observed. In the presence of ZnCrO_x , a signal of mass/charge ratio (m/z) = 42.01 appeared in the effluents at a photon energy $h\nu$ = 9.72 eV (Fig. 2D) in addition to stable hydrocarbon products. Further varying the photon energy (fig. S10) (9) confirmed that this signal was unambiguously attributed to ketene CH_2CO , considering the m/z ratio and the ionization energy (22–24). In comparison, propene (m/z = 42.05) was only distinguishable at $h\nu$ > 9.73 eV (fig. S10e) (9), and it became prominent at $h\nu$ = 11.40 eV (the black signal in the inset of Fig. 2D). Additional signals in Fig. 2D were assigned to stable products of C_4H_8 and C_6H_6 , and their derivatives from stepwise addition of CH_2 monomers up to m/z = 126.

In addition to ketene and the stable products, signals of methanol (m/z = 32) and its dissociated product methoxyl group (m/z = 31) were also detected at a high $h\nu$ (11.40 eV) in the presence of ZnCrO_x catalyst. However, the reaction did not appear to go via methanol in this OX-ZEO process because the yield of C_2^- – C_4^- dramatically dropped to 3% within 22 hours when feeding methanol (50 mbar in He) directly to the composite catalyst (fig. S11). Figure S12 shows that

MSAPO alone as a methanol-to-olefin (MTO) catalyst also deactivated quickly within 30 hours, even at a methanol partial pressure as low as 5 mbar, and 0.18 mol C/g_{cat} was converted before deactivation. By contrast, the composite catalyst delivered rather stable performance in OX-ZEO. No obvious degradation of CO conversion was observed for operation as long as 650 hours (fig. S13), and 9.6 mol C/g_{cat} was converted within this period of time. The total coke deposit was only 11 weight % (wt %) (fig. S14) (9). In contrast, fast deactivation remains a major issue for MTO in that coke deposits can mount up about 10 wt % within 15 min (25). Furthermore, very little water is produced in OX-ZEO, in contrast to the MTO process, where two moles of H_2O are produced for each mole of ethylene (assumed as the only product) from methanol (9). In addition, O from CO is removed mainly by producing CO_2 with a selectivity of 40 to 45% in OX-ZEO, whereas little CO_2 forms in MTO. The above results show that reaction via methanol may not be the dominating pathway in OX-ZEO, although it cannot be excluded completely, whereas ketene likely plays an important role.

Such CH_2 species are very active and readily react with CO in the presence of CO, forming a relatively less reactive ketene (26, 27), which is detectable by SVUV-PIMS. Thus, CH_2 species are likely the primary intermediates. By forming ketene, the reaction pathway of surface polymerization of CH_x is blocked, hence circumventing the ASF limits of FTS. Subsequently, in the presence of confined acidic environment of zeolite pores, CH_2CO can be converted to olefins (Fig. 2A). This was validated by feeding ketene directly as the reactant to the MSAPO catalyst, with the effluents monitored by the online SVUV-PIMS. Ketene was synthesized via pyrolysis of acetic anhydride following the reported procedure (fig. S15) (24, 28). Comparison of the results in the blank reactor and in the presence of the catalyst (Fig. 3A and fig. S15) demonstrates the capability of MSAPO catalyzing conversion of ketene to light olefins.

Figure 3B and fig. S16 (9) demonstrate that the product selectivity can be modulated by the medium strength acidity, characterized by temperature-programmed-desorption (TPD) of NH_3 , with the peak maximum located in the range from 350° to 410°C. For example, a commercially available

SAPO-34 exhibiting NH_3 desorption at ~394°C had a C_2^- – C_4^- selectivity of 43% and an olefin/paraffin ratio (C_2^- – $\text{C}_4^-/\text{C}_5^-$ – C_6^-) of 0.9. The olefin/paraffin ratio increased with the decreasing NH_3 desorption temperature and reached 4.7 for a MSAPO sample with NH_3 desorption peak at 350°C (Fig. 3C). In contrast, a composite catalyst with almost no medium strength acidic sites had a similar product distribution, as the catalyst contained no zeolite (fig. S17 and table S3) (9). Thus, it is reasonable to assume that there may exist an optimum acidity with NH_3 desorption temperature <350°C for olefin formation. However, it is still a challenge to synthesize zeolites with a weaker acidity but without reducing the number of active sites (necessary to achieve a reasonable conversion). In addition, the preliminary results in fig. S18 (9) show that the distribution of different-sized hydrocarbons might be tunable through the shape selectivity of zeolites, because a larger pore generally yields higher hydrocarbons. However, further elucidation of the relation between the structure (pore size/acidity) and the activity/selectivity will require much more sophisticated experiments because the acidity frequently varies simultaneously with the pore structure and crystallinity.

The capability of the partially reduced oxide in activating CO but incapability of catalyzing surface polymerization of CH_x makes it possible to manipulate C–C coupling with confined acidic zeolite pores. Thus, the CO conversion and selectivity can be tuned at the same time—i.e., CO conversion is manipulated via the surface structure of the oxides and the ratio of oxides/zeolite, whereas the olefin selectivity is controlled by the properties of zeolites, particularly the pore structure and acidity. These findings open up a new avenue for development of syngas-to-olefin technologies, which may allow utilization of coal- and biomass-derived syngas with a low H_2/CO ratio.

REFERENCES AND NOTES

1. R. Snel, *Catal. Rev. Sci. Eng.* **29**, 361–445 (1987).
2. Y. D. Xu, D. W. Goodman, *Catal. Lett.* **24**, 31–35 (1994).
3. Z. Yang, S. Guo, X. Pan, J. Wang, X. Bao, *Energy Environ. Sci.* **4**, 4500–4503 (2011).
4. H. M. Torres Galvis *et al.*, *Science* **335**, 835–838 (2012).
5. X. Chen, D. Deng, X. Pan, Y. Hu, X. Bao, *Chem. Commun. (Camb.)* **51**, 217–220 (2015).
6. H. M. Torres Galvis, K. P. de Jong, *ACS Catal.* **3**, 2130–2149 (2013).

7. R. A. Friedel, R. B. Anderson, *J. Am. Chem. Soc.* **72**, 1212–1215 (1950).
8. I. Puskas, R. S. Hurlbut, *Catal. Today* **84**, 99–109 (2003).
9. Supplementary materials are available on Science Online.
10. G. Yang, N. Tsubaki, J. Shamoto, Y. Yoneyama, Y. Zhang, *J. Am. Chem. Soc.* **132**, 8129–8136 (2010).
11. K. Fujimoto, H. Saima, H. O. Tominaga, *J. Catal.* **94**, 16–23 (1985).
12. Q. Ge, X. Li, H. Kaneko, K. Fujimoto, *J. Mol. Catal. Chem.* **278**, 215–219 (2007).
13. Y. Yu et al., *React. Kinet. Mech. Catal.* **112**, 489–497 (2014).
14. J. Eñeña, J. M. Arandes, J. Bilbao, A. T. Aguayo, H. I. de Lasa, *Ind. Eng. Chem. Res.* **37**, 1211–1219 (1998).
15. P. Mohanty, K. K. Pant, J. Parikh, D. K. Sharma, *Fuel Process. Technol.* **92**, 600–608 (2011).
16. Y. Tamaura, M. Tahata, *Nature* **346**, 255–256 (1990).
17. G. Melaet et al., *J. Am. Chem. Soc.* **136**, 2260–2263 (2014).
18. J. Xiao, T. Frauenheim, *J. Phys. Chem. Lett.* **3**, 2638–2642 (2012).
19. C. Jia et al., *Phys. Chem. Chem. Phys.* **16**, 7538–7547 (2014).
20. F. Qi, *Proc. Combust. Inst.* **34**, 33–63 (2013).
21. J. D. Savee et al., *Science* **347**, 643–646 (2015).
22. NIST Chemistry WebBook, <http://webbook.nist.gov/chemistry/mw-ser.html>.
23. T. A. Cool et al., *J. Chem. Phys.* **119**, 8356–8365 (2003).
24. B. Yang et al., *Int. J. Mass Spectrom.* **309**, 118–128 (2012).
25. D. Chen, K. Moljord, A. Holmen, *Micro. Meso. Mater.* **164**, 239–250 (2012).
26. J. Channugam, M. Burton, *J. Am. Chem. Soc.* **78**, 509–519 (1956).
27. Z. H. Zhang, Y. Zhang, J. B. Wang, *ACS Catal.* **1**, 1621–1630 (2011).
28. J. W. Williams, C. D. Hurd, *J. Org. Chem.* **5**, 122–125 (1940).

ACKNOWLEDGMENTS

This work was financially supported by the National Natural Science Foundation of China (grant nos. 21425312, 21321002, and 91545204), the Ministry of Science and Technology of China

(no. 2013CB933100), the “Strategic Priority Research Program” of the Chinese Academy of Sciences (grant XDA09030101), and Dalian Institute of Chemical Physics Fundamental Research Program for Clean Energy (DICP M201308). The Advanced Light Source is supported by the Director, Office of Science, Office of Basic Energy Sciences, of the U.S. Department of Energy under contract no. DE-AC02-05CH11231. A Chinese patent and an international patent application under the Patent Cooperation Treaty are pending.

SUPPLEMENTARY MATERIALS

www.sciencemag.org/content/351/6277/1065/suppl/DC1
Materials and Methods
Figs. S1 to S18
Tables S1 to S4
References (29, 30)

3 January 2016; accepted 22 January 2016
10.1126/science.aaf1835

QUANTUM COMPUTING

Realization of a scalable Shor algorithm

Thomas Monz,^{1*} Daniel Nigg,¹ Esteban A. Martinez,¹ Matthias F. Brandl,¹ Philipp Schindler,¹ Richard Rines,² Shannon X. Wang,² Isaac L. Chuang,² Rainer Blatt^{1,3}

Certain algorithms for quantum computers are able to outperform their classical counterparts. In 1994, Peter Shor came up with a quantum algorithm that calculates the prime factors of a large number vastly more efficiently than a classical computer. For general scalability of such algorithms, hardware, quantum error correction, and the algorithmic realization itself need to be extensible. Here we present the realization of a scalable Shor algorithm, as proposed by Kitaev. We factor the number 15 by effectively employing and controlling seven qubits and four “cache qubits” and by implementing generalized arithmetic operations, known as modular multipliers. This algorithm has been realized scalably within an ion-trap quantum computer and returns the correct factors with a confidence level exceeding 99%.

Shor’s algorithm for factoring integers (*1*) is one example in which a quantum computer (QC) outperforms the most efficient known classical algorithms. Experimentally, its implementation is highly demanding (*2–7*) because it requires both a sufficiently large quantum register and high-fidelity control. Such challenging requirements raise the question of whether optimizations and experimental shortcuts are possible. Optimizations, especially system-specific or architectural optimizations, are certainly possible, but for a demonstration of Shor’s algorithm in a scalable manner, special care must be taken to not oversimplify the implementation—for instance, by employing knowledge about the solution before the actual experimental application (*8*).

How does Shor’s algorithm work? First, we consider a classical factoring recipe, assuming

that the number we want to factor is $N = 15$. We pick a random number $a \in [2, N - 1]$ (the base)—say, $a = 7$. We evaluate whether the greatest common divisor $\text{gcd}(a, N) = 1$; if not, a factor is already determined. This is the case for $a = \{3, 5, 6, 9, 10, 12\}$. Next, we calculate the modular exponentiation $a^x \bmod N$ for $x = 0, 1, 2, \dots$ and find its period r : the first value of $x > 0$ such that $a^x \bmod N = 1$. Given r , finding the factors of N requires calculating the greatest common divisors of $a^{r/2} \pm 1$ and N , which is efficiently possible with a classical approach—for instance, using Euclid’s algorithm. For our example ($N = 15$, $a = 7$), the modular exponentiation yields 1, 7, 4, 13, 1, ..., which has a period of 4. The greatest common divisors of $a^{r/2} \pm 1 = 7^{4/2} \pm 1 = \{48, 50\}$ and $N = 15$ are $\{3, 5\}$, the nontrivial factors of N . In this example, the cases $a = \{4, 11, 14\}$ have period $r = 2$ and require a single multiplication step ($a^2 \bmod N = 1$), which is considered an “easy” case (*8*). Note that the periodicity for a chosen a cannot be predicted.

How can this recipe be implemented in a QC? A QC also has to calculate $a^x \bmod N$ in a computational register for $x = 0, 1, 2, \dots$ and then extract r . Using the quantum Fourier transform (QFT) applied to the period register, the period of

$a^x \bmod N$ can be extracted from a number of measurements not increasing with the size of the number to be factored.

What are the requirements and challenges of implementing Shor’s algorithm? We first focus on the period register and subsequently address modular exponentiation in the computational register. Factoring N , an $n = \lceil \log_2(N) \rceil$ -bit number (with the quantity in brackets rounded up to next integer number), requires a minimum of n qubits in the computational register (to store the results of $a^x \bmod N$) and generally about $2n$ qubits in the period register (*9, 10*). Thus, even a seemingly simple example, such as factoring 15 (an $n = 4$ -bit number), requires $3n = 12$ qubits. These qubits then have to be manipulated with high-fidelity gate operations. Given the current state-of-the-art control over quantum systems (*11*), such an approach would probably yield an unsatisfactory performance. However, a full quantum implementation of this part of the algorithm is not necessary. As noted by Kitaev (*12*), if only the classical information of the QFT (such as the period r) is of interest, $2n$ qubits subject to a QFT can be replaced by a single qubit. Still, this approach requires qubit recycling (specifically, in-sequence single-qubit readout and state reinitialization) paired with feed-forward behavior to compensate for the reduced system size.

In the following, Kitaev’s QFT will be referred to as KQFT^(M). It replaces a QFT acting on M qubits with a semiclassical QFT acting repeatedly on a single qubit. Similar applications of Kitaev’s approach to a semiclassical QFT in quantum algorithms have been investigated (*13–15*). For the implementation of Shor’s algorithm, Kitaev’s approach provides a reduction from the previous n computational qubits and $2n$ QFT qubits (in total, $3n$ qubits) to only n computational qubits and 1 KQFT⁽²ⁿ⁾ qubit (in total, $n + 1$ qubits).

The second key ingredient of Shor’s algorithm—and a notably more challenging aspect than the QFT—is modular exponentiation, which admits the following general simplifications.

1) Considering Kitaev’s approach (Fig. 1), the input state $|1\rangle$ (in decimal representation) is subject to a conditional multiplication based on the most significant bit k of the period register. At most, there will be two results after this first step.

¹Institut für Experimentalphysik, Universität Innsbruck, Technikerstraße 25, A-6020 Innsbruck, Austria. ²Center for Ultracold Atoms, Massachusetts Institute of Technology, 77 Massachusetts Avenue, Cambridge, MA 02139, USA. ³Institut für Quantenoptik und Quanteninformation, Österreichische Akademie der Wissenschaften, Otto-Hittmair-Platz 1, A-6020 Innsbruck, Austria.

*Corresponding author. E-mail: thomas.monz@uibk.ac.at

It follows that, for the very first step, it is sufficient to implement an optimized operation that conditionally maps $|1\rangle \rightarrow |a^{2^k} \bmod N\rangle$. Considering the importance of a high-fidelity multiplication (with its performance being fed forward to all subsequent qubits), this efficient simplification improves the overall performance of experimental realizations.

2) Subsequent multipliers can similarly be replaced with maps by considering only possible outputs of the previous multiplications. However, using such maps will become intractable, as the number of input and output states to be considered grows exponentially with the number of steps: After n steps, $2^n > N$ possible outcomes need to be considered, a numerical task as challenging as factoring N by classical means. Thus, controlled full modular multipliers should be implemented. Figure 2 shows the experimentally obtained truth table for the modular multiplier $2 \bmod 15$ [see also (16) for modular multipliers with bases $\{7, 8, 11, 13\}$]. These quantum circuits can be efficiently derived from classical procedures by using a variety of standard techniques for reversible quantum arithmetic and local logic optimization (17, 18).

3) The very last multiplier allows one more simplification: Considering that the results of the modular exponentiation are not required for Shor's algorithm (as only the period encoded in the period register is of interest), the last multiplier only has to create the correct number of correlations between the period register and the computation register. Local operations after the conditional (entangling) operations may be discarded to facilitate the final multiplication without affecting the results of the implementation.

4) In rare cases, certain qubits are not subject to operations in the computation. Thus, these qubits can be removed from the algorithm entirely.

For large-scale quantum computation, optimization steps 1, 3, and 4 will only marginally affect the performance of the implementation. These steps represent merely a small subset of the entire computation, which mainly consists of the full modular multipliers. Thus, the realization of these modular multipliers is a core requirement for the implementations of a scalable Shor algorithm.

Furthermore, Kitaev's approach requires in-sequence measurements, qubit recycling to reset the measured qubit, feed-forward behavior of gate settings on the basis of previous measurement results, and controlled quantum operations—tasks that have not been realized in a combined experiment to date.

We demonstrate these techniques in our realization of Shor's algorithm in an ion-trap QC, with five $^{40}\text{Ca}^+$ ions in a linear Paul trap. The qubit is encoded in the ground state $S_{1/2}(m = -1/2) = |1\rangle$ and the metastable state $D_{5/2}(m = -1/2) = |0\rangle$ (where m denotes the Zeeman sublevel) [for more details, see (16, 19)]. Unitary operations, illustrated in Fig. 1, are decomposed into primitive components, such as two-target controlled-NOT (C-NOT) and C-SWAP gates (or gates with global symmetries, such as the four-target C-NOT gate employed

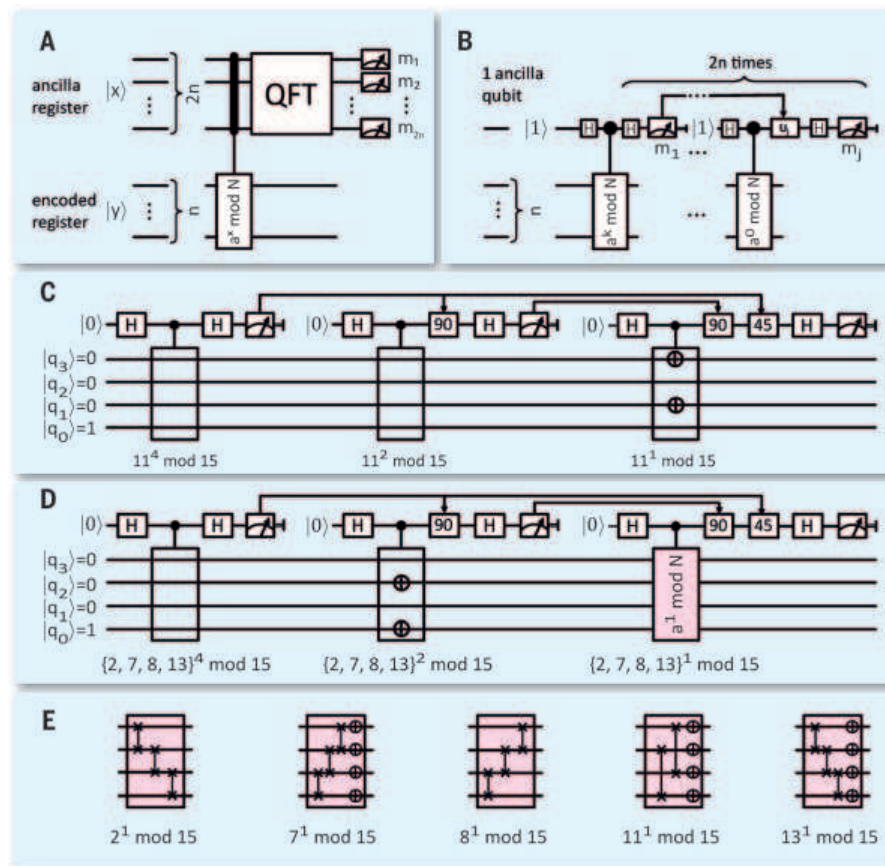


Fig. 1. Quantum circuits. Diagrams of Shor's algorithm for factoring $N = 15$, using a generic textbook approach (A) compared with Kitaev's approach (B) for a generic base a . (C) The actual implementation for factoring 15 to base 11, optimized for the corresponding single-input state. Here q_i corresponds to the respective qubit in the computational register. (D) Kitaev's approach to Shor's algorithm for the bases $\{2, 7, 8, 13\}$. Here, the optimized map of the first multiplier is identical in all four cases, and the last multiplier is implemented with full modular multipliers, as depicted in (E). In all cases, the single QFT qubit is used three times, which, together with the four qubits in the computation register, totals seven effective qubits. (E) Circuit diagrams of the modular multipliers of the form $a \bmod N$ for bases $a = \{2, 7, 8, 11, 13\}$.

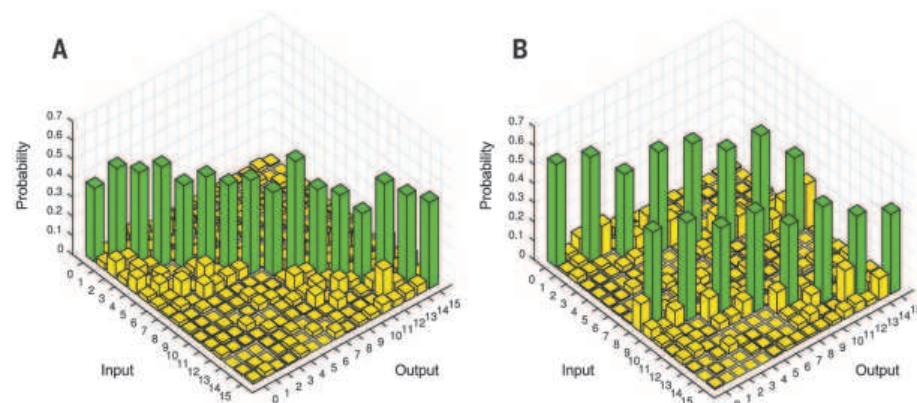
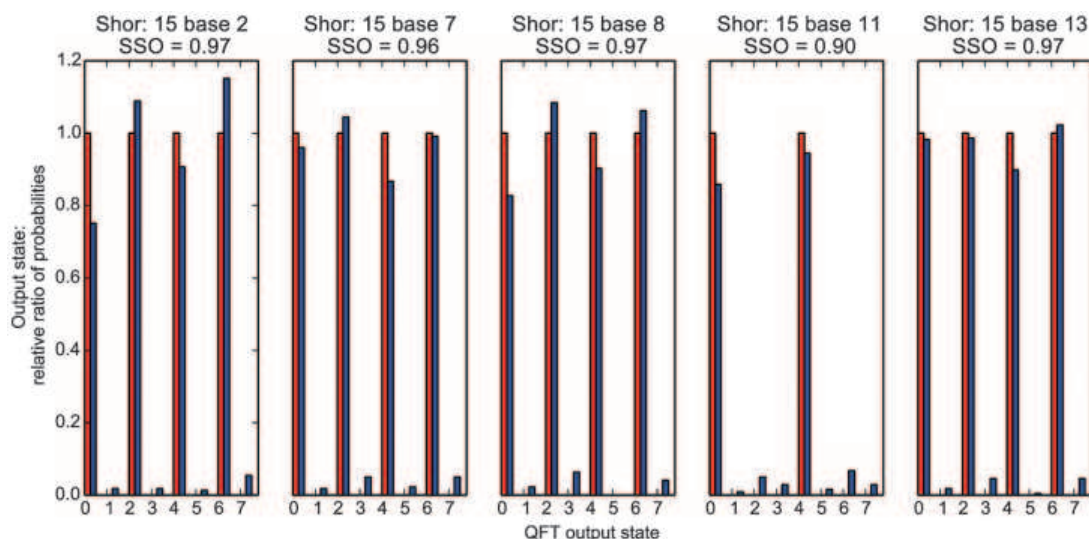


Fig. 2. Truth table. Experimentally obtained truth table of the controlled $2 \bmod 15$ multiplier. (A) With the control-qubit being in state 0, the truth table corresponds to the identity operation. (B) When the control qubit triggers the multiplication, the truth table illustrates the multiplication of the input state with $2 \bmod 15$. The mean fidelity with respect to the expected output state is 48(5)%.

Fig. 3. Experimental findings. Results and correct order-assign probability for the different implementations to factor $N = 15$. Three-digit results (in decimal representation) of Shor's algorithm for the different bases. The ideal data (red) for period $\{2, 4\}$ are shown adjacent to the raw data (blue). The squared statistical overlap is larger than 90% for all cases.



here), from which an adaptation of the gradient-ascent pulse engineering algorithm (20) can efficiently derive an equivalent sequence of laser pulses acting on only the relevant qubits. The problem with this approach is that the resulting sequence generally includes operations acting on all qubits. Implementing the optimized three-qubit operations for a five-ion string therefore requires decoupling the remaining qubits from the computation space. We spectroscopically decouple qubits by transferring any information from $|S\rangle$ to $|D'\rangle = D_{5/2}(m = -5/2)$ and from $|D\rangle$ to $|S'\rangle = S_{1/2}(m = 1/2)$. Here, the subspace $\{|S'\rangle, |D'\rangle\}$ serves as a readily available “quantum cache” to store and retrieve quantum information for the purpose of facilitating quantum computations.

Finally, to complete the toolbox necessary for Kitaev's approach to Shor's algorithm, we also implement (i) single-qubit readout, by encoding all other qubits in the $\{|D\rangle, |D'\rangle\}$ subspace and subsequent electron shelving (21) on the $S_{1/2} \leftrightarrow P_{1/2}$ transition; (ii) feed-forward behavior, by storing counts detected during the single-qubit readout (22) in a classical register and subsequent conditional laser pulses; and (iii) state reinitialization, using optical pumping for the ion, and Raman cooling (23, 24) for the motional state of the ion string. The pulse sequences and additional information on the implementation of the modular multipliers are available in (16).

The measurement results for base $a = \{2, 7, 8, 11, 13\}$ with period $r = \{4, 4, 4, 2, 4\}$ are shown in Fig. 3. To quantify the performance of the implementation, previous realizations focused mainly on the squared statistical overlap (SSO) (25), the classical equivalent to the Uhlmann fidelity (10). Although we achieved an SSO of $\{0.968(1), 0.964(1), 0.966(1), 0.901(1), 0.972(1)\}$ for the case of $a = \{2, 7, 8, 11, 13\}$, we argue that this does not answer the question “What is the period?” Shor's algorithm allows one to deduce the period with high probability from a single-shot measurement, as the output of the QFT (x) is, in the exact case, a ratio of integers, where the denominator gives the desired period. This period is extracted by using

a continued fraction expansion applied to $x/2^k$, a good approximation of the ideal case when k , the number of qubits, is sufficiently large. In our realizations with bases $a = \{2, 7, 8, 11, 13\}$, the probabilities (and their error estimates in parentheses) to obtain output states that allow the derivation of the correct period are $\{56(2), 51(2), 54(2), 47(2), 50(2)\}\%$. Thus, to obtain a confidence level of $>99\%$ for the periodicity, the experiment has to run about eight times.

We have presented the realization of Kitaev's vision of Shor's algorithm based on scalable building blocks with three-digit resolution to factor $N = 15$, using bases $\{2, 7, 8, 11, 13\}$. To do this, we successfully employed a semiclassical QFT combined with single-qubit readout, feed-forward behavior, and qubit recycling. Compared with the traditional algorithm, our realization of Shor's algorithm reduces the required number of qubits by nearly a factor of 3. Furthermore, the entire quantum register has been subject to the computation in a “black-box” fashion. Employing the equivalent of a quantum cache by spectroscopic decoupling facilitated the derivation of the necessary pulse sequences to achieve high-fidelity results. We envision that our scalable algorithm implementation will be combined with a scalable trap architecture (26) and quantum error correction to enable arbitrary long quantum computation.

REFERENCES AND NOTES

- P. W. Shor, in *Proceedings of the 35th Annual Symposium on Foundations of Computer Science* (IEEE Computer Society Press, 1994), pp. 124–134.
- A. Politi, J. C. F. Matthews, J. L. O'Brien, *Science* **325**, 1221 (2009).
- E. Martín-López et al., *Nat. Photonics* **6**, 773–776 (2012).
- E. Lucero et al., *Nat. Phys.* **8**, 719–723 (2012).
- C. Y. Lu, D. E. Browne, T. Yang, J. W. Pan, *Phys. Rev. Lett.* **99**, 250504 (2007).
- B. P. Lanyon et al., *Phys. Rev. Lett.* **99**, 250505 (2007).
- L. M. K. Vandersypen et al., *Nature* **414**, 883–887 (2001).
- J. A. Smolin, G. Smith, A. Vargo, *Nature* **499**, 163–165 (2013).
- E. G. Rieffel, W. H. Polak, *Quantum Computing: A Gentle Introduction* (Scientific and Engineering Computation) (The MIT Press, ed. 1, 2011).
- M. A. Nielsen, I. L. Chuang, *Quantum Computation and Quantum Information* (Cambridge Series on Information and the Natural Sciences, Cambridge Univ. Press, ed. 1, 2004).

- J. Stajic, *Science* **339**, 1163 (2013).
- A. Y. Kitaev, <http://arxiv.org/abs/quant-ph/9511026> (1995).
- R. B. Griffiths, C. S. Niu, *Phys. Rev. Lett.* **76**, 3228–3231 (1996).
- S. Parker, M. B. Plenio, *Phys. Rev. Lett.* **85**, 3049–3052 (2000).
- M. Mosca, A. Ekert, in *Quantum Computing and Quantum Communications*, vol. 1509 of *Lecture Notes in Computer Science*, C. P. Williams, Ed. (Springer, 1999), pp. 174–188.
- Supplementary materials are available on Science Online.
- V. Vedral, A. Barenco, A. Ekert, *Phys. Rev. A* **54**, 147–153 (1996).
- R. Van Meter, K. M. Itoh, *Phys. Rev. A* **71**, 052320 (2005).
- P. Schindler et al., *New J. Phys.* **15**, 123012 (2013).
- V. Nebendahl, H. Häffner, C. F. Roos, *Phys. Rev. A* **79**, 012312 (2009).
- H. Dehmelt, *Bull. Am. Phys. Soc.* **20**, 60 (1975).
- M. Riebe et al., *Nature* **429**, 734–737 (2004).
- D. J. Wineland et al., *J. Res. Natl. Inst. Stand. Technol.* **103**, 259 (1998).
- I. Marzoli, J. I. Cirac, R. Blatt, P. Zoller, *Phys. Rev. A* **49**, 2771–2779 (1994).
- J. Chiaverini et al., *Science* **308**, 997–1000 (2005).
- D. Kielpinski, C. Monroe, D. J. Wineland, *Nature* **417**, 709–711 (2002).

ACKNOWLEDGMENTS

We acknowledge support from the Austrian Science Fund (FWF), through the SFB FoQus (FWF project no. F4002-N16); the European Commission (AQUTE), the NSF Interdisciplinary Quantum Information Science and Engineering (iQuISE) Integrative Graduate Education and Research Traineeship (IGERT); and the Institut für Quantenoptik und Quanteninformation. E.A.M. is a recipient of a DOC Fellowship of the Austrian Academy of Sciences. This research was funded by the Office of the Director of National Intelligence (ODNI), Intelligence Advanced Research Projects Activity (IARPA), through Army Research Office grant W911NF-10-1-0284. All statements of fact, opinion, or conclusions contained herein are those of the authors and should not be construed as representing the official views or policies of IARPA, the ODNI, or the U.S. government. T.M., D.N., and P.S. developed the research, on the basis of theoretical ideas derived with R.R., S.X.W., and I.L.C.; T.M., D.N., E.A.M., M.F.B., P.S., and S.X.W. performed the experiments; T.M. and D.N. analyzed the data; T.M., D.N., E.A.M., P.S., M.F.B., and R.B. contributed to the experiment; T.M., D.N., R.R., M.F.B., I.L.C., and R.B. wrote the manuscript; and all authors contributed to discussions about the results and the manuscript. We declare no competing financial interests.

SUPPLEMENTARY MATERIALS

www.sciencemag.org/content/351/6277/1068/suppl/DC1
Supplementary Text
Figs. S1 and S2
Tables S1 and S2
References (27, 28)

25 November 2015; accepted 1 February 2016
10.1126/science.1249480

FLEXIBLE ELECTRONICS

Highly stretchable electroluminescent skin for optical signaling and tactile sensing

C. Larson,^{1*} B. Peele,^{1*} S. Li,^{2*} S. Robinson,² M. Totaro,³ L. Beccai,³
B. Mazzolai,³ R. Shepherd^{1,2,†}

Cephalopods such as octopuses have a combination of a stretchable skin and color-tuning organs to control both posture and color for visual communication and disguise. We present an electroluminescent material that is capable of large uniaxial stretching and surface area changes while actively emitting light. Layers of transparent hydrogel electrodes sandwich a ZnS phosphor-doped dielectric elastomer layer, creating thin rubber sheets that change illuminance and capacitance under deformation. Arrays of individually controllable pixels in thin rubber sheets were fabricated using replica molding and were subjected to stretching, folding, and rolling to demonstrate their use as stretchable displays. These sheets were then integrated into the skin of a soft robot, providing it with dynamic coloration and sensory feedback from external and internal stimuli.

Biological systems employ a host of strategies for visual display and camouflage. Cephalopods, for example, can mimic their environment by changing skin color and texture, as well as posture (*1*). Recent developments in soft robotics (*2, 3*), bioinspired design (*4, 5*), and stretchable electronics (*6*) reveal strategies that enable us to engineer some of the functions of cephalopod skin synthetically. For example, microfluidic networks filled with liquid dyes have been used as active camouflage and displays for soft mobile robots, giving them the ability to change their appearance via color, texture, and luminescence (*7*). More recently, electro-mechanically responsive films were exploited to render fluorescent patterns under the control of electric fields (*8*), and adaptive optoelectronic camouflage systems have been used to mimic the visual appearance of cephalopod skin (*9*). Another approach is the use of active display technologies, such as polymeric light-emitting devices (PLEDs) and organic light-emitting diodes (OLEDs), which use stretchable transparent electrodes based on indium tin oxide (ITO) films (*10*), graphene (*11*), single- or multi-walled carbon nanotubes (SWNTs or MWNTs) (*12, 13*), polyethylene-dioxythiophene: polystyrene-sulfonate (PEDOT:PSS) (*14*), or other percolated networks of conductive colloids or nanowires (*15*). Despite the broad applicability of LED-based systems for consumer displays, their electrical function is limited to ultimate strains, $\epsilon_{ult} < 120\%$ (*16*), well below the ultimate strain of elastomers (such as silicones; $\epsilon_{ult} \sim 400$ to 700%)

that are used in soft robotics to mimic the movements of animals.

Biological skin also enables animals to sense their environments. A number of approaches have been used to create pressure-sensitive electronic skins, including arrays of organic field-effect transistors (FETs) deposited on flexible parylene-polyamide substrates (*17, 18*) and inside stretchable rubber (*19*), as well as thin Au films and liquid metal embedded in polydimethylsiloxane (PDMS) (*20, 21*). More recently, dielectric elastomer transducers (DETs), which are stretchable capacitors composed of highly extensible ionic hydrogels, have been used. These hydrogels are intrinsically soft, highly transparent in the visible spectrum (extinction coefficient $\mu_{ext} \sim 10^{-6} \text{ } \mu\text{m}^{-1}$) (*22*), can exhibit very high ultimate strain ($\epsilon_{ult} \sim 2000\%$) and toughness ($U \sim 9 \text{ kJ m}^{-2}$) (*23*), and have relative changes in resistivity with strain that are orders of magnitude less than those of electrodes based on percolated networks of conductive particles (such as metal nanoparticles, carbon powder, or nanotubes) (*24*).

Presently, soft robots are primarily used because their low mechanical compliance enables safe human-robot interaction; however, their potential is limited by a lack of suitable electronics that can stretch continuously with their bodies. No soft robot can dynamically display information on its body, and there are relatively few examples that can sense external and internal stimuli. Here we present a hyperelastic light-emitting capacitor (HLEC) that enables both light emission and touch sensing in a thin rubber sheet that stretches to $>480\%$ strain (Fig. 1A). These HLECs are composed of ionic hydrogel electrodes and composites of doped ZnS phosphors embedded in a dielectric matrix of silicone elastomer. We used electroluminescent (EL) phosphor powders that emit light via excitations within intrinsic heterojunctions under an AC electric

field; unlike current-driven LEDs, which require lithography to form p-n junctions, this material system can be processed using replica molding. Application of an AC electric field causes luminescence within the semiconducting phosphor at wavelength centers corresponding to the dopants in the ZnS lattice. Green and blue centers are typically produced using low [~ 0.01 weight % (wt %)] and high (~ 0.1 wt %) concentrations of Cu, whereas yellow is produced using Mn (~ 1 wt %) (*25*). White light can be achieved using combinations of these dopants.

The HLEC (Fig. 1B) is a five-layer structure consisting of an electroluminescent dielectric layer that is sandwiched between two electrodes and encapsulated in low elastic modulus ($E \sim 30 \text{ kPa}$) (*26*) silicone (Ecoflex 00-30, Smooth-on Inc.). Our hydrogel electrodes are designed with a balance of high mechanical toughness, low volatility, and low electrical resistance under deformation (fig. S1 and data table S1). Aqueous lithium chloride (LiCl) is used as the ionic conductor because of its high conductivity ($\sim 10 \text{ S m}^{-1}$), ionic strength, and hygroscopic nature, whereas polyacrylamide (PAM) is used as the elastomeric matrix because of its high toughness (*27*) and optical transparency. Electrodes are synthesized by first dissolving acrylamide monomer (AAM), polyacrylamide, and *N,N'*-methylenebisacrylamide crosslinker in aqueous LiCl and casting the solution onto an ultraviolet (UV)-ozone-treated silicone (Ecoflex 00-30) substrate. The aqueous PAM-AAM solution is then crosslinked under UV light (*28*), producing a highly stretchable and transparent electrode. The EL layer is formed by mixing commercially available phosphor powders (Global Tungsten & Powders) ($25 \text{ } \mu\text{m}$, $\sim 8\%$ by volume) into silicone (Ecoflex 00-30) and then molding the dispersion into a 1-mm-thick sheet. Finally, we bond the EL layer between the two electrode-patterned silicone substrates and encapsulate the capacitor in an insulating layer of silicone.

The stress-strain curves of the HLEC and its silicone-containing layers (Ecoflex and Ecoflex-EL composite) are all coincident, whereas the elastic modulus of the hydrogel is two orders of magnitude lower, allowing the HLEC to stretch freely without delaminating. Mechanical testing data (Fig. 1C and data table S2) and images (Fig. 2A, data table S3, and movie S1) show the excellent adhesion between the layers. The HLEC achieved a mean strain of $487 \pm 59\%$ (SD), as measured at five locations across the width of the illuminated section, with portions exceeding 500% before the external copper leads lost contact with the hydrogel electrodes. For these tests, the HLECs were operated at 700 Hz under a nominal electric field of $\sim 25 \text{ kV cm}^{-1}$, with a power consumption of 0.2 W and a luminous efficacy of $43.2 \text{ millilumens per watt (mlm W}^{-1})$ (*28*). We used this same replica molding technique to form an 8-by-8 array of 4-mm pixels (Fig. 3A). This HLEC display can undergo many deformation modes, including stretching, rolling, folding, and wrapping (Fig. 3, B to E, and movie S2). Dynamic control of the pixels is shown in Fig. 3, F to I.

¹Department of Mechanical and Aerospace Engineering, Cornell University, Ithaca, NY 14853, USA. ²Department of Materials Science and Engineering, Cornell University, Ithaca, NY 14853, USA. ³Center for Micro-BioRobotics@SSSA, Istituto Italiano di Tecnologia, Viale Rinaldo Piaggio 34, I-56025 Pontedera, Italy.

*These authors contributed equally to this work. †Corresponding author. E-mail: rfs247@cornell.edu

In addition to emitting light, the HLEC also serves as a dielectric elastomer sensor (DES), due to its construction as a parallel-plate capacitor. Changes in the electrode area (A) and separation distance (d) cause the capacitance (C) to change according to $C/C_0 \propto Ad^{-1}$, allowing the HLEC to sense deformations from pressure and stretching. The capacitance of the HLEC changes as it

is stretched under uniaxial (Fig. 2B and data S4) and biaxial (fig. S2 and data S5) tension (28). We model the capacitance by expressing A and d in terms of the principal stretches, λ_1 , λ_2 , and λ_3 , which represent the axial, transverse, and out-of-plane orientations, respectively (supplementary text). For uniaxial boundary conditions, we observe that the relative capacitance increases lin-

early as the sample is stretched (eq. S11). For biaxial test conditions, we observe that the relative change in capacitance follows $C/C_0 = \lambda^4$ (eq. S12); however, at higher strains, the measured values are slightly lower, due to a decrease in the permittivity of the dielectric (24).

The illuminance of the HLEC also increases as the device is stretched. We attribute this change

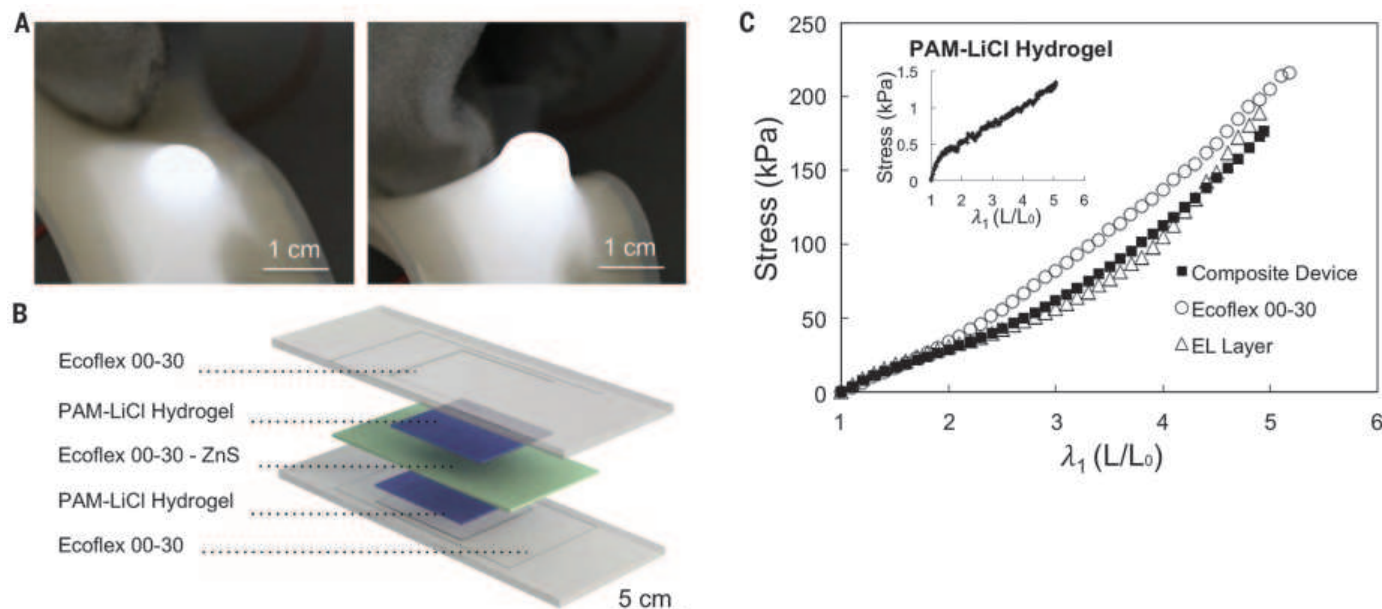


Fig. 1. HLEC. (A) Image of the HLEC conforming to the end of a pencil. (B) Exploded view of the HLEC showing its five-layer structure consisting of a ~1-mm-thick electroluminescent layer (ZnS-Ecoflex 00-30) that is sandwiched between two PAM-LiCl hydrogel electrodes and encapsulated in Ecoflex 00-30. (C) Stress-stretch curves of Ecoflex 00-30, the electroluminescent layer, and the composite device. The hydrogel data are shown in the inset because of its much lower elastic modulus.

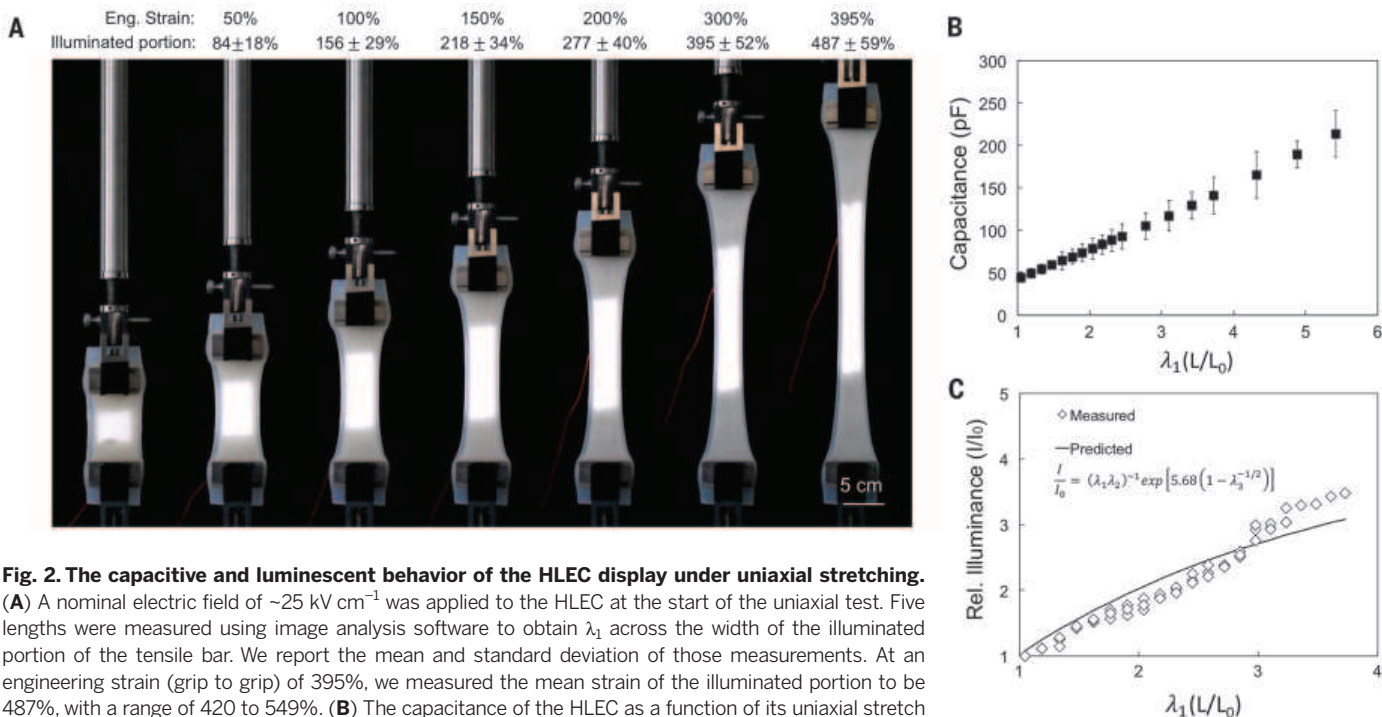


Fig. 2. The capacitive and luminescent behavior of the HLEC display under uniaxial stretching. (A) A nominal electric field of $\sim 25 \text{ kV cm}^{-1}$ was applied to the HLEC at the start of the uniaxial test. Five lengths were measured using image analysis software to obtain λ_1 across the width of the illuminated portion of the tensile bar. We report the mean and standard deviation of those measurements. At an engineering strain (grip to grip) of 395%, we measured the mean strain of the illuminated portion to be 487%, with a range of 420 to 549%. (B) The capacitance of the HLEC as a function of its uniaxial stretch (number of samples, $n = 4$). (C) The relative illuminance of the HLEC versus its uniaxial stretch ($n = 4$), plotted alongside predicted values (supplementary text).

to two interrelated phenomena: (i) the increase in electric field (E) as d decreases and (ii) the decrease in areal number density of phosphor particles (η) as A increases. Starting with the Alfrey-Taylor equation (eq. S13, fig. S3, and data table S6) (29), we predict the scaling law in Eq. 1 by expressing E/E_0 as a function of the principal stretches and by correcting for the change in η with stretching ($\eta/\eta_0 \propto A_0/A$) (supplementary text). The predicted trend is shown alongside

luminescence measurements in Fig. 2C (data table S7)

$$\frac{I}{I_0} = (\lambda_1 \lambda_2)^{-1} \exp[5.68(1 - \lambda_3^{1/2})] \quad (1)$$

To demonstrate the ability to monolithically integrate the HLEC into soft systems, we embedded three HLEC panels in a crawling soft robot by bonding six layers together. The top four layers make up the electroluminescent

skin, whereas the bottom two are used for pneumatic actuation (Fig. 4A). Inspired by architectures developed for mobile soft robots (30), our pneumatic actuator uses a series of inflatable chambers embedded in silicone, with a bottom layer composed of an inextensible fiber-elastomer composite (28). The inextensible layer induces a net bending moment as the pneumatic chambers are inflated; the resulting curvature is exploited to create an undulating gait.

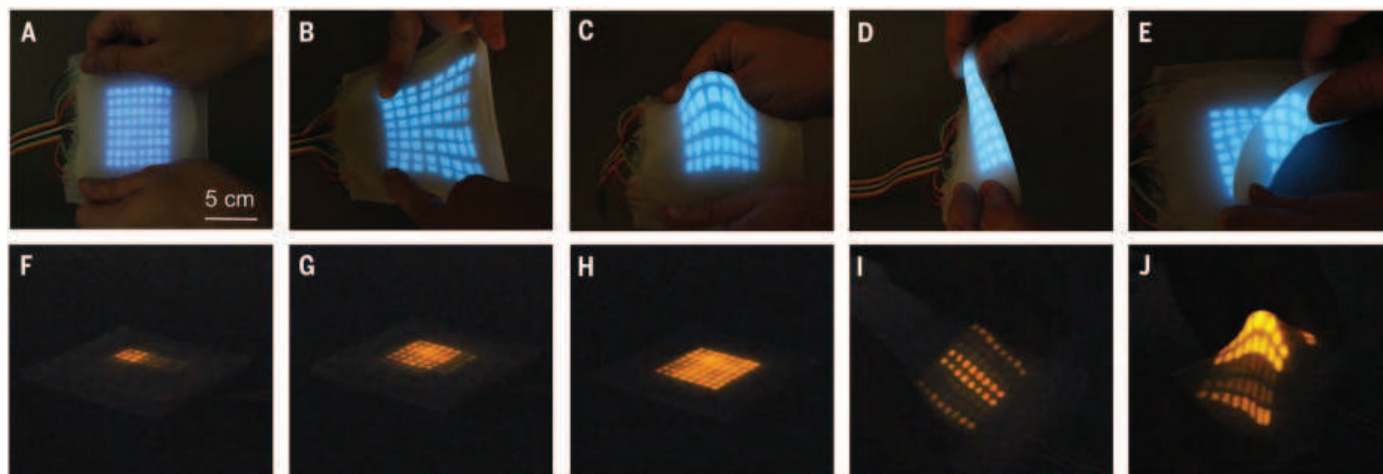


Fig. 3. Multipixel electroluminescent displays fabricated via replica molding. The device measures 5 mm thick, with each of the 64 pixels measuring 4 mm. We show the devices in various states of deformation and illumination: (A) undeformed, (B) stretched, (C) wrapped around a finger, (D) folded, (E) rolled, (F to H) with subsets of pixels activated, and (I and J) subsets of pixels activated while being deformed.

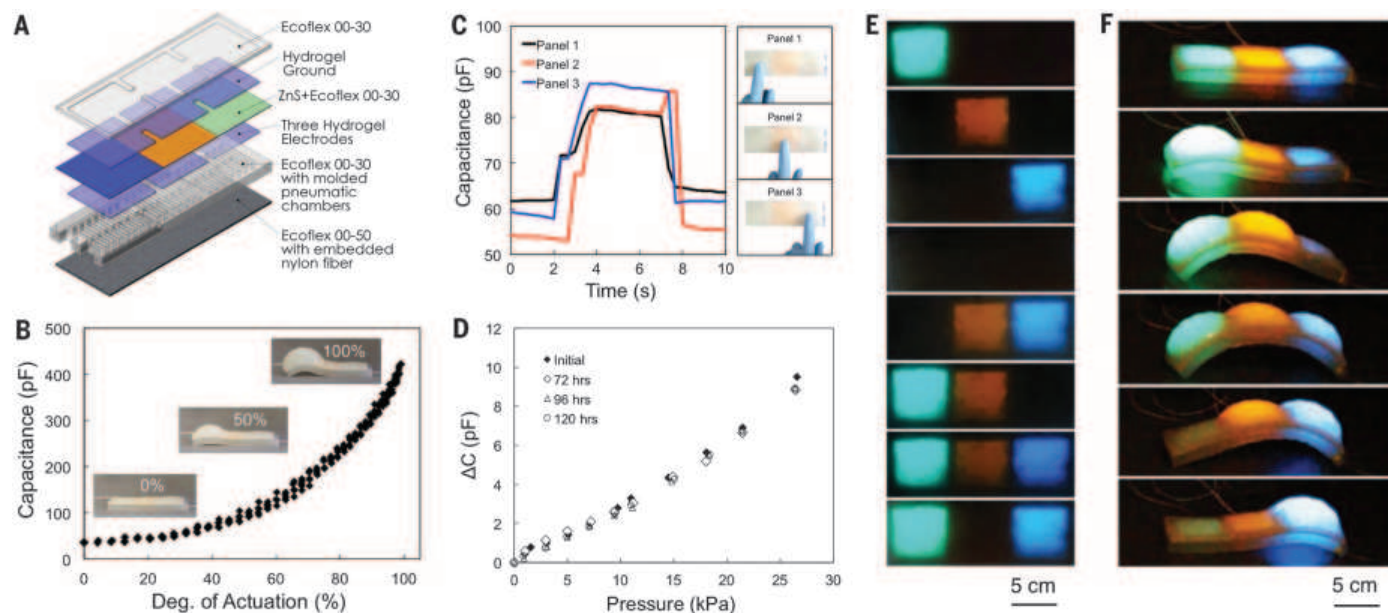


Fig. 4. HLEC skins endow soft robots with the ability to sense their actuated state and environment and communicate optically. (A) Schematic of a three-chambered soft robot. A series of three independently actuated pneumatic chambers is embedded between the HLEC skin (top) and a strain-limiting layer (bottom). (B) Capacitance plotted versus the actuation amplitude, defined as the relative change in deflection between the uninflated and fully inflated states (number of samples, $n = 5$). (C) A firm finger press induces an ~25% increase in capacitance. (D) Change in capacitance versus applied pressure. We observed

a negligible change in the capacitive response of the sensors over a period of 120 hours. (E) Array of three HLEC panels, each emitting a different wavelength through selective doping of the EL phosphor layer. Each HLEC panel is activated independently. (F) An undulating gait is produced by pressurizing the chambers in sequence along the length of the crawler. This sequence produces forward locomotion at a speed of $\sim 4.8 \text{ m hour}^{-1}$ ($\sim 32 \text{ body lengths hour}^{-1}$). As each pneumatic chamber is pressurized, the outer electroluminescent skin is stretched, increasing the electric field across the EL layer and thus the luminescence.

The crawling robot uses its HLEC skin to sense its physical state and environment (i.e., proprioception and exteroception). The capacitance of the HLEC changes with pneumatic actuation (Fig. 4B and data S8) and externally applied pressure (Fig. 4, C and D, and data table S9) (10). Actuation of the three underlying pneumatic chambers results in capacitance changes (ΔC) of up to 1000% when the chambers are fully inflated. Additionally, each HLEC panel is largely decoupled from the state of the surrounding pneumatic chambers (fig. S4 and data table S11) (28). The ability to identify the actuated state of the robot using the capacitive sensor readings enables proprioception. To demonstrate the tactile sensing capabilities of the electronic skin, we pressed each of the HLEC panels on the robot and measured the capacitive response (Fig. 4C). A firm finger press resulted in a ~25% increase in capacitance. The relative capacitance versus applied pressure, ranging from 0.9 to 30.9 kPa, remained nearly constant over a period of 120 hours (Fig. 4D). Arrays of these tactile sensors enable exteroception in soft robotic systems.

An array of three HLEC panels patterned into the three-chambered crawling robot enables eight distinct illuminated states (Fig. 4E). The embedded HLEC remains functional as the robot is actuated through its crawling sequence (Fig. 4F and movie S3). During actuation, the embedded HLEC undergoes stretches of $\lambda_1 = 2.63$ and $\lambda_2 = 2.42$ in the longitudinal (front to rear) and transverse (side to side) directions, respectively, to produce a ~635% increase in the skin's surface area (fig. S5). Similar to the single-panel HLEC (movie S1), the luminescence of the embedded skin increases during actuation as its thickness is decreased.

Integrating these highly stretchable and compliant displays into soft actuators enables two new capabilities in soft electronics: (i) displays that actively change their shape and (ii) robots that actively change their color. Using replica molding, we fabricated a multipixel array of individually addressable HLECs, and we used the same process to monolithically integrate these displays into a soft robot capable of changing posture. The HLEC array imparts both dynamic coloration and the potential for feedback control, which would be useful in epidermal electronics (31) and robotics (32). Although the luminous efficacy of our HLEC (43.2 mlm W^{-1}) is not as high as that of commercial AC powder electroluminescent devices ($\sim 4 \text{ lm W}^{-1}$) (32), it can be greatly improved by tuning the materials system and device architecture (such as higher-transmissivity encapsulation layers, reduced thickness, and optimized particle size). For applications requiring higher display resolution, HLECs could be made compatible with photolithography and other microfabrication techniques by using photopolymerizable polymers. These techniques would also allow us to decrease the thickness of the electroluminescent layer, thereby reducing the voltage required to power the HLEC.

REFERENCES AND NOTES

1. A. Barbosa, J. J. Allen, L. Mäthger, R. T. Hanlon, *Proc. R. Soc. London Ser. B* **279**, 84–90 (2012).
2. F. Ilievski, A. D. Mazzeo, R. F. Shepherd, X. Chen, G. M. Whitesides, *Angew. Chem. Int. Ed. Engl.* **50**, 1890–1895 (2011).
3. D. Rus, M. T. Tolley, *Nature* **521**, 467–475 (2015).
4. M. J. Spenko et al., *J. Field Robot.* **25**, 223–242 (2008).
5. E. Kreit et al., *J. R. Soc. Interface* **10**, 20120601 (2012).
6. J. A. Rogers, T. Someya, Y. Huang, *Science* **327**, 1603–1607 (2010).
7. S. A. Morin et al., *Science* **337**, 828–832 (2012).
8. Q. Wang, G. R. Gossweiler, S. L. Craig, X. Zhao, *Nat. Commun.* **5**, 4899 (2014).
9. C. Yu et al., *Proc. Natl. Acad. Sci. U.S.A.* **111**, 12998–13003 (2014).
10. P. E. Burrows et al., *Displays* **22**, 65–69 (2001).
11. T. H. Han et al., *Nat. Photonics* **6**, 105–110 (2012).
12. T. Sekitani et al., *Nat. Mater.* **8**, 494–499 (2009).
13. M. K. Shin et al., *Adv. Mater.* **22**, 2663–2667 (2010).
14. M. S. White et al., *Nat. Photon.* **7**, 811–816 (2013).
15. L. Hu, H. S. Kim, J. Y. Lee, P. Peumans, Y. Cui, *ACS Nano* **4**, 2955–2963 (2010).
16. J. Liang, L. Li, X. Niu, Z. Yu, Q. Pei, *Nat. Photon.* **7**, 817–824 (2013).
17. T. Someya et al., *Proc. Natl. Acad. Sci. U.S.A.* **102**, 12321–12325 (2005).
18. K. Takei et al., *Nat. Mater.* **9**, 821–826 (2010).
19. T. Someya et al., *Proc. Natl. Acad. Sci. U.S.A.* **101**, 9966–9970 (2004).
20. Y. L. Park, B. R. Chen, R. J. Wood, *IEEE Sens. J.* **12**, 2711–2718 (2012).
21. D. P. J. Cotton, I. M. Graz, S. P. Lacour, *IEEE Sens. J.* **9**, 2008–2009 (2009).
22. C. Keplinger et al., *Science* **341**, 984–987 (2013).
23. J. Y. Sun et al., *Nature* **489**, 133–136 (2012).
24. J. Y. Sun, C. Keplinger, G. M. Whitesides, Z. Suo, *Adv. Mater.* **26**, 7608–7614 (2014).
25. A. Kitai, *Luminescent Materials and Applications* (Wiley, West Sussex, UK, 2008), pp. 249–268.
26. R. F. Shepherd, A. A. Stokes, R. M. D. Nunes, G. M. Whitesides, *Adv. Mater.* **25**, 6709–6713 (2013).
27. Y. Bai et al., *Appl. Phys. Lett.* **105**, 151903 (2014).
28. Materials and methods are available as supplementary materials on Science Online.
29. G. F. Alfrej, J. B. Taylor, *Proc. Phys. Soc. B* **68**, 775–784 (1955).
30. R. F. Shepherd et al., *Proc. Natl. Acad. Sci. U.S.A.* **108**, 20400–20403 (2011).
31. D. H. Kim et al., *Science* **333**, 838–843 (2011).
32. J. Kim et al., *Nat. Commun.* **5**, 5747 (2014).

ACKNOWLEDGMENTS

Data reported in the paper are included in the supplementary materials. This work was supported by the Army Research Office (grant no. W911NF-15-1-0464), the Air Force Office of Scientific Research (grant no. FA9550-15-1-0160), the NSF MRSEC program (DMR-1120296), and an NSF Graduate Research Fellowship (grant no. DGE-1144153). The hyperelastic electroluminescent capacitors presented in this work have been filed under a provisional patent application, no. 62/250,172 for Stretchable Electroluminescent Devices. The listed inventors are Chris Larson, Shuo Li, Bryan Peele, Sanlin Robinson, and Robert Shepherd.

SUPPLEMENTARY MATERIALS

www.sciencemag.org/content/351/6277/1071/suppl/DC1
Materials and Methods
Supplementary Text
Figs. S1 to S7
Table S1
Reference (33)
Movies S1 to S3
Data Tables S1 to S11 (single Excel workbook)
5 May 2015; accepted 4 February 2016
10.1126/science.aac5082

HUMAN ALTRUISM

The brain's functional network architecture reveals human motives

Grit Hein,^{1*} Yosuke Morishima,^{1,2,3} Susanne Leiberg,¹ Sunhae Sul,⁴ Ernst Fehr¹

Goal-directed human behaviors are driven by motives. Motives are, however, purely mental constructs that are not directly observable. Here, we show that the brain's functional network architecture captures information that predicts different motives behind the same altruistic act with high accuracy. In contrast, mere activity in these regions contains no information about motives. Empathy-based altruism is primarily characterized by a positive connectivity from the anterior cingulate cortex (ACC) to the anterior insula (AI), whereas reciprocity-based altruism additionally invokes strong positive connectivity from the AI to the ACC and even stronger positive connectivity from the AI to the ventral striatum. Moreover, predominantly selfish individuals show distinct functional architectures compared to altruists, and they only increase altruistic behavior in response to empathy inductions, but not reciprocity inductions.

The theory of revealed preference (1) provides the choice-theoretic foundations for modern economics. In this view, preferences cannot be identified independently of behavior, and motives play no causal role in economists' explanatory toolbox—a view that is in direct contradiction to the neuroeconomic approach (2–4). In psychology, motives are also considered to be independent drivers of goal-directed human behavior (5). Motives are, however, mental constructs that are not directly observable and frequently not even accessible introspectively, meaning that asking people does not provide rel-

evant information about motives (6, 7). Therefore, human motives have been typically inferred from individuals' behavior by assuming that different motives lead to different behaviors.

¹Laboratory for Social and Neural Systems Research, Department of Economics, University of Zurich, Switzerland.

²Division of Systems Neuroscience of Psychopathology, Translational Research Center, University Hospital of Psychiatry, University of Bern, Switzerland. ³Japanese Science and Technology Agency, PRESTO, Japan.

⁴Department of Psychology, Pusan National University, Pusan, South Korea.

*Corresponding author. E-mail: grit.hein@econ.uzh.ch (G.H.); ernst.fehr@econ.uzh.ch (E.F.)

Here we ask whether different motives have a distinct neurophysiological representation that is generalizable across individuals. That is, even if we had no information about individuals' behaviors or if these behaviors would not allow us to

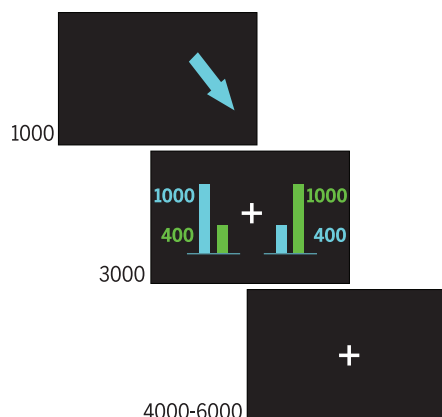


Fig. 1. Example trial in the allocation task in which subjects could allocate money to themselves (indicated by the green bars in the second screen) and one of their partners (indicated by the blue bars in the second screen). Subjects could either maximize their own monetary payoff (selfish decision) or maximize the paired partner's monetary payoff by giving up their own payoff (altruistic decision). They faced several trials during the allocation task that differed in the subject's cost of maximizing the partner's payoff (21). In each trial, subjects from the empathy induction group were paired with the empathy partner (empathy condition) or the baseline partner (baseline condition). Likewise, in each trial, subjects from the reciprocity induction group were paired with a reciprocity partner (reciprocity condition) or the baseline partner (baseline condition). The arrow in the first screen indicates the partner with whom the subject was paired in a trial. The choice problems in the empathy, the reciprocity, and the baseline conditions were identical.

make inferences about motives, could we still identify and predict their motives merely on the basis of their functional neural network architecture?

We tackled this question in the context of human altruistic decisions (8–14). Subjects participated in an allocation task in which they could make selfish or altruistic decisions. We studied the role of two key motives for altruistic behaviors—the empathy motive and the reciprocity motive, two important drivers for human altruism (8–14). We induced these motives experimentally in two different groups of subjects, i.e., subjects were randomly assigned to either the empathy induction group or the reciprocity induction group. After the motive inductions, subjects participated in the allocation task in which they could allocate money to other individuals at a cost to themselves. All subjects faced the same allocation task regardless of the previous motive-induction group. Therefore, their underlying motive cannot be inferred from the mere fact that they behave altruistically. Can we now predict the induced motive solely on the basis of the subject's functional neural architecture?

We used dynamic causal models (DCMs) of functional magnetic resonance imaging data (15–17) collected during the allocation task and used the estimated DCM parameters to predict subjects' "hidden" motivational state with machine learning—an approach known as generative embedding (17). More specifically, the DCM analyses of subjects' brain data during altruistic decision-making gave us information about individuals' network architecture in the different motive conditions. These parameters then provided the "raw" material for our predictions and for the mechanistic insights that follow from our examination (17).

Both in the empathy and the reciprocity induction group, subjects were paired with two partners (confederates of the experimenter), who were sitting on either side of the subject. In the empathy induction group, the subject repeatedly observed one of the confederates (the empathy

partner) receiving pain shocks in a number of trials, a situation known to elicit an empathic response (18, 19). The reciprocity motive is defined as the desire to reciprocate perceived kindness with a kind behavior (13, 14). Therefore, in the reciprocity induction group, we activated the reciprocity motive by instructing one of the confederates (the reciprocity partner) to give up money in several trials to save the subject from painful shocks (13, 14, 20). No motives were induced toward the respective second partner (baseline partner), who played the same role in both the empathy- and the reciprocity induction group [for details of motive induction, see supplementary materials (21)]. It is important to stress that the subjects received painful shocks not only in the reciprocity induction group but also in the empathy induction group, and that the number of painful shocks was identical across conditions (21). This feature has two advantages. First, by equalizing the shock frequency across conditions, we can be sure that the two motive inductions contain the same number of aversive events. Second, the application of painful shocks to the subject in the empathy condition is likely to enhance the ability to empathize with the empathy partner because subjects know how the shock feels. Finally, to assess the success of the motive inductions, the subjects also completed emotion ratings where they indicated in each trial how they felt.

In the allocation task, subjects were in the scanner. In each trial, they allocated money between themselves and one of the partners (Fig. 1). They could choose between maximizing the other person's monetary payoff by reducing their own monetary payoff (altruistic behavior), or maximizing their own payoff (selfish behavior) at a cost to the partner. Depending on the type of partner subjects faced in the allocation task, there were three conditions—the empathy condition, the reciprocity condition, and the baseline condition. Because neither reciprocity nor empathy motives were induced in the baseline condition

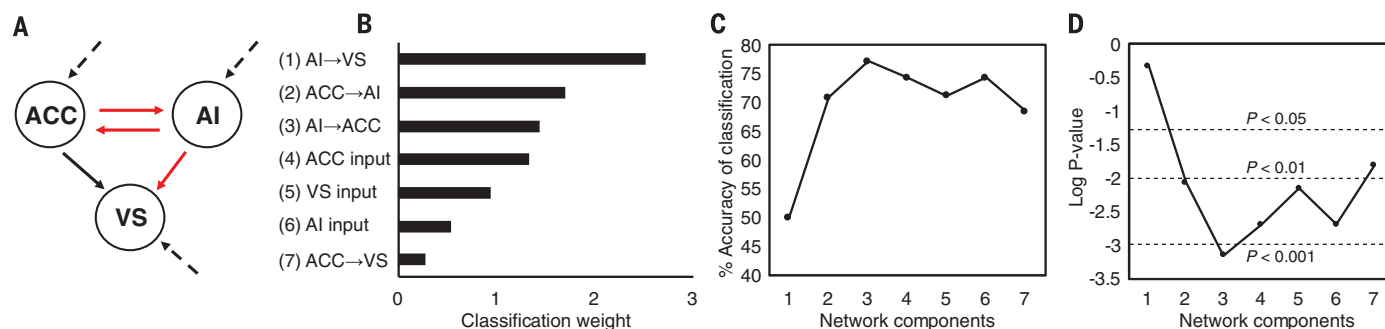


Fig. 2. DCM-based classification of different motives that resulted in the same altruistic decision. (A) Dynamic causal model (DCM) that was used to investigate the impact of the empathy and the reciprocity motive on brain connectivity during altruistic decisions. Straight arrows indicate interregional connections (four components), and dashed arrows represent stimulus inputs from outside of the network (three components). (B) Discriminative components. The figure visualizes the weights with which each of the seven network components contributed to the classification of the empathy and reciprocity

motive. (C) Accuracy for each level of the stepwise classification, based on the order of classification weights in (B). (D) Log P-value of stepwise classification, based on the order of classification weights in (B). AI, anterior insula; ACC, anterior cingulate cortex; VS, ventral striatum. Network components: 1 = AI→VS; 2 = plus ACC→AI; 3 = plus AI→ACC; 4 = plus ACC input; 5 = plus VS input; 6 = plus AI input; 7 = plus ACC→VS. The highest accuracy is reached when only the first three of the seven connectivity and input parameters are used to classify the empathy and the reciprocity motive [(A), highlighted in red].

(i.e., vis-à-vis the baseline partner), the behavior in this condition measures subjects' "raw" or "homegrown" unconditional altruism. This altruism is unconditional in the sense that the baseline partner did not do anything during the motive induction on which the subjects could condition their behavior during the allocation task. Homegrown unconditional altruism can play a role in all three conditions, but the induced empathy motive plays an additional role in the empathy condition and the reciprocity motive plays an additional role in the reciprocity condition.

Empathy means that if an individual observes someone else in pain, the individual also feels or "shares" that pain (18). Stronger empathizing during the empathy induction should therefore induce worse feelings (due to "shared" pain), which should then lead to a stronger empathy motive for altruistic behavior. We indeed observed that the worse a subject felt when seeing the empathy partner in pain, the more frequent the altruistic decision toward this person in the subsequent allocation task [$r(18) = -0.51$, $P = 0.03$]. Because the reciprocity partner is willing to incur cost to remove painful shocks, the partner is likely to be perceived as kind, which should result in positive feelings and higher frequencies of altruistic decisions toward the reciprocity partner. We found indeed that the better a subject felt after the reciprocity partner's decision during motive induction, the more altruistic the decisions toward this person in the subsequent allocation task [$r(16) = 0.57$, $P = 0.021$]. Reciprocity induction also induced significantly higher likability ratings—which were collected after scanning ("How much do you like the other person"? 9 = very much to 1 = not at all)—for the reciprocity partner as compared to the baseline partner [$t(15) = 3.24$, $P = 0.005$]. The overall frequency of altruistic decisions toward the empathy partner and the

reciprocity partner was significantly higher than toward the baseline partner [motive induction versus baseline, $F(1,32) = 12.5$, $P = 0.001$; empathy versus baseline, $t(17) = 2.5$, $P = 0.022$; reciprocity versus baseline, $t(15) = 2.7$, $P = 0.017$]. There was, however, no significant difference in the increase of altruistic decisions between the two motive inductions [empathy versus baseline compared to reciprocity versus baseline, $F(1,32) = 0.2$, $P = 0.64$]. In addition, the results of a Bayesian analysis show that the null hypothesis that the two motive inductions cause the same increase in altruism relative to baseline is more than five times more likely (84% versus 16%) than the hypothesis of a differential increase (21).

Our imaging analyses focused on altruistic decisions during the allocation task. First we used a conventional general linear model (GLM) analysis for a whole-brain search of regions with significantly different activity during altruistic decisions driven by empathy versus altruistic decisions driven by reciprocity. There were no significant differences even at the very liberal threshold of $P_{\text{uncorrected}} < 0.05$. This suggests that empathy-driven and reciprocity-driven altruism activate similar brain regions. We therefore compared brain activations under altruistic decisions in both motive-induction conditions with the activations involved in altruistic decisions in the baseline condition. The results revealed a network consisting of left anterior insula (AI), left ventral striatum (VS), and anterior cingulate cortex (ACC) [$P < 0.05$; family-wise error (FWE) corrected; see table S1 for details]—regions that were reported by previous studies on the reciprocity (22–24) and the empathy motive (18, 19, 25).

In a second step, we determined the pattern of neural connectivity within this network for each subject, using DCM. We extracted the time series of activations during altruistic decisions toward the empathy partner, the reciprocity part-

ner, and the respective baseline partner from individual regions of interest (ROIs) in left AI, left VS, and ACC (table S2).

The DCM analyses were based on the anatomical model shown in Fig. 2A, which is characterized by seven components: three inputs (dashed arrows) and four interregional connectivities (solid arrows). Because most VS projections target the cortex via the thalamus (26, 27), ascending projections from VS were not included in the anatomical model. We used Bayesian model averaging (28) to determine the DCM parameters for the seven components for each subject. For a subject of the empathy group, for example, we calculated (i) how activation in ACC, AI, and VS during altruistic decisions is changed as a result of impulses from outside the network under the empathy and under the baseline conditions (dashed arrows in Fig. 2A), and (ii) how activation in every (target) region is changed by the level of activation in the other regions during altruistic decisions under the empathy and the baseline conditions (effective connectivity, solid arrows in Fig. 2A). The same computations were also done for subjects of the reciprocity group. We thus obtained 14 DCM parameters per subject, seven for altruistic decisions under the respective motive-induction condition (empathy or reciprocity), and seven for altruistic decisions under the baseline condition. We then subtracted the individual DCM parameters of the baseline condition from the DCM parameters of the motive-induction condition. The resulting seven Δ -DCM parameters reflect the individual pattern of neural connectivity specific for altruistic decisions driven by empathy or reciprocity.

In a third step, we submitted these individual Δ -DCM parameters to a classification algorithm (support vector machine, SVM) to test if the individual patterns of brain connectivity can be used to detect the specific motive for altruism that the experimenter induced (17). This approach

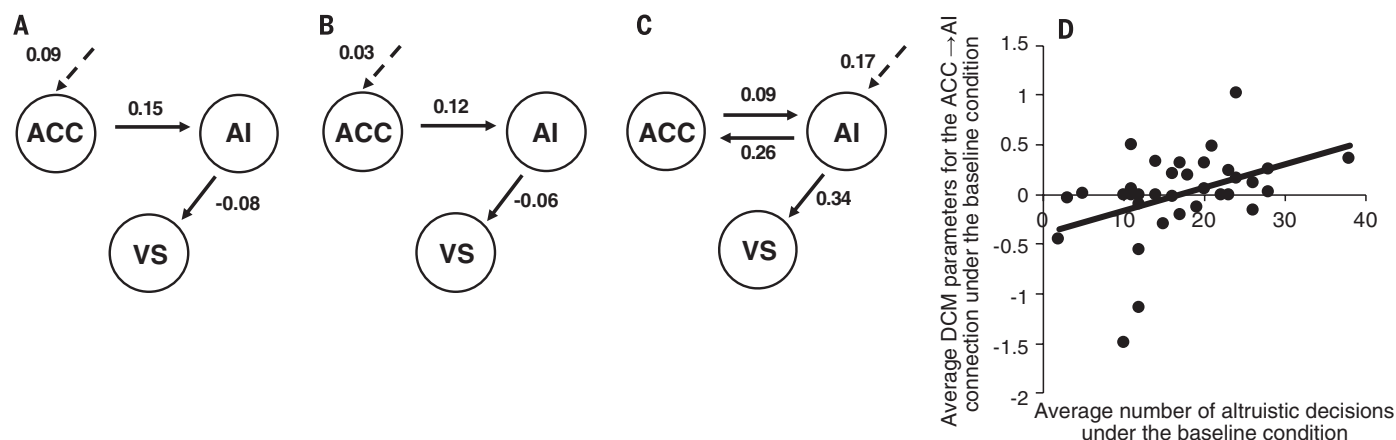


Fig. 3. Average best models and mean DCM parameters. Best models and mean DCM parameters for (A) Altruistic decisions driven by the empathy motive, (B) altruistic decisions driven by "homegrown" unconditional altruism in the baseline condition, and (C) altruistic decisions driven by the reciprocity motive. For visualization purposes, the baseline data for subjects from the empathy and the reciprocity group were pooled in (B), because there were no significant differences in the corresponding best-model parameters [ACC→AI,

$t(1,32) = -0.57$, $P = 0.58$; AI→VS, $t(1,32) = -1.03$, $P = 0.31$; ACC input, $t(1,32) = 0.55$, $P = 0.59$]. In (A) to (C), dashed arrows indicate direct inputs to an area; solid arrows indicate directed interregional connectivities. AI, anterior insula; ACC, anterior cingulate cortex; VS, ventral striatum. (D) Correlation between the individual parameters of the ACC→AI connection under baseline conditions and the individual average number of altruistic decisions toward the baseline partner.

significantly predicted the subjects' induced altruistic motives, i.e., whether subjects went through the empathy or the reciprocity induction condition (classification accuracy = 68.4%, $P = 0.016$). The computation of classification accuracy with the associated P -value is based on the posterior probability of balanced accuracy as in (17). We also tested if the two motives can be classified on the basis of conventional functional activations. We extracted the corresponding beta values from the traditional GLM analysis (empathy versus baseline condition; reciprocity versus baseline condition) from the same ROIs that were used for the DCM analyses and submitted them to

the classification algorithm. This analysis did not yield classification accuracy significantly above chance (classification accuracy = 55.2%, $P = 0.3$). It was also not possible to classify the motives based on the increases in the frequency of altruistic decisions in the two motive-induction conditions relative to the baseline condition [classification accuracy = 41%, $P = 0.93$; see also (29)].

To better understand which DCM parameters jointly enabled the distinction between the empathy and the reciprocity motive, we calculated the average classification weights with which each of the seven different network components contributed to the classification (Fig. 2B), and the stepwise classification performance of the sequential combination of network components (Fig. 2, C and D). The strongest classification weight was attached to the connection from AI to VS, followed by the directional connection from the cingulate cortex to the insular cortex and vice versa (see red arrows in Fig. 2A). The combination of these three network components was sufficient for classifying the induced motives behind subjects' altruistic decisions with an accuracy of 77% ($P = 0.0007$; Fig. 2, C and D).

To identify the motive-specific functional network architectures, we selected the best average network for altruistic decisions under the empathy, reciprocity, and baseline conditions. The selection procedure was based on 28 different models (fig. S3). To define this model space, we used the criteria of anatomical plausibility, network coherence, and functional plausibility [see methods section in supplementary materials (27) for details]. We used random-effect Bayesian model selection (30) to select the models whose structure and patterns of inputs and effective connectivity fit best with the neural processes evoked by altruistic decisions under the different conditions (27).

Figure 3 shows the best models of neural connectivity during empathy-driven, reciprocity-driven, and "homegrown" altruism in the baseline condition (see figs. S3 and S4 for details). A comparison between Fig. 3, A and B, shows a marked similarity in the functional network architecture of empathy-driven and homegrown altruism. Both models show a positive connectivity between ACC and AI, and a slightly negative connectivity between AI and VS, with no significant differences in the respective DCM parameters [ACC to AI, $t(1,17) = -0.24$, $P = 0.8$; AI to VS, $t(1,17) = -0.66$, $P = 0.52$; ACC input, $t(1,17) = 0.89$, $P = 0.34$]. This contrasts sharply with the best model for reciprocity-driven altruism (Fig. 3C). In this model there is, first, a strong bidirectional projection between AI and ACC. Second, there is a strong positive connectivity between AI and VS, which significantly differs from the negative AI-to-VS connectivity under the baseline [$t(1,15) = 2.8$, $P = 0.015$] and empathy conditions [$t(1,32) = 2.91$, $P = 0.006$; α (Bonferroni-corrected) < 0.025]. There were no significant differences with regard to the connectivity from ACC to AI [reciprocity versus baseline, $t(1,15) = 0.03$, $P = 0.9$; reciprocity versus empathy, $t(1,32) = -0.28$, $P = 0.78$].

These findings also raise the question whether the differential network components present in the reciprocity condition are related to particular psychological features. Inspired by previous evidence that has linked the social evaluation of other individuals to activation in ventral striatal regions (31, 32), we correlated subjects' likability ratings of the reciprocity partner with the individual strengths of the AI→VS connectivity. There was a significant positive correlation [$r(16) = 0.59$, $P = 0.016$], whereas no such correlation was present in the empathy and the baseline conditions [empathy condition: $r(18) = -0.29$, $P = 0.25$; baseline condition: $r(16) = 0.001$, $P = 0.99$].

There is, however, also a common network feature—the ACC→AI connectivity—that is present in all three conditions. We thus hypothesized that this component of the network might reflect basic prosocial motivation. To test this conjecture, we correlated individuals' frequency of altruistic decisions toward their baseline partner with their DCM parameters of the ACC→AI connection. The results show a significant positive correlation [$r(34) = 0.4$, $P = 0.017$] (Fig. 3D). The stronger a person's connectivity from ACC to AI, the higher the baseline level of altruism. Indeed, if we divide our sample of subjects in prosocial and selfish individuals on the basis of a median split in the frequency of altruistic decisions in the baseline condition, we find that prosocial individuals display a positive connectivity from ACC to AI of 0.16, whereas selfish individuals show a negative connectivity of -0.17 —a difference that is highly significant [$F(1,32) = 9.49$, $P = 0.004$].

If selfish and prosocial subjects display different network architectures, they may also respond differently to the empathy and the reciprocity induction. We sorted the selfish and prosocial individuals by the respective motive-induction condition; this resulted in nine prosocial subjects in both the empathy and the reciprocity condition, nine selfish subjects in the empathy condition, and seven selfish subjects in the reciprocity condition. Figure 4A shows that the induction of the empathy motive significantly increased altruistic decisions in selfish individuals, whereas there was no such effect after the induction of reciprocity. In contrast, the induction of reciprocity resulted in a further enhancement of altruistic behavior in prosocial individuals, whereas the empathy induction had no effect on these individuals. Thus, the two types of subjects respond very differently to the two motive inductions [motive induction \times individual type, $F(1,30) = 8.8$, $P = 0.006$].

We next compared the differences in brain connectivity between the motive-induction and the baseline conditions. Empathy induction increased effective connectivity from ACC to AI in selfish subjects, while there was no such effect after the selfish subjects received a reciprocity induction and in prosocial individuals [motive induction \times individual type, $F(1,30) = 4.1$, $P = 0.05$] (Fig. 4B). In contrast, the reciprocity induction led to an enhancement of neural connectivity from AI to VS in prosocial individuals, which is not the case

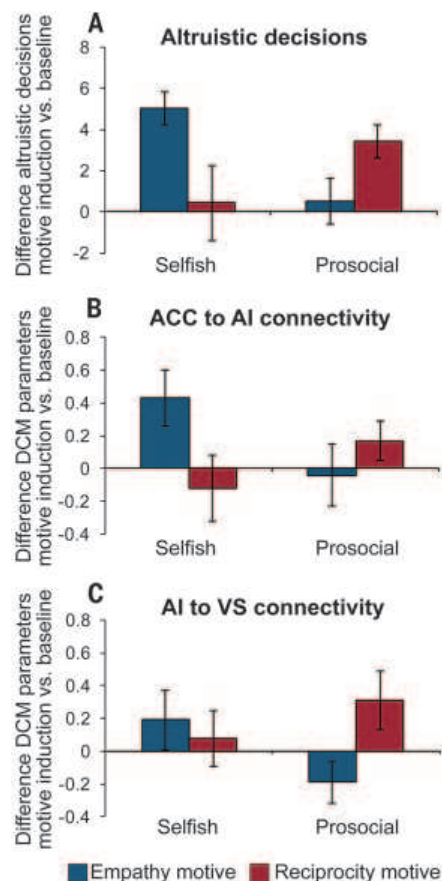


Fig. 4. Differential impact of the empathy and the reciprocity motive on individuals with predominantly selfish and prosocial preferences.

(A) Change in the frequency of altruistic decisions after the empathy and the reciprocity induction, compared to baseline, in selfish and prosocial individuals. The empathy induction only increases the frequency of altruistic decisions in more selfish subjects, whereas the reciprocity induction only increases the frequency of altruistic decisions in subjects with more prosocial preferences. (B) Change in brain connectivity from the ACC to the AI after the empathy and reciprocity induction, compared to baseline, in selfish and prosocial individuals. (C) Change in brain connectivity from the AI to the VS after the empathy and reciprocity induction, compared to baseline, in selfish and prosocial individuals. Error bars indicate SEM.

after the empathy induction and in selfish types [motive induction \times individual type, $F(1,30) = 4.9$, $P = 0.034$] (Fig. 4C).

Motives are purely mental constructs that are not directly observable. Here we show, however, that distinct motives have a distinct neurophysiological representation in the brain. Although the empathy and the reciprocity motive increase the frequency of altruistic acts by the same amount relative to the baseline condition, they are associated with different patterns of brain connectivity that enabled us to predict the different motives with relatively high accuracy. We predicted each subject's induced motive with a classifier whose parameters were not influenced by that subject's brain data (nor by that subject's behavioral data). Instead, the parameters of the classifier were solely informed by other subjects' brain data. This means that the motive-specific brain connectivity patterns are generalizable across subjects. The distinct and across-subject-generalizable neural representation of the different motives thus provides evidence for a distinct neurophysiological existence of motives.

The findings also provide mechanistic insights into the neural underpinnings of important altruistic motives and how motive inductions change the underlying neural network. In particular, predominantly selfish individuals were characterized by a low or even negative connectivity from ACC→AI in the baseline condition, whereas predominantly prosocial individuals displayed a positive connectivity between these regions. However, when we induce the empathy motive, the selfish, but not the prosocial, types become more altruistic and show a substantial increase in ACC→AI connectivity. Thus, after the empathy induction, selfish individuals resemble "homegrown" unconditional altruists in terms of both brain connectivity and altruistic behavior. This contrasts with the effect of inducing the reciprocity motive, which renders the prosocial, but not the selfish, types more altruistic and increases only the prosocial types' AI→VS connectivity.

We obtain these mechanistic insights because the inputs into the support vector machine are not merely brain activations but small brain models of how relevant brain regions interact with each other (i.e., functional neural architectures). Thus, by correctly predicting the induced motives, we simultaneously determine those mechanistic models of brain interaction that best predict the motives. And it is these models that deliver the mechanistic insights into brain function and how changes in brain function relate to behavioral changes due to motive inductions. Our study, therefore, also demonstrates how "mere prediction" and "insights into the mechanisms" that underlie psychological concepts (such as motives) can be simultaneously achieved if functional neural architectures are the inputs for the prediction.

REFERENCES AND NOTES

- P. A. Samuelson, *Economica* **15**, 243–253 (1948).
- P. W. Glimcher, A. Rustichini, *Science* **306**, 447–452 (2004).
- A. Rangel, C. Camerer, P. R. Montague, *Natl. Rev.* **9**, 545–556 (2008).
- E. Fehr, A. Rangel, *J. Econ. Perspect.* **25**, 3–30 (2011).
- K. Lewin, *Field Theory in Social Science* (Harper, New York, 1951).
- R. B. Zajonc, *Am. Psychol.* **35**, 151–175 (1980).
- R. E. Nisbett, T. D. Wilson, *Psychol. Rev.* **84**, 231–259 (1977).
- C. D. Batson, *The Altruism Question: Toward a Social-Psychological Answer* (Erlbaum, Hillsdale, NJ, 1991).
- E. Fehr, U. Fischbacher, *Nature* **425**, 785–791 (2003).
- J. Moll et al., *Proc. Natl. Acad. Sci. U.S.A.* **103**, 15623–15628 (2006).
- W. T. Harbaugh, U. Mayr, D. R. Burghart, *Science* **316**, 1622–1625 (2007).
- Y. Morishima, D. Schunk, A. Bruhin, C. C. Ruff, E. Fehr, *Neuron* **75**, 73–79 (2012).
- M. Rabin, *Am. Econ. Rev.* **83**, 1281–1302 (1993).
- A. Falk, U. Fischbacher, *Games Econ. Behav.* **54**, 293–315 (2006).
- K. J. Friston, L. Harrison, W. Penny, *Neuroimage* **19**, 1273–1302 (2003).
- K. E. Stephan et al., *Neuroimage* **42**, 649–662 (2008).
- K. H. Brodersen et al., *PLOS Comput. Biol.* **7**, e1002079 (2011).
- T. Singer et al., *Science* **303**, 1157–1162 (2004).
- G. Hein, G. Silani, K. Preusschoff, C. D. Batson, T. Singer, *Neuron* **68**, 149–160 (2010).
- R. A. Emmons, M. E. McCullough, *The Psychology of Gratitude* (Oxford Univ. Press, 2004).
- Methods and materials, supplementary analyses, supplementary figures, and supplementary tables are available as supporting material on Science Online.
- D. Tomlin et al., *Science* **312**, 1047–1050 (2006).
- J. K. Rilling et al., *Neuropsychologia* **46**, 1256–1266 (2008).
- K. L. Phan, C. S. Sripada, M. Angstadt, K. McCabe, *Proc. Natl. Acad. Sci. U.S.A.* **107**, 13099–13104 (2010).
- C. Lamm, J. Decety, T. Singer, *Neuroimage* **54**, 2492–2502 (2011).
- S. N. Haber, B. Knutson, *Neuropsychopharmacol.* **35**, 4–26 (2010).
- A. Parent, L. N. Hazrati, *Brain Res. Brain Res. Rev.* **20**, 91–127 (1995).
- J. A. Hoeting, D. Madigan, A. E. Raftery, C. T. Volinsky, *Stat. Sci.* **14**, 382 (1999).
- If we use both the number of altruistic decisions in the baseline condition and the increase in the frequency of altruistic decisions in the motive-induction conditions, the behavioral classification becomes marginally significant (classification accuracy of 64.2%, $P = 0.051$). However, if we perform the same classification analysis with connectivity data—i.e., in addition to the Δ -DCM parameters we also use the level of the DCM parameters in the baseline condition for classification purposes—the classification accuracy increases even to 83%, $P = 0.00004$. Thus, the classification based on brain connectivity data clearly outperforms the behavior-based classification (see also supplementary materials).
- K. E. Stephan, W. D. Penny, J. Daunizeau, R. J. Moran, K. J. Friston, *Neuroimage* **46**, 1004–1017 (2009).
- M. R. Delgado, R. H. Frank, E. A. Phelps, *Nat. Neurosci.* **8**, 1611–1618 (2005).
- A. Tusche, T. Kahnt, D. Wisniewski, J. D. Haynes, *Neuroimage* **72**, 174–182 (2013).

ACKNOWLEDGMENTS

We thank K. E. Stephan for useful comments on early versions of the manuscript and K. Treiber and S. Klein for assistance with data collection. We also thank two anonymous referees for their helpful comments. The paper is part of the advanced European Research Council grant on the "Foundations of Economic Preferences and the Synergia grant of the Swiss National Science Foundation on the neuroeconomics of value-based decision making (CRSII3_141965)." The data are stored on the server of the Laboratory for Social and Neural Systems Research at the University of Zurich.

SUPPLEMENTARY MATERIALS

www.sciencemag.org/content/351/6277/1074/suppl/DC1
Materials and Methods
Figs. S1 to S4
Tables S1 and S2
References (33–37)

15 June 2015; accepted 22 January 2016
10.1126/science.aac7992

EBOLA VIRUS

Isolation of potent neutralizing antibodies from a survivor of the 2014 Ebola virus outbreak

Zachary A. Bornholdt,¹ Hannah L. Turner,² Charles D. Murin,^{1,2} Wen Li,³ Devin Sok,¹ Colby A. Souders,⁴ Ashley E. Piper,⁵ Arthur Goff,⁵ Joshua D. Shamblyn,⁵ Suzanne E. Wollen,⁵ Thomas R. Sprague,⁵ Marnie L. Fusco,¹ Kathleen B. J. Pommert,¹ Lisa A. Cavacini,⁴ Heidi L. Smith,⁴ Mark Klempner,⁴ Keith A. Reimann,⁴ Eric Krauland,³ Tillman U. Gerngross,³ Karl D. Wittrup,³ Erica Ollmann Saphire,¹ Dennis R. Burton,^{1,6} Pamela J. Glass,⁵ Andrew B. Ward,² Laura M. Walker^{3*}

Antibodies targeting the Ebola virus surface glycoprotein (EBOV GP) are implicated in protection against lethal disease, but the characteristics of the human antibody response to EBOV GP remain poorly understood. We isolated and characterized 349 GP-specific monoclonal antibodies (mAbs) from the peripheral B cells of a convalescent donor who survived the 2014 EBOV Zaire outbreak. Remarkably, 77% of the mAbs neutralize live EBOV, and several mAbs exhibit unprecedented potency. Structures of selected mAbs in complex with GP reveal a site of vulnerability located in the GP stalk region proximal to the viral membrane. Neutralizing antibodies targeting this site show potent therapeutic efficacy against lethal EBOV challenge in mice. The results provide a framework for the design of new EBOV vaccine candidates and immunotherapies.

In recent years, Ebola virus (EBOV) outbreaks have increased in frequency, duration, and geographical spread, underscoring the need for pre- and post-exposure treatments (1). The membrane-anchored EBOV glycoprotein (GP)

trimer is the sole known target for protective antibodies and is currently the primary target for antiviral vaccines and therapies (2, 3). A small number of protective monoclonal antibodies (mAbs) to GP have been isolated from immunized mice,

and recent structures of these antibodies in complex with GP have illuminated key sites of vulnerability on the EBOV glycoprotein (3–7). However, only a small number of mAbs to GP have been isolated from human EBOV survivors (8–10), and therefore the characteristics of the human antibody response to EBOV GP remain largely undefined.

In this study, we aimed to comprehensively profile the human B cell response to EBOV GP by cloning an extensive panel of mAbs to GP from the peripheral B cells of a convalescent donor (subject 45) who survived the 2014 EBOV Zaire outbreak. Three months after primary infection, the donor plasma showed strong immunoglobulin G (IgG) binding reactivity to EBOV GP and potent neutralizing activity, suggesting that this donor had mounted a robust neutralizing antibody (Nab) response to GP by this time point (fig. S1, A and B). To assess the magnitude of the B cell response to EBOV GP, B cells were stained with a fluorescently labeled EBOV GP ectodomain (GPΔTM) (4) and analyzed by flow cytometry. Approximately 3% of IgG⁺ B cells were specific for GPΔTM (fig. S2), which is comparable to the percentage of circulating antigen-specific peripheral B cells observed during chronic HIV infection and after primary dengue infection (11, 12). Cognate antibody heavy- and light-chain pairs were rescued from 420 individual GPΔTM-reactive B cells by single-cell polymerase chain reaction and were subsequently cloned and expressed as full-length IgGs in an engineered strain of *Saccharomyces cerevisiae* (13). Of the 420 cloned

mAbs, 349 bound to EBOV GP in preliminary binding screens (table S1). Analysis of the heavy- and light-chain variable regions (V_H and V_κ, respectively) revealed that the anti-GP repertoire was highly diverse, containing 294 independent clonal lineages (fig. S3A and table S2). This result contrasts with previously described anti-HIV and anti-influenza repertoires, which show a significantly higher degree of clonal restriction (11, 14). Comparison to non-GP-reactive antibodies (15) revealed that the EBOV GP-specific repertoire was skewed toward Ig light-chain kappa (Igκ) versus Ig light-chain lambda (Igλ) and longer heavy-chain complementarity-determining region 3 (CDRH3) lengths (fig. S3, B and C, and table S2). Similar biases have also been observed in HIV-1-infected patient repertoires (11, 12). V_H and V_κ germline gene usage in the GP-specific repertoire was similar to non-GP-specific repertoires (15, 16) (fig. S3, D and E, and table S2). As expected for antibodies derived from IgG⁺ B cells, almost all of the GP-specific clones were somatically mutated, with an average of 5.1 and 2.7 nucleotide substitutions in V_H and V_L, respectively (fig. S3F and table S2).

To map the antigenic specificities of the mAbs to GP, we produced 321 IgGs in larger quantities and performed biolayer interferometry (BLI) binding experiments with several GP variants. We first tested binding to EBOV GPΔTM and a mucin-like domain deletion construct (GPΔmuc) (6). Unexpectedly, only two mAbs failed to bind to GPΔmuc, indicating that less than 1% of the GP-specific antibody response in this donor is directed against epitopes within or dependent on the mucin-like domain (Fig. 1A and table S3). About 30% of the mAbs showed increased binding responses and faster association rates to GPΔmuc as compared to GPΔTM (fig. S4), suggesting that these mAbs probably recognize epitopes that are partially occluded by the mucin-like domain. We next tested the mAbs for binding to a secreted GP isoform, sGP, which is expressed as a disulfide-linked GPI dimer containing the majority of the mucin-like

domain-free GPI core and glycan cap sequence (fig. S5) (17, 18). This analysis revealed that 39% of GPΔmuc-reactive mAbs failed to bind to sGP, 2% bound with similar apparent affinity to both GPΔmuc and sGP, and 59% reacted with both proteins but bound with higher apparent affinity to sGP (Fig. 1, B and C, and table S3). The latter result is consistent with previous studies showing that sGP is secreted in large quantities during natural infection and may behave as an antigenic decoy by redirecting the immune response toward epitopes that are either inaccessible on surface GP or shared between the two proteins (17, 19).

To further define the epitopes targeted by the mAbs to GP, we performed competitive binding experiments (20). We first tested the 321 mAbs for competition with two well-characterized murine mAbs, 1H3 and 13C6, that recognize overlapping epitopes in the glycan cap (4). The vast majority of sGP cross-reactive binders competed with one or both mAbs, suggesting that they also bind within the glycan cap (Fig. 2A and fig. S6A). We next tested the GP-specific mAbs for competition with KZ52, a human antibody that binds at the interface of GP1 and GP2 (6, 8). Approximately half of the GP-specific binders competed with KZ52 (Fig. 2A and fig. S6B), suggesting that this antigenic site is a common target for antibodies elicited by natural EBOV infection, at least for the donor studied. Because KZ52 has been shown to exhibit specificity for Zaire GP (6), we next tested selected KZ52 competitors for cross-reactivity with Sudan (SUDV) GP and Bundibugyo (BDBV) GP. Similar to KZ52, most of these mAbs did not show broad species cross-reactivity (Fig. 2B and fig. S7A). However, in contrast to KZ52 and other well-characterized GP base binders (4), most of the KZ52 competitor mAbs failed to react with a minimal thermolysin-processed GP core, in which both the mucin domain and glycan cap regions had been proteolytically removed (GP_{CL}) (4) (Fig. 2C). Thus, this class of antibodies appears to target specific epitopes that either directly overlap with the KZ52 epitope or are sterically inhibited

¹Department of Immunology and Microbial Science, The Scripps Research Institute, La Jolla, CA 92037, USA.

²Department of Integrative Structural and Computational Biology, The Scripps Research Institute, La Jolla, CA 92037, USA. ³Adimab, Lebanon, NH 03766, USA. ⁴MassBiologics, University of Massachusetts Medical School, Boston, MA 02126, USA. ⁵U.S. Army Medical Research Institute of Infectious Diseases, Frederick, MD 21702, USA. ⁶Ragon Institute of Massachusetts General Hospital, Massachusetts Institute of Technology, and Harvard University, Cambridge, MA 02142, USA.

*Corresponding author. E-mail: laura.walker@adimab.com

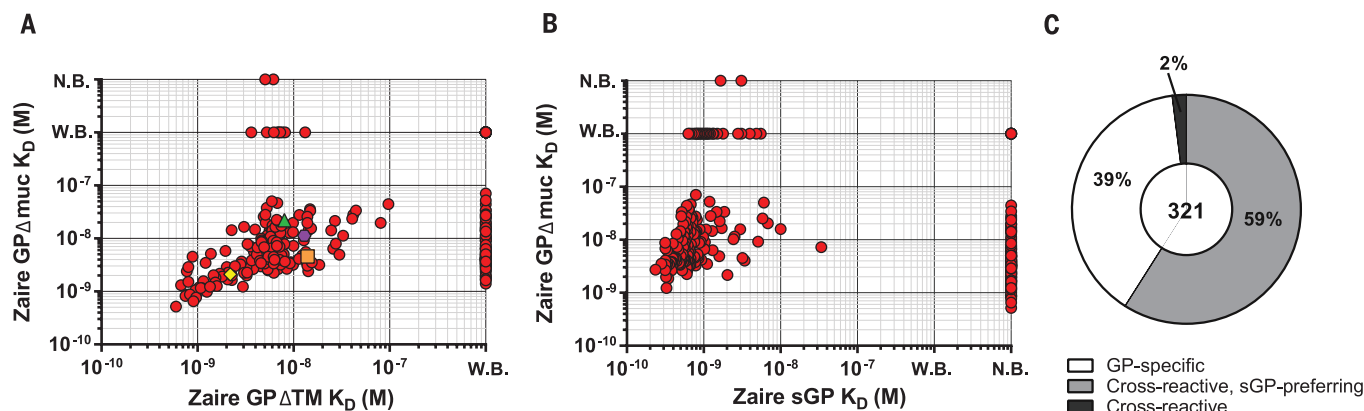


Fig. 1. Antigen-binding properties of mAbs to GP. (A) Apparent binding affinities of GP-specific IgGs to Zaire GPΔTM and Zaire GPΔmuc constructs as determined by BLI measurements. Newly discovered mAbs to GP are shown as red circles. KZ52 IgG (yellow diamond), 13C6 IgG (green triangle), 1H3 IgG (orange square), and 2G4 IgG (purple hexagon) are included for comparison. (B) Apparent binding affinities of GP-specific IgGs to Zaire sGP and Zaire GPΔmuc as determined by BLI measurements.

(C) Pie chart summarizing antibody binding profiles. Cross-reactive mAbs refer to those that bind to both GP and sGP. N.B., nonbinder; W.B., weak binder. IgG equilibrium dissociation constants were calculated for mAbs with BLI responses >0.1 nm. mAbs with BLI responses <0.05 nm were designated as N.B.s; mAbs with BLI responses between 0.05 and 0.1 nm were designated as W.B.s. All data are representative of two or more independent experiments.

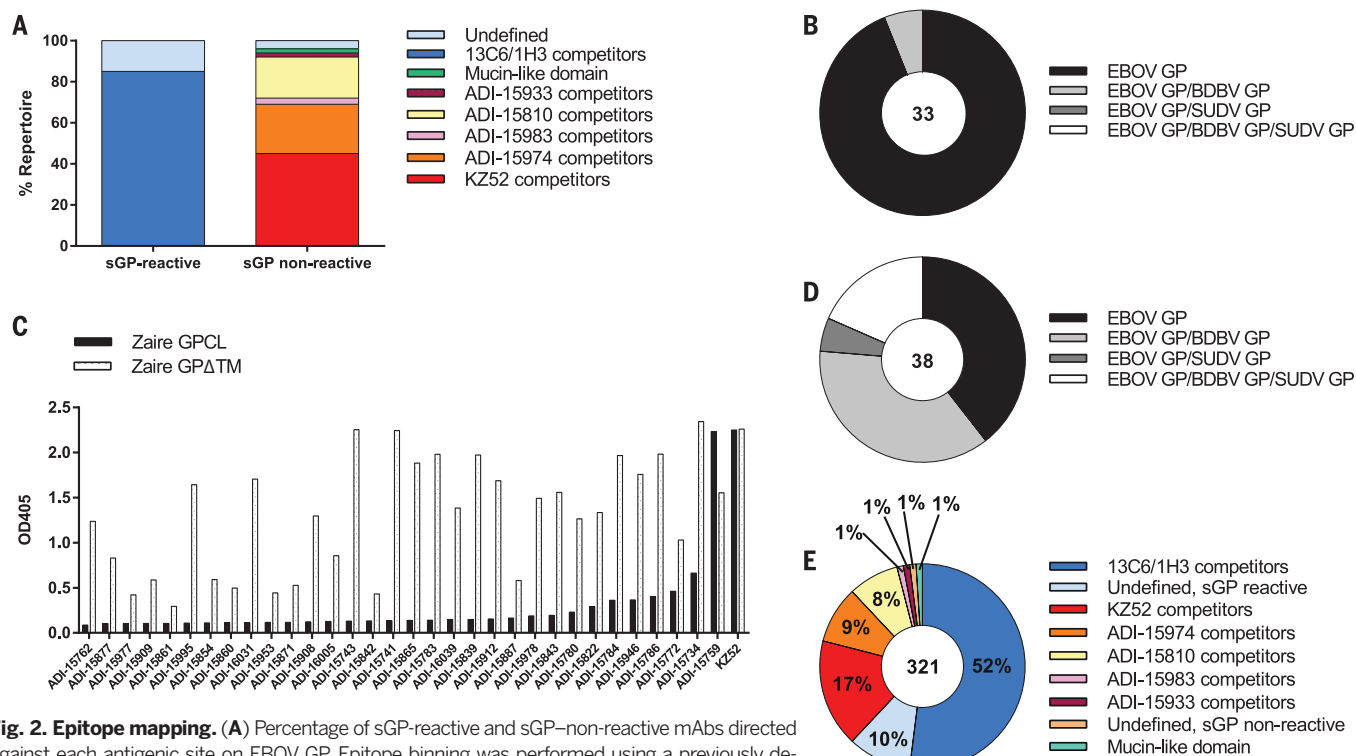
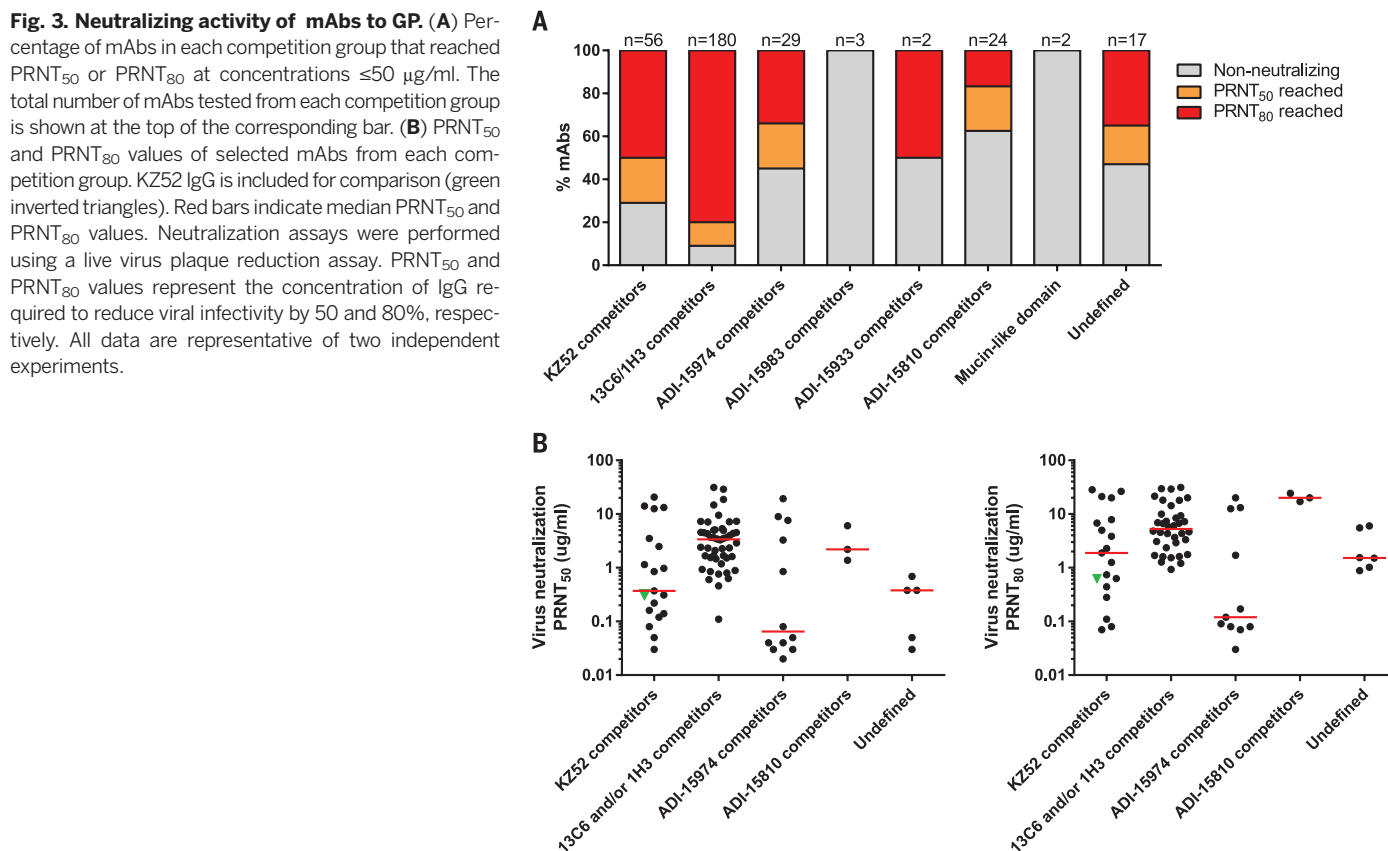


Fig. 2. Epitope mapping. (A) Percentage of sGP-reactive and sGP-non-reactive mAbs directed against each antigenic site on EBOV GP. Epitope binning was performed using a previously described yeast-based competition assay (20). (B) Percentage of selected KZ52 competitors that cross-react with SUDV GP and BDBV GP. Binding cross-reactivity was assessed by enzyme-linked immunosorbent assay (ELISA). (C) ELISA binding of selected KZ52 competitors to a minimal GP core that contains deletions in the mucin-like domain and glycan cap (GP_{CL}). ELISA binding is expressed as the optical density at 405 nm (OD₄₀₅) reading at a concentration of 0.2 µg/ml. (D) Percentage of selected KZ52 noncompetitors that cross-react with SUDV GP and BDBV GP. Binding cross-reactivity was assessed by ELISA. (E) Summary of the antigenic sites targeted by the mAbs to GP. All data are representative of two or more independent experiments.



by the KZ52 Fab. To estimate the number of different antigenic sites recognized by the remaining GP-specific mAbs, we performed competitive binding experiments with four high-affinity mAbs from the panel (ADI-15974, ADI-15933, ADI-15810, and ADI-15983) that did not show significant competition with KZ52 or with each other (table S4). Eighty percent of the non-KZ52-competitive GP-specific mAbs bound to epitopes overlapping that of ADI-15974 or ADI-15810 (Fig. 2A and fig. S6B). This group of mAbs also showed significantly broader cross-species GP-binding reactivity than the KZ52 competitors (Fig. 2D and fig. S7B). Overall, these data show that the anti-GP repertoire in this patient is primarily composed of clones that target four non-overlapping antigenic sites on EBOV GP (Fig. 2E).

We next measured the neutralizing activity of the B cell-derived mAbs using a live virus plaque reduction neutralization (PRNT) assay. Because of the large number of mAbs and the high-throughput nature of our study, initial neutralization screening was performed using a single concentration of purified IgG (table S5 and fig. S9). Remarkably, 77 and 63% of the mAbs reduced viral infectivity by 50 and 80% (PRNT₅₀ and PRNT₈₀), respectively, at concentrations ≤ 50 μ g/ml (Fig. 3A and table S5). Control experiments with yeast-produced and CHO-produced (CHO, Chinese hamster ovary cells) IgGs demonstrated that functional activity is probably not affected by the host production system (fig. S8). Analysis of neutralizing activity by a competition group revealed that the majority of competition groups contained a pro-

portion of NABs, with the KZ52 and 13C6/1H3 competition groups containing the highest proportion of NABs (Fig. 3A and table S5). The latter result was unexpected, because 13C6 and 1H3 only weakly neutralize in the absence of complement (7, 21). We next performed neutralization titration experiments in order to evaluate neutralization potency. These results showed that several NABs, particularly those in the ADI-15974 and KZ52 competition groups, exhibited extraordinary potency. Half of the NABs tested from the ADI-15974 competition group, and two of the NABs tested from the KZ52 competition group, neutralized with PRNT₅₀ values ≤ 0.05 μ g/ml (Fig. 3B and table S5). In contrast, the majority of 13C6 and/or 1H3 competitor mAbs neutralized with relatively modest potency, with PRNT₅₀ values averaging 3.3 μ g/ml. We conclude that the GP-specific antibody repertoire in the donor studied contains a high proportion of NABs, the most potent of which bind to epitopes overlapping those of KZ52 or ADI-15974.

To structurally define the epitopes recognized by the NABs, we used single-particle electron microscopy (EM) to examine five potent NABs, representing each of the four major competition groups, in complex with fully glycosylated EBOV GPATM. These NABs included ADI-15731 (a 13C6 competitor), ADI-15734 and ADI-15762 (KZ52 competitors), ADI-15758 (an ADI-15974 competitor), and ADI-15859 (an ADI-15810 competitor). We were able to obtain negative-stain two-dimensional (2D) class averages for all five complexes of Fabs bound to EBOV GPATM (fig. S10) and 3D reconstructions for four of the Fab:EBOV GPATM complexes at 18 to 24 Å resolution (Fig. 4 and fig. S11). In agreement with the competitive binding data, the EM reconstruction of ADI-15731 showed that this NAB binds within the glycan cap, with a footprint approximately between the epitopes recognized by 13C6 and 1H3 and with a similar angle of approach (Fig. 4 and fig. S12A). We next examined the two KZ52 competing NABs, ADI-15734 and ADI-15762. As anticipated, ADI-15734 bound to EBOV GPATM at the GP1/GP2 interface, slightly adjacent to the KZ52 epitope and at a similar angle of approach (Fig. 4 and fig. S12C). In contrast, ADI-15762 actually binds within the glycan cap, but with a shallow binding angle that probably sterically occludes the KZ52 epitope (Fig. 4 and fig. S12B). Last, we determined the structure of EBOV GPATM in complex with ADI-15758 (an ADI-15974 competitor), one of the most potent NABs described in this panel. The EM reconstruction shows that ADI-15758 binds to a region proximal to the viral membrane, distal to all previously described epitopes, and below the body of the trimeric EBOV GP structure (Fig. 4 and fig. S12D). Although this region has not yet been structurally characterized at high resolution in the pre-fusion GP context, it corresponds to the α -helical heptad repeat 2 (HR2; residues 613 to 637) defined in the post-fusion conformation (22). Docking of the EBOV GP crystal structure into the reconstruction suggests that the ADI-15758 epitope is within the C-terminal 24 residues of GP2 contained in the EBOV GPATM construct (6). Three Fab molecules

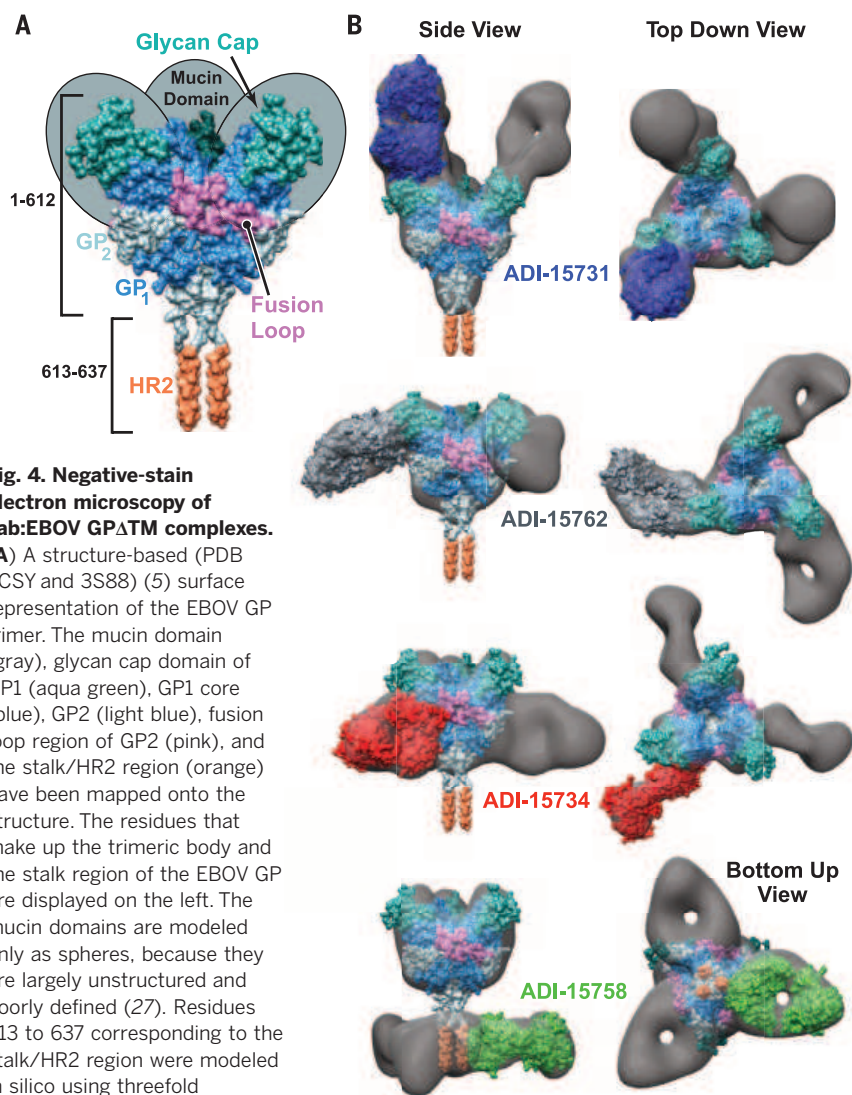


Fig. 4. Negative-stain electron microscopy of Fab:EBOV GPATM complexes.

(A) A structure-based (PDB 3CSY and 3S88) (5) surface representation of the EBOV GP trimer. The mucin domain (gray), glycan cap domain of GP1 (aqua green), GP1 core (blue), GP2 (light blue), fusion loop region of GP2 (pink), and the stalk/HR2 region (orange) have been mapped onto the structure. The residues that make up the trimeric body and the stalk region of the EBOV GP are displayed on the left. The mucin domains are modeled only as spheres, because they are largely unstructured and poorly defined (27). Residues 613 to 637 corresponding to the stalk/HR2 region were modeled in silico using threefold symmetry and peptide structure prediction for the HR2 region (28). (B) Corresponding 3D reconstructions of four Fab:EBOV GPATM complexes are shown in transparent surface representation (gray) with the model from (A) fitted in the density. Additionally, structural models for each Fab variable region were generated using the ROSIE server (29, 30) and then fitted into the density maps as surface representations. Each structure is shown as side (left) and top (right) views, with the exception of ADI-15758, which is shown from the bottom up, relative to the viral membrane.

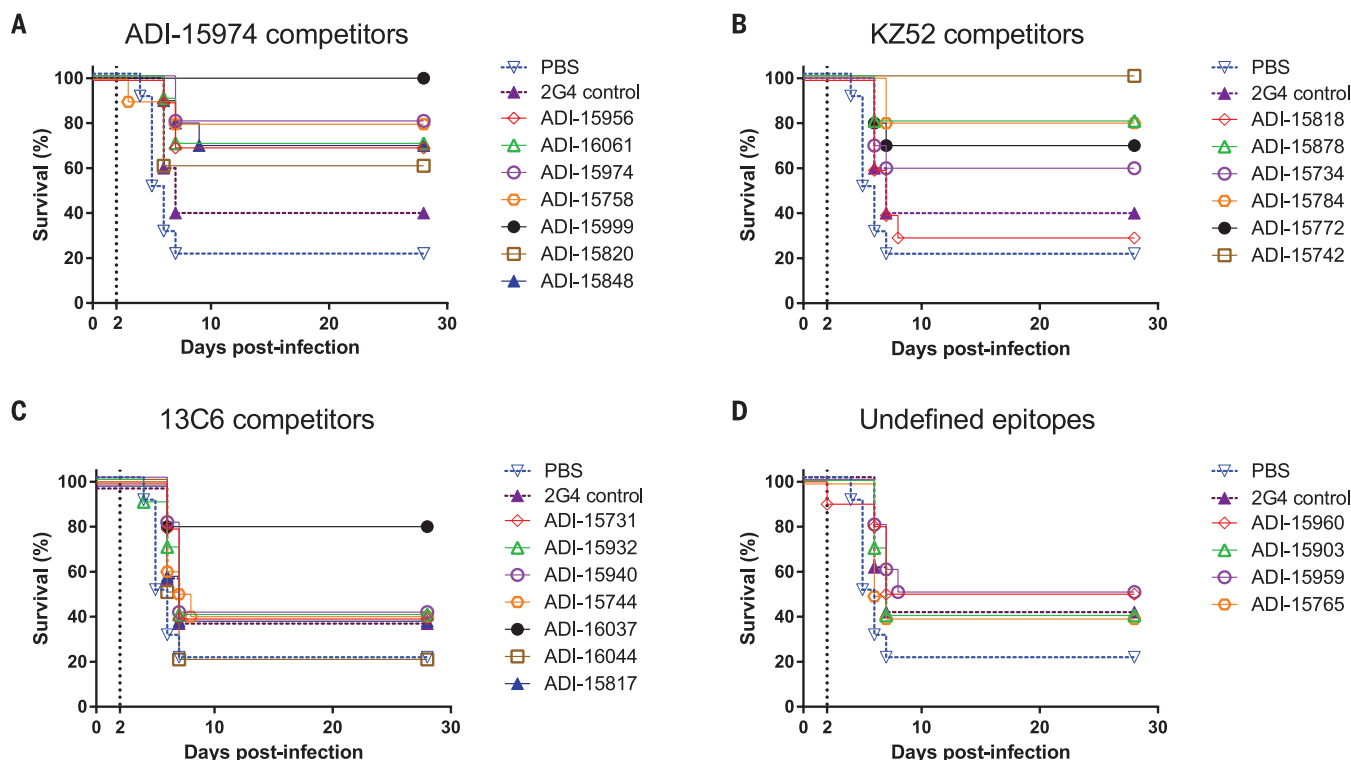


Fig. 5. Therapeutic efficacy of NAb against MA-EBOV. Kaplan-Meier survival curves for ADI-15974 competitor NAb (A), KZ52 competitor NAb (B), 13C6 competitor NAb (C), and NAb targeting undefined epitopes (D). Mice were infected with 100 PFU of MA-EBOV and treated intraperitoneally with a single dose of the indicated mAbs at 2 dpi (dotted black line). Negative control mice were treated with phosphate-buffered saline. MAb 2G4 is included for comparison. Data are representative of one experiment with 10 mice per group.

could be visualized in the 2D class averages (fig. S10), suggesting that the HR2 region may exist as a three-helix bundle in the pre-fusion GP structure (6). Additionally, although we were not able to generate a 3D reconstruction of ADI-15859 (an ADI-15810 competitor) bound to EBOV GP Δ TM, the negative-stain 2D class averages indicate that this mAb also binds within the GP stalk region. Collectively, these data suggest that the GP stalk region containing the HR2 helices is an accessible antigenic region targeted by NAb, a proportion of which exhibit remarkable neutralization potency.

Finally, we sought to determine whether certain NAb to GP showed greater *in vivo* efficacy than others. For this experiment, several NAb were selected from each competition group and evaluated for post-exposure therapeutic efficacy against lethal EBOV challenge in a murine infection model (23). Groups of mice were challenged with a target dose of 100 plaque-forming units (PFU) of mouse-adapted EBOV (MA-EBOV), followed by a single 100 μ g dose of mAb at 2 days post-infection (dpi). The previously described neutralizing mAb 2G4, a component of the ZMapp cocktail, was also included for comparison (3). Of significance, all of the ADI-15974 competitor NAb (GP stalk binders) provided significant post-exposure protection, with survival rates ranging from 60 to 100% and average weight loss ranging between 8 and 10% (Fig. 5A, fig. S13, and table S6). Five out of the six NAb in the KZ52 compe-

tion group were also highly effective in protection, with survival rates ranging between 60 and 100% (Fig. 5B and table S6). With the exception of ADI-15818 (a KZ52 competitor), all of the NAb in these two competition groups showed greater therapeutic efficacy than 2G4, which only provided 40% protection under these conditions. In contrast to the ADI-15974 and KZ52 competitor NAb, the NAb targeting the glycan cap (13C6/1H3 competitors) and undefined epitopes generally showed little to no therapeutic efficacy (Fig. 5, C and D, fig. S13, and table S6). Only ADI-16037 (a 13C6 competitor NAb) provided potent protection, yielding 80% survival and 7% average weight loss. The remaining NAb in these groups yielded \leq 50% survival, which in most cases was not a statistically significant increase in protection over the negative control (Fig. 5, C and D, and table S6). This result is consistent with previous studies showing that mAb targeting the glycan cap generally do not afford significant protection when administered at 1 to 2 dpi (3, 24). In summary, most of the NAb targeting the GP stalk region (ADI-15974 competitors) and the GP1/GP2 interface (KZ52 competitors) provided significant post-exposure protection against lethal EBOV challenge, whereas NAb targeting the glycan cap (13C6/1H3 competitors) and undefined regions generally showed little to no therapeutic efficacy under these conditions.

We have shown that the human B cell response to EBOV GP is composed of a broad diversity of

clones that primarily target three non-overlapping antigenic sites on the GP spike: the glycan cap; the GP1/GP2 interface; and the stalk, inclusive of the HR2 helices (fig. S14). A substantial fraction of the mAb cloned from GP-specific B cells show neutralizing activity, demonstrating that at least in this donor, NAb responses can develop relatively early after EBOV infection. The most potentially neutralizing and therapeutically effective mAb in our panel target the GP1/GP2 interface and the GP stalk region, suggesting that these epitopes may be promising targets for rational vaccine design. In addition, the observation that EBOV escape variants can emerge after treatment with the MB-003 antibody cocktail highlights the need for protective mAb that target new antigenic sites, such as those described here targeting the GP stalk (25, 26).

REFERENCES AND NOTES

1. P. Roddy, *Viruses* **6**, 3699–3718 (2014).
2. A. Marzi et al., *Science* **349**, 739–742 (2015).
3. X. Qiu et al., *Nature* **514**, 47–53 (2014).
4. C. D. Murin et al., *Proc. Natl. Acad. Sci. U.S.A.* **111**, 17182–17187 (2014).
5. J. M. Dias et al., *Nat. Struct. Mol. Biol.* **18**, 1424–1427 (2011).
6. J. E. Lee et al., *Nature* **454**, 177–182 (2008).
7. G. G. Olinger Jr. et al., *Proc. Natl. Acad. Sci. U.S.A.* **109**, 18030–18035 (2012).
8. T. Maruyama et al., *J. Virol.* **73**, 6024–6030 (1999).
9. W. B. Oswald et al., *PLOS Pathog.* **3**, e9 (2007).
10. A. I. Flyak et al., *Cell* **164**, 392–405 (2016).
11. J. F. Scheid et al., *Nature* **458**, 636–640 (2009).
12. M. Beltramello et al., *Cell Host Microbe* **8**, 271–283 (2010).
13. Y. Xu et al., *Protein Eng. Design Select.* **26**, 663–670 (2013).

14. J. Wrammert *et al.*, *Nature* **453**, 667–671 (2008).
15. S. D. Boyd *et al.*, *J. Immunol.* **184**, 6986–6992 (2010).
16. K. J. Jackson *et al.*, *Immunogenetics* **64**, 3–14 (2012).
17. A. Sanchez, S. G. Trappier, B. W. Mahy, C. J. Peters, S. T. Nichol, *Proc. Natl. Acad. Sci. U.S.A.* **93**, 3602–3607 (1996).
18. S. K. Gire *et al.*, *Science* **345**, 1369–1372 (2014).
19. G. S. Mohan, W. Li, L. Ye, R. W. Compans, C. Yang, *PLOS Pathog.* **8**, e1003065 (2012).
20. D. R. Bowley, A. F. Labrijn, M. B. Zwick, D. R. Burton, *Protein Eng. Design Select.* **20**, 81–90 (2007).
21. J. Audet *et al.*, *Sci. Rep.* **4**, 6881 (2014).
22. W. Weissenhorn, A. Carfi, K. H. Lee, J. J. Skehel, D. C. Wiley, *Mol. Cell* **2**, 605–616 (1998).
23. M. Bray, K. Davis, T. Geisbert, C. Schmaljohn, J. Huggins, *J. Infect. Dis.* **179**, S248–S258 (1999).
24. X. Qiu *et al.*, *PLOS Negl. Trop. Dis.* **6**, e1575 (2012).
25. J. R. Kugelman *et al.*, *Cell Rep.* **12**, 2111–2120 (2015).
26. X. Qiu *et al.*, *Sci. Transl. Med.* **4**, 138ra81 (2012).
27. T. Hashiguchi *et al.*, *Cell* **160**, 904–912 (2015).
28. Y. Shen, J. Maupetit, P. Derreumaux, P. Tufféry, *J. Chem. Theory Comput.* **10**, 4745–4758 (2014).
29. S. Lysov *et al.*, *PLOS One* **8**, e63906 (2013).

30. A. Sivasubramanian, A. Sircar, S. Chaudhury, J. J. Gray, *Proteins* **74**, 497–514 (2009).

ACKNOWLEDGMENTS

We thank T. Bolland and M. Vasquez for assistance with antibody sequence analysis, C. Williams and S. M. Eagol for assistance with figure preparation, R. Pejchal for providing helpful comments on the manuscript, and M. Haynes for assistance with flow cytometry. All of the IgGs were sequenced by Adimab's Molecular Core and produced by the High Throughput Expression group. BLI binding experiments were performed by Adimab's protein analytics group. The ZMapp cocktail mAb 2G4 was generously provided by Mapp Biopharmaceutical. The data presented in this manuscript are tabulated in the main paper and in the supplementary materials. GenBank accession numbers for the antibody variable-region gene sequences reported in this study can be found in table S7. The cryo-EM maps have been deposited to the Electron Microscopy Data Bank (accession numbers EMD-6586, EMD-6587, EMD-6588, and EMD-6589). E.O.S., Z.A.B., M.L.F., K.B.J.P., A.B.W., H.L.T., and C.D.M. acknowledge support from the NIH/National Institute of Allergy and Infectious Diseases Center for Excellence in Translational Research Grant

U19AI109762, "Consortium for Immunotherapeutics Against Viral Hemorrhagic Fevers." E.O.S. was also supported by R01AI067927. C.D.M. was supported by a predoctoral fellowship from NSF. This study was supported in part by U.S. NIH grants U19 AI109762 and R01 AI067927 awarded to E.O.S. Research was funded in part by the Defense Advanced Research Projects Agency (DARPA-BAA-13-03). D.R.B. and D.S. acknowledge support from Center for HIV/AIDS Vaccine Immunology and Immunogen Discovery Grant UMI1A100663. This is manuscript no. 29237 from The Scripps Research Institute. Opinions, interpretations, conclusions, and recommendations are those of the authors and are not necessarily endorsed by the U.S. Army.

SUPPLEMENTARY MATERIALS

www.sciencemag.org/content/351/6277/1078/suppl/DC1
Materials and Methods
Figs. S1 to S14
Tables S1 to S7
References (31–39)

7 October 2015; accepted 8 February 2016
10.1126/science.aad5788

IMMUNOGENOMICS

Regulatory evolution of innate immunity through co-option of endogenous retroviruses

Edward B. Chuong, Nels C. Elde,*† Cédric Feschotte*†

Endogenous retroviruses (ERVs) are abundant in mammalian genomes and contain sequences modulating transcription. The impact of ERV propagation on the evolution of gene regulation remains poorly understood. We found that ERVs have shaped the evolution of a transcriptional network underlying the interferon (IFN) response, a major branch of innate immunity, and that lineage-specific ERVs have dispersed numerous IFN-inducible enhancers independently in diverse mammalian genomes. CRISPR-Cas9 deletion of a subset of these ERV elements in the human genome impaired expression of adjacent IFN-induced genes and revealed their involvement in the regulation of essential immune functions, including activation of the AIM2 inflammasome. Although these regulatory sequences likely arose in ancient viruses, they now constitute a dynamic reservoir of IFN-inducible enhancers fueling genetic innovation in mammalian immune defenses.

Changes in gene regulatory networks underlie many biological adaptations, but the mechanisms promoting their emergence are not well understood. Transposable elements (TEs), including endogenous retroviruses (ERVs), have been proposed to facilitate regulatory network evolution because they contain regulatory elements and can amplify in number and/or move throughout the genome (1–3). Genomic studies support this model (4), revealing that a substantial fraction of TE-derived noncoding sequences evolve under selective constraint (3, 5), are frequently bound by transcription factors (6–10), and often exhibit cell type-specific chromatin states consistent with regulatory activity (11, 12). These observations implicate TEs as a potential source of lineage-

specific cis-elements capable of rewiring regulatory networks, but the adaptive consequences of this process for specific physiological functions remain largely unexplored.

We investigated the evolution of gene regulatory networks induced by the proinflammatory cytokine interferon- γ (IFN γ). Interferons are proinflammatory signaling molecules that are released upon infection to promote transcription of innate immunity factors, collectively defined as IFN-stimulated genes (ISGs) (13). ISGs are regulated by cis-regulatory elements that are bound by IRF (interferon regulatory factor) and STAT (signal transducer and activator of transcription) transcription factors upon activation of IFN signaling pathways (13). Although innate immune signaling pathways are conserved among mammals, the transcriptional outputs of these pathways differ across species (14, 15), likely reflecting lineage-specific adaptation in response to independent host-pathogen conflicts. Thus, these pathways provide useful systems that allow us to

investigate whether TE-derived regulatory elements influence biological outcomes.

To explore the influence of TEs on IFN γ -inducible regulatory networks, we examined their contribution to IRF1 and STAT1 binding sites with the use of published chromatin immunoprecipitation sequencing (ChIP-seq) data for three human cell lines treated with IFN γ : K562 myeloid-derived cells, HeLa epithelial-derived cells, and primary CD14⁺ macrophages (16, 17). Our initial analysis revealed 27 TE families enriched within IFN γ -induced binding peaks in at least one of the data sets examined (18) (table S1 and fig. S1, A and B) and included TEs previously predicted to be cis-regulatory elements (11, 19). These sequences contained evolutionarily young to ancient TE families, of which the majority (20 of 27) originated from long terminal repeat (LTR) promoter regions of ERVs (Fig. 1A). These data suggest that ERVs, which arose from ancient retroviral infections and currently constitute 8% of the human genome (20), represent a source of novel binding sites bound by IFN γ -inducible transcription factors.

We next investigated whether these ERVs may contribute to IFN γ -inducible regulation of adjacent cellular genes. ERVs bound by STAT1 and/or IRF1 in CD14⁺ macrophages were strongly enriched near ISGs (binomial test, $P = 1.4 \times 10^{-87}$; Fig. 1B and fig. S2), determined from a matched RNA-seq data set (table S2) (18, 21). A complementary approach using the genomic regions enrichment of annotations tool (GREAT) (22) revealed enrichment of CD14⁺ STAT1-bound and/or IRF1-bound ERVs near genes annotated with immune functions (fig. S3, A and B). These findings suggest a potentially widespread role for ERVs in the regulation of the human IFN γ response.

MER41 is an endogenized gammaretrovirus that invaded the genome of an anthropoid primate ancestor ~45 to 60 million years ago with 7190 LTR elements, from six subfamilies (MER41A, B, C, D, E, and G), now fixed in the human genome (fig. S4A). Our analysis revealed the primate-specific MER41 family of ERVs as a source of IFN γ -inducible binding sites (fig. S4B), with nearly 1000 copies in humans ($N = 962$) bound by

Department of Human Genetics, University of Utah School of Medicine, Salt Lake City, UT 84112, USA.

*Corresponding author. E-mail: nelde@genetics.utah.edu (N.C.E.); cedric@genetics.utah.edu (C.F.). †These authors contributed equally to this work.

STAT1 and/or IRF1 in at least one cell type (table S3 and fig. S4C). In CD14⁺ macrophages, STAT1-bound MER41 elements exhibited stereotypical induction of histone H3 Lys²⁷ (H3K27) acetylation upon IFNG stimulation, a hallmark of cis-regulatory enhancer activity (23) (Fig. 1C).

Consistent with the idea that this ERV family affects IFNG-inducible regulation, MER41B sequences were identified as enriched within STAT1 ChIP-seq peaks in IFNG-stimulated HeLa cells (19). A tandem pair of predicted STAT1 binding sites coincided with STAT1 ChIP-seq peak localization (Fig. 1D). These sites also occur in the ancestral (consensus) sequence of the MER41B subfamily (Fig. 1D) but not in the MER41A subfamily, which is characterized by a 43–base pair (bp) deletion that has eliminated these binding sites (fig. S5). MER41A sequences showed no enrichment within IFNG-inducible binding sites, despite otherwise sharing 99% sequence identity with MER41B (figs. S4B and S5). Together, these data suggest that many MER41 elements are directly bound by STAT1 upon IFNG treatment, likely owing to the presence of ancestral STAT1 binding motifs within their LTR sequences.

Next, we focused on the MER41AIM2 ERV, which is located 220 bp upstream of the gene *Absent in Melanoma 2* (*AIM2*), an ISG that encodes a sensor of foreign cytosolic DNA and acti-

vates an inflammatory response (24). *AIM2* is IFNG-inducible in humans but is constitutively transcribed in mice (24). In humans, MER41AIM2 appears to provide the only STAT1 binding site within 50 kb of the *AIM2* gene, and the element gained H3K27 acetylation upon IFNG stimulation (Fig. 2A). Therefore, the regulation of *AIM2* has undergone evolutionary divergence across mammalian lineages, which in turn suggests that the transposition of MER41 upstream of *AIM2* may have conferred regulation by IFN signaling in anthropoid primates.

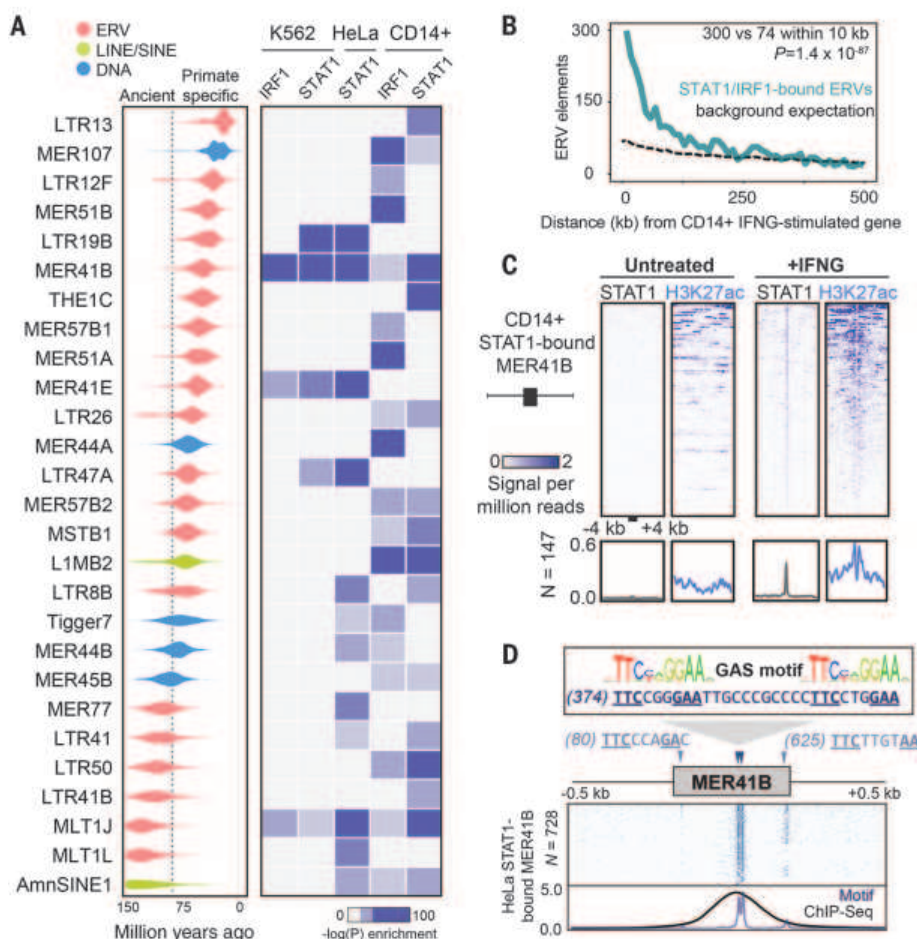
We used the CRISPR-Cas9 system to delete the MER41AIM2 element in HeLa cells (fig. S6) (18). Cells homozygous for the MER41AIM2 deletion (Δ MER41AIM2) failed to express *AIM2* upon IFNG treatment, in contrast to control cells in which *AIM2* transcript levels were robustly induced by IFNG (Fig. 2B). IFNG-induced *AIM2* protein levels were undetectable in Δ MER41AIM2 cells (Fig. 2C), thus demonstrating that MER41AIM2 is necessary for endogenous IFNG-inducible regulation of *AIM2*.

We further delineated the regulatory activity of MER41AIM2 by means of luciferase reporter assays (18). MER41AIM2 was sufficient to drive IFNG-inducible reporter expression in HeLa cells, and this activity was significantly diminished by point mutations ablating the predicted STAT1

binding motifs (Fig. 2D). These binding sites are conserved across anthropoid primates (fig. S7A), and IFNG-inducible reporter activity is conserved across orthologous MER41AIM2 elements cloned from chimpanzee, rhesus macaque, and marmoset (Fig. 2D). We also confirmed that orthologs of *AIM2* were all IFNG-inducible in primary fibroblasts from these species (fig. S7B). These results establish MER41AIM2 as an IFNG-inducible enhancer and suggest that it was co-opted for *AIM2* regulation in an ancestor of anthropoid primates.

The binding of *AIM2* to cytoplasmic double-stranded DNA from intracellular bacteria and viruses promotes the assembly of a molecular platform known as an inflammasome, which initiates pyroptotic cell death by cleaving and activating caspase-1 (25). To test whether MER41AIM2 is required for this response to infection, we infected Δ MER41AIM2 cells with vaccinia virus (VACV) for 24 hours and assayed secretion of the active cleaved form of caspase-1 (subunit p10) as the readout of inflammasome activity. Secreted levels of activated caspase-1 were markedly reduced in Δ MER41AIM2 cells relative to wild-type cells, and caspase-1 activation was restored by transient transfection with an *AIM2* overexpression construct [pCMV-*AIM2* plasmid (Fig. 2E)]. Collectively these experiments demonstrate

Fig. 1. Dispersion of IFNG-inducible regulatory elements by ERVs. (A) Age distribution (left) and enrichment within ChIP-seq data sets (right) of 27 TE families that were enriched within binding sites for IFNG-stimulated cells (18). Estimated primate/rodent divergence time (82 million years ago) is from (34). (B) Frequency histogram of absolute distances from each ERV to the nearest ISG, for CD14⁺ cells. The background expectation is from the genome-wide ERV distribution (18). Statistical significance of the observed enrichment within the first 10 kb of the nearest ISG was assessed by binomial test. (C) Heat map of CD14⁺ ChIP-seq signals centered across STAT1 peak summits within MER41B elements. Bottom metaprofiles represent average normalized ChIP signal across bound elements. (D) Schematic of the MER41B LTR consensus sequence. Triangles indicate gamma activated site (GAS; TTCNNGGAA, where N = any nucleotide) motifs predicted to bind STAT1 in response to IFNG (13). Heat map depicts the presence of GAS motifs across 728 extant STAT1-bound MER41B copies in HeLa cells (18). Bottom metaprofile represents average presence of STAT1 motifs relative to the MER41 consensus sequence, overlain with normalized STAT1 ChIP-seq density across the same elements.



that MER41.AIM2 is likely a necessary element of the inflammatory response to infection.

The dispersion of cis-regulatory elements propagated by the same TE family might facilitate the recruitment of multiple genes into the same regulatory network (3). We identified three additional MER41 elements within 20 kb of *APOL1*, *IFI6*, and *SECTM1*, which all are involved in human immunity (26–28) (Fig. 3A). As with MER41.AIM2,

we used CRISPR-Cas9 to generate genomic deletions of MER41.APOL1, MER41.IFI6, and MER41.SECTM1 in HeLa cells (figs. S8 and S9). Upon treatment with IFNG, each mutant cell line exhibited significantly decreased transcript levels of the corresponding ISG relative to wild-type levels (Fig. 3B), indicating that these MER41 elements had also been co-opted as IFNG-inducible enhancers. However, in contrast to *AIM2*, deletion

of these MER41 elements did not completely abolish IFNG-induced transcript levels of these genes. This difference may be due to additional STAT1 binding sites located near these genes (Fig. 3A). In such cases, MER41 elements may contribute regulatory robustness as partially redundant or “shadow” enhancers (29).

ERVs related to the primate-specific MER41 family (“MER41-like”) have been identified in

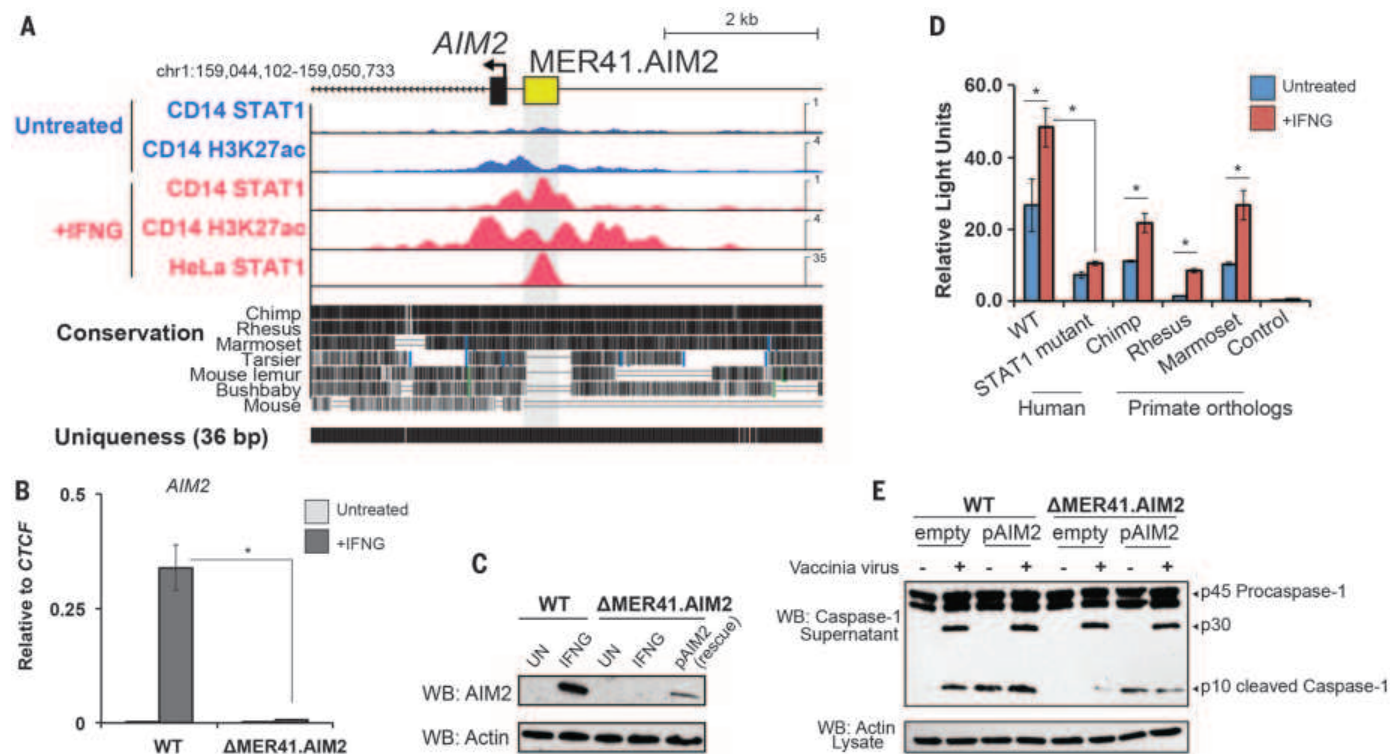


Fig. 2. A MER41 element is essential for AIM2 inflammasome activation. (A) Genome browser view of *AIM2*. ChIP-seq tracks are normalized per million reads. The “uniqueness” track displays genome-wide short-read alignability. (B) Quantitative polymerase chain reaction (qPCR) of *AIM2* levels in wild-type and Δ MER41.AIM2 HeLa cells after 24 hours of IFNG treatment. (C) Western blot of *AIM2* in wild-type and Δ MER41.AIM2 cells after IFNG treatment. (D) Luciferase reporter assays of MER41.AIM2, MER41.AIM2 with mutations in the predicted STAT1 sites, and primate orthologs of MER41.AIM2 (see fig. S7A). (E) Western blot of caspase-1 from supernatants of wild-type and Δ MER41.AIM2 cells infected with vaccinia virus (18). * $P < 0.05$, Student’s t test. Error bars denote SD.

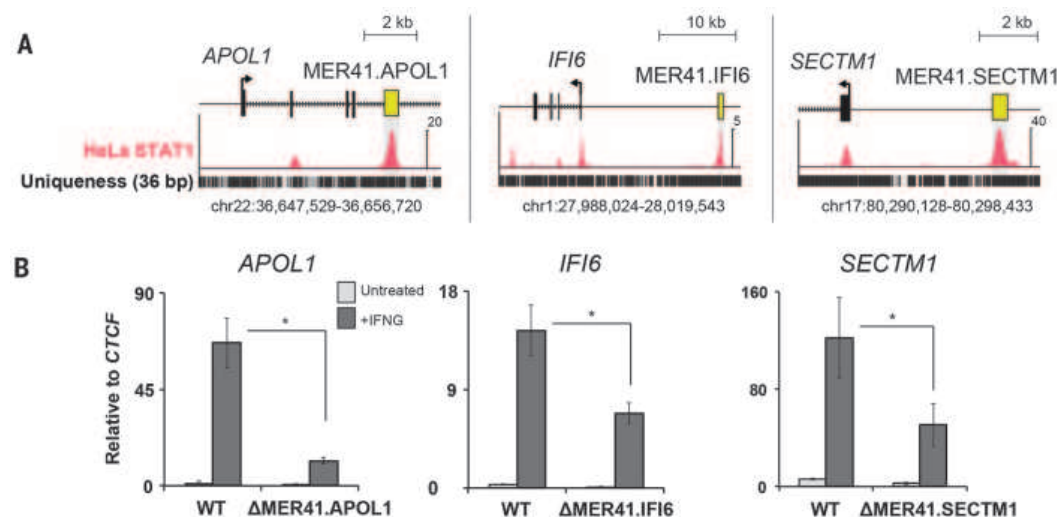


Fig. 3. Multiple MER41 elements have been co-opted to regulate the IFNG response.

(A) Genome browser views of MER41 elements located near *APOL1*, *IFI6*, and *SECTM1*. ChIP-seq data are depicted as normalized signal per million reads. (B) qPCR of each gene comparing IFNG-inducible levels in wild-type HeLa cells and MER41 deletion mutants. * $P < 0.05$, Student’s t test. Error bars denote SD.

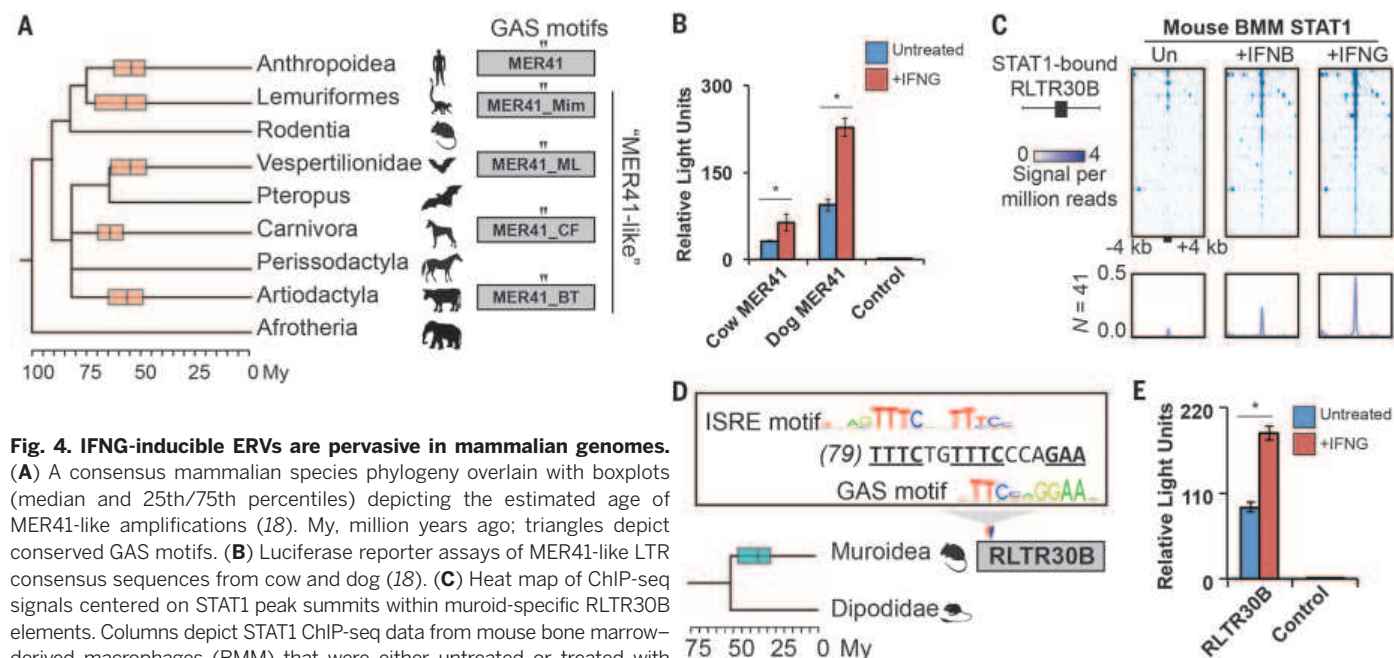


Fig. 4. IFNG-inducible ERVs are pervasive in mammalian genomes.

(A) A consensus mammalian species phylogeny overlain with boxplots (median and 25th/75th percentiles) depicting the estimated age of MER41-like amplifications (18). My, million years ago; triangles depict conserved GAS motifs. (B) Luciferase reporter assays of MER41-like LTR consensus sequences from cow and dog (18). (C) Heat map of ChIP-seq signals centered on STAT1 peak summits within murid-specific RLTR30B elements. Columns depict STAT1 ChIP-seq data from mouse bone marrow-derived macrophages (BMM) that were either untreated or treated with IFNB or IFNG. Only RLTR30B elements that are bound by STAT1 upon IFNG treatment are shown. Bottom metaprofiles represent average normalized ChIP signal across bound elements. (D) Rodent phylogeny overlain with a boxplot depicting the amplification of RLTR30B, as in (A). ISRE denotes interferon-stimulated response element motif (TTTCNNTTTC) predicted to bind STAT1 in response to IFNB (13). (E) Luciferase reporter assay of RLTR30B consensus sequence, as in (B). [Time-calibrated phylogenies in (A) and (D) are from (34).] * $P < 0.05$, Student's t test. Error bars denote SD.

most major mammalian lineages (30), raising the possibility of similar contributions to immune regulation. Further analysis, including cross-species genomic alignments, confirmed that multiple mammalian lineages were independently colonized by related MER41-like gammaretroviruses ~50 to 75 million years ago (table S4). Remarkably, we found that the tandem STAT1 binding motifs present in anthropoid MER41 are conserved in MER41-like relatives found in lemuri-formes, vesper bats, carnivores, and artiodactyls (Fig. 4A and fig. S10), which suggests that they might also have dispersed IFN-inducible enhancers in the genomes of these species. Consistent with this prediction, we found that reconstructed ancestral (consensus) sequences of MER41-like LTRs from dog and cow can drive robust IFNG-inducible reporter activity in HeLa cells (Fig. 4B).

These results suggest that ERVs may have independently expanded the IFN regulatory network in multiple mammalian lineages. To further investigate this possibility, we analyzed a STAT1 ChIP-seq data set of IFNG- and IFN- β (IFNB)-stimulated primary macrophages from mouse (31), a species that lacks MER41-like elements but harbors a diverse repertoire of lineage-specific ERVs (30). Our analysis revealed a murid-specific endogenous gammaretrovirus named RLTR30B enriched for both IFNG- and IFNB-inducible STAT1 binding events (Fig. 4C and fig. S11A), which coincide with overlapping motifs corresponding to both IFNG- and IFNB-induced STAT1 binding sites located in the 5' end of the LTR consensus sequence (Fig. 4D). Reporter assays revealed that the consensus sequence

of RLTR30B also provides IFNG-inducible enhancer activity in HeLa cells (Fig. 4E). GREAT analysis also revealed significant enrichment of mouse STAT1-bound ERVs near functionally annotated immunity genes (fig. S11B).

Together, our findings reveal IFN-inducible enhancers introduced and amplified by ERVs in many mammalian genomes. On occasion, these elements have been co-opted to regulate host genes encoding immunity factors. Although we have shown that ERVs play a functional role regulating innate immune pathways in human HeLa cells, further studies will be necessary to extend our findings to primary hematopoietic cells and other species such as mouse. We speculate that the prevalence of IFN-inducible enhancers in the LTRs of these ancient retroviruses is not coincidental, but may reflect former viral adaptations to exploit immune signaling pathways promoting viral transcription and replication (32). Indeed, several extant viruses, including HIV, possess IFN-inducible cis-regulatory elements (33). It would be ironic if viral molecular adaptations had been evolutionarily recycled to fuel innovation and turnover of the host immune repertoire. Regardless of how these sequences originated, our study illuminates how selfish genetic elements have contributed raw material that has been repurposed for cellular innovation.

REFERENCES AND NOTES

- R. J. Britten, E. H. Davidson, *Science* **165**, 349–357 (1969).
- B. McClintock, *Proc. Natl. Acad. Sci. U.S.A.* **36**, 344–355 (1950).

- C. Feschotte, *Nat. Rev. Genet.* **9**, 397–405 (2008).
- R. Rebollo, M. T. Romanish, D. L. Mager, *Annu. Rev. Genet.* **46**, 21–42 (2012).
- C. B. Lowe, G. Bejerano, D. Haussler, *Proc. Natl. Acad. Sci. U.S.A.* **104**, 8005–8010 (2007).
- T. Wang et al., *Proc. Natl. Acad. Sci. U.S.A.* **104**, 18613–18618 (2007).
- G. Kunarso et al., *Nat. Genet.* **42**, 631–634 (2010).
- D. Schmidt et al., *Cell* **148**, 335–348 (2012).
- E. B. Chuong, M. A. K. Rumi, M. J. Soares, J. C. Baker, *Nat. Genet.* **45**, 325–329 (2013).
- J. H. Notwell, T. Chung, W. Heavner, G. Bejerano, *Nat. Commun.* **6**, 6644 (2015).
- P.-É. Jacques, J. Jeyakani, G. Bourque, *PLOS Genet.* **9**, e1003504 (2013).
- V. Sundaram et al., *Genome Res.* **24**, 1963–1976 (2014).
- L. C. Platanius, *Nat. Rev. Immunol.* **5**, 375–386 (2005).
- L. B. Barreiro, J. C. Marioni, R. Blekman, M. Stephens, Y. Gilad, *PLOS Genet.* **6**, e1001249 (2010).
- K. Schroder et al., *Proc. Natl. Acad. Sci. U.S.A.* **109**, E944–E953 (2012).
- M. B. Gerstein et al., *Nature* **489**, 91–100 (2012).
- Y. Qiao et al., *Immunity* **39**, 454–469 (2013).
- See supplementary materials on Science Online.
- C. D. Schmid, P. Bucher, *PLOS ONE* **5**, e11425 (2010).
- E. S. Lander et al., *Nature* **409**, 860–921 (2001).
- X. Su et al., *Nat. Immunol.* **16**, 838–849 (2015).
- C. Y. McLean et al., *Nat. Biotechnol.* **28**, 495–501 (2010).
- R. Ostuni et al., *Cell* **152**, 157–171 (2013).
- V. Hornung et al., *Nature* **458**, 514–518 (2009).
- T. Fernandes-Alnemri et al., *Nat. Immunol.* **11**, 385–393 (2010).
- L. Vanhamme et al., *Nature* **422**, 83–87 (2003).
- K. Meyer et al., *Sci. Rep.* **5**, 9012 (2015).
- T. Wang et al., *J. Leukoc. Biol.* **91**, 449–459 (2012).
- M. Lagha, J. P. Bothma, M. Levine, *Trends Genet.* **28**, 409–416 (2012).
- W. Bao, K. K. Kojima, O. Kohany, *Mob. DNA* **6**, 11 (2015).
- S.-L. Ng et al., *Proc. Natl. Acad. Sci. U.S.A.* **108**, 21170–21175 (2011).

32. R. E. Randall, S. Goodbourn, *J. Gen. Virol.* **89**, 1–47 (2008).
 33. M. Sgarbanti et al., *J. Virol.* **82**, 3632–3641 (2008).
 34. R. W. Meredith et al., *Science* **334**, 521–524 (2011).

ACKNOWLEDGMENTS

Accession numbers for the published data sets analyzed in this study are available in the supplementary materials. We thank all members of the Elde and Feschotte labs for insightful discussions. We thank A. Kapusta, A. Lewis, D. Downhour,

J. Carleton, and K. Cone for technical assistance, and D. Hancks and J. F. McCormick for their critical input. Supported by a Pew Charitable Trusts award and NIH grants GM082545 and GM114514 (N.C.E.) and by NIH grants GM112972 and GM059290 (C.F.). E.B.C. is a Howard Hughes Medical Institute postdoctoral fellow of the Jane Coffin Childs Fund. N.C.E. is a Pew Scholar in the Biomedical Sciences and Mario R. Capecchi Endowed Chair in Genetics. The authors declare no financial conflicts of interest.

SUPPLEMENTARY MATERIALS

www.sciencemag.org/content/351/6277/1083/suppl/DC1
 Materials and Methods
 Tables S1 to S6
 Figs. S1 to S11
 References (35–49)

30 September 2015; accepted 2 February 2016
 10.1126/science.aad5497

GENE EXPRESSION

Expression homeostasis during DNA replication

Yoav Voichek,* Raz Bar-Ziv,* Naama Barkai†

Genome replication introduces a stepwise increase in the DNA template available for transcription. Genes replicated early in S phase experience this increase before late-replicating genes, raising the question of how expression levels are affected by DNA replication. We show that in budding yeast, messenger RNA (mRNA) synthesis rate is buffered against changes in gene dosage during S phase. This expression homeostasis depends on acetylation of H3 on its internal K56 site by Rtt109/Asf1. Deleting these factors, mutating H3K56 or up-regulating its deacetylation, increases gene expression in S phase in proportion to gene replication timing. Therefore, H3K56 acetylation on newly deposited histones reduces transcription efficiency from replicated DNA, complementing its role in guarding genome stability. Our study provides molecular insight into the mechanism maintaining expression homeostasis during DNA replication.

The synthesis of mRNA depends on protein factors binding to the DNA template. During the cell cycle, DNA dosage increases at discrete times in S phase, whereas cell volume increases continuously, introducing considerable temporal variations in DNA concentration. How these variations in DNA level affect mRNA synthesis was examined in classical studies (1). In bacteria, mRNA production follows gene dosage, so that the expression of each gene increases rapidly after its replication (2–4). By contrast, experiments in eukaryotic cells, ranging from yeast to mammals (5–7), indicate a limited dependency of gene expression on DNA dosage, prompting the hypothesis that transcription of newly replicated DNA is transiently repressed (8).

We extended previous studies, which measured total mRNA synthesis (9, 10), or focused on individual genes (11, 12) by directly comparing the expression of early- versus late-replicating genes during S phase. If replicated loci produce more mRNA than unreplicated ones, then expression of genes that replicate early should increase relative to the expression of late-replicating genes during S phase (fig. S1A). In contrast, we find that the relative expression of early- versus late-replicating genes remained relatively constant in budding yeast, progressing synchronously through S phase after release from α -factor or hydroxyurea (HU) arrest and did not correlate

with DNA replication timing (Fig. 1, A and B, and figs. S1 and S2). Further, the synthesis rates of early-replicating genes increased by only ~20% relative to late-replicating genes, significantly less than the ~70% increase in DNA content (Fig. 1A). We also examined cells arrested in the beginning of S phase after 3-hour treatment with HU. Despite the stable increase in DNA content of early-replicated genes, their expression increased by a mere 5% relative to that of late nonreplicated genes, suggesting that buffering under this S phase-arrested condition is even stronger than in cycling cells (Fig. 1C and fig. S8D). Taken together, our results are consistent with previous studies showing that during S phase, DNA dosage has a limited influence on mRNA synthesis rates.

In contrast to mRNA levels, the binding of RNA polymerase II to DNA did correlate with DNA content in HU-arrested cells and after release into S phase. Still, the increase in PolII binding to replicated genes (30%) was lower than expected by the increase in DNA content (Fig. 2A and fig. S3). In HU-arrested cells, early-replicated genes were depleted of elongating PolII (Fig. 2B). However, this difference was specific to HU arrest and disappeared upon release, before the completion of replication. Therefore, reduced PolII binding to replicated DNA may partially account for the buffering of gene expression, with additional differences in elongation capacity that increases buffering in HU-arrested cells.

We hypothesized that chromatin regulators may suppress transcription from replicated DNA. To identify such factors, we examined a pub-

lished data set describing how individual deletions of 165 chromatin-associated factors affect the genome-wide expression profile (13). Deleting a factor that limits transcription from replicated DNA will increase gene expression in proportion to the time at which the gene is replicated in S phase, so that early-replicated genes will increase in expression more than genes replicated late. We therefore searched for mutants in which gene expression levels were (on average) negatively correlated with gene replication timing (Fig. 3A). Of the three mutants showing the strongest correlation between gene expression and replication timing, two were involved in H3 acetylation: the acetyltransferase Rtt109 and its histone chaperone cofactor Asf1 (14–16). A similar effect was detected in expression data from fission yeast deleted of the Asf1 paralogue (fig. S4A) (17, 18). The third candidate, Tos4, is a less-characterized putative transcription factor (19). All three genes increase in expression during G1, just before DNA replication (20).

The correlation between gene expression and replication timing were highly significant in all three mutants, but the difference in expression between early- and late-replicated genes was small. This is expected, as measurements were taken in asynchronous cultures in which only a minority of cells are in S phase. To amplify the difference in mRNA levels between early- and late-replicated genes, we profiled gene expression in all three mutants synchronized by HU (Fig. 3B). In both $\Delta rtt109$ and $\Delta asf1$ cells (but not $\Delta tos4$), expression levels correlated with DNA content, with genes that were already replicated showing 24 to 28% increase in expression relative to the nonreplicated genes. We next measured the mRNA levels and synthesis rates in $\Delta rtt109$ cells progressing synchronously through S phase. Indeed, expression and synthesis rates of early-replicated genes increased transiently during mid-S phase relative to late-replicating genes (Fig. 3C and fig. S5). Therefore, Rtt109 is required for buffering mRNA synthesis during DNA replication (Fig. 3C, red line).

A similar loss of buffering was observed for $\Delta asf1$ (Fig. 3D) and also for $\Delta tos4$ cells (fig. S7). The latter is particularly notable because $\Delta tos4$ did not abrogate buffering in HU-arrested conditions, consistent with an additional buffering mechanism acting upon HU arrest. To examine whether the three candidates act through the same pathway, we measured gene expression in the double deletions $\Delta rtt109 \Delta asf1$ and $\Delta rtt109 \Delta tos4$. The increased expression of early-replicated genes was similar to the single deletions for the two pairs, suggesting that the three genes function

Department of Molecular Genetics, Weizmann Institute of Science, Rehovot 76100, Israel.

*These authors contributed equally to this work. †Corresponding author. E-mail: naama.barkai@weizmann.ac.il

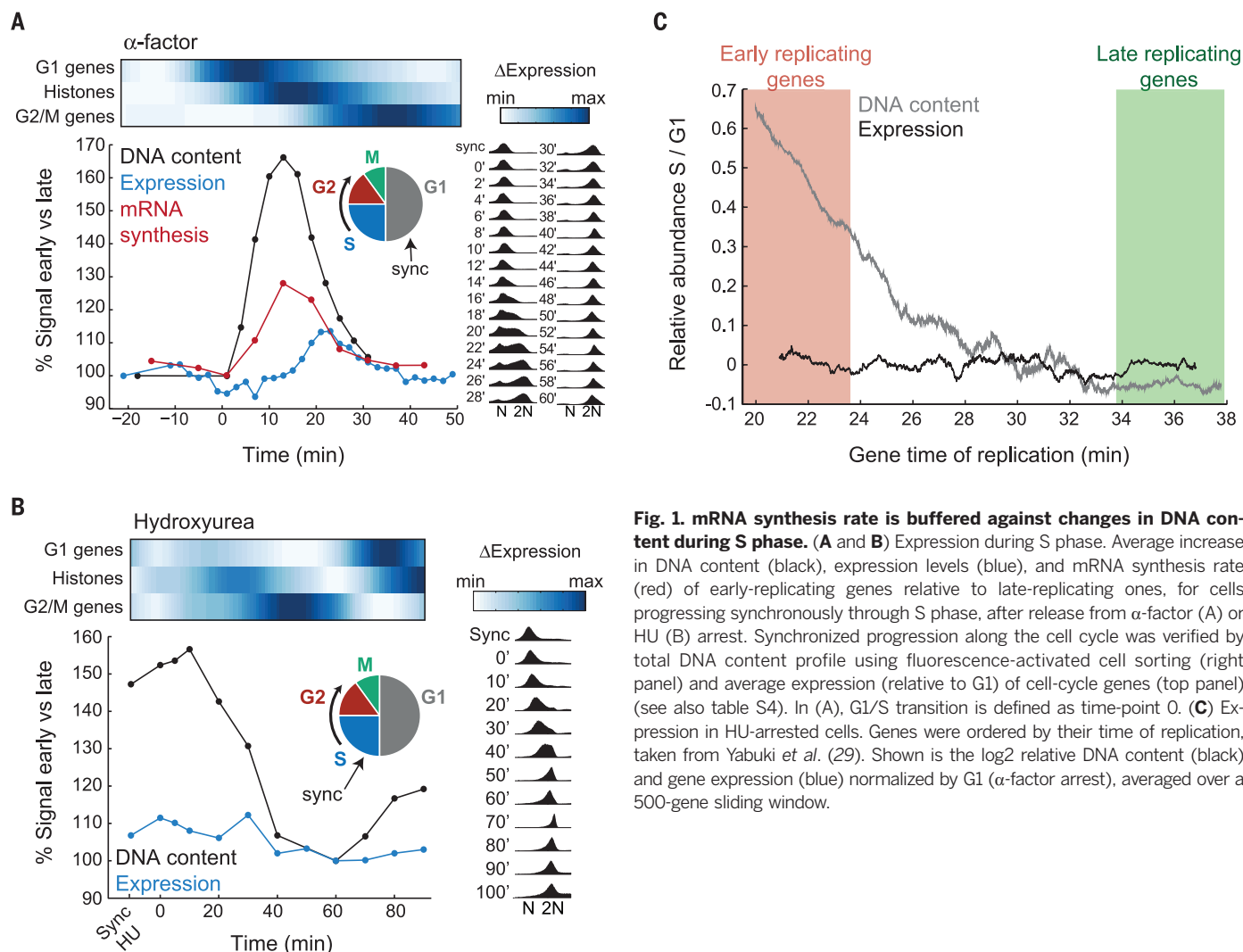
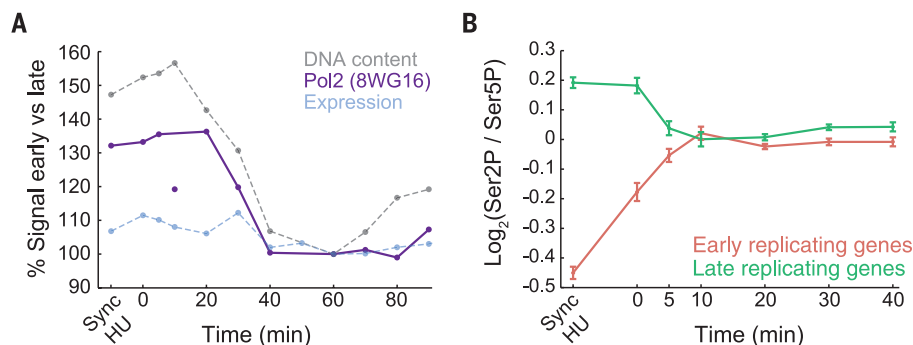


Fig. 1. mRNA synthesis rate is buffered against changes in DNA content during S phase. (A and B) Expression during S phase. Average increase in DNA content (black), expression levels (blue), and mRNA synthesis rate (red) of early-replicating genes relative to late-replicating ones, for cells progressing synchronously through S phase, after release from α -factor (A) or HU (B) arrest. Synchronized progression along the cell cycle was verified by total DNA content profile using fluorescence-activated cell sorting (right panel) and average expression (relative to G1) of cell-cycle genes (top panel) (see also table S4). In (A), G1/S transition is defined as time-point 0. (C) Expression in HU-arrested cells. Genes were ordered by their time of replication, taken from Yabuki *et al.* (29). Shown is the log₂ relative DNA content (black) and gene expression (blue) normalized by G1 (α -factor arrest), averaged over a 500-gene sliding window.

Fig. 2. RNA polymerase binding increases on replicated genes.

(A) PolII binding during S phase. The ratio between PolII binding of early- versus late-replicating genes (purple) as measured by chromatin immunoprecipitation sequencing (ChIP-Seq). A line is presented to guide the eye, omitting the 10-min time point. DNA content (black) and gene expression (blue) were sampled in the same experiment and shown also in Fig. 1B. See fig. S3A for other antibodies. (B) PolII phosphorylation on Ser2 and Ser5. The log₂ ratio of Ser2P (initiating PolII) versus Ser5P (elongating PolII) abundance on early- (red) and late- (green) replicated genes in HU-arrested cells and after their release into S phase as measured by ChIP-Seq. Error bars represent standard error.



through the same pathway (Fig. 3, D and E, and figs. S6A and S7).

Rtt109 acetylates histone H3 on two residues, K56 and K9, and Asf1 is required for both functions (21). To differentiate which of these residues is responsible for the reduced transcription efficiency of replicated DNA, we considered mutants in which K56 or K9 were replaced by residues that mimic constant nonacetylation (lysine

to alanine, K→A) or constant acetylation (lysine to glutamine, K→Q) (22). Mutating K9 did not affect buffering of early-replicated gene expression in HU-arrested cells (Fig. 4A). In contrast, the relative expression of early-replicating genes was significantly higher in cells mutated for K56 (average 34%, compared with a 5% increase in wild-type cells). As expected, both modifications (K→A and K→Q) eliminated the asymmetry be-

tween late- and early-replicated genes. Consistently, buffering was also lost upon overproducing the H3K56ac-specific histone deacetylases, Hst3 and Hst4 (23) (Fig. 4B and fig. S8). Therefore, H3K56 acetylation is required for the reduced gene expression from newly replicated DNA.

In summary, we find that Rtt109/Asf1-dependent H3K56ac suppresses transcription from newly replicated DNA during S phase, thereby maintaining

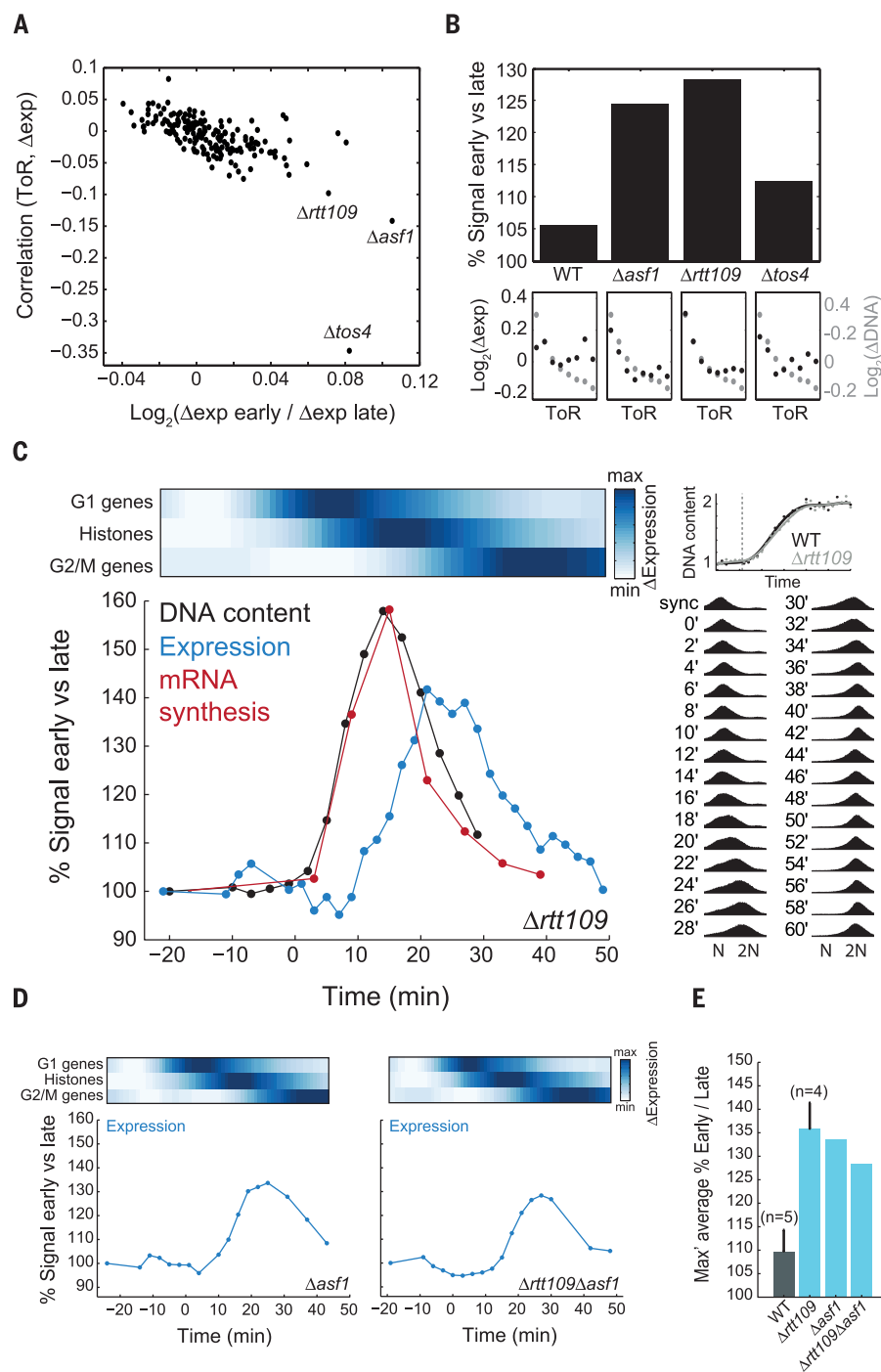


Fig. 3. *Rtt109* and *Asf1* are required for expression homeostasis during S phase. (A) Expression in asynchronous cultures. Each dot represents a single mutant. Correlation between replication timing and change in gene expression is shown on the y axis, and the difference in the expression of early- and late-replicating genes is shown on the x axis. The two measures are expected to be correlated. Expression data from a data set by Lenstra *et al.* (13). (B) Expression in HU-synchronized cells. Increase in the expression of replicated genes (early) relative to nonreplicated (late) ones for the indicated strains (top), in cells arrested with HU for 3 hours. Correlations of gene expression with replication timing is also shown (bottom). (C) Expression during S phase in $\Delta rtt109$. Same as in Fig. 1A for $\Delta rtt109$ after α -factor synchronization. Average DNA content from $\Delta rtt109$ and wild-type (WT) are plotted along the time course (top right) (DNA content from WT same as in Fig. 1A). (D and E) Expression during S phase in mutants. The average increase in expression levels (blue) of early-replicating genes relative to late-replicating ones is depicted for the indicated mutants progressing through S phase after release from α -factor arrest. The maximal increase in the expression of early- versus late-replicating genes is summarized in (E) over 5 and 4 repeats for WT and $\Delta rtt109$, respectively (see also figs. S7B and S8D).

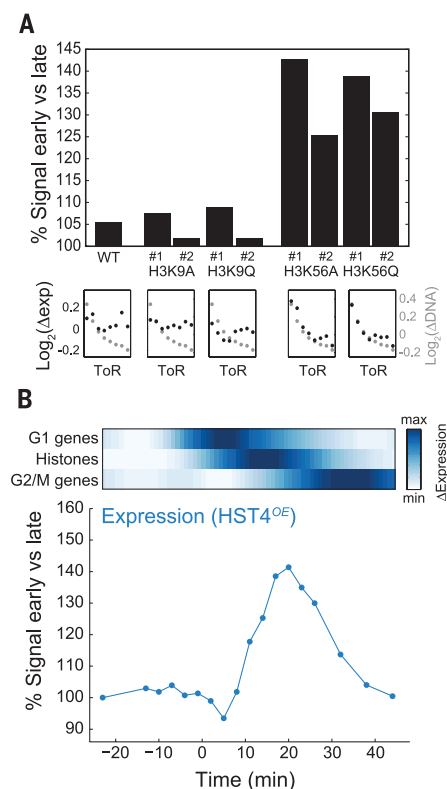


Fig. 4. H3K56 acetylation is required for expression homeostasis during S phase. (A) Expression in HU-synchronized cells of H3K56 or H3K9 point mutations. The indicated strains were HU-arrested for 3 hours. Shown is the increase in expression of replicated genes (early) relative to nonreplicated (late) ones for the indicated strains (top). Correlations of gene expression with the replication timing are also shown (bottom). (B) Expression during S phase in a strain overexpressing Hst4: the average increase in gene expression levels of early-replicating genes relative to late-replicating ones for cells overexpressing Hst4, progressing synchronously through S phase after release from α -factor arrest (see also table S4). A milder overexpression of Hst3 led to an intermediate effect (fig. S8C).

expression homeostasis during this time when the DNA dosage of different genes transiently differs. H3K56 is an internal site that is acetylated on newly synthesized histones before incorporation onto DNA (15, 24) (fig. S8E). Previous studies associated this modification with active transcription of specific genes (25), showing that it promotes nucleosome disassembly (26). H3K56ac, however, is primarily a marker of replicated DNA during S phase (27) (fig. S11), when it promotes nucleosome assembly and guards genome stability (14, 16, 28). Our study ascribes a complementary role to H3K56ac in maintaining expression homeostasis during S phase.

REFERENCES AND NOTES

1. S. Marguerat, J. Bahler, *Trends Genet.* **28**, 560–565 (2012).
2. M. G. Chandler, R. H. Pritchard, *Mol. Gen. Genet.* **138**, 127–141 (1975).

3. M. B. Schmid, J. R. Roth, *J. Bacteriol.* **169**, 2872–2875 (1987).
4. C. Sousa, V. de Lorenzo, A. Cebolla, *Microbiology* **143**, 2071–2078 (1997).
5. S. G. Elliott, C. S. McLaughlin, *Proc. Natl. Acad. Sci. U.S.A.* **75**, 4384–4388 (1978).
6. D. Killander, A. Zetterberg, *Exp. Cell Res.* **38**, 272–284 (1965).
7. S. E. Pfeiffer, *J. Cell. Physiol.* **71**, 95–104 (1968).
8. S. G. Elliott, *Mol. Gen. Genet.* **192**, 204–211 (1983).
9. R. S. Fraser, F. Moreno, *J. Cell Sci.* **21**, 497–521 (1976).
10. R. S. Fraser, P. Nurse, *Nature* **271**, 726–730 (1978).
11. S. Yungler, L. Rosenfeld, Y. Garini, Y. Shav-Tal, *Nat. Methods* **7**, 631–633 (2010).
12. O. Padovan-Merhar et al., *Mol. Cell* **58**, 339–352 (2015).
13. T. L. Lenstra et al., *Mol. Cell* **42**, 536–549 (2011).
14. R. Driscoll, A. Hudson, S. P. Jackson, *Science* **315**, 649–652 (2007).
15. J. Han, H. Zhou, Z. Li, R.-M. Xu, Z. Zhang, *J. Biol. Chem.* **282**, 14158–14164 (2007).
16. Q. Li et al., *Cell* **134**, 244–255 (2008).
17. C. Heichinger, C. J. Penkett, J. Bähler, P. Nurse, *EMBO J.* **25**, 5171–5179 (2006).
18. K. Yamane et al., *Mol. Cell* **41**, 56–66 (2011).
19. C. E. Horak et al., *Genes Dev.* **16**, 3017–3033 (2002).
20. P. T. Spellman et al., *Mol. Biol. Cell* **9**, 3273–3297 (1998).
21. E. Radovani et al., *Eukaryot. Cell* **12**, 654–664 (2013).
22. J. Dai et al., *Cell* **134**, 1066–1078 (2008).
23. I. Celic et al., *Curr. Biol.* **16**, 1280–1289 (2006).
24. C. A. Davey, D. F. Sargent, K. Luger, A. W. Maeder, T. J. Richmond, *J. Mol. Biol.* **319**, 1097–1113 (2002).
25. F. Xu, K. Zhang, M. Grunstein, *Cell* **121**, 375–385 (2005).
26. S. K. Williams, D. Truong, J. K. Tyler, *Proc. Natl. Acad. Sci. U.S.A.* **105**, 9000–9005 (2008).
27. H. Masumoto, D. Hawke, R. Kobayashi, A. Verreault, *Nature* **436**, 294–298 (2005).
28. M. Clemente-Ruiz, R. González-Prieto, F. Prado, *PLOS Genet.* **7**, e1002376 (2011).
29. N. Yabuki, H. Terashima, K. Kitada, *Genes Cells* **7**, 781–789 (2002).

ACKNOWLEDGMENTS

We thank D. Rosin and M. Krupkin for technical assistance and J. Karagiannis for yeast strains. We also thank members of our laboratory and B. Z. Shilo for fruitful discussions and comments on the manuscript. This work was supported by the European Research Council, Israel Science Foundation, and Binational Science Foundation. RNA-seq, ChIP-seq, and DNA-seq data are deposited in the European Nucleotide Archive (ENA) under accession number PRJEB11977.

SUPPLEMENTARY MATERIALS

www.sciencemag.org/content/351/6277/1087/suppl/DC1
Materials and Methods
Figs. S1 to S11
Tables S1 to S4
References (30–61)

28 July 2015; accepted 19 January 2016
10.1126/science.aad1162

TRANSCRIPTION

Multiplexed protein-DNA cross-linking: Scrunching in transcription start site selection

Jared T. Winkelman,^{1,2,3,4*} Irina O. Vvedenskaya,^{1,3*} Yuanchao Zhang,^{1,5*} Yu Zhang,^{2,3*†} Jeremy G. Bird,^{1,2,3} Deanne M. Taylor,^{1,5,6,7} Richard L. Gourse,⁴ Richard H. Ebricht,^{2,3†} Bryce E. Nickels^{1,3‡}

In bacterial transcription initiation, RNA polymerase (RNAP) selects a transcription start site (TSS) at variable distances downstream of core promoter elements. Using next-generation sequencing and unnatural amino acid-mediated protein-DNA cross-linking, we have determined, for a library of 4¹⁰ promoter sequences, the TSS, the RNAP leading-edge position, and the RNAP trailing-edge position. We find that a promoter element upstream of the TSS, the “discriminator,” participates in TSS selection, and that, as the TSS changes, the RNAP leading-edge position changes, but the RNAP trailing-edge position does not change. Changes in the RNAP leading-edge position, but not the RNAP trailing-edge position, are a defining hallmark of the “DNA scrunching” that occurs concurrent with RNA synthesis in initial transcription. We propose that TSS selection involves DNA scrunching prior to RNA synthesis.

During bacterial transcription initiation, RNA polymerase (RNAP) holoenzyme binds to promoter DNA through sequence-specific interactions with core promoter elements, unwinds a turn of promoter DNA to form an RNAP-promoter open complex (RPO) with an unwound “transcription bubble,” selects a tran-

scription start site (TSS), and aligns the TSS template-strand nucleotide with the RNAP active center (7). There is variability in the position of the TSS relative to core promoter elements (2–6). The mechanistic basis for this variability has remained unclear. In addition, although DNA-sequence determinants for TSS selection within the TSS region have been defined (2), it has remained unclear whether there also are DNA-sequence determinants for TSS selection outside the TSS region.

To investigate whether there are sequence determinants for TSS selection outside the TSS region, we applied a next-generation-sequencing approach that enables comprehensive analysis of sequence determinants during transcription: “massively systematic transcript end readout” (MASTER) (2). MASTER entails generating transcripts from a library of bar-coded randomized sequences and sequencing transcript ends (fig. S1) (2). In previous work, we defined TSS-region sequence de-

terminants for TSS selection, using a library containing all 4⁷ (~16,000) sequences at positions 4 to 10 base pairs (bp) downstream of the –10 element of a consensus bacterial promoter (MASTER-N7; Fig. 1A and fig. S1) (2). Here, to define effects on TSS selection of sequences outside the TSS region, we analyzed a template library containing all 4¹⁰ (~1,000,000) sequences at positions 1 to 10 bp downstream of the –10 element, extending the randomized sequence to include the “discriminator” (7–10), located between the TSS region and the –10 element (MASTER-N10; Fig. 1A and fig. S1). Results of MASTER-N10 analysis reveal that the discriminator affects TSS selection (Fig. 1, B to D; figs. S2 to S4; and table S1). Changes in the discriminator change TSS selection by up to ~3 bp (Fig. 1D and fig. S4) and change the mean TSS, averaged over the ~16,000 templates analyzed for each of the 64 discriminator sequences, by ~1 bp (Fig. 1B). Discriminators having a purine at each position (RRR), particularly GGG, favor TSS selection at upstream-shifted positions, whereas discriminators having a pyrimidine at each position (YYY), particularly CCT, favor TSS selection at downstream-shifted positions (modal TSS for RRR, 7 bp downstream of –10 element; modal TSS for YYY, 8 bp downstream of –10 element; Fig. 1, B and C, and fig. S2B). Results from MASTER-N10, where the discriminator is GTG, match results from MASTER-N7, where the discriminator is GTG, demonstrating the reproducibility of the approach (Fig. 1, C and D, and fig. S2B). We conclude that the discriminator is a determinant of TSS selection.

A conserved region of transcription initiation factor σ , “ σ region 1.2” ($\sigma_{1.2}$), makes sequence-specific protein-DNA interactions with the nontemplate strand of the discriminator in the transcription bubble in RPO (7, 8). These interactions confer specificity for GGG (7–9). To determine whether sequence-specific $\sigma_{1.2}$ -discriminator interactions affect TSS selection, we used MASTER-N10 to compare wild-type σ to a σ derivative having alanine substitutions that disrupt sequence-specific discriminator- $\sigma_{1.2}$ interactions: $\sigma_{1.2}$ -mut (7, 11). The results show that disrupting $\sigma_{1.2}$ -discriminator interactions markedly alters TSS selection for templates containing a GGG discriminator, resulting

¹Department of Genetics, Rutgers University, Piscataway, NJ 08854, USA. ²Department of Chemistry and Chemical Biology, Rutgers University, Piscataway, NJ 08854, USA.

³Waksman Institute, Rutgers University, Piscataway, NJ 08854, USA.

⁴Department of Bacteriology, University of Wisconsin-Madison, Madison, WI 53705, USA. ⁵Department of Biomedical and Health Informatics, Children’s Hospital of Philadelphia, Philadelphia, PA 19104, USA. ⁶Department of Pediatrics, Perelman School of Medicine, University of Pennsylvania, Philadelphia, PA, 19104, USA. ⁷Department of Obstetrics, Gynecology and Reproductive Sciences, Rutgers Robert Wood Johnson Medical School, New Brunswick, NJ 08901, USA.

*These authors contributed equally to this work. †Present address: Chinese Academy of Sciences, Shanghai, 200032, China.

‡Corresponding author. E-mail: bnickels@waksman.rutgers.edu (B.E.N.); ebricht@waksman.rutgers.edu (R.H.E.)

in a downstream shift in mean TSS (Fig. 1E). We conclude that $\sigma_{1,2}$ -discriminator interactions are a determinant of TSS selection.

The results in Fig. 1 and figs. S2 to S4 show that TSS selection can occur at any of five positions downstream of the -10 element—i.e., positions 6 to 10,

with position 7 generally being preferred—and that discriminator sequence affects TSS selection. These results imply that RPo can accommodate ~ 17 Å (5 bp $\times 3.4$ Å/bp) variation in the position of the TSS and that discriminator sequence affects the ability to accommodate this variation.

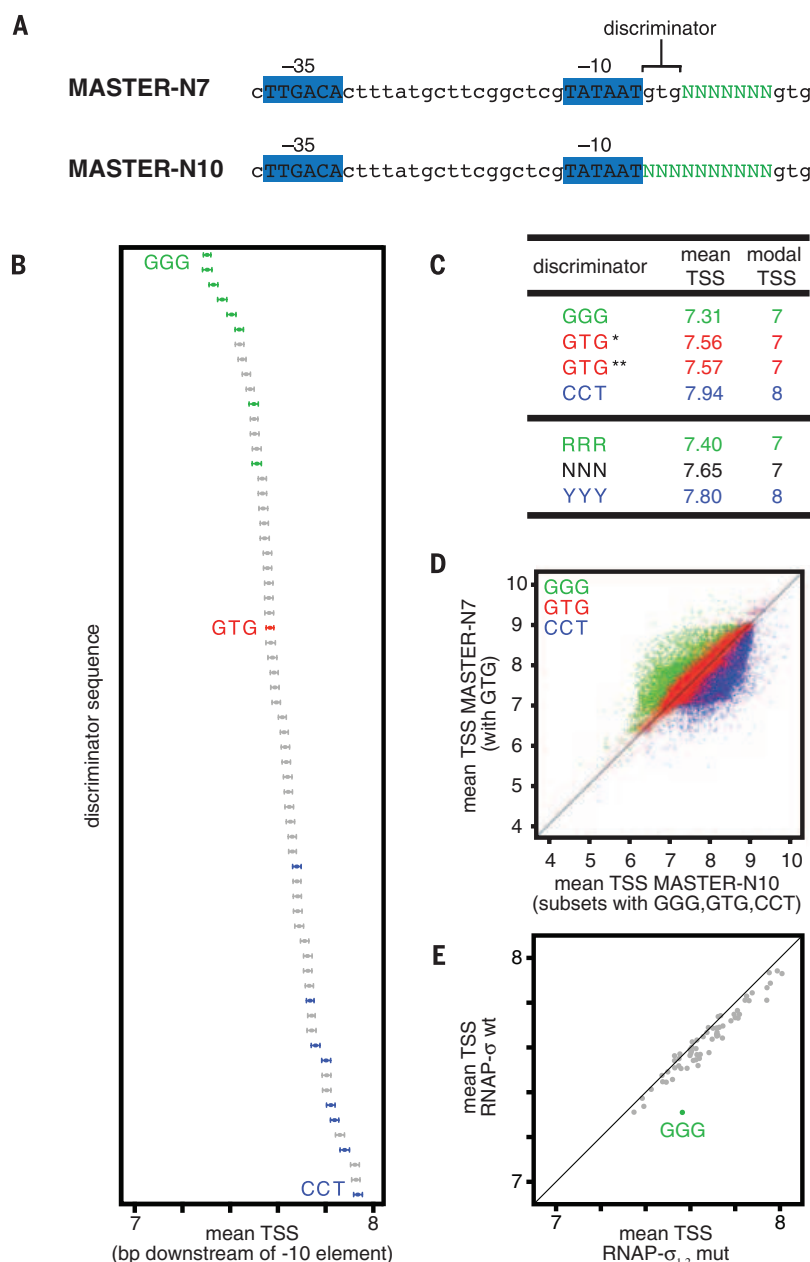


Fig. 1. Sequences upstream of TSS region affect TSS selection. (A) Promoter sequences analyzed in MASTER-N7 (2) and MASTER-N10. Promoter -35 , -10 , and discriminator elements are indicated. Green, randomized nucleotides. (B) Effect of discriminator on position of TSS (numbered in base pairs downstream of -10 element). Data show means and 99.9% confidence intervals for each of the 64 discriminator sequences ($\sim 16,000$ templates analyzed for each discriminator). Green, GGG and other RRR discriminators; blue, CCT and other YYY discriminators; red, GTG discriminator. (C) Mean and modal TSS. *, GTG data from MASTER-N7; **, GTG data from MASTER-N10. (D) Upstream and downstream shifts in TSS selection with the $\sim 16,000$ GGG and $\sim 16,000$ CCT discriminators (green and blue, respectively) relative to the $\sim 16,000$ GTG discriminators (red). (E) Effect of $\sigma_{1,2}$ -discriminator interactions on TSS selection (downstream shift in mean TSS for $\sim 16,000$ GGG-discriminator templates on replacement of σ by $\sigma_{1,2}$ mutant).

It has been hypothesized that TSS selection at positions downstream of the modal TSS (generally position 7; Fig. 1C and fig. S2A) involves transcription-bubble expansion (“scrunching”; fig. S5), and TSS selection at positions upstream of the modal TSS involves transcription-bubble contraction (“anti-scrunching”; fig. S5) (2, 12). According to this hypothesis, RPo generally contains a 13-bp transcription bubble that places position 7 in the RNAP active-center initiating nucleoside triphosphate (NTP) site (“i site”) and position 8 in the RNAP active-center NTP addition site (“i+1 site”; fig. S5, TSS = 7). For TSS selection to occur at positions 8, 9, or 10, it is hypothesized that the downstream DNA duplex is unwound by 1, 2, or 3 bp; the unwound DNA is pulled into and past the RNAP active center, and the unwound DNA is accommodated as bulges within the transcription bubble, yielding a scrunched complex (fig. S5, TSS = 8, 9, or 10). For TSS selection to occur at position 6, it is hypothesized that the opposite occurs: Downstream DNA is rewound by 1 bp, downstream DNA is extruded from the RNAP active center, and the extrusion of DNA is accommodated by stretching DNA within the transcription bubble, yielding an anti-scrunched complex (fig. S5, TSS = 6). Two lines of evidence support this hypothesis: Single-molecule fluorescence resonance energy transfer results suggest that transcription-bubble size in RPo can vary (12); and negative supercoiling, which provides a driving force for transcription-bubble expansion, favors TSS selection at downstream positions (2). However, direct evidence for this hypothesis has not been reported.

Transcription-bubble expansion (scrunching) occurs in initial transcription, where it is coupled to RNA synthesis (13–15) (fig. S5). A hallmark of scrunching during initial transcription is that the RNAP trailing edge remains stationary relative to DNA, whereas the RNAP leading edge moves relative to DNA (13–15) (fig. S5). Here, we investigated whether this hallmark of scrunching is a feature of TSS selection. We used unnatural amino acid-mediated protein-DNA photo-cross-linking to define the RNAP trailing-edge position and RNAP leading-edge position in RPo on a MASTER-N10 library (MASTER-N10-XL; Fig. 2A and fig. S6). To perform MASTER-N10-XL, we incorporated the photoactivatable unnatural amino acid *p*-benzoyl-L-phenylalanine (Bpa; fig. S6) (15, 16) at specific sites at the RNAP trailing edge and RNAP leading edge; formed RPo between the Bpa-containing RNAP derivatives and the MASTER-N10 library; and irradiated complexes with ultraviolet light to induce cross-linking between Bpa and adjacent DNA nucleotides (Fig. 2A and fig. S6). We then mapped positions of cross-links on each of the 4^{10} sequences by primer extension and high-throughput sequencing (Fig. 2A). The method defines the mean RNAP trailing-edge position, the mean RNAP leading-edge position, and the mean distance between them (RNAP trailing-edge/leading-edge distance; Fig. 2 and table S2).

The results show that changes in the discriminator change the RNAP trailing-edge/leading-edge distance in the same manner that changes in the discriminator change TSS selection (Figs. 1 and 2

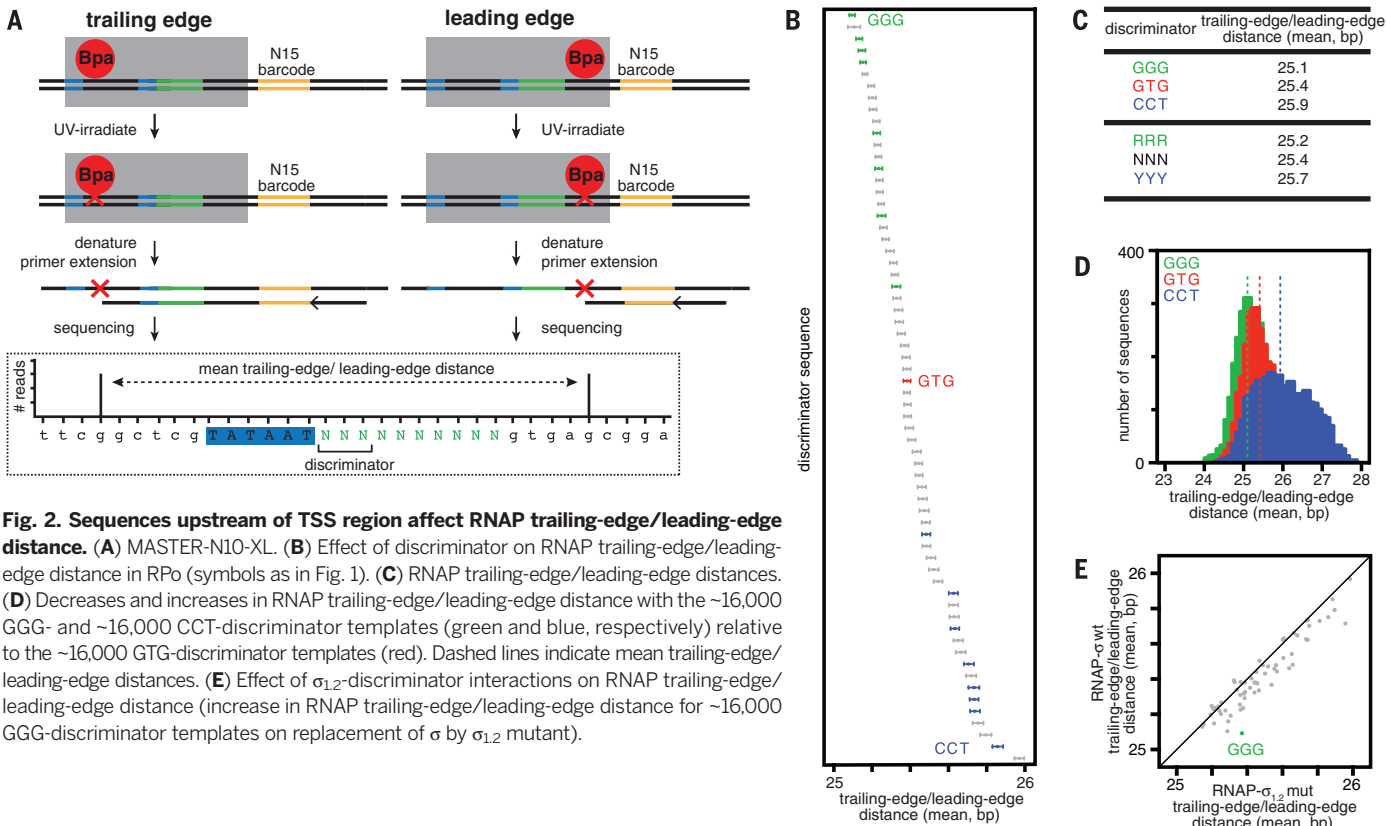
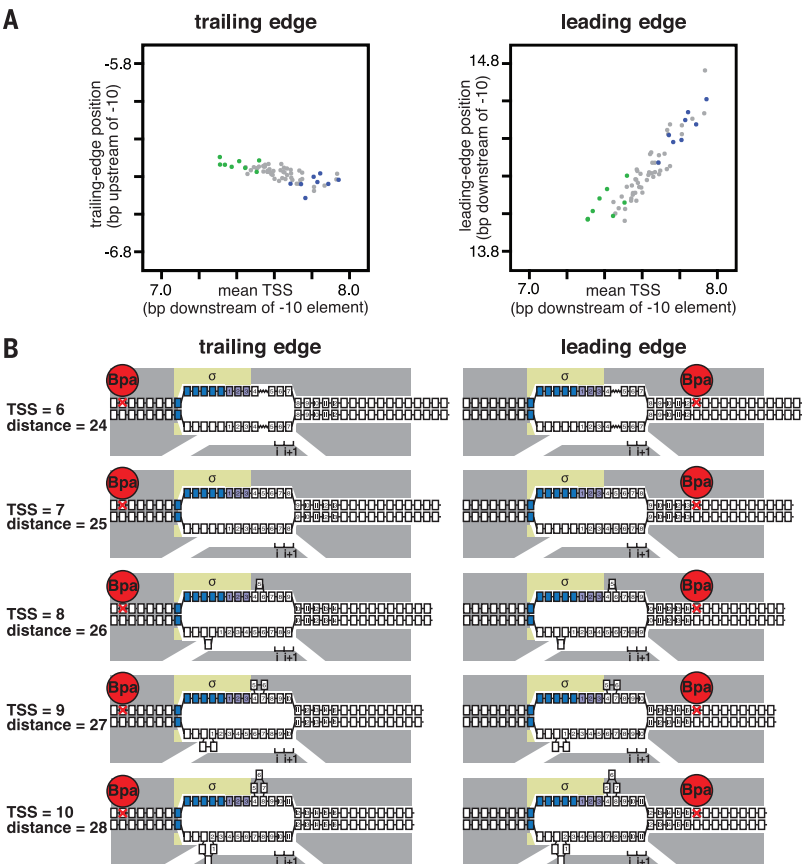


Fig. 3. As TSS changes, RNAP leading-edge position changes, but RNAP trailing-edge position does not change. (A) RNAP trailing-edge position (left; slope ~0) and RNAP leading-edge position (right; slope ~1) as a function of mean TSS for each of the 64 discriminator sequences (~16,000 templates analyzed for each discriminator; green, RRR discriminators; blue, YYY discriminators). (B) Interpretation: Changes in TSS selection result from changes in DNA scrunching. Gray, RNAP; yellow, σ ; blue, -10 element nucleotides; purple, discriminator nucleotides; i and i+1, NTP binding sites; red, Bpa and nucleotide cross-linked to Bpa; boxes, DNA nucleotides (nontemplate-strand nucleotides above template-strand nucleotides; nucleotides downstream of -10 element numbered). Scrunching is indicated by bulged-out nucleotides. Anti-scrunching is indicated by a “stretched” nucleotide-nucleotide linkage.



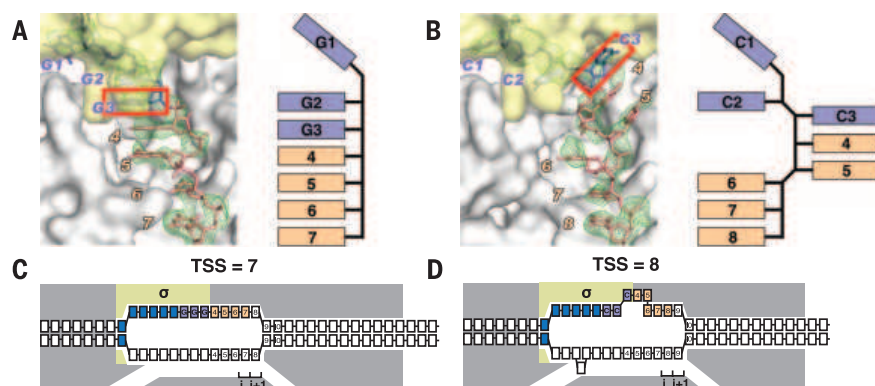


Fig. 4. Crystal structures define paths of DNA nontemplate strands with representative RRR and YY discriminators. (A) Crystal structure of an initiation complex with RRR discriminator and nontemplate-strand length corresponding to TSS at position 7 (RPo-GGG-7). Left, simulated annealing $|F_o - F_c|$ omit map contoured at 2.3σ and atomic model for interactions of RNAP with DNA nontemplate strand. Right, schematic path of DNA. Gray, RNAP; yellow, σ ; purple, discriminator nucleotides; pink, nontemplate-strand nucleotides downstream of discriminator; green, omit map. Red box, third nucleotide of discriminator. (B) Crystal structure of an initiation complex with YY discriminator and nontemplate-strand length corresponding to TSS at position 8 [RPo-CCC-8; symbols as in (A)]. Nucleic-acid scaffolds used for crystallization included short oligoribonucleotides (see Methods). (C and D) Interpretation: The different position of the third nucleotide of the discriminator in the structure with a YY discriminator increases the distance between the third nucleotide of the discriminator and downstream duplex DNA, accommodating an additional nucleotide in the connector.

and fig. S7). Changes in the discriminator change the RNAP trailing-edge/leading-edge distance by up to ~ 3 bp (fig. S8) and change the RNAP trailing-edge/leading-edge distance, averaged over the $\sim 16,000$ templates analyzed for each of the 64 discriminator sequences, by ~ 1 bp (Fig. 2B and fig. S7). The RNAP trailing-edge/leading-edge distance is shortest for RRR, especially GGG, discriminators and longest for YY, especially CCT, discriminators (Fig. 2, B to D). Disruption of $\sigma_{1,2}$ -discriminator interactions results in a marked increase in RNAP trailing-edge/leading-edge distance for templates containing a GGG discriminator (Fig. 2E).

We next compared effects of discriminator sequence on TSS selection (Fig. 1) to effects of discriminator sequence on RNAP trailing-edge position and RNAP leading-edge position (Figs. 2 and 3 and fig. S9). The results show that, as the position of the TSS changes by 1 bp, the RNAP leading-edge position changes by 1 bp (Fig. 3A and fig. S9, right), but the RNAP trailing-edge position does not change (Fig. 3A and fig. S9, left). Thus, TSS selection exhibits a defining hallmark of scrunching: namely, the RNAP leading edge moves, whereas the RNAP trailing edge does not move (Fig. 3B). The results provide support for the hypothesis that flexibility in TSS selection is mediated by scrunching/anti-scrunching, and that the discriminator affects TSS selection by modulating the extent of scrunching/anti-scrunching.

To define the path of the DNA nontemplate-strand in RPo having an RRR discriminator and a nontemplate-strand length corresponding to its modal TSS at position 7, and to define the path of the DNA nontemplate-strand in RPo having a YY discriminator and a nontemplate-

strand length corresponding to its modal TSS at position 8, we determined crystal structures of representative initiation complexes of each: RPo-GGG-7 and RPo-CCC-8 (Fig. 4, figs. S10 and S11, and table S3). For RPo-GGG-7, the first nucleotide of the discriminator is unstacked and inserted into a pocket in $\sigma_{1,2}$, and the next six nucleotides of the nontemplate-strand form a continuous stack (Fig. 4A and fig. S10) (8). In contrast, for RPo-CCC-8, the third nucleotide of the discriminator occupies a different position, being unstacked, rotated by $\sim 180^\circ$, and inserted into a pocket in σ region 2 (σ_2 ; Fig. 4B and figs. S10 and S11). As a result of the difference in the position of the third nucleotide of the discriminator, the distance between the third nucleotide of the discriminator and the downstream duplex is ~ 4 – 5 Å greater in RPo-CCC-8 than in RPo-GGG-7, and the DNA segment between the third nucleotide of the discriminator and the downstream duplex accommodates an additional nucleotide (Fig. 4B and fig. S10). Two factors account for the difference in the position of the third nucleotide of the discriminator in the RPo-CCC-8: (i) weak stacking between YY, as compared to RR, at the second and third nucleotides of the discriminator (Fig. 4B and fig. S10); and (ii) the ability of Y at the third nucleotide of the discriminator to fit in a pocket in σ_2 that has size and hydrogen-bonding character specific for Y (Fig. 4B and fig. S11).

Our results indicate that flexibility in TSS selection occurs through changes in scrunching/anti-scrunching in RPo. We propose that RPo uses thermally driven DNA fluctuations to access an ensemble of transcription-bubble sizes (Fig. 3 and fig. S5). Transcription-bubble expansion (scrunching) places downstream DNA in contact

with the RNAP active center, facilitating downstream TSS selection; and transcription-bubble contraction (anti-scrunching) places upstream DNA in contact with the RNAP active center, facilitating upstream TSS selection. According to this model, the discriminator alters TSS selection by altering the energy landscape describing the ensemble of transcription-bubble sizes in RPo (Fig. 4). The scrunching that occurs in TSS selection is mechanistically analogous to the scrunching that occurs during initial transcription (13–15) (fig. S5). However, scrunching in TSS selection occurs before NTP binding and nucleotide incorporation and, in the absence of an additional energy source, is driven by energy available from the thermal bath and therefore limited to ~ 1 to 3 bp—rather than occurring after NTP binding and nucleotide incorporation, being driven by a combination of thermal energy, NTP binding, and nucleotide incorporation, and being able to span tens of base pairs. We suggest that, in the presence of an additional energy source, scrunching in TSS selection could access a larger range of TSS positions, and, in particular, we speculate that this occurs with transcription factor IIH (TFIIH)-dependent adenosine 5'-triphosphate (ATP) hydrolysis as the additional energy source in the long-range “TSS scanning” observed with eukaryotic RNAP II in some species (17).

REFERENCES AND NOTES

- E. F. Ruff, M. T. Record Jr., I. Artsimovitch, *Biomolecules* **5**, 1035–1062 (2015).
- I. O. Vvedenskaya et al., *Mol. Cell* **60**, 953–965 (2015).
- W. Jeong, C. Kang, *Nucleic Acids Res.* **22**, 4667–4672 (1994).
- J. Liu, C. L. Tumbough Jr., *J. Bacteriol.* **176**, 2938–2945 (1994).
- K. A. Walker, R. Osuna, *J. Bacteriol.* **184**, 4783–4791 (2002).
- D. E. Lewis, S. Adhya, *Mol. Microbiol.* **54**, 692–701 (2004).
- S. P. Haugen et al., *Cell* **125**, 1069–1082 (2006).
- Y. Zhang et al., *Science* **338**, 1076–1080 (2012).
- A. Feklistov et al., *Mol. Cell* **23**, 97–107 (2006).
- A. A. Travers, *J. Bacteriol.* **141**, 973–976 (1980).
- S. P. Haugen, W. Ross, M. Manrique, R. L. Gourse, *Proc. Natl. Acad. Sci. U.S.A.* **105**, 3292–3297 (2008).
- N. C. Robb et al., *J. Mol. Biol.* **425**, 875–885 (2013).
- A. Revyakin, C. Liu, R. H. Ebright, T. R. Strick, *Science* **314**, 1139–1143 (2006).
- A. N. Kapanidis et al., *Science* **314**, 1144–1147 (2006).
- J. T. Winkelman et al., *Mol. Cell* **59**, 768–780 (2015).
- J. W. Chin, A. B. Martin, D. S. King, L. Wang, P. G. Schultz, *Proc. Natl. Acad. Sci. U.S.A.* **99**, 11020–11024 (2002).
- F. M. Fazal, C. A. Meng, K. Murakami, R. D. Kornberg, S. M. Block, *Nature* **525**, 274–277 (2015).

ACKNOWLEDGMENTS

Work was supported by NIH grants GM37048 (R.L.G.), GM041376 (R.H.E.), GM088343 (B.E.N.), and GM115910 (BEN). Protein Data Bank accession codes are 5E17 and 5E18.

SUPPLEMENTARY MATERIALS

www.sciencemag.org/content/351/6277/1090/suppl/DC1
Materials and Methods
Figs. S1 to S11
Tables S1 to S4
References (18–23)

21 October 2015; accepted 25 January 2016
10.1126/science.aad6881

DNA REPAIR

Stochastic activation of a DNA damage response causes cell-to-cell mutation rate variation

Stephan Uphoff,^{1,2*} Nathan D. Lord,² Burak Okumus,² Laurent Potvin-Trottier,^{2,3} David J. Sherratt,¹ Johan Paulsson^{2*}

Cells rely on the precise action of proteins that detect and repair DNA damage. However, gene expression noise causes fluctuations in protein abundances that may compromise repair. For the Ada protein in *Escherichia coli*, which induces its own expression upon repairing DNA alkylation damage, we found that undamaged cells on average produce one Ada molecule per generation. Because production is stochastic, many cells have no Ada molecules and cannot induce the damage response until the first expression event occurs, which sometimes delays the response for generations. This creates a subpopulation of cells with increased mutation rates. Nongenetic variation in protein abundances thus leads to genetic heterogeneity in the population. Our results further suggest that cells balance reliable repair against toxic side effects of abundant DNA repair proteins.

The integrity of the genome is constantly threatened by DNA damage. Most damage events are reversed by active repair systems, but the ones that escape repair can cause cell death or mutations. An intriguing question is what causes those failures. Specifically, the classic perspective suggests that failures to repair reflect the intrinsic error rate of the repair enzymes, for example, because of the random search for lesions (1, 2). Alternatively, most failures could occur in an error-prone subpopulation of cells (3, 4) in which repair is compromised by fluctuations in the abundances of the repair proteins (5–7).

To distinguish between these possibilities we quantitatively analyzed, with single-molecule resolution in single cells, the adaptive response that protects *Escherichia coli* against the toxic and mutagenic effects of DNA alkylation damage (8). The Ada protein functions not only in the direct repair of alkylated DNA but also as the transcriptional activator of the adaptive response (Fig. 1A) (9, 10). Specifically, *ada* expression is induced by methylated Ada (meAda) after irreversible methyl transfer from DNA phosphotriester and O⁶MeG lesions onto cysteine residues of Ada. Because Ada is present in low numbers before damage, this positive-feedback gene regulation may amplify stochastic fluctuations and create cell-to-cell heterogeneity in the repair system (2, 11).

We imaged the endogenous expression of a functional Ada-mYPet fluorescent protein fusion (fig. S1), in cells treated with methyl methane-sulfonate (MMS) (Fig. 1B). We observed a strong and uniform expression of Ada in most cells, but

20% of the cells did not respond at all, even at saturating doses of MMS (Fig. 1, B and C). Quantitatively similar results were obtained with a transcriptional fluorescent reporter in cells with untagged Ada (fig. S2), which showed that the protein fusion did not affect the observations.

To visualize the dynamics of the process, we monitored Ada-mYPet abundance in real time in a microfluidic device that allows imaging of single cells over tens of generations during constant DNA damage treatment (fig. S3 and movies S1 and S2) (12, 13). At low-to-intermediate MMS concentrations (<200 μ M MMS), cells showed random unsynchronized pulses of Ada expression (Fig. 1D). The pulse frequency increased proportionally to the MMS concentration (fig. S4), as expected when triggering is limited by the probability that Ada finds a lesion. At higher MMS concentrations, most cells rapidly induced a persistent and uniform response (Fig. 1E). However, 20 to 30% of cells were lagging even at saturating MMS and triggered the response after exponentially distributed delays with an average of one generation time (Fig. 1F and fig. S5). Some cells thus failed to respond for several generations.

To identify the molecular determinants of this heterogeneity, we measured the Ada abundance before MMS treatment. Ada-mYPet was undetectable over the autofluorescence background of cells, which suggested that absolute amounts were on the order of a few molecules per cell. We therefore turned to single-molecule microscopy to directly count individual proteins in live cells (Fig. 1G and fig. S6). The abundance of Ada was extremely low: The observed population average was 1.4 ± 0.1 molecules per cell (\pm SEM) and 20 to 30% of the cells did not contain a single Ada molecule. Because the *ada* gene is strictly autoregulatory, i.e., it can only be induced by the Ada protein (8–10, 14), cells with zero Ada molecules should be unable to trigger the adaptive response, despite great amounts of damage. This is supported by

the quantitative agreement between the percentages of cells with a delayed response and with zero Ada molecules. Consequently, the delay before response activation should match the time until the first random expression event occurs in these cells. Indeed, the distribution of Ada copies before damage was very close to a Poisson distribution (Fig. 1G) with an average production rate of one molecule per cell cycle (fig. S6), and the late-responding cells also activated the response with a Poisson rate of once per cell cycle (Fig. 1F).

These findings also mean that most cells reliably launch the response with just one or two Ada molecules to sense the damage and to induce *ada* expression (Fig. 2A). We indeed observed distinct single-molecule signatures: The rates of Ada production displayed staircase patterns with equidistant states during response activation and deactivation at low MMS concentrations (Fig. 2B and fig. S7), indicative of discrete production and loss events of the meAda molecules that control Ada expression. To further confirm the low numbers, we titrated meAda using promoter sites on a low copy-number plasmid (15), which markedly decreased steady-state Ada induction, as expected (fig. S8). Furthermore, the discrete production rate steps disappeared when meAda abundance was increased using high MMS concentrations (fig. S7).

Because failure to trigger the adaptive response seems to be the result of a complete lack of Ada molecules in a fraction of cells, it should be possible to reduce this fraction with a slight increase in the average abundance of Ada. Specifically, for many distributions (including the Poisson) the probability mass in the tails depends sensitively on the average. We therefore moderately increased Ada numbers per cell either by inhibiting cell division—keeping the concentrations constant (16)—or by expressing additional unlabeled Ada from the P_{Ada} promoter on a very low copy-number plasmid (MiniF; ~2 copies per cell). In both cases, we observed the predicted uniform MMS response and disappearance of the late-responding cell subpopulation (Fig. 2, C and D).

These observations raise the question of why the native *ada* gene is expressed at such low basal amounts. Following the fates of single cells over time showed that a failure to activate the adaptive response during MMS treatment lowered the viability of those cells, as expected (Fig. 3A and fig. S9). However, the moderate overexpression of Ada resulted in severe toxicity of MMS treatment (Fig. 3A and fig. S10) (14, 17) and caused spontaneous triggering of the response in the absence of MMS (Fig. 3B and fig. S10), something we never observed at native *ada* expression (Fig. 3B and fig. S3). The extremely low abundance of Ada can thus be advantageous to the population as a whole, which implies that the repair system faces a trade-off to repair exogenous alkylation damage without introducing harmful effects. In fact, given the low numbers of molecules, the *ada* regulation is remarkably precise: First, the Poisson distribution before damage shows an almost complete absence of gene expression bursts or “extrinsic” noise (Fig. 3C and fig. S6), in stark contrast to the regulation

¹Department of Biochemistry, University of Oxford, Oxford OX1 3QU, UK. ²Department of Systems Biology, Harvard Medical School, Boston, MA 02115, USA. ³Biophysics Ph.D. Program, Harvard Medical School, USA.

*Corresponding author. E-mail: stephan.uphoff@bioch.ox.ac.uk (S.U.); johan_paulsson@harvard.edu (J.P.)

of most genes studied (5, 6, 7, 18). This can be explained by a short half-life and inefficient translation of *ada* mRNAs (19, 20), as well as the tendency of Poisson noise to dominate at very low abundances. Second, a dual reporter assay (5) that simultaneously monitors expression of the endogenous P_{Ada} *ada*-mYPet and an ectopic P_{Ada} *cfp* insertion (Fig. 3, D and E, and fig. S11) showed that both the activation time after MMS treatment and the subsequent expression dynamics were closely correlated between the two genes, with little uncorrelated noise that would indicate transcriptional bursting. Considering the central role of meAda in *ada* regulation (8–10, 14), these expression dynamics likely reflect fluctuations in meAda numbers. Indeed, the normalized standard deviation was inversely proportional to the square root of the expected average number of DNA damage sites, quantitatively consistent with the simplest model, where varying damage levels determine meAda abundances that then reliably control *ada* expression (fig. S12). Third, *ada* transcription activation is inhibited by unmethylated Ada. This may

control response deactivation after the damage has been repaired (21). Indeed, removal of MMS caused all cells to switch off the adaptive response uniformly, and Ada was diluted because of cell growth (Fig. 3F).

The total number of Ada molecules directly determines a cell's repair capacity: each Ada molecule can only act once to remove one mutagenic O⁶MeG lesion (10). Furthermore, a lack of Ada repair capacity cannot be compensated for by the DNA mismatch repair pathway, because unrepaired O⁶MeG lesions miscode for T instead of C. This leads to futile mismatch repair cycles, which eventually cause stable mutations during the next round of replication (17). We therefore tested whether heterogeneity in Ada concentrations affects mutation rates. To directly measure genomic mutation rates in single cells, we used the DNA mismatch recognition protein MutS as a marker for labeling nascent mutations (22). Specifically, photoactivated single-molecule tracking (23) allowed us to classify individual MutS-PAmCherry fusion proteins as DNA-bound or mobile (24, 25),

while also imaging Ada-mYPet in the same live cells (Fig. 4). Without MMS treatment, the apparent mutation frequency was low (fig. S13), and most MutS molecules were mobile (average 6% bound) (fig. S14). MMS treatment of Ada-deficient cells (Δada) increased both the mutation frequency (fig. S13) and MutS binding (56% bound) (Fig. 4 and fig. S14). MMS treatment of wild-type cells resulted in highly variable amounts of bound MutS molecules between cells. This variation could be entirely explained by the heterogeneity in Ada expression (Fig. 4 and fig. S15): MutS binding was increased only in the subpopulation of cells with low Ada expression (30% bound), whereas cells with abundant Ada retained low MutS activity (10% bound). Stochastic activation of the adaptive response therefore leads to an error-prone cell subpopulation that does not efficiently repair DNA alkylation damage and accumulates mutations.

We found that a cell's fate after DNA damage can be accurately predicted by the presence or absence of a single protein molecule. The resulting cell heterogeneity increases the chance

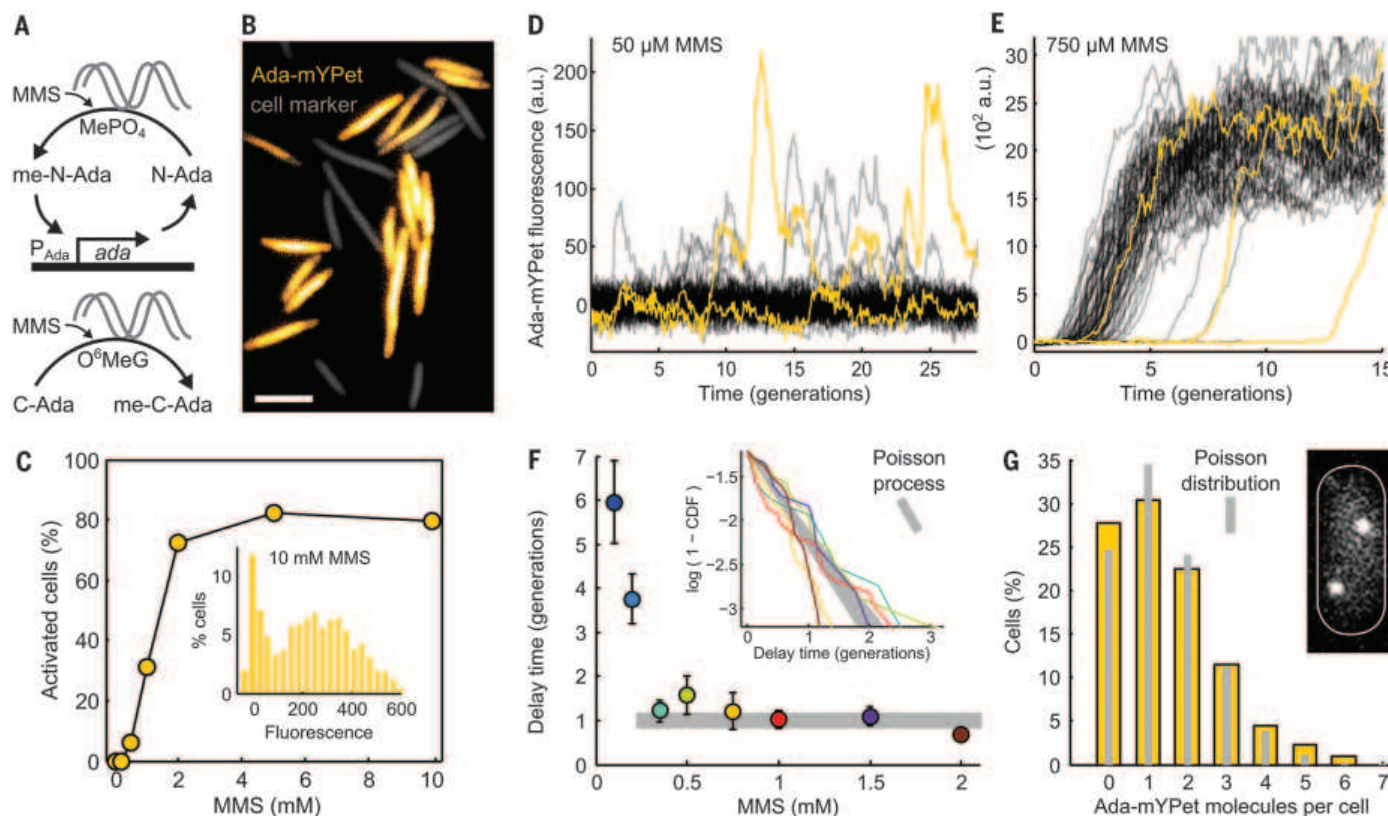


Fig. 1. Stochastic gene expression delays Ada response activation in a cell subpopulation. (A) Methylation of Ada N- and C-terminal domains functions as a damage sensor, turning Ada into an autoregulatory activator of genes involved in DNA alkylation repair. (B) Ada-mYPet fluorescence (yellow) in cells treated with 10 mM MMS for 1 hour. Constitutive mKate2 serves as fluorescent cell marker (gray). Scale bar, 5 μ m. (C) Percentage of cells that activated Ada-mYPet expression after 1 hour in MMS. (Inset) Histogram of Ada-mYPet fluorescence per cell with 10 mM MMS. (D and E) Time traces of Ada-mYPet fluorescence in single cells treated with 50 μ M and 750 μ M MMS (added at time 0). Example cells in yellow; time in units of average generation times (42 min) throughout. (F) (Inset) Transformed cumulative distribution

log(1-CDF) of response delay times for the last 30% of cells to activate Ada-mYPet expression after MMS treatment in the microfluidic chip. Different MMS concentrations in colors as in main plot. Straight lines on log scale reflect exponential distributions as generated by a Poisson process; the slope corresponds to the average-delay time constant. Gray area: Poisson process with a rate of 1 ± 0.1 per generation. Main plot: Average delay time constants from the inset data (\pm SEM). (G) Single-molecule counting of Ada-mYPet without MMS. Example cell shown. Poisson model was generated using measured production rate of 1 molecule per generation. Note that the actual value may be closer to 1.2 because of delayed maturation of mYPet (see supplementary materials).

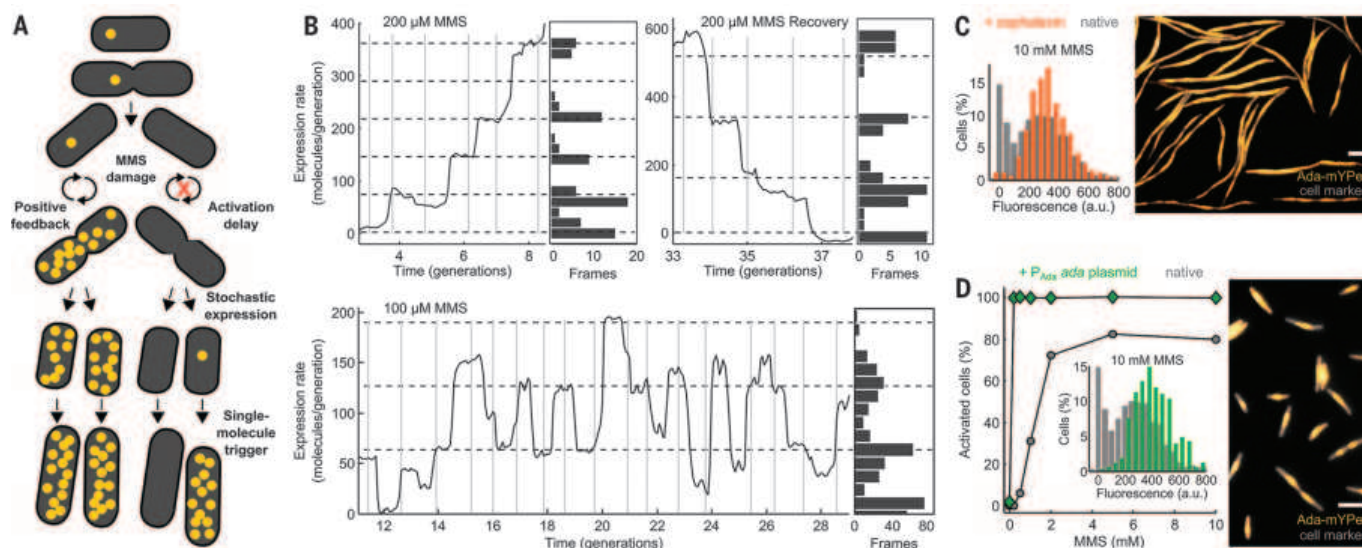


Fig. 2. Single-molecule trigger of the Ada response. (A) Stochastic expression and random segregation of molecules at cell division creates a subpopulation of cells with zero Ada molecules which therefore fails to auto-induce the adaptive response. (B) Sections of time traces showing distinct steps in Ada-mYPet expression rates during response activation upon 200 μM MMS treatment, deactivation after MMS removal, and stochastic activation and deactivation transitions with 100 μM MMS. Vertical lines indicate cell divisions.

Histograms show number of frames spent in the expression rate states. Losses can occur because of rare meAda degradation or by segregation at cell division. At very low numbers, all meAda molecules should sometimes remain in the same cell, maintaining expression rates, as observed. (C) Uniform Ada-mYPet induction when cell division was inhibited with cephalixin before MMS treatment (orange). (D) Uniform accumulation of endogenous Ada-mYPet with additional MiniF plasmid carrying P_{Ada} ada (green). Scale bars, 5 μm.

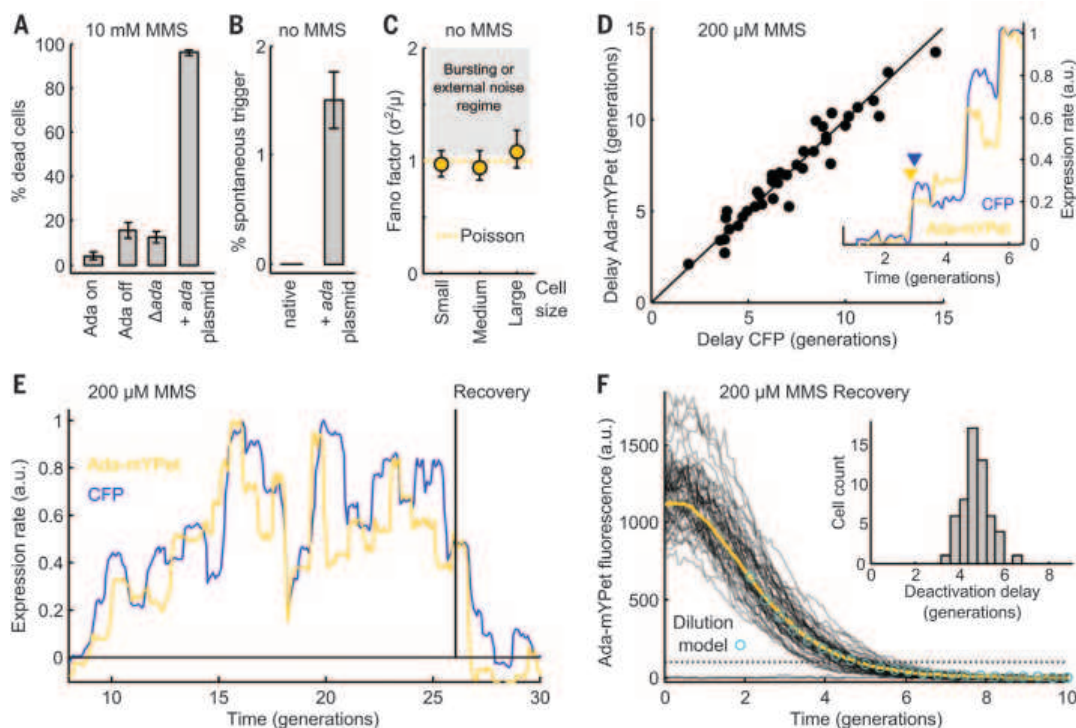


Fig. 3. High precision of the Ada response. (A) Cell fates after treatment with 10 mM MMS for 1 hour: Percentages of cells failing to recover growth during time-lapse microscopy without MMS for 3 hours (±SEM). Cells were distinguished if they had activated (Ada on) or failed the response (Ada off). (B) Percentages of cells spontaneously triggering Ada-mYPet expression without MMS (±SEM). (C) Fano factors (variance/mean) for Ada-mYPet without MMS, using single-molecule counting data from Fig. 1G (±SEM bootstrapped). Cells grouped by size. Expression bursting would give Fano factors above Poisson limit of 1. (D) Dual reporter assay: Delay times between MMS addition and response

activation for endogenous *ada-mYPet* and ectopic P_{Ada} *cfp* are closely correlated. Each dot represents one cell. (Inset) Example expression-rate time traces with simultaneous activation of both genes. (E) Example time traces showing correlated expression-rate fluctuations of the dual reporter genes and simultaneous response deactivation after MMS removal. (F) Deterministic response deactivation: Time traces after MMS removal at time 0 (average: yellow). The dilution model (circles) has an exponential decay constant equal to the average generation time. (Inset) Narrow distribution of delay times from MMS removal until response is deactivated (dotted line threshold).

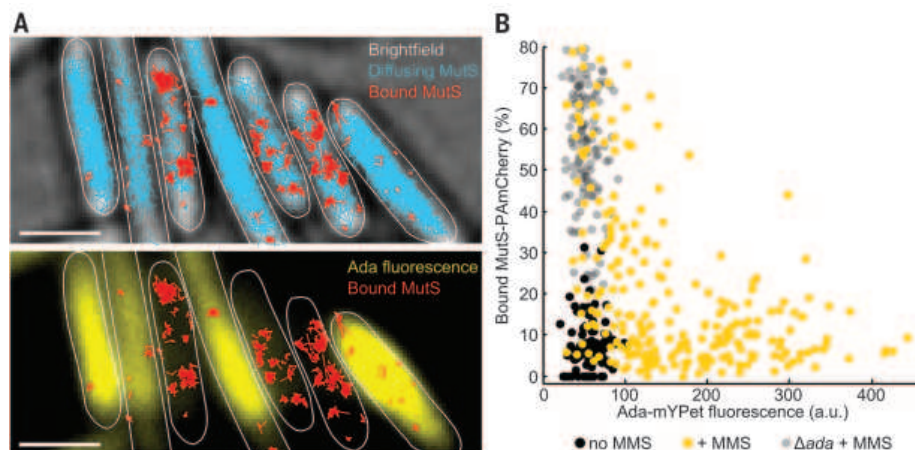


Fig. 4. Increased binding of mismatch recognition protein MutS in cells with delayed Ada response. Photoactivated single-molecule tracking of MutS-PAmCherry and Ada-mYPet fluorescence in single cells treated with 10 mM MMS for 1 hour. **(A)** Tracks of bound (red) and mobile MutS (blue). Cell outlines drawn; scale bars, 2 μ m. **(B)** Percentage of bound MutS molecules versus Ada-mYPet fluorescence per cell. Native strain with (yellow) and without MMS (black); Δ ada with MMS (gray).

of genetic adaptation in a hypermutagenic subpopulation of cells without jeopardizing the genetic integrity in the majority of the population during stress (3, 26). However, our observations that high Ada expression is toxic and that cells appear to minimize the heterogeneity in several ways suggest that this is not an adaptive bet-hedging strategy, but rather a side effect of maximizing short-term fitness: Because proteins with the capacity to modify DNA can be detrimental, cells may be forced to express them in low amounts, such that random fluctuations are unavoidable. Mutations can then result from stochastic variation in the concentrations of DNA repair proteins. Just as genetic heterogeneity can cause phenotypic heterogeneity, the reverse is thus also true.

REFERENCES AND NOTES

1. N. M. Kad, B. Van Houten, *Prog. Mol. Biol. Transl. Sci.* **110**, 1–24 (2012).

2. S. Uphoff, A. N. Kapanidis, *DNA Repair (Amst.)* **20**, 32–40 (2014).
3. R. S. Galhardo, P. J. Hastings, S. M. Rosenberg, *Crit. Rev. Biochem. Mol. Biol.* **42**, 399–435 (2007).
4. A. Marusyk, V. Almendro, K. Polyak, *Nat. Rev. Cancer* **12**, 323–334 (2012).
5. M. B. Elowitz, A. J. Levine, E. D. Siggia, P. S. Swain, *Science* **297**, 1183–1186 (2002).
6. I. Golding, J. Paulsson, S. M. Zawilski, E. C. Cox, *Cell* **123**, 1025–1036 (2005).
7. P. J. Choi, L. Cai, K. Frieda, X. S. Xie, *Science* **322**, 442–446 (2008).
8. L. Samson, J. Cairns, *Nature* **267**, 281–283 (1977).
9. P. Landini, M. R. Volkert, *J. Bacteriol.* **182**, 6543–6549 (2000).
10. B. Sedgwick, *Nat. Rev. Mol. Cell Biol.* **5**, 148–157 (2004).
11. U. Alon, *Nat. Rev. Genet.* **8**, 450–461 (2007).
12. P. Wang *et al.*, *Curr. Biol.* **20**, 1099–1103 (2010).
13. T. M. Norman, N. D. Lord, J. Paulsson, R. Losick, *Nature* **503**, 481–486 (2013).
14. D. E. Shevell, P. K. LeMotte, G. C. Walker, *J. Bacteriol.* **170**, 5263–5271 (1988).
15. R. C. Brewster *et al.*, *Cell* **156**, 1312–1323 (2014).
16. J. C. W. Locke, J. W. Young, M. Fontes, M. J. Hernández Jiménez, M. B. Elowitz, *Science* **334**, 366–369 (2011).

17. D. Fu, J. A. Calvo, L. D. Samson, *Nat. Rev. Cancer* **12**, 104–120 (2012).
18. H. Maamar, A. Raj, D. Dubnau, *Science* **317**, 526–529 (2007).
19. J. A. Bernstein, A. B. Khodursky, P.-H. Lin, S. Lin-Chao, S. N. Cohen, *Proc. Natl. Acad. Sci. U.S.A.* **99**, 9697–9702 (2002).
20. G.-W. Li, D. Burkhardt, C. Gross, J. S. Weissman, *Cell* **157**, 624–635 (2014).
21. B. M. Saget, G. C. Walker, *Proc. Natl. Acad. Sci. U.S.A.* **91**, 9730–9734 (1994).
22. M. Elez *et al.*, *Curr. Biol.* **20**, 1432–1437 (2010).
23. S. Manley *et al.*, *Nat. Methods* **5**, 155–157 (2008).
24. S. Uphoff, R. Reyes-Lamothé, F. Garza de Leon, D. J. Sherratt, A. N. Kapanidis, *Proc. Natl. Acad. Sci. U.S.A.* **110**, 8063–8068 (2013).
25. Y. Liao, J. W. Schroeder, B. Gao, L. A. Simmons, J. S. Biteen, *Proc. Natl. Acad. Sci. U.S.A.* **112**, E6898–E6906 (2015).
26. J.-W. Veening, W. K. Smits, O. P. Kuipers, *Annu. Rev. Microbiol.* **62**, 193–210 (2008).

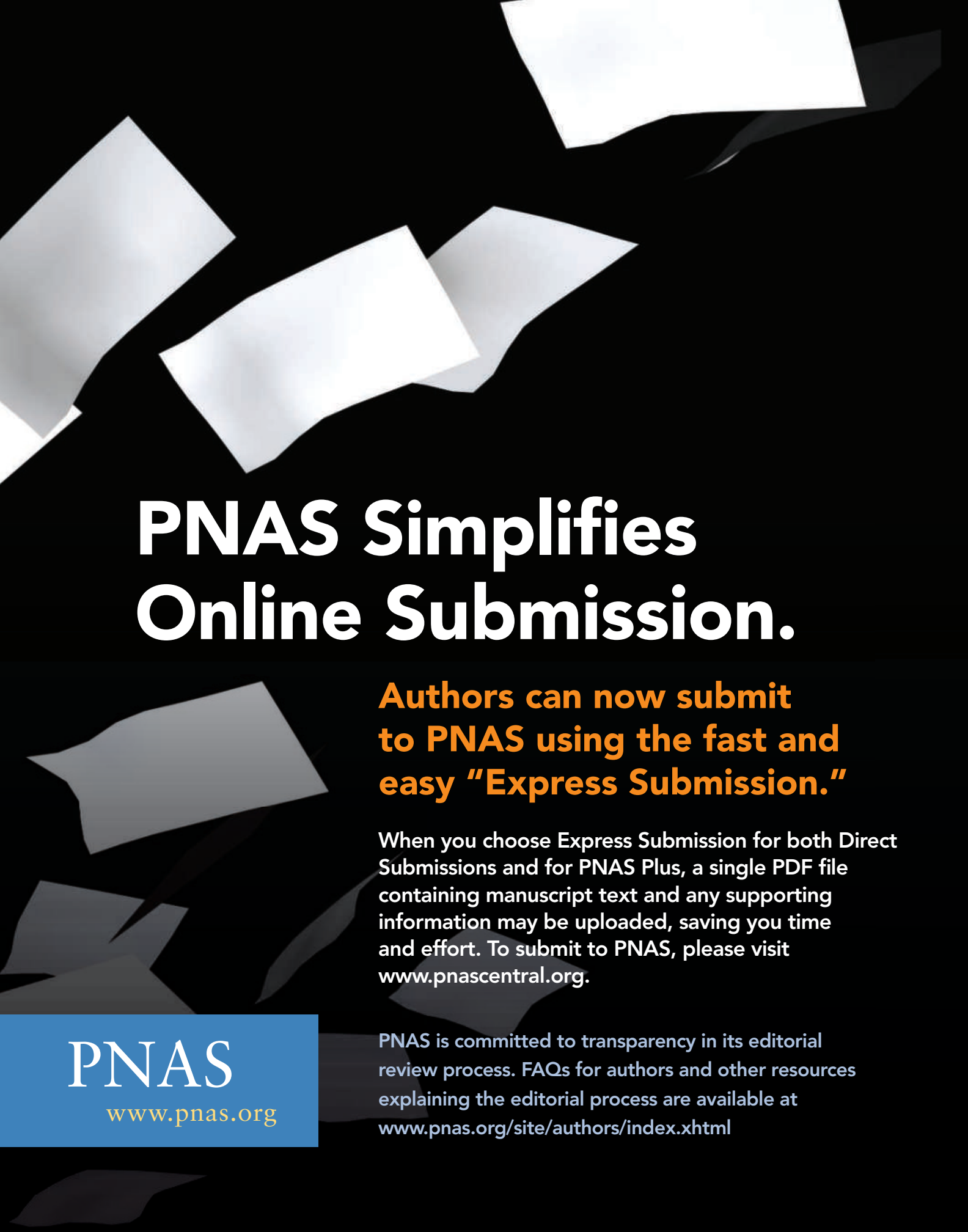
ACKNOWLEDGMENTS

We thank R. Reyes-Lamothé, U. Alon, J.-Y. Bouet, A. Kapanidis, C. Lesterlin, A. Upton, and P. Zawadzki for reagents and discussions. We thank C. Saenz and the Microfluidics Core Facility at Harvard Medical School. Microscopy at Micron Oxford was supported by a Wellcome Trust Strategic Award (091911) and Medical Research Council grant (MR/K01577X/1). S.U. is funded by a Sir Henry Wellcome Fellowship by the Wellcome Trust and a Junior Research Fellowship at St John's College, Oxford. J.P., N.D.L., L.P.-T., and B.O. are funded by NIH grant GM095784. L.P.-T. acknowledges fellowship support from the Natural Sciences and Engineering Research Council of Canada (NSERC) and the Fonds de recherche du Québec-Nature et technologies. D.J.S. is funded by a Wellcome Trust Investigator Award (099204/Z/12Z). The primary data described in the manuscript is available upon request. Author contributions: S.U. conceived the study, generated cell strains, and designed and performed experiments and analysis. S.U., D.J.S., and J.P. interpreted the data. N.L. and L.P.-T. developed the microfluidic imaging methods. B.O. developed the single-molecule counting method. S.U., D.J.S., and J.P. wrote the manuscript. The authors declare competing financial interests. A U.S. Patent Application 20150247790 entitled "Microfluidic assisted cell screening" was filed on behalf of B.O., J.P., and co-workers by the President and Fellows of Harvard College.

SUPPLEMENTARY MATERIALS

www.sciencemag.org/content/351/6277/1094/suppl/DC1
Materials and Methods
Figs. S1 to S15
Table S1
Movies S1 and S2
References (27–35)

8 July 2015; accepted 5 February 2016
10.1126/science.aac9786



PNAS Simplifies Online Submission.

**Authors can now submit
to PNAS using the fast and
easy "Express Submission."**

When you choose Express Submission for both Direct Submissions and for PNAS Plus, a single PDF file containing manuscript text and any supporting information may be uploaded, saving you time and effort. To submit to PNAS, please visit www.pnascentral.org.

PNAS
www.pnas.org

PNAS is committed to transparency in its editorial review process. FAQs for authors and other resources explaining the editorial process are available at www.pnas.org/site/authors/index.xhtml

Open Minds



The American Association for the Advancement of Science (AAAS) is the world's most trusted resource for science across disciplines and a leader in empowering scientific information in the public sphere.

By joining, you are bridging a gap between science and society. You are strengthening an organization that develops evidence-based policy making, enhances science education, and communicates unbiased science to the public. Your member benefits include:

- 51 weekly issues of *Science*, the leading journal of original science research
- Career resources and networking opportunities
- Member-only webinars, videos, blogs, online courses, podcasts, and more
- Advocacy, community outreach, and volunteer opportunities
- Timely science and technology news
- Access to research dating back to 1880
- Discounts on journals, meetings, products, and services



Visit www.aaas.org/join. Together, we can make a difference.



AAAS 2017 ANNUAL MEETING

FEBRUARY 16-20 • BOSTON

SERVING SOCIETY THROUGH SCIENCE POLICY

To make decisions, societies rely on knowledge and multiple perspectives. Policies both within and outside science should be informed by the best available evidence. Science alone cannot translate knowledge into viable policy options; other factors include societal norms and cultural values.

One aspect of science policy is advancing the practice of science: How do we continually improve scientific methods, mechanisms, and outputs to increase the value of science to society?

Another aspect of science policy is providing the best available scientific evidence to policymakers, community leaders, and citizens. How can we most effectively provide scientific evidence that informs policy? What are the roles for scientists as individuals and for the scientific enterprise as a whole in the policy landscape? What emerging and established areas of science are essential to future policy decisions?

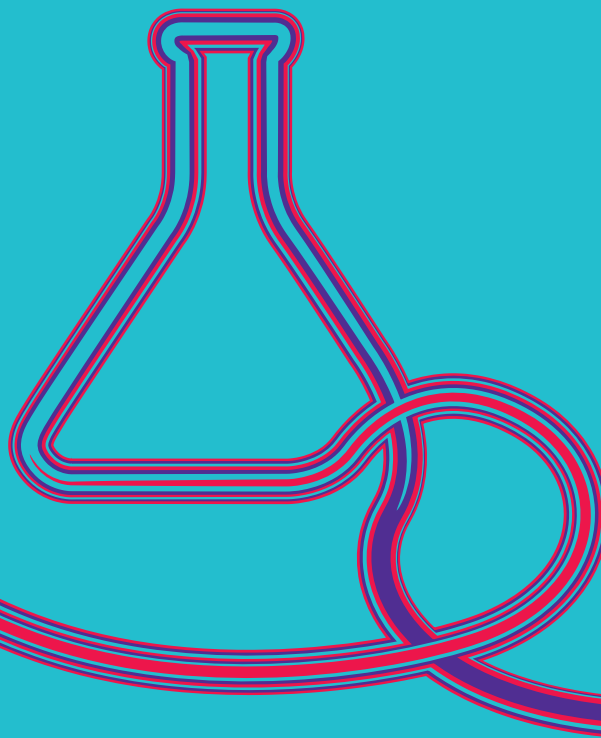
Call for Session Proposals

Session proposals for the 2017 AAAS Annual Meeting are now being solicited. To submit a proposal, visit aaas.org/meetings. The deadline for submission is **April 22, 2016**.

aaas.org/meetings

CHEMISTRY EXPERTISE

EMD MILLIPORE + SIGMA-ALDRICH
have joined forces to simplify your world
– so you can focus with confidence on
tackling life science's biggest challenges.



MilliporeSigma now offers an expanded global network that extends across more than 66 countries, a world-class e-commerce platform that simplifies transactions, and a combined portfolio that has grown to include over 300,000 products – from Catalytic Screening to Chromatography and more.

Visit us at
ACS Spring Booth #919
March 13-17, San Diego CA

Learn more at
sigma-aldrich.com/acs

**MilliporeSigma is a
business of Merck KGaA,
Darmstadt, Germany**



**Biotech
AND The Law**
2016 Global Conference
*Connecting Science, Law,
and Opportunity*


May 5-7, 2016
Monona Terrace
Convention Center
Madison, Wisconsin

REGISTER NOW

Visit biotechandthelaw.org

 **PINNACLE**



DF-SCOPE™
Multiphoton
Imaging
For Your
Olympus
BX51WI
Microscope

NEW

The DF-Scope™ is a customer-inspired, multiphoton, imaging package that provides the necessary optics and electronics for the BX51WI to be used for multiphoton imaging (with the addition of a Ti:Sapphire laser). The design incorporates subassemblies from our MOM® (Movable Objective Microscope®) system including resonant and galvo scan boxes and controllers, detector paths, PMTs, PMT power supplies, scan lenses and tube lenses.

FEATURES

- Includes detector(s) and "whisper-quiet" resonant scan box.
- Upper and lower photodetectors for increased collection efficiency.
- Fully compatible with the Sutter MPC-78 Large Moving Stage.
- Designed to be controlled with the Sutter MCS Imaging Software and MScan 2.0.
- Fully compatible with most multiphoton freeware (ScanImage 5.0, Helioscan, and MPScope).
- Breadboard format in scan pathway allows easy addition of photomanipulation light sources to the main scanned laser path.

SUTTER INSTRUMENT

PHONE: 415.883.0128 | FAX: 415.883.0572
EMAIL: INFO@SUTTER.COM | WWW.SUTTER.COM

Cambridge Healthtech Institute's Fifteenth Annual

Bio-IT World

CONFERENCE & EXPO '16

APRIL 5 - 7, 2016 | Seaport World Trade Center | Boston, MA

**REGISTER EARLY FOR
MAXIMUM SAVINGS!**

MENTION KEYCODE 1620L35

*Building a global network
for precision medicine by
uniting the Bio-IT community*

CONFERENCE TRACKS

- | | |
|--|---|
| 1 Data & Storage Management | 8 Data Visualization & Exploration Tools |
| 2 Data Computing | 9 Pharmaceutical R&D Informatics |
| 3 Software Applications & Services | 10 Clinical Genomics |
| 4 Cloud Computing | 11 Open Source Innovations |
| 5 Bioinformatics | 12 Cancer Informatics |
| 6 Next-Gen Sequencing Informatics | 13 Data Security |
| 7 Clinical Research & Translational Informatics | |

PLENARY KEYNOTE SPEAKERS



Howard Jacob, Ph.D.

Executive Vice President for Medical Genomics and
Chief Medical Genomics Officer, HudsonAlpha



Heidi L. Rehm, Ph.D., FACMG,

Chief Laboratory Director, Laboratory for Molecular Medicine,
Partners Healthcare Personalized Medicine; Clinical Director,
Broad Institute Clinical Research Sequencing Platform; Associate
Professor of Pathology, Brigham & Women's Hospital and Harvard Medical School



Yaron Turpaz, Ph.D., MBA

Chief Information Officer,
Human Longevity, Inc.

Enabling Technology. Leveraging Data. Transforming Medicine.

Bio-ITWorldExpo.com

advantage New Promotion March 1 – June 30, 2016



Macro-offers for Microbiologists

Premium solutions for your microbiological processes – now save up to 25 %!

Our new Eppendorf Advantage™ special offers include Eppendorf premium products ideally suited for the most important steps of your microbiology workflow.

> Buy a Mastercycler® nexus gradient PCR cycler and save 25 %

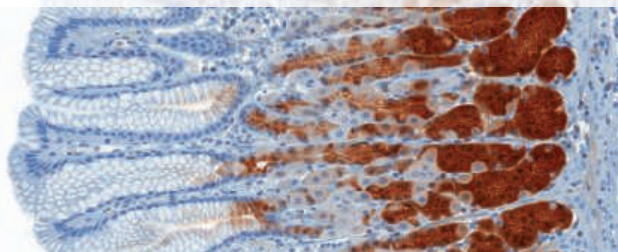
> Purchase any Eppendorf Xplorer® or Xplorer plus electronic pipette with 20 % off

> Save 20 % on the epMotion® 96

> Get the Eppendorf HeatSealer S100 with 20 % savings

www.eppendorf.com/advantage

Eppendorf®, the Eppendorf logo, epMotion®, Eppendorf Xplorer®, and Mastercycler® are registered trademarks of Eppendorf AG, Hamburg, Germany. Eppendorf Advantage™ is a trademark of Eppendorf AG, Hamburg, Germany. U.S. Design Patents are listed on www.eppendorf.com/ip. Offers may vary by country. All rights reserved, including graphics and images. Copyright © 2016 by Eppendorf AG.



Immunohistochemistry for the 21st Century

Immunohistochemistry (IHC) dates back decades, but that doesn't mean it's stagnant. Automated sample processors, digital slide scanners, image analysis software, and more have given the aged procedure a decidedly 21st century flair.

See the full story on page 1098.

Upcoming Features

General Lab Equipment—April 29

Microscopy—May 13

Exosomes/Microvesicles—June 10

Produced by the Science/AAAS Custom Publishing Office

AAAS Travels

In Search of

AMELIA EARHART

Explore one of the greatest mysteries of all time!

On the 80th Anniversary of
Amelia's World Flight & Disappearance!

June 21–July 11, 2017



On July 2, 1937, Amelia Earhart and her navigator Fred Noonan went missing on one of the last legs of their round the world flight after they departed

New Guinea for Howland Island. Our colleagues at the International Group for Historic Aircraft Recovery (TIGHAR), believe they turned their Electra south and landed at Nikumaroro Island. On board the *Reef Endeavour*, we'll sail north from Fiji for 1,000 miles, stopping at Rotuma Island en route to Niku. We will join TIGHAR scientists in their research at Niku and look for artifacts which may indicate Amelia and Fred did land there! From \$8,995 + air.

For a detailed brochure, call (800) 252-4910

All prices are per person twin share + air



BETCHART EXPEDITIONS Inc.

17050 Montebello Rd, Cupertino, CA 95014

Email: AAASInfo@betchartexpeditions.com

www.betchartexpeditions.com

myIDP:

A career plan customized for you, by you.



For your career in science, there's only one **Science**



Recommended by
leading professional
societies and the NIH

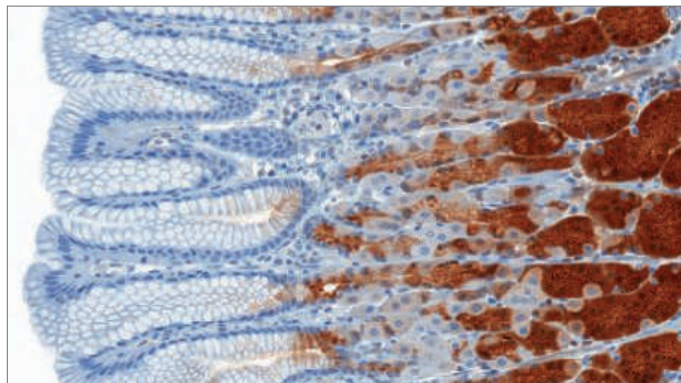
Features in myIDP include:

- Exercises to help you examine your skills, interests, and values
- A list of 20 scientific career paths with a prediction of which ones best fit your skills and interests
- A tool for setting strategic goals for the coming year, with optional reminders to keep you on track
- Articles and resources to guide you through the process
- Options to save materials online and print them for further review and discussion
- Ability to select which portion of your IDP you wish to share with advisors, mentors, or others
- A certificate of completion for users that finish myIDP.

Visit the website and start planning today!
myIDP.sciencecareers.org

Science Careers In partnership with:





Immunohistochemistry for the 21st Century

Immunohistochemistry (IHC) dates back decades, but that doesn't mean it's stagnant. Automated sample processors, digital slide scanners, image analysis software, and more have given the aged procedure a decidedly 21st century flair. **By Jeffrey M. Perkel**

Immunohistochemistry is all about spatial relationships. If researchers want to know whether or not a given piece of tissue expresses a particular protein, they can use mass spectrometry or Western blotting. But to determine where in the tissue that protein is found, they have to visualize it in its cellular context.

That's where IHC comes in. Employing antibodies as probes for specific antigens, the method produces images of thin slivers of tissue—a tumor biopsy, for example—stained to display the expression and spatial distribution of one or more proteins.

"It answers the fundamental question of localization, of where you're going to find a particular target antigen," says Kevin Long, senior manager of the technical and scientific content development team at **MilliporeSigma** (a life science business of Merck KGaA in Darmstadt, Germany).

Spatial data can be used by researchers, for instance, to track lymphocyte infiltration at a site of disease; clinicians can use the data to grade tumors or assess a patient's likely response to a therapy.

The IHC laboratory at the **Naval Medical Center San Diego** (NMCS) sees some 18,000 surgical cases a year, according to Director Greg Gates. Each yields anywhere from 2 to over 100 slides, depending on the size of the sample and the complexity of the case, but on average, Gates says, each case generates about 4 slides apiece—some 72,000 slides in all. Most pathology slides don't require IHC; about 80% of cases can be diagnosed from histologic staining (such as hematoxylin and eosin) alone, estimates Andreas Hoel, director of marketing for IHC at **Agilent Technologies**. But the remainder require more extensive evaluation.

Requiring from four to eight hours, the process is tedious but not complicated; starting with tissue on a microscope slide, the general process includes antigen retrieval, incubation with primary and secondary antibodies, washing, and development with a chromogenic reagent. The data are then interpreted using a light microscope.

"The best way I can describe IHC is, it's so easy a high school student can do it," says Stephen Hewitt, head of the Experimental Pathology Laboratory at the **National Institutes of Health** and editor-in-chief of the *Journal of Histochemistry and Cytochemistry*.

The problem is, each of these steps can be tweaked, and there is no one "standard" IHC protocol. As in many areas of biology, researchers don't always document their methods in sufficient detail for others to replicate them. And in any event, the resulting images are typically read by eye, an inherently subjective approach. As a result, variability from day to day and lab to lab can be considerable. But researchers have developed strategies for locking down that variability and improving other IHC pain points as well.

Automated sample preparation

One approach to decreasing IHC variability is using automation—employing systems that will treat every slide precisely the same, while at the same time freeing technicians and pathologists to tend to other tasks. "What we talk about as two pillars we improve on are laboratory efficiency and diagnostic accuracy," says Hoel, whose Dako Omnis system, for instance, automates both IHC and fluorescence in situ hybridization (FISH) staining.

The NMCS pathology lab has purchased systems to automate two stages of the IHC process, says Gates: Sample processing systems from **Polaris** and **Leica** dehydrate and rehydrate the fixed specimens, while a **BenchMark Ventana** system from **Roche** automates the IHC staining itself.

For those with considerably lighter workloads—up to about 100 assays a week—the **SNAP i.d. 2.0** IHC system from **MilliporeSigma** provides a vacuum manifold to increase the efficiency and reproducibility of manual slide staining, says Long. Researchers can process up to 24 slides simultaneously as reagents are removed from all slides at once via vacuum suction, he says.

Automation, says Hewitt, offers incontrovertible benefits—for clinical laboratories. But he notes that most academics engaged in basic research have little need for such power. After all, automation is just another word for robotics, he explains. "If you're just an investigator who needs to do a few experiments for your study, either find a good collaborator, or do it by hand."

Digital pathology

Another transformative development in IHC is the advent of so-called digital pathology. Instead of viewing and analyzing IHC slides under a microscope, digital pathology systems scan the stained slides in their entirety, storing the resulting whole-slide images in a digital format that can then be viewed and manipulated on a computer.

Upcoming Features

General Lab Equipment—April 29 ■ Microscopy—May 13 ■ Exosomes/Microvesicles—June 10



That approach offers several benefits, says Catherine Conway, senior product manager for image analysis and pathology imaging at **Leica Biosystems**, which sells both brightfield- and fluorescence-based slide scanners under the Aperio brand. For one thing, whole-slide imaging facilitates medical education by ensuring that students have access to interesting and rare cases they might not otherwise see when sharing physical slides. But it also simplifies the process of sharing data with remote colleagues and obtaining second opinions—a process called “telepathology.”

The **University of Pittsburgh Medical Center (UPMC)**, for instance, offers a web portal through which distant researchers can upload slides for evaluation by the hospital’s pathologists for between \$50 and \$150 per slide. Anthony Demetris, the Starzl Professor of Liver and Transplant Pathology at UPMC, who coauthored a 2012 study documenting the university’s experience with telepathology, says he has evaluated samples from as far away as Australia and Asia. “It makes the interaction much more fluid than it would be otherwise.”

In one case, Demetris remotely evaluated a liver biopsy of an elderly patient that the primary physician suspected was simply inflammation. Demetris’ review of the data suggested a tumor, so he asked the on-site physician to perform and upload some follow-up stains for T and B lymphocytes and Epstein-Barr virus (EBV) nucleic acids. In just a few days, he says, the proper diagnosis emerged: EBV-related lymphoma.

Whole-slide imaging also simplifies sample storage and retrieval by providing an easily accessible record of the slide (as opposed to physical slides), and it facilitates data analysis and subsequent reanalysis. “You can go back again and again to the same image and ask different questions,” Demetris says. “It actually becomes a reusable data resource.”

In addition to Leica, slide scanners are available from **Hamamatsu, Olympus, Philips, Roche, and Zeiss**, among others. But because each system uses a proprietary image format, researchers are generally restricted in what they can do with the images, especially if they have scanners from multiple vendors.

Mahadev Satyanarayanan (“Satya”), the Carnegie Group Professor of Computer Science at **Carnegie Mellon University** in Pittsburgh, Pennsylvania has had firsthand experience with that problem. Several years ago, Satya was working with pathologists to translate an image search algorithm he had developed to analyze digital slide images. He very quickly hit a wall—there was no way to search across different image formats. “The only software around that could interpret those formats was proprietary software,” he says.

So, Satya’s team worked out the details of the different file formats, codifying that knowledge in OpenSlide, an open-source C programming library. OpenSlide, he explains, functions like a computer printer driver, freeing programmers from needing to understand how a given scanner works. “You just say ‘print,’ and it’s assumed that the device driver underneath will provide the appropriate translation to the specific idiosyncrasies of that printer.” Similarly, programmers using OpenSlide can simply direct the software to read a file without having to know how it is actually structured.



Digital pathology systems scan the stained slides in their entirety, storing the resulting whole-slide images in a digital format that can then be viewed and manipulated on a computer.

Researchers have used Open Slide to build other applications as well, such as telepathology portals and an educational resource called “SlideTutor.” For his part, Satya has used it to implement his own search tool, called “Diamond,” with which pathologists can ask such questions as, “Among all patients seen at this hospital between this date and this date who were taking this medication, do you see any [patients] where the following properties are similar to what I see in the slide?” OpenSlide, he says, “greatly increases the number of degrees of freedom you have as a designer.”

Image analysis

Another benefit of digital pathology is the ability to perform sophisticated image analyses. Given a whole-slide image, these software packages identify cells and sub-cellular compartments (usually the cytoplasm, nucleus, and cell membrane), outputting such values as cell counts and staining intensity.

The Halo software package from **Indica Labs**, for instance, includes modules for counting cells expressing one or two proteins in the nucleus or cytoplasm, counting cells positive for membrane staining, assessing in situ hybridization, and more. Researchers can even assess spatial relationships, says Indica’s chief scientific officer Kate Lillard. “For example, how many CD8-positive lymphocytes are within 50, 100, or 200 microns of the nearest tumor cells?” In one recent study, a research team led by Antoni Ribas at the University of California, Los Angeles used Halo to quantify lymphocyte subtypes within different tissue compartments in myeloma tumors. They observed a positive correlation between the presence of CD8+ cells specifically at the tumor margin with patient responses to antibodies targeting the “programmed death-1” receptor—data suggesting that it may be possible to increase the efficacy of such therapeutics by selecting the patients most likely to benefit from them.

Image analysis isn’t new, of course, says Lillard—software for analyzing photomicrographs has been available for years. “The big difference here is that we’re working on gigabyte-sized images.” As a result, the software must be specially optimized to squeeze as much power as **cont.>**

Featured Participants

Agilent Technologies
www.agilent.com

Carnegie Mellon University
www.cmu.edu

Hamamatsu Photonics
www.hamamatsu.com/jp/en/5007.html

Indica Labs
www.indicalab.com

Laboratory of Pathology, NIH
ccr.cancer.gov/laboratory-of-pathology

Leica Biosystems
www.leicabiosystems.com

MilliporeSigma
www.emdmillipore.com

Naval Medical Center San Diego
www.med.navy.mil/sites/nmcscd

Olympus Life Science Solutions
www.olympus-lifescience.com/en

Philips Healthcare
www.philips.co.uk/healthcare/solutions/pathology

University of Pittsburgh Medical Center
www.upmc.com

Ventana Medical Systems
www.ventana.com

Yale Pathology Tissue Services
medicine.yale.edu/pathology/research/tissueservices

Zeiss
www.zeiss.com

Additional Resources

CellProfiler
cellprofiler.org

OpenSlide
openslide.org

SlideTutor
slidetutor.upmc.edu

possible from a computer's hardware. In an analysis of 50 whole-slide images, for instance, total Halo processing time ranged from 21.7 hours with one CPU core to 0.9 hours (64 cores).

A number of companies sell such tools, including Definenes (recently acquired by MedImmune), PerkinElmer, and Visiopharm. Alternatively, Anne Carpenter of the Broad Institute of the Massachusetts Institute of Technology (MIT) and Harvard has developed CellProfiler and CellProfiler Analyst, a pair of open-source software packages that accomplish many of the same tasks.

In theory, such tools could make life simpler in the clinic, for instance, by quickly flagging and counting cells and regions of interest. However, says Lillard, image analysis tools are used mainly in research and drug development rather than clinical laboratories, a result of regulatory obstacles. But that could change, she says. At the moment, researchers are using Halo and related software to identify interesting biomarkers that correlate with drug response or survival. But to be of use, they will have to translate those discoveries from bench to bedside. "The hope is that those will eventually transition into the clinic."

Quantitative immunofluorescence

Thanks to digital pathology and image analysis software, pathologists can score staining intensity not in relatively crude bins (0, 1+, 2+, 3+) as is done today, but as a contin-

uous variable (say, 0–1000)—a change that should allow researchers to identify more subtle biomarkers.

Yet according to David Rimm, professor of pathology at Yale University and director of **Yale Pathology Tissue Services**, the traditional method of IHC isn't really compatible with continuous variables, and thus isn't truly quantitative. IHC, he says, "is not linear and it's not reproducible."

In traditional IHC, he explains, a secondary antibody conjugated to horseradish peroxidase converts a chromogenic substrate into a dark brown or red precipitate. But as light cannot easily penetrate that material—what Rimm calls "mud"—the method is at best semiquantitative.

Rimm's alternative is to use a fluorogenic substrate instead, a strategy called "quantitative immunofluorescence" (QIF). With such a strategy, small changes in protein abundance lead to comparable changes in light output, and coupled with whole-slide scanning and digital image analysis, that technique can provide a powerful platform for IHC analysis.

Breast cancer biopsies, for instance, are commonly tested for human epidermal growth factor receptor 2 (HER2) expression to determine whether the HER2-targeting drug Herceptin is likely to be effective. Herceptin binds the protein's extracellular domain, yet most of the antibodies used for HER2 IHC in the clinic target the protein's intracellular domain, notes Rimm.

In 2014 and 2015, Rimm and his team used QIF to assess whether they could detect a difference in staining with antibodies targeting the HER2 intra- or extracellular domains. As it turns out, they could. Using the chromogenic substrate 3,3'-diaminobenzidine and IHC, other teams found no observable difference between patients when using the cytoplasmic domain antibody and the extracellular domain antibody—staining intensity with both antibodies was identical. But using QIF, differences emerged. "About 10% to 20% of the patients' HER2 protein does not have any extracellular domain," he says. "So they're not likely to benefit from trastuzumab [Herceptin]."

Such seemingly minor fluctuations could make the difference between a successful drug and a failure, says Rimm. Referring to the staining categories used today, he says, "Science isn't ordinal"—it's continuous. And it's possible that the value of many potential biomarkers will only become apparent when using finer shades of intensity.

"Who knows how many other markers are out there that ultimately failed because there was not acceptance of the methods required to measure them quantitatively, and you needed to be above a certain level before the drug was effective?" asks Rimm.

That's not to say every histopathologist needs to switch to QIF and digital scanning. "Most of what pathologists do for IHC is, by design, nonquantitative," says Rimm. "It's 'fit-for-purpose.'" Indeed, IHC has been fit-for-purpose for over 70 years, with no apparent end in sight.

Jeffrey M. Perkel is a freelance science writer based in Pocatello, Idaho.

DOI: 10.1126/science.opms.p1600103



Stem Cell Counting Technology

Since the beginnings of mammalian tissue stem cell biology, counting has been the bane of both basic research and clinical stem cell studies. Biomarkers, such as CD34 and CD133, do not identify tissue stem cells with sufficient specificity for counting them. Asymmetrex's AlphaSTEM technology, developed with AlphaSTAR Corporation, provides precise determinations of the number, viability, and self-renewal pattern (asymmetric versus symmetric) of stem cells in complex tissue cell preparations, including both research and medical specimens. AlphaSTEM technology uses computer simulation to extract tissue stem cell properties from specially prescribed serial culture data. The AlphaSTEM tissue stem cell counting technology has many exciting applications, including determining the number of stem cells in experimental samples, determining the stem cell dose for transplantation treatments, identifying agents that can improve the vitality of transplanted tissue stem cells, and identifying agents that are toxic to tissue stem cells.

Asymmetrex

For info: 617-990-6819
www.asymmetrex.com

Cancer Stem Cell Identification Kit

The new AldeRed ALDH Detection Kit is designed for identifying and isolating cancer stem cells. The AldeRed reagent is used to label cancer stem cells with a red fluorescent dye, making it possible to distinguish cancer stem cells in live cell populations where specific identification was previously impossible. Aldehyde dehydrogenase (ALDH), a cancer stem cell marker enzyme, causes the AldeRed reagent to fluoresce in the far-red spectrum, allowing the cancer cells to be identified and isolated with concurrent use of green fluorescent cell lines, transgenic animals, and reporter assays. Previous ALDH reporters exhibited green fluorescence, which made it difficult to identify positive cells in an otherwise green fluorescent background.

EMD Millipore

For info: 800-645-5476
www.emdmillipore.com/stemcells



Pathology Imaging System

The Vectra 3 is an automated, high-throughput quantitative pathology imaging system. The system's new seven-color multiplexing and visualization capabilities are designed to enable pathologists and oncologists conducting research to gain a deeper level of understanding of disease mechanisms related to new cancer immunotherapy approaches. The system visualizes, analyzes, quantifies, and phenotypes immune cells in situ in formalin-fixed paraffin-embedded (FFPE) tissue sections. It incorporates 10x whole slide imaging and the Phenochart whole slide viewer, allowing researchers to annotate and navigate slides with interactive interfaces to better identify regions of interest for detailed multispectral acquisition. The multiplexing capability enables identification and quantification of multiple biomarkers and reveals spatial context within a digital workflow to assist researchers with better, faster decisions. Combined with PerkinElmer's inForm image analysis software, which automatically identifies and quantifies cell populations in tissue, the Vectra 3 system provides researchers the power of multiplexed biomarker imaging and quantitative analysis within a familiar digital workflow.

PerkinElmer

For info: 877-754-6973
www.perkinelmer.com

Monoclonal Antibody

A new immunohistochemistry (IHC)-approved, human-specific, VISTA rabbit monoclonal antibody (mAb) is now available for use in biomedical research. VISTA (V-domain Ig suppressor of T-cell activation, C10orf54, GI24, SISP1) is a negative checkpoint control protein that regulates T-cell activation and immune response. Its role in negative checkpoint control has made it an important target in the field of tumor immunology, a field that seeks to develop better therapeutic options by dismantling the mechanisms tumors use to generate and thrive in their own immunosuppressive microenvironments. VISTA (D1L2G) XP Rabbit mAb #64953 is validated using Cell Signaling Technology's rigorous standards, to recognize human VISTA in IHC and Western blot research applications.

Cell Signaling Technology

For info: 877-616-2355
www.cellsignaling.com

ChIP-Validated Antibodies

A new range of chromatin immunoprecipitation (ChIP)-validated antibodies are now available. The use of high-quality and specific ChIP-validated antibodies is essential for the success of a ChIP assay. The antibody must recognize and bind to native protein that is bound to DNA. Antibodies from other applications do not always work well in ChIP. These top-quality validated antibodies will give our customers confidence in their protocols and their results, safe in the knowledge that a ChIP-validated antibody was at the heart of their assay. Chromatrap currently offers a range of ChIP kits for quantitative polymerase chain reaction (qPCR) or sequencing and has now launched the first nine antibodies in its validated antibody program, which are H3, RNA pol II (S), RNA pol II (S5), H3K9me3, 5mC, AcH3, AcH4, AR, and Sin3a. Chromatrap validated antibodies are available in 100- μ L aliquots at a concentration of 1 mg/ml, delivered overnight.

Chromatrap

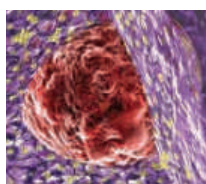
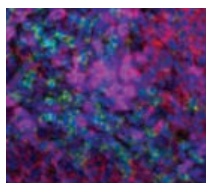
For info: +44-1978-666222
www.chromatrap.com

Electronically submit your new product description or product literature information! Go to www.sciencemag.org/about/new-products-section for more information.

Newly offered instrumentation, apparatus, and laboratory materials of interest to researchers in all disciplines in academic, industrial, and governmental organizations are featured in this space. Emphasis is given to purpose, chief characteristics, and availability of products and materials. Endorsement by *Science* or AAAS of any products or materials mentioned is not implied. Additional information may be obtained from the manufacturer or supplier.

want new technologies?

antibodies
apoptosis
biomarkers
cancer
cytometry
data
diseases
DNA
epigenetics
genomics
immunotherapies
medicine
microbiomics
microfluidics
microscopy
neuroscience
proteomics
sequencing
toxicology
transcriptomics



watch our **webinars**

Learn about the latest breakthroughs, new technologies, and ground-breaking research in a variety of fields. Our expert speakers explain their quality research to you and answer questions submitted by live viewers.

VIEW NOW!

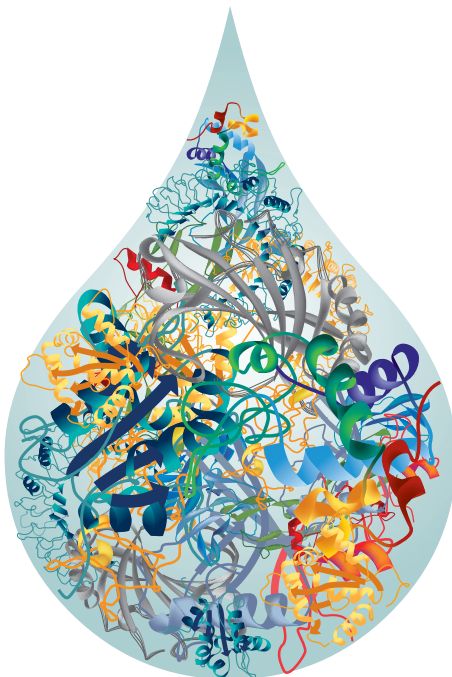
webinar.sciencemag.org

Science
AAAS

Brought to you by the *Science*/AAAS
Custom Publishing Office



@SciMagWebinars



What's in Your Sample?
Find Your Answers!



[rndsystems.com/
Immunoassays](https://rndsystems.com/Immunoassays)



There's only one **Science**

Science Careers Advertising

For full advertising details, go to ScienceCareers.org and click For Employers, or call one of our representatives.

Tracy Holmes

Worldwide Associate Director
Science Careers
Phone: +44 (0) 1223 326525

THE AMERICAS

E-mail: advertise@sciencecareers.org

Fax: +1 (202) 289 6742

Tina Burks

Phone: +1 (202) 326 6577

Nancy Toema

Phone: +1 (202) 326 6578

Online Job Posting Questions

Phone: +1 (202) 312 6375

EUROPE / INDIA / AUSTRALIA / NEW ZEALAND / REST OF WORLD

E-mail: ads@science-int.co.uk

Fax: +44 (0) 1223 326532

Sarah Lelarge

Phone: +44 (0) 1223 326527

Kelly Grace

Phone: +44 (0) 1223 326528

Online Job Posting Questions

Phone: +44 (0) 1223 326528

JAPAN

Katsuyoshi Fukamizu (Tokyo)

E-mail: kfukamizu@aaaas.org

Phone: +81 3 3219 5777

Hiroyuki Mashiki (Kyoto)

E-mail: hmashiki@aaaas.org

Phone: +81 75 823 1109

CHINA / KOREA / SINGAPORE / TAIWAN / THAILAND

Ruolei Wu

Phone: +86 186 0082 9345

E-mail: rwu@aaaas.org

All ads submitted for publication must comply with applicable U.S. and non-U.S. laws. Science reserves the right to refuse any advertisement at its sole discretion for any reason, including without limitation for offensive language or inappropriate content, and all advertising is subject to publisher approval. Science encourages our readers to alert us to any ads that they feel may be discriminatory or offensive.

Science Careers

FROM THE JOURNAL SCIENCE AAAS

ScienceCareers.org



University
of Glasgow

College of Medical, Veterinary and Life Sciences
Research Institute of Infection, Immunity and Inflammation
(Centre for Virus Research)

Professor – Chair in Infectious Diseases (Virology)

Ref: M00659

The MRC-University of Glasgow Centre for Virus Research (CVR) is a distinctive international research centre with a critical mass of researchers dedicated to the multidisciplinary study of human and animal viruses. We are seeking a distinguished researcher to establish a programme in the general area of emerging viruses complementing the existing strengths of the CVR, either in basic, clinical or translational research. Research programmes focused on any aspect of emerging virus infections, including virus genomics, evolution and virus-host interactions are welcome. The appointee will have a distinguished track record of research achievement, an international reputation and a demonstrated ability to attract national and international funding. They will take on a research leadership role within and beyond the CVR.

The CVR has a collegiate and collaborative environment and it is well positioned to offer an attractive start-up package and resources.

For further information, please visit www.cvr.ac.uk and www.facebook.com/centreforvirusresearch. Informal enquiries should be directed to Prof Massimo Palmarini (massimo.palmarini@glasgow.ac.uk). For further details and to submit an electronic application online visit: www.gla.ac.uk/about/jobs/

Closing date 31 March 2016

The University has been awarded the Athena SWAN Institutional Bronze Award.

The University is committed to equality of opportunity in employment.

The University of Glasgow, charity number SC004401.



www.glasgow.ac.uk

JOB FOCUS: CHEMISTRY

PRINCETON UNIVERSITY DEPARTMENT OF CHEMISTRY

The Princeton University Department of Chemistry seeks two postdoctoral research associates for ultrafast laser experimental positions in the group of Professor Herschel Rabitz. The first research position involves ultrafast laser control in biology of multiple optogenetic switches and fluorescent protein sensors *in vitro* and *in vivo*. The second position concerns exploring the systematics of laser control of chemical reactions. Applicants with experience in ultrafast lasers and ideally quantum control are particularly encouraged to apply. Applications must be submitted electronically to website: <https://jobs.princeton.edu> (Requisition No. 1600157) and submit Curriculum Vitae, list of publications, and contact information for three references. Ph.D. required. These positions are subject to the University's background check policy.

Princeton University is an Equal Opportunity Employer and all qualified applicants will receive consideration for employment without regard to race, color, religion, sex, sexual orientation, gender identity, national origin, disability status, protected veteran status, or any other characteristic protected by law.

Download the Science Careers Job App

SEARCH JOBS
ON THE GO!

apps.sciencemag.org



POSITIONS OPEN

**BELL MUSEUM
OF NATURAL HISTORY**
UNIVERSITY OF MINNESOTA
Driven to Discover™

The University of Minnesota is seeking an **Executive Director** who will oversee the Bell Museum of Natural History and Planetarium's (BMNHP) mission through its personnel, research/programs and facilities. The BMNHP mission is to ignite curiosity and wonder, explore our connections to nature and the universe, and create a better future for our evolving world. For more information about this position and to apply, go to the University of Minnesota employment website and search for **requisition #307546**.



Regulatory Pharmaceutical Analysis Program OFFICE OF REGULATORY AFFAIRS (ORA)

The FDA's Office of Regulatory Affairs is seeking Ph.D. level scientists with advanced experience in chemical analysis of complex pharmaceutical products to work at one of Office of Regulatory Affairs field laboratories located in Jamaica, New York or Irvine, California. Candidates must have expertise either in mass spectrometry or NMR spectroscopy. Salary range: \$75,000 - \$120,000 per year and will be commensurate with experience. Interested persons can send curriculum vitae or resume to email: ORSJOBSEARCH@fda.hhs.gov Attention: Gail Tarry.

MY WORK IS A STORY OF SUSTAINABILITY.

I help save the environment. I'm part of a group that works to improve processes for our customers, including replacing hazardous chemicals with more environmentally friendly alternatives. It's rewarding to be part of a team that's having a real impact by promoting smarter, safer chemistries.

Our innovations have even earned Thermo Fisher Scientific the Environmental Protection Agency's Presidential Green Chemistry Challenge Award. With the largest R&D budget in the industry, we are fully committed to promoting innovative thinking and pursuing a sustainable future.

Matt
Scientist

When you're ready for sustainable success in your career, you'll discover that, at Thermo Fisher Scientific, each one of our 50,000 extraordinary minds has a unique story to tell. And we all contribute to a singular mission—enabling our customers to make the world healthier, cleaner and safer.

What story will you tell?



Explore our opportunities at
jobs.thermofisher.com and join our team.

ThermoFisher
SCIENTIFIC

Thermo Fisher Scientific is an Equal Employment
Opportunity/ Affirmative Action employer and a
VEVRAA Federal Contractor.

IN SEARCH OF REMARKABLE SCIENTISTS

Molecular Technologist, Houston, Texas

Do you have a PhD in microbiology or biochemistry with a strong desire to change the world to biofuels? Then we'd like you to help us pilot an exciting new project.

Joining our in-house microbial biofuels team, you'll be working with transformable host organisms to efficiently produce different biofuel components at both lab and pilot scale. You'll need experience in one or more of the following areas: metabolic pathway improvement via transformation, microbial/pathway evolution, transformation of non-standard hosts, solid or liquid fermentation (batch or continuous flow at pilot scale).

Find out more and apply online at www.shell.com/careers. In the "Students and Graduates" section, click on "Shell Recruitment Day" and then create an account. When entering your contact details, select "Other" in response to "Where you found out about this Shell opportunity," click "Next" and then type in "Biofuels."

DISCOVER WHAT YOU CAN ACHIEVE AT SHELL



Minority, Female, Disabled and Veteran EEO/AA Employer.

Advance
your career
with expert
advice from
Science
Careers.



Download Free Career
Advice Booklets!

ScienceCareers.org/booklets



ScienceCareers

FROM THE JOURNAL SCIENCE AAAS



Sandia National Laboratories is seeking a **Co-Director** for the **Center for Integrated Nanotechnology (CINT)**, who will also lead the Integrated Nanotechnologies Department.

The Integrated Nanotechnologies Department, within CINT, oversees the operations of several departments and provides oversight in the areas of Basic Energy Sciences and Materials Science.

CINT is a Department of Energy/Office of Science Nanoscale Science Research Center jointly supported by Sandia National Labs and Los Alamos National Lab, operating as a national user facility devoted to establishing nanoscale science by developing the scientific principles that govern the design, performance and integration of nanoscale materials. With sites in both Albuquerque, NM and Los Alamos, NM, CINT provides world-class facilities and expertise to the broad scientific community with the mission to support and accelerate the progress of nanoscience. Proposal-based access is offered to tools and expertise focused around CINT scientific thrust areas: nanoscale electronics, mechanics and systems, nanophotonics and optical nanomaterials, soft and biological nanomaterials, theory and simulation of nanoscale phenomena.

Job Summary: The Senior Manager will work closely with management colleagues at Los Alamos to:

- Provide leadership to ensure the success of the overall scientific and user program of CINT
- Maintain and grow strong and effective partnership between the Laboratories
- Grow the impact of CINT to the missions of DOE and the two host Laboratories
- Develop and execute CINT's scientific vision and strategy as it relates to the broader set of sponsors beyond BES
- Serve as the primary point of contact for CINT's external advisory bodies

The advancement plan for this role is excellent, as the Co-Director is expected to succeed the Director at a future point.

Apply by completing an online application at: <http://www.sandia.gov/careers>. Click on "View all jobs" and enter Job Number "652668" into the Keyword search.

GRADUATE PROGRAMS

Patent Agents *in High Demand*

The Masters in Patent Practice at **Case Western Reserve University School of Law** prepares students with an undergraduate degree in engineering, computer science, or a physical or biological degree for careers as patent agents without a 3-year JD degree!

- Merit Scholarships Available
- Salary Range of \$63,500 - \$120,700
- Rolling admissions, but June 1st application submission strongly encouraged

For more information visit or to apply visit:
law.case.edu/Academics/Degrees/Masters-in-Patent-Practice



SCHOOL OF LAW

CASE WESTERN RESERVE
UNIVERSITY

CROSS THE BOUNDARIES TO NEW HORIZONS



The Living Systems Institute (LSI) is a major new initiative by the University of Exeter (Global Top 100, *Times Higher Education World University Rankings*) designed to promote interdisciplinary research that transcends the boundaries of mathematics, engineering and the biological, medical and physical sciences. Its mission is to analyse living cells and organisms as integrated systems, with the aim of unravelling how diseases disrupt biological processes at the molecular, cellular and organismal level.

The LSI will open in autumn 2016 under the direction of eminent geneticist, Philip Ingham FRS. Our vision is to build a team of researchers who will work together across disciplines to identify new ways to diagnose, treat and cure disease in plants and animals, especially humans. Our goal is to identify common signatures of disease, irrespective of host or the precise mechanism of disease pathogenesis (i.e. whether caused by genetic changes or environmental agents).

We are now seeking to appoint ambitious investigators committed to working in this interdisciplinary manner, who will explore the basis of disease and translate

fundamental understanding into predictive capability, to secure human health and wellbeing.

A total of twenty appointments will be made at a variety of career stages, based on experience and potential. A demonstrable interest in the fundamental principles that govern how living-systems operate and how they breakdown in disease is essential, as is a commitment to working across traditional discipline boundaries. We are particularly keen to recruit investigators with expertise in mathematics, physics, chemistry or engineering, as well as in the life sciences.

Candidates for Full and Associate Professorial appointments will be leaders in their field of research as evidenced by outstanding publication and funding track records. Early career stage investigators will be considered for appointment to fixed term (five year) Fellowships with the opportunity for progression to Group Leader and a proleptic permanent appointment. All appointees will be highly innovative and collaborative with strong interdisciplinary research interests and activities that provide an excellent fit for collaboration within the LSI and beyond.

Professors in Living Systems (Ref: P00582)

Associate Professors in Living Systems (Ref: P00583)

Senior Lecturers in Living Systems (Ref: P00584)

Research Fellows in Living Systems (Ref: P00585)

The closing date for applications is 11 April 2016

Interviews are expected to take place between 31 May and 3 June 2016.

For more information go to www.exeter.ac.uk/livingsystems/recruitment

For an informal discussion about opportunities within LSI please contact:

info@exeter.ac.uk



The University of Exeter is an equal opportunity employer which is 'Positive about Disabled People'. Whilst all applicants will be judged on merit alone, we particularly welcome applications from groups currently underrepresented in the workforce.

By Elizabeth Pennisi

Making a game of science

When Ariel Marcy was 7 years old, her physician father gave her an electronic game to help her understand what he did all day. Playfully exploring the human body as a child, she says, set her on the path to where she is today: working to inspire the next generation with her own science games and beefing up her credentials by pursuing a biology Ph.D. at the University of Queensland in Brisbane, Australia. One of her creations, “Go Extinct!,” a board game in which players explore evolutionary trees, is already in a second printing. To fashion this dual career in science and game design, Marcy had to think beyond the standard routes in science training and take the initiative to make her own way.

As an undergraduate student in biology at Stanford University in Palo Alto, California, Marcy came under the wing of evolutionary biologist Elizabeth Hadly, whose outreach work made Marcy keenly aware of the value of doing more than just research. Eager to branch out from her science studies and broaden her skills, Marcy went on to take design classes and build games in a computer science course. As she was finishing her bachelor’s degree, she didn’t want to head down the expected path of graduate school. Instead, she realized that she could combine her loves of evolutionary biology and building games to become an educational game designer. While working as a human biology instructor, she made her first foray into the game world. She developed a digital game to help students master cell signaling pathways, with the aid of lots of books and advice from game designers.

At the same time, she recalls, “I was noticing that my students were having a tough time wrapping their heads around evolutionary trees.” To make the concept easier to grasp, she put her design skills and gaming experience to work. She spent hours combing through the scientific literature to develop “Go Extinct!” and took an early prototype to the Society of Vertebrate Paleontology annual meeting to get feedback from researchers. Her biology training helped with more than just the content. Both research and game development “require a lot of experimentation and testing to see what works,” Marcy explains. In addition, success in either arena “requires working with a lot of people and taking advantage of their expertise.” She also built on past experience—and missteps, a tactic learned from lab work. She only tried out her first game, “Cancer Avenger,” on student players after launching it, when it was too late to fix design flaws. So from the very



“She could combine her loves of evolutionary biology and building games.”

beginning of this new game, she teamed up with several schools to get students to test early versions.

With the design in hand, she turned to the crowdfunding site Kickstarter and raised more than \$16,000, enough to pay for an artist and print 1000 games. Eight months after the first printing, the game was sold out and she had 3000 more printed. She’s now working on a new game, “Suddenly Cute,” in which players learn how small changes early in a vertebrate’s embryonic development can lead to big differences in adults.

Even with “Go Extinct!” under her belt, she found she needed more credentials to make it in the game design world, so her pendulum swung back toward research. Now a Ph.D. student, she plans to scale back her

game design efforts, temporarily. She sees her Ph.D. as important for a long-term career in science outreach and education. “As a person advocating for science and science careers, it gives me more authority and shows more integrity for me to have actually pursued the advanced degree required for the discipline,” she says.

Her experience designing games has also helped prepare her for academic work. “I have a better understanding of what the public thinks biology is,” she says, which “will help me in communicating my research.” She’s learned that she needs to work on listening, too. “It’s really easy to come up with an idea that you are really in love with,” she says. “The most challenging part for me is listening to feedback and acting on it. But receiving criticism and feedback is a huge part of science.” ■

Elizabeth Pennisi is a senior correspondent for Science. Send your story to SciCareerEditor@aaas.org.

ILLUSTRATION: ROBERT NEUBECKER